ADDENDUM

Section 2.2.1 p51: *Application of emplacement models to the Pul Pul Rhyolite* In conclusion, I nominate progressive aggradation as the preferred model for pyroclastic flow transport, based on the convincing evidence supporting this mechanism for emplacement of the Middle Ignimbrite Member, as outlined on p53.

p 66 insert after para 1: *Effects of greenschist facies metamorphism* All samples selected for geochemical analysis exhibit good preservation of primary mineralogy, and only minor alteration associated with greenschist facies metamorphism. Feldspars are fresh to slightly sericitised. Fe-oxides are unaltered and (volcanic) quartz grains are not recrystallised. Chlorite and epidote alteration is largely restricted to mafic lithic clasts, although partial replacement of feldspars and fiamme occurs in some samples. Secondary minerals (chlorite, epidote, calcite) comprise only 0.1-10% (average 3.5%) of the recrystallised matrix. Scatter in CaO and MgO indicates these elements were mobile during alteration and metamorphism, which is consistent with chlorite-epidote alteration. Scatter of Na_2O suggests some post-alteration alkali movement, perhaps reflecting minor albitisation of feldspars. K_2O, Rb and Ba exhibit relatively coherent linear trends, indicating these elements were largely immobile, and that sericite alteration had little effect on geochemistry. All other elements exhibit reasonably coherent linear trends once the effects of xenolithic contamination are removed (see below), indicating they were largely immobile during metamorphism. It can therefore be concluded that for most elements, these patterns of variation reflect original magmatic trends.

p73 insert before Section 2.3: The compositional zonation in the ignimbrites suggests a zoned or stratified magma chamber. The existence of zoned magma bodies, in which relatively evolved, low density, cooler magma overlies a more dense mafic liquid, is well established and widely documented (e.g. Smith and Bailey 1966; Lipman 1967; Hildreth 1979, 1981; Wolff and Storey 1984; Bacon and Druitt 1988). The most widely accepted mechanism for producing this compositional stratification is convective fractionation, involving sidewall crystallisation and the rise of buoyant residual liquid to pool at the top of the closed magma chamber (McBirney 1980; Turner 1980). Theoretical studies of the fluid dynamics of magma withdrawal from stratified magma chambers have shown that compositional gradients in the eruptive products are not simply inversions of pre-eruptive gradients in magma chambers (Spera et al 1986). When a given combination of magma discharge rate, magma density contrast and kinematic viscosity is attained, magma from the lower layer can be drawn up through the upper layer, and complex mixing can occur across density stratified layers (Blake and Ivey 1986). The compositional profile of the Pul Pul Rhyolite ignimbrites can be explained in terms of this mechanism, as being a function of variations in eruption intensity during discharge of a two-layered stratified magma chamber.

The vertical composition profile of the Pul Pul Rhyolite is similar to geochemical variations that occurred during the 79 AD plinian eruption of Vesuvius (Sigurdsson et al. 1990). For the Vesuvius eruption, the initial eruptive product is a white, evolved pumice. At mid-level in the deposit there is an abrupt transition to denser grey, less evolved pumice, with the fraction of white evolved pumice increasing again in the upper levels. Sigurdsson et al. (1990) noted a correlation between the magma discharge rate and the composition of eruptive products, with maximum eruptive intensity corresponding to the largest fraction of evolved pumice. They postulated that the eruption tapped a two-layer stratified magma chamber. Evolved magma from the upper levels of the magma chamber was tapped in the early stages of eruption. At the peak of magma discharge rate, the withdrawal depth was greater than the thickness of the evolved magma layer and tapping of the less evolved magma in the lower levels of the chamber occurred. As the more evolved material was drawn up though the conduit, the silica-enriched magma at the top of the chamber would have been simultaneously displaced up towards the roof of the chamber and away from the conduit, where it remained trapped in the reservoir and untapped (Spera et al. 1986). Eventually this more evolved magma was tapped again, as eruption intensity began to wane and the interface between the two magma layers migrated away from the conduit. A similar process is proposed to explain the concentric geochemical pattern of the Pul Pul Rhyolite.

p93 para 3 insert after 2nd sentence: The incompatible elements are partitioned into late-stage accessory minerals during final crystallisation of the granite (e.g. monozite, allanite, zircon). These accessory minerals do not incorporate large quantities of major elements, which explains why they do not display a comparable degree of variation during this late-stage fractionation of the suite.

p94 para 2: NB: one sample of the sparsely porphyritic rhyolites (sample 89123109) was collected near a fault zone, and is altered and aberrant in the plots (Figure 2.39). The sample is silicified (77.99% SiO2), elevated in HFS elements (La, Ce, Nd, Ga) and has an anomalously high ASI index (Figure 2.37). When the altered sample is removed, the remaining sparsely porphyritic rhyolites have a silica range of 74.55-76.77%, which is broadly the same as that of the granite (75-76.5%). Volcanic rocks, or in this case, subvolcanic intrusions, erupt at an incomplete stage of magmatic crystallisation, and late-stage crystallising minerals such as K-feldspar, and accessory

minerals like zircon, monozite and allanite, are therefore not yet present as phenocrysts. This explains why the sparsely porphyritic rhyolites do not show an increase in the incompatibles to the same level as the granites.

Section 7.2.1 p278: This section of my thesis attempted comparison of the volcaniclastic megaturbidites with their nearest sedimentological analogues. Drawing a direct analogy between these two different types of deposits did not turn out to be appropriate, and the comparison was not effective in resolving the issue of contemporary flow transformation vs post-eruptive slumping. Two specific points were raised. (1) In response to my comments that: (a) epiclastic megaturbidites occur as isolated beds within thick packages of 'normal' sedimentation; and (b) the frequency of occurrence of volcaniclastic megaturbidites supports their association with volcanic eruptions, Professor Carey brought my attention to recent ODP studies of the Madeira Abyssal Plain. This area contains hundreds of thick turbidites sourced from the African Shelf, Canary Islands and nearby seamounts, which are stacked continuously with only a few cm of hemipelagic sediment separating adjacent deposits. Some are clearly associated with large-scale sector collapse of volcanic islands in the Canaries. i.e. in this region there is a high frequency of slump-related turbidite events of juvenile volcaniclastic material. However, the pattern of sedimentation in this is different to that in the Turondale and Merrions Formations. The deposits in the Madeira Abyssal Plain are much thinner (< 4m) and occur much more frequently. The volcaniclastic megaturbidites in the Hill End Trough are occasionally amalgamated, but are regularly interspersed with intervals of hemipelagic sedimentation. If these volcaniclastic megaturbidites were slump-related and not associated with penecontemporaneous volcanism, a pattern similar to turbidites of the Madeira Abyssal Plain would occur (i.e. if regular epiclastic processes such as periodic sector collapse occurred, you would see frequent repetition of many smaller-scale events).

(2) In response to my argument that the volcaniclastic megaturbidites are not likely to represent slump deposits because they do not show the debris flow-to-turbidite facies changes observed in some epiclastic deposits, Professor Carey pointed out that this evolution is likely to be strongly linked to the clay content (and therefore cohesiveness) of the slumping material. Pyroclastic flow material is virtually devoid of cohesive clay and is therefore more easily mixed, segregated and diluted with water. However, if the volcaniclastic megaturbidites were cold, slumped deposits, you would expect them to preserve a granulometry more similar to pyroclastic flows, particularly closer to the entry point into water. Thus the fines depletion in the volcaniclastic megaturbidites still argues for a substantial modification of juvenile material, more consistent with ash removal processes associated with interactions between hot, gas supported pyroclastic flow and seawater.

p287 & 334 append to end of second paras: As discussed in section 3.3.6, further fractionation of the dense and light components is likely to occur within the derivative water-supported mass flows, fine ash is entrained by upward convection during buoyant liftoff of parts of the flow.

Add to reference list:

Bacon, C.R. and Druitt, T.H. 1988. Compositional evolution of the zoned, calcalkaline magma chamber of Mount Mazama, Crater Lake, Oregon. *Contributions to Mineralogy and Petrology* **98**: 224-256.

Blake, S. and Ivey, G.N. 1986. Magma-mixing and the dynamics of withdrawal from stratified reservoirs. *Journal of Volcanology and Geothermal Research* **27**: 153-178.

Lipman, P.W. 1967. Mineral and chemical variations within an ash-flow sheet from Aso Caldera, Southwestern Japan. *Contributions to Mineralogy and Petrology* **16**: 300-327.

McBirney, A.R. 1980. Mixing and unmixing of magmas. *Journal of Volcanology and Geothermal Research* **7**: 357-371.

McLeod, P., Carey, S. and Sparks, R.S.J. 1999. Behaviour of particle-laden flows into the ocean: experimental simulation and geological implications. *Sedimentology* **46**: 523-536.

Sigurdsson, H., Cornell, W. and Carey, S. 1990. Influence of magma withdrawal on compositional gradients during the AD 79 Vesuvius eruption. *Nature* **345**: 519-521.

Smith R.L. and Bailey, R.A. 1966. The Bandalier Tuff: a study of ash-flow eruption cycles from zoned magma chambers. *Bulletin of Volcanology* **29**: 83-103.

Spera, F.J., Yuen D.A., Greer, J.C. and Sewell, G. 1986. Dynamics of magma withdrawal from stratified magma chambers. *Geology* **14**: 723-726.

Turner, J.S. 1980. A fluid-dynamic model of differentiation and layering in magma chambrs. *Nature* **285**: 213-215.

Willis, I.L., Brown, R.E., Stroud, W.J. and Stevens, B.P.J. 1983. The Early Proterozoic Willyama Supergroup: stratigraphic subdivision and interpretation of high to low-grade metamorphic rocks in the Broken Hill Block, New South Wales. *Journal of the Geological Society of Australia* **30**: 195-224.

Wolff, J.A. and Storey, M. 1984. Zoning in highly alkaline magma bodies. *Geological Magazine* **121**: 563-575.

The facies architecture and geochronology of the subaerial to subaqueous Palaeoproterozoic El Sherana Group, Northern Territory, and the submarine Early Devonian Crudine Group, New South Wales: implications for eruption and depositional processes.

Elizabeth Anne Jagodzinski
BSc Hons (University of Adelaide)

Submitted for the degree of Doctor of Philosophy
in the Department of Earth Sciences,
Monash University, Australia

September 1999

Contents

INDEX OF FIGURES

Chapter 5

Chapter 6

Chapter 7

Chapter 8

Chapter 9

INDEX OF TABLES

ABSTRACT

The El Sherana Group is a succession of fluvial and lacustrine sedimentary rocks and bimodal volcanics outcropping in a NW-trending faulted belt in the South Alligator Valley area of the Proterozoic Pine Creek Inlier, Northern Territory, Australia. The El Sherana Group comprises, in ascending stratigraphic order, the Scinto Breccia, Coronation Sandstone, Pul Pul Rhyolite and Big Sunday Formation. The Pul Pul Rhyolite represents a major period of silicic volcanism during deposition of the El Sherana Group. It contains an association of rhyolitic volcanic, volcaniclastic and intrusive facies, dominated by welded ignimbrites. The volcanic succession is thickest (over 1 km thick) around the southern margin of the Malone Creek Granite, thinning to under 200m to the northwest, where it outcrops discontinuously throughout the South Alligator Valley Mineral Field, and around the base of the Mt Callanan Basin. In the southeast, where the formation is thickest, the Pul Pul Rhyolite is disconformably overlain by the Big Sunday Formation, a succession of volcaniclastic turbidites interpreted to represent a local lacustrine environment in the predominantly subaerial palaeo-landscape.

The thick volcanic succession south of the Malone Creek Granite is interpreted to represent the preserved remnant of an ancient caldera structure that developed incrementally through partial collapse in the early stages of eruption, followed by downsagging in the later stages. The thinner succession to the northwest is interpreted to represent the associated outflow (i.e. extracaldera) deposits. The position of the caldera margin between the proximal and distal deposits is marked by a series of faults, including an early collapse scarp interpreted as a preserved remnant of the early caldera margin, which correspond spatially to a significant change in the thickness of the ignimbrite succession. sparsely porphyritic quartz monzonite porphyries at this locality may correspond to a ring dyke associated with this fracture system. Because the Big Sunday Formation overlies the intracaldera facies, it is interpreted to have accumulated within the topographic depression remaining after caldera collapse. The spatial relationship between the Pul Pul Rhyolite and the central Malone Creek Granite pluton suggests that late-stage resurgence of the volcanic pile accompanied emplacement of the granite.

The Pul Pul Rhyolite and Big Sunday Formation depocentres developed within a large braidplain river system flowing to the northwest, which is represented by the sedimentary successions of the underlying Coronation Sandstone and overlying Kurrundie Sandstone (Edith River Group). The outflow facies of the Pul Pul Rhyolite appears to have travelled down the regional northwest palaeoslope of the fluvial braidplain. Palaeocurrents for the

turbidite succession of the Big Sunday Formation suggest a southeast facing palaeoslope, suggesting that Pul Pul Rhyolite volcanism temporarily interrupted regional braidplain sedimentation, and either through caldera formation and/or damming of the braidplain drainage, caused local ponding of a lake with its own palaeodrainage pattern.

The Big Sunday Formation contains thick deposits of juvenile volcaniclastic detritus, comprising thick, massive beds of crystal-rich volcaniclastic sandstone (CRVS), local diffusely-bound pumice- and ash-rich, non-welded domains and horizons of fluidally-shaped welded ignimbrite intraclasts in a CRVS matrix. These facies were generated when subaerial pyroclastic flows containing both agglutinated and particulate domains (i.e. undergoing partial primary agglutination and welding), encountered water at the shoreline of the lake. The agglutinated component of the flows, represented by the fluidally-shaped welded ignimbrite intraclasts in the final deposits, survived the transition beyond the shoreline relatively intact, experiencing only partial disruption through ductile stretching, brittle disaggregation and quenching upon contact with water. In contrast, the particulate component of the flows underwent complete disruption at the shoreline, through phreatic explosions and/or ingestion of water, and transformation in transit into water-supported mass flows. The flow transformation process was accompanied by very efficient winnowing of pumice and ash, with only small local, diffusely-bound pumice- and ash-rich domains remaining intact within the predominantly crystal-rich facies.

Deriving a magmatic age for the Pul Pul Rhyolite presents a difficult dating prospect, because the volcanic succession is dominated by ignimbrites containing abundant lithic clasts and xenocrysts. These provide an obvious (potential) source of inheritance to the zircon population. To avoid any consequent problems with data interpretation, a careful sampling strategy was conducted, targeting several different volcanic and intrusive facies. Ion microprobe ages of 1827±3.5 Ma and 1828.1±3.5 Ma for rhyolite prophyries, and 1828.6±5.1 Ma for a lithic-poor ignimbrite, tightly constrain the age of the volcanic succession. The latter age is taken as the stratigraphic age of the Pul Pul Rhyolite. This age is about 40 m.y. younger than previous estimates of the age of the El Sherana Group. It indicates, in conjunction with ion microprobe ages available for the overlying Edith River Group (1822±6 Ma) and the Cullen Supersuite (ranging between 1830-1810 Ma), that there are two main magmatic episodes in the Pine Creek Inlier. The first is related to the major compressional deformation event (Nimbuwah Event) and occurred between 1870-1850 Ma (represented by granitoid rocks of the Nimbuwah and Litchfield Complex). The second, defined as the 'Cullen Event', occurred between about 1830-1810 Ma and is marked by intrusion of the Cullen Supersuite and shallow level plutons of the Jim Jim Suite and emplacement of volcanic successions within the El Sherana and Edith River Groups.

The Hill End Trough of central-western New South Wales was an elongate deep marine basin that existed in the Lachlan Fold Belt of eastern Australia, from the early Late Silurian to the late Early Devonian. It is represented by a regionally extensive sequence of interbedded turbidites and hemipelagites, which passes laterally into contemporaneous shallow-water deposits of the adjacent Molong and Capertee Highs. The Turondale and Merrions Formations of the Early Devonian Crudine Group are two prominent volcanogenic formations within the predominantly sedimentary trough succession. Both formations contain a range of primary and resedimented volcanic facies. These include widespread subaqueous silicic lavas and/or lava cryptodomes in the Merrions Formation and compositionally equivalent porphyries intruding the older Turondale Formation as sills, and thick, massive deposits of syn-eruptive, crystal-rich volcaniclastic sandstone (CRVS). The volcaniclastic deposits reflect periods of large-scale silicic volcanism on the adjacent shallow marine to emergent highs, and are interpreted to be generated by interaction between contemporaneous subaerial pyroclastic flows and the sea.

'Normal' basin sedimentation within the Turondale Formation is represented by thick, hemipelagic intervals of shale and interbedded siltstone, which represents ambient deep-water sedimentation, below the influence of storm wave activity. This ambient sedimentation was periodically interrupted by the emplacement of various volcaniclastic mass-flow facies, including CRVS (turbidites and megaturbidites) and associated cherty tuffaceous sandstones and siltstones, normally graded volcaniclastic breccia/sandstone (megaturbidites) and polymictic volcaniclastic conglomerates. The volcaniclastic detritus was derived from penecontemporaneous subaerial to shallow marine explosive eruptions of a volcanic source to the south or southeast of Sofala, probably located on the adjacent Capertee High. The source region may be represented by the Huntingdale Volcanics outcropping in the Capertee Valley about 30 km east of Sofala.

Ion microprobe dating of the Turondale and Merrions Formations by means of the commonly used SL 13 zircon standard yields ages ranging between 411.3±5.1 and 404.8±4.8 Ma. Calibrating the data against a different zircon standard (QGNG) yields preferred slightly older mean ages that range between 413.4±6.6 and 407.1±6.9 Ma. These ages broadly approximate the Early Devonian age that has been historically associated with the Crudine Group. However, the biostratigraphically inferred late Lochkovian-early Emsian (mid-Early Devonian) age for the Merrions Formation is inconsistent with the 410 Ma age assigned to the Silurian-Devonian boundary, as defined on both the Australian Phanerozoic Timescale (Young and Laurie 1996), and the IUGS global stratigraphic chart (Cowie and Bassett 1989), and with the ages of 404.5 Ma and 395.5 Ma assigned to the base and top of the Pragian, respectively (Young and Laurie 1996). There is, however, good agreement if the new ages

are compared with the most recently published revision of the Devonian time scale (Tucker et al. 1998). This suggests that the Early Devonian stage boundaries of the Australian Phanerozoic Timescale need to be revised downward. The new ages for the Merrions Formation could also provide a time point on this time scale for the Pragian to early Emsian, for which no data are presently available.

One outcome of studying crystal-rich volcaniclastic sandstone (CRVS) facies has been an assessment of how magmatic compositions are modified through the loss of pumice and ash during the eruption and transportation of pyroclastic flows and associated syn-eruptive volcaniclastic mass flows. In general compatible elements, which partition into early phenocryst phases, are enriched in ignimbrites and syn-eruptive volcaniclastic products relative to the parent magma. Conversely, incompatible elements, which partition into the melt and consequently the vitric fraction of the erupting magma, are depleted. Where this chemical modification can be quantified, it is possible to predict the composition of the source magma, which has important applications in provenance studies. This knowledge of chemical modification is also potentially useful for interpreting facies in high grade metamorphic terranes, where determining metamorphic precursors can be difficult due to the obliteration of primary textures and structural features.

A sound understanding of volcanic processes and facies is essential when selecting samples for U-Pb dating. Whereas pyroclastic rocks or syn-eruptive pumiceous and/or crystal-rich volcaniclastic facies (CRVS) provide the best stratigraphic markers in subaerial and submarine successions, they are the most likely facies to contain significant crustal contamination, which can introduce a significant inherited component into the zircon population. Conversely, coherent facies such as lavas and syn-sedimentary sills and intrusions are less affected by crustal lithic contamination (although they may still contain xenocrysts derived from the magmatic source), and generally should have comparatively simple zircon populations. However, they have limited value for correlation purposes and can be difficult to distinguish from post-depositional intrusions. Therefore no volcanic facies can be singled out as ideally suitable for isotopic dating studies. An accurate interpretation of geochronological results requires: (1) an awareness of the potential difficulties inherent in dating each type of facies; and (2) careful elucidation of eruptive and emplacement processes of volcanic facies selected for dating. If crustal contamination is likely to introduce significant inheritance in the zircon population, or if the origin of the facies is equivocal (e.g. if there is a problem determining the timing of emplacement of coherent bodies, or distinguishing primary from reworked tuffaceous units), then information independently constraining the age of the facies is required to ensure the correct age interpretation.

ACKNOWLEDGEMENTS

I was lucky enough to have the best supervisors to guide me in my studies; Professor Ray Cas (supervisor) and Dr Lesley Wyborn (co-supervisor). Both have achieved excellence and acclaim in their chosen field, and both are committed to sharing their knowledge with the greater scientific community. For these reasons, they are excellent mentors and role models. As supervisors, Ray and Lesley not only expanded my knowledge, but through example, taught me the principles of problem solving and conducting rigorous scientific research. I thank them both for this excellent grounding. Ray is also thanked for his thorough reviews and astute comments, which led to great improvement of the final manuscript.

Thanks to Dr Chris Pigram, Chief of the Regional Geology and Minerals Division of the Australian Geological Survey Organisation (AGSO), for approving the time and resources to complete this thesis. AGSO has provided logistical support for much of this project, and I have been able to draw on the great breadth of knowledge of my colleagues. Morrie Duggan is particularly thanked for putting up with my heavy utilisation of his skills as a gun petrologist, and Lance Black for offering me guidance in the processing of SHRIMP U-Pb data, and for reviewing my efforts in Chapter 5. Thanks also to all my colleagues at the New South Wales Geological Survey for discussion and free exchange of ideas and information as we worked on the Bathurst and Dubbo 1: 250 000 mapsheets, with special thanks to Simone Meakin and Gary Colquhoun for our great fun and companionable times together in the field. At Monash University, discussions with Ray's other students, particularly Adrian McArthur, Ceinwen Scutter and Scott Bryan, were stimulating and interesting, and enabled me to keep up with the latest developments in the field of physical volcanology. Thanks to Gordon Packham, Dave Nelson, Lesley Wyborn, Rod Page, Barry Fordham, Gary Colquhoun and Tony Wright, for reviews and comments on Chapter 8. I believe that good science involves the integration of knowledge and ideas from a range of disciplines, and an attempt to strive for some consensus, and my interaction with the geologists mentioned above has enabled me to pursue this goal.

Mum (Mary Jagodzinski), Andrew Roberts and Carla Bos took on the onerous task of final proof-reading and editing of chapters (thanks, thanks and thanks again!) and Lesley Wyborn stepped in during the final frantic hours to make short work of the references.

I have received a great deal of encouragement and support from family and friends over the years, and I thank the following people for being there through thick and thin (especially thin!): Hazel and Lauren McFadden, Simone Meakin, Gary Colquhoun, Digna Smit-Martin, Cornelia Cefai and Penny Ursem. Finally, my partner Andrew Roberts must be thanked for cooking a long line of great meals, generally looking after me, building my office and for cheerfully enduring a grumpy PhD student for two years!

INTRODUCTION AND SCOPE OF THE THESIS

The behaviour of ignimbrite-forming pyroclastic flows upon passage into subaqueous environments has been a much debated issue in volcanology in recent years (e.g. Cas and Wright 1991), with research directed towards determining whether pyroclastic flows can travel significant distances as hot gas-particle dispersions under water, allowing them to weld in wholly subaqueous environments. Some authors claim that this should be possible, through the development of a steam carapace which would insulate the flow from heat loss and ingestion of water (e.g. Sparks et al. 1980a,b; Francis and Howells 1973; Howells et al. 1985), and through the conversion of any incorporated water into steam, with only minor heat loss from the interior of the flows (Sparks et al. 1980a,b). Other authors envisage that many hot pyroclastic flows are likely to disintegrate upon contact with cold water, due to unstable turbulent boundary conditions that promote rapid ingestion of water, and the triggering of phreatomagmatic explosions (Cas and Wright 1991; McArthur 1995). Resolving the issue hinges on identifying unequivocal examples of pyroclastic flow deposits in submarine successions. This requires both the host depositional setting to be adequately constrained, and evidence for heat retention in the subaqueous deposits to be established (Cas and Wright 1991). One of the most reliable indicators of hot emplacement is welding, and authors advocating models of flow disintegration consider it significant that very few welded ignimbrites have been recognised in subaqueous successions. This is despite the fact that many volcanic centres are situated adjacent to marine basins, and the passage of hot pyroclastic flows into the sea must be a fairly common occurrence. However, examples of welding in ancient marine successions are becoming more widely recognised (e.g. Schneider et al. 1992; Fritz and Stillman 1996; White and McPhie 1997), and so the debate continues, and models determining the conditions under which subaqueous pyroclastic flow may be plausible, continue to be refined.

One of the main aims of this study is to address the above issue, and consider the likely processes and deposits arising from the interaction between pyroclastic flows and water. This is approached through the study of a distinctive crystal-rich volcaniclastic sandstone facies (CRVS) found in subaqueous settings, which is considered likely to be generated by complex

interaction between subaerial pyroclastic flows and the sea (Cas and Wright 1991; White and McPhie 1997). This style of deposit has been categorised as a 'syn-eruptive resedimented volcaniclastic deposit', emphasising the genetic connection with active volcanism (McPhie et al. 1993). The facies comprises volcaniclastic megaturbidites, orders of magnitude larger than normal siliciclastic turbidites, that are composed of large volumes of unmodified dense juvenile pyroclasts (predominantly crystals and crystal fragments), but contain no pumice and are significantly depleted in fine ash (relative to subaerial pyoclastic flow deposits).

Two reasonably exposed examples of the CRVS facies have been identified and selected for study. The first is preserved within the Big Sunday Formation of the El Sherana Group in the Palaeoproterozoic Pine Creek Inlier, Northern Territory (Section 1). The second occurs within the Turondale Formation of the Crudine Group in the Siluro-Devonian Hill End Trough, central-western New South Wales, which is part of the Palaeozoic Lachlan Fold Belt of eastern Australia (Section 2). The examples chosen for study illustrate two very different palaeoenvironments in which these crystal-rich volcaniclastic sandstones can occur. CRVS of the Big Sunday Formation were deposited in a restricted lacustrine setting in a predominantly subaerial volcano-sedimentary landscape, whereas those of the Turondale Formation were deposited in a deep marine basin. Each study involves an assessment of facies characteristics of the crystal-rich volcaniclastic sandstones, and subsequent discussion of what these characteristics infer about the likely behaviour of pyroclastic flows upon entering subaqueous environments (Chapters 3 and 7, respectively). In the Big Sunday Formation, breccia units composed of welded ignimbrite clasts in a crystal-rich sandstone matrix are of particular interest, and an assessment of this distinctive facies association provides important information about the contrasting behaviour of particulate and non-particulate flow components as they interact with water (Chapter 3).

The results of this study supplement a growing body of literature on these subaqueous crystal-rich volcaniclastic deposits. Other examples of this facies have been recorded in the: (1) Merrions Formation of the Hill End Trough, New South Wales (Cas 1979, 1983a); (2) Kowmung Volcaniclastics and Tangerang Formation of the Bindook Volcanic Complex, which lies beyond the southern margin of the Hill End Trough (Cas et al. 1981; Simpson et al. 1997); and (3) Tyndall Goup of the Mt Read Volcanics, Tasmania (White and McPhie 1996, 1997). These studies all focus on volcanological and sedimentary aspects of the facies. The present study expands on this earlier work, by also conducting a geochemical and geochronological evaluation of the facies. Issues addressed include: (1) determining how original magmatic compositions are modified through the loss of pumice and ash during eruption, transportation and deposition of the facies (Chapters 3 and 7); (2) exploring the

implications of these post-eruptive geochemical modifications to provenance studies and recognition of the facies in high-grade terrains (Chapters 7 and 9); and (3) assessing whether this type of resedimented (but essentially syn-eruptive) facies is suitable to target for isotopic dating (specifically U-Pb zircon dating) and the implications for volcanology of the homogeneity of zircon populations (Chapter 9).

The study also involves a detailed evaluation of the environments hosting the crystal-rich volcaniclastic sandstones, through facies analysis of host successions. In each case, the palaeogeography and volcanic history of the region are reconstructed. In the first study of the El Sherana Group (Section 1), the scope of the thesis is expanded to include a detailed assessment of the subaerial volcanic succession of the Pul Pul Rhyolite (Chapter 2), which underlies the Big Sunday Formation lacustrine succession. This first study is therefore also of significance in addressing eruption and emplacement mechanisms for subaerial pyroclastic flows as well as subaqueously-deposited pyroclastic flows. It is also an excellent example of how caldera settings can be reconstructed in partially preserved and tectonically dismembered ancient (specifically, Proterozoic) volcanic successions, by comparing preserved facies associations in the remnant sequences with caldera-based facies models constructed from modern volcanic centres.

The final aim of this thesis is to provide some numerical age control to the regional stratigraphy of both the Palaeoproterozoic Pine Creek Inlier and the Siluro-Devonian Hill End Trough, by obtaining U-Pb zircon ages for volcanic and volcaniclastic facies within the two successions selected for study. Very few isotopic age constraints are presently available for either the Pine Creek Inlier (Section 1) or the Hill End Trough (Section 2), and the reasonably fresh, unaltered silicic volcanic successions selected for study provide excellent targets for geochronological studies. A range of primary and syn-eruptive volcanic facies, in both subaerial and submarine ancient successions, were selected for dating. In the final chapter of the thesis, the results of both studies contribute to an overall discussion of the suitability of different types of volcanic facies for U-Pb dating, some problems that may be encountered when dating each type of facies.

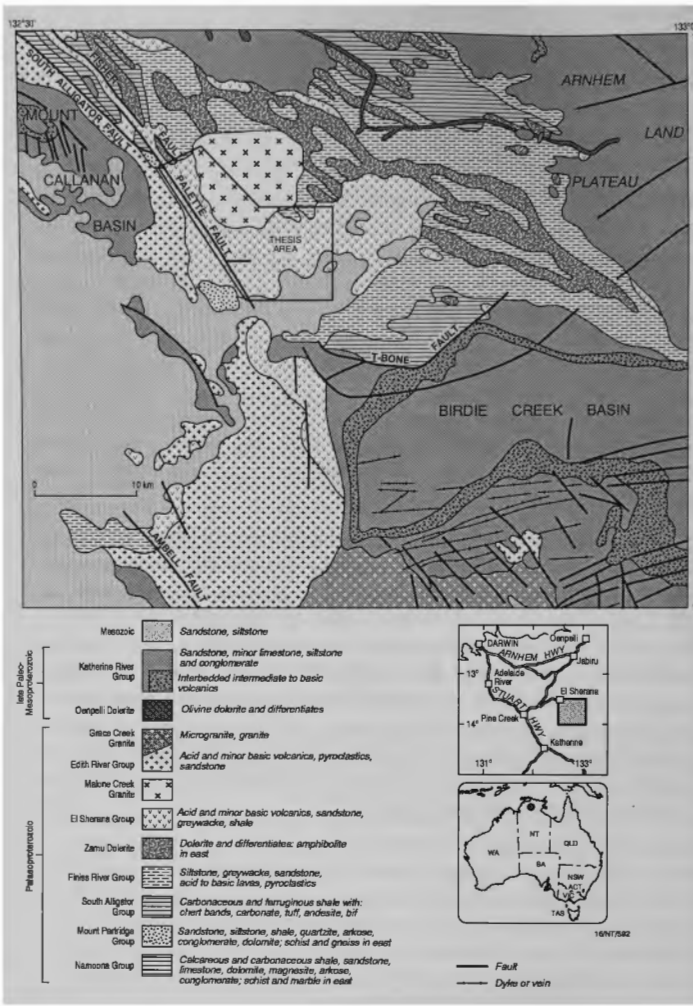

Figure 1.1: Solid geology map of the Stow 1:100 000 mapsheet (map number 5740) showing the distribution of the El Sherana Group, which is largely confined in outcrop to this mapsheet. The thesis area covers the El Sherana Group where it outcrops around the southern and western margins of the Malone Creek Granite, and east of the Palette Fault.

CHAPTER 1

Introduction

1.1 Aims of the study

The Pul Pul Rhyolite is a silicic volcanic suite that outcrops in the South Alligator Valley region of the Palaeoproterozoic Pine Creek Inlier, Northern Territory, Australia (Figure 1.1). The formation is part of the El Sherana Group, a sequence of terrestrial sedimentary and volcanic rocks deposited on metamorphosed and deformed Proterozoic basement rocks during a period of extension postdating the main compressional orogenic event in the Pine Creek Inlier (Needham et al. 1988). The Pul Pul Rhyolite represents a major period of silicic volcanism during deposition of the post-orogenic El Sherana Group. The study area covers the thickest exposed sequence of the Pul Pul Rhyolite where it outcrops at the southern margin of the Malone Creek Granite (Figure 1.1). Here it comprises a thick package of welded ignimbrites (~ 1 km thick) with minor non-welded ignimbrite, associated felsic dykes and intrusions, derivative volcaniclastic sediments and minor mafic intrusive bodies. This facies association is similar to that occurring in many modern silicic volcanic centres (e.g. Cas and Wright 1987), suggesting the sequence may represent the erosional relic of a volcanic centre within the Pul Pul Rhyolite.

In recent years considerable progress has been made in understanding volcanic processes and deposits. This has been largely due to adopting a sedimentological-style facies analysis approach to the study of modern volcanic centres. These studies have shown that volcanically active regions are dynamic, recording a complex interplay between progradational and aggradational processes, and accompanying ground movements. This results in a complex stratigraphy characterised by rapid lateral and vertical lithological changes, abundant faults, local unconformities and disconformities and irregular contacts between facies. Mapping and reconstructing these complex successions in ancient terrains can be hampered by poor outcrop, preferential preservation of primary volcanic facies most resistant to erosion, and overprinting of original stratigraphic and structural features by post-volcanic deformation, metamorphism and alteration. Key features diagnostic of eruptive centres, such as caldera rims, ring faults or ring dyke complexes

may fail to be preserved in outcrop, or be deformed beyond recognition. Several studies, however, have shown that the depositional context of partially preserved and/or deformed ancient volcanic successions can be established by the lithofacies preserved, by comparing the associations of facies with facies models for modern silicic centres (e.g. Cas and Wright 1987; McPhie 1988; Orth et al. 1989). One aim of this study is to apply such a facies analysis approach to the volcanic succession of the Pul Pul Rhyolite in order to

1. assess the characteristics of each facies to determine their mode of deposition and environmental conditions at their time of emplacement (Chapter 2).

2. determine the spatial distribution and stratigraphic relationships of facies to reconstruct the palaeovolcanological history of the sequence (Chapter 4).

3. use the association of facies to determine the original context of the preserved succession relative to the source eruption centre (Chapter 4).

Another aim of the study is to provide some numerical age control on the Pine Creek Inlier sequence, by obtaining a stratigraphic age for the El Sherana Group through U-Pb zircon dating of volcanic facies of the Pul Pul Rhyolite. There are very few numerical age constraints available on the constituent units of the Pine Creek Inlier. This is because the predominantly sedimentary clastic succession contains few interbedded volcanic rocks suitable for isotopic (U-Pb) dating. At present there are no age data directly constraining the age of the El Sherana Group, but the reasonably fresh, unaltered silicic volcanic succession of the Pul Pul Rhyolite provides an excellent target for a U-Pb dating study. The study also explores the importance of applying a sound understanding of volcanic processes and facies to the field of geochronology, using in particular the SHRIMP (sensitive high resolution ion microprobe) U-Pb method applied to the dating of zircon crystals and grains (Chapter 5). It illustrates the problems that can arise when making age determinations on fragmental volcanic facies (particularly ignimbrites). It is important to be aware that obtaining a crystallisation or deposition age for fragmental facies can be hampered by the presence of lithic or xenocrystic contaminants that can have a primary and/or secondary origin. Lithic or xenocrystic contamination of the parent magma can potentially introduce inheritance into the zircon population, creating complex isotopic signatures that can be difficult to interpret. The study offers solutions to overcome the problem of xenocrystic contamination in fragmental rocks.

This study also provides an opportunity to consider the behaviour of pyroclastic flows as they enter a standing body of water. This issue has been the subject of much debate (e.g. Cas and Wright 1991), and of particular interest is whether pyroclastic flows can

maintain their integrity and continue as gas-particle dispersions under water, or if they are more likely to disintegrate and transform into water-supported systems. The Big Sunday Formation overlying the Pul Pul Rhyolite represents a locally developed lacustrine sequence within the predominantly subaerial volcanic landscape. The turbidite succession contains thick deposits of massive, crystal-rich volcaniclastic sandstones (CRVS), which are interpreted to have been generated by the interaction of subaerial pyroclastic flows with water. The succession is unique, in that a genetic relationship can be inferred between the syn-eruptive volcaniclastic units deposited in a subaqueous setting, and the underlying subaerial pyroclastic flow deposits. This allows a direct comparison to be made of the features of the deposits of pyroclastic flows emplaced in subaerial and subaqueous settings. The other important feature of the crystal-rich subaqueous deposits is that locally they contain (1) diffusely bounded non-welded pumice- and ash-rich domains; and (2) horizons of welded ignimbrite clasts, which are genetically related to the crystal-rich matrix in which they occur. Interpreting the origin of these unusual textural features within the crystal-rich volcaniclastic sandstones, and discussing their relevance to the subaqueous pyroclastic flow debate, provides the main focus for Chapter 3.

1.2 GEOLOGICAL AND TECTONIC SETTING OF THE PINE CREEK INLIER

Regional setting

The Pine Creek Inlier (Needham et al. 1988) is a Palaeoproterozoic basin of northern Australia, traditionally known as the Pine Creek Geosyncline (Ferguson and Goleby 1980). It is exposed over an area of about 66 000 km^2, and it is believed to extend beneath younger basins to the east and south. The basin unconformably overlies a late Archaean (~2500 to 2700 Ma) granitic basement which is exposed as three small complexes within the inlier (Rum Jungle, Waterhouse Complex and Nanambu Complex; Figure 1.2) and intersected in drill holes beneath thin Mesozoic cover in the Woolner area 65 km east of Darwin (Woolner Granite). The basin is overlain with marked unconformity by the Palaeo- to Mesoproterozoic McArthur Basin to the east, the Mesoproterozoic Victoria River Basin and Palaeozoic Daly Basin to the south, the Palaeozoic Bonaparte Gulf Basin to the west and the Mesozoic Bathurst Terrace to the north (Needham et al. 1980; Figure 1.2).

The regional geology, stratigraphy, metamorphism and structural setting of the Pine Creek Inlier are described by Walpole et al. (1968), Needham et al. (1980, 1988), Needham and Stuart-Smith (1985a,b) and Stuart-Smith et al. (1993). The stratigraphy of the Pine Creek Inlier is presented in Figure 1.3, and simplified geology of the inlier is shown in Figure 1.4. From west to east, Needham et al. (1988) divide the Pine Creek

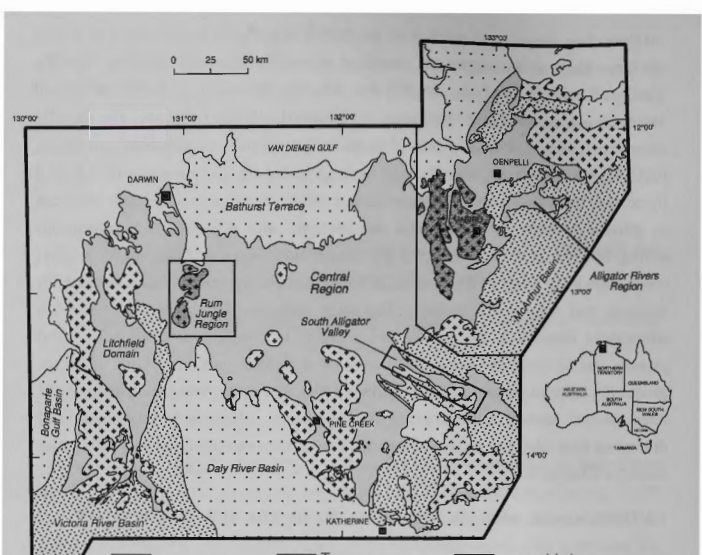

Figure 1.2: Generalised geology of the Pine Creek Inlier showing its location and structural setting, and division of the inlier into five sub-regions; the Litchfield Domain, Rum Jungle Region, Central region, South Alligator Valley and Alligator Rivers Region (modified after Needham and Stuart-Smith 1985a and Needham et al. 1988).

Inlier into five sub-regions; the Litchfield domain, Rum Jungle region, Central region, South Alligator Valley region and Alligator Rivers region (Figure 1.2). The Rum Jungle region represents Archaean crust and exhibits polyphase upright folds, domes and basins. The Palaeoproterozoic Litchfield domain and Nimbuwah domain (Alligator Rivers region) are characterised by complex multiple folding and medium-grade metamorphism (upper amphibolite facies). The Central region and the South Alligator Valley exhibit relatively simple structures dominated by north- to northwest-trending upright folds, and lower grade metamorphism (lower greenschist facies).

Geological history

The tectonic evolution of the Pine Creek Inlier is described by Needham et al. (1988). Their model for the evolution of the South Alligator Valley region is presented in Figure 1.5 and summarised below. Formation of the Palaeoproterozoic intracratonic basin is

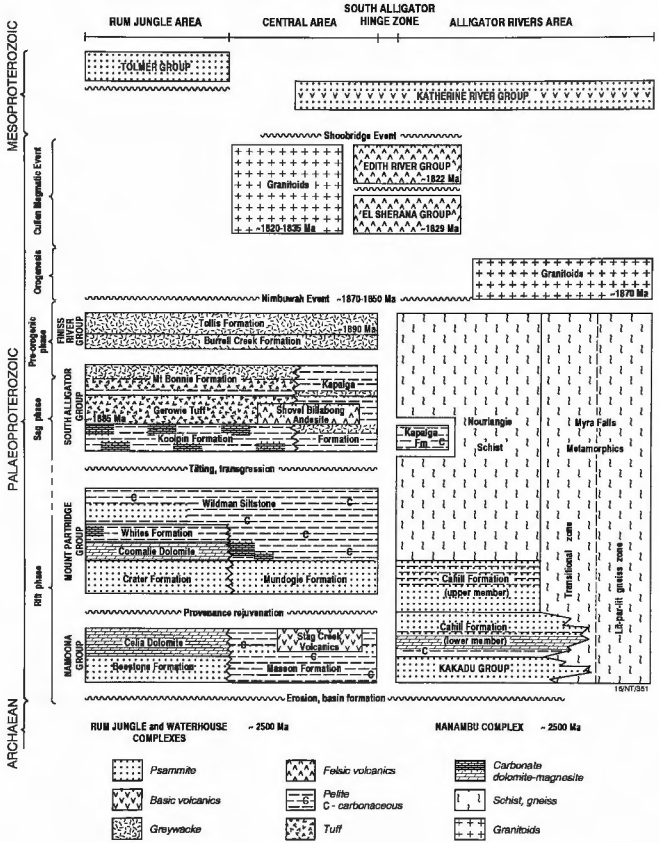

Figure 1.3: Diagrammatic stratigraphy of the Pine Creek Inlier, showing tectonic stages and events, and age determinations. Adapted from Needham et al (1988).

thought to have resulted from extension of late Archaean crust (~2500 to 2700 Ma; Page et al. 1980). About 10km of clastic, organic and chemical sedimentary rocks with minor volcanics filled the basin during sagging related to post-extensional subsidence. Initial depositional environments ranged from neritic to intertidal to fluviatile, followed by deeper marine 'flysch'-like sedimentation as subsidence rates increased towards the end of sedimentation. Needham et al. (1988) refer to this sedimentary succession as the 'Pine Creek Geosyncline Sequence', comprising (in ascending stratigraphic order) the *Namoona Group, Mount Partridge Group, South Alligator Group* and *Finniss River Group* (Figure 1.3). The age of the Pine Creek Geosyncline Sequence is constrained between 2470 and 1870 Ma (Page et al. 1980). U-Pb SHRIMP age determinations on tuff horizons in the *Gerowie Tuff* and *Mount Bonnie Formation* suggest a stratigraphic age of 1885±2 Ma for the *South Alligator Group* (Needham et al. 1988; Figure 1.3), providing a direct numerical constraint on the depositional timing of the basin system. The upper age limit of deposition is constrained by post-depositional granitoid intrusions of the Nimbuwah Complex, dated at 1866±8 Ma (Page et al. 1980). Combining this sparse age control with broad estimates of sedimentation rates, Needham et al. (1988) speculated that extension took place about 2000 Ma ago, and that sedimentary infill was complete by about 1880 Ma.

Needham et al. (1988) divide the basin succession into three tectonic stages; a rift phase, sag phase and orogenic phase. Sedimentation in the initial rift phase is represented by the *Namoona, Kakadu* and *Mount Partridge Groups* (Figure 1.3). The oldest sedimentary rocks of the basin include fluviatile to shallow marine conglomerate and arkosic sandstone (*Beestons Formation, Kakadu Group*), succeeded by supratidal to intertidal carbonate facies (*Masson Formation, Celia Dolomite).* The overlying *Mount Partridge Group* contains conglomerate, arkose, sandstone and minor siltstone deposited in an extensive fluvial fan system across the centre of the inlier (*Mundogie Sandstone, Crater Formation*). Fluvial/alluvial fans to fan delta successions grade distally and vertically to subtidal, high energy, finely banded pelites (grey siltstone and black carbonaceous shale) of the *Wildman Siltstone*. In the west, near exposed Archaean highlands (at Rum Jungle) supratidal to subtidal carbonate facies of the *Coomalie Dolomite* and *Whites Formation* were deposited. The overlying sag phase is represented by the *South Alligator* and *Finniss River Groups*, thought to have been deposited during thermal subsidence of extended lithosphere following cessation of major extension and normal faulting (Needham et al. 1988). The *South Alligator Group* was deposited under shallow marine, low-energy conditions and includes pyritic carbonaceous shale, chert, carbonate and banded iron formation (*Koolpin Formation*). Koolpin-type sedimentation was interrupted

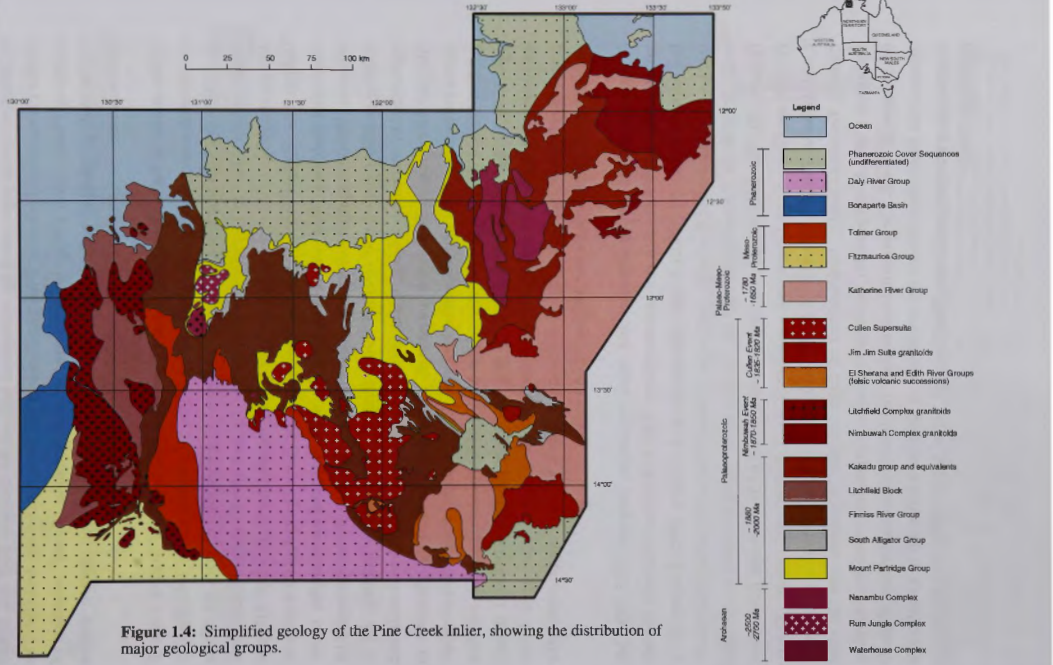

Figure 1.4: Simplified geology of the Pine Creek Inlier, showing the distribution of major geological groups.

by felsic volcanism represented by widespread tuffs of the *Gerowie Tuff* and *Mount Bonnie Formation* and restricted felsic lava flows of the *Shovel Billabong Andesite*. The overlying *Finniss River Group* is represented by a monotonous 'flysch' sequence of interbedded greywacke and siltstone deposited in high energy, deeper marine environments.

Sedimentation in the intracratonic basin was terminated by a period of high T - low P compressional orogenesis at about 1870 Ma, named the 'Nimbuwah Event' (Needham et al. 1988), which deformed and metamorphosed the sedimentary pile. Overall, the effects of this orogeny were more pronounced on the western and eastern margins (Litchfield domain and Alligator Rivers region) than in the Central region (including South Alligator Valley). The orogenic phase began with intrusion of the *Zamu Dolerite*, a thick suite of continental tholeiites. This was followed by the main structural-metamorphic event. Johnston (1984) recognised five deformations related to this event. D_1 is represented by bedding-parallel foliation and isoclinal folds, usually subparallel to bedding. D_2 is represented by recumbent folding, which is more common in the Litchfield domain and Alligator Rivers region. D_3 is more widespread, and takes the form of upright north- to northwest-trending folds and associated cleavage. D_4 is associated with syn-orogenic granite intrusion (Nimbuwah Complex; ~1866 Ma), and has produced easterly trending tight folds in the Nimbuwah domain. D_5 is a late kink foliation related to dextral movements along major faults. Regional metamorphic grades range from lower greenschist facies in the Central region and South Alligator Valley to upper amphibolite facies in the Litchfield domain and Alligator Rivers region.

A major period of granite intrusion and felsic volcanism between 1835-1820 Ma followed regional deformation and metamorphism. This widespread magmatic episode has been defined as the 'Cullen Event' (Jagodzinski and Wyborn 1995; Chapter 5). It involved emplacement of the *Cullen Supersuite* (formerly Cullen Batholith; Stuart-Smith et al. 1993) in the Central region and the *Jim Jim Suite* in the southeast of the inlier (Figure 1.3). The latter includes the felsic volcanics of the *El Sherana* and *Edith River Groups*, the *Grace Creek Granite* and a number of small shallow level plutons (*Malone Creek Granite, Jim Jim Granite, Nabarlek Granite, Tin Camp Granite, Eva Valley Granite, Yeuralba Granite*). Emplacement of large volumes of magma into the crust during the Cullen Event probably accompanied post-compressional relaxation following the Nimbuwah Event. The terrestrial sedimentary and (bimodal) volcanic rocks of the *El Sherana* and *Edith River Groups* are considered to have been deposited in a continental extensional or transtensional basin (Needham and Stuart-Smith 1985b; Friedmann and Grotzinger 1994).

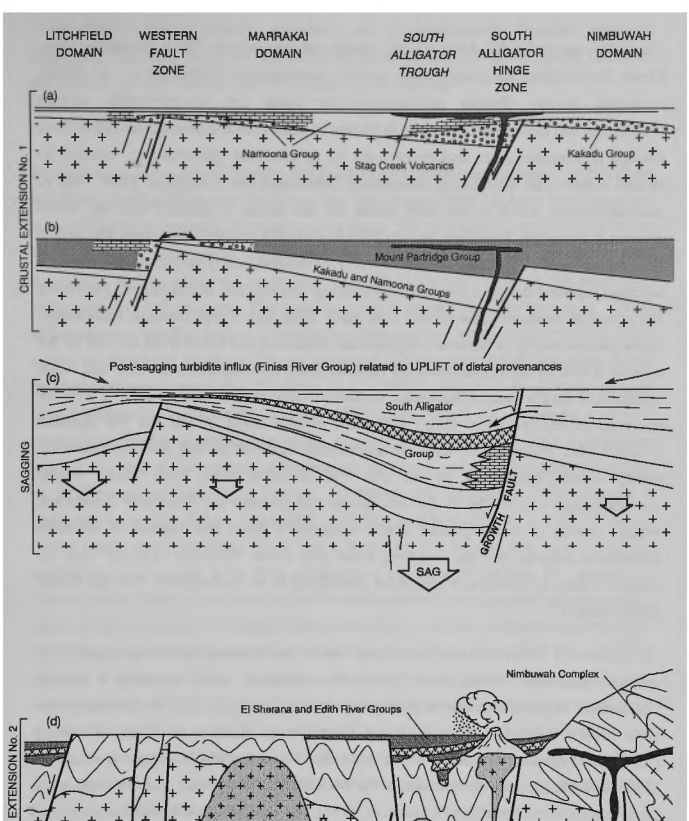

Figure 1.5: Tectonic model for the evolution of the South Alligator Valley region, from Needham et al. (1988): (a) crustal extension to form a shallow half graben; (b) subsequent deepening to form tilt blocks; (c) rapid infill in the last stages of basin sedimentation prior to onset of the major orogenic event ('Nimbuwah Event'); and (d) a second extensional event leading to reactivation of major fault zones, to form a graben over the South Alligator Valley area. These reactivated faults were the loci of felsic and mafic magmatism represented by the El Sherana and Edith River Groups.

The *El Sherana* and *Edith River Groups* overlie the pre-orogenic basin succession (Pine Creek Geosyncline Sequence) with marked unconformity (Needham et al. 1988), onlapping steeply dipping palaeotopography along the unconformable contact (Friedmann and Grotzinger 1994). Each formation within the *El Sherana* and *Edith River Groups* is separated from underlying units by an erosional unconformity, marked by incised valleys with 40-150m of palaeorelief (Friedmann and Grotzinger 1994). The *El Sherana Group*, which is the main focus for this study, is divided into the *Scinto Breccia*, *Coronation Sandstone*, *Pul Pul Rhyolite* and *Big Sunday Formation*. The *Scinto Breccia* is a basal phosphatic, siliceous breccia, developed locally on carbonate rocks as a siliceous saprolite during a period of weathering and regolith development. Following this period of weathering, the valleys were partly filled with coarse fluviatile sedimentary rocks (predominantly polymictic conglomerate, sandstone and minor shale derived by the erosion of underlying metasedimentary basement) and contemporaneous felsic and mafic volcanics of the *Coronation Sandstone*. Volcanism culminated with extrusion of massive columnar jointed ignimbrite sheets and minor rhyolite flows of the *Pul Pul Rhyolite* (1829±5 Ma). Volcaniclastic turbiditic sedimentary facies of the *Big Sunday Formation* locally overlie ignimbrites of the *Pul Pul Rhyolite*. The *Edith River Group* unconformably overlies the *El Sherana Group* and contains the *Kurrundie Sandstone*, which consists of coarse-grained clastic sedimentary rocks that formed in fluviatile palaeoenvironments, and the overlying *Plum Tree Creek Volcanics* (1822±6 Ma), an extensive sheet of crystal-rich ignimbrite considered to be co-magmatic with the *Grace Creek Granite*.

The Palaeo- to Mesoproterozoic McArthur Basin was initiated following a period of volcanic quiescence (Kruse et al. 1994). The timing of basin formation is poorly constrained. Deposition is known to have commenced prior to 1712 Ma (the age of the *West Branch Volcanics*, upper *Katherine River Group*; Kruse et al. 1994). Rawlings (1994) estimates that deposition of the McArthur Basin succession ranges from about 1780-1650 Ma. Initial sedimentation in the McArthur Basin appears to have been on a broad epicontinental platform (Kruse et al. 1994), and is represented by thick deposits of fluvial and shallow marine quartzose sandstone (*Kombolgie Formation)* and bimodal volcanism (*Nungbalgarri Volcanic Member*, *Birdie Creek Volcanic Member*, *McAddens Creek Volcanic Member*).

The final Palaeoproterozoic igneous event was the intrusion of a series of continental tholeiitic dolerite lopoliths and minor dykes in the east (*Oenpelli Dolerite*). Stuart-Smith and Ferguson (1978) interpret the contact relationship between the *Oenpelli Dolerite* and the *Kombolgie Formation* as unconformable, with the Kombolgie Formation overlying the dolerite. However, on the Millingimbi 1:250 000 mapsheet (Rix 1968) the dolerite

clearly intrudes the *Kombolgie Formation* and its emplacement therefore postdates deposition of at least the lower part of the *Katherine River Group*. A Rb-Sr total-rock and mineral age of 1718± 65 Ma is available for the dolerite.

Tectonic setting of the El Sherana and Edith River Groups

As mentioned above, the El Sherana and Edith River Groups are considered by Needham and Stuart-Smith (1985b) and Friedmann and Grotzinger (1994) to have been deposited in a continental extensional or transtensional basin. The true extent and geometry of the basin, however, are poorly constrained due to erosion of much of the original succession, lack of preserved margins or marginal facies, and burial of the succession under younger platform cover. The basin has been interpreted by Needham et al. (1988) as a north-west trending graben controlled by older, northwest-trending subvertical faults several kilometres in length, within the deformed and metamorphosed basement. Based on their subvertical geometry, Needham et al. (1988) considered these faults to have chiefly strike-slip displacement. Valenta (1991) documented S-C foliations and fault lineations indicating dextral displacement, supporting this conclusion, but showed that most of this fault movement post-dates deposition of the Kombolgie Formation overlying the El Sherana and Edith River Groups. Friedmann and Grotzinger (1994) describe a small sub-basin (the Palette sub-basin) recording sedimentation in a local strike-slip setting within the larger basin. They found, however, that beyond this local setting the sedimentary succession lacks thick sedimentary packages dominated by coarsening-upward cycles, debris-flow deposits and fan-delta deposits, or dispersed palaeocurrents, which provide evidence for major deformation and syntectonic sedimentation typical of transform zones and major strike-slip faults. They concluded, therefore, that the basin was not of strike-slip origin, and that the structural patterns, facies patterns and sense and style of syntectonic deposition are consistent with an extensional or transtensional regional setting. Their evidence for regional extension was the bimodal volcanism and normal-sense growth faulting recorded throughout the sedimentary succession. Local strike-slip tectonism as recorded within the Palette sub-basin is also consistent with a dominantly extensional setting.

1.3 PREVIOUS WORK

Early investigations (pre-1950's) of the South Alligator Valley region, in which the El Sherana Group is exposed, were mostly reconnaissance work and reports of mineral occurrences, listed by Walpole et al. (1968). The area was first mapped by a Bureau of Mineral Resources (BMR) survey in 1954 and 1955 as part of a regional evaluation of the Katherine-Darwin region, resulting in the publication of a 1:12 000 geological map of the area. Walpole et al. (1968) produced the first comprehensive interpretation of the

Proterozoic stratigraphy of the area based on the results of this mapping. Stewart (1965) made a more detailed petrographic study of the volcanic rocks of the El Sherana, Edith River and Katherine River Groups.

In the 1970's and early 1980's, the area was mapped by the BMR and Northern Territory Geological Survey using 1:25 000 colour air photos, during systematic 1:100 000 scale mapping of the Pine Creek Inlier (Stuart-Smith et al. 1988). This work resulted in substantial revision of the stratigraphy of the Pine Creek Inlier (Needham and Stuart-Smith 1985a) and led to the current interpretation of the tectonic setting of the Pine Creek Inlier (Etheridge et al. 1987; Needham et al. 1988). The structural evolution and mineralisation of the Pine Creek Inlier are summarised by the work of Johnston (1984).

The South Alligator Valley region contains the South Alligator Valley Mineral Field (Needham 1988), which has a history of mining and exploration spanning back to the early 1950's, when uranium was first discovered at Coronation Hill in 1953. Intensive prospecting by small companies located a further 13 deposits spread over 24 kms along the South Alligator River, and a total quantity of 874 tonnes of U_3O_8, ~0.3t Au and minor Ag were mined between 1956 and 1964. Exploration through the 1970's concentrated on prospecting for U, Au and base metal deposits. Open file company reports from this period are lodged with the Northern Territory Department of Mines and Energy in Darwin.

Interest in the region as a gold district developed in the 1980's, and in 1984, BHP discovered a potentially economic gold-platinum-palladium deposit at Coronation Hill. Development of the deposit and further exploration in the area has been restricted since the extension of the Kakadu National Park over the region was proposed in 1980. This conflict in land use purposes led to the most recent activity by the BMR in the area. In 1987 the BMR designed a program to provide the Australian government with an assessment of the 'Conservation Zone', an area within Stage 3 of the Kakadu National Park set aside for exploration, in terms of mineral reserves and future prospectivity. This program produced a detailed study of the geochronology, geochemistry, geophysics, structural geology, stratigraphy, sedimentology, volcanology, regional metamorphism and mineralisation of the South Alligator Valley and surrounding area (Valenta 1991; Wyborn et al. 1990; Warren and Kamprad 1990; Friedmann and Grotzinger 1994). As part of this program, Friedmann and Grotzinger (1994) carried out a detailed study of the stratigraphy, sedimentology and tectonic evolution of the El Sherana and Edith River Groups. The field work for this thesis study of felsic volcanism in the El Sherana Group was also carried out as part of this program.

CHAPTER 2

Facies and origin of the Pul Pul Rhyolite

2.1 INTRODUCTION

2.1.1 Stratigraphy and Distribution

The Pul Pul Rhyolite of the El Sherana Group is well exposed in the headwaters of the South Alligator and Katherine River systems, where it forms a thick volcanic succession striking around the southern margin of the Malone Creek Granite. It also extends discontinuously along the South Alligator Valley, northwest through El Sherana and Rockhole (abandoned uranium mines), and around the rim of a syncline surrounding the Mt Callanan Basin (Figure 2.1). Discontinuous exposure of the Pul Pul Rhyolite covers an area of approximately 55 x 20 km.

Walpole et al. (1968) first ascribed the term 'Pul Pul Rhyolite Member' of the 'Edith River Volcanics' to the rhyolitic volcanic rocks that overlie the Coronation Sandstone between Rockhole and Coronation Hill (abandoned uranium mines of the South Alligator Valley Mineral Field; Figure 2.1). Needham and Stuart-Smith (1985b) elevated the Pul Pul Rhyolite to formation status and placed it within their newly created El Sherana Group. They expanded the formation to include the thick felsic volcanic succession surrounding the Malone Creek Granite to the east, previously mapped as undifferentiated Edith River Volcanics by Walpole et al. (1968). The formation is named after Pul Pul Hill, a prominent peak in the South Alligator Valley (GR 383990). The type section is registered as Pul Pul Hill, but no description of it exists in the literature, and on the Stow 1:100 000 mapsheet, Pul Pul Hill is now mapped as part of the Coronation Sandstone (Stuart-Smith et al. 1988).

The Pul Pul Rhyolite is thickest around the southern and western margins of the Malone Creek Granite. In this area it comprises a package of welded ignimbrites (about 1 km thick), with minor non-welded ignimbrite, associated felsic intrusions and volcaniclastic sedimentary rocks (Figure 2.2). This facies association is similar to that

Figure 2.1: Interpreted solid geology of the South Alligator Valley region, Pine Creek Inlier, N.T. (adapted from Needham 1988), showing the distribution of the Pul Pul Rhyolite, El Sherana Group, and the location of the study area.

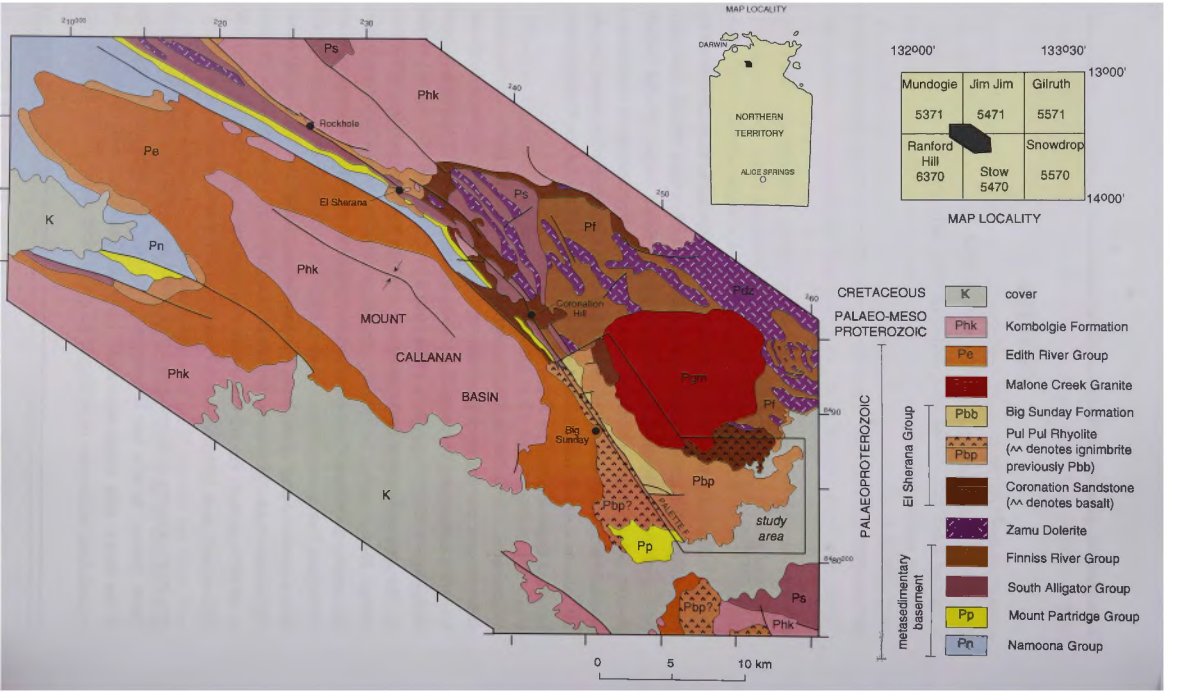

occurring in many modern silicic volcanic centres (e.g. Cas and Wright 1987), suggesting it may represent the remains of a volcanic centre within the Pul Pul Rhyolite (this possibility is explored further in Chapter 4). Beyond the northwest margin of the Malone Creek Granite, the Pul Pul Rhyolite has a different association of facies and is considerably thinner, attaining a maximum thickness of only 190m around Monolith (an abandoned U prospect near El Sherana). The predominant facies is a porphyritic rhyolite lava with a maximum thickness of about 130 m near Monolith, which is locally underlain by a thin (60-100m thick) layer of ignimbrite (Friedmann and Grotzinger 1994; Figure 2.3). The fact that rhyolite lavas do not generally travel far from their source vent (Walker 1973; Cas and Wright 1987) implies a second volcanic centre or eruption point probably existed in the Monolith area, where the rhyolite lava is thickest. The underlying rhyolitic ignimbrite may also have been sourced from this local eruption point, or it may represent an outflow unit that correlates with the thick ignimbrite pile adjacent to the Malone Creek Granite (see Chapter 4).

The Pul Pul Rhyolite overlies a major erosional surface which removed up to 100 m of the Coronation Sandstone stratigraphy (Friedmann and Grotzinger 1994). In places the Pul Pul Rhyolite overlaps the Coronation Sandstone to rest unconformably on the older Pine Creek Geosyncline Sequence. In the Malone Creek Granite region, this older basement sequence consists of metamorphosed greywackes, schists, phyllites and phyllitic siltstone of the Burrell Creek and Masson Formations and medium-grained tholeiitic dolerite of the Zamu Dolerite, which intrudes the Burrell Creek Formation as thick sills (Figure 2.1). In the El Sherana-Rockhole region the older basement comprises mainly the Koolpin Formation, and around the rim of the Mt Callanan Basin it consists of metasediments of the Namoona and Mount Partridge Groups.

2.1.2 Location and description of the study area

The study area covers the thick volcanic succession south of the Malone Creek Granite and north of the Palette Fault, where the Pul Pul Rhyolite is most fresh and best exposed (Figure 1.1, 2.1). The thinner succession to the northwest of this area is not included in the present study for two reasons. Firstly, Friedmann and Grotzinger (1994) provide detailed facies and petrographic descriptions of the Pul Pul Rhyolite in this region. Secondly, this area contains abundant U deposits of the South Alligator Valley Mineral Field (Needham 1988), and the volcanic rocks have been significantly affected by alteration related to U(Au-PGE) mineralisation (see Section 2.1.3). This alteration renders the volcanic rocks unsuitable for geochemical and geochronological analysis, and mineralogical changes have largely obliterated microtextures and primary mineralogy (Friedmann and Grotzinger 1994).

Figure 2..2: Geology of the Pul Pul Rhyolite, Stow Region, Pine Creek Inlier.

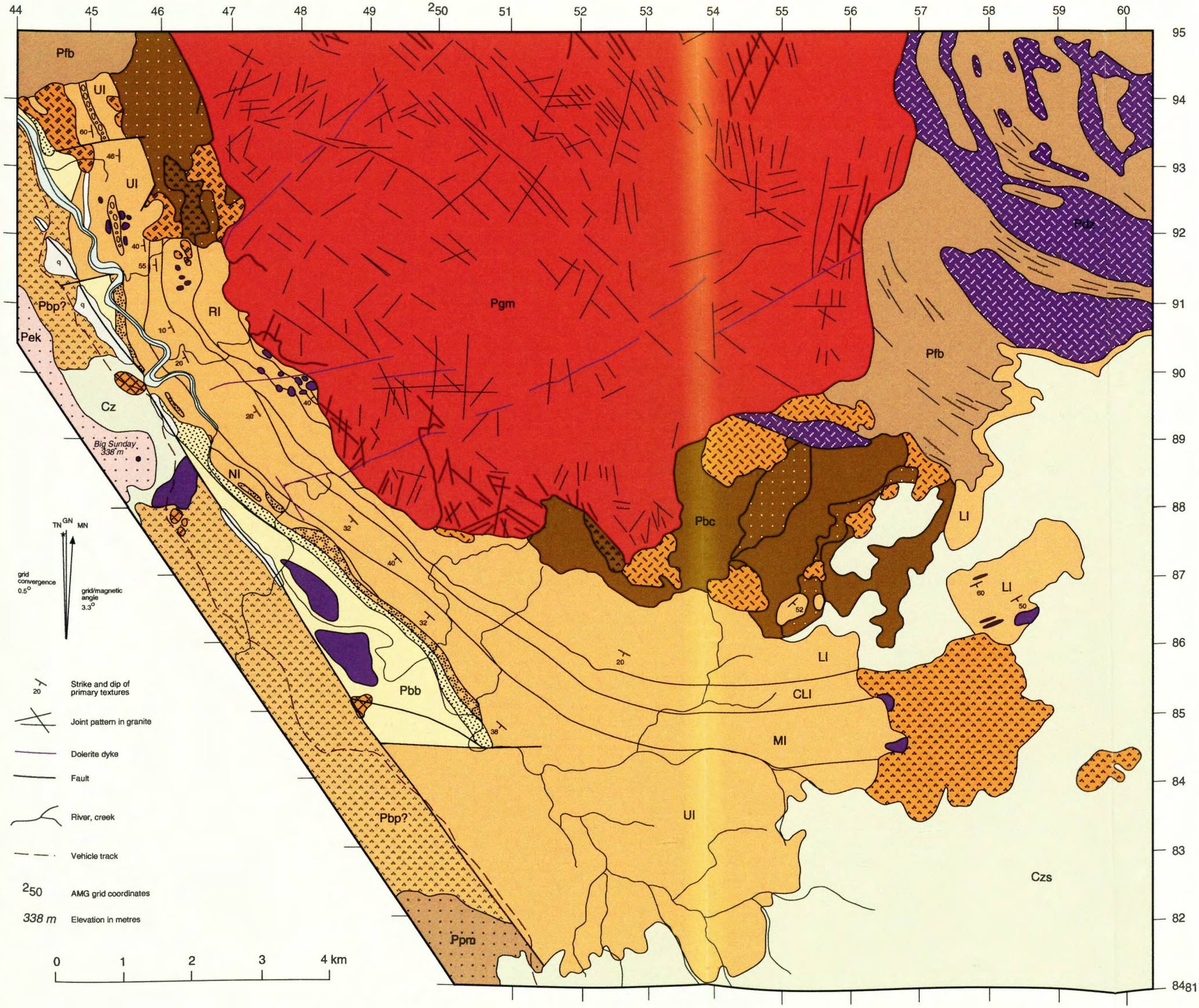

Map Legend

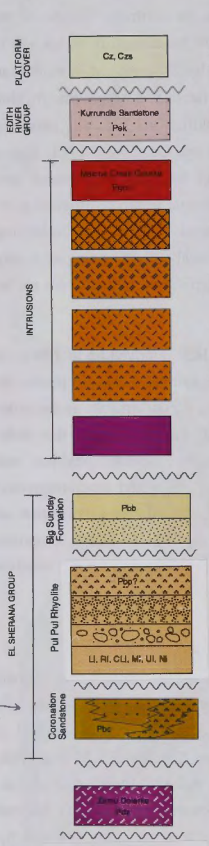

Cz: Skeletal soils, gradational red soils and yellow earth soils
Czs: Unconsolidated sand, ferruginous and clayey sand.

Medium to coarse lithic sandstone, polymictic pebble and cobble conglomerate, fine to coarse quartz sandstone, minor micaceous sandy siltstone.

Fine- to coarse-grained, even to porphyritic alkali feldspar granite with abundant quartz and greisen veins.

Megacrystic quartz monzonite porphyry.

Sparsely-porphyryic quartz monzonite porphyry.

Rhyolite porphyry.

Massive to flow banded, pink to brick red, fine-grained, aphyric to sparsely-porphyrytic rhyolite.

Medium- to coarse-grained dolerite and amygdaloidal dolerite.

Interbedded volcaniclastic siltstone and sandstone turbidite sequence.

Crystal-rich volcaniclastic sandstones, locally containing diffusely bound pumice-bearing horizons, and welded ignimbrite intraclasts.

Rhyolite and ignimbrite. Previously mapped as part of the Big Sunday Formation.

Interbedded fluvial sandstones, conglomerates and minor siltstones. Predominantly massive to diffusely stratified beds, with local planar and cross stratification.

Heterolithic co-ignimbrite boulder breccia (lag).

Ignimbrites. Ll = Lower Ignimbrite Member, Rl = Rheomorphic Ignimbrite, CLl = Cognate lithic-bearing Ignimbrite, Ml = Middle Ignimbrite Member, Ul = Upper Ignimbrite Member, Nl = Non-welded Ignimbrite.

Predominantly fine- to medium-grained basalt and amygdaloidal basalt. Dots denote medium- to coarse-grained arkosic sandstone and conglomerate. Inverted v's denote flow banded to autobrecciated high-Si basalts that display evidence of magma mixing and/or mingling (see Chapter 3).

Nimbuwah Event - regional deformation and lowgrade regional metamorphism ~ 1870 Ma

Massive medium to coarse grey quartz dolerite and foliated amphibolite.

Foliated fine to madium metafeldspathic greywacke, chlorite-muscovite quartz schist, phyllite and phyllitic sandstone.

Very coarse sericitic foliated quartzite and minor pebble conglomerate. Lenticular cross bedding common. Minor carbonaceous silty phyllite.

Figure 2.3: Fence diagram illustrating the stratigraphy of the El Sherana Group in the South Alligator Valley mineral field, northwest of the study area (adapted from Friedmann and Grotzinger 1994). The greatest preserved thickness of the Pul Pul Rhyolite in this region is in the Monolith-El Sherana area (~190m), where it comprises mainly coherent quartz-feldspar porphyry, interpreted to be a lava flow by Friedmann and Grotzinger (1994) .

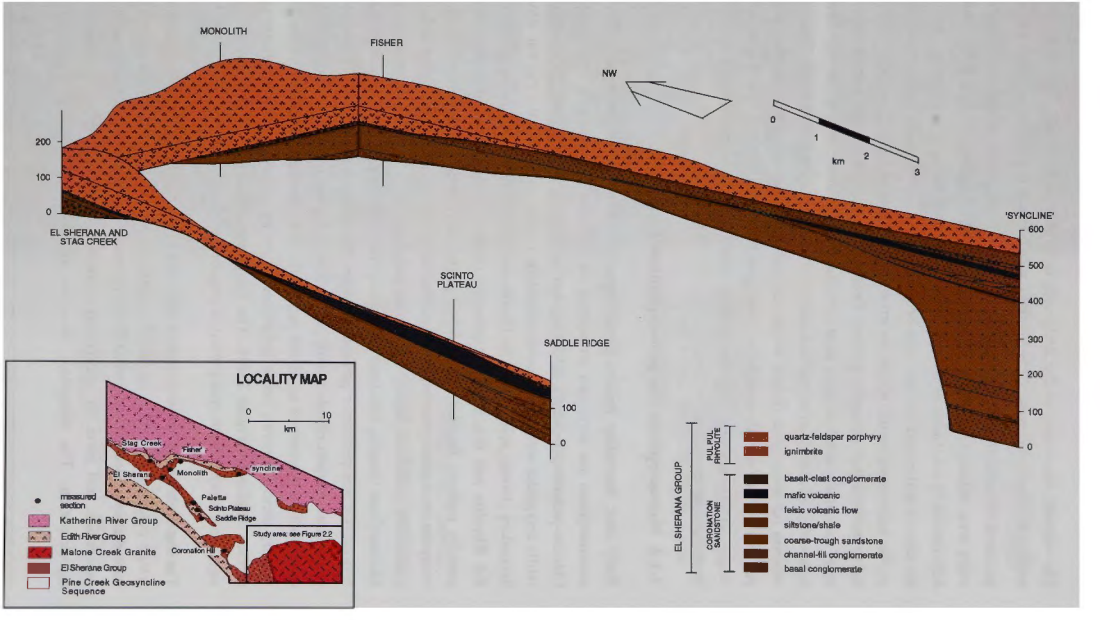

The volcanic succession in the study area is largely undeformed, and strikes openly around the southern margin of the Malone Creek Granite, dipping radially away from the granite at an angle of between 20-60°. It is reasonably exposed in the western half of the study area, although outcrop is discontinuous. The topography consists of undulating hills incised by a network of fluvial gullies. Outcrop is best exposed and most fresh on the sides of gullies and in some creek beds. The outcrop tends to be bouldery and sparse on the intervening crests, which are strewn with rubble and partly covered by soil and tall to medium-high perennial grasses. Detailed facies mapping was carried out in this area, and stratigraphic sections were measured through some units at the best available exposures. Further east (beyond the eastern termination of the Palette Fault; Figure 2.1), outcrop becomes more deeply weathered and discontinuous where the formation is partially buried beneath sandplains. The ignimbrite succession in this region remains largely undifferentiated, and stratigraphic boundaries are extrapolated, based on the limited available outcrop.

2.1.3 Metamorphism and post-depositional alteration

Study area: Secondary mineral assemblages consistent with lower greenschist facies metamorphism are developed throughout the volcanic succession in the study area. Chlorite-prehnite-pumpellyite-calcite±epidote±actinolite overprints the groundmass and infills amygdales within Coronation Sandstone basalts underlying the Pul Pul Rhyolite. Secondary chlorite, epidote, calcite, fluorite and sericite are recorded throughout the Pul Pul Rhyolite and Big Sunday Formation (Figure 2.4a-c). The secondary minerals partially replaces fiamme and feldspar grains in ignimbrites (Figure 2.4a,b), and overprint the matrix/groundmass of volcanic and sedimentary rocks (Figure 2.4c). The Coronation Sandstone basalts are contact metamorphosed immediately adjacent to the Malone Creek Granite, with local development of biotite and hornblende overprinting the regionally-developed lower greenschist facies metamorphic assemblage. There are few contact metamorphic effects recorded in the felsic volcanic rocks of the Pul Pul Rhyolite, apart from the presence of aplite and pegmatite veins emanating from the granite into the country rock. However, some ignimbrites samples collected near the granite contact contain amphibole (Figure 2.4d). The samples containing amphibole do not exhibit significant recrystallisation as a result of contact metamorphism.

The top of the volcanic succession is truncated by the northwest-trending Palette Fault, which outcrops as a resistant silicified strike ridge. Silicification is recorded in rocks immediately adjacent to the Palette Fault. Hematite alteration is common throughout the succession, and gives the matrix and fiamme of most ignimbrites a distinctive red discolouration. The ubiquitous hematite alteration is probably related to both

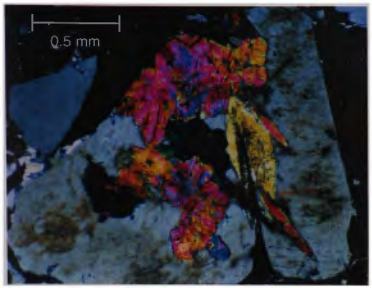

Figure 2.4a: Photomicrograph showing the replacement of K-feldspar by epidote. Sample 89123099; Upper Ignimbrite Member.

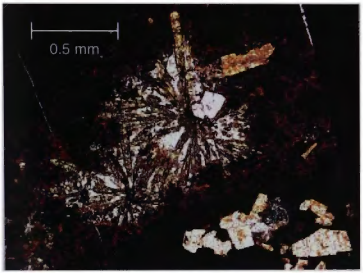

Figure 2.4b: Pumice clast, showing hematite alteration of the groundmass, and chlorite, illite and quartz replacing glomeroporphyritic crystal clusters. Sample 89123193d; Upper Ignimbrite Member.

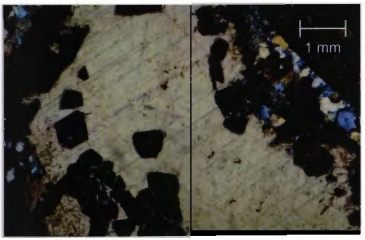

Figure 2.4c: Photomicrograph showing fluorite and calcite overprinting the ignimbrite matrix. Sample 89123106; Lower Ignimbrite Member.

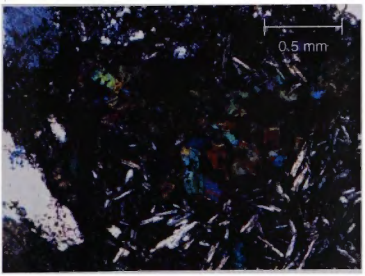

Figure 2.4d: Photomicrograph showing the development of amphibole (hornblende), resulting from contact metamorphism of ignimbrite near the margin of the Malone Creek Granite. Sample 89123191; Cognate lithic-bearing Member.

devitrification of matrix/groundmass and hydrothermal alteration by oxidised fluids associated with later faulting and mineralisation. Mesoscopic volcanic textures such as eutaxitic foliation and flow banding are well preserved in outcrop. The original glassy matrix/groundmass of volcanic rocks has been devitrified and hematised to form a very fine-grained microgranular quartz and feldspar mosaic. Microtextures such as relic welding textures are variably preserved.

South Alligator Valley Mineral Field: In the South Alligator Valley Mineral Field northwest of the study area, volcanic rocks within the Coronation Sandstone and Pul Pul Rhyolite have been significantly affected by alteration related to U(Au-PGE) mineralisation. Alteration zones extend over 1 km away from the mineralisation. The alteration is characterised by muscovite (sericite)-chlorite±kaolinite±hematite (Mernagh et al. 1998). Mg-metasomatism and the formation of late-stage Mg-rich chlorite is common. Geochemically, alteration is characterised by very high Fe^{3+}/Fe^{2+} and U/Th ratios, U and Mg enrichment and significant SiO_2, Na_2O, CaO and Th depletion, with enhancement of Ni and Cr in mafic rocks, Ba and P_2O_5 in feldspar-rich rocks and Mn in iron-rich rocks (Mernagh et al. 1998). Although felsic volcanic rocks still retain some recognisable macroscopic volcanic textures, microtextures and primary mineralogy are largely obliterated (Friedmann and Grotzinger 1994).

2.1.4 Research methods

The descriptions and interpretations of facies in this chapter are based on 1:25 000 and local 1:10 000 scale mapping of the outlined study area, and on stratigraphic sections measured through some units at the best available exposures (presented in Appendix A4). Sample locations are listed in Appendix A1, and geochemical data are presented in Appendix A2. Modal percentages quoted are based on point count data in Appendix A3, and average modal abundances for each ignimbrite unit, and for volcaniclastic sedimentary facies, are presented in Table 2.1. It is important to note that for the ignimbrite samples, which contain a wide range of particle sizes from ash- to cobble-sized grains, the modal percentages are not representative of the whole-rock lithic, pumice and matrix contents. Point counting only provides modal information for the interstitial matrix supporting the outsized lithic and pumice clasts, which comprises crystals, small lithics and pumice (sand- to gravel-sized clasts) and a fine-grained microgranular quartz and feldspar mosaic, representing a devitrified and recrystallised vitric matrix component. Lithic and pumice clasts over 1-2 cm in diameter are too large to be represented in thin sections and are therefore excluded from modal analyses. As a result, the modal percentages may underestimate the total lithic and pumice content of the ignimbrites. In contrast to the lithic and pumice contents, the crystal component of the ignimbrites is accurately represented by modal analysis.

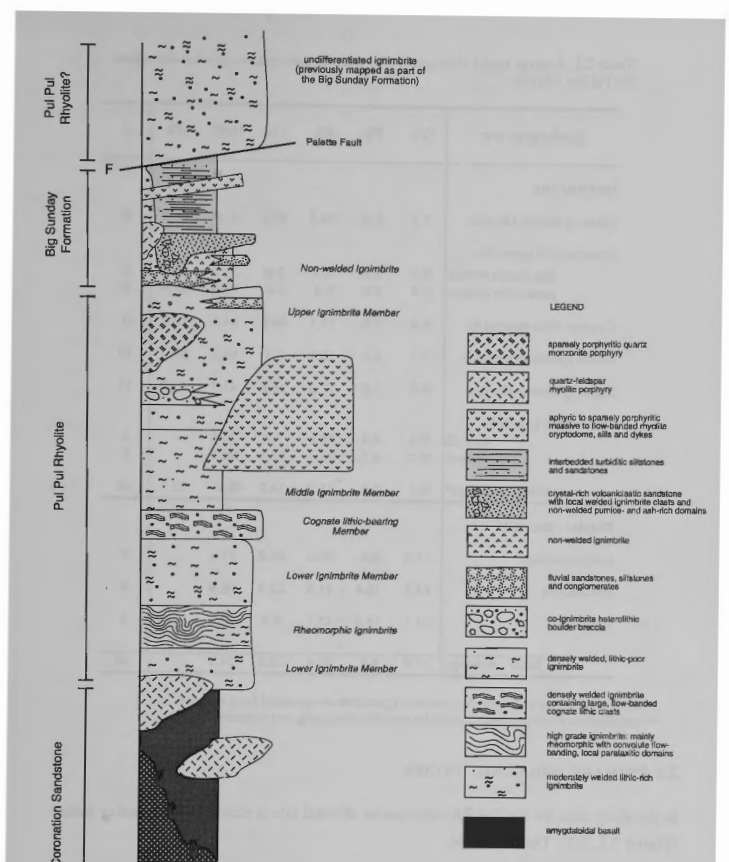

Figure 2.5: Simplified schematic graphic log depicting facies associations of the El Sherana Group in the study area. The total thickness of the Pul Pul Rhyolite is about 1 km. The ignimbrite succession is divided into informal units as discussed in the text. Note that ignimbrite overlying the Palette Fault is assigned tentatively to the Pul Pul Rhyolite, whereas it was previously assigned to the Big Sunday Formation (see Chapter 3).

Table 2.1: Average modal abundances of ignimbrite units and fluvial deposits within the Pul Pul Rhyolite. Q = quartz, F = feldspar, X = total crystals, L = total lithics, M = matrix, P = pumice

Stratigraphic unit	Q%	F%	X%	L%	Mat%	P%	n
Ignimbrites							
Lower Ignimbrite Member	8.0	5.4	14.5	24.9	41.7	18.9	8
Rheomorphic Ignimbrite							
flow folded domain	2.2	3.2	5.9	2.6	91.5	-	2
parataxitic domain	3.4	2.9	6.4	4.0	48.3	41.5	2
Cognate lithic-bearing Ig.	5.4	7.3	13.1	32.4	44.9	9.6	5
Middle Ignimbrite Member	3.2	6.5	10.1	3.4	56.5	30.0	10
Upper Ignimbrite Member	7.8	8.3	16.5	15.7	47.6	20.2	11
Non-welded Ignimbrite							
layer 2b	9.9	6.4	16.6	7.0	76.5	-	5
ground layer	21.3	11.4	32.7	29.6	37.8	-	5
total average*	6.3	6.7	13.5	14.3	52.6**	19.6	48
Fluvial deposits							
conglomerates	17.6	5.4	23.0	55.9	21.1		6
sandstones	24.5	12.4	37.5	23.6	38.9		8
siltstones	24.1	13.0	38.4	8.3	53.4		2
total average	21.9	9.8	32.2	33.8	34.0		16

* NB: ground layers within the Non-welded Ignimbrite are excluded from calculations
** calculation of average matrix excludes welded ignimbrite samples containing no recognisable pumice.

2.2 PRIMARY VOLCANIC FACIES

In the study area, the Pul Pul Rhyolite can be divided into a number of distinctive facies (Figure 2.2, 2.5). These include:

1. Primary fragmental volcanic facies, consisting of welded and non-welded ignimbrite, and co-ignimbrite breccias.

2. Secondary volcaniclastic facies.

3. Coherent intrusive facies, which are categorised into several subfacies on the basis of different mineralogy and geochemical composition. The subfacies comprise: (1) rhyolite porphyry stocks; (2) quartz monzonite porphyry stocks; (3) the Malone Creek

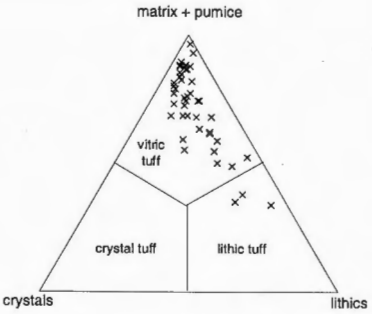

Figure 2.6: Classification of the Pul Pul Rhyolite ignimbrites after Schmid (1986).

Granite; (4) an aphyric to sparsely porphyritic fine-grained rhyolite which occurs as a large intrusive sill or dome and as smaller sills and dykes; and (5) late-stage dolerite dykes and intrusive bodies.

2.2.1 Welded Ignimbrites

Description: Welded ignimbrites comprise the main volcanic facies within the Pul Pul Rhyolite in the study area, forming a conformable sequence of up to 1 km preserved thickness. The Pul Pul Rhyolite contains five regionally mappable welded ignimbrite subunits (Figure 2.2, 2.5). The three thickest and most laterally extensive units are informally termed the Lower, Middle and Upper Ignimbrite Members. Two thinner, less extensive units are also defined and described; a densely welded to rheomorphic ignimbrite near the base of the succession (Rheomorphic Ignimbrite) and a thin ignimbrite unit containing abundant cognate lithic clasts, which locally outcrops between the Lower and Middle Ignimbrite Members in the centre of the study area (Cognate lithic-bearing Member). All welded ignimbrite units share the following characteristics:

1. They have a framework consisting of crystals, pumice and lithic fragments, and classify as vitric tuffs, using the classification system of Schmid (1981; Figure 2.6). Average modal proportions of crystal:lithic:matrix:pumice are about 13:14:49:23 (Table 2.1). That is, the ignimbrites contain roughly equal proportions of crystals and small (sand- to gravel-sized) lithic clasts. Outsized lithic and pumice clasts (pebble- to boulder-sized) have a heterogeneous distribution, and lithic breccias (layer 2bL lithic cocentration zones) and pumice-rich domains are recognised in some ignimbrite units.

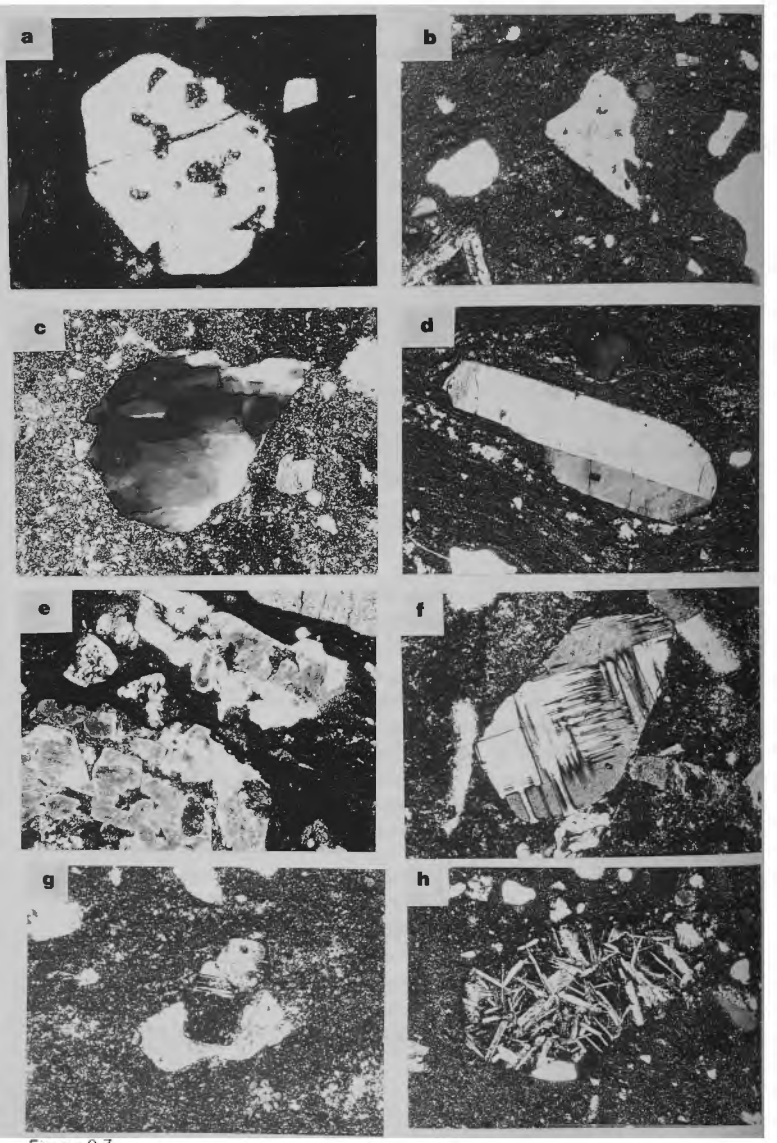

Figure 2.7

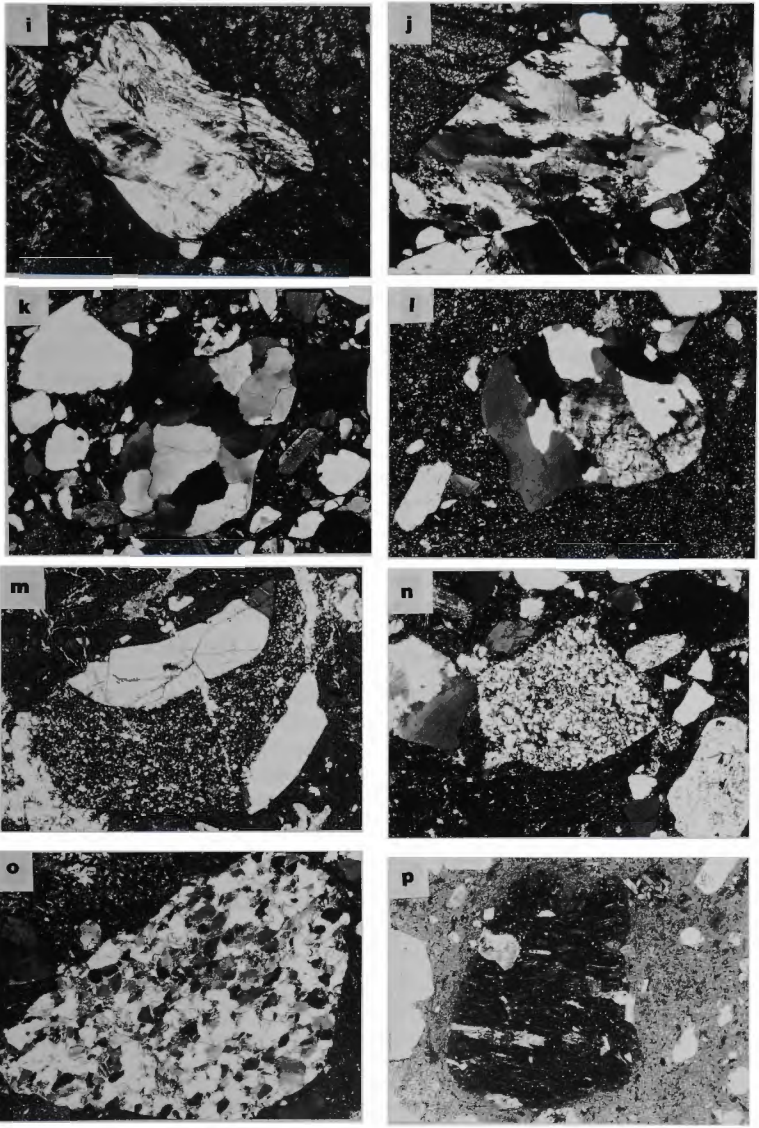

Figure 2.7

2. The crystal assemblage is dominated by K-feldspar, quartz and plagioclase. Quartz and feldspar crystals have an average grainsize of 0.25-0.5 mm, and range up to 4 mm in diameter.

   Both volcanic quartz and monocrystalline metamorphic quartz are recognised. The volcanic quartz exhibits bipyramidal euhedral or round-cornered, resorbed margins (Figure 2.7a), or displays angular, fragmental outlines (Figure 2.7b). Embayed crystals, reflecting magmatic resorption, are common (Figure 2.7a). The volcanic quartz is monocrystalline and undeformed, exhibiting straight to slightly undulose extinction, and is clear and free of inclusions. The monocrystalline metamorphic quartz consists of predominantly rounded grains (although some are angular) that exhibit strong undulose extinction indicative of high strain (Figure 2.7c). They generally contain vapour fluid inclusion trails that imply annealing of grain sutures at depth, and rutile inclusions are common.

   Feldspar occurs as euhedral to broken crystals, and is variably altered by sericite, chlorite, epidote and clay. K-feldspar is most common, and is commonly albitised. Some K-feldspar crystals exhibit simple twinning (Figure 2.7d). Resorption has produced rounded corners and strong embayments in some grains (Figure 2.7e). Some feldspars exhibit perthitic textures (Figure 2.7f). Smaller crystals of plagioclase (albite) are distinguished by the presence of multiple twinning, and glomeroporphyritic aggregates of feldspar are common (Figure 2.7g).

   Zircon, magnetite, and titanite (after ilmenite) occur as accessory mineral phases.

3. In order of predominance, lithic clasts include dolerite (Figure 2.7h), basalt, basement-derived composite quartz grains (Figure 2.7 i-l), rhyolite porphyry (Figure 2.7m), chert, which may represent the groundmass/matrix component of volcanic rocks (Figure 2.7n), sandstone (Figure 2.7o) and minor ignimbrite clasts (Figure 2.7p). The composite quartz grains may be highly strained and exhibit strong

Figure 2.7 (previous pages): Representative photomicrographs illustrating the most common crystal and lithic species that occur within the ignimbrites and fluvial deposits of the Pul Pul Rhyolite, and the overlying crystal-rich volcaniclastic sandstones (CRVS) of the Big Sunday Formation, as described in the text of Chapters 2 and 3. The photomicrographs are taken from various representative samples of all three facies. (a) euhedral volcanic quartz exhibiting resorption features; (b) fragmented, angular quartz crystal; (c) basement-derived metamorphic quartz exhibiting strong undulose extinction; (d) broken euhedral K-feldspar crystal; (e) resorbed K-feldspar crystals; (f) perthite; (g) composite plagioclase aggregate (glomeroporphyritic cluster); (h) dolerite; (i) highly strained basement clast (gneiss or mylonite); (j) strained metamorphic basement clast (composite quartz) with sutured internal grain boundaries; (k) & (l) less strained metamorphic basement clasts (composite quartz) exhibiting straighter internal grain boundaries and a more equigranular appearance; (m) rhyolite porphyry; (n) fine-grained chert (ignimbrite matrix or porphyry groundmass); (o) sandstone; and (p) welded ignimbrite.

undulose extinction and sutured internal grain boundaries (Figure 2.7 j,k), or have a more equigranular appearance, containing larger interlocking grains that exhibit straight extinction (Figure 2.7l,m). In hand specimen and outcrop they appear as small, milky-white pebbles. Both types are interpreted to be derived from the metasedimentary basement unconformably underlying the ignimbrite succession.

The lithic fragments are angular to rounded, and range in diameter between 0.5-30 cm. Coarse lithic clasts are generally well to moderately rounded, whereas small lithic clasts are more angular in shape. The distribution of small lithic clasts (< 5 cm in diameter) is fairly even throughout the ignimbrite succession. The proportion of outsized lithic clasts (5-25 cm in diameter) is more variable, and can range from 5-20% within pumiceous ignimbrite facies, with some notable lithic concentration zones (layer 2bL) containing 25-40% lithics. Pumice clasts within lithic concentration zones are generally less than 2 cm in length. Outsized pumice clasts may be pulverised to fine ash in lithic-rich domains, whereas in lithic-poor domains, abrasion of pumice is reduced.

4. The densely welded ignimbrites display a prominent planar foliation defined by aligned, flattened pumice clasts that commonly have wispy, flame-like terminations (fiamme). The fiamme usually range between 0.5-20 cm in length, with larger clasts in local pumice concentration zones attaining maximum dimensions of 100x40 cm. A simple compaction factor obtained by measuring the length:width ratio of fiamme yielded results between 5 and 10. Larger clasts in pumice concentration zones generally display higher degrees of attenuation, attaining a maximum value of 22. The pumice clasts contain fewer crystals than the host ignimbrites (about 2-5%), indicating there has been loss of vitric ash during emplacement of the ignimbrites (Sparks and Walker 1977). The phenocryst population of the pumice clasts is dominated by euhedral equant, tabular and lath-shaped feldspar crystals and glomeroporphyritic feldspar clusters (predominantly K-feldspar), with subordinate quartz phenocrysts. In contrast, the host ignimbrite contains quartz and feldspar in roughly equal proportion, suggesting that much of the quartz in the ignimbrite is of xenocrystic origin. This accords with the metamorphic origin of about half the quartz grains (basement-derived). The size of the feldspar and quartz crystals in the pumice is comparable to unfragmented crystals in the surrounding matrix, averaging 0.5 mm and ranging up to about 2 mm in diameter (glomeroporphyritic clusters up to 4 mm). Highly fragmented crystals in the ignimbrite matrix are naturally smaller. In thin section the pumice clasts have a spherulitic texture (Figure 2.8), or comprise a microgranular mosaic of quartz and hematite-stained feldspar, that is characteristic of granophyric crystallisation of

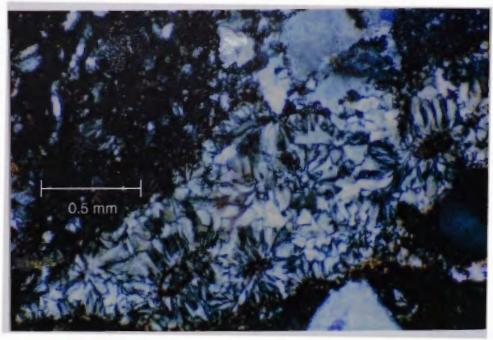

Figure 2.8a: Pumice clasts exhibiting extensive spherulitic crystallisation. Sample 89123099; Upper Ignimbrite Member.

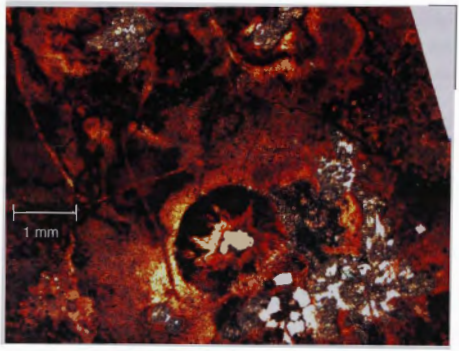

Figure 2.8b: Spherulitic crystallisation locally overprinting the fabric of a pumice clast. In this case, spherulites have nucleated on euhedral phenocrysts. Sample 89123193d; Upper Ignimbrite Member.

glass. The degree of internal granophyric or spherulitic crystallisation is more intense than that observed in the surrounding ignimbrite matrix, which is a common characteristic of pumice (e.g. Briggs 1976). Hematite, chlorite, epidote, calcite and/or sericite alteration of pumice is common.

5. The matrix of the ignimbrites is usually red to maroon coloured and aphyric in outcrop and hand specimen. It consists of devitrified volcanic glass altered to a fine-grained microgranular quartz and feldspar mosaic, with disseminated sericite and chlorite. This granophyric crystallisation completely overprints any pre-existing vitriclastic textures in some samples. However, a relic welding texture is commonly preserved in thin section, defined by a strong compaction of pumice clasts and shards, especially near the edges of crystals and lithic clasts (eutaxitic texture). In some ignimbrite units, where shards display an extreme degree of attenuation, a parataxitic texture is defined (Cognate Lithic-bearing Member, Middle Ignimbrite Member and parts of the Rheomorphic Ignimbrite).

Lower Ignimbrite Member

The Lower Ignimbrite Member occurs at the base of the ignimbrite succession, outcropping around the margin of the Malone Creek Granite and unconformably overlying basalts, rhyolite porphyries, sandstones and conglomerates of the Coronation Sandstone (Figure 2.2, 2.5). Over much of its strike length, the Lower Ignimbrite Member is intruded by the Malone Creek Granite and its thickness cannot be estimated. However, it is approximately 300 m thick where the basal contact with the Coronation Sandstone is exposed. To the northwest, the Lower Ignimbrite Member terminates abruptly against a buttress unconformity comprising a vertical wall of Coronation Sandstone, which may represent original palaeotopography, or a pre-existing fault scarp. In the eastern half of the study area, the unit is largely buried beneath sandplains and outcrop is weathered and discontinuous.

The Lower Ignimbrite Member contains an average modal abundance of 14% crystals, 24% lithics, 42% matrix and 19% pumice, with quartz and feldspar in roughly equal proportion (Table 2.1). Lithic clasts comprise mainly dolerite and basalt. Rhyolite porphyry, sandstone and metasedimentary basement clasts are also abundant. The lithic clast assemblage matches the rock types of the underlying succession. Basalt, sandstone and rhyolite porphyry clasts are likely to be derived from the Coronation Sandstone, dolerite from the Zamu Dolerite, and pelites, psammite and schistose fragments from the Burrell Creek Formation, Masson Formation and/or Koolpin Formation. No epiclasts of the adjacent Malone Creek Granite were recorded, supporting the interpretation that granite intrusion postdated ignimbrite emplacement (see Section 2.4.4).

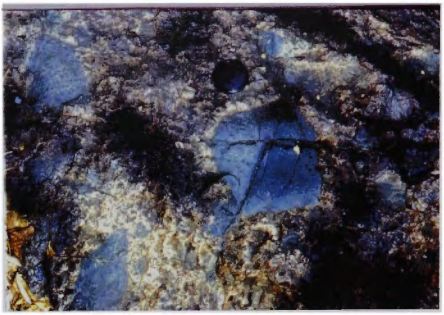

Figure 2.9a: Layer 2bL lithic concentration zone within the Lower Ignimbrite Member, comprising mainly outsized dolerite clasts. GR 248500 8488700.

Figure 2.9b: Outsized rhyolite porphyry clast within the Lower Ignimbrite Member, also showing a planar foliation defined by attenuated pumice clasts. The eutaxitic fabric deforms around the clast. The large, red fiamme are typical of this ignimbrite unit (and also the Upper Ignimbrite Member). GR 252500 8485800.

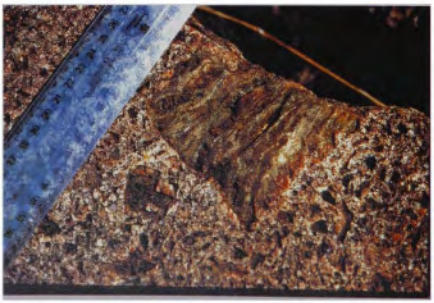

Figure 2.9c: Outsized metamorphic basement clast (perhaps derived from the Burrell Creek Formation) in the Lower Ignimbrite Member. The unit is less welded at this locality (c.f. Figure 2.9b), and small pumice clasts are not significantly attenuated. GR 258600 8486500.

The lithic clasts range up to 30 cm in diameter, and are sub-angular to rounded in shape. Small clasts (< 5 cm in diameter) are abundant and evenly distributed throughout the unit. Outsized clasts (5-30 cm) have a heterogeneous distribution. Layer 2bL lithic breccias with lithic concentrations of 25-40% are locally recorded near the base of the unit (Figure 2.9a), and isolated outsized lithic clasts are dispersed throughout the overlying pumiceous ignimbrite facies (Figure 2.9b,c). The basal lithic breccias could not be traced laterally due to outcrop discontinuity, so the number of layers, their lateral extent and precise stratigraphic position remains equivocal. The dominant clast type varies along strike. In the centre of the study area the lithic breccias contain abundant basalt, sandstone and rhyolite porphyry clasts derived from the underlying Coronation Sandstone (Figure 2.9a,b), whereas further east, where the unit outcrops in the Recent sandplains, the clast assemblage comprises dolerite and metasedimentary basement clasts (Figure 2.9c).

In fresh outcrop and hand specimen the ignimbrite is red to red-brown in colour, weathering to a buff colour. Large (5-15 cm) pumice clasts are a distinctive red colour, and are generally flattened to define a well developed eutaxitic texture (Figure 2.9b), and welding microtextures (plastically deformed shards and pumice) are commonly preserved in thin section. However, the degree of welding is variable. In some outcrops in the east of the study area, the ignimbrite is only slightly welded, with pumice clasts only slightly compacted (Figure 2.9c). In thin section, some shards within these less welded ignimbrites retain original cuspate shapes. However, those adjacent to crystal and lithic components show the effects of slight welding and are partly deformed and compacted. No non-welded zones were recorded in the Lower Ignimbrite Member. Welding zonation patterns within the unit could not be delineated due to discontinuity and lack of outcrop.

Rheomorphic Ignimbrite

The Rheomorphic Ignimbrite occurs within the Lower Ignimbrite Member in the northwest of the study area, outcropping discontinously over a strike length of 3 km (Figure 2.2). Outcrop of the Rheomorphic Ignimbrite is subordinate, and confined only to some creek beds. The unit has a apparent thickness of about 100 m. As with the Lower Ignimbrite Member, the Rheomorphic Ignimbrite terminates against a buttress unconformity against a vertical wall of Coronation Sandstone to the northwest. It is cross cut by the Malone Creek Granite to the east, so its original lateral extent cannot be estimated. However, the unit does not reappear further east (where the basal contact of the Pul Pul Rhyolite is exposed), suggesting it pinches out in this direction. The contacts between the Lower Ignimbrite Member and the Rheomorphic Ignimbrite are sharp, not gradational, and the two units differ markedly in appearance and composition. The

Figure 2.10a: Rheomorphic flow folding in a hand specimen of weathered Rheomorphic Ignimbrite. Small angular dolerite clasts occur within the facies, which supports its interpretation as a high-grade rheomorphic ignimbrite, as opposed to a coherent, flow-banded lava or cryptodome. Sample 89123179, GR 247100 8490600.

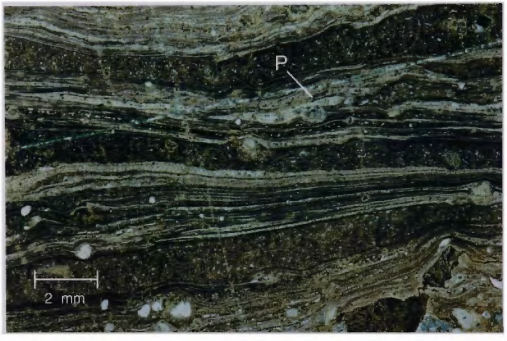

Figure 2.10b: Photomicrograph of the Rheomorphic Ignimbrite, showing a gradation in welding density from a parataxitic texture (at the base of the photograph) into a rheomorphic texture with well developed flow layering. Small, highly attenuated pumice clasts can be detected between the flow layers (P). Sample 89123090.

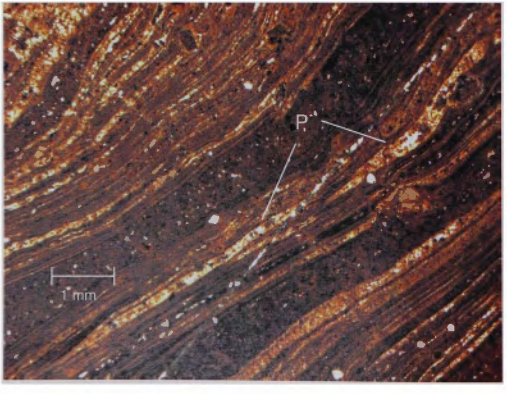

Figure 2.10c: Close-up of the rheomorphic domain in Figure 2.10b, showing in more detail, the low aspect lenticular terminations of highly attenuated pumice clasts within flow bands.

Rheomorphic Ignimbrite is more vitric than the adjacent Lower Ignimbrite Member (~90% vitric material (pumice+matrix) c.f. 67%; Table 2.1), has a significantly lower crystal and lithic content and is devoid of outsized lithic and pumice clasts. A higher proportion of crystals occur as euhedral, unbroken grains. These features suggest that the Rheomorphic Ignimbrite does not represent a more intensely welded rheomorphic zone within the Lower Ignimbrite Member, but is instead a separate entity, representing a discrete eruption and depositional event. The local occurrence of the Rheomorphic Ignimbrite within the Lower Ignimbrite Member suggests that the latter comprises at least two flow units, and may contain several more, although there is no other definitive evidence that this is the case (e.g. intercalated epiclastic deposits, indicative of a time interval between successive flows).

The Rheomorphic Ignimbrite is a dense, finely flow banded rock (laminae are generally $\leq$ 1 mm), that locally exhibits small-scale flow folds with centimetre-scale wavelengths (Figure 2.10a). Flow bands alternate pink and brown in colour in fresh outcrop. Modal abundances indicate the unit comprises about 91% matrix (including attenuated pumice), 6% crystals and crystal fragments (with quartz and feldspar in roughly equal proportion) and 3% small lithic clasts up to 2 cm in diameter (mainly dolerite). Due to the absence of outsized lithic and pumice clasts ($\geq$ 5 cm in size), the modal percentages quoted for this unit are a reasonable estimate of the whole rock abundance of each component. The unit is similar in appearance to the Middle Ignimbrite Member (described below), which is also densely welded, and contains small pink fiamme in a brown-coloured matrix. Both units are vitric in appearance, containing only scattered framework grains and small lithic fragments.

The flow banded component of the Rheomorphic Ignimbrite grades locally into less densely welded parataxitic domains, in which extremely attenuated shards are recognised, appearing as long, narrow lenses that define a prominent planar foliation (Figure 2.10b). Within the flow banded domains, shards have been completely smeared into laminations and are no longer discernible. However, highly attenuated fiamme are recognised between the flow bands in thin section (Figure 2.10b,c).

The gradation between flow banded and parataxitic textures, and the presence of pumice, fragmental crystals and angular lithic clasts, indicate that this unit is a high grade rheomorphic ignimbrite rather than a lava flow (e.g. Branney et al. 1992; Branney and Kokelaar 1992).

Figure 2.11a: Flow banded cognate lithic clasts showing a compaction alignment near the top of the unit. The juvenile clasts have a fluidal form, and exhibit ragged, wispy terminations. GR 247600 8489600.

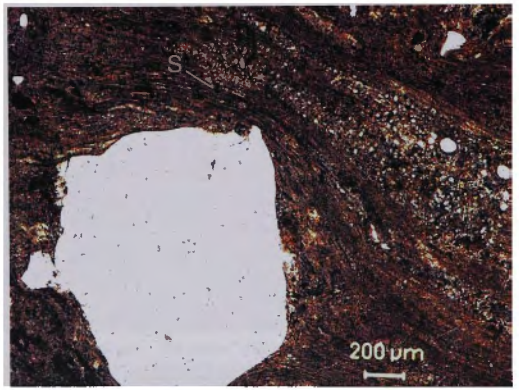

Figure 2.11b: In thin section, the Cognate lithic-bearing Member exhibits strong compaction and welding of pumice and shards, especially near the edges of crystals. Shards (S) are compacted to form narrow lenses, defining a parataxitic texture. Note also, the angularity of the crystal and lithic fragments. Sample 89123052.

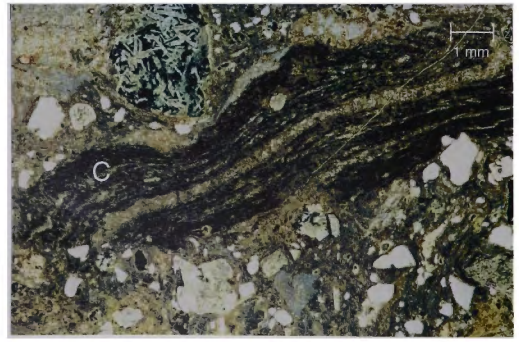

Figure 2.11c: Photomicrograph of a cognate lithic clast (C), showing the fine flow banding and scattered euhedral feldspar crystals. Sample 89123180.

Cognate lithic-bearing Member

A distinctive welded ignimbrite unit containing abundant large, flow banded clasts, outcrops conformably between the Lower and Middle Ignimbrite Members (Figure 2.11a). The unit varies in thickness along strike, ranging from about 20-90 m. The flow banded clasts are confined exclusively to this unit, and constitute about 15-30% of the total volume. The clasts are evenly distributed throughout the unit, apart from an upward decrease in clast frequency in the top 10 m. The unit also contains outsized dolerite and rare sandstone and rhyolite porphyry lithics (5-10 cm in diameter), which occur as isolated clasts or in small local concentrations near its base. The unit contains small, pink-coloured pumice clasts (up to 5 cm), similar to those in the overlying Middle Ignimbrite Member (described below). No outsized pumice clasts were observed. On average, the ignimbrite comprises 13% crystals, 30% lithics, 45% matrix and 12% pumice, in modal abundance. The ignimbrite matrix exhibits well preserved, parataxitic welding microtextures in which shards and small clasts of tube pumice are extremely attenuated, especially near the margins of crystals and lithic clasts (Figure 2.11b).

The flow banded clasts range from 2 to 25 cm in diameter, and commonly display irregular, fluidal outlines, with ragged, wispy terminations. At the base of the unit the clasts are chaotic and randomly oriented and folded. Up section they flatten out and align with the strike of the unit (Figure 2.11a). The clasts are non-vesiculated, and contain a sparse population of phenocrysts (~2-5%) comprising mainly glomeroporphyritic feldspar clusters (K-feldspar and/or plagioclase) and euhedral feldspar crystals (predominantly K-feldspar), with subordinate quartz crystals. The size of the crystals in the clasts is similar to euhedral crystals in the surrounding ignimbrite matrix (fragmented crystals in the ignimbrite matrix are slightly smaller). Glomeroporphyritic feldspar clusters are up to 5 mm in size. Euhedral crystals average about 0.5 mm and range up to 2 mm in diameter. The groundmass of the clasts comprises a recrystallised mosaic of quartz and feldspar, similar to that of the surrounding ignimbrite matrix, and the flow bands are defined by variable degrees of granophyric crystallisation (i.e. alternating fine- and coarser-grained bands; Figure 2.11c). Some clasts exhibit a microspherulitic texture, indicating an original dense glassy nature.

The flow banded clasts are unlike any lithofacies observed in successions immediately underlying the ignimbrite pile, suggesting they are not accidental lithic fragments. An interpretation of the clasts as cognate rather than accessory lithic fragments is supported by: (1) a crystal population corresponding to that of vesicular pumice clasts within the

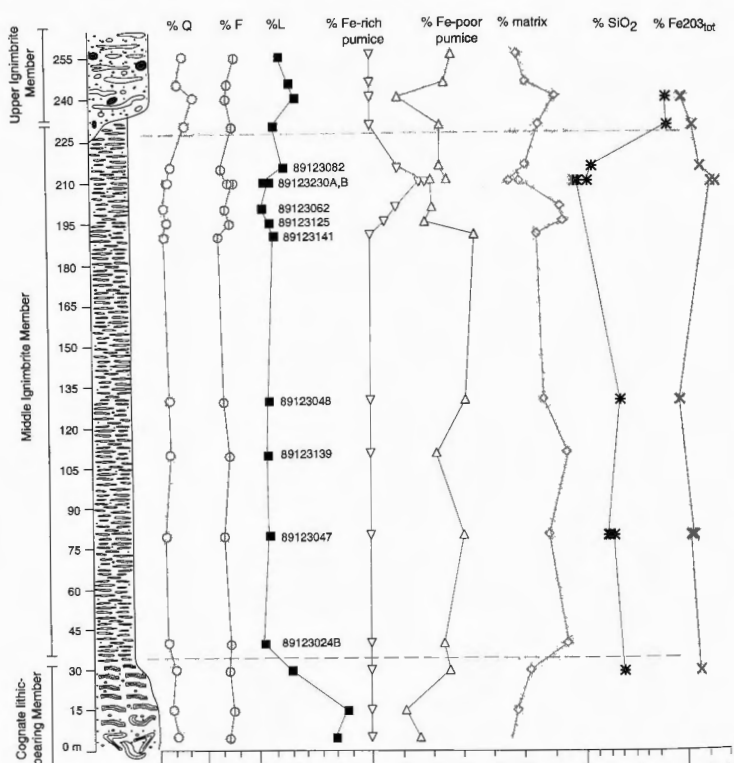

Figure 2.12: Measured section through the Middle Ignimbrite Member (GR 484882-478880) showing variation in crystal, lithic, matrix and pumice contents. The unit is homogeneous in appearance, and densely welded from base to top. There is very little compositional variation throughout the unit apart from an influx of Fe-rich pumice in the top 20 m, which corresponds with a slight change in silica and Fe content.

ignimbrite units; (2) the local development of spherulites, indicating an original glassy groundmass; and (3) the fluidal outlines of the clasts, reflecting incorporation into the pyroclastic flow in a semi-consolidated state. Cognate lithic fragments are dense, non-vesiculated juvenile magmatic fragments derived from solidified parts of the erupting magma, such as magma chilled against the conduit or magma chamber walls, or portions of magma that crystallised in the magma chamber prior to vesiculation and explosive volcanism.

Middle Ignimbrite Member

The Middle Ignimbrite Member conformably overlies the Cognate lithic-bearing Member, and forms a distinctive thick, tabular unit about 200 m thick, in the middle of the ignimbrite succession. To the northwest the Middle Ignimbrite Member terminates against a buttress unconformity, against a vertical wall of Coronation Sandstone, and to the east it is intruded by a rhyolite cryptodome or sill (Figure 2.2).

The Middle Ignimbrite Member has a markedly different appearance and composition to the two other laterally extensive ignimbrite sheets (the Lower and Upper Ignimbrite Members), and therefore provides an excellent marker horizon within the ignimbrite succession. The main differences are:

(1) it is less oxidised and altered (hematised), and the matrix appears brown, rather than red in colour in outcrop and hand specimen;

(2) it has a more homogenous appearance, exhibiting no vertical or lateral variation in crystal, lithic and pumice clast contents, and containing no layer 2bL lithic breccias (Figure 2.12);

(3) it is more densely welded, and exhibits a compaction layering and well developed columnar jointing (Figure 2.13a,b). The unit is densely welded from base to top, and exhibits no welding zonation;

(4) it has a lower lithic content, averaging 3.4%, (compared with 16-30% in the Lower and Upper Ignimbrite Members and the underlying Cognate lithic-bearing Member), and the lithic fragments are much smaller (< 2 cm in diameter c.f. 5-30 cm);

(5) it is more vitric in composition and appearance. Pumice+matrix (ash) contents range between 81-90%, compared with 35-75% in layer 2b and 2bL deposits of the Lower and Upper Ignimbrite Members, and 76-82% in layer 2bP deposits of the Upper Ignimbrite Member (Appendix A3);

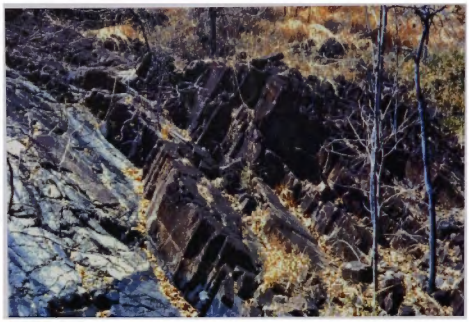

Figure 2.13a: Profile of well developed columnar jointing near the top of the Middle Ignimbrite Member. The unit is densely welded from its base to its top, and exhibits no welding zonation. GR 247200 8488800.

Figure 2.13b: Plan view of the columnar jointing in Figure 2.12a.

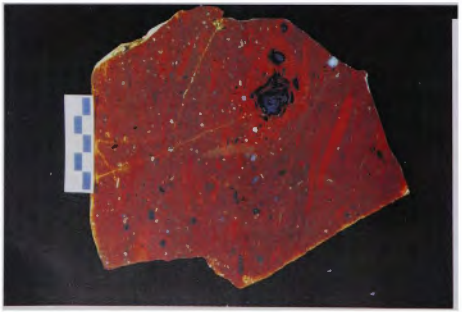

Figure 2.13c: Hand specimen of the Middle Ignimbrite Member, showing compaction of the small, pink fiamme typical of the unit, and the presence of rare, small lithic clasts. The size and colour of the fiamme differ markedly from those of the Lower Ignimbrite Member (Figure 2.9b) and Upper Ignimbrite Member (Figure 2.14a). Sample 89123055.

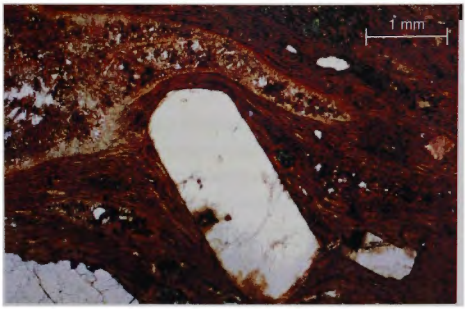

Figure 2.13d: Photomicrograph of the densely welded Middle Ignimbrite Member, showing extreme deformation and compaction of shards and pumice clasts around the margin of a euhedral K-feldspar crystal (parataxitic texture). Note that granophyric crystallisation is coarser-grained in the pumice clast than in the surrounding matrix. Sample 89123048.

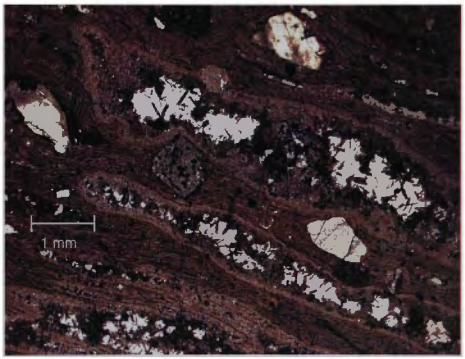

Figure 2.13e: Photomicrograph of the most common pumice type, showing granophyric crystallisation becoming coarser-grained towards the centre of the clast, and the presence of cavities containing drusy K-feldspar laths, infilled with large, interlocking quartz grains. Sample 89123048.

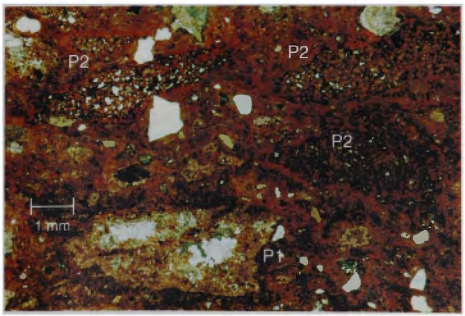

Figure 2.13f: Photomicrograph showing the two pumice clast types; the most common clast type, as depicted in Figure 2.13e (P1), and the less common Fe-rich, hematite-stained pumice clasts (P2), which only occur in the top 20 m of the unit. Sample 89123230.

(6) pumice clasts are a distinctive pink colour, quite different in appearance and considerably smaller than the large red fiamme in the Lower and Upper Ignimbrite Members, which average 5-20 cm in length. The pink pumice clasts are generally less than 1-2 cm, but range up to 5-8 cm in length (Figure 2.13c).

(7) the unit contains more feldspar than quartz in the framework (about 3% quartz and 7% feldspar), whereas the other ignimbrite units generally contain roughly equal proportions of these minerals (Table 2.1). This mineralogical difference is reflected in the geochemistry of the Middle Ignimbrite Member, which has a lower SiO_2 content and is less fractionated than the other ignimbrite units (see Section 2.2.4).

The Middle Ignimbrite Member contains 56.5% matrix, 30% pumice, 10.1% crystals and 3.4% lithics (mainly dolerite) in average modal abundance (Table 2.1). As with the Rheomorphic Ignimbrite, the unit is devoid of outsized lithic and pumice clasts, so the quoted modal percentages are a reasonable estimate of the whole rock abundance of each component. The average crystal content of the unit is also slightly lower than other units, apart from the Rheomorphic Ignimbrite (Table 2.1), and the crystals are generally less fragmented, with a higher proportion of grains retaining their euhedral shape and occurring as glomeroporphyritic clusters. The matrix exhibits well preserved, strongly developed welding microtextures, in which plastically-deformed shards and pumice exhibit an extreme degree of attenuation (Figure 2.13d). The shards appear only as narrow lenses defining a prominent planar foliation, and original cuspate and tricuspate outlines are obscured, defining a parataxitic welding fabric (Figure 2.13d).

In thin section, two types of pumice can be distinguished on the basis of slight compositional and textural differences. The most common type exhibits granophyric recrystallisation of the original glassy groundmass, resulting in a mosaic of quartz and feldspar that is coarser-grained than that observed in the surrounding ignimbrite matrix (Figure 2.13d,e). Some clasts are finely banded, with the layers defined by variable degrees of crystallisation. Others exhibit an increase in grainsize of the quartz-feldspar mosaic towards the centre of the clast (Figure 2.13e). Many clasts contain cavities rimmed by small, drusy alkali feldspar laths, and infilled with coarse, interlocking quartz grains (Figure 2.13e). The second type of pumice is comparatively rare, and is most abundant in samples collected from the top 20 m of the unit (Figure 2.12). The clasts exhibit a higher degree of hematite alteration (Figure 2.13f), reflecting a higher original Fe content. The Fe-rich pumice clasts also exhibit granophyric textures, but are devoid of the cavities prevalent in the more common pumice type. Both pumice types have a similar phenocryst assemblage, comprising about 5% euhedral feldpar crystals (and minor quartz) and glomeroporphyritic clusters of feldspar.

Upper Ignimbrite Member

The Upper Ignimbrite Member conformably overlies the Middle Ignimbrite Member over most of the study area. In the northwest, however, the underlying ignimbrite units are absent, and the Upper Ignimbrite Member unconformably overlies lithofacies of the Coronation Sandstone. To the east, it is intruded by a rhyolite cryptodome or sill (Figure 2.2). The top of the ignimbrite is irregular with a high relief suggesting the unit has been significantly eroded. It therefore varies markedly in thickness along strike, and is thinnest in the centre of the study area (60 m) where it is overlain by a non-welded ignimbrite and incised by fluvial channels and lacustrine deposits. To the west and east of this central eroded area, the unit attains a maximum thickness of about 500 m. As with the Lower Ignimbrite Member, the Upper Ignimbrite Member is red in colour in outcrop and hand specimen, and has a well developed planar foliation or eutaxitic texture, defined by large attenuated red pumice clasts. These are commonly flame-like in appearance, with ragged wispy terminations (Figure 2.14a). Columnar jointing is locally developed.

Modal analyses indicate that the framework consists of euhedral to fragmental crystals of quartz and feldspar in equal proportion (~8% each), small angular lithics (~10% and up to ~45% in lithic concentration zones), and small pumice clasts (~20-30%) in a devitrified aphanitic matrix (45-60%). Pumice+matrix values are lower in lithic concentration zones (averaging 55% c.f. 75%). In many samples welding microtextures comprising plastically deformed shards and tube pumice are excellently preserved (Figure 2.14b,c). Shards are fluidally deformed but not highly attenuated, and clear cuspate and tricuspate morphologies are visible, defining a eutaxitic, as opposed to parataxitic, welding fabric (c.f. the Middle Ignimbrite Member; Figure 2.13d).

The Upper Ignimbrite Member is heterogeneous, and pumice and lithic contents are highly variable. Several regionally mappable lithic- and pumice-rich domains were delineated in the northwest region of the study area (Figure 2.15). An 80 m thick lithic-rich ignimbrite, occurs near the base of the unit, outcropping over a strike length of about 2 km before lensing out to the south. It is locally overlain by the co-ignimbrite boulder breccia described in Section 2.2.2 (Figure 2.16b). The lithic-rich ignimbrite has a distinctive grey colour and gravelly appearance in outcrop (Figure 2.16c,d), and contains relatively low concentrations of small pumice clasts (< 5 cm), which are not greatly compacted. The large red fiamme that characterise the Upper Ignimbrite Member are absent. The lithic-rich ignimbrite contains several layer 2bL lithic breccias, 1-2m thick, which contain about 25-35% outsized lithic clasts, in a matrix-supported configuration (Figure 2.16d). The clasts are dominantly large sub-rounded to rounded dolerite clasts, with subordinate rhyolite porphyry and sandstone clasts. They average about 5 cm and

Figure 2.14a: Eutaxitic texture in the densely welded Upper Ignimbrite Member. The planar foliation is defined by large, attenuated red fiamme that have wispy, flame-like ends. GR 246800 8489000.

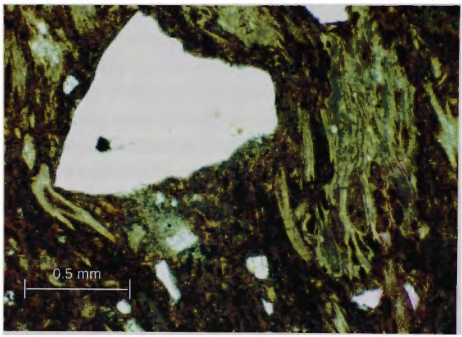

Figure 2.14b: In thin section, the Upper Ignimbrite Member exhibits strong compaction and welding of pumice and shards, especially near the edges of crystals. Pumice clasts display ragged terminations and collapsed tube vesicles. Note the angularity of the fragmented quartz crystal. Sample 89123043.

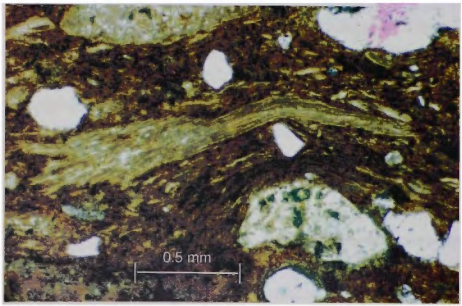

Figure 2.14c: Photomicrograph exhibiting the strong welding fabric and tube pumice. Sample 89123043.

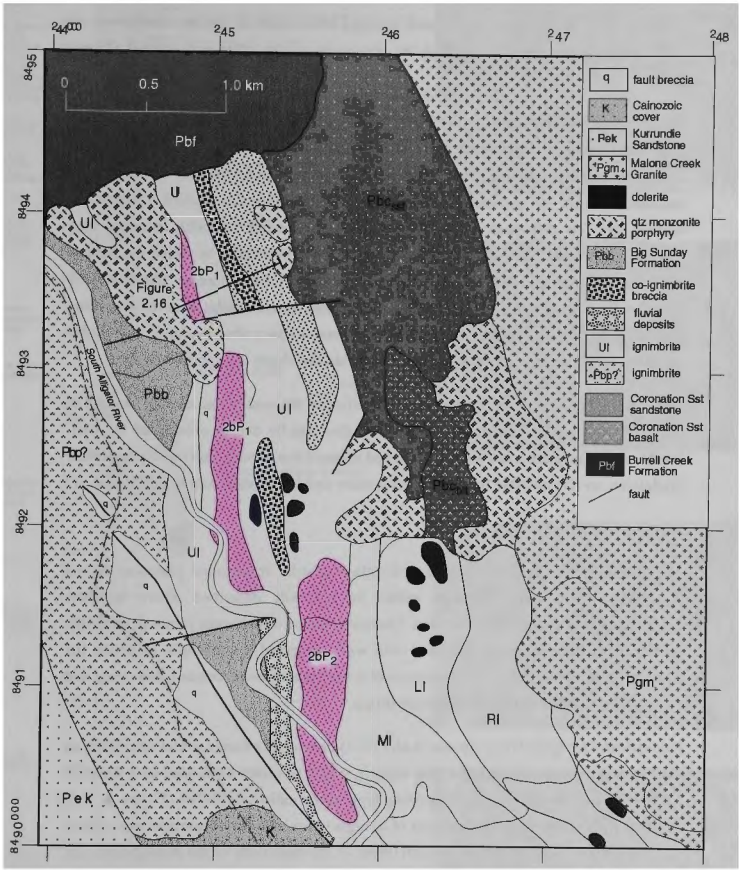

Figure 2.15: Detailed geology of the northwestern margin of the study area, showing the distribution of lithic- and pumice-rich domains and co-ignimbrite lithic breccias within the Upper Ignimbrite Member (Ul) of the Pul Pul Rhyolite. Lithic-rich ignimbrite is denoted by black stipple, co-ignimbrite boulder breccia by coarse black stipple and pumice concentration zones (layer 2bP) by red stipple. $2bP_1$ contains abundant, very large, highly attenuated fiamme (up to 100x40 cm) that exhibit reverse grading, and $2bP_2$ contains a high concentration of small fiamme (2-5 cm) that are ungraded. LI = Lower Ignimbrite Member, RI = Rheomorphic Ignimbrite, MI = Middle Ignimbrite Member. The location of the measured section in Figure 2.16 is marked for reference.

range up to 25 cm in diameter. Isolated outsized lithic clasts of similar dimensions are also irregularly dispersed throughout the remainder of the lithic-rich subunit (Figure 2.16c).

Several pumice-rich domains (layer 2bP), 10-20 m thick, outcropping over a maximum strike length of about 1 km, were also recorded in the northwest region of the study area. Their distribution is illustrated in Figure 2.15. They appear to be laterally discontinuous, and either lens out, or are terminated by faulting along strike. The pumice-rich domains contain very few dispersed, small lithics. Some pumice-rich domains comprise high concentrations (~40-50%) of very small fiamme (2-5 cm in length), in which the fiamme are evenly distributed, and exhibit no reverse grading. Others contain abundant very large (up to 100x40 cm), highly attenuated fiamme which exhibit a reverse grading (Figure 2.16a). The pumice concentration zones contain lower abundances of small lithic clasts (≤ 2 cm) than normal layer 2b deposits within the Upper Ignimbrite Member.

Pumice- and lithic-rich domains were not identified in the central and eastern regions of the study area. In the centre of the study area, this may be due to erosion of the unit. Further east, the ignimbrites were not mapped in detail due to poor outcrop in the Recent sandplains, so it is possible that lithic- and pumice-rich layers also exist in this region.

Interpretation

The abundance of flattened pumice, relic glass shards, fragmented phenocrysts and abundant angular lithic fragments within the deposits described above indicates fragmentation by pyroclastic processes. The development of columnar jointing, eutaxitic, parataxitic and rheomorphic textures, with well preserved microscopic evidence for compaction and welding, provide evidence of a hot state of emplacement, indicating that the ignimbrites are of primary pyroclastic origin.

Facies model for ignimbrites: Sparks et al. (1973) developed a facies model describing an ideal section through a pyroclastic flow deposit, which has since been used as a standard framework for identifying and interpreting high aspect-ratio ignimbrites (Figure 2.17a). Their ideal section through the products of a single ignimbrite-forming eruption consisted of a basal stratified ground surge deposit (layer 1); the main body of the deposit (layer 2), which is divided into a thick, poorly-sorted massive layer (layer 2b), underlain by a thin, reverse-graded, fine-grained basal layer (layer 2a); and a fine ash deposit (layer 3). Layer 2b is characterised by coarse-tail grading (normal grading of large lithic clasts and reverse grading of large pumice clasts; Sparks 1976), which can result in the development of well-defined lithic concentration zones (layer 2bL) at the base, and pumice concentration zones (layer 2bP) at the top of the layer. Wilson and Walker (1982) further developed

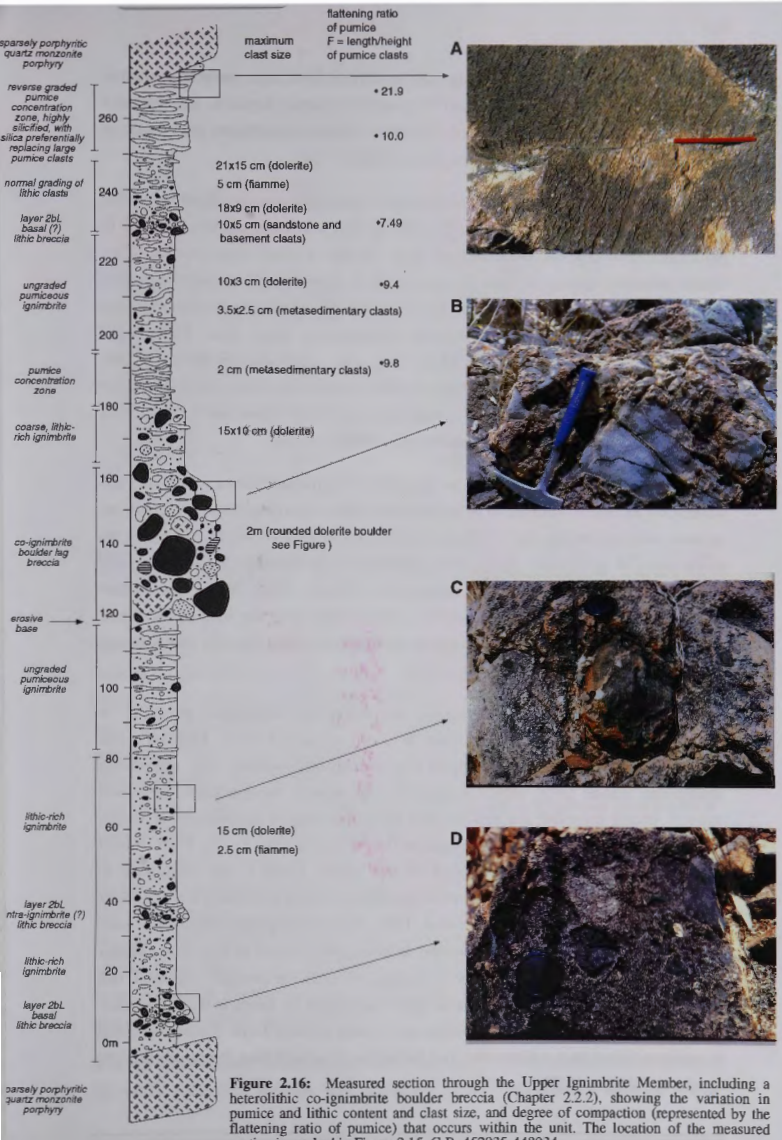

Figure 2.16: Measured section through the Upper Ignimbrite Member, including a heterolithic co-ignimbrite boulder breccia (Chapter 2.2.2), showing the variation in pumice and lithic content and clast size, and degree of compaction (represented by the flattening ratio of pumice) that occurs within the unit. The location of the measured section is marked in Figure 2.15. G.R. 452935-448934.

this model to include low aspect-ratio ignimbrites derived from more energetic eruptions, by expanding Layer 1 to include jetted fines-depleted pumice deposits, and lithic-rich ground layers deposited from the highly fluidised, inflated and turbulent head region of very energetic and turbulent pyroclastic flows (Figure 2.17b).

By comparison with the standard facies model for ignimbrite deposits described above, the welded ignimbrites of the Pul Pul Rhyolite are interpreted as a stacked sequence of pyroclastic flow deposits dominated by layer 2b-type textural characteristics. They exhibit definitive features of layer 2b facies such as poor sorting, a matrix-supported configuration in which crystals, lithics and pumice are supported by large volumes of ash matrix, with layer 2bL and 2bP domains developed in some units. Fairly rapid successive eruption and emplacement of the flow units is indicated by the lack of any intercalated epiclastic deposits (apart from thin beds near the top of the Upper Ignimbrite Member), or evidence of incision and erosion that might result if there were a significant time break in deposition between emplacement of units.

Models of ignimbrite emplacement: The deposition of pyroclastic flows is still not fully understood, and there continues to be research and debate regarding this topic. There are currently two main models that should be taken into consideration when considering the emplacement of ignimbrites: (1) *en masse* 'freezing' of the flow as it loses momentum, so that the final deposit mirrors the moving flow (Sparks 1976; Wright and Walker 1981); and (2) progressive aggradation by sedimentation from the base of the flow, operating continuously over the entire runout extent (Fisher 1966; Branney and Kokelaar 1992).

Sparks (1976) attributed the poor sorting and absence of sedimentary structures in ignimbrites to high particle concentration in poorly expanded flows. Following this interpretation, it became widely accepted that ignimbrites (especially high aspect-ratio ignimbrites; Walker 1983) were emplaced by high particle concentration, high yield strength, poorly expanded and non-turbulent flows that stopped and deflated *en masse*, so that deposit thickness was roughly equal to flow thickness (e.g. Sparks 1976; Wright and Walker 1981; Carey 1991). Based on this model, Layer 1 was interpreted to represent deposits resulting from processes operating within or in advance of the front of the flow (Sparks et al. 1973; Walker et al. 1981; Wilson and Walker 1982). The main body of the pyroclastic flow was envisaged as undergoing laminar or plug flow, similar to debris flows (Johnson 1970) prior to stopping *en masse* to produce a massive unit (layer 2b), with an inversely graded base (layer 2a) formed by shearing at the boundary layer between the moving pyroclastic flow and ground surface. Layer 3 was interpreted to represent fallout from a dilute ash cloud tailing the pyroclastic flow (co-ignimbrite ash; Sparks and Walker 1977).

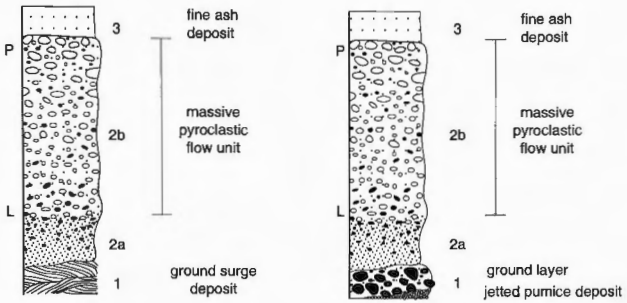

Figure 2.17: Idealised sections through: (a) a high aspect ratio ignimbrite (HARI); and (b) an energetic low aspect ratio ignimbrite (LARI). Modified from Sparks et al. (1973).

More recently, the significance of turbulent transport regimes in pyroclastic flows has been reconsidered (Fisher 1966; Branney and Kokelaar 1992; Buesch 1992; Cole and Scarpati 1993). Branney and Kokelaar (1992) questioned the debris-flow analogy and *en masse* emplacement of ignimbrites, and suggested an alternative model of progressive aggradation from the base of a sustained or semi-continuous turbulent current. They envisaged deposition occurring in a zone of laminar flow developed at the base of a more dilute turbulent flow, where increased particle concentration and frictional shear results in a lowered flow velocity and suppressed turbulence. The basal depositional regime is fed by continuous fallout from the overlying passing dilute and turbulent transport regime. Particles are incrementally added to the bed load so that a particle by particle or layer by layer concentration of material builds up with time, resulting in stratified deposits. Because the bed load accumulates continuously rather than *en masse*, the bedding and sorting characteristics of the final deposit only reflect the depositional processes in the dense basal part of the flow, and not the transport regime of the entire flow, as previously assumed by Sparks (1976).

Branney and Kokelaar (1992) noted that features such as textural stratification (defined by vertical changes in sorting), various grading patterns and chemical zonation within

ignimbrites are difficult to reconcile with plug flow and *en masse* deflation (c.f. Wright and Walker 1981). They suggested that progressive aggradation from a sustained current provided a better framework to explain the varying deposit characteristics of ignimbrites (including the facies defined by Sparks et al. 1973), attributing them to supply-controlled effects. Textural stratification, layering and various grading patterns in ignimbrites are interpreted to reflect flow unsteadiness during progressive aggradation. Vertical chemical zonation can be explained by incremental deposition from a flow sourced by an eruption whose magma composition changes with time. Branney and Kokelaar (1992) cited these vertical changes in chemistry within individual flow units as evidence that massive (2b) layers can also aggrade progressively, representing deposition from a more steady current, fed from a continuous column-collapse eruption. Under the high rates of sedimentation produced by these conditions, traction and turbulence are inhibited by the high particle concentration, resulting in a poorly sorted, massive deposit (hindered settling; e.g. Lowe 1988; Druitt 1992, 1995; Branney and Kokelaar 1992). Inverse coarse-tail graded pumice (layer 2bP) is attributed to hindered settling through buoyancy within the dense depositional boundary layer. Normal coarse-tail grading of lithics (i.e. layer 2bL) is explained as a function of variable supply of lithics during deposition, either due to a decreasing supply from vent with time, and/or to a reduction in the transport capacity in a waning current over time, so that the largest lithics are deposited progressively closer to the source. Branney and Kokelaar (1992) also noted that inverse-graded, fine-grained layers (2a) do not necessarily record flow unit boundaries as conventionally interpreted by Sparks (1976), but may reflect fluctuating input into the depositional regime. Thus a single flow unit could contain several 2a layers (or none), and multilayered deposits conventionally interpreted as multiple flow units, may instead have accumulated by progressive aggradation at the base of a single (unsteady) flow.

The occurrence of lithic breccias at or near the top of ignimbrites, and multiple lithic breccia layers within a single, massive ignimbrite, also pose problems in terms of the laminar/plug flow model of Sparks (1976). In this model, layer 2bL lithic concentration zones develop in response to gravitational settling, and should therefore occur towards the base of a massive ignimbrite. Therefore multilayered arrangements of lithic breccia layers must result from the rapid emplacement of several flows (e.g. Roobol et al. 1987), or high flow yield strengths need to be evoked to prevent gravitational sinking of lithics through the flow (e.g. Cole et al. 1993). The progressive aggradation model provides a more simple explanation for these features, explaining the position of lithic breccias in an ignimbrite as a function of supply processes, rather than processes operating during transport. Multilayered lithic breccias at various heights within massive ignimbrites reflect temporal changes in supply, flow competence and capacity (Bryan et al. 1998; Allen and Cas 1998). A late flux of lithics may be either sourced from the vent, reflecting

episodes of vent erosion, conduit wall instability and possibly onset of vent wall and/or caldera collapse, or locally derived, recording substrate erosion that may be related to topographic irregularities or breaks in slope.

Application of emplacement models to the Pul Pul Rhyolite: It is difficult to interpret most of the Pul Pul Rhyolite ignimbrite units in light of these opposing models of ignimbrite emplacement, as in many cases, the features exhibited could be explained in terms of either model. The best unequivocal evidence for progressive aggradation would be the occurrence of lithics high in the deposit of a single flow, or evidence of vertical compositional zonation within a single flow.

Lower Ignimbrite Member: In the Lower Ignimbrite Member, layer 2bL lithic breccias are only recorded near the base of unit. If the laminar/plug flow model is evoked, these basal lithic breccias are interpreted to have developed in response to gravitational settling of coarse, dense lithic clasts through the pyroclastic flow. Based on a model of progressive aggradation, they could be interpreted as reflecting a major vent-clearing episode at the onset of explosive eruption, that produced a pyroclastic density current initially rich in lithics (e.g. Allen and Cas 1998).

Cognate lithic-bearing Member: The distribution of lithic clasts within the Cognate lithic-bearing Member is best explained in terms of the progressive aggradation model. In this case, the local basal concentrations of outsized dolerite, sandstone and rhyolite porphyry clasts are unlikely to reflect gravitational settling of the coarse lithic fraction, as similar-sized non-vesiculated, dense, flow banded cognate lithics are evenly distributed throughout the unit, and not likewise concentrated at the base of the flow. The basal concentrations of exotic lithic clasts are therefore interpreted to represent either locally-derived accidental lithic clasts, and/or an early influx of vent-derived lithics sourced by a vent-clearing episode at the onset of eruption. The eruption provided a continuous, but waning, supply of cognate lithic clasts to the derivative pyroclastic density current, resulting in a progressive decrease in their abundance in the top 10 m of the deposit.

Upper Ignimbrite Member: It is likely that the Upper Ignimbrite Member is composed of several flow units, as it is heterogeneous in appearance and composition and contains intercalated co-ignimbrite lag breccias in the northwest (Figure 2.16), and intercalated epiclastic deposits in the central region of the study area (Figure 2.2, Section 2.3). It is therefore unlikely that all layer 2bL lithic breccias recorded within the measured section in Figure 2.16 occur within a single flow unit. Their presence may delineate interruptions in ignimbrite emplacement, with each marking the onset of a new phase of eruption and the base of a new flow unit. If this is the case, these basal breccias could be interpreted to have accumulated by coarse-tail gravity settling if the plug-flow model is applied.

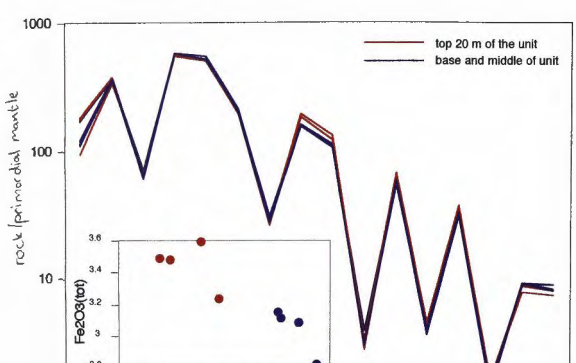

Figure 2.18: Extended trace element diagram for samples collected from the Middle Ignimbrite Member, showing a slight compositional variation in the top 20 m of the unit. Samples collected from the top of the unit show a slight enrichment in light rare earth elements (La, Ce), Nd and Zr. The inset shows they are also slightly more basic in composition, with a lower silica content (see also Figure 2.12). The higher Fe content corresponds with a late-stage influx of Fe-rich pumice.

Conversely, they may be interpreted to reflect major vent-clearing episodes at the start of each eruption, producing pyroclastic density currents initially rich in lithics. The heterogeneous distribution of pumice could also be explained in terms of either emplacement model. Pumice concentration zones could be interpreted in terms of flow mechanics processes (such as upward buoying of pumice in a high particle concentration plug flow), or in terms of a vent supply control and changes in material supply (inferring progressive aggradation).

Another possibility is that some of the layer 2bL deposits are intra-ignimbrite lithic breccias. This scenario is preferred for lithic breccias within the 80 m thick lithic-rich ignimbrite at the base of the Upper Ignimbrite Member (e.g. at 40 m in Figure 2.16), as they are surrounded by texturally identical ignimbrite, and neither overlie an erosive base, nor are laterally continuous. The intra-ignimbrite lithic breccia layers may reflect small-scale vent-clearing or caldera collapse episodes, or periodic collapse of country rock near the conduit during a sustained eruption, which generated slugs of accessory lithic clasts within the contemporaneous pyroclastic density currents.

Middle Ignimbrite Member: In contrast to the Lower and Upper Ignimbrite Members, the Middle Ignimbrite Member can be interpreted as a single flow unit with confidence, as it is markedly homogeneous in composition and appearance (Figure 2.12), and displays an even (dense) welding profile. However, vertical variations in the relative abundance of Fe-poor and Fe-rich pumice clasts are recorded, with the latter becoming notably more abundant in the top 20 m of the unit (Figure 2.12). The late flux of Fe-rich pumice is accompanied by a subtle change in the bulk-rock chemistry of the unit towards a less evolved composition (Figure 2.12, 2.18). This internal compositional zonation is more readily explained as a function of vent supply, than by fluid dynamic processes operating during transport. It supports the model of progressive incremental aggradation from the base of a flow whose magmatic source was compositionally inhomogeneous. The temporal progression to a slightly more mafic composition suggests that the eruption feeding the pyroclastic flow progressively tapped different levels or domains within a compositionally zoned or stratified magma chamber (e.g. Lipman et al. 1966, Hildreth 1979, 1981, 1983).

Ignimbrite grade and lithofacies characteristics: implications for eruption processes: The ignimbrite succession has a zoned vertical welding profile (Figure 2.19). A high grade parataxitic zone is developed within the central units (Cognate lithic-bearing and Middle Ignimbrite Members), flanked by lower grade eutaxitic zones within the underlying and overlying Lower and Upper Ignimbrite Members. A relatively thin local deposit of non-welded ignimbrite locally overlies the welded ignimbrite succession (Section 2.2.3). This zoned welding profile appears to reflect *en masse* cooling of the pyroclastic flow deposits, to produce a simple cooling unit (Smith 1960). However, the different welding intensity between flow units coincides with other variable lithofacies characteristics such as lithic content and degree of crystal fragmentation. These features infer different eruption styles for each unit, suggesting that variable welding density may be a function of eruption and emplacement mechanics, instead of reflecting post-depositional load.

Branney et al. (1992) and Branney and Kokelaar (1992) have expanded the concept ignimbrite grade (Walker 1983), to define a continuum of ignimbrite types (Figure 2.20). The low-grade end of the spectrum is represented by non-welded high- and low aspect-ratio ignimbrites, Extremely high-grade ignimbrite facies comprise rheomorphic and lava-like ignimbrites, with high-temperature, fountain-fed lava flows representing the high-grade end-member of the continuum. Their model outlines some characteristic features of high- and low-grade facies, and equate these with likely eruption and emplacement processes. Based on this system, the welded ignimbrites of the Pul Pul Rhyolite classify as moderate-grade, non-rheomorphic welded ignimbrites to high-grade rheomorphic ignimbrites (Figure 2.19).

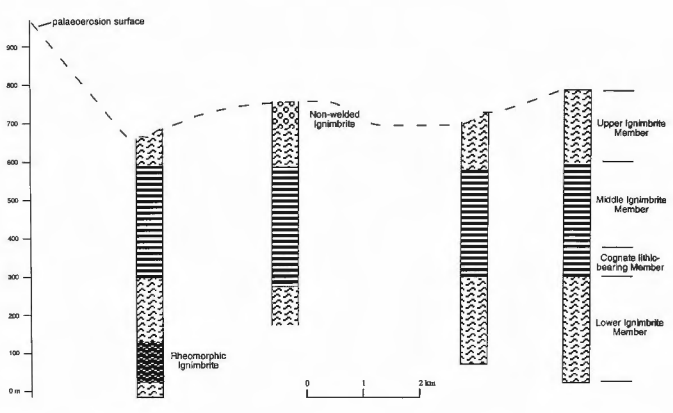

Figure 2.19: Welding profile of the ignimbrite succession of the Pul Pul Rhyolite (central study area), showing a concentric vertical pattern with the highest ignimbrite grade in the centre. The sections are correlated using the base of the Middle Ignimbrite Member as a fixed reference line.

The nature of the eruption column is an important factor influencing ignimbrite grade, as the column height influences the degree of cooling during collapse. Column height also influences the velocity and degree of expansion and turbulence in the derivative pyroclastic flows, which will also affect the degree of heat loss, and consequently the intensity of welding. The densely welded parataxitic and rheomorphic fabrics displayed by the Middle Ignimbrite Member, Rheomorphic Ignimbrite and Cognate lithic-bearing Member indicate a high degree of heat retention. This is consistent with collapse of a low eruption column or a 'boiling-over' eruptive style, involving the continuous supply of a low fountain of low volatile magma from the vent. Other textural features of the Middle Ignimbrite Member and Rheomorphic Ignimbrite units are also consistent with a less violent style of eruption. These units have very low lithic contents relative to the other ignimbrite units and a low degree of crystal fragmentation, as indicated by the presence of a significant proportions of euhedral and resorbed crystals and glomeroporphyritic crystal aggregates (Branney and Kokelaar 1992; Figure 2.20). They also have higher ash+pumice contents, suggesting less turbulence in the eruption column and derivative pyroclastic flows. The other ignimbrite units have much higher lithic contents (Table 2.1) and exhibit a higher degree of crystal fragmentation, and the Lower and Upper

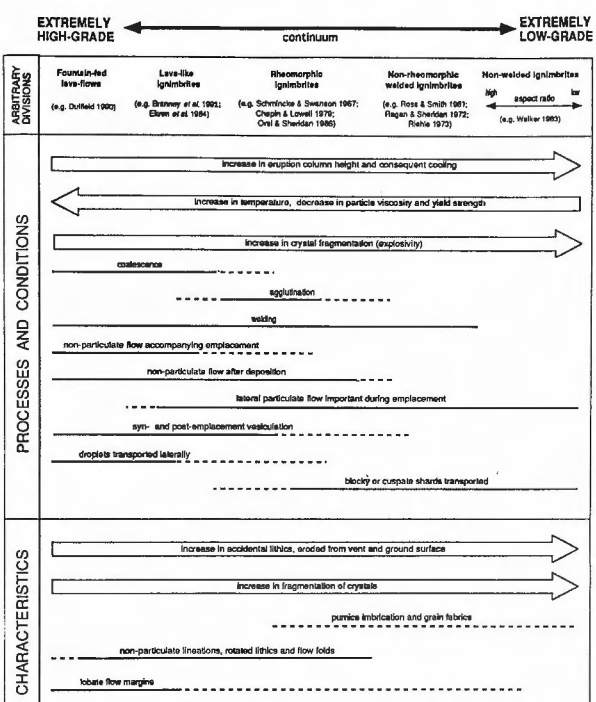

Figure 2.20: The ignimbrite grade continuum, illustrating associated eruption and emplacement processes, conditions and products (from Branney and Kokelaar 1992). Solid lines indicate some characteristic features ; dotted lines indicate possible features. The ignimbrites of the Pul Pul Rhyolite classify as medium- to high grade within the continuum.

Ignimbrite Members are less welded. These features suggest a more violent style of eruption for these units, and the development of a higher (plinian) eruption column.

A low fountain boiling-over eruptive style and consequent deposition from poorly expanded (high aspect-ratio) pyroclastic flows could also account for the absence of pyroclastic facies other than welded layer 2b deposits. In the generation of high eruption columns, plinian fall deposits are common precursors to the main flow deposits, and no fall deposits were recognised within the welded ignimbrite sequence. The distribution of fall deposits is strongly dependent on vent position and wind dispersal patterns, so it could be argued that pyroclastic fall facies existed but were distributed elsewhere. However, fall deposits generally have a wide dispersal, and at least some material should deposit in the vicinity of the ignimbrites, especially if they were deposited in close proximity to vent (as is inferred in Chapter 4). Alternatively, their absence could be accounted for by erosion, as fall deposits are generally non-welded and have a low preservation potential in ancient successions (Cas and Wright 1987). However, their preservation potential improves if they are rapidly capped by welded ignimbrite, so that erosion should not have been entirely effective in removing the facies. It is possible that the consistent absence of plinian fall deposits beneath the ignimbrite units indicates that the ignimbrites were not generated through the collapse of a high, convective eruption column, arguing for immediate column overload and collapse, or a boiling-over eruption style.

Deposition by poorly expanded, relatively non-turbulent pyroclastic flows could also account for the absence of layer 1 ground surge or head deposits and layer 3 co-ignimbrite ash surges and falls. A low eruption column would not promote ingestion of air, and consequently the development of a dilute turbulent sheath around the eruption column would be minimised, and the potential development of layer 1 ground surge deposits generated by the collapse of such a sheath and/or by flow head processes would be low. Low column collapse heights would result in slow-moving, poorly expanded and fluidised flows (high aspect-ratio ignimbrites) which would not develop inflated and turbulent flow heads resulting in ground layer deposits (Walker et al. 1980, 1981; Wilson and Walker 1982; Walker 1985). If turbulence is dampened through high particle concentrations near the ground surface, ash winnowing would also be minimised, accounting for the absence of co-ignimbrite ash surges and fall deposits. The absence of layer 3 deposits could also be explained through continuous successive emplacement of ignimbrite, or by erosion either by successive pyroclastic flow heads or normal surface processes. As with plinian deposits, co-ignimbrite ash deposits are generally non-welded and have a low preservation potential, which improves if they are rapidly capped by welded ignimbrite.

2.2.2 Heterolithic co-ignimbrite boulder breccia

Description: The heterolithic boulder breccia is a distinctive facies that occurs within the Upper Ignimbrite Member. The unit is confined to the northwest of the study area, where it outcrops as two lenses, about 30-50m thick (Figure 2.15). The first lens forms a ridge with a continuous strike length of 800 m which is conformable with the strike trends (~350°) of the adjacent ignimbrites. The lens is truncated to the south by an east-trending fault. The second lens outcrops a further 700 m to the south, is about 1 km in length and passes laterally into pumiceous ignimbrites. The lithic breccias have sharp basal contacts, and both lenses overlie a distinctive grey-coloured lithic-rich ignimbrite, indicating they occupy a similar stratigraphic position within the Upper Ignimbrite Member. Upper boundaries are gradational with the overlying pumiceous ignimbrite. The gradation involves a progressive increase in the proportion of pumice and decrease in the proportion and size of lithic clasts. A diffuse internal stratification is locally observed.

The facies comprises abundant large lithic clasts, from centimetres up to 2 m in diameter, in a matrix of slightly welded rhyolitic ignimbrite. Coarse lithic clasts (> 5-10 cm in diameter) are generally well to moderately rounded, whereas smaller lithic clasts are more angular in shape. The proportion of matrix in the breccia is variable and clast organisation varies from clast-supported, to closely spaced grains in a matrix-supported configuration with some clasts exhibiting grain contacts.

The clast population is heterolithic and clast compositions are consistent with the lithic assemblage observed in the surrounding ignimbrite succession, comprising dolerite, basalt, rhyolite porphyry, sandstone and metasedimentary basement clasts (Figure 2.21a,b,c). However, the lithic clasts are an order of magnitude coarser than those within the overlying pumiceous ignimbrites (Figure 2.16). Rounded dolerite boulders range in size up to 2 m maximum diameter (Figure 2.21d), rhyolite porphyry clasts average 30 cm and have a maximum diameter of 1 m, and sandstone and basement clasts are up to 50 cm in diameter.

The matrix is fine-grained and red in colour, and similar in appearance to the adjacent welded ignimbrite deposits. It consists of a hematised, fine-grained microgranular quartz and feldspar mosaic, supporting euhedral crystals and crystal fragments (volcanic quartz, K-feldspar and minor plagioclase), angular to sub-rounded metamorphic quartz grains and small angular to sub-rounded lithic clasts (Figure 2.21e,f). The small lithic clasts (up

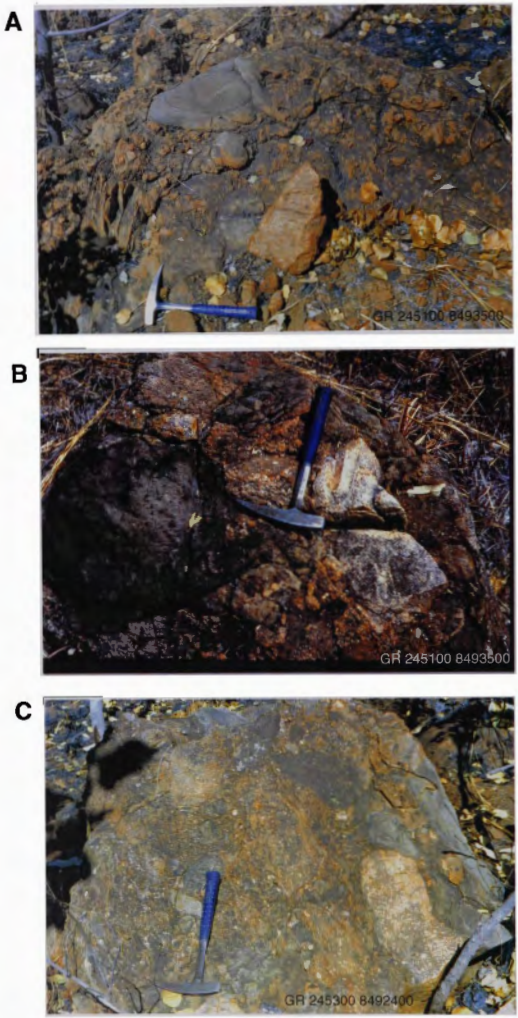

Figure 2.21a-c: Field photographs of the heterolithic co-ignimbrite boulder breccia. Lithic boulders include dolerite, crenulated metamorphic basement clasts (middle LHS; Figure 2.21a), rhyolite porphyry and sandstone.

Figure 2.21d: A 2 m diameter rounded dolerite boulder in the heterolithic co-ignimbrite boulder breccia. GR 245100 8493500.

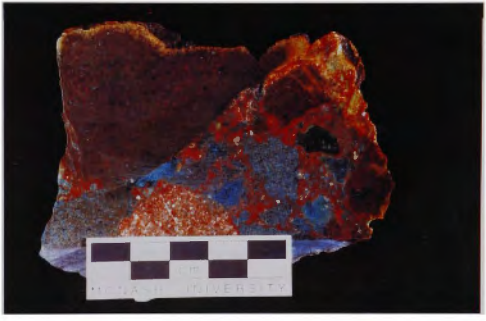

Figure 2.21e: Handspecimen of the heterolithic co-ignimbrite boulder breccia, showing small angular lithic clasts supported by a red, aphanitic volcanic matrix. Sample 89123076.

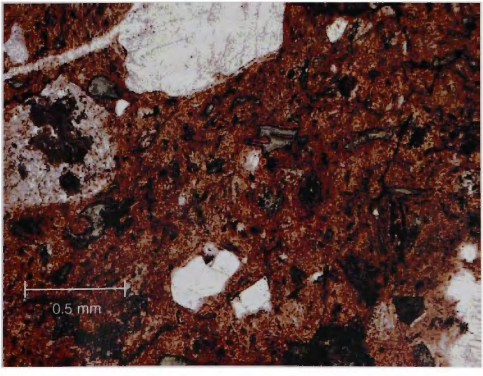

Figure 2.21f: Photomicrograph of the matrix to the heterolithic co-ignimbrite boulder breccia. Although granophyric crystallisation and alteration have largely overprinted pre-existing vitriclastic textures, some remnants are recognisable. In this photograph, chloritised shards retain original bubble-wall shapes. Elsewhere within the same sample, however, the shards show the effects of slight welding and are partly deformed and compacted adjacent to crystal and lithic components. Sample 89123076.

to 2 cm in diameter) are predominantly dolerite fragments, and also include a high abundance of metasedimentary basement-derived composite quartz grains. In thin section, remnants of the original vitriclastic textures are recognisable within the altered and recrystallised matrix. Although many chloritised shards retain original bubble-wall shapes (Figure 2.21f), those adjacent to crystal and lithic components show the effects of slight welding and are partly deformed and compacted.

Interpretation:: The facies is interpreted to represent a co-ignimbrite lithic breccia based on its close spatial association and gradational contacts with pumiceous ignimbrites. The matrix is compositionally and texturally identical to that of the adjacent welded ignimbrites and relic pumice and shards exhibiting welding textures are preserved, confirming that this facies is of pyroclastic origin.

Walker (1985) summarised the types of lithic breccias associated with ignimbrites. The most common are: (1) lithic concentration zones near the base of ignimbrites (layer 2bL deposits; Sparks et al. 1973), which are strongly lithic enriched but not fines depleted, have a matrix-supported ignimbrite fabric and may be coarse tail graded; (2) ground layer deposits, which are laterally extensive lithic breccia horizons at the base of, and in sharp contact with overlying ignimbrite; and (3) proximal lag deposits developed close to vent.

Co-ignimbrite lag or lag-fall breccias are thick, near-vent accumulations of coarse lithic clasts that are internally stratified, up to 30 m thick and fines depleted (Wright and Walker 1977; Druitt and Sparks 1982; Walker 1985). Lag-fall breccias are emplaced by the fall out of lithics at the base of the eruption column (Wright and Walker 1977). Lag breccias are interpreted to develop from a highly inflated gas/particle mixture formed at the site of column collapse, and are the temporal and lateral equivalents of ignimbrites (Wright and Walker 1977; Eichelberger and Koch 1979; Walker 1985). Compression of the gas-particle mixture at the base of a collapsing eruption column generates a high particle concentration flow body with high pore pressures. As the flow moves away laterally, gas decompression causes strong fluidisation within the body and segregation of lithics to generate a lag breccia.

Ground layers are widespread fines-depleted, clast-supported lithic-rich accumulations that occur at the base of an ignimbrite or above jetted fines-depleted ignimbrite (Walker et al. 1981; Druitt and Sparks 1982; Wilson 1985). They are usually less than 1 m thick and have sharp upper and lower contacts, and are generally thinner and finer grained than lag breccias. The ground layer was first defined from studies of the Taupo ignimbrite (Walker et al. 1981; Wilson and Walker 1982; Walker 1983; Wilson 1985). These studies proposed that fast-moving pyroclastic flows such as the Taupo pyroclastic flow

can be divided into a head, body and tail region. Ingestion of air into the flow front results in vigorous fluidisation of the head, generating a lithic-rich and fines-depleted ground layer (layer 1H), and causing segregation of fine and light pyroclasts into the body and tail regions of the flow.

Interpretation of the heterolithic boulder breccia as a lag breccia is supported by the coarseness and thickness of the deposits, their fines-depletion and their gradational relationship with adjacent ignimbrites. Ground layers and layer 2bL deposits seldom exceed 1 m in thickness (Walker 1985), whereas the 30-50 m thickness of the heterolithic boulder breccia is comparable to documented thicknesses of co-ignimbrite lag deposits (up to 30 m thick). In addition, the maximum clast size is an order of magnitude coarser than within the overlying pumiceous ignimbrite (2 m c.f. 25 cm), whereas in ground layers the maximum clast size is typically only 3-4 times greater (Walker 1985).

2.2.3 Non-welded ignimbrite

Description: In the centre of the study area a relatively thin deposit of non-welded ignimbrite overlies the Upper Ignimbrite Member (Figure 2.2, 2.5). The unit is volumetrically minor compared with the underlying welded ignimbrite sequence, and occurs as a broadly lensoidal body extending approximately 3 km along strike, with an average thickness of 60 m. The top of the facies is highly eroded and along strike it interfingers with and is overlain by fluvial epiclastic sediments, which also occur locally as smaller lenses within the Non-welded Ignimbrite and underlying welded Upper Ignimbrite Member.

The facies is a massive, matrix supported breccia with poorly sorted euhedral and fragmented crystals and lithic clasts in an aphanitic siliceous matrix that comprises 70-80% of the deposit. The facies is geochemically and mineralogically identical to the underlying welded ignimbrites (Table 2.1). It contains about 16% fragmented to euhedral crystals of quartz, K-feldspar, minor plagioclase and accessory zircon and opaques, and between 3 to 11% small lithic clasts (maximum diameter of 3 cm). For this unit, the modal percentages are a reasonable estimate of the whole rock abundance of each component, as the unit contains no pumice or outsized lithic clasts. Lithic fragments include dolerite, welded ignimbrite, presumably derived from the underlying ignimbrite sequence, basement-derived composite quartz (metasedimentary fragments) that appears as distinctive large milky white quartz grains in hand specimen, chert and sandstone. Unlike the underlying welded ignimbrites, the unit is clearly unwelded. It has no eutaxitic texture in outcrop and hand specimen, and the matrix contains non-welded chloritised shard that retain original cuspate shaps, and unflattened tube pumice (Figure 2.22a).

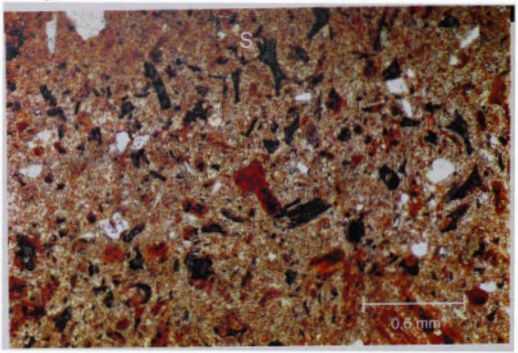

Figure 2.22a: Non-welded chloritised shards (S) with cuspate and platy shapes, from the Non-welded Ignimbrite. Sample 89123033.

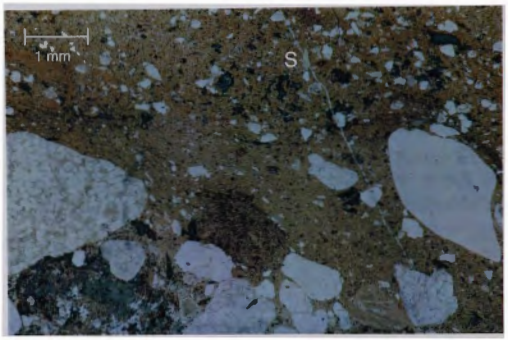

Figure 2.22b: Contact between a clast-supported crystal (+lithic) concentration zone and the overlying matrix-supported non-welded ignimbrite. Small chlorite shards are visible in the centre of the photograph (S). Sample 89123033.

Interpretation: The fragmented morphology of the crystal component, the angularity of lithic fragments and the presence of undeformed pumice fragments and chloritised cuspate shards in the matrix of the unit indicate initial fragmentation by pyroclastic processes. The massive, poorly sorted, matrix supported texture indicates emplacement by mass flow processes perhaps with yield strength. In the absence of evidence of a hot state of emplacement, the facies could represent either a non-welded ignimbrite, or mass-flow redeposition of essentially unreworked pyroclastic debris. The thick massive nature of the unit suggests that it is likely to be a non-welded ignimbrite, and this is supported by the fact that the unit is compositionally and mineralogically identical to the underlying welded ignimbrites. This interpretation is also supported by associated subfacies that occur within the unit (described below), which are consistent with deposition by pyroclastic flow processes.

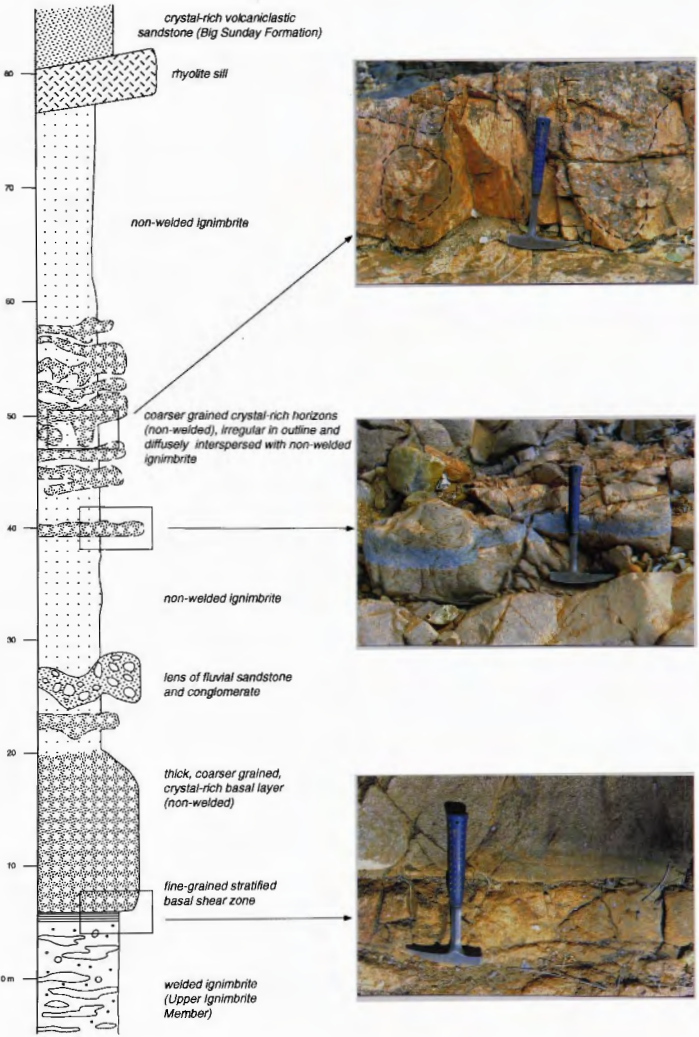

Figure 2.23: Measured section through the non-welded ignimbrite, showing various sub-facies described the text (GR 479 880 - 476 878).

Sub-facies of the non-welded ignimbrite

A thin (10 cm), fine-grained and finely stratified layer occurs at the base of the non-welded ignimbrite (Figure 2.23a). The basal layer is crystal-rich and lacks the larger lithic clasts present in the overlying deposit, and has sharp conformable contacts. It is overlain by a 15 m thick coarse-grained, crystal- and lithic-rich layer that exhibits normal size-grading and has a higher concentration of crystals and lithics at the base (55%) than at the top (39%). The layer grades into the overlying non-welded ignimbrite described above, and has a higher concentration of grains, in a grain supported to matrix supported (upwards) configuration. This coarse-grained, graded crystal-rich facies occurs repeatedly upsection, irregularly interbedded with the non-welded ignimbrite, occurring as 20 cm - 1 m thick layers that cross-cut the non-welded ignimbrite over a 25 m interval (Figure 2.23b). The crystal-rich layers have a tightly packed framework and little interstitial matrix, with crystal and lithic concentrations as high as 67-73% (Figure 2.22b). The thinner layers (< 1m) are extremely irregular in form and exhibit load structures at their base, including load balls which form when pebbly material detaches from the crystal-rich layer and sinks into the underlying non-welded ignimbrite (Figure 2.23c). These structures indicate that the underlying unwelded ignimbrite was soft and deformable under the increased load resulting from deposition of the crystal and lithic-rich layers. The top contacts of the denser crystal-rich layers with non-welded ignimbrite are sharp to gradational, with isolated large lithic clasts occurring above the crystal-rich layers in the base of the overlying non-welded ignimbrite.

The crystal-rich layers have a similar crystal and lithic population to the host non-welded ignimbrite, suggesting a genetic association. An interesting variation within the crystal-rich facies is that upsection, the layers show a progressive increase in lithic content (Figure 2.24)

Interpretation: The fine-grained basal layer is interpreted as a layer 2a deposit, occurring at the base of a more massive layer 2b. The coarser-grained crystal-rich layers have a gradational relationship with the non-welded ignimbrite and have the same mineralogical composition, but are fines-depleted, and enriched in crystals and lithic clasts. They are interpreted as small ground layers deposited from the head of the pyroclastic flow. The head is the most fluidised part of a pyroclastic flow, into which large quantities of air can be ingested (Wilson 1985). Strong fluidisation and turbulence in the flow head promotes elutriation of fines which stream into the main body of the flow. This results in the ground layer being fines depleted and enriched in crystals and lithics. The presence of some large lithic fragments near the base of the non-welded ignimbrite immediately above

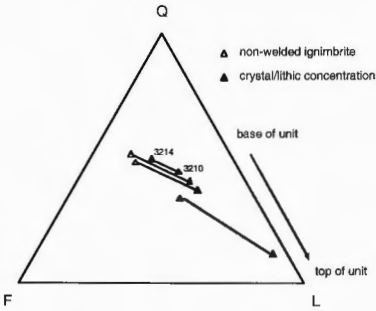

Figure 2.24: Modal analyses of facies of the Non-welded Ignimbrite. Tie lines link ash-rich ignimbrite domains with underlying crystal-lithic concentration zones (tie line between samples 3210 and 3214 link upper and lower levels of the basal crystal-lithic concentration zone). Both the ash-rich domains and the concentration zones become progressively more lithic-rich upsection.

the coarser layers (Figure 2.22b) suggests that there is some exchange of material between the flow head and the overriding body of the flow.

Repetition of successive crystal- and lithic-rich intervals with gradational contacts into the overlying non-welded ignimbrite suggests pulsating deposition in a series of close spaced events. The repetition could result from aggradational deposition from a pulsating current (corresponding to fluctuations in the eruption rate) or from the overlapping of flow lobes in a single pyroclastic flow (i.e. ramping of the flow over itself; Cole et al. 1993). The progressive increase in lithic content indicates a progressive increase in sediment supply, which reflects a change in flow capacity and competence with time. The increase in lithics may result from vent flaring as eruption rates progressively increase, so that progressively more accessory lithic material is incorporated into the pyroclastic flow during the course of the eruption. Alternately if the lithics are accidental, their increase in abundance would indicate increased fluidisation and erosive capacity of the flow head.

2.2.4 Petrography and geochemistry of the ignimbrites

In the following section, the whole-rock geochemistry of the ignimbrites is presented in conjunction with petrographic analyses, in order to discern and evaluate any significant

compositional trends within the succession. Classification of the ignimbrites occurs in section 2.5. Interpreting the significance of geochemical trends in ignimbrites can be difficult, even in modern settings, as the original magmatic composition may be modified by post-eruptive processes. These include depletion of juvenile ash, concentration of crystals and incorporation of xenoliths and xenocrysts during eruption and emplacement. In ancient successions, the effects of diagenetic and metamorphic alteration by processes such as leaching of Na, K, Si and other elements from the metastable glass (e.g. Noble 1967; Scott 1971), vapour phase (secondary) crystallisation, and metasomatism, must also be considered. Alkali elements are the most highly mobile and prone to redistribution during devitrification, diagenesis and regional metamorphism (Vallance 1965, Lipman 1965), and scatter of K_2O, Na_2O and CaO may be attributed to post-depositional alteration. The moderate to high degree of scatter exhibited by most other elements is likely to have been introduced by the combined effect of all the above processes. Despite this scatter, broad geochemical trends can still be recognised, and an attempt is made to eliminate some of the effects of these post-eruptive processes, and delineate primary trends.

Effects of crystal-enrichment: Most pyroclastic flow deposits exhibit some degree of crystal enrichment relative to their source magmas, due to the selective segregation of vitric ash and pumice from the eruption column and plume during eruption, and from the ash cloud of the derivative pyroclastic flow (e.g. Walker 1972; Sparks and Walker 1977). As a consequence, the composition of ignimbrites may depart notably from that of their parent magmas, being enriched in those chemical elements contained in higher proportion by the crystals, and depleted in elements contained in higher proportion in the glass (Walker 1972). The overall geochemical effect is analogous to removing the minimum melt component of the eruptive magma, and consequently the crystal-enriched ignimbrites will have a less evolved composition and, except where quartz is an abundant phenocryst, will have a lower SiO_2 content. Studies by Flood et al. (1980) showed that a 3.7% loss of SiO_2 is consistent with the loss of about 36% of the vitric fraction during eruption and transportation. Studies of the compositional effects of pumice- and ash-depletion in crystal-rich volcaniclastic sandstones of the Turondale Formation (Chapter 7.3.2, this study) yielded similar results, suggesting a 4% loss of SiO_2 resulting from 25% ash-loss.

In the case of the Pul Pul Rhyolite, crystals constitute about 2-5% of pumice clasts (all units) and non-vesicular juvenile clasts within the Cognate lithic-bearing Member, inferring that the vitric component at the time of eruption was about 95%. This compares with about 90% for the Rheomorphic Ignimbrite, 86% for the Middle Ignimbrite Member, and about 72% for all other ignimbrite units (average values of

pumice+matrix+non-vesicular juvenile components), indicating between 5-20% depletion of vitric material during eruption and emplacement. Thus the original magmatic composition is likely to have been more evolved than the bulk-rock composition of the ignimbrites. The expected loss of SiO_2, however, will have been counteracted to some extent by the introduction of a pure silica contaminant, in the form of basement-derived quartz xenocrysts and quartz-rich xenoliths. As discussed in Section 2.2.1, the phenocryst population of the pumice and non-vesicular juvenile clasts is dominated by euhedral equant, tabular and lath-shaped feldspar crystals and glomeroporphyritic feldspar clusters (predominantly K-feldspar), with subordinate quartz phenocrysts, whereas most ignimbrite units contain quartz and feldspar in roughly equal proportion (the Middle Ignimbrite Member is an exception). This infers that much of the quartz is introduced as a xenocrystic contaminant. In addition, basement-derived quartz-rich xenoliths are the most common lithic contaminant after dolerite/basalt. The composition of the Middle Ignimbrite Member and Rheomorphic Ignimbrite will most closely approximate original magmatic compositions, as these units have undergone the least amount of ash-depletion and crystal enrichment (these units also contain the lowest xenolith abundances; Table 2.1).

Effects of xenolithic contamination: The high degree of xenolithic contamination in the ignimbrites is likely to introduce a significant source of error into the geochemical analyses. Because the distribution of pumice and lithic clasts is heterogeneous, outsized lithic clasts can be avoided during sampling. However, even the finer grained component of the ignimbrite units contains between 5-45% small lithic clasts, which can be expected to affect their geochemical composition. In order to assess the effect of lithic contamination on the original magmatic composition, 17 ignimbrite samples were jaw-crushed and the rock chips hand-picked to remove lithic fragments. Analyses of the hand-picked are plotted on major and trace element variation plots and compared with the bulk-rock ignimbrite analyses (Figure 2.25). As dolerite comprises the main lithic component, representative samples of the Coronation Sandstone basalts, Zamu Dolerite and one dolerite clast extracted from the Lower Ignimbrite Member, are also plotted to represent the composition of the main contaminant. For the Middle Ignimbrite Member and the Rheomorphic Ignimbrite which contain less than 5% total lithics, there was no significant compositional difference between the hand-picked and bulk-rock samples, indicating that lithic contamination does not greatly affect the geochemical composition of these lithic-poor units. For the remaining units, however, lithic contamination has a significant effect on the geochemical trends.

It is clear that many of the trends for the bulk-rock samples seen on the variation plots do not represent magmatic trends, but are mixing lines generated between felsic melt and the

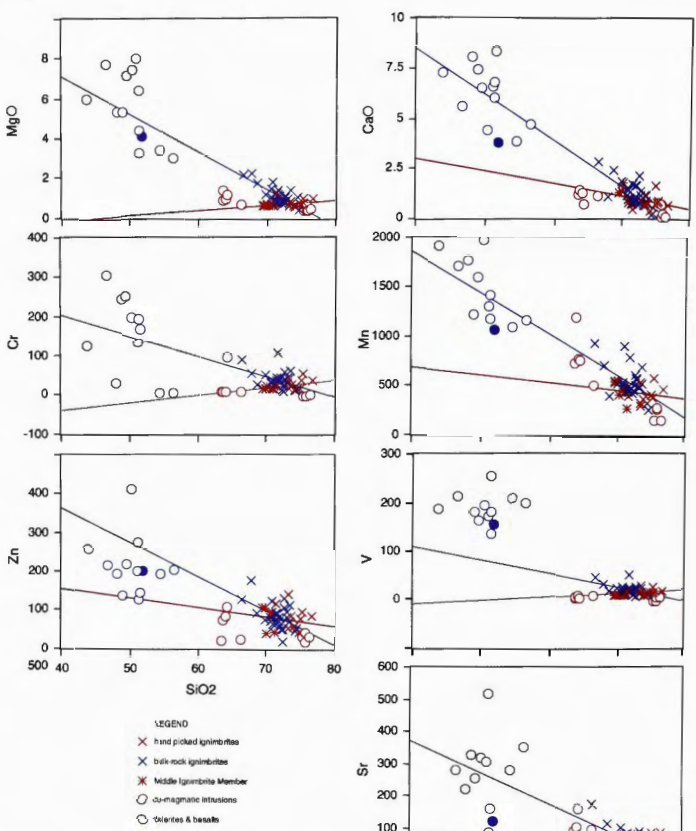

Figure 2.25: Geochemical fractionation trends for ignimbrites of the Pul Pul Rhyolite. The blue vectors are generated by linear regression through bulk-rock analyses of ignimbrite units with a high lithic contents (Lower, Cognate lithic-bearing, and Upper Ignimbrite Members, and Non-welded Ignimbrite). For most elements, these vectors intersect the composition of dolerites and basalts in the underlying succession (Zamu Dolerite and Coronation Sandstone), indicating they represent mixing lines between the original felsic melt composition and a mafic lithic contaminant. The red vectors are generated by linear regression through ignimbrite samples that were hand-picked to remove much of the dolerite lithic contaminant. For most elements, these vectors intersect bulk-rock analyses of relatively uncontaminated (i.e. lithic-poor) units (Middle Ignimbrite Member and Rheomorphic Ignimbrite) and co-magmatic intrusions (quartz monzonite porphyries (63-66% SiO_2) and rhyolite porphyries (~76% SiO_2), and are therefore believed to more closely represent original magmatic trends.

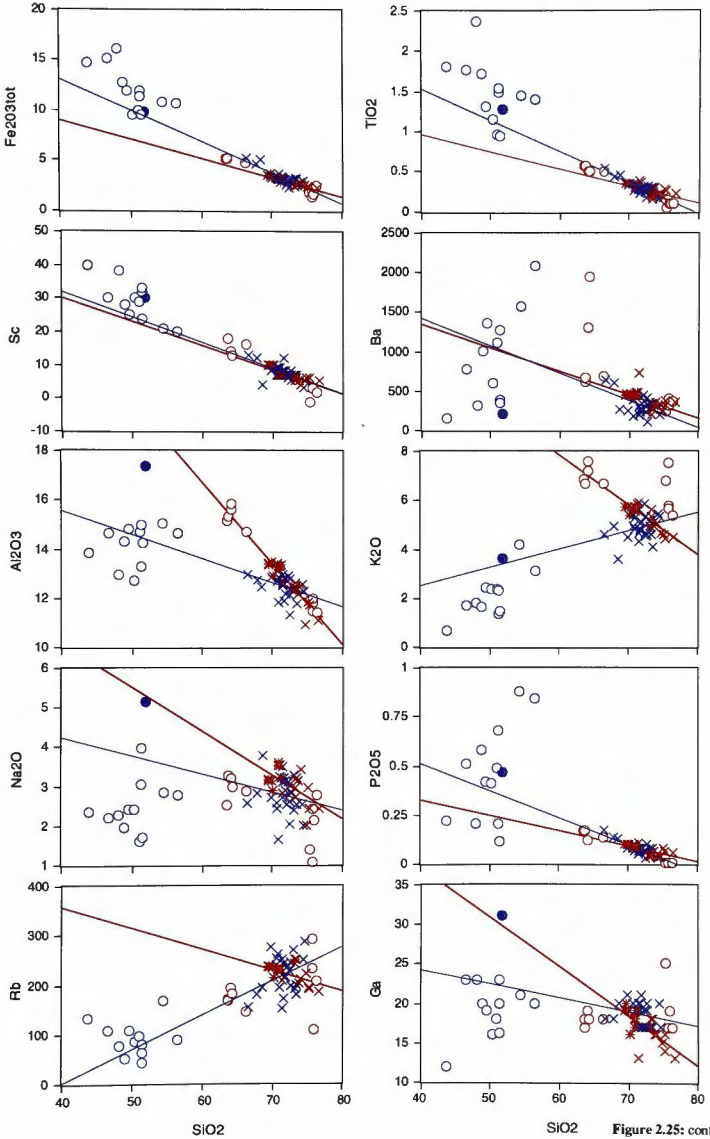

Figure 2.25: cont'd.

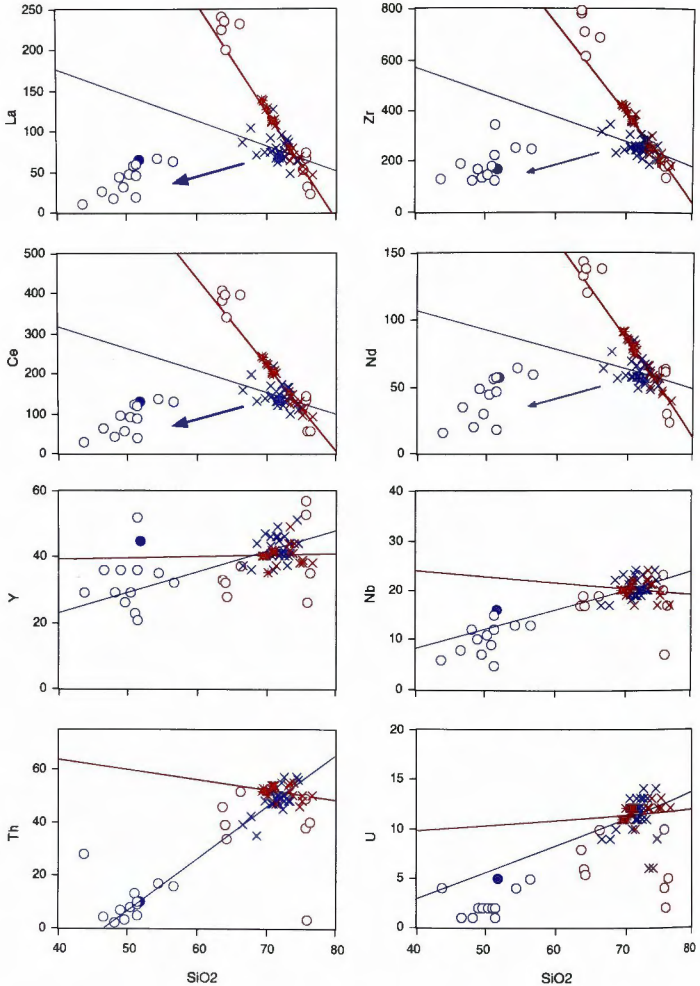

Figure 2.25: cont'd.

lithic (dolerite+basalt) contaminant end members. The transition elements are the most affected by mafic lithic contamination, particularly MgO, Cr, V, Mn, Zn, CaO and Sr (Figure 2.25a), and to a lesser extent Fe_2O_3(tot) and TiO_2, due to the high concentration of mafic mineral phases (olivine, pyroxene, chlorite, epidote) in the dolerite and basalt clasts. These elements exhibit fairly flat magmatic trends in the hand-picked ignimbrite samples, whereas the bulk-rock samples exhibit strong mixing trends with the dolerite contaminant. For other transition metals (Sc and P_2O_5) and also for Ba, the dolerite mixing line mimics the linear trend of magmatic descent, so although scatter may be introduced to the data, the overall trend is largely unaffected. The light rare earth elements (LREE) elements (La, Ce), Al_2O_3, Zr and Nd are also markedly affected by the addition of a mafic lithic contaminant. Linear regression through the hand-picked ignimbrites generates steep, linearly descending magmatic trend lines for these elements, that intersect co-magmatic intrusions associated with the ignimbrite succession. In contrast, linear regression through the bulk-rock samples are flatter, due to the incorporation of mafic clasts that contain these elements in comparatively low abundance. For large ion lithophile (LIL) elements (K_2O, Rb), Na_2O, Ga, Al and high field strength (HFSE) elements (Th, U, Y and Nb), magmatic trends as defined by the hand-picked ignimbrites are constant or decrease with increasing SiO_2. The effect of mafic contaminant is less severe, and samples with over 70% SiO_2 exhibit only minor scatter along a mixing line with the doleritic contaminant.

Magmatic trends: When the most contaminated samples are removed from the ignimbrite dataset (see Appendix A2), the geochemical trends are controlled by magmatic fractionation over an SiO_2 range of 69.5-77% (represented by red trend-lines in Figure 2.25), which intersect associated co-magmatic intrusions for most elements. Fractionation trends are consistent with the progressive removal of feldspars, a ferromagnesian mineral (perhaps biotite or amphibole, now converted to chlorite and epidote by greenschist facies metamorphism) and accessory phases such as zircon and apatite, from the melt. It is difficult to discern small-scale compositional variations within the ignimbrite succession due to the high degree of scatter exhibited by most elements on variation diagrams. However, when the average values of SiO_2 and other representative major and trace elements are compared for each unit, a broad concentric compositional zonation is delineated (Figure 2.26), suggesting that the ignimbrites were derived from a series of eruptions that tapped different levels or domains of a compositionally zoned or stratified magma chamber. The Middle Ignimbrite Member in the centre of the succession has the least evolved geochemical composition. It has a lower SiO_2 content, ranging between 69.5-71.5% (c.f. 71-77% SiO_2 in other units) and less fractionated trace element pattern (Figure 2.27). There are two factors that confirm that this geochemical difference is primary and not induced by any of the secondary (post-eruptive) processes

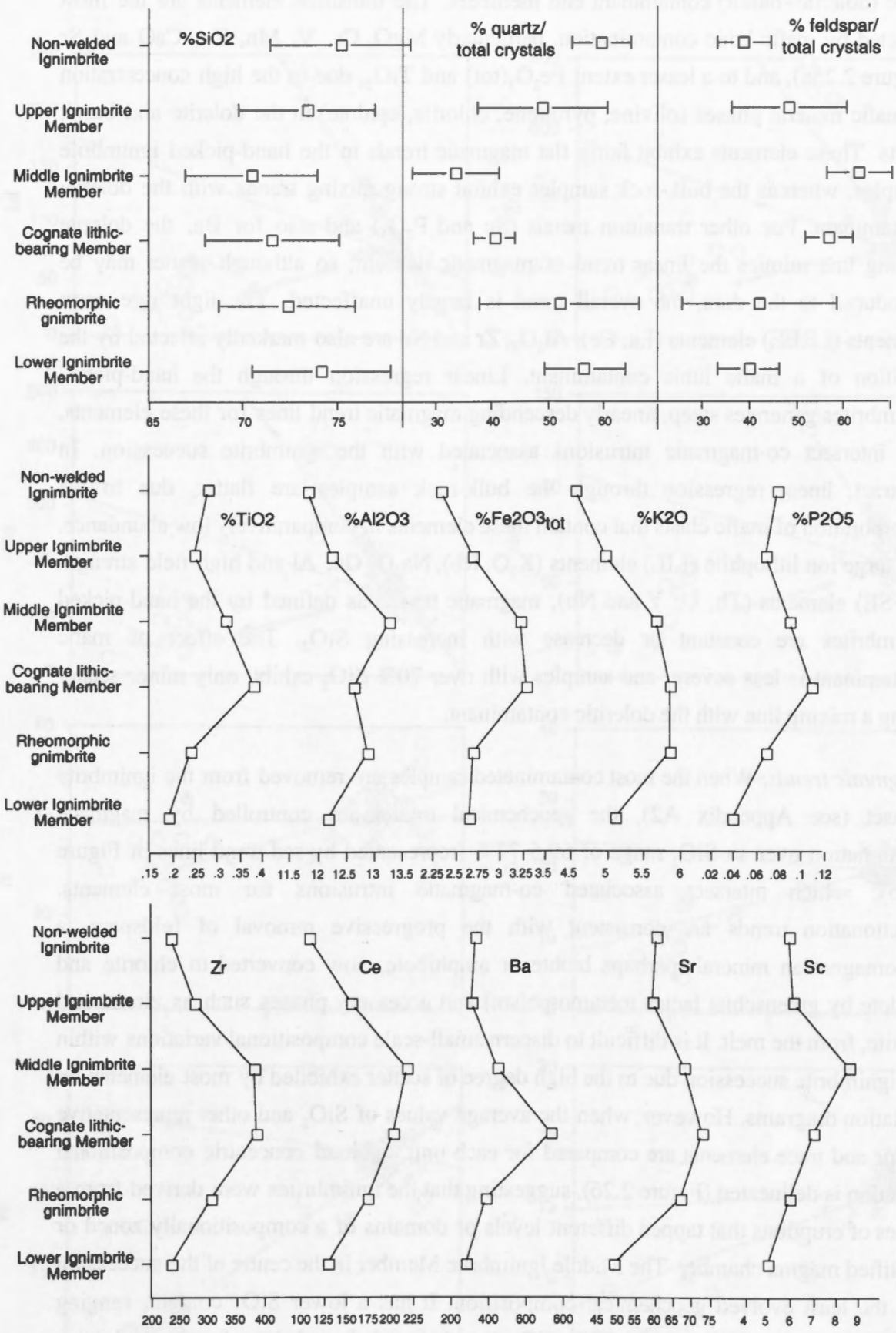

Figure 2.26: Average values of quartz and feldspar (as a percentage of total lithic content) and select major and trace elements for ignimbrite units of the Pul Pul Rhyolite, illustrating vertical compositional trends within the succession. The trends define a concentric pattern, in which ignimbrites in the centre of the succession have the least evolved composition. Average values for each unit are calculated from a refined dataset, from which samples exhibiting the greatest effects of lithic contamination were eliminated (see Appendix A2).

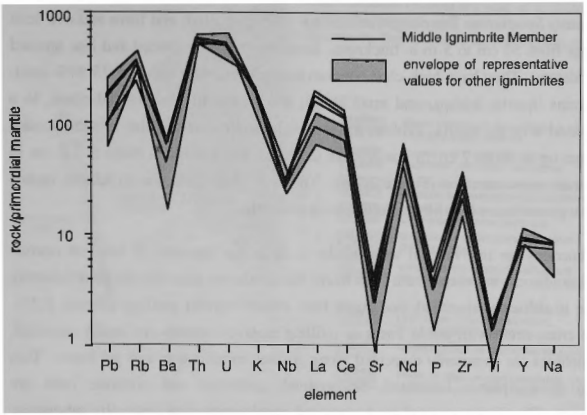

Figure 2.27: Extended trace element diagram comparing trace element patterns of the Middle Ignimbrite Member with other ignimbrites of the Pul Pul Rhyolite. The Middle Ignimbrite Member plots as the least fractionated end-member of the ignimbrite suite.

described above: (1) it is accompanied by a difference in mineralogy, as the Middle Ignimbrite Member contains a higher abundance of feldspar (and less quartz) than other units; and (2) there is a notable compositional difference between the Middle Ignimbrite Member and Rheomorphic Ignimbrite. The geochemistry of these units is interpreted to have been largely unaffected by ash-depletion, crystal enrichment and xenolithic contamination.

2.3 SECONDARY VOLCANICLASTIC FACIES

Description: The top 100 m of the ignimbrite succession interfingers with and is unconformably overlain by lensoidal packages of polymictic volcaniclastic rocks, comprising up to 60m of conglomerate, fine- to very coarse-grained sandstone and minor siltstone. The polymictic volcaniclastic facies outcrops over a preserved lateral extent of about 8 km. The main succession erodes into the underlying non-welded ignimbrite and has a broad channel geometry (Figure 2.28). Smaller lenses, 5-20 m thick, are also recorded within the Non-welded Ignimbrite and Upper Ignimbrite Member. The facies is unconformably overlain by the predominantly fine-grained volcanogenic sedimentary facies of the Big Sunday Formation (described in Chapter 3), interpreted as a locally developed lacustrine sequence.

Sedimentary Structures: The conglomerates are clast-supported, and form massive beds that range from 50 cm to 5 m in thickness. Some are normally graded and fine upward into sandstone. They have high clast concentrations, containing between 75-84% sand-sized grains (quartz, feldspar and small lithics) and gravel- to pebble-sized clasts, in a fine-grained siltstone matrix. Pebbles in the conglomerates are angular to sub-rounded and range up to about 7 cm in size (Figure 2.29a), but gravel-sized clasts ≤ 1.5 cm in diameter are most common (Figure 2.29b). The beds form lenticular to tabular bodies that have planar bases or infill shallow erosive channels.

Conglomerates are interspersed with tabular to lenticular intervals of fine- to coarse-grained sandstone, between 50 cm -7 m thick. The sandstone intervals are predominantly massive to diffusely stratified, and some beds exhibit normal grading (Figure 2.28). Trough cross-strata with planar bases or infilling erosive channels are locally recorded. Small pebbles are commonly dispersed along foreset stratification and set bases. Thin (2-5 m thick), planar laminated, fine-grained sandstone and siltstone beds are subordinate. The clast-supported sandstones and conglomerates are texturally submature. Sandstones are generally well sorted, whereas conglomerates are more poorly sorted. Angular to rounded clast and grain morphologies reflect variable degrees of reworking.

One fine-grained volcaniclastic sandstone beds, 10 m thick, has a massive, matrix-supported internal structure in which small angular quartz and feldspar grains (0.1-0.2 mm) are dispersed throughout a finer-grained siliceous (siltstone) matrix (measured section 3; Figure 2.28). This matrix-supported volcaniclastic sandstone is compositionally and texturally less mature than the polymictic clast-supported sandstones and conglomerates described above, comprising angular, unabraded crystal fragments and very few lithics. The siliceous matrix is interpreted to have been originally composed of fine glassy ash, recrystallised to a fine quartz-feldspar mosaic. No pumice or shards were observed within the unit.

Composition: Crystals of quartz, K-feldspar and plagioclase occur in abundances of 8-54%. Conglomerates have the highest lithic contents (averaging 60%) and conversely the lowest matrix abundance (21%), where the matrix is defined as the very fine-grained siliceous material interstitial to sand-sized fragments and larger lithic clasts. By comparison, the sandstones average 23.6% lithics and 39% matrix, and siltstones average 8.3% lithics and 53.4% matrix (Table 2.1). Based on Folk (1980) the deposits classify as lithic feldsarenites to litharenites (Figure 2.30a). The dominant lithic component comprises sub-rounded to rounded metasedimentary basement clasts, which include highly deformed gneisses and mylonites, and variably strained basement-derived composite quartz grains (quartzites). Basalt, dolerite, sandstone, siltstone, chert, devitrified fine-grained volcanic fragments and rhyolite porphyry clasts occur in minor

Figure 2.28: Distribution of fluvial deposits of the Pul Pul Rhyolite, and the overlying lacustrine deposits of the Big Sunday Formation (mapped at a scale of 1: 10 000). Note the lensoidal character of the fluvial deposits. The crystal-rich volcaniclastic sandstones of the Big Sunday Formation cut across the fluvial deposits and erode into the underlying welded ignimbrites (Upper Ignimbrite Member), indicating that an unconformable relationship exists between the two formations. Representative sections through the fluvial deposits are also presented, and their locations are marked on the map.

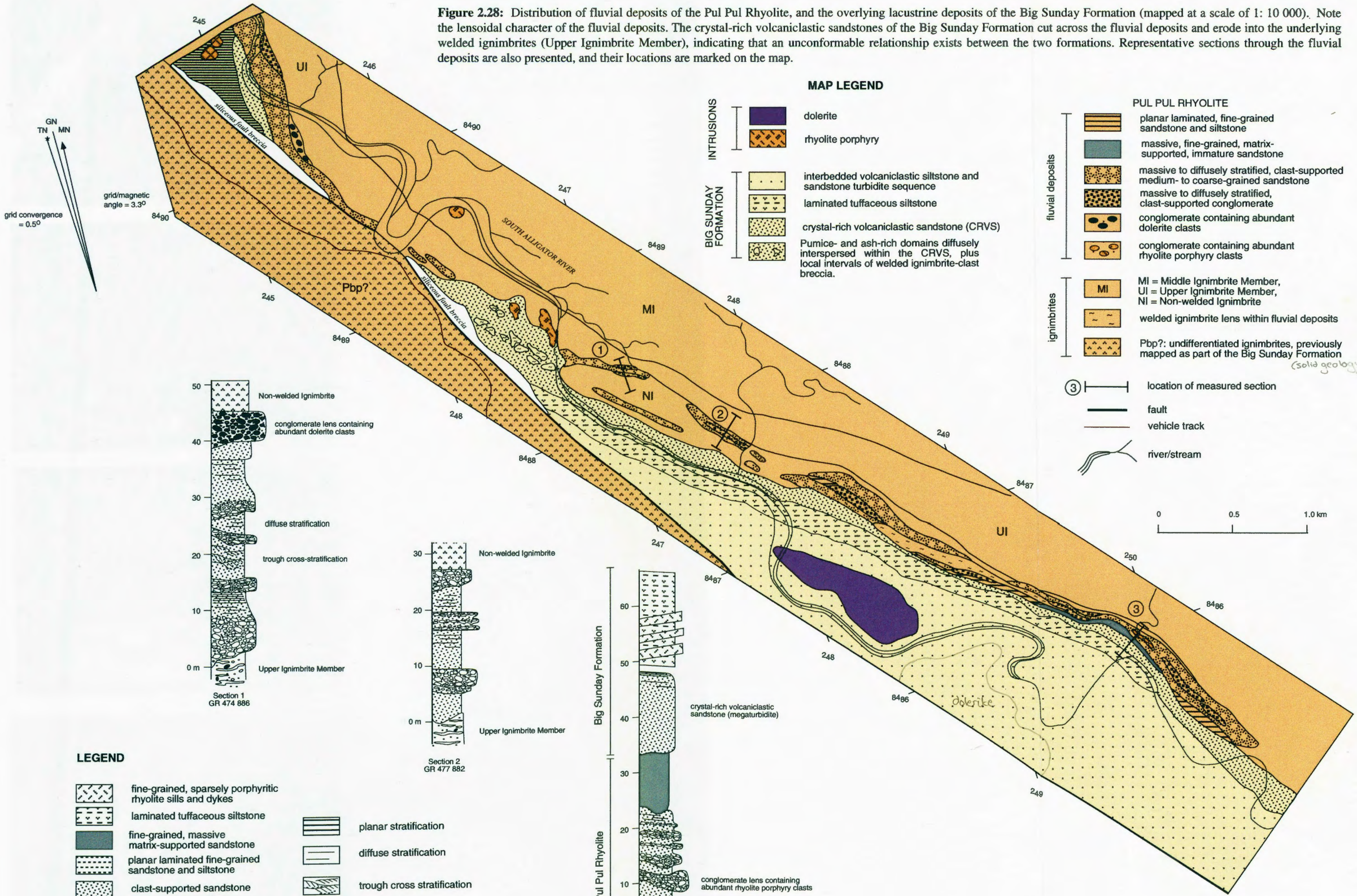

Figure 2.29a: Interbedded conglomerate and sandstone, showing the massive internal structure of each bed. Conglomerate layers contain well-rounded quartzite cobbles. GR 245400 8491100.

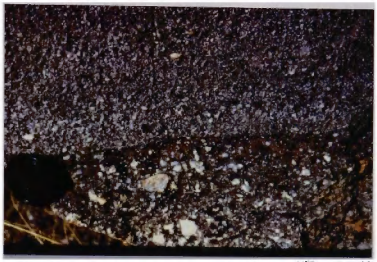

Figure 2.29b: Contact between coarse-grained massive sandstone and massive gravelly conglomerate. GR 248000 8487600.

Figure 2.29c: Hand specimen of a poorly-sorted conglomerate containing abundant large angular to sub-rounded dolerite clasts. GR 245450 8490550.

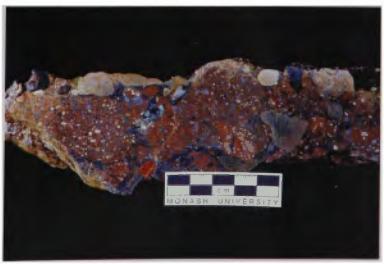

Figure 2.29d: Hand specimen of a poorly-sorted conglomerate containing abundant large sub-rounded to rounded rhyolite porphyry clasts. GR 250550 8485000.

proportions. Two conglomerate lenses within the volcaniclastic facies have distinctive coarse-lithic components. The first underlies an interbedded sandstone and conglomerate sequence and contains abundant angular basalt fragments in a finer-grained siliceous matrix (measured section 1 in Figure 2.28; Figure 2.29c). The second forms a lens surrounded by medium-grained massive sandstone and contains large, sub-rounded to rounded rhyolite porphyry cobbles (measured section 3 in Figure 2.28; Figure 2.29d). These conglomerates differ from the majority of beds, which contain predominantly metasedimentary lithic clasts, and must have been sourced from areas locally enriched in the lithology of the dominant clast-type.

The crystal and lithic components are consistent with the assemblage observed in the underlying ignimbrite succession. However, the dominant crystal and lithic species differ. Quartz is more abundant than feldspar, whereas they occur in roughly equal proportion in the ignimbrites (Table 2.1; Figure 2.30a). This reflects a greater abundance of basement-derived metamorphic quartz in the polymictic volcaniclastic deposits (Figure 2.30b). In the sandstones and conglomerates, metasedimentary basement-derived clasts are the dominant lithic component (Figure 2.30c), whereas in the ignimbrites, dolerite and basalt are more abundant (Figure 2.30d).

Interpretation: . The polymictic volcaniclastic sandstones and conglomerates record rapid deposition under predominantly high energy conditions, within an active subaerial volcanic landscape, and are interpreted as high energy fluvial deposits sourced from erosion of the underlying ignimbrites and an older basement provenance. A thin lens of welded ignimbrite (15 m thick) is locally interbedded with the facies (GR 490860; Figure 2.28), indicating that pyroclastic activity was ongoing during its deposition. The restricted geography of the facies association, its overall broadly lensoidal, channel-form geometry and substantial thinning of the underlying Non-welded Ignimbrite beneath the deposits suggest deposition within an incised fluvial valley topography eroded into the underlying ignimbrite succession.

The massive to diffusely stratified conglomerate and sandstone intervals record rapid, steady to pulsing deposition from sediment-laden, high flow regime currents, consistent with hyperconcentrated flood flow processes (Smith 1986). Deposition from hyperconcentrated flood flow is thought to occur by both tractional and suspension processes. The high sediment concentrations dampen turbulence within the flow, and dispersive pressures generated by grain collisions and/or buoyancy play a significant role in particle support (Smith 1986). Sand- and gravel-sized particles are typically carried in suspension, whereas outsized clasts are transported as bedload (Pierson and Scott 1985). Normal grading reflects flow deceleration, and stratification is better developed in upper fine-grained parts of normally graded depositional units. Planar lamination in some fine-

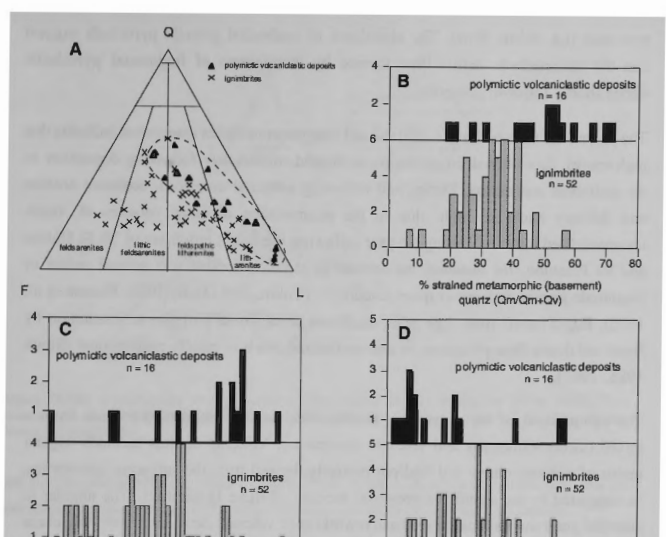

Figure 2.30: (a) Petrographic-based classification (Folk 1980) of polymictic volcaniclastic sandstones and siltstones of the Pul Pul Rhyolite. The underlying ignimbrites are plotted for comparison, illustrating the lower abundance of feldspar in the polymictic volcaniclastic sandstones; (b) comparison of the proportion of basement-derived metamorphic quartz grains in the polymictic volcaniclastic deposits and underlying ignimbrites; (c) comparison of the proportion of quartz-rich basement clasts in the two facies; and (d) comparison of the poportion of mafic clasts (dolerite and basalt) in the two facies.

grained sandstone and siltstone beds reflects tractional sedimentation (planar bed flow), probably also under high flow regime conditions. Isolated sets of trough cross-strata within predominantly massive to diffusely laminated sandstone intervals reflect streamflow reworking of these deposits by moderate flow-regime currents, following flood flow events or during waning flow stages.

The massive, fine-grained volcaniclastic sandstone bed contains unabraded juvenile pyroclasts (angular quartz and feldspar crystals), and has a poorly sorted, matrix-supported internal structure that is consistent with pyroclastic flow facies characteristics. However, the massive facies preserves no evidence for a hot state of emplacement, and the internal structure may also reflect *en masse* deposition by water-supported mass flow

processes (i.e. debris flow). The abundance of unabraded juvenile pyroclasts suggest that the volcaniclastic debris flow formed by mobilisation of fragmental pyroclastic debris shortly following eruption.

The polymictic volcaniclastic sandstone and conglomerate facies association indicates that high energy depositional processes predominated immediately following deposition of the ignimbrite succession. During and following subaerial eruptions, sediment erosion and delivery rates are high, due to the accumulation of large volumes of loose, unconsolidated material. During the year following the recent eruptions of Mt St Helens and Mt Pinatubo, for instance, the amount of sediment eroded was several orders of magnitude greater than pre-eruption conditions (Collins and Dunne 1986; Pierson et al. 1992). Rapid runoff from high relief catchment areas would promote sedimentation by flood and debris flow processes, as unconsolidated debris is rapidly redistributed (Smith 1986, 1987).

The composition of the polymictic volcaniclastic deposits reflects derivation from a mixed (meta)sedimentary and volcanic provenance. Volcanic detritus includes angular grains of volcanic quartz and feldspar probably derived from the subjacent ignimbrites, as suggested by the significant erosional incision of these ignimbrites. The angular to euhedral grain shapes indicate minimal reworking of volcanic detritus. Some lithic clasts could also be derived from erosion of the underlying ignimbrites. However, the polymictic volcaniclastic facies is enriched in quartz-rich metasedimentary basement clasts relative to the underlying ignimbrites, and a dominance of quartz over feldspar is recorded in their crystal population. These features infer a sediment contribution from an older basement provenance in addition to the penecontemporaneous volcanic landscape, indicating the fluvial drainage system extended headward into the exposed basement beyond the margins of the volcanic terrain.

2.4 INTRUSIVE FACIES

Numerous porphyry bodies are associated with the volcanic succession of the Pul Pul Rhyolite. The porphyries are divided into three groups based on their geochemical composition, mineralogy and texture (Figure 2.31): (1) fine-grained, aphyric to sparsely-porphyritic rhyolites; (2) rhyolite porphyries; and (3) quartz monzonite porphyries (with both megacrystic and sparsely porphyritic varieties). The main body of fine-grained rhyolite occurs as a large, tabular body covering a surface area of about 6 km^2, and sills and dykes of similar composition also occur throughout the ignimbrite succession. The rhyolite and quartz monzonite porphyries occur as small hypabyssal stocks (maximum diameter about 1 km). The texture of these units indicates they were emplaced as coherent masses. Phenocrysts are unbroken and euhedral in shape (Figures 2.32-2.34),

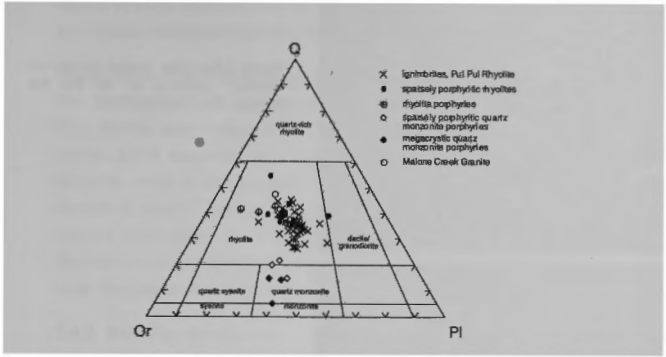

Figure 2.31: Classification of the intrusions using the system of Streckeisen (1976, 1979). The compositions are based on CIPW-normative values for Q-Or-Pl. Ignimbrites of the Pul Pul Rhyolite are plotted for comparison.

and glomeroporphyritic aggregates of quartz and feldspar are common, indicating that in contrast to the ignimbrites, these units are not the product of explosive volcanism.

2.4.1 Rhyolite dome and related sills and dykes

The main body of fine-grained rhyolite occurs in the southeast of the study area, as a large, coherent, tabular body about 6 km in length, which cross-cuts the ignimbrite succession (Figure 2.2). However, small rhyolite dykes about 1m wide, of similar composition and appearance to the large rhyolite body, intrude the top of the ignimbrite succession at several other localities, distinctly cross-cutting the fabric of the ignimbrites at a low angle (Figure 2.32a), and numerous small sills and dykes also intrude the overlying turbidite succession of the Big Sunday Formation (Figure 2.32b). The rhyolites have a narrow silica range (between 74.5-78% SiO_2). They are pink to brick-red in hand specimen (Figure 2.32c), and may be massive or flow banded, and aphanitic or sparsely porphyritic. They contain up to 5% dispersed crystals of embayed and resorbed volcanic quartz, K-feldspar and plagioclase that are up to 2 mm in diameter, with minor opaques. Feldspars commonly form glomeroporphyritic clusters and are replaced by sericite and chlorite. The groundmass of the large rhyolite body is devitrified to form abundant micro-spherulites of radiating clusters of alkali feldspar fibres about 0.5 mm in diameter (Figure 2.32d). The flow banding is defined by the differential development of micro-spherulitic textures in the different layers. The groundmass of the

Figure 2.32a: Flow banded rhyolite sill intruding ignimbrite of the Pul Pul Rhyolite. GR 247600 8487800.

Figure 2.32b: Rhyolite dyke intruding tuffaceous siltstone of the Big Sunday Formation. GR 249800 8485600.

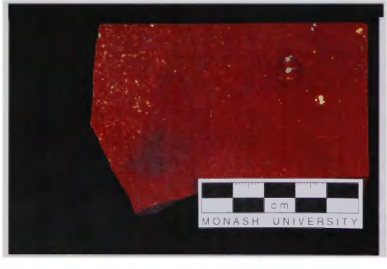

Figure 2.32c: Handspecimen of the aphyric to sparsely porphyritic rhyolite. Sample 89123111. GR 257800 8484700.

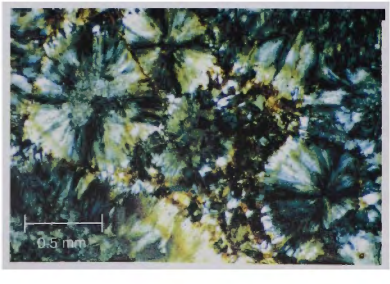

Figure 2.32d: Photomicrograph of the aphyric to sparsely porphyritic rhyolite, showing spherulitic crystallisation of the groundmass. Sample 89123111.

rhyolite dykes is devitrified and recrystallised to a fine granophyric aggregate of quartz and feldspar which exhibits some alteration to clay, even in the freshest samples.

Emplacement of the rhyolite sills and dykes clearly postdates deposition of the ignimbrite (Pul Pul Rhyolite) and overlying turbidite succession (Big Sunday Formation). The larger rhyolite body is likely to have been emplaced coevally with these smaller rhyolite bodies, and is interpreted to be a high-level intrusive dome. The rhyolite body cuts across the strike of the ignimbrite succession suggesting an intrusive contact, and the absence of rhyolite clasts in younger ignimbrites suggests that the rhyolite was not exposed at the surface as a lava flow. As discussed in more detail in Section 2.5, the rhyolites are compositionally related to the ignimbrites, and are interpreted to be a late-stage, fractionated derivative of the same magma body.

2.4.2 Rhyolite porphyries

Rhyolite porphyries occur within the Coronation Sandstone, Pul Pul Rhyolite and Big Sunday Formation in the central to eastern region of the study area (Figure 2.2). The rhyolite porphyries range in size from small bodies no larger than 2-4 m^2 in outcrop size (Figure 2.33a), to larger stocks covering areas of about 1 km^2. The larger bodies are mostly confined to the base of the ignimbrite succession of the Pul Pul Rhyolite, and the underlying Coronation Sandstone. In most cases, their contact relationship with other units is difficult to discern, but one cliff exposure along the South Alligator River (GR 468890) shows a large rhyolite porphyry body that clearly intrudes the turbidite succession of the Big Sunday Formation. The porphyry has an irregular contact, contains inclusions of the country rock near its margins and cross cutting veins of porphyry emanate from the main body into the adjacent sedimentary rocks. The widespread occurrence of rhyolite porphyry clasts within the ignimbrites of the Pul Pul Rhyolite indicates there were several phases of porphyry emplacement. Rhyolite porphyries emplaced prior to ignimbrite eruption, either as small high level intrusions or lavas were eroded and incorporated into the ignimbrite-forming eruptions as accessory or accidental lithics. Using the SHRIMP (Sensitive High Resolution Ion Microprobe) U-Pb zircon technique, a crystallisation age of 1827.3±3.5 Ma was obtained for a rhyolite porphyry intrusion. A rhyolite porphyry clast within the ignimbrites, eroded from an earlier porphyry phase, yielded a crystallisation age of 1828.1±3.5 Ma. By comparison, a numerical age of 1828.6±5.2 Ma was obtained for the ignimbrite succession (see Chapter 5).

The rhyolite porphyries are massive and homogeneous, non-vesicular and moderately to highly porphyritic. Most bodies have 25-30% crystals, but some are more porphyritic with crystal concentrations of 50%. They classify as rhyolites based on their high silica

Figure 2.33a: Small rhyolite porphyry body intruding the Lower Ignimbrite Member of the Pul Pul Rhyolite. GR 252700 8486100.

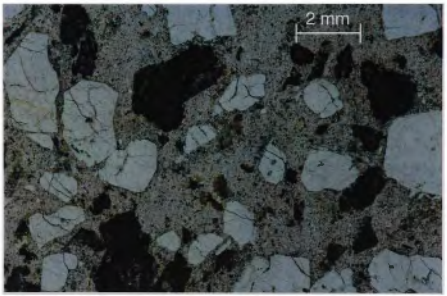

Figure 2.33a: Photomicrograph of a rhyolite porphyry. Sample 89123002.

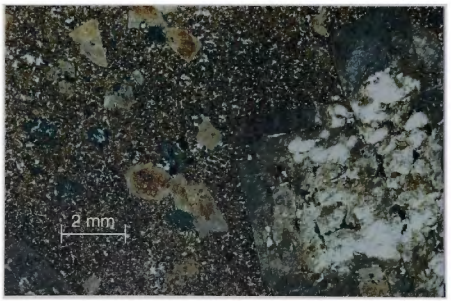

Figure 2.33a: Photomicrograph of a megacrystic quartz monzonite porphyry body, showing a cluster of K-feldspar megacrysts in the lower right hand corner. Sample 88126007.

content (>75% SiO_2) and mineralogy (Figure 2.31). Phenocrysts consist of euhedral quartz, K-feldspar and plagioclase up to 5 mm in diameter, and minor fine-grained opaques (Figure 2.33b). Glomeroporphyritic aggregates of quartz and feldspar are common. The quartz is monocrystalline with straight extinction, it contains fluid inclusion trails, and has rounded corners and embayments indicating resorption. K-feldspar is the most abundant feldspar, with minor plagioclase crystals. Feldspar is fresh to slightly altered to sericite, minor chlorite and clay minerals, giving the altered crystals a dusty appearance. This alteration also affects the groundmass of some samples. The groundmass is devitrified and recrystallised to a fine granophyric aggregate or, less commonly, consist of micro-spherulites up to 0.5 mm in diameter.

2.4.3 Quartz monzonite porphyries

The quartz monzonite porphyries can be subdivided on the basis of their phenocryst abundance and grainsize, into megacrystic and sparsely porphyritic varieties. The megacrystic quartz monzonite porphyries have a silica content of about 64% SiO_2. They were originally classified as syenites by Stuart-Smith et al. (1988), probably due to the abundance of large, randomly orientated, white tabular K-feldspar phenocrysts, which are prominent in hand-specimen. However, plagioclase is an equally ubiquitous groundmass and phenocryst phase, and the porphyries classify as quartz monzonites based on the classification system of Streckeisen (1976; Figure 2.31). The sparsely porphyritic quartz monzonite porphyries have a similar geochemical composition (63-66% SiO_2) and mineralogy, but are markedly different in texture.

Megacrystic quartz monzonite porphyries: Megacrystic quartz monzonite porphyry dykes and stocks, up to 500 m across, are exposed 2 to 3 km from the Malone Creek Granite around its southwestern and eastern margins, where they intrude the Pul Pul Rhyolite and Big Sunday Formation, and earlier Palaeoproterozoic geosynclinal metasediments that form a basement to the El Sherana Group (Stuart-Smith et al. 1988). The megacrystic quartz monzonite porphyries are massive and homogeneous, non-vesicular and highly porphyritic, with 40-50% phenocrysts of K-feldspar and plagioclase (Figure 2.33c). Quartz does not occur as a phenocryst phase. Tabular K-feldspar phenocrysts are commonly 5 mm in diameter, and glomeroporphyritic aggregates of K-feldspar are up to 1-2 cm in size, appearing as large megacrysts in outcrop and hand specimen. Plagioclase phenocrysts are slightly smaller, with single grains about 1 mm in diameter, and aggregates 2-5 mm in size. The groundmass is devitrified, recrystallised to coarse granophyric aggregates of quartz, K-feldspar and plagioclase, with minor chlorite, epidote and carbonate. All feldspars are partly altered to hematite, sericite, chlorite and clay. The megacrystic quartz monzonite porphyries mainly intrude along or near the

Figure 2.34a: Sparsely porphyritic quartz monzonite porphyry, exhibiting a fine network of veinlets and silica-filled fractures. Hematite and chlorite alteration emanate from the fracture system. GR 244800 8493600.

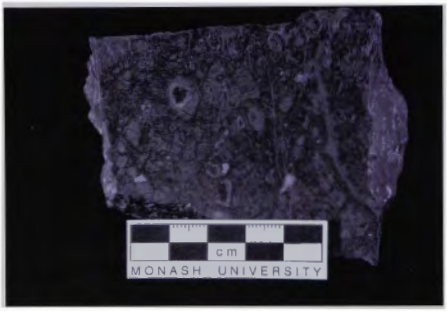

Figure 2.34b: Handspecimen of sparsely porphyritic quartz monzonite porphyry, collected near a cross-fault running perpendicular to the main Palette Fault. Siliceous alteration emanating from the pervasive fracture system gives the rock a nodular appearance. Sample 89123073. GR 244900 8493100.

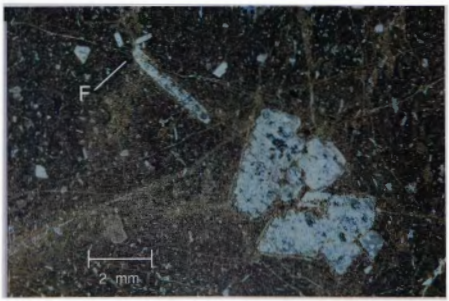

Figure 2.34c: Photomicrograph of the sparsely porphyritic quartz monzonite porphyry. Small feldspar microlites are ubiquitous throughout the groundmass. Fractures cross-cut feldspar phenocrysts (F), indicating fracturing post-dated initial crystallisation of magma. Sample 89123095.

Palette Fault, and this close spatial association suggests the fault was used as a conduit providing a pathway for the intrusive magma.

Sparsely porphyritic quartz monzonite porphyries: The sparsely porphyritic quartz monzonite porphyries contain significantly less phenocrysts (less than 10%), which are much smaller than those in the megacrystic porphyries described above (≤ 5 mm in diameter). The sparsely porphyritic quartz monzonite porphyries are confined to the northwest region of the study area (Figure 2.2), and outcrop as several large stocks (up to 1.5 x 0.5 km in size) and smaller bodies (up to 250 m in diameter) within the Pul Pul Rhyolite and underlying Coronation Sandstone. The largest stocks discordantly cross-cut the volcanic stratigraphy, inferring an intrusive relationship. They contain 5-10% phenocrysts and glomeroporphyritic clusters of K-feldspar (2-5 mm in diameter) and plagioclase (1-2 mm in diameter), in roughly equal proportion. The plagioclase is commonly sericitised. K-feldspar phenocrysts are fresh, or altered to clay (± epidote, sericite). Quartz does not occur as a phenocryst phase. The groundmass consists of a fine granophyric aggregate of quartz and K-feldspar, with abundant plagioclase microlites, about 0.25-0.5 mm in diameter. The sparsely-porphyritic quartz monzonite porphyries are highly altered (hematised) and red in colour. They are laced with a network of fine quartz veinlets, and fractures rimmed by hematite and chlorite alteration (Figure 2.34a). Along a splay of the main Palette Fault, the siliceous alteration emanating from fine fractures and veinlets gives the rocks a nodular appearance, and the rock is light grey in colour (Figure 2.34b). This pervasive fracturing and fluid circulation suggests pressure fluctuations between lithostatic and hydrostatic. The fracturing of phenocrysts postdated initial crystallisation of the magma (Figure 2.34c). The porphyry bodies are spatially associated with a series of faults cross-cutting the ignimbrite succession near its northwest margin. These faults may have provided a pathway for the intrusive dacitic magma, then later acted as conduits for circulating fluids, which pervasively fractured the porphyries.

2.4.4 Malone Creek Granite

The Malone Creek Granite is an almost circular pluton about 10 km in diameter. The ignimbrite succession trends around the south to south-west margins of the pluton (Figure 2.2). The numerical age of the Malone Creek Granite is very poorly constrained, but available data suggest that the granite is younger than the Pul Pul Rhyolite. All attempts to determine the crystallisation age of the Malone Creek Granite using the SHRIMP U-Pb technique have been largely unsuccessful. Most analyses obtained are highly discordant due to the high U contents of zircons in the granite. Williams (1992) commented on the relationship between radioactivity and discordance in zircon grains, observing that in the case of the Watersmeet gneiss (an early Archaean tonalitic gneiss in

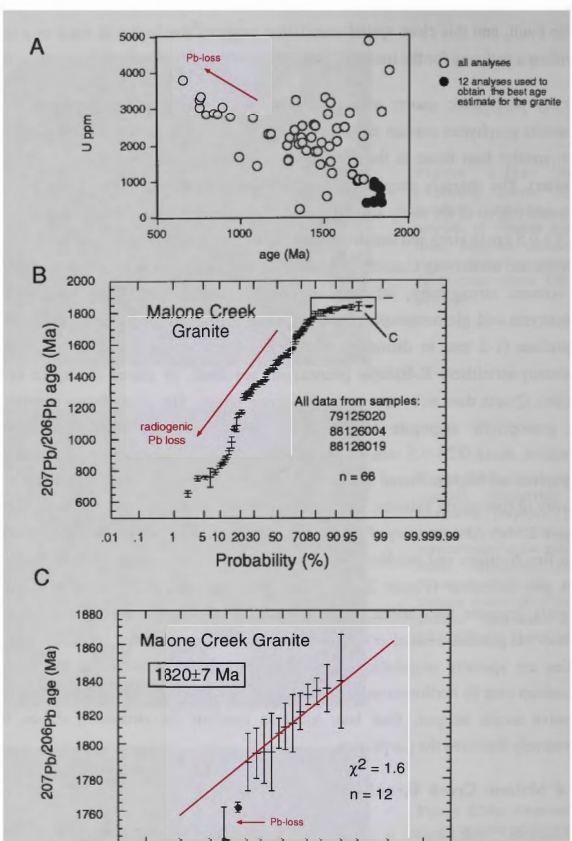

Figure 2.35: (a) U contents of zircons from the Malone Creek Granite. The correlation between U content and $^{207}Pb/^{206}Pb$ age, indicates that the degree of Pb loss is controlled by the U content of the grains. (b) & (c): Probability plots of individual zircon ages for all samples analysed of the Malone Creek Granite (unpublished data extracted from AGSO's OZCHRON database). A normal distribution is represented by a straight line, the slope of which is proportional to the standard deviation: (a) all data (200-5000 ppm U). A large tail in the distribution reflects radiogenic lead loss in high U grains; and (b) analyses containing below 1000 ppm U. 12 ages are within error of each other, and yield an age of 1820±7 Ma (χ^2 = 1.6). Three younger values plot below the normal distribution of this age population, reflecting radiogenic Pb loss.

northern Michigan), metamorphism had the least effect on the lowest U parts of zircon grains. As U contents increased, the likelihood of metamorphic effects and their possible magnitude also increased, and over a threshold U content of 700 ppm, isotopic disturbance was inevitable and usually profound, resulting in complete loss of radiogenic Pb in most such zircon. By comparison, unpublished data for the Malone Creek Granite obtained from the Australian Geological Survey Organisation's OZCHRON database show that most zircons analysed have U contents between 1000-5000 ppm (mean ~ 1500 ppm). These contents far exceed the threshold above which radiogenic Pb loss is likely to pose a significant problem. Only 15 of 66 analyses from three granite samples contained less than 1000 ppm U, containing between 234-969 ppm U. The three youngest analyses from this group of lower U zircons are rejected as outliers resulting from Pb loss. The remaining 12 analyses yield a weighted mean age of 1820±7 Ma, with a χ^2 of 1.6, which is the best available estimate for the age of the Malone Creek Granite (Figure 2.35). By comparison, a U-Pb zircon age of 1828.6±5.1 Ma was obtained for the ignimbrite succession of the Pul Pul Rhyolite in this study (see Chapter 5).

The Malone Creek Granite clearly intrudes the Lower Proterozoic siltstones of the Burrell Creek Formation (Figure 2.36a) and the Zamu Dolerite (Bryan 1962), with contact metamorphic effects extending 200m from the granite margin (Stuart-Smith et al. 1988). Coronation Sandstone basalts underlying the ignimbrites also show signs of contact metamorphism, with local development of biotite and actinolite overprinting the regional lower greenschist facies metamorphic assemblage in the basalts. The only notable change in the ignimbrites is the presence of aplite and pegmatite veins emanating from the granite into the country rock, and the presence of hornblende in some samples collected near the granite contact. On an outcrop scale, the granite margin cross cuts the fabric of the ignimbrites, inferring an intrusive relationship. No granite epiclasts are recorded in the ignimbrite succession, supporting the interpretation that granite emplacement postdated ignimbrite extrusion.

The granite is a quartz-rich alkali feldspar variety. The major constituents are quartz, kaolinised and sericitised K-feldspar and plagioclase and biotite, with accessory fluorite (Figure 2.36b), allanite, zircon, apatite and titanite. The quartz and alkali feldspar are commonly graphically intergrown (Figure 2.36c). The pluton has been mapped as three broadly concentric gradational zones (Stuart-Smith et al. 1988) based mainly on textural criteria rather than mineralogical or geochemical. It has a porphyritic centre, a fine to coarse even-grained middle zone and a fine, even-grained rim with widespread quartz veins and greisens (Stuart-Smith et al. 1988).

Figure 2.36a: Contact between the Malone Creek Granite and the Burrell Creek Formation. The granite contact cross-cuts the fabric of the metasediments, and is clearly intrusive. Clasts of Burrell Creek Formation are incorporated into the Granite near its margin.

Photograph: Dr Lesley Wyborn.

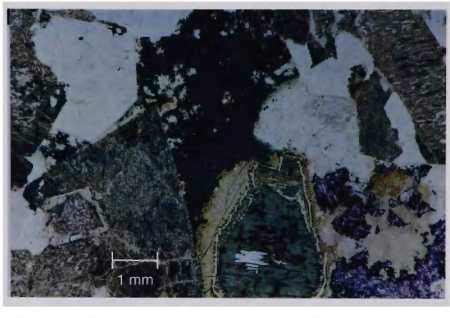

Figure 2.36b: Photomicrograph of the Malone Creek Granite showing a coarsely crystalline texture, and the presence of accessory fluorite (lower right hand corner). Sample 79125023.

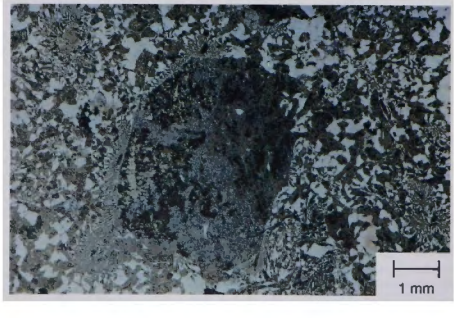

Figure 2.36c: Photomicrograph of porphyritic Malone Creek Granite, with a myrmeckitic texture (plagioclase and quartz intergrowths) developed around the margins of K-feldspar crystals. Sample 88126004.

2.4.5 Dolerite dykes and intrusions

Swarms of east-northeast-trending vertical dolerite dykes intrude the ignimbrites of the Pul Pul Rhyolite, and the Malone Creek Granite (Figure 2.2). These dykes are regional features, also intruding Lower Proterozoic sedimentary succession and filling major joints in the overlying Plum Tree Creek Volcanics, Grace Creek Granite, Cullen Granite, Birdie Creek Volcanics and lower members of the Kombolgie Formation (Stewart 1965; Stuart-Smith et al. 1988). Stuart-Smith et al. (1988) suggest they correlate with a dyke dated at 1370 Ma (Page et al. 1980), which transgresses the Ranger uranium ore body in the northeast of the Pine Creek Inlier. The dykes are clearly late-stage features and unrelated to the magmatic event forming the igneous rocks of the Pul Pul Rhyolite. The dykes have ophitic textures and are composed of andesine, augite, chlorite and magnetite. They are variably metamorphosed to form an albite-sericite-chlorite-epidote assemblage.

A prominent body of dolerite about 1 km long and 30 m wide, intrudes the volcaniclastic sedimentary rocks of the Big Sunday Formation (Figure 2.2), about 16 km SSE of Coronation Hill. It is composed of sericitised and albitised plagioclase, augite, chlorite and minor calcite, with a subophitic texture, and contains large amygdales infilled with chalcedony, calcite and chlorite. The body was originally interpreted as an amygdaloidal basalt, and included as part of the depositional sequence of the Big Sunday Formation (Stuart-Smith et al. 1988). However, it is medium to coarse-grained indicating a doleritic texture, and the grainsize decreases markedly from the centre of the body towards the margins. In addition, it clearly cross-cuts the strike of the volcaniclastic sediments, and so has been reinterpreted as a dolerite intrusion. Smaller outcrops of dolerite (up to 400 m in diameter) intrude the ignimbrites of the Pul Pul Rhyolite. Where fresh, the dolerites contain plagioclase laths up to 2 mm in diameter forming spherulitic clusters or penetrating larger augite crystals to form a subophitic texture. Prehnite and chlorite form interstitially to the plagioclase and augite, and the plagioclase is commonly sericitised. Opaques are abundant. Where altered, the plagioclase is albitised and primary ferromagnesian minerals alter to chlorite, epidote and opaques (magnetite).

2.5 Geochemistry of the magmatic suite

Available geochemical data are used to determine whether the intrusive units form a coherent geochemical suite with the ignimbrites of the Pul Pul Rhyolite, if they evolved from the same magmatic source, or if they are geochemically unrelated. In particular, the geochemical relationship between the Malone Creek Granite and volcanics of the Pul Pul Rhyolite is examined, as this has important implications for interpreting the

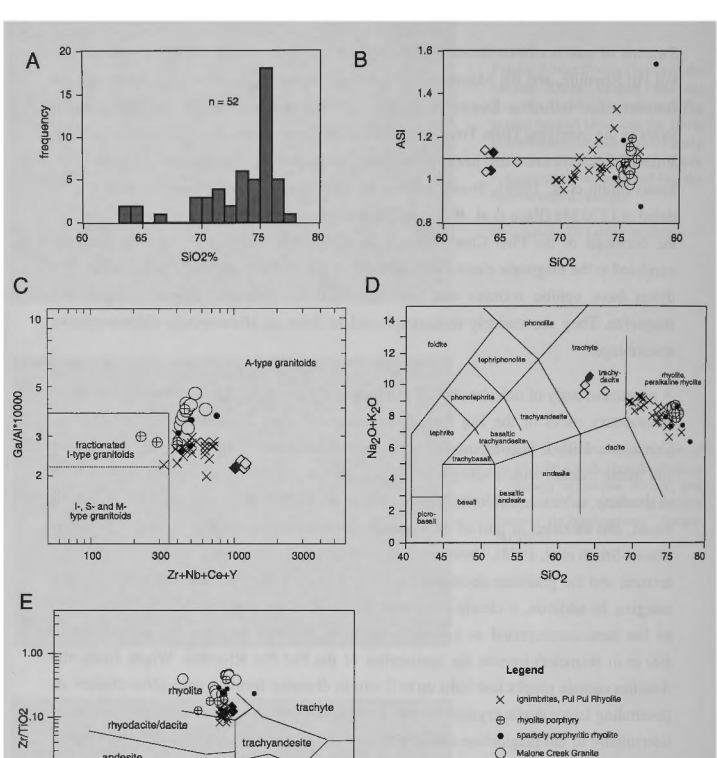

Figure 2.37: Classification of the Pul Pul Rhyolite-Malone Creek Granite magmatic suite: (a) Frequency histogram showing the silica range of the suite; (b) ASI ratios; (c) Ga/Al vs HFSE (high field strength elements) classification system of Eby (1990); (d) the geochemical classification system for volcanic rocks of LeBas et al. (1986); and (e) a classification system based on immobile trace elements (Winchester and Floyd 1977).

palaeovolcanology and palaeogeographic context of the succession. The spatial association between the Malone Creek Granite and the Pul Pul Rhyolite is suggestive of a resurgent dome intruding a co-magmatic ignimbrite pile (Chapter 4), and geochemical analysis is used to test whether these units are intrusive and extrusive derivatives of the same magmatic episode.

The Pul Pul Rhyolite ignimbrites and associated intrusions form a geochemical suite of silicic igneous rocks (quartz monzonites, rhyolites, granites) with a silica range of 63-79% SiO_2. (Figure 2.37a). The suite is metaluminous to mildly peraluminous with ASI (aluminium saturation index) ratios mainly < 1.1 (Figure 2.37b), and has less than 1% normative corundum. These features define the rocks as I-type or 'infracrustal', based on the criteria of Chappell and White (1984). The suite plots in the A-type field as defined by Eby (1990) for Palaeozoic granites (Figure 2.37c), and both the ignimbrites and the Malone Creek Granite have high F contents and contain visible fluorite. Most facies classify as rhyolites (granites, in the case of the Malone Creek Granite) using classification systems based on both alkali elements (Figure 2.37d) and immobile elements (Figure 2.37e). There is a small compositional gap between the quartz monzonite porphyries (63-66% SiO_2) and the rhyolitic ignimbrites (69.5-77% SiO_2; Figure 2.37a). All other intrusions, including the Malone Creek Granite, plot as high-silica end-members to the ignimbrites.

The suite begins to fractionate significantly at about 76% SiO_2. The Malone Creek Granite is highly fractionated relative to the ignimbrites (Figure 2.38, 2.39). Once fractionation commences, the SiO_2 level remains fairly constant, as the values of incompatible elements such as Nb, Th, U, Y, Ga, Nd and Rb rise exponentially. If all samples of the Malone Creek Granite are plotted, it also appears to be strongly enriched in K_2O, but this enrichment is a secondary potassium alteration effect involving conversion of plagioclase to K-feldspar, and consequent enrichment of K_2O and depletion of Na_2O. If the samples affected by alteration are removed (those with < 2% Na_2O), the remaining unaltered samples are only slightly K_2O enriched (Figure 2.39). The granite is markedly depleted in Ba, Sr, Fe_2O_{3tot}, TiO_2, MgO, V, Sc, and P_2O_5, and less depleted in La, Ce, Zr, Zn and CaO relative to the ignimbrites. K/Rb decreases with increasing SiO_2. Depletion in Ba and Pb may be explained by fractionation of plagioclase and K-feldspar. Enrichment of Ga can result from fractionation of feldspars and quartz. Also, in high fluorine granites, Ga is concentrated in the melt by forming GaF^{3-}_6 complexes (Collins et al. 1982). MgO, Fe_2O_3, FeO, and TiO_2 depletion suggest biotite, magnetite and ilmenite may also control the fractionation trends. Depletion of Zr and LREE's is consistent with fractionation of zircon, monozite and allanite. This interpretation is consistent with the mineral assemblage observed in the granite. Nb, F,

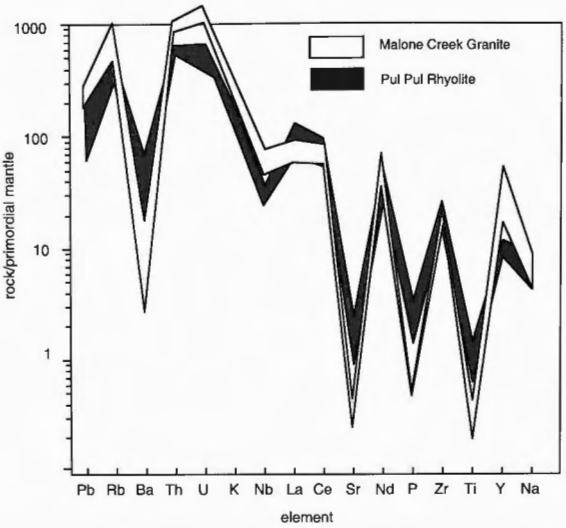

Figure 2.38: Extended trace element diagram comparing trace element patterns of the Malone Creek Granite with the Pul Pul Rhyolite. The Malone Creek granite has a more fractionated trace element pattern than the Pul Pul Rhyolite.

Rb and the incompatible elements (Th, U, Y) are strongly partitioned into the melt of felsic magmas, explaining their enrichment in the more differentiated samples. Thus the geochemical data are consistent with the Malone Creek Granite having evolved by fractional crystallisation from the same melt that sourced the ignimbrites, with crystal fractionation controlled by the removal of K-feldspar, albite, some quartz, biotite, ilmenite, magnetite and accessory phases from the melt.

The fine-grained, aphyric to sparsely porphyritic rhyolite dome and associated sills and dykes that intrude the Pul Pul Rhyolite are compositionally similar to the Malone Creek Granite, and are also fractionated relative to the ignimbrites. On variation diagrams, the fine-grained rhyolites plot consistently with the Malone Creek Granite for most elements. They do not show the same high degree of enrichment of incompatible and high field strength elements as the granite, but these elements are enriched relative to the most evolved ignimbrites, and have the same degree of enrichment as the least fractionated granite samples. The fine-grained rhyolites are interpreted to be early differentiates of the

final melt phase, extracted and emplaced before the final stages of fractional crystallisation in the pluton (Malone Creek Granite).

The rhyolite porphyries also plot as high-silica end-members to the ignimbrite suite, but unlike the Malone Creek Granite and late stage, fine-grained rhyolites, the rhyolite porphyries are not significantly fractionated relative to the ignimbrites. The spatial relationship between the ignimbrites and rhyolite porphyries, and their near-identical U-Pb ages, suggest they were emplaced coevally, with several episodes of porphyry emplacement occurring before, during and after ignimbrite emplacement. The rhyolite porphyries are therefore interpreted to have been extracted from early phases of the melt, whereas the Malone Creek Granite and aphyric lavas represent fractionated, late-stage differentiates of the magma body.

In summary, a genetic association is inferred for the ignimbrites of the Pul Pul Rhyolite, the rhyolite porphyries, the Malone Creek Granite and the late-stage fine-grained rhyolite dome and associated sills and dykes. These units are interpreted to be derived from the same batch of magma, in which crystal fractionation was most significant in the late stages of magmatic evolution. After extraction of the ignimbrites and the rhyolite porphyries, the remaining liquid fractionated to produce the fine-grained rhyolites, then continued to fractionate significantly during final crystallisation at depth to produce the small circular stock of the Malone Creek Granite.

The quartz monzonite porphyries define fairly linear trends with the ignimbrites for all major oxides and trace elements (Figure 2.39), suggesting they are also part of the same suite of igneous rocks. The emplacement of these intrusions following eruption of more silicic ignimbrites may reflect vertical differentiation of the source magma chamber, with the quartz monzonites tapping the lower parts of the magma chamber, and the silicic ignimbrites erupting from the more silicic chamber top (e.g. Lipman 1975).

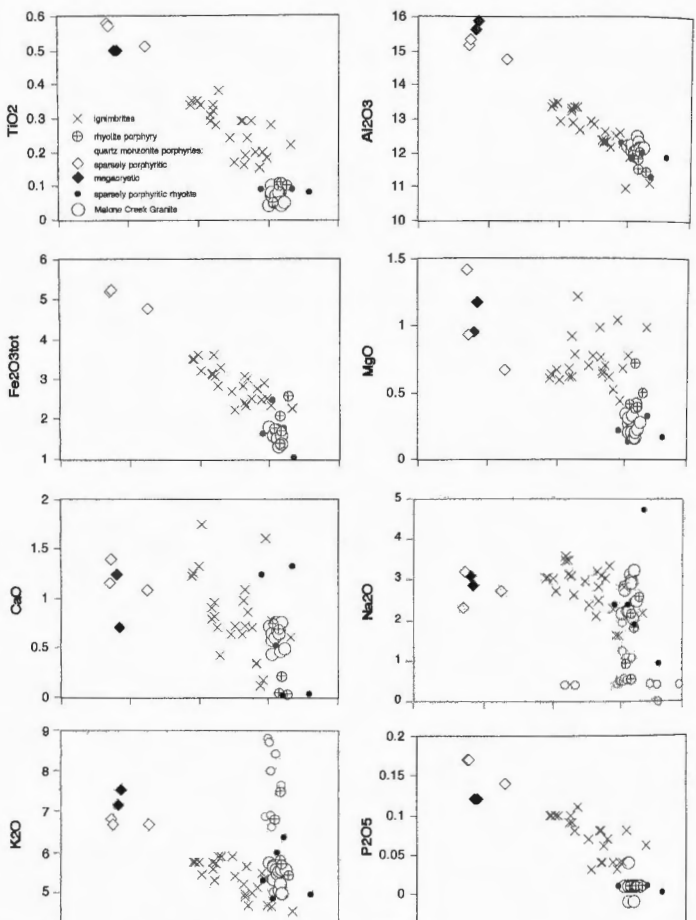

Figure 2.39: Geochemical fractionation plots comparing the Pul Pul Rhyolite ignimbrites and associated intrusions. Only the least altered samples of the Malone Creek Granite have been plotted (those with > 2% Na_2O). The red circles on the Na_2O and K_2O plots represent the full range of values for the granite, and show that its chemstry is greatly affected by post-emplacement alteration.

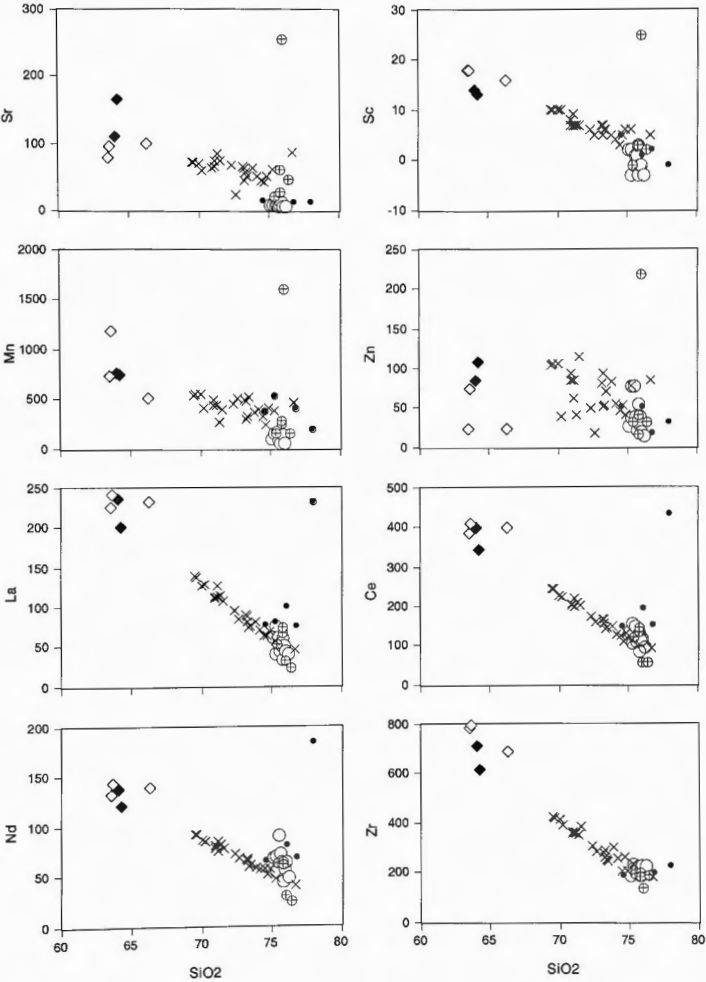

Figure 2.39: cont'd.

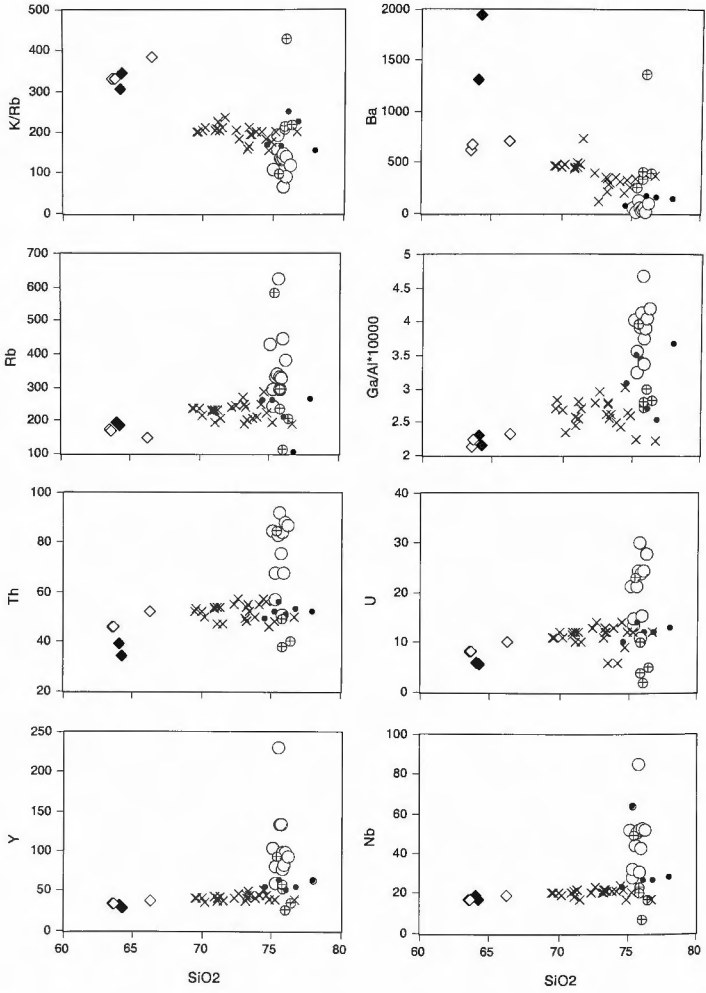

Figure 2.39: cont'd.

CHAPTER 3

Crystal-rich volcaniclastic deposits of the Proterozoic Big Sunday Formation, Northern Territory, Australia: recording the passage of pyroclastic flows into water.

3.1 INTRODUCTION

The Big Sunday Formation overlies the Pul Pul Rhyolite, and is the youngest unit of the El Sherana Group. As presently defined, the Big Sunday Formation is confined to the east of the South Alligator Valley, on the Stow 1:100 000 mapsheet, outcropping continuously over a 17 km strike length east of Big Sunday, and in the Mount Stow and Turnoff Creek areas, further southwest (Stuart-Smith et al. 1988; Figure 3.1). Stuart-Smith et al. (1988) interpreted the contact between the Pul Pul Rhyolite and the Big Sunday Formation as conformable, but at one location sediments of the Big Sunday Formation infill a buttress unconformity against a vertical wall of welded ignimbrite, suggesting local downfaulting and/or landscape erosion to form a palaeovalley or canyon with a relief of about 30m.

The formation was first defined by Needham and Stuart-Smith (1985b), who named it after Big Sunday, a prominent hill 2 km northwest of the type section (GR 457890). The type section runs along the bank of the South Alligator River and minor tributaries, from GR 480875 (bottom) to GR 472867 (top). The type section is described by Stuart-Smith et al. (1988) as consisting of: (1) a lower 280 m thick sequence of fine- to coarse-grained feldspathic greywackes and tuffaceous sedimentary rocks interpreted as a subaqueous 'volcaniclastic-flyschoid' sequence; and (2) an upper sequence, at least 200m thick, comprising amygdaloidal basalt, flow banded rhyolite and ignimbrite. The northwest-trending Palette Fault separates the volcaniclastic sediments and amygdaloidal basalt from the predominantly ignimbritic upper sequence (Figure 3.1). The 'amygdaloidal basalt' described by Stuart-Smith et al. (1988) has been reinterpreted in this study as a medium-grained dolerite intrusion (Chapter 2.4.5), and therefore is not part of the original depositional sequence. The rhyolitic ignimbrites west of the Palette Fault are identical in appearance and composition to the Upper Ignimbrite Member of the Pul Pul Rhyolite east

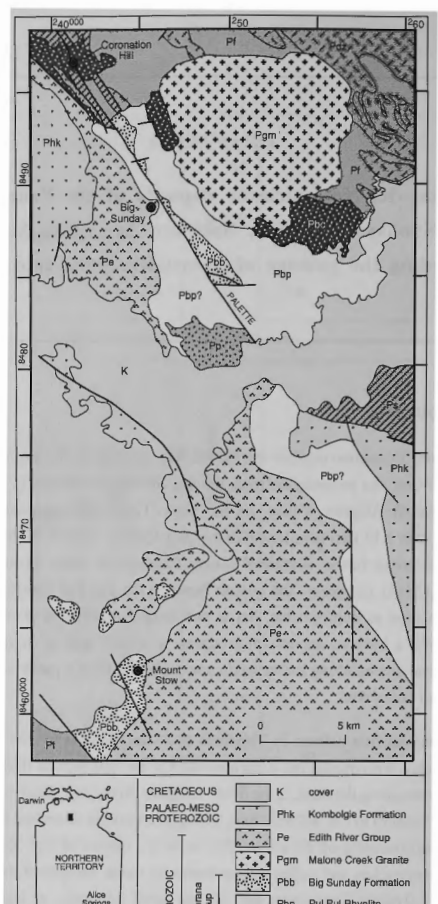

Figure 3.1: Simplified map of the South Alligator Valley region southeast of Coronation Hill, showing the distribution of the Big Sunday Formation and other major lithostratigraphic units.

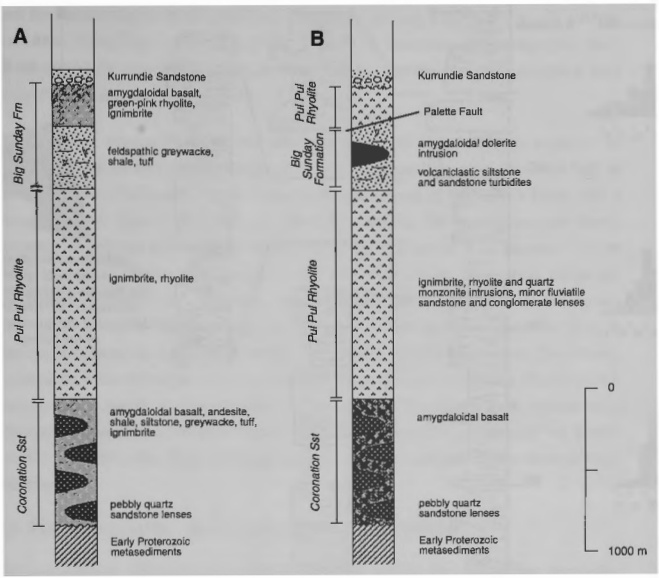

Figure 3.2: (a) Stratigraphy of the El Sherana Group north of Big Sunday (and southeast of Coronation Hill), as interpreted by Stuart-Smith et al. (1988). This interpretation assumes the succession is conformable across the Palette Fault. (b) An alternative interpretation, as suggested in the text, is that fault repetition of the Pul Pul Rhyolite ignimbrite succession occurs across the Palette Fault. If this is correct, the Big Sunday Formation is reduced to representing only the volcaniclastic turbidite succession that lies at the base of the unit as it is presently defined.

of the Palette Fault (described in Chapter 2.2.1). Originally, the entire ignimbrite succession was mapped as a single unit ('undifferentiated Edith River Volcanics'; Stewart 1965; Walpole et al. 1968). By dividing the ignimbrites into separate stratigraphic formations, Stuart-Smith et al. (1988) made an (unjustified) assumption that the ignimbrites west of the Palette Fault conformably overlie the ignimbrites (Pul Pul Rhyolite) and tuffaceous sedimentary rocks (Big Sunday Formation) east of the Palette Fault. An alternative possibility that needs to be considered, is that fault repetition of the ignimbrite succession occurs across the Palette Fault. This alternative scenario would place the entire ignimbrite succession within the Pul Pul Rhyolite, and the Big Sunday Formation could be redefined as containing only the 'tuffaceous sedimentary rocks' that

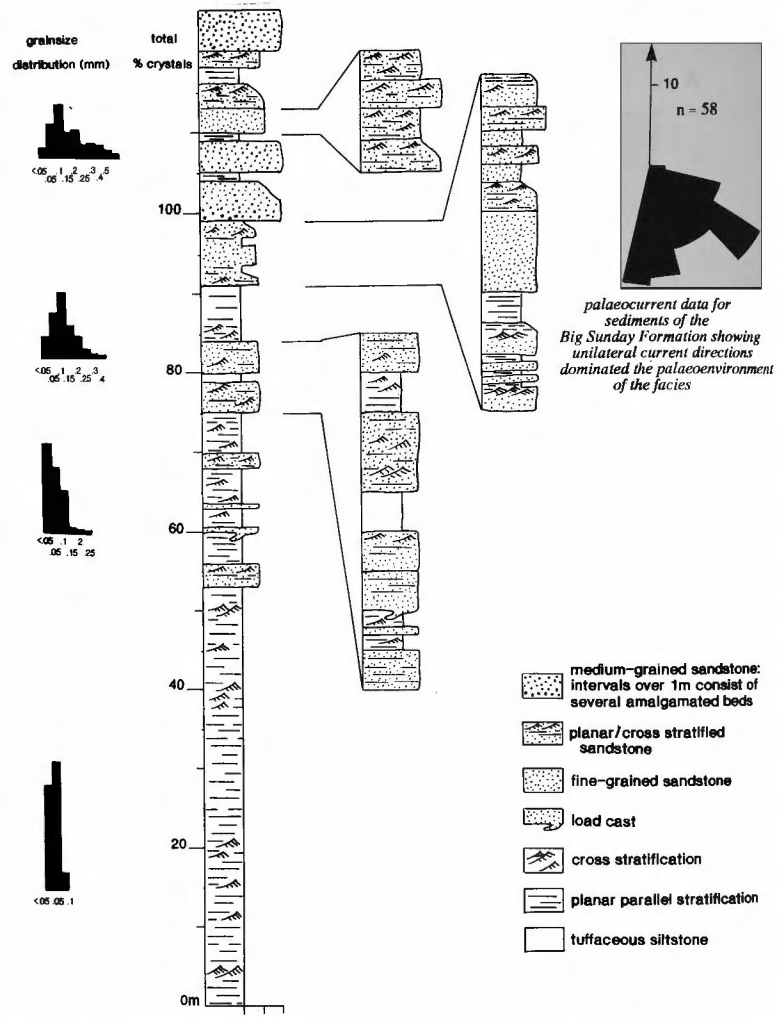

Figure 3.3: Measured section through the interbedded volcaniclastic siltstone and sandstone turbidite sequence of the Big Sunday Formation (Type Section: GR 470875-477875). Palaeocurrent data are from Friedmann and Grotzinger 1994).

presently comprise the lower half of the formation (Figure 3.2). This would significantly limit the aerial extent of the Big Sunday Formation, confining it to small areas of outcrop east of the Palette Fault, and in the Mount Stow area. Resolving this stratigraphic issue conclusively is beyond the scope of the present study, however, as the ignimbrites west of the Palette Fault were not studied in detail.

The following chapter describes and interprets the genetic origin of the sequence of 'tuffaceous sedimentary rocks' which, as presently defined, comprise the lower half of the Big Sunday Formation. The sequence outcrops to east of the Palette Fault over a strike length of about 6 km and unconformably overlies the ignimbrites and fluvial epiclastic sandstones and conglomerates of the Pul Pul Rhyolite. The sequence can be divided into two major facies associations. The main facies association comprises interbedded volcaniclastic siltstones and sandstones (equivalent to the 'tuffaceous sedimentary rocks' of Stuart-Smith et al. 1988). This association is described first, in order to determine the depositional setting for the Big Sunday Formation. The second facies association comprises several amalgamated, thick, massive deposits of crystal-rich volcaniclastic sandstone, that outcrop at the base of the interbedded volcaniclastic siltstone and sandstone sequence (described as a 'volcanolithic greywacke' by Stuart-Smith et al. 1988). The origin of this second, older facies association is the main focus of this chapter.

3.2 VOLCANICLASTIC SILTSTONES AND SANDSTONES

The volcaniclastic siltstones and sandstones which comprise the main facies association of the Big Sunday Formation form a sequence estimated to be about 280 m thick (Stuart-Smith et al. 1988). Approximately 120 m of the sequence is continuously exposed along the type section of the Big Sunday Formation, and a section was measured at this location (Figure 3.3). The basal 50 m of the section consists of fine-grained, massive to finely laminated siltstones that conformably overlie the massive crystal-rich volcaniclastic deposits at the base of the Big Sunday Formation (discussed below in Section 3.3). The siltstones exhibit planar and cross laminations (Figure 3.4a,b). Where exposed, upper bedding surfaces form pavements of exhumed climbing ripples (Figure 3.4c). The basal contacts of thicker massive siltstone beds (2-5 cm) display scouring and flame and load structures (Figure 3.4d). Petrographic analysis of the siltstones indicate they are volcaniclastic in composition, with abundant fine-grained angular volcanic quartz and feldspar dominating grain populations, in a fine siliceous matrix. The siltstones do not contain preserved juvenile vitric pyroclasts such as shards and pumice.

In the upper half of the section, the siltstones are interlayered with coarser-grained sandstone intervals (Figure 3.3). The sandstone beds are also volcaniclastic in

Figure 3.4a: Massive to planar laminated tuffaceous siltstone from the basal 50 m of the volcaniclastic turbidite succession. GR 248600 8484800.

Figure 3.4b: Massive sandstone passing upward into cross laminated then planar laminated sandstone (representing Bouma divisions A, C and D, respectively). GR 246750 8486850.

Figure 3.4c: Exhumed upper bedding surface forming a pavement of assymetrical climbing ripples, showing unilateral current directions. From the basal tuffaceous siltstone interval of the volcaniclastic turbidite sequence. GR 249800 8485600.

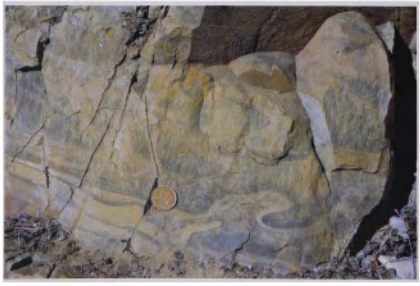

Figure 3.4d: Load casts at the base of a massive sandstone bed (Bouma division A). GR 246750 8486850.

composition, containing abundant grains of angular volcanic quartz, K-feldspar and minor plagioclase in a fine-grained siliceous matrix. Quartz and feldspar occur in sub-equal proportions, with slightly more quartz in most samples, and using the classification scheme of Folk (1980), the sandstones are described as feldsarenites. Small lithic fragments include polycrystalline quartz grains derived from a plutonic source, and minor chert, gneiss and dolerite (Table 3.1). The sandstones are texturally sub-mature, with angular to subrounded grains, and poor to moderate sorting. Some quartz grains have sutured margins, or polycrystalline siliceous overgrowths, indicating some removal of silica and some recrystallisation has occurred. The primary mineralogy is overprinted by a metamorphic assemblage of chlorite+calcite+epidote+sericite.

The sandstone beds exhibit features such as graded bedding, sharp bases with flute and load casts and internal structural features consistent with the Bouma sequence (Bouma 1962; Figure 3.4b,d), and are identified as turbidites. Sandstone beds are medium-grained and become coarser-grained up section. Sandstone beds in the upper stratigraphic horizons have a lower percentage of matrix material and a higher percentage of quartz and lithic fragments than those lower in the sequence. Bed thicknesses increase towards the top of the sequence, from < 10 cm to over one metre and siltstone intervals are less frequent near the top of the succession. Beds in the middle of the section are dominated by divisions B and C of the Bouma sequence (plane parallel laminae, and ripples and cross laminae respectively). Near the top of the succession more beds begin with the massive Bouma A division and individual sandstone beds amalgamate to form thick sandstone intervals.

Interpretation: Although the siltstones at the base of the sequence are composed entirely of volcanically derived, siliceous ashy material, a pyroclastic mode of deposition is ruled out by the extreme thickness of the siltstone interval. Planar laminated fine tuffs of pyroclastic fall deposits are rarely > 10 m thick (Cas and Wright 1987) and the basal siltstones have an uninterrupted thickness of over 50 m. In addition, structures such as ripple pavements, and basal scours and flame structures preserved within the siltstones indicate an element of lateral current transport, so that individual layers represent discrete episodes of deposition rather than semi-continuous fallout from an ash cloud. The siltstones are interpreted to have been deposited by suspension sedimentation (represented by planar laminations) within a standing body of water with periodic deposition under short-lived, higher energy events. Given the restricted preserved lateral extent of the subaqueous facies in a predominantly subaerial environment, the sequence is interpreted as lacustrine in origin. Palaeocurrent data for the Big Sunday Formation have a unimodal distribution which indicate a flow towards the southeast (Friedmann and Grotzinger 1994; Figure 3.3). Sediment-laden currents fed from fluvial currents draining

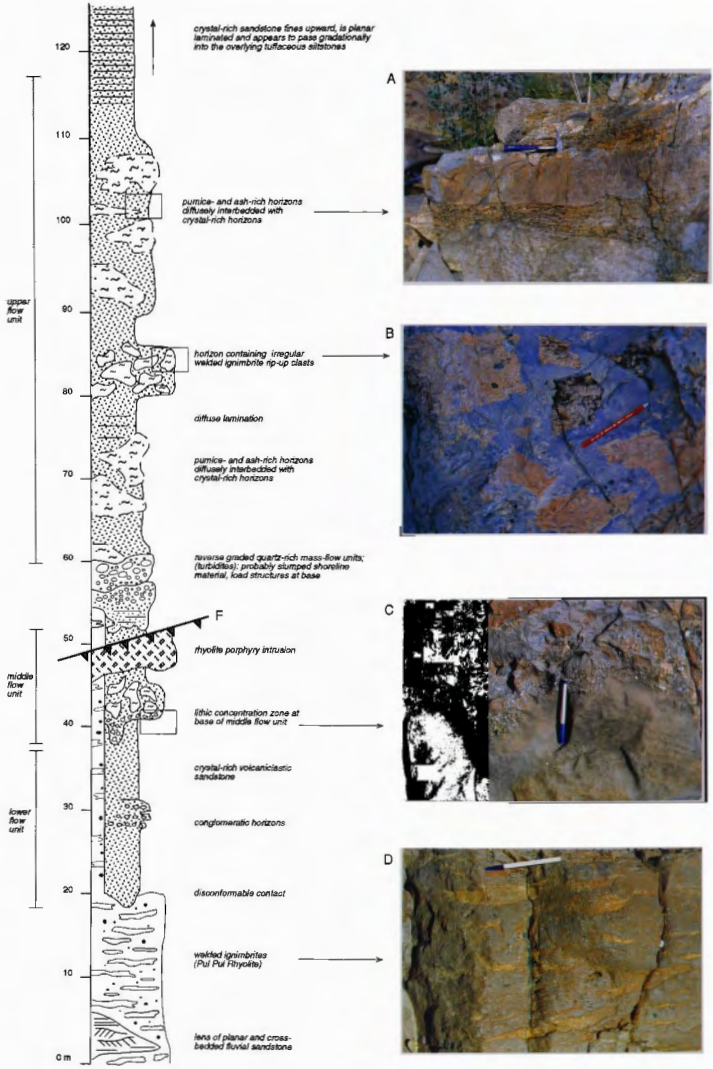

Figure 3.5: Measured section through the thickest exposure of the CRVS (the palaeovalley), exposed in a section along the South Alligator River (GR 468 891 - 466 886).

into the lake through the underlying ignimbritic volcanic succession are considered to source the thick siltstone interval. The thicker, massive siltstone layers record fluctuations in the sediment load of the river.

An increasing influx of clastic sediment into the lacustrine environment is recorded by the thickening- and coarsening- upward sandstone beds in the top half of the sequence. The thicker, coarser-grained beds, increase in sandstone-siltstone ratio and occurrence of amalgamated sandstone beds, and the progressive increase of proximal turbidites (beginning with the Bouma A division) over distal turbidites (divisions B-D) up section, all indicate deposition under conditions of higher to lower flow regime, reflecting closer proximity to the source, which in this case is interpreted to be the river mouth. This pattern is consistent with trends identified in prograding deltas (Walker 1984; Reading 1996). The absence of wave-generated sedimentary structures infers a below storm wave base setting, and deposition in relatively deep water.

Given the volcaniclastic nature of the lacustrine deposits and their close spatial relationship with the thick ignimbrite sequence, it is likely that the siltstones and sandstones were derived from reworking of the subjacent volcanic landscape. The thick volcaniclastic siltstone interval may have been derived from reworking of co-ignimbrite ash-fall deposits associated with the underlying ignimbrites, or from unwelded ignimbrites at the top of the welded ignimbrite sequence. Both co-ignimbrite ash deposits and unwelded ignimbrites have poor preservation potential in subaerial environments, and erosion and resedimentation by fluvial processes may have resulted in the transport of unconsolidated volcanic debris into the lacustrine environment.

3.3 Syn-eruptive crystal-rich volcaniclastic sandstones

Thick, massive crystal-rich volcaniclastic sandstones (CRVS) occur at the base of the Big Sunday Formation, beneath the lacustrine turbidite succession described above. The CRVS fine upward and locally grade into the overlying laminated siltstones, indicating their relationship is conformable. The CRVS disconformably overlie the subaerial ignimbrites and fluvial facies of the Pul Pul Rhyolite. The facies mainly comprises a single, massive, 30 m thick sandstone bed which forms a laterally extensive horizon with a sheet-like geometry. Locally the facies thickens to about 100 m where it overlies and fills a palaeovalley or box canyon with buttress unconformity margins against a vertical wall of ignimbrite (Figure 3.5). The relief on the buttress unconformity suggests the palaeovalley was at least 30 m deep. At least three separate crystal-rich flow units 20-50 m thick can be recognised within this palaeovalley (referred to below as the lower, middle and upper palaeovalley units). The laterally extensive 30 m bed may be the lateral or

outflow equivalent of the upper palaeovalley unit or may overlie the palaeovalley sequence.

Within the palaeovalley the CRVS facies is interbedded with massive, reverse graded, clast-supported, quartz-rich coarse sandstone and conglomerate turbidites, about 2-4 m thick (at ~60m; Figure 3.5). The beds exhibit no tractional sedimentary structures, and the facies characteristics are consistent with transport and deposition by high-density turbidity currents or debris flows (e.g. Lowe 1982). Sub-rounded to rounded lithic clasts (dolerite, metasedimentary basement clasts and chert) within the conglomerate bed infer the material passed through a shallow marine or fluvial environment prior to resedimentation into the deeper water setting, and the beds are interpreted as slumped shoreline material, possibly comprising fluvial epiclastic material similar to that which underlies much of the CRVS facies.

3.3.1 Description of the facies

Sedimentary structures

The CRVS form very thick (30-50 m), massive sedimentation units that lack internal stratification apart from zones of diffuse lamination. The sedimentation units show no sedimentary structures or bedforms, and cross-bedding or other structures indicating tractional deposition are conspicuously absent. Normal grading is mainly confined to the upper levels of the thick sedimentation units, where they fine-upward into fine-grained, diffuse to planar laminated sandstone ± siltstone.

The lower palaeovalley unit (20 m thick), is in sharp contact with the welded ignimbrite that forms the canyon walls, and there is a relief of about 1 m on the underlying surface. The unit has a fine-grained, inversely graded basal layer a few centimetres thick. Fine planar laminations in this layer are defined by a few finer-grained (average grainsize 0.1 mm) ash-rich layers. The contact between the basal layer and the main body of the unit is gradational. The basal layer has a finer-grained crystal population and higher matrix content (50 modal %) than the main body of the unit (20-40 modal %). This basal layer is interpreted as a basal shear zone or traction carpet layer, developed as the basal part of the flow acquires yield strength due to friction between particles (cf. S_2 of Lowe 1982).

The lower and middle palaeovalley units are amalgamated, and the base of the latter is marked by a thin volcaniclastic lithic breccia, about 5 cm thick, which loads into the underlying crystal-rich volcaniclastic sandstone (Figure 3.5c). The basal breccia has a framework comprising angular to rounded pebble-size clasts (dominantly dolerite, composite quartz grains representing metasedimentary basement and chert) supported in a

coarse-grained sandstone matrix. The lithic clasts decrease in size and abundance upwards (coarse-tail grading), and the breccia grades into at least 15 m of massive crystal-rich volcaniclastic sandstone. The middle palaeovalley unit is overlain by a 3 m thick, reverse-graded, quartz-rich pebbly sandstone turbidite. The presence of load structures at the base of the quartz-rich sandstone turbidite indicates the underlying CRVS was unconsolidated during its emplacement.

The base of the upper palaeovalley unit is in contact with a 2.5 m thick, reverse-graded, quartz-rich conglomeratic turbidite, and the presence of load structures at the basal contact indicates the underlying quartz-rich sediments were unconsolidated during emplacement of the CRVS. The unit is about 65 m thick, and grades up into laminated, fine-grained siltstone in the top 10 m.

Texture

The CRVS comprise a clast-supported framework of sand-sized crystals, crystal fragments and lithic fragments in a fine-grained altered matrix. The framework of the sandstones is generally well sorted. The crystals and lithics show a range in grainsize from a maximum of 2 mm down to fine silt-sized grains, with an average diameter of about 0.5 - 1 mm. The sandstones have an immature to submature texture. Crystals are euhedral to fragmented (angular), and generally show no effects of abrasion. Some volcanic quartz, and less commonly K-feldspar, are embayed and have a slightly rounded margins, but this rounding reflects magmatic resorption, and not mechanical abrasion. Lithic fragments are subangular to rounded, reflecting some abrasion by sedimentary processes, but these grains were probably rounded in an earlier sedimentary event, rather than during deposition of the massive sedimentation units.

Composition

The CRVS facies contains abundant crystals and crystal fragments (30-65%), comprising quartz (of volcanic and metamorphic origin), K-feldspar and plagioclase with minor magnetite and zircon, and angular lithic clasts (10-30%). Vitriclasts (largely altered pumice clasts) are a minor component of the lithic population. Shards are not visible or not preserved. Modal abundances derived from point count data are presented in Appendix A3 and summarised in (Table 3.1), and geochemical compositions of representative samples are presented in Appendix A2. The CRVS plot as lithic feldsarenites or felsic litharenites on modal analysis plots (Folk 1980; Figure 3.6), and classify as rhyolites in composition using both geochemical and petrographic-based classification systems (Figure 3.7).

Table 3.1: Summary of modal analyses of facies within the Big Sunday Formation.

Sample no.	Facies	Q%	F%	L%	Mat%	crystals						lithics			matrix	n
						Qv	Qm	Kfs	Pl	Mt	Zr	Lms	Lv	Ld		
89123188	normal' v'clastic turbidite	38.5	29.8	7.5	25.3	231		150	29		2	37	7	1	175	632
89123189	normal' v'clastic turbidite	27.6	24.5	1.6	37.3	221		158	38	1		7	4	2	336	767
89123194	CRVS (basal shear zone)	28.2	11.5	10.1	50.2	163	119	96	19			79	14	8	502	1000
89123154	CRVS (crystal-rich domain)	38.8	24.4	15.0	21.6	105	89	106	16		1	65	8	2	108	500
89123156	CRVS (crystal-rich domain)	34.4	15.6	21.2	28.6	241	103	126	30		2	142	21	49	286	1000
89123035	CRVS (crystal-rich domain)	31.5	8.7	27.3	32.4	126	189	75	12	1		194	21	58	324	1000
89123068	CRVS (crystal-rich domain)	30.5	17.1	19.8	32.5	189	116	132	39	1		115	67	16	325	1000
89123192A	CRVS (crystal-rich domain)	28.7	14.9	22.0	34.3	131	70	77	27		1	105	22	27	240	700
89123077	CRVS (pumice-bearing domain)	18.5	12.9	9.1	59.5	128	57	89	40			83	2	6	595	1000
89123079	CRVS (pumice-bearing domain)	18.2	12.9	14.1	54.8	112	70	97	32			106	24	11	548	1000
89123195A	CRVS (pumice-bearing domain)	32.1	17.0	12.4	38.5	192	129	139	23			70	48	6	385	992
89123195B	CRVS (pumice-bearing domain)	22.3	11.4	8.6	57.4	137	92	107	10	3		66	12	10	589	1026
89123158	CRVS (ignimbrite clast)	10.1	3.9	13.4	72.4	102	40	46	8		1	98	17	73	1015	1400
89123192B	CRVS (ignimbrite clast)	8.0	6.4	14.3	71.3	90	30	83	14			97	15	103	1074	1506

NB: Qv = volcanic qtz, Qm = metamorphic qtz, Kfs = K-feldspar, Pl = plagioclase, Mt = opaques, Zr = zircon,
Lms = metasedimentary basement clasts, Lv = acid volcanic clasts, Ld = dolerite and basalt clasts

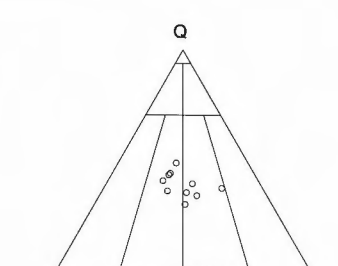

Figure 3.6: Petrographic-based classification of the CRVS, Big Sunday Formation (after Folk 1980).

Quartz is the most abundant framework constituent (~50%), and is of volcanic and metamorphic origin. Volcanic quartz is monocrystalline, and occurs as angular crystal fragments or as unfragmented crystals that exhibit bipyramidal euhedral to slightly rounded, resorbed margins. It is free of inclusions and generally exhibits straight extinction, although weak undulose extinction is observed, and may be due to a low-grade metamorphic overprint. Grainsize is up to 1 mm. About a third of the quartz grains are interpreted to be metamorphic crystals, derived from metasedimentary basement unconformably underlying the El Sherana Group. The metamorphic quartz consists of predominantly rounded grains (although some are angular), that exhibit strong undulose extinction, vapour fluid inclusion trails that imply annealing of grain sutures at depth, and abundant rutile inclusions.

Quartz and feldspars occur at a ratio of roughly 2:1, with feldspar grains forming 20-30% of the framework. K-feldspar is the most common feldspar-type, and occurs as well-formed euhedral crystals and as crystal fragments, that typically range from 0.5-2 mm in length. Microperthites are common and may have a plutonic source or could result from low-grade metamorphic unmixing of original volcanic potassium feldspar. The rest of the K-feldspar is either sanidine or orthoclase, both of which can occur as a volcanic phenocryst phase. Some grains exhibit simple twinning. Most K-feldspar grains are albitised and overprinted by clay minerals, giving the grains a dusty appearance, or are overprinted by sericite ± calcite. Plagioclase is a minor framework constituent. Crystals are typically smaller than the K-feldspar crystals (up to 1 mm in diameter).

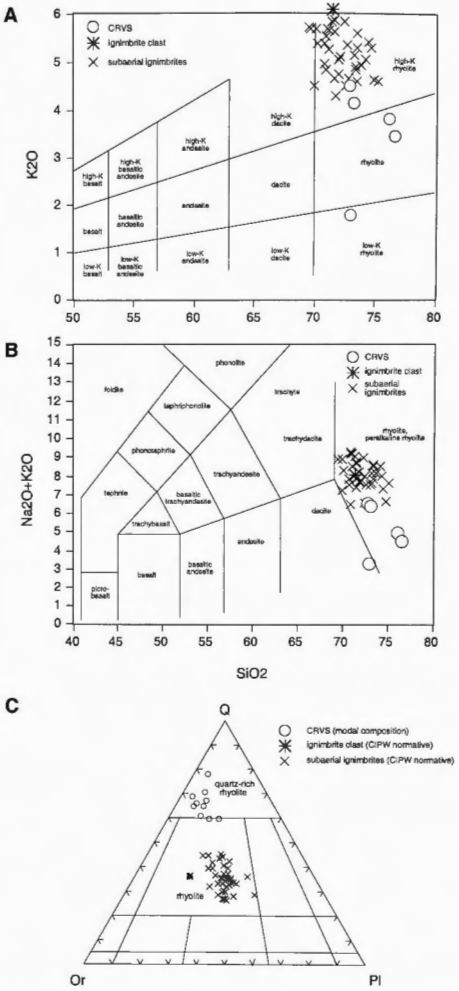

Figure 3.7: Classification of CRVS of the Big Sunday Formation using: (a) the geochemical system of Peccerillo and Taylor (1976), modified after Gill (1981); (b) the geochemical system of LeBas et al. (1986); and (c) the petrographic-based classification system of Streckeisen (1979). The underlying ignimbrites of the Pul Pul Rhyolite, and a welded ignimbrite clast within the CRVS, are plotted for comparison. NB: CIPW normative compositions are used for ignimbrites, because their high matrix content results in inaccurate modal estimates of the three endmember components.

Lithic clasts constitute 20-40% of the framework grains, and in order of abundance, consist of composite quartz, dolerite and chert, with rare clastic sedimentary rock fragments and vitriclasts. About 60% of the composite quartz grains consist of highly strained grain aggregates that exhibit highly variable grainsize, strong undulose extinction and sutured internal grain boundaries. The remainder have a more equigranular appearance. The internal grains are coarser and more even grained, have comparatively straight grain boundaries, and exhibit straight to mildly undulose extinction. Both types are interpreted to be derived from the metasedimentary basement unconformably underlying the El Sherana Group. Other metasedimentary basement fragments include quartz-feldspar aggregates or quartz-(±feldspar)-phyllosilicate aggregates. They are probably phyllite, schist and gneissic fragments derived from the Burrell Creek Formation.

Dolerite fragments consist predominantly of albitised plagioclase laths with interstitial chlorite and opaques, and occasionally larger, tabular K-feldspar crystals. Dolerite clasts are sometimes deformed during compaction of the host arenite to form a pseudomatrix infilling the interstitial spaces between crystals, or breaks down to form plagioclase aggregates. The dolerite is probably of Zamu Dolerite generation, derived from the sills which form part of the basement to the Pul Pul Rhyolite and outcrop to the north and west of the succession. The basic clasts could also be derived from coarse-grained basalts within the Coronation Sandstone.

Sedimentary rock fragments are extremely rare and consist of sandstone or finer-grained siltstone clasts. Rare vitriclasts occur locally and are most common in the arenites which are diffusely mixed with welded ignimbrites. The vitriclasts are sand-sized and lack phenocrysts. They are granophyric aggregates of quartz and feldspar with locally spherulitic textures, and are interpreted to be devitrified, aphanitic volcanic rock fragments, or volcanic rock fragments consisting entirely of groundmass material. They may be derived from the underlying ignimbrites, from rhyolite porphyries intruding these ignimbrites or from contemporaneous pyroclastic flows. Chert grains are likely to represent fragments of recrystallised ignimbrite or porphyry matrix, derived from the underlying volcanic sequence.

A matrix component consisting of a fine-grained microgranular quartz and feldspar mosaic fills the intergranular spaces. The matrix is commonly overprinted by secondary minerals of metamorphic origin such as calcite, chlorite, epidote and sericite. The matrix has the same composition and texture as the ignimbrite matrix of the Pul Pul Rhyolite, and it is likely it was also originally glassy ash which has devitrified and been recrystallised to a secondary mineral assemblage, although in this case, shard forms are

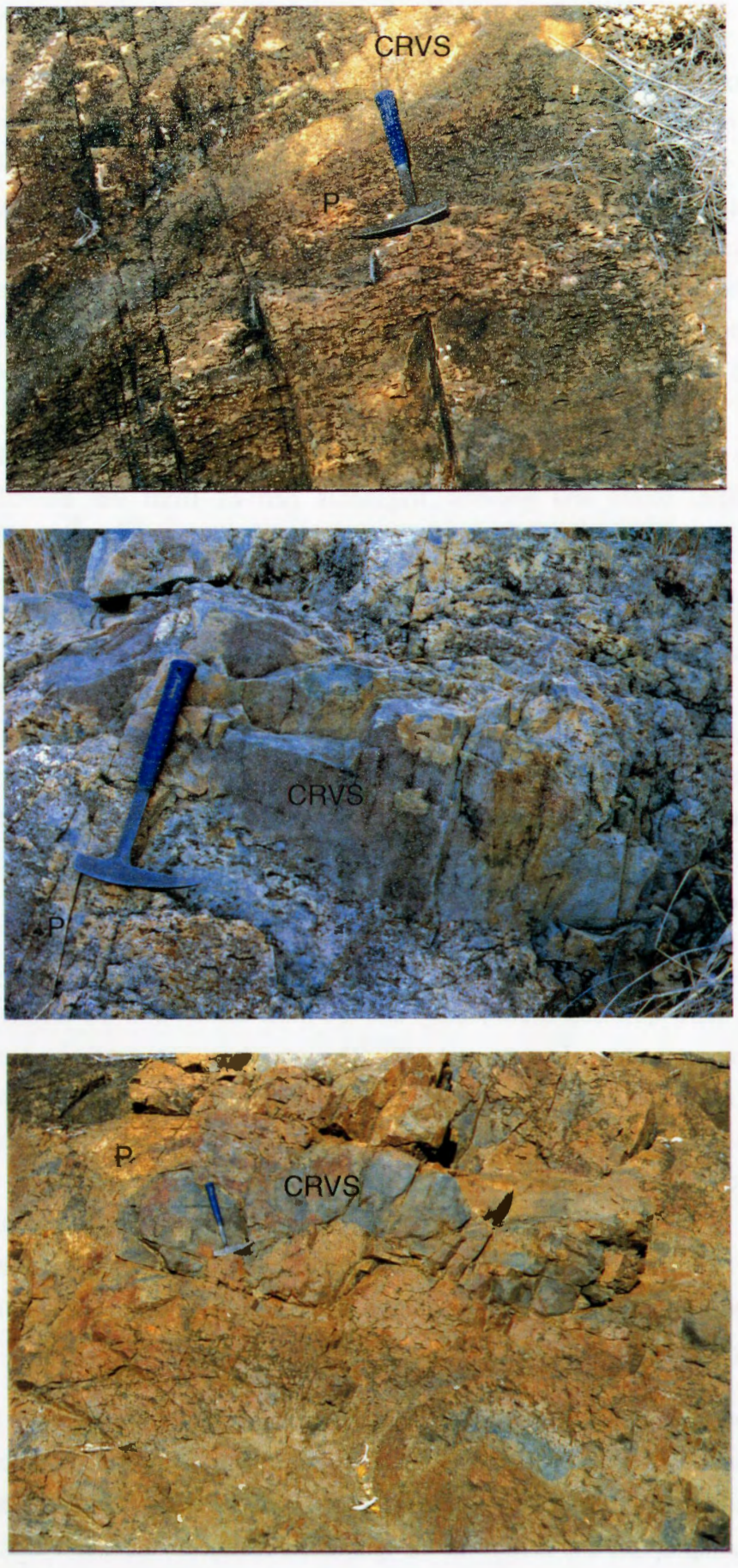

Figure 3.8: Pumice-bearing domains within the CRVS. These horizons also contain a higher proportion of volcanic ash (represented by fine-grained siliceous matrix) than the surrounding crystal-rich domains (~60% pumice+ash c.f. ~30% ash and no pumice). Boundaries between the crystal-rich and pumice- and ash-rich domains are extremely irregular and diffuse, and gradational in terms of crystal content. The pumice (P) is compacted to form a pseudo-eutaxitic texture, and the crystal-rich domains (CRVS) commonly cross-cut this fabric (as illustrated in Figure 3.8a). GR 246700 8488700.

not preserved. The matrix component ranges between 20-40 modal %. The original matrix component may have been higher, but intergranular spaces have been reduced by compaction, and pressure solution at grain boundaries forming siliceous overgrowths on the grains. However, it was probably no more than about 40%, given the clast-supported aspect of the rock.

Pumice- and ash-rich domains

The CRVS facies is dominantly composed of crystal and lithic fragments which have a combined modal abundance of 60-80% (mainly crystals). However, the upper palaeovalley unit also contains non-welded, pumice- and ash-rich domains, in which flattened pumice clasts are compacted and aligned to form a pseudo-eutaxitic texture (Figure 3.5a, 3.8). These domains have a lower crystal+lithic content than is usual for the CRVS (40-60%). The boundaries between the pumice-bearing domains and the crystal-rich domains containing no pumice are extremely irregular and diffuse, and gradational in terms of crystal-lithic content.

The crystal-rich sandstones are texturally immature to submature. Sorting is generally good, but is poor in the pumice-bearing horizons, due to the higher component of volcanic ash (matrix) and the presence of large pumice clasts.

Outsized welded ignimbrite clasts

The palaeovalley contains two 5-10 m thick intervals of monomictic volcanic breccia, comprising outsized clasts of welded ignimbrite supported by a matrix of crystal-rich volcaniclastic sandstone (CRVS). One interval occurs at the base of the Middle palaeovalley unit, and the other within the upper palaeovalley unit (Figure 3.5). The welded ignimbrite clasts range between 5-50 cm in size, and are prominent in outcrop as they are red in colour, and contrast with the grey sandstone matrix. They commonly display irregular angular and fluidal outlines (Figure 3.5b).

In thin section the ignimbrite clasts have a matrix-supported fabric, which contrasts markedly to the clasts-supported framework of the host CRVS (Figure 3.9a). The clasts consist of angular crystals and lithic fragments (30%) supported by an aphanitic siliceous matrix (70%). The framework constituents are the same as for the welded ignimbrites underlying the CRVS, comprising crystals and lithics in roughly equal proportion, with quartz and feldspar in a ratio of approximately 2:1. Dolerite is the main component of the lithic population. The geochemical composition of the clasts is identical to the underlying welded ignimbrites. Welding textures are poorly preserved due to metamorphic overprinting of the matrix, but some clasts exhibit preserved spherulitic textures, and relic vitriclastic textures (attenuated shards and pumice shreds) that suggest plastic

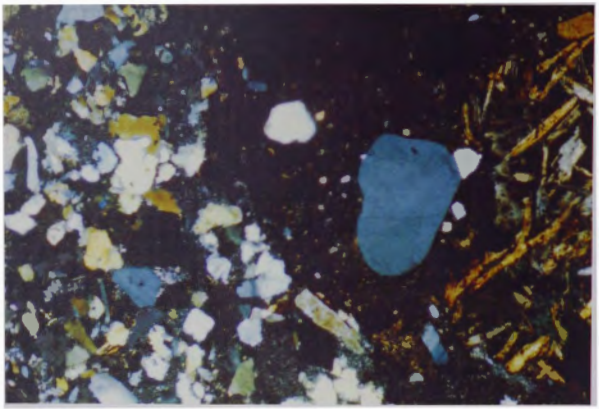

Figure 3.9a: Photomicrograph showing the difference in texture between the CRVS (left) and the welded ignimbrite clasts (right).

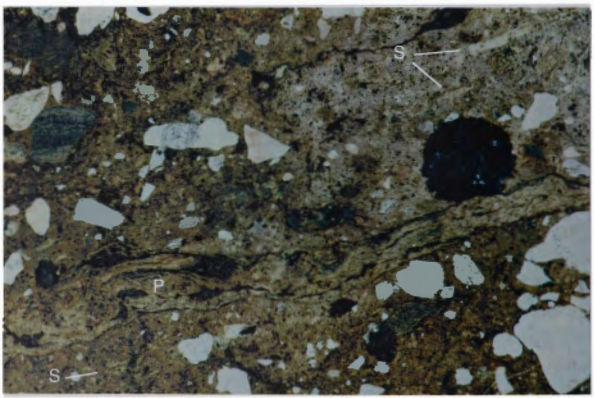

Figure 3.9b: In thin section the ignimbrite clasts exhibit relic vitriclastic textures. Compacted and flattened shards (S) and pumice (P) indicate that the clasts are welded.

deformation and welding (Figure 3.9b). Macroscopically, the clasts exhibit a subtle eutaxitic foliation that lies in random orientations from one clast to another.The ignimbrite clasts commonly display fluidal outlines that exhibit delicate apophyses and globular features (Figure 3.10a), and some clasts thin dramatically towards their margins (Figure 3.10b). They are similar in form to mudstone rip-up intraclasts found within turbidite sequences (e.g. Figure 7.12, Chapter 7.1), and their fluidal outlines indicate that they fragmented in a ductile manner, and were incorporated into the deposits in a semi-consolidated state. Their highly irregular shape indicates that they did not experience reworking or significant abrasion either before or during transport, and were therefore not derived from erosion and resedimentation of the older consolidated welded ignimbrite deposits underlying the CRVS. The clasts are interpreted as rip-up clasts of recently deposited, semi-solidified, ductile welded ignimbrite. Some clasts have angular outlines, with sharp corners and planar to curved surfaces indicative of quenching and brittle fracture, but these are rare (Figure 3.10c).

Many clasts exhibit internal fracturing and preserve jigsaw-fitted textures, indicating either: (1) that they quenched in situ at the final site of deposition; and/or (2) they quenched, or were mechanically fractured in transit and prevented from mixing by a high particle concentration matrix in the flow. The clasts exhibit a gradation in fracture morphology between brittle fractures, slightly modified brittle fractures and totally irregular and contorted fracture surfaces (Figure 3.11a,b,c, respectively), which suggests that initial fracturing was by quenching, but that the clast margins were deformed upon intrusion of sediment into the fractures. Very few of the original internal brittle quench fracture surfaces are preserved. Most of the internal fractures have a modified morphology and are highly fluidal in shape. This infers that the interiors of most clasts were still hot and ductile at the time of quenching of the clasts. During the quench fragmentation process, the unconsolidated wet sediments hosting the clasts have a high dispersive pressure due to the presence of fluids and gases in the pore space. When the quench fractures within the clasts open up, they create an area of low pressure into which the surrounding sediment is conveyed under high pressure. In solid clasts that have quenched completely, the dispersal of the sediment through the interior of the clast is controlled and channelled by the fracture. The fracture surface remains brittle and the clast rotates open as sediment enters the fracture. In clasts that have only quenched at the margins and remain hot and ductile in the interior, the sediment intruding the fracture under high pressure is able to deform the interior clast margins, and the original brittle fracture surfaces are completely modified.

Figure 3.10a: Outsized welded ignimbrite clasts (red) in a crystal-rich volcaniclastic sandstone matrix (grey). Many clasts have an irregular and fluidal shape, and thin apophyses are preserved, suggesting they have not been significantly abraded during transportation. GR 246800 8489000.

Figure 3.10b: Close-up of one clast (pink) embedded in a crystal-rich matrix (grey), showing the extremely irregular, fluidal outline and delicate apophyses in more detail. The margins of these fluidal clasts exhibit annular and globular features, which suggest they were soft and ductile when eroded.

Figure 3.10c: Close-up of an ignimbrite clast that exhibits sharp, planar to curved exterior surfaces produced by brittle fracture (quench fragmentation).

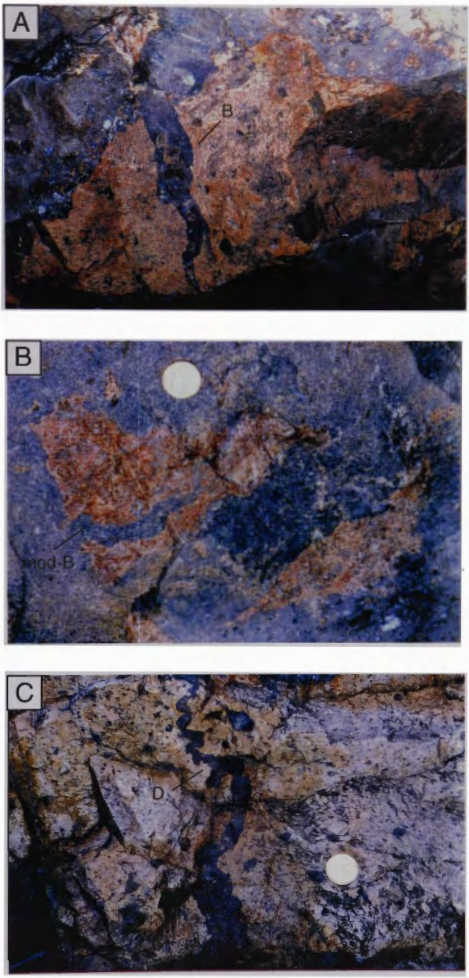

Figure 3.11: Close-up of welded ignimbrite clasts (red) within the CRVS (grey) showing a gradation in internal fracture morphology from (a) brittle fracture (sharp, planar to curved fracture surfaces: B); (b) slightly modified brittle fracture (mod-B); and (c) totally fluidal (globular) fracture surfaces (D). GR 246800 8489000.

3.3.2 Depositional setting

The CRVS facies lies between the subaerial volcanic succession of the Pul Pul Rhyolite, and a subaqueous, deep-water volcaniclastic turbidite succession, interpreted to represent a short-lived, restricted lacustrine environment. The lake developed within a topographic depression that remained after the bulk of the ignimbrites associated with the Pul Pul Rhyolite depocentre had erupted. Lake formation may have occurred in response to fault subsidence, downsagging and erosion associated with caldera formation (see Chapter 4), and/or by local ponding of the palaeodrainage following deposition of the thick ignimbrite succession. Given that its stratigraphic position is transitional between a subaerial and subaqueous setting, the depositional environment of the facies must be carefully established.

The contact relationships between the facies suggest that the CRVS facies is hosted by the overlying lacustrine turbidite sequence, and is not part of the underlying subaerial succession. A period of erosion removing up to 30m of welded ignimbrite stratigraphy suggests a significant hiatus occurred between deposition of the subaerial facies and the CRVS, during which palaeodrainage was altered, resulting in a local lacustrine environment in the subaerial volcanic setting. The CRVS fine upward and grade into the overlying laminated siltstones, indicating the two facies are conformable, and in the palaeovalley, CRVS are interbedded with quartz-rich coarse sandstone and conglomerate turbidites. These relationships indicate that the facies is part of the lacustrine turbidite succession, which implies a relatively deep water, below storm wave base depositional environment for the facies. This is also inferred by the facies characteristics of the CRVS, described above, as such thick, crystal-rich, monomictic mass flows have only been recorded in deep water settings (e.g. Cas 1983a; Cas and Wright 1991; White and McPhie 1997; Simpson et al. 1997).

3.3.3 Character and setting of the source

The CRVS contain large volumes of texturally juvenile pyroclasts (euhedral crystals, fragmented crystals and lithic fragments, pumice and outsized ignimbrite clasts), which reflect a volcanic source terrain. The quartz and two feldspar (predominantly K-feldspar) assemblage of the volcaniclastic sandstones, and their geochemical composition, are consistent with a rhyolitic volcanic provenance, as for the underlying welded ignimbrites of the Pul Pul Rhyolite. The abundance of angular and fragmented juvenile pyroclasts and lithic clasts within the volcaniclastic facies indicates an explosive magmatic and/or phreatomagmatic eruption style.

Certain criteria have been established to distinguish syn-eruptive from post-eruptive volcaniclastic deposits (Stix 1991; White and McPhie 1997). Syn-eruptive deposits are transported and deposited during the eruptive cycle (deposited as little as days to weeks after eruption), and may be identified by the following criteria: (1) evidence of hot emplacement of the deposits; (2) a high proportion of juvenile volcanic components, reflecting a homogenous volcanic source; (3) thick sedimentation units, reflecting the periodic influx of volcaniclastic debris in large volumes (comparable to the volumes of pyroclasts released during pyroclastic eruptions); (4) lack of evidence for sedimentary reworking of the pyroclasts; (5) inversely graded pumice (Kano et al. 1996); and (6) double-grading (Fiske and Matsuda 1964). Post-eruptive volcaniclastic deposits record denudation of the source terrain following eruption, and are distinguished by: (1) thinner deposits; (2) a more heterogeneous clast and textural population, indicating the material originated from more than one source; (3) evidence of reworking and the presence of abraded epiclasts; (4) normally graded pumice (Fisher 1984; Kano et al. 1996); and (5) no evidence of hot emplacement. The lithofacies characteristics of the CRVS are most consistent with being syn-eruptive, based on the above criteria.

Depth constraints on explosive eruptions generally imply either a subaerial or a shallow water volcanic centre. Studies by McBirney (1963) indicate that sustained explosive eruptions of silicic magma are constrained to water depths of less than 1 km, and that significant vesiculation of silicic magma should only occur in water depths of several hundred metres or less. At greater depth, gas expansion is impeded by the hydrostatic pressure exerted by the overlying water column, so the facies is not likely to have been sourced from a deep water eruption. Several lines of evidence indicate the eruptive centre was subaerial rather than subaqueous:

1. The compositional similarity of the CRVS, the ignimbrite rip-up clasts within the facies and the underlying subaerial welded ignimbrites infers a genetic relationship between the facies.

2. There is compositional evidence to suggest that the CRVS comprise an admixture of pyroclastic material similar in composition to the underlying subaerial ignimbrites, and some foreign material derived from subaerial epiclastic deposits, suggesting detritus was transported over a subaerial environment prior to deposition in a deep water setting.

The welded ignimbrite clasts within the CRVS are identical to the underlying subaerial ignimbrites of the Pul Pul Rhyolite, and the CRVS contain the same framework components as these ignimbrites and ignimbrite clasts. A genetic relationship between the ignimbrites and the CRVS is therefore inferred. The most notable petrographic

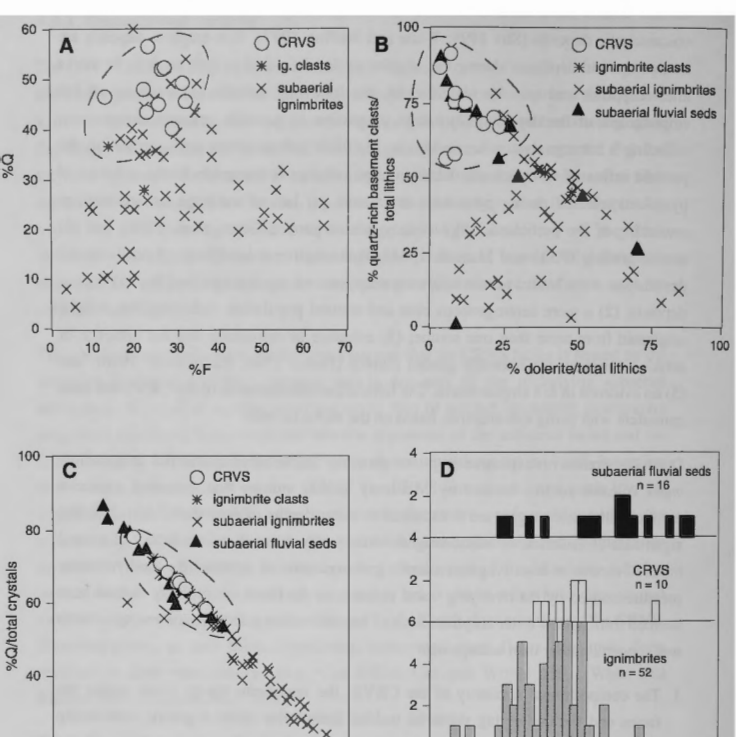

Figure 3.12: Petrographic comparisons between the CRVS, welded ignimbrite clasts contained within the facies and subaerial ignimbrites of the Pul Pul Rhyolite: (a) quartz:feldspar ratios plotted as percentage of framework (i.e. Q+F+L). The CRVS have a higher average quartz content, and a narrower range of quartz and feldspar contents; (b) ratio of the dominant lithic components of the CRVS and ignimbrites. Fluvial epiclastic deposits (Pul Pul Rhyolite) are plotted for comparison; (c) quartz and feldspar ratio of the crystal populations. Fluvial epiclastic deposits (Pul Pul Rhyolite) are plotted for comparison; and (d) histogram comparing the proportion of strained metamorphic quartz (basement-derived xenocrysts; Qm), as a percentage of total quartz. Figures (c) and (d) show that the CRVS can be interpreted as comprising an admixture of pyroclastic debris contaminated by fluvial epiclastic material.

differences between the facies are that the CRVS are slightly enriched in quartz (Figure 3.12a), and contain a higher ratio of quartz-rich, basement-derived clasts to dolerite clasts in the lithic assemblage (Figure 3.12b). The lower dolerite count in the CRVS could be in part a statistical aberration caused by the problem of point counting inhomogeneous grainsize populations, as occur in the ignimbrites. The dolerite clasts in the ignimbrites are usually 3-4 times larger than the crystal fraction and basement-derived lithic clasts, and are subsequently over-counted, introducing a bias into the statistical analyses. In contrast, the CRVS are better-sorted, and dolerite clasts have a similar grainsize as the crystals and other lithic fragments. It is possible that the larger dolerite clasts were preferentially removed from the clastic population by hydraulic sorting processes operating in the sediment mass-flows. The presence of coarse-tail grading in the middle palaeovalley unit indicates that hydraulic sorting of the more dense, coarser-grained fraction did occur.

Another possibility, which also explains the enrichment of quartz and basement-derived lithics in the CRVS, is that the facies was contaminated by an extraneous source of lithics and crystals. A possible source of foreign sedimentary material is fluvial epiclastic deposits near the shoreline of the lake, similar to those which underlie much of the CRVS. These fluvial deposits have a mixed source of contemporaneous pyroclastic and older basement detritus (Chapter 2.3), are enriched in quartz relative to the welded ignimbrites (Figure 3.12c), and basement clasts dominate over dolerite grains in the lithic population of most deposits (Figure 3.12b). Contamination from this source would increase the abundance of basement-derived lithics in the CRVS, and the quartz enrichment is explained by the addition of basement-derived quartz xenocrysts to the volcanic-derived crystal population. Figure 3.12d shows that the CRVS contain a higher proportion of highly strained, basement-derived quartz grains than the subaerial ignimbrites, and the source of these grains can be explained by the incorporation of fluvial epiclastic sediments. In support of this proposal that the CRVS comprises an admixture of primary pyroclastic debris and some contaminant from fluvial deposits, small, diffusely bound lenses of quartz-rich coarse to pebbly sandstones occur within the CRVS (Figure 3.5). The lenses are equivalent in composition to the fluvial epiclastic deposits underlying much of the CRVS and are interpreted to be sedimentary material from the shoreline of the palaeolake, incorporated into final deposits.

3.3.4 Mode of emplacement of the CRVS

The general homogeneity and massive nature of the CRVS, and the absence of tractional sedimentary features, indicates they were emplaced by mass-flows. The CRVS are an order of magnitude thicker than: (1) other turbidites within the Big Sunday Formation lacustrine succession (Figure 3.3, 3.5); and (2) turbidites generated by normal surface

processes in sedimentary terrains, which rarely exceed a thickness of several metres (e.g. Bouma 1962; Bailes 1980). The thick, amalgamated beds are therefore interpreted to be deposited by megaturbidites with particle mass-flux rates considerably greater than those produced by normal sedimentary processes. The large volumes of juvenile pyroclasts within the CRVS are sourced by (pene)contemporary pyroclastic eruptions, and represent high particle mass flux rates, similar to those of pyroclastic flows. The thickness of the sedimentation units is also comparable with those of pyroclastic flow deposits. There is however, no evidence of heat retention or welding in the crystal-rich deposits, or the pumice-bearing domains, which would infer gas-supported transportation of the pyroclastic material. Such evidence would include columnar jointing, welding textures (eutaxitic textures and plastically deformed pumice or shards), high temperature crystallisation textures (e.g. spherulites, lithophysae) or perlitic fracturing of the matrix. In the absence of any other evidence of heat retention, the flattening and alignment of pumice clasts within the diffuse pumice-bearing horizons, is interpreted as a pseudo-eutaxitic texture, formed by diagenetic compaction of the deposits.

Without clear evidence for hot emplacement, it is likely that the material was transported and deposited in a cold state, by water-supported mass flows. The lack of internal stratification and the presence of grading in the upper parts of the massive units suggests suspension sedimentation from high particle concentration, poorly-expanded mass flows. The suggested flow mechanism is analogous to that of high-density turbidity currents, in which the flow is sustained by grain support mechanisms such as fluid turbulence, dispersive pressure related to shear stress between grains, buoyancy uplift driven by escaping steam and water and hindered settling (Middleton and Hampton 1976; Lowe 1982; Druitt 1995). The deposition of coarse, massive sandstones from high-density turbidity currents has been commonly attributed to the rapid dumping of material due to flow unsteadiness developed as the grains begin to settle, grain concentration in suspension decreases, and the flow can no longer be supported by grain interactions (e.g. Lowe 1982). Kneller and Branney (1995) propose an alternative deposition mechanism involving the gradual aggradation of sand beneath a sustained, steady or quasi-steady current, as opposed to 'freezing' of the flow en masse. The principal grain support mechanisms are the same for both models, with the Kneller and Branney model involving a high concentration depositional basal zone in the flow.

The high sediment concentration and rapid deposition rate in high density flows limits particle freedom so that total size grading is not developed or is only poorly developed. Coarse-tail grading of only the most dense or coarsest grains is a common feature of high concentration turbidity currents (Stauffer 1967; Allen 1970), and would account for the development of a lithic concentration zone at the base of the middle palaeovalley unit. The

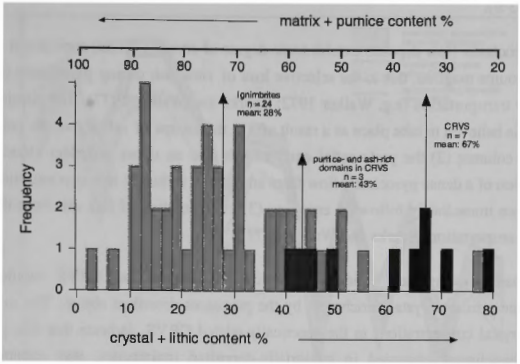

Figure 3.13: Comparison of the crystal and matrix contents of the CRVS (black) and the underlying ignimbrites (light grey). The pumice-bearing zones within the CRVS (dark grey) are intermediate between the two facies.

thin, normally graded flow tops of some units represent the eventual waning of the sustained high-density current, leaving a residual current containing finer material in low-density turbulent suspension. The thin (3 cm) planar-laminated, reverse graded layer that occurs at the base of the lower palaeovalley unit is interpreted to represent a boundary layer effect, developed due to intense shearing in the basal part of the flow, where it is in contact with the substrate. Diffuse layering within the massive units may reflect flow unsteadiness, or a minor component of laminar flow and internal shear stress in the basal depositional sub-layer at the time of deposition (Johnson 1970). The outsized welded ignimbrite clasts would have been supported by matrix buoyancy, as a result of the higher concentration of dispersed finer detritus (Hampton 1975).

3.3.5 Crystal enrichment and its geochemical consequences

The inferred genetic relationship between the CRVS and underlying welded ignimbrites suggests that both facies were derived from the same subaerial volcanic source. However, the subaqueously-emplaced CRVS contain more than twice the amount of crystals (+lithics) as the subaerially-emplaced welded ignimbrites (Figure 3.13). The welded ignimbrites comprise, on average, 27% crystals+lithics, 23% pumice and 50% ash (matrix). By comparison, the CRVS contain an average of 67% crystals+lithics, are substantially depleted in ash, and contain only minor pumice concentrated in local horizons within the palaeovalley. It should be noted that the pumice-bearing domains

within the CRVS do not show the same degree of crystal-enrichment as the rest of the facies (43%).

Most pyroclastic flow deposits exhibit some degree of crystal (+lithic) enrichment relative to their source magmas, due to the selective loss of vitric ash during pyroclastic eruption and flow transportation (e.g. Walker 1972; Sparks and Walker 1977). The elutriation of fine ash is believed to take place as a result of: (1) the escape of ash above the collapsing eruption column; (2) the preferential entry of ash into an upper turbulent cloud as the segregation of a dense pyroclastic flow from an initially turbulent low-concentration flow takes place immediately following eruption; (3) the elutriation of fine ash from the flow during transportation (Sparks and Walker 1977).

The subaerially-emplaced welded ignimbrites underlying the CRVS would have undergone primary crystal enrichment by the processes described above. The markedly higher crystal concentrations in the genetically-related CRVS, indicate that this primary crystal enrichment observed in subaerially-deposited ignimbrites, was enhanced by further separation of ash and pumice, probably as a consequence of their final deposition in a subaqueous environment.

One consequence of crystal concentration in ignimbrites, is that their geochemical composition is likely to depart notably from that of the parent magma, being enriched in those chemical elements contained in higher proportion by the crystals, and depleted in those contained in higher proportion in the glass (Walker 1972). The overall geochemical effect is analogous to removing the minimum melt component of the eruptive magma. Except where quartz is an abundant phenocryst, this will result in a deposit with a lower SiO_2 value than that of the parent magma, and with a less fractionated or less evolved geochemical composition overall. The loss of pumice and ash during transportation of the CRVS would have had the same consequent effect on their geochemical composition as that proposed by Walker (1972) for primary crystal-enrichment in ignimbrites. The greater loss of pumice and ash in the CRVS can be expected to substantially modify their geochemical signature relative to the genetically-related welded ignimbrites. By comparing the CRVS with the genetically related ignimbrites, the geochemical changes which occur as a result of pumice and ash loss can be quantified.

Four of the samples selected for geochemical analysis from the CRVS represent the crystal-rich deposits containing no pumice. These samples are slightly enriched in SiO_2 relative to the ignimbrites, due to concentration of quartz crystals and lithics. They are depleted in Al_2O_3, which is incompatible with removal of the vitric component, as Al will partition into the feldspar crystals, and therefore should be enriched in the crystal concentrate. However, the Al_2O_3 depletion may reflect the lower dolerite content of the

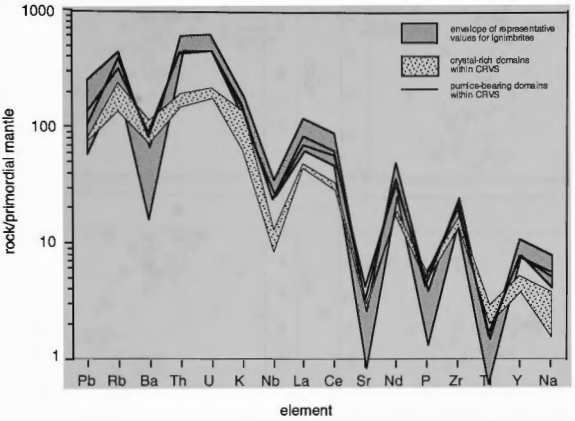

Figure 3.14: Extended trace element diagram comparing trace element patterns of the subaerial ignimbrites with the CRVS. The CRVS have a less fractionated pattern, as would be expected with the removal of the glassy fraction (as volcanic ash and pumice). The two samples that have a trace element signature similar to the ignimbrites are from pumice-bearing domains within the CRVS, which have undergone only minor crystal enrichment relative to the rest of the facies.

CRVS, as the dolerite clasts almost entirely consist of calcic plagioclase, which is high in Al. All other element trends are consistent with the removal of vitric material. The trace element pattern of the CRVS is less fractionated than the more vitric ignimbrites (Figure 3.14), and they show higher abundances of compatible elements (Ba, Fe_2O_3, TiO_2, CaO, MgO, Ni, V, Mn, Sc, P_2O_5, Cr), which would be contained in higher proportion by the crystals, and lower abundances of incompatible elements (i.e. LIL elements (K_2O, Rb), HFSE elements (Zr, Y, U, Th, Nb, Nd) and LREE (La, Ce)) which would be progressively concentrated through fractionation in the melt (Figure 3.15).

The two remaining samples analysed (samples 89123077 and 89123079) were collected from the pumice-bearing domains within the CRVS. These domains are closer in geochemical composition to the subaerial ignimbrites, because the degree of pumice and ash-loss, and crystal-enrichment, is less pronounced.

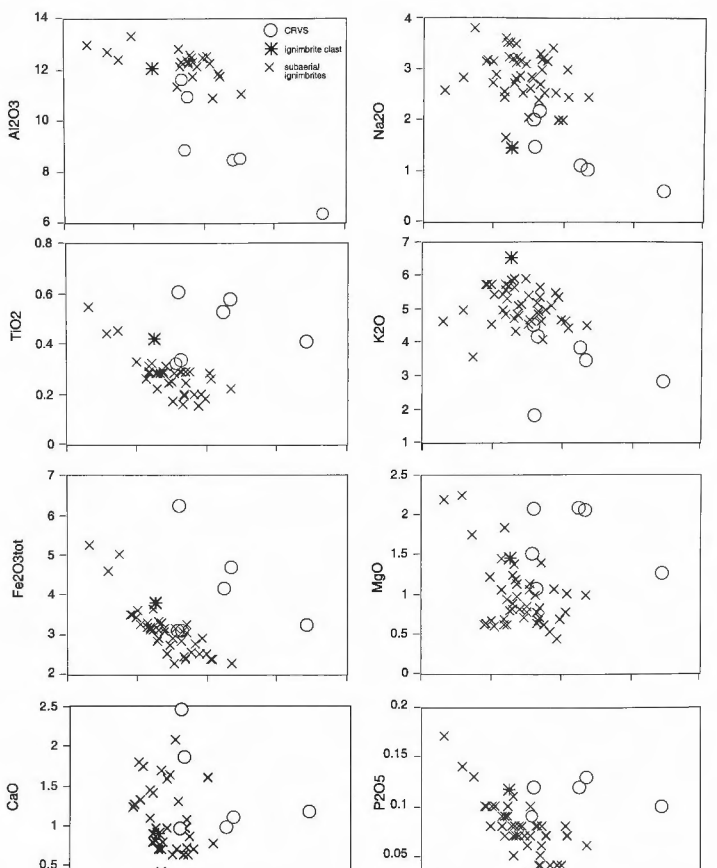

Figure 3.15: A comparison of geochemical trends in the subaerial ignimbrites of the Pul Pul Rhyolite and the CRVS facies of the Big Sunday Formation. A welded ignimbrite clast within the CRVS has the same geochemistry as the underlying subaerial ignimbrites. The two samples within the CRVS that have a similar geochemical signature to the ignimbrites are from pumice-bearing domains that have not undergone extensive crystal enrichment, and therefore still retain a high proportion of ash matrix and pumice.

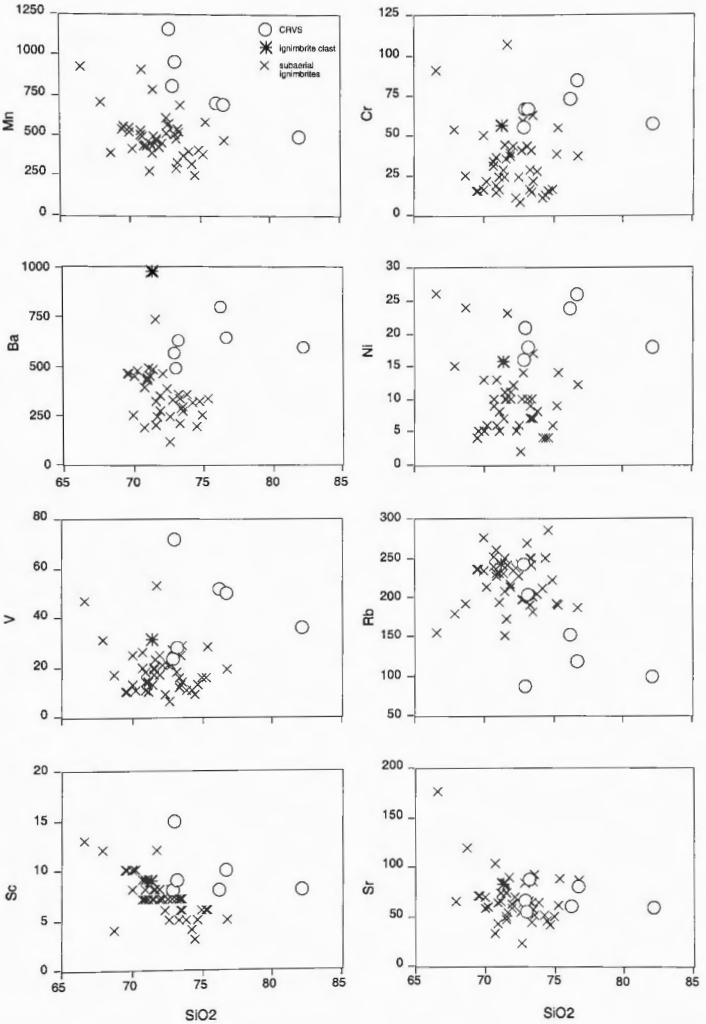

Figure 3.15: cont'd.

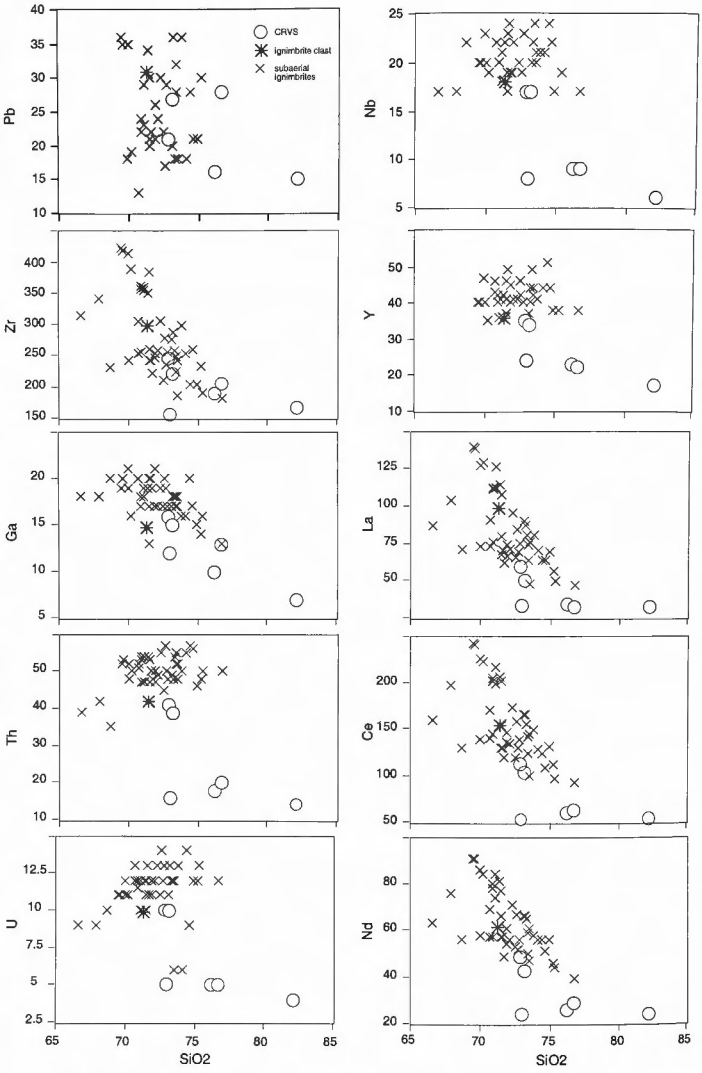

Figure 3.15: cont'd.

3.3.6 Origin and emplacement of the CRVS

Contemporaneous flow transformation vs post-eruptive slumping

From the above discussions, it is clear that the CRVS originated from (pene)contemporary subaerial pyroclastic eruptions, but that their final emplacement in a subaqueous environment was by water-supported mass flows with high-particle mass-flux rates (megaturbidites). Water-supported mass flows carrying large volumes of juvenile pyroclasts could be generated in two ways. Because their particle mass-flux rates are comparable to those of pyroclastic flow-forming eruptions, they may represent the subaqueous continuation of subaerial pyroclastic flows, directly and continuously fed by a steady eruptive source and pyroclastic density current. Alternatively, they may have been generated by slumping and remobilisation of large volumes of unconsolidated pyroclastic material surrounding the basin. Distinguishing between deposits formed by these two mechanisms is difficult, and can be impossible in cases where the volcaniclastic detritus is emplaced at a low temperature, because the resultant flow processes are the same in both cases (Wright and Mutti 1981; Cas and Wright 1987, 1991; Stix 1991; Cole and Stanley 1994). In this case, however, two features of the deposits suggest that the water-supported mass flows were the subaqueous derivatives of subaerial pyroclastic flows: (1) the welded ignimbrite clasts and diffusely-bound, pumice- and ash-rich domains contained within the CRVS are interpreted to represent relatively unmodified remnants (intraclasts) of the parent pyroclastic flow deposits; and (2) the in situ quenching of the outsized welded ignimbrite clasts provides unequivocal evidence of heat retention within the flow, indicating only a short time factor between eruption and emplacement.

The pumice-and ash-rich domains within the CRVS are interpreted to be preserved remnants (intraclasts) of non-welded parts of the parent pyroclastic flows, that were largely unmodified by the crystal enrichment process that affected much of the facies. The irregular ignimbrite clasts are interpreted as rip-up clasts of recently deposited, semi-solidified ductile welded ignimbrite. It is likely that they are also intraclasts, derived from agglutinating domains within the pyroclastic flows. It has long been proposed that high-grade ignimbrites may undergo primary welding during flow emplacement (e.g. Schmincke and Swanson 1967; Chapin and Lowell 1979), and this concept has been expanded more recently by Branney et al. (1992) and Branney and Kokelaar (1992). Under the model of plug and laminar transport regimes (Sparks 1976; Wright and Walker 1981), welding could occur in the final stages of motion as a flow begins to 'freeze' and deflate, bringing hot 'sticky' glass particles into contact, and forming viscous plugs of agglutinating material within the body of the flow. Under the model of deposition by the

aggradation of pyroclasts from a sustained, turbulent pyroclastic flow (Branney and Kokelaar 1992), particle coalescence or agglutination is more likely to occur within the basal high-concentration layer of a pyroclastic flow during emplacement. Particle interactions occur frequently within this basal layer, and if particles are sufficiently hot and fluid, they could coalesce upon contact, adhering to the top of an upwards-accreting, non-particulate deposit forming at the base of the particulate flow. Temporal variations in current steadiness may then increase the viscous shear exerted by the overriding particulate part of the flow, resulting in erosion of the agglutinated non-particulate layer, and incorporation of fluidal welded rip-up clasts into the main body of the flow. Intraclasts of this type have been identified in the zoned Arico ignimbrite from Tenerife (Canary Islands), which contains rip up clasts of orange welded ignimbrite from the basal zone incorporated into the overlying dark grey middle zone of the same subaerial ignimbrite deposit (Bryan et al. 1998).

The welded ignimbrite intraclasts exhibit internal fracturing and preserve jigsaw-fitted textures, indicating that they quenched and fragmented in situ. The fact that the clasts were still hot when they reached the final site of deposition indicates a short time factor between eruption and emplacement of the flows. Emplacement of the CRVS was therefore contemporaneous with eruption, which supports the case for deposition by the water-transformed derivatives of subaerial pyroclastic flows.

Model for flow transformation and crystal enrichment

The transition process from subaerial pyroclastic flows to subaqueous water-supported mass flows must have involved the removal of significant volumes of pumice and ash, to account for the crystal enrichment in the CRVS compared to the genetically-related ignimbrites. This could be achieved through a combination of: (1) flow disruption at the shoreline; (2) initial flow (or partial flow) over the water surface; and (3) entrainment and dispersal of fine ash in the derivative water-supported mass flows.

Local disruption of pyroclastic flows may occur at the shoreline as water is ingested into the vigorously advancing turbulent flow front. The high thermal contrast between the pyroclastic flows and the cold ambient water is likely to generate steam and trigger phreatomagmatic explosions during this process, generating rootless vents at the shoreline (e.g. Rotoehu Ash, New Zealand, Walker 1979; Pitts Head Tuff, Wales, Wright and Coward 1977). The explosions are likely to cause fragmentation of the larger pumice clasts (Wright and Mutti 1981), and fine ash may be elutriated in the secondary eruption columns, providing the high moisture content of the plumes does not favour retention of fines by mud fallout and formation of accretionary lapilli.

Recent analogue experiments provide new insights into pyroclastic flow behaviour upon entering the sea (McLeod et al. 1999). The experimental mixtures simulate density stratified pyroclastic flows. The stratified flows split into a dense basal flow which descends along the sea floor, and a buoyant upper flow which travels across the ocean surface. These experimental results accord with empirical observations of the 1883 eruption of Krakatau, for which deposits from both subaqueous and sea surface flows are described (Mandeville et al. 1996; Carey et al. 1996). As most pyroclastic flows are density stratified as a result of gravitational segregation, entrainment and turbulent mixing processes during subaerial runout (e.g. Sparks et al. 1973; Valentine 1987), it can therefore be assumed that at least some component of the flow will always continue over the water surface.

As the buoyant upper flow component travels over the surface, it decelerates and deflates away from the shoreline and segregates into a highly concentrated basal flow enriched in the denser components (crystals and lithics), and an overriding lower concentration turbulent flow containing the lighter pyroclasts (pumice and ash). The dense basal flow Sedimentation from the base of the flow is therefore initially dominated by the denser components, while pumice and ash remain in the transport system longer (Cas and Wright 1991; Carey et al. 1996). Settling of the juvenile material through the water column beneath the portion of the pyroclastic flow travelling over water would further fractionate and sort the dense and light components very effectively, with the lighter clasts remaining in suspension to be dispersed by currents.

Thus the shoreline area can be considered a complex mixing environment in which dense and light components are fractionated and sorted due to complex interaction between subaerial pyroclastic flows and the sea. The rapid accumulation of this fractionated material would then contribute to the rapid development of high particle concentration turbidity currents that continued on into deeper water.

Further fractionation of the dense and light components is likely to have occurred within the derivative water-supported mass flows. Although these flows will have a bulk density greater than the surrounding seawater, the interstitial fluid may be less dense if the entrained water has been heated by contact with pyroclasts. Recent analogue experiments show that the flow dynamics of a warm water-supported mass flow may be quite different to a normal turbidity current, with buoyant uprise occurring as a result of the thermal contrast between the interstitial water and ambient seawater (McLeod et al. 1999). As sedimentation of dense particles occurs at the base of the flow its bulk density is reduced and the remaining material becomes buoyant and rises up into the overlying water, producing convective clouds analogous to co-ignimbrite plumes generated by subaerial pyroclastic flows. Fine ash is entrained by upward convection and may be

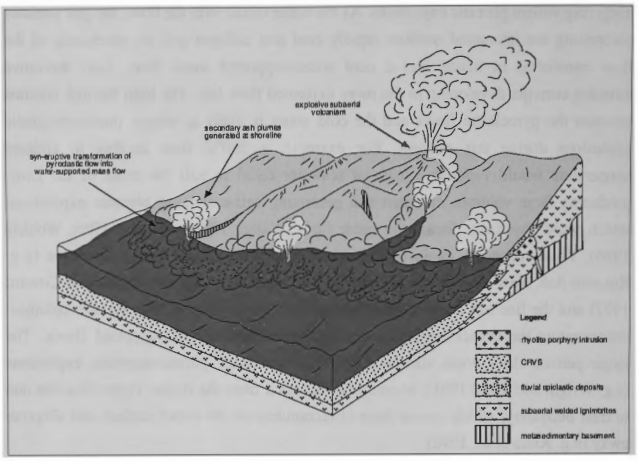

Figure 3.16: Schematic block diagram illustrating eruption and emplacement of the CRVS.

dispersed by oceanic currents, or eventually settle to produce a thin ash layer capping the deposit. Lithic clasts sedimented from the secondary buoyant flow will sink directly to the ocean floor, while pumice will float in a raft until becoming water saturated.

The diffusely bound pumice- and ash-rich horizons which occur randomly throughout the CRVS in the palaeovalley area are interpreted as pockets of the original non-welded pyroclastic flow that largely escaped interaction with water, and the consequent ash-winnowing process. These pumice-bearing horizons do not occur outside the palaeovalley area, where the CRVS forms a laterally extensive horizon. It is possible that the pyroclastic flows were channelled by the palaeovalley and then spread along the shoreline of the basin (Figure 3.16). The pumice and ash winnowing process may have been more effective as the pyroclastic flows spread out along the shoreline, exposing a greater surface area, and thus allowing more efficient mixing with water.

Behaviour of the non-particulate component of the flow

The preservation of welding textures in the outsized ignimbrite clasts has important implications for the physical state of the original subaerial pyroclastic flows. The textures indicate that through primary welding and agglutination, the flows were in a partially rheomorphic state as they approached the lacustrine shoreline, and they therefore contained both particulate and non-particulate components (Figure 3.17). The response of these separate components upon encountering water would have varied according to their different flow dynamics and boundary conditions. Whereas the particulate components disintegrated through interaction with water as described above, the non-particulate components were preserved relatively intact. The agglutinating domains would have behaved as viscous fluids with a rheology similar to rhyolite lavas, and may have been partially insulated by film boiling, a process which produces an insulating carapace of superheated steam (Liedenfrost Effect; Mills 1984), preventing heat loss and ingestion of water. As a result, they largely escaped interaction with water, and remained hot and fluidal as they were carried within the derivative water-supported mass flows. Larger plugs of viscous material may have disaggregated into smaller clasts through quench fragmentation upon contact with water, as suggested by the brittle exterior margins displayed by some clasts, through ductile stretching induced by flow shear and/or by brittle fragmentation during flow, and fracturing as large, cold clasts were rafted, flexed and collided. However, the preservation of jigsaw-fit textures suggests that quenching of most clasts occurred at the final site of deposition, when they came into contact with large volumes of wet sediment, and not during transportation.

3.4 DISCUSSION

The behaviour of subaerial pyroclastic flows when they encounter water continues to be an issue that attracts debate and controversy. Some authors maintain that pyroclastic flows will interact explosively with water (Walker 1979) and/or mix with water, and transform into cold-state, subaqueous volcaniclastic debris flows (e.g. Carey and Sigurdsson 1980; Cas 1983a; Whitham 1989). The presence of welded ignimbrites within marine sequences has led others to conclude that pyroclastic flows may maintain their integrity and continue to travel under water in a primary state (e.g. Sparks et al. 1980a,b; Francis and Howells 1973; Howells et al. 1985).

The debate hinges on the nature of the boundary layer of pyroclastic flows, and whether or not film boiling can operate to produce an insulating steam carapace that would enable flows to travel considerable distances under water. This process has been observed at the margins of effusive, viscous basaltic lavas (Moore et al. 1973), and is therefore known

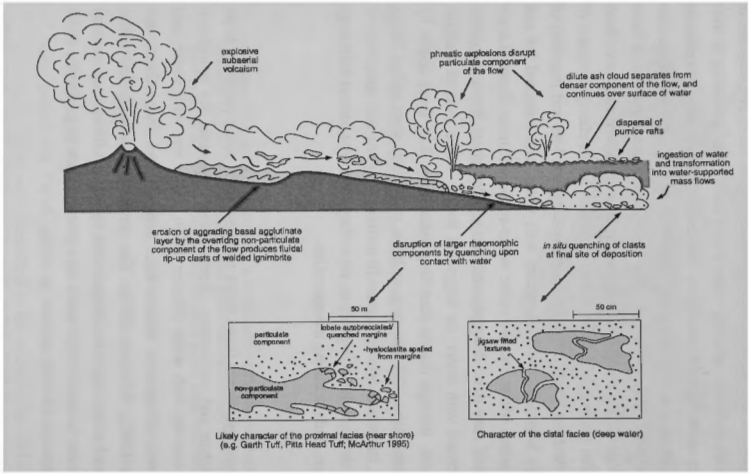

Figure 3.17: Model for the entry of a pyroclastic flow undergoing rheomorphism into water. The particulate component of the flow enters the water, disintegrates and transforms into a water-supported mass flow through phreatic explosion and/or ingestion of water into the turbulent flow head. Ash and pumice are winnowed out through eruption columns at the shoreline, resulting in crystal-enrichment in the derivative subaqueous flows. The agglutinated component of the flow may have been partially insulated through film boiling, as it survived the transition beyond the shoreline relatively intact, experiencing only partial disruption through: (1) ductile stretching induced by flow shear; (2) brittle disaggregation during flow as large clasts were rafted, flexed and collided; and (3) quenching upon contact with water. The agglutinated component of the flow is represented in the distal (deep water) deposits by fluidally-shaped welded ignimbrite intraclasts that display evidence of ductile shear and brittle disaggregation at clast margins, and evidence of insitu quenching at the site of final deposition (internal fracturing exhibiting jigsaw-fitted textures).

to be viable under stable, laminar boundary conditions. However, it is unlikely to operate effectively at the unstable margins of a vigorously advancing turbulent flow front of a pyroclastic flow. On the contrary, fluid instabilities in the turbulent boundary layer would promote the ingestion of water across the head and body of the flow, and cold water would be driven into the flow front by the substantial fluid pressure gradient existing between the gas-particulate system and the denser body of water (Orton 1989; McArthur 1995).

The development of a steam carapace has been invoked to explain most occurrences of primary subaqueous emplacement and welding (e.g. Sparks et al. 1980a,b; Howells et al. 1985; Schneider et al. 1992). However, an alternative explanation is that transportation by primary pyroclastic flow in subaqueous environments can be feasible under special circumstances where the pyroclastic flow was prevented from interacting with surrounding water, either through emergence or through rapid emplacement of large volumes of material near vent. Convincing examples of primary pyroclastic flow in subaqueous settings are restricted to: (1) shallow water, near-shore settings; (2) near-vent settings in deep marine basins (Cas and Wright 1991); and (3) localities where temporary shoaling of deep water basins occurs (White and McPhie 1997). In the first case, the flows are prevented from interacting with water, either because significant thicknesses of the deposit were emergent during and following emplacement (e.g. Mweelrea Group, Ireland, Dewey 1963, Pudsey 1984; Koura Formation, Japan, Kano 1990; Capel Curig Formation, Orton 1991, McArthur 1995), and/or because welding commenced prior to encroaching the shoreline, enabling the resultant viscous, rheomorphic flows to be insulated by film boiling (e.g. Capel Curig Formation and Pitts Head Tuff Formation, Wales, McArthur 1995). In the second case, the flows were insulated from interaction with water through the ponding of thick, rapidly accumulated deposits within wholly or partially submerged calderas (e.g. Vandever Mountain Tuff, Mineral King, USA, Busby-Spera 1984; Kokelaar and Busby 1992) or through high eruption discharge rates from subaqueous fissures, and rapid emplacement of material near vent (southern Vosges, France, and Anatolia, Turkey, Schneider et al. 1992). In both cases, deposits that can be traced laterally exhibit features that indicate the flows began to disintegrate a short distance from the shoreline or vent, through the progressive entrainment of water along flow bases and flow fronts. (e.g. lack of welding, fine-grained normally-graded flow tops, quenching of pyroclasts, incorporation of bioclastic material; Orton 1989; McArthur 1995; Cole and Decelles 1991, Schneider et al. 1992). The third scenario, involving temporary shoaling of deep marine basins, is suggested to explain the occurrence of thin welded ignimbrite deposits in the Tyndall Group, Mt Read Volcanics in western Tasmania (White and McPhie 1996, 1997). The ignimbrites are associated with thick intervals of crystal-rich volcaniclastic sandstone, which record the sudden influx of large

volumes of pyroclastic material. This material is considered to have overwhelmed the prevailing deep-water sedimentation system, creating temporary local shallow marine to emergent conditions, so that the welded ignimbrites were in fact deposited subaerially or in very shallow water.

Models advocating explosive interaction between pyroclastic flows and water, and their transformation to water-supported mass flows in subaqueous settings, infer that the majority of pyroclastic flows do not survive as such beyond the shoreline. This is consistent with the fact that most deep-water deposits of pyroclastic debris are emplaced by cold, water-supported mass flows (Cas and Wright 1991). Many examples of volcanigenic deposits emplaced by water-supported mass flows have been described in both marine (e.g. Stanton 1960; Fiske 1963; Fiske and Matsuda 1964; Niem 1977; Dimroth and Demarke 1978; Tassé et al. 1978; Cas 1983a; Wright and Mutti 1981; Whitham 1989; Cole and Stanley 1994; Kano 1996; Kano et al. 1996; White and McPhie 1996, 1997) and lacustrine environments (Yamazaki et al. 1973; Yamada 1973). Submarine eruptions have been proposed for some of these deposits, but many are considered to be generated from subaerial vents. In most cases, however, the subaerial sources have not been identified, and because the deposits are emplaced in a cold state, it cannot be proven unequivocally whether they are the subaqueous, syn-eruptive equivalents of subaerial pyroclastic flows, or if they were generated by secondary slumping and remobilisation of previously deposited pyroclastic debris. The examples described herein are therefore important, because: (1) a close genetic relationship with the underlying ignimbrites is established, providing a rare opportunity to compare the characteristics of subaerial pyroclastic flow deposits with their likely subaqueous volcaniclastic derivatives; and (2) the original pyroclastic flows were undergoing primary agglutination and welding as they encountered water, enabling the behaviour of particulate and non-particulate components of the same flows to be compared. The non-particulate components of the flows, represented by the preserved welded ignimbrite intraclasts, may have been partially insulated through film boiling and survived the transition beyond the shoreline relatively intact, experiencing only minor disaggregation through quenching upon contact with water. The particulate components of the flows, however, clearly did not maintain their integrity as they passed into a subaqueous setting. Final sedimentation of the particulate component was by cold water-supported mass flow, which infers a process of flow transformation, which involved significant loss of pumice and ash. This process could have occurred through vigorous mixing with water and disruption of the flow through phreatic explosions as the flows penetrated below the surface, and/or through sedimentation from the bases of flows that travelled across the surface. The different behaviour of the particulate and non-particulate components of the same flow strongly supports models that predict the explosive disintegration and transformation of pyroclastic flows upon encountering water, because it suggests that only the coherent domains may be insulated through film boiling.

CHAPTER 4

Palaeogeography: could the Pul Pul Rhyolite contain the remnants of an ancient caldera structure?

4.1 Depositional setting of the Pul Pul Rhyolite

The facies association of the Pul Pul Rhyolite comprises mainly primary volcanic products that are predominantly rhyolitic in composition, indicating they are the products of a silicic volcanic centre. Silicic volcanic centres occur in environments ranging from subaerial through shallow marine to deep marine, but the predominance of welded ignimbrites in the volcanic succession supports a subaerial depositional environment for the Pul Pul Rhyolite. As discussed in Chapter 3, welded ignimbrites have been described in subaqueous successions (e.g. Howells et al. 1979; Francis and Howells 1983), but occurrences are rare, and require special circumstances in which the pyroclastic flow is prevented from interacting with water. In general, welding in ignimbrites is a good indication of subaerial environments.

The depositional setting of the Pul Pul Rhyolite volcanic succession can be determined by considering the sedimentary facies associations bounding the formation (within the underlying Coronation Sandstone El Sherana Group and overlying and Kurrundie Sandstone; Figure 4.1). Friedmann and Grotzinger (1994) present a detailed study of the stratigraphy and sedimentology of these units, and the summary below is based largely on their work.

4.1.1 Sedimentary facies of the Coronation Sandstone

The Coronation Sandstone is irregularly distributed, and mostly confined to the South Alligator Valley between El Sherana and Coronation Hill (Figure 2.1). It also outcrops beneath the Pul Pul Rhyolite around the southern margin of the Malone Creek Granite, and as small outliers farther to the east and north (Stuart-Smith et al. 1988). It unconformably overlies older Palaeoproterozoic basement that was deformed, metamorphosed (to lower greenschist facies), uplifted and eroded. The basement rocks formed a steep palaeotopography, with resistant units forming palaeoridges and less

Figure 4.1: Fence diagram illustrating El Sherana/Edith River Group stratigraphy in the South Alligator Valley, northwest of the study area, showing the distribution of sedimentary facies within the Coronation Sandstone and Kurrundie Sandstone (from Friedmann and Grotzinger 1994).

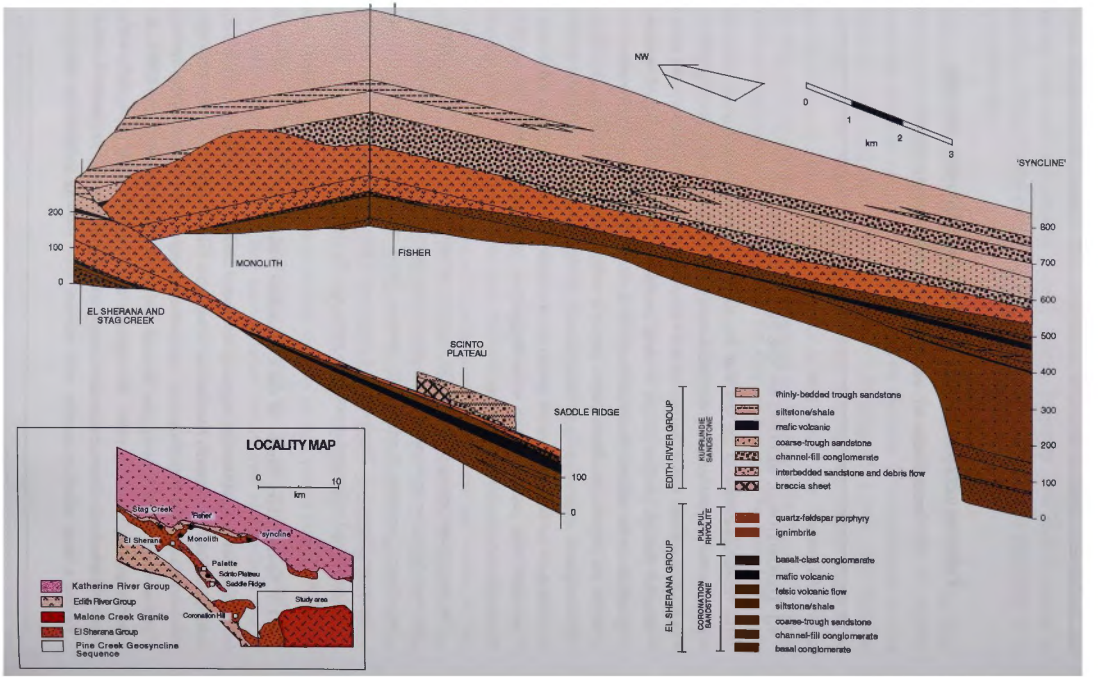

resistant units forming palaeovalleys. This antecedent northwest-trending valley-and-ridge topography roughly parallels the regional structural trends within the basement units. Large faults and fold limbs within the basement uniformly trend northwest-southeast (Needham et al. 1980; Johnston 1984; Valenta 1991). Thickness variations in the Coronation Sandstone are a function of antecedent topography. The Coronation Sandstone is typically less than 100m thick, but locally exceeds 600m in thickness (Friedmann and Grotzinger 1994; Figure 4.1). Its thickness varies by as much as 400m across only several kilometres, and units pinch out abruptly against basement palaeohighs.

Friedmann and Grotzinger (1994) divide the sedimentary facies of the Coronation Sandstone into a coarse-grained, heterogeneous lower assemblage comprising mainly conglomerates, and a homogeneous, trough-cross-bedded upper unit. The lower assemblage contains five facies (Figure 4.1). In ascending stratigraphic order they consist of: (1) 1-5 m thick beds of massive, clast-supported, imbricated cobble conglomerates, that are commonly amalgamated to form sequences up to 45m thick; (2) planar-laminated sandstone with matrix- and clast-supported conglomerate interbeds that have local imbricated clast texture; (3) poorly-sorted, medium to coarse-grained, massively bedded sandstones; (4) fine to medium-grained sandstones containing centimetre- to metre-scale scours; and (5) planar to cross-bedded, clast-supported gravels that exhibit numerous scour surfaces (with up to 4m relief), commonly overlain by lags of coarse, imbricated clasts, which grade upward into planar cross-bedded pebbly sandstone. The basal conglomerate sequence described above is incised and overlain by a thick (75m maximum thickness) interval of coarse to pebbly trough-cross bedded sandstone. The sandstones range in composition from quartz to lithic sandstone, with a minor feldspar and detrital mica component. Cobbles and boulders are typically well-rounded and mainly consist of foliated quartzite, greywacke, phyllite siltstone and vein quartz (Stuart-Smith et al. 1988). In contrast to the basal facies assemblage, the trough-cross-bedded sandstones are predominantly composed of monocrystalline quartz and chert, and are better sorted. The petrology of the framework grains reflects derivation from a low-grade continental block with few granitic bodies, consistent with provenance from the underlying low-grade metasedimentary basement.

Friedmann and Grotzinger (1994) interpret the sedimentary facies of the Coronation Sandstone to represent a mature medial braidplain environment (Figure 4.2), with clast-supported, imbricated-clast cobble conglomerates and pebble sandstones indicating bar-avalanche and channel-migration deposition. The paucity of fine sand and the general absence of mudstones suggest a lack of overbank deposits. In the lower conglomeratic assemblage, sedimentation is characterised by deep, narrow migrating channels with

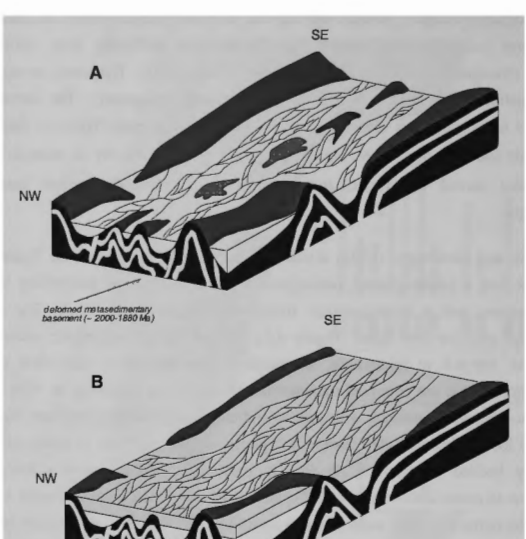

Figure 4.2: Schematic block diagram of Coronation Sandstone deposition showing the effect of antecedent strucure on palaeotopography and drainage, from Friedmann and Grotzinger (1994). Unshaded beds in Figure 4.2a represent narrow-channel epsilon cross-bedded units of the lower conglomeratic assemblage. Shaded beds in Figure 4.2b represent broad-channel trough-cross-bedded pebbly sandstone of the upper unit.

abundant scour-filled conglomerates and epsilon cross-stratification (Figure 4.2a). In contrast, the trough cross-bedded facies of the upper unit suggests a broad channel containing large migrating three-dimensional dunes (Figure 4.2b). This change in depositional style may reflect a change in drainage patterns owing to the infilling of antecedent topography, allowing a broader braidplain to eventually develop. At all times, sedimentation was confined within palaeovalleys cut into the underlying bedrock. As a result, palaeoflow ran parallel to antecedent topography, which was controlled by the northwest-southeast structural grain of the metasedimentary basement. Palaeocurrent patterns suggest flow to the northwest with low dispersion (Figure 4.3a).

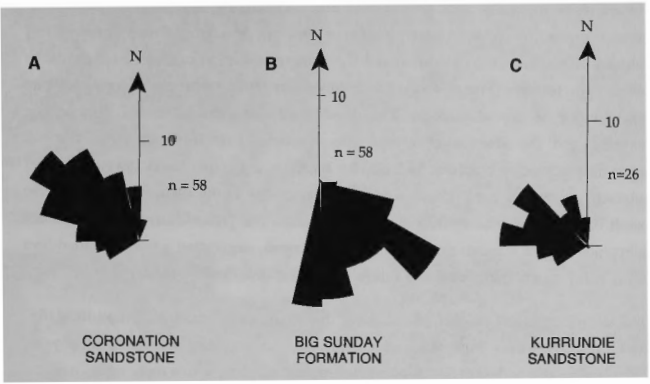

Figure 4.3: Palaeocurrent data from the South Alligator Valley region, organised in ascending stratigraphic order from A-C (from Friedmann and Grotzinger 1994).

4.1.2 Bimodal volcanism in the Coronation Sandstone

Mafic volcanics: The braidplain sequence of the Coronation Sandstone is associated with bimodal volcanism. Volcanic rocks are volumetrically minor and are normally poorly exposed between sandstone lenses (Figure 4.1), except around the Malone Creek Granite, where volcanic units are predominant (Figure 2.1). Northwest of Coronation Hill, a mafic volcanic unit up to 40m thick occurs near the top of the predominantly sedimentary succession (Figure 4.1). Friedmann and Grotzinger 1994 describe this unit as highly altered, with some phenocryst pseudomorphs, predominantly silica after plagioclase laths, preserved in the fresher samples. Amygdales infilled with chert or calcite are recorded in the top 10m of the unit. It is overlain by sandstone, or by ignimbrite of the Pul Pul Rhyolite where erosion has incised the Coronation Sandstone succession down to and including this mafic marker horizon (e.g. Saddle Ridge section, Figure 4.1). The main locus of extrusion was south of the Malone Creek Granite, where the mafic volcanics form a thick unit outcropping over a strike length of about 5 km (Figure 2.3). Their thickness in this area is uncertain, as the base of the succession is intruded by the Malone Creek Granite, and the strike and dip of the beds could not be determined.

The mafic volcanics south of the Malone Creek Granite can be subdivided into two facies based on textural and compositional differences. The first consists of massive, medium-

grained basalt to basaltic andesite (50-56% SiO_2), containing large olivine phenocrysts pseudomorphed by chlorite (+opaques+minor epidote), in a groundmass composed of euhedral plagioclase laths (andesine) and clinopyroxene (augite) exhibiting subophitic to subtrachytic textures (Figure 4.4a). Large amygdales infilled with chalcedony, prehnite and pumpellyite are ubiquitous. The development of subophitic and subtrachytic textures, and the absence of crystal fragmentation, pyroclasts or other features suggesting explosive eruption, indicate the basalt is coherent. Local development of subtrachytic textures may indicate some flow movement during cooling, suggesting the basalt is a lava flow rather than an intrusive body. The predominant medium-grained subophitic texture suggests slow cooling of the magma, suggesting a thick, ponded lava flow. This facies is interpreted as a valley-fill basaltic lava flow (or flows).

The second facies has a higher silica content that suggests an andesitic composition (61-64% SiO_2). However, mineralogically the facies consists of an aphanitic to porphyritic basalt (or basaltic andesite) that displays evidence of mingling with a more silicic magma. The porphyritic basalts contain olivine phenocrysts pseudomorphed by quartz+opaques (Figure 4.4b), and glomerophyric aggregates of tabular plagioclase and clinopyroxene phenocrysts (Figure 4.4c), in a very fine-grained groundmass composed of a microcrystalline aggregate of clinopyroxene, plagioclase and opaques (magnetite and titanomagnetite). They also contain strongly resorbed quartz xenocrysts rimmed by coronas of clinopyroxene, which indicate that the quartz crystals are in disequilibrium with the basaltic melt (Figure 4.4d). Composite plagioclase-anorthoclase feldspar aggregates within the basalts are also likely to be of xenocrystic origin, derived from a more felsic magmatic source. The xenocryst-bearing basalts outcrop at two localities. At GR 520875 (Figure 2.3), the basalt occurs as a thin, elongate body exhibiting near-vertical flow folding (Figure 4.4e). The restricted, elongate form of this body suggests the basalt may have cooled in a conduit rather than extruding as a lava, with more rapid cooling in the narrow conduit producing an aphanitic to porphyritic texture, in contrast to the medium-grained interlocking texture of the thicker basaltic lava flow(s) of facies 1. At this location, the basalts also exhibit mingling with a fine-grained rhyolite (75% SiO_2) that has an orthophyric texture in thin section (Figure 4.4f,g). The margins of the

Figure 4.4: Mafic volcanic rocks of the Coronation Sandstone: (a) subophitic intergrowths of clinopyroxene and plagioclase. Sample 89123001; (b) olivine phenocryst pseudomorphed by quartz and opaques. Sample 89123018; (c) glomeroporphyritic aggregate of clinopyroxene in a fine-grained basaltic (cpx-plag-opaques) groundmass. Sample 89123019; (d) quartz xenocryst rimmed by a reaction corona of amphibole, in a fine-grained basaltic groundmass. Sample 89123019; (e) vertical flow folding in an elongate pipe-like body of fine-grained basalt. GR 520875; (f) magma mingling of rhyolite (light grey) and basalt (dark grey). The basalt contains quartz xenocrysts. GR 525870; (g) thin section showing the highly irregular contact between rhyolite (top of photograph) and basalt domains, with small blebs of rhyolite incorporated into the basalt. Sample 89123013; and (h) autobrecciated margin of high-silica basalt. GR 463921.

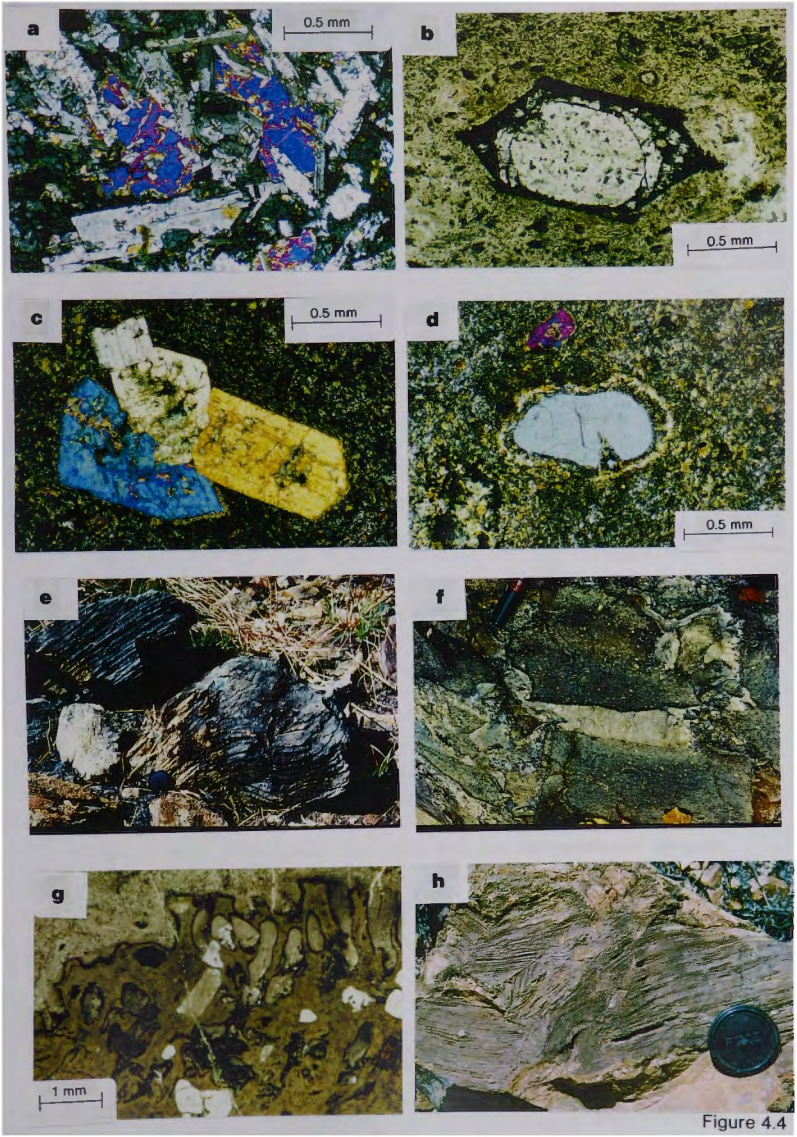

Figure 4.4

rhyolite and basalt are highly irregular and small blebs of the rhyolite have broken off and are included in the basalt. A second outcrop of xenocryst-bearing basalt occurs at GR 463921. The basalt is predominantly massive in character, but its upper surface is locally autobrecciated (Figure 4.4h).

Felsic volcanics: Felsic magmatism in the Coronation Sandstone is represented by coarse-grained rhyolite porphyries that outcrop within the thick basalt lavas south of the Malone Creek Granite (Figure 2.1). The porphyries are similar in composition and geochemistry to the rhyolite porphyries intruding the overlying Pul Pul Rhyolite and Big Sunday Formation (Chapter 2.4.2). Some of these coherent porphyry bodies may intrude the Coronation Sandstone basalts. However, porphyry clasts are locally incorporated into the basalt, suggesting at least some of the porphyry bodies were exposed at the surface as lavas, and eroded prior to basalt extrusion.

The bimodal pattern of volcanism recorded by the Coronation and Pul Pul Rhyolite of the El Sherana Group, is also characteristic of the Plum Tree Volcanics of the overlying Edith River Group, which consists of a mix of felsic (dacitic) volcanics and minor mafic volcanics (Needham and Stuart-Smith 1985b).

4.1.3 Sedimentary facies of the Kurrundie Sandstone

Northwest of Coronation Hill, the Kurrundie Sandstone of the Edith River Group (> 300 m thick) disconformably overlies the Pul Pul Rhyolite. Incised valleys with 40-60m of relief cut into the Pul Pul Rhyolite, and are infilled with boulder conglomerates of the Kurrundie Sandstone (Friedmann and Grotzinger 1994). Southeast of Coronation Hill, the Kurrundie Sandstone overlies ignimbrites assigned to the Big Sunday Formation (Needham and Stuart-Smith 1985a), that are separated from the lower turbidite succession of the Big Sunday Formation by the Palette Fault (Figure 2.1). These ignimbrites probably represent either fault repetition of the underlying Pul Pul Rhyolite ignimbrite succession or result from ongoing volcanism from the same volcanic source (Chapter 3). The contact of the Kurrundie Sandstone with the Big Sunday Formation ignimbrites has not been studied in detail, but is probably also disconformable.

Friedmann and Grotzinger (1994) describe the facies of the Kurrundie Sandstone as follows: (1) a basal cobble-boulder channel-fill conglomerate containing imbricated rounded clasts of Pul Pul Rhyolite; (2) coarse to fine-grained planar-laminated sandstone; (3) coarse to fine-grained trough-cross-bedded sandstone; (4) a 40m interval of planar-laminated siltstones, shales and finely-laminated, rippled quartz sandstone; and (5) quartz-pebble conglomerates. The relationship between these facies is illustrated in

Figure 4.1. The Kurrundie Sandstone is very similar in composition to the Coronation Sandstone, consistent with provenance from the underlying low-grade metasedimentary basement (Friedmann and Grotzinger 1994). The main difference is the greater abundance of felsic volcanic fragments in the Kurrundie Sandstone, derived from the underlying Pul Pul Rhyolite.

Friedmann and Grotzinger (1994) interpret the succession of facies within the Kurrundie Sandstone to record the transition from medial braidplain (represented by boulder channel-fill conglomerates and trough-cross-bedded sandstone) to distal braidplain and possibly subaqueous strata (represented by the siltstones, shales and well-bedded fine sandstone). As with the Coronation Sandstone, palaeoflow was to the northwest, with low dispersion (Figure 4.3c).

4.1.4 Depositional and tectonic setting

The regional landscape was the same preceding and following deposition of the Pul Pul Rhyolite and Big Sunday Formation, consisting of a large braidplain river system flowing to the northwest. The volcanic succession of the Pul Pul Rhyolite is therefore interpreted to have accumulated in terrestrial sedimentary basin under subaerial conditions. The Pul Pul Rhyolite and Big Sunday Formation depocentres developed independently of the regional palaeoslope, which throughout the history of El Sherana/Edith River Group deposition, remained to the northwest. The turbiditic siltstones and sandstones of the Big Sunday Formation, which locally overlie the Pul Pul Rhyolite at the southeastern end of the South Alligator Valley, record subaqueous sedimentation in relatively quiet water (i.e. below storm-wave base; Chapter 3). However, the local distribution of the formation, and the presence of subaerial units both directly above and below the turbidite succession, suggests that the formation is non-marine, and probably represents a short-lived lacustrine environment within the predominantly terrestrial succession. Palaeocurrents for the turbidite succession suggest a southeast facing palaeoslope, directly opposite to the regional northwest palaeoslope (Figure 4.3b). This suggests that Pul Pul Rhyolite volcanism temporarily interrupted regional braidplain sedimentation, and either through caldera formation and/or damming of the braidplain drainage, caused local ponding of a lake with its own palaeodrainage pattern, not influenced by the regional palaeoslope.

Bimodal volcanism within the El Sherana and Edith River Groups, in conjunction with normal-sense growth faulting recorded throughout the sedimentary succession, led Friedmann and Grotzinger (1994) to interpret the tectonic setting as a continental extensional or transtensional basin.

4.2 FACIES MODELS FOR SUBAERIAL SILICIC VOLCANIC CENTRES

From the facies descriptions of the Pul Pul Rhyolite in Chapter 2, it is known that in the study area, it comprises a complex association of primary rhyolitic volcanic products and subordinate epiclastic deposits (the lacustrine deposits of the Big Sunday Formation, described in Chapter 3, are included as part of the association). The facies association of ignimbrite, co-ignimbrite breccia, sub-volcanic stocks, sills and dykes and restricted volcaniclastic sedimentary rocks (confined to fluvial and lacustrine environments), is similar to that occurring in many modern subaerial silicic volcanic centres (Cas and Wright 1987). In the following section the palaeoenvironmental context of the Pul Pul Rhyolite is determined by interpreting the facies association in terms of its proximity to volcanic vent. In the case of modern silicic volcanic centres, the most widely recognised type of volcanic centre is the caldera-style vent, and so the facies association of the Pul Pul Rhyolite is assessed in terms of caldera models, by comparing the sequence with modern caldera centres, and a facies model devised for ancient successions.

4.2.1 Modern subaerial silicic volcanic centres

Some of the most comprehensive studies of modern calderas have been carried out in the large silicic volcanic provinces of the Western United States (e.g. San Juan Volcanic Field; Lipman 1976; Steven and Lipman 1976). Based on the study of 'resurgent cauldrons' in this region, Smith and Bailey (1968) proposed a seven stage cycle for the evolution of silicic volcanic centres. In a landmark paper based on a review of subsequent studies of caldera complexes in the western United States (e.g. Lipman 1976; Steven and Lipman 1976; Bailey et al. 1976, Christiansen 1979; Mahood 1980, 1981; Bacon 1983, Nelson et al. 1986), Lipman (1984) updated this model and divided caldera evolution into three stages:

1. *Pre-caldera stage:* The caldera cycle, which typically lasts between 100 000 years to 1 million year, is initiated by the emplacement of a mid-high level magma chamber which may cause regional tumescence, resulting in the development of a vertical to inward-dipping arcuate ring fracture system which outlines the area within which caldera collapse will later occur (Lipman 1984). These fracture systems and the shape of the caldera complex may be partly controlled by pre-existing basement structures (e.g. Valles Caldera; Self et al. 1986). Pre-caldera volcanism is commonly more intermediate in composition than the main caldera-forming eruptions, which may reflect fractionation in the magma chamber and the progressive evolution of a more felsic source. At this early stage in the caldera cycle, magma pressure must exceed lithostatic pressure in order to create vents and initiate eruptions. Magma ejected under

high pressure produces high eruption columns resulting in plinian fallout deposits and small pyroclastic flows. As a result, the earliest volcanic activity typically produces clusters of small intermediate stratovolcanoes. (e.g. Taupo Volcanic Zone; Wilson et al. 1984). These early vents are usually destroyed during caldera formation (Steven and Lipman 1976).

2. *Caldera collapse:* As magma chamber pressure is released following initial plinian airfall eruption, the roof of the magma chamber collapses resulting in the opening of additional vents. Vent position may transfer from a central vent to multiple vents located around the ring fracture system (e.g. Bandelier Tuff; Self et al. 1986). At this stage the major ignimbrite-forming eruption takes place. As vent widening occurs, a higher volume of material is erupted and the eruption column becomes difficult to sustain, resulting in column collapse and the generation of large-scale pyroclastic flows. Ignimbrite eruption may be synchronous with caldera subsidence, which results from the rapid evacuation of the magma chamber and roof collapse. Syn-volcanic subsidence results in intracaldera deposits that may be an order of magnitude thicker than the corresponding outflow sheets. Intracaldera ignimbrite deposits are commonly thicker than 500m and deposits up to 1.5 km or more are recorded, whereas outflow ignimbrite sheets are typically tens of metres to 100-200m thick. The ignimbrites generated during caldera formation may be compositionally zoned, becoming more mafic upsection (e.g. Crater Lake Caldera; Bacon 1983). The zoning reflects continuous draining of a compositionally zoned magma chamber (Steven and Lipman 1976; Christiansen 1979). Collapse of the caldera floor and vent widening results in shattering of the wallrock, supplying abundant coarse lithic debris which is incorporated into the pyroclastic flows and forms co-ignimbrite lag breccias (e.g. Thira Caldera; Druitt and Sparks 1982). Oversteepened caldera margins may collapse, forming landslide mesobreccias and megabreccias which interleave with the intracaldera ignimbrites.

   The mechanics of caldera formation has been a much studied issue, and varied processes have been inferred as important (Lipman 1997), including: (1) plate (piston) subsidence of a relatively coherent floor bounded by ring faults (Smith and Bailey 1968; Steven and Lipman 1976); (2) complex piecemeal fracturing of caldera floors (Scandone 1990; Branney and Kokelaar 1994); (3) trap-door subsidence, bounded by an incomplete ring fault and a hinged segment (Steven and Lipman 1976; Christiansen et al. 1977); (4) downsag subsidence without large bounding faults (Walker 1984; Branney 1995); and (5) funnel-shaped subsidence into an areally restricted central vent (Yokoyama 1983,1987; Aramaki 1984). In addition to syn-eruptive subsidence, many calderas are topographically enlarged by late-stage

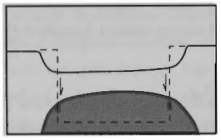

A

Plate (piston) collapse

single, large volume eruptions from
large shallow magma chambers

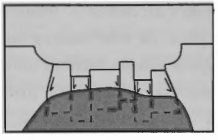

B

Piecemeal disruption

- multicyclic (ie incremental subsidence during successive eruptions
- interaction with prevolcanic structural grain
-intricate fracturing of the caldera floor during a single eruption

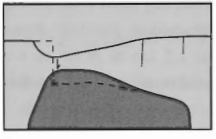

C

Trap-door subsidence

- asymmetrical pluton
- early downsagging and incipient plate collapse related to smaller eruptions
- regional tectonic influences

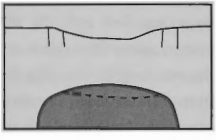

D

Downsag subsidence

- small volume/deep magma chamber
- small volume eruptions
- components of downsag accompany plate-subsidence and trap-door subsidence

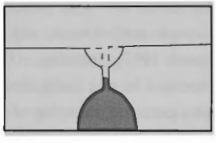

E

Funnel calderas

small calderas (<3-5 km diameter)
small/deep pluton?
dominant enlargement by slumping into an areally restricted vent

Figure 4.5: Models of alternative caldera subsidence geometries in relation to size of eruption, and depth and geometry of the underlying magma (from Lipman 1997). Dashed lines indicate depths of downdropped caldera floor blocks, which are inferred to have been partly removed by stoping into the magma chamber during and immediately after collapse.

subsidence (downsag) or collapse (Lipman 1997), creating depressions that are later filled with fluvio-lacustrine sedimentary successions. Lipman (1997) noted that caldera-forming processes are highly variable in terms of vent types and eruptive histories, resulting in a wide range of deposit types and configurations. Lipman (1997) proposed that the geometric diversity of ash-flow calderas represents a continuum of features and processes bounded by the five simplified geometric end members described above, and illustrated in Figure 4.5, and related subsidence mechanisms to factors such as eruption size and magma chamber geometry.

Regardless of the mechanism, caldera collapse results in structural complexity within the caldera structure, generating abundant faults and unconformities, and a complex facies geometry with rapid vertical and lateral facies changes. The resultant caldera structure is usually circular to elliptical in shape. Average diameters range between 10-20 km. The largest caldera has a dimension of 100x40 km (Toba Caldera, Indonesia).

3. *Post-caldera stage:* Post-caldera activity involves a period of relative quiescence with only minor volcanic activity, including the emplacement of shallow intrusive domes and/or extrusive lava domes and flows of intermediate to acidic composition, accompanied by small volume pyroclastic eruptions. These are commonly emplaced around the ring fracture (e.g. Valles Calderas; Smith and Bailey 1968; Self et al. 1986) or along reactivated basement faults within the caldera (e.g. La Primavera Caldera; Mahood 1980, 1981). Sedimentation may be initiated in the new caldera depression. Deposits include talus and landslides resulting from mass wasting due to the high topographic relief. Impounded drainage can result in the formation of fluvial systems and caldera lakes (e.g. Crater Lake Caldera; Nelson et al. 1986; La Primavera Caldera; Walker et al. 1981; San Luis and Creede Calderas; Steven and Lipman 1976). In the post-caldera phase, hydrothermal systems may be active along fault conduits. These hydrothermal systems may be associated with base and precious metal mineralisation.

In the final stages of the caldera cycle, resurgence or structural doming of the caldera floor may result from recharging of the sub-volcanic magma chamber causing local tumescence, or from the rise of the residual subvolcanic magma body to intrude and uplift its cogenetic volcanic pile (Smith and Bailey 1968; Lipman 1984). Resurgence usually follows a relatively short time after caldera collapse, with simple cycles requiring no more than hundreds of thousands of years, and more complicated cycles no more than one to two million years to complete (Smith and Bailey 1968; Lipman 1984; Elston 1984). Resurgent domes are characterised by radially outward-dipping intracaldera ignimbrites and fill (Lipman 1984). At depth these ignimbrites may

surround a central intrusive dome (Smith and Bailey 1968). The classic example of doming is held to be the Creede Caldera (Steven and Lipman 1976).

4.2.2 A facies model for ancient successions

The general model of caldera formation described above provides a good synthesis of the common features of modern caldera centres, and can be used to construct a facies model for subaerial silicic volcanic centres. This facies model can then be applied to the interpretation of less well preserved or exposed ancient volcanic sequences. Facies models devised for volcanic successions use the eruptive centre as the focal element (e.g. Vessel and Davies 1981; Cas and Wright 1987; McPhie 1988; Orth et al. 1989). In this case, the eruptive centre is a caldera-style eruptive vent. The model outlined below recognises two broad facies associations related to distance from source vent, designated the proximal and distal facies associations. The proximal facies association corresponds to the intracaldera sequence and the extra-caldera or outflow deposits are assigned to the distal facies association. The facies characteristics and facies associations that characterise each region are outlined below, and illustrated in Figure 4.6.

Proximal Facies

The scale of caldera structures is approximately hundreds of square kilometres. Calderas range in diameter from 5 km to 100 x 40 km (Toba Caldera, Indonesia) and average about 10-20 km in diameter. The caldera structure is usually circular to elliptical in shape, although significant basement structural controls can impose more irregular shapes. The margins of the caldera may be abrupt, steep scarps or gently inward-dipping slopes and may be flanked by caldera margin collapse breccias (Cas and Wright 1987).

1. Primary volcanic facies

- The primary volcanic facies association principally comprises thick ignimbrite deposits (commonly > 500 m), which may be the product of a single, voluminous eruption (e.g. Self and Wright 1983; Busby-Spera 1984; Lipman 1984), or many moderate-sized to small-scale eruptions (e.g. Wright 1981; Christiansen 1979). Intracaldera ignimbrites are typically densely welded, because the great thickness of the sequence promotes heat conservation. The ignimbrites are lithic-rich because they are erupted synchronously with caldera formation, during which shattering of the caldera floor and activity on the margin faults create a significant supply of coarse lithic clasts which are incorporated into the pyroclastic flows.

- An abundance of coarse lithic breccias associated with the ignimbrite deposits indicates a near-source environment. These include genetically-related co-ignimbrite

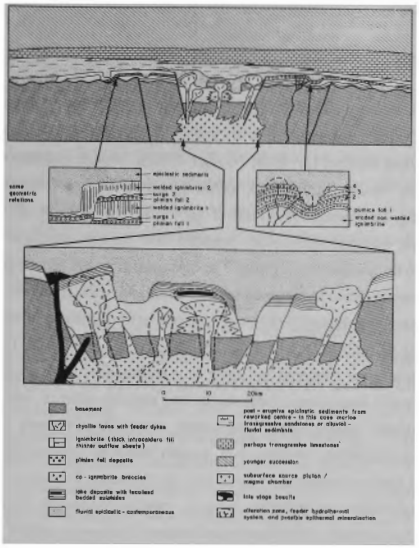

Figure 4.6: Facies model for continental silicic volcanoes developed by Cas and Wright (1987), depicting proximal facies associations (from the focal caldera complex) through to distal facies associations of the ignimbrite plateau or shield outside the caldera.

lag breccias, comprising large lithic clasts in an ignimbrite matrix, which are generated as the largest and densest lithic clasts are deposited closest to the source. Other clastic deposits include landslide meso- and megabreccias generated by fault scarp collapse at the caldera margins, which interleave with syn-eruptive ignimbrite deposits.

- Plinian fall deposits are relatively thick and exhibit near-vent characteristics such as coarse pumice and lithic clast size. If the deposits are thick enough they may retain enough heat to weld (Cas and Wright 1987). Being unconsolidated, they have low preservation potential unless rapidly capped by welded ignimbrite.

- Intrusive to extrusive lava domes and dome complexes are emplaced within the central caldera region and at its margins, or just outside the caldera margins (Walker 1984). They are generated both immediately prior to and following caldera collapse, but the post-caldera domes are best preserved.

- Pyroclastic surge and associated airfall material can form at phreatomagmatic vents or in association with extrusive lava domes that encountered surface water.

2. Sedimentary facies

- Epiclastic deposits are volumetrically minor relative to primary volcanic facies. Caldera centres usually have strong relief caused by magma movement producing uplift and downsag (Self et al. 1986; Walker 1984), violent eruptions producing evacuation holes and/or differential eruption-related or post-eruptive vertical movements along fault scarps (Fridrich et al. 1991). In periods of repose, the unstable volcanic landscape is rapidly denuded and primary volcanic material is incorporated into the sedimentary system. The epiclastic deposits are characterised by a textural and compositional immaturity, and are commonly rich in unabraded pumice and vitric components (Mahood 1980), feldspar and ferromagnesian phases. Deposits reflect a diversity of sedimentary environments and processes. Talus, landslide and debris flow deposits are triggered by uplift and earthquakes and originate on the flanks of high-profile lava domes, fault scarps and unstable piles of volcanic debris. Fluvial environments ranging from intermittent stream environments to relatively mature alluvial/fluvial/deltaic systems may contain relatively coarse-grained, thick-bedded deposits that are tractional or mass flow in character. Relatively fine-grained deposits can accumulate in lacustrine systems, which commonly develop within caldera structures as a result of the impounded drainage following caldera subsidence.

3. Intrusive component

- Small-volume sub-volcanic stocks and plugs intrude along caldera-related faults, or reactivated pre-existing basement structures. Magmatic resurgence can result in the emplacement of a roughly circular central pluton into the volcanic pile at depth (Smith and Bailey 1968).

4. Structural features

- Caldera fills are complex sequences of fluvial and lacustrine epiclastic deposits, pyroclastic rocks, and lavas. Facies relationships are further complicated by intrusion of rhyolite domes and structural disturbances. Ground movements related to volcanic activity cause significant faulting, tilting and deformation of strata, generation of unconformities and abrupt lateral facies relationships.

- The presence of magma bodies close to the surface creates a high geothermal gradient which, coupled with faulting and ground movement, promotes fluid circulation and the development of hydrothermal systems. Features include hydrothermal alteration zones, hydraulic breccias, mineralisation and geothermal activity (sinter deposits, sulphurous lakes and mud pools).

Distal Facies

The distal facies encompasses the outflow setting of caldera structures. Distal environments cover a greater area than the proximal environment (hundreds to thousands of square kilometres), but the deposits are much thinner. Primary volcanic facies are subordinate in volume relative to sedimentary facies, as the distal environment is characterised by active erosion and normal sedimentary surface processes, which are periodically interrupted by the sudden influx of large volumes of pyroclastic material.

1. Primary volcanic facies

- Ignimbrites have a sheet-like geometry, and generally infill and mantle old topography, constructing a low-profile slope that generally dips shallowly away from the vent (Wright 1981), although in some sag calderas such as Taupo, extracaldera slopes are inward dipping (Walker 1984). They are generally an order of magnitude thinner than proximal ignimbrite deposits (tens to 100-200 m, compared to hundreds to thousands of metres thick), less strongly welded and generally contain smaller lithic clasts than their proximal counterparts. Grainsize, thickness and degree of sorting and welding vary systematically with distance from source. The geological record is biased towards the preservation of welded sheets, because non-welded ignimbrites are rapidly eroded.

- Lavas and vent-produced base surges typically do not flow far enough from their sources to be incorporated into distal sequences (McPhie 1988).

- Airfall deposits and co-ignimbrite ashes are common components of the distal environment, but as with non-welded ignimbrites, they are generally poorly preserved. They are thin (1-2 m maximum thickness) and generally contain smaller pumice and lithic clasts than their proximal counterparts, and fewer lithic clasts (Walker et al. 1981).

2. Sedimentary facies

- The distal facies association encompasses a diverse range of subaerial to shallow and deep marine sedimentary environments, due to the vast lateral extent of the setting. Significant erosion occurs between ignimbrite eruptions. Steep-sided valleys are rapidly incised into freshly erupted ignimbrite as drainage patterns are re-established (Cas and Wright 1987). Local, shallow lakes may form in valley or develop on the low slopes of the shield. Large volumes of eroded volcaniclastic debris rapidly accumulate and are redeposited by mass-flow processes, so that drainage of distal

settings is repeatedly choked by the influx of lahars (McPhie 1988). The volcaniclastic debris is eventually deposited in fluvial outwash plains flanking the ignimbrite shield or transported into adjacent marine basins.

3. Structural features

- There is a complex interplay between epiclastic sedimentation and ignimbrite deposition in the distal environment. Palaeovalleys will be periodically choked with ignimbrite or lahars then cleared to re-establish the pre-existing drainage pattern (McPhie 1983). This leads to the repeated infilling and excavation of the same valley, and the generation of disconformities. However, the overall facies geometry is relatively regular compared with the proximal environment, and consists of a stack of ignimbrites interbedded with volcaniclastc sedimentary rocks.

- The distal facies is generally free of hydrothermal alteration, being remote from the locus of intrusive magmatic activity.

4.3 Palaeogeography of the Pul Pul Rhyolite

In Chapter 2, the Pul Pul Rhyolite was subdivided into facies, which were documented in detail. For each facies, the genetic origin was determined by its characteristics, and its relationships with other facies. The following section describes the spatial association of these facies (including their relationship to the underlying Coronation Sandstone, and the overlying lacustrine sequence of the Big Sunday Formation) and interprets their temporal and spatial relationships. The palaeogeography of the Pul Pul Rhyolite is determined by interpreting the facies associations in terms of the facies model for silicic volcanic centres described above, and a depositional model for the El Sherana Group in the study area is presented.

4.3.1 Facies associations of the Pul Pul Rhyolite

The Pul Pul Rhyolite can be divided into two domains that have distinctive facies associations (Figure 4.7). Domain 1, which lies to the southeast of Dinner Creek (Figure 4.7), contains the thickest stratigraphic package. Domain 2 encompasses the Pul Pul Rhyolite where is outcrops discontinuously along the South Alligator Valley and around the rim of a syncline surrounding the Mt Callanan Basin (northwest of Dinner Creek; Figure 2.1). The formation is considerably thinner in Domain 2, and has a less complex association of facies.

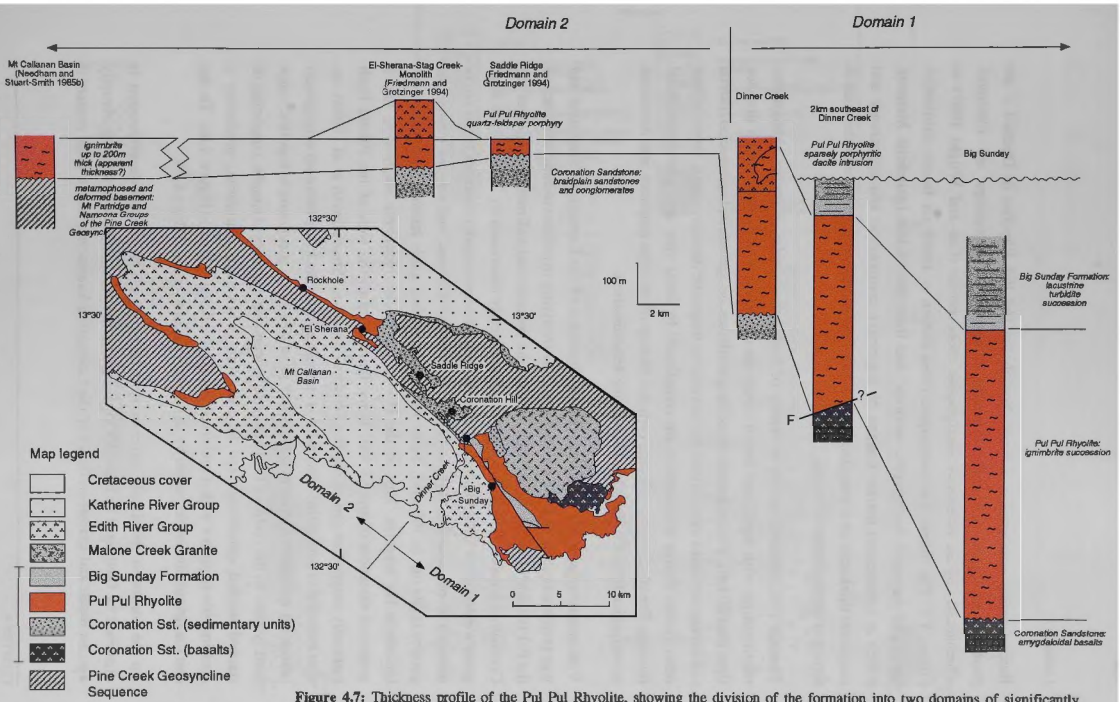

Figure 4.7: Thickness profile of the Pul Pul Rhyolite, showing the division of the formation into two domains of significantly different thickness, which contain distinctive facies associations. The map insert shows the spatial distribution of the Pul Pul Rhyolite and section locations.

Domain 1

Representative stratigraphic sections through the Pul Pul Rhyolite in Domain 1 are presented in Figure 4.8 and interpreted stratigraphic relationships are illustrated schematically by an interactive stratigraphic cross-section (Cas and Wright 1987) in Figure 4.9. The interactive stratigraphic cross-section is based on facies distribution maps and measured stratigraphic sections, and uses the Middle Ignimbrite Member, which is a prominent marker horizon of distinctive composition and appearance and consistent thickness, as a time plane to establish stratigraphic correlations and the relative timing of emplacement of facies.

Domain 1 is characterised by a variety of facies that display complex stratigraphic relationships, with significant lateral variations occurring over a short strike distance (less than 20 km). Facies include rhyolitic ignimbrites, co-ignimbrite lag breccias, fluvial and lacustrine facies associations and several co-magmatic intrusive units, cross-cutting other facies. Facies relationships are complicated by local syn- and post-depositional faulting. The stratigraphy reflects a complex history of multiple eruptions and intrusions accompanied by block faulting and on-going sedimentation.

Volcanism commenced in Domain 1 during deposition of the Coronation Sandstone and was predominantly basaltic in composition. The overlying rhyolitic volcanic sequence of the Pul Pul Rhyolite disconformably overlies the volcanic and sedimentary facies of the Coronation Sandstone. The sequence is volumetrically dominated by moderate to high grade welded ignimbrites that have a high coarse-lithic component (clasts up to 30 cm in diameter) concentrated in layer 2bL lithic concentration zones, and contain coarse and pumice clasts (up to 100 cm). Some of the ignimbrites grade laterally into coarse co-ignimbrite lag breccias. East of the Palette Fault, the ignimbrite succession has a preserved thickness of over 1 km. If the ignimbrites to the west of the Palette Fault (presently mapped as part of the Big Sunday Formation; Stuart-Smith et al. 1988) are also included as part of this succession, the total apparent thickness becomes even greater (about 1.4 km), although there may be fault repetition of the succession across this major fault system. In the centre of Domain 1, the volcanic stratigraphy is simple, consisting of stacked welded ignimbrites and an overlying non-welded ignimbrite, producing a conformable sequence with a preserved thickness of about 800m (Figure 4.8). To the east the ignimbrites are truncated by an intrusive rhyolite dome (Figure 4.9).

To the northwest the simple 'layer-cake' stratigraphy of the ignimbrite succession is disturbed by faulting. The basal 350m of the ignimbrite succession terminates abruptly against basalt and sandstone facies of the Coronation Sandstone, and a fault contact is

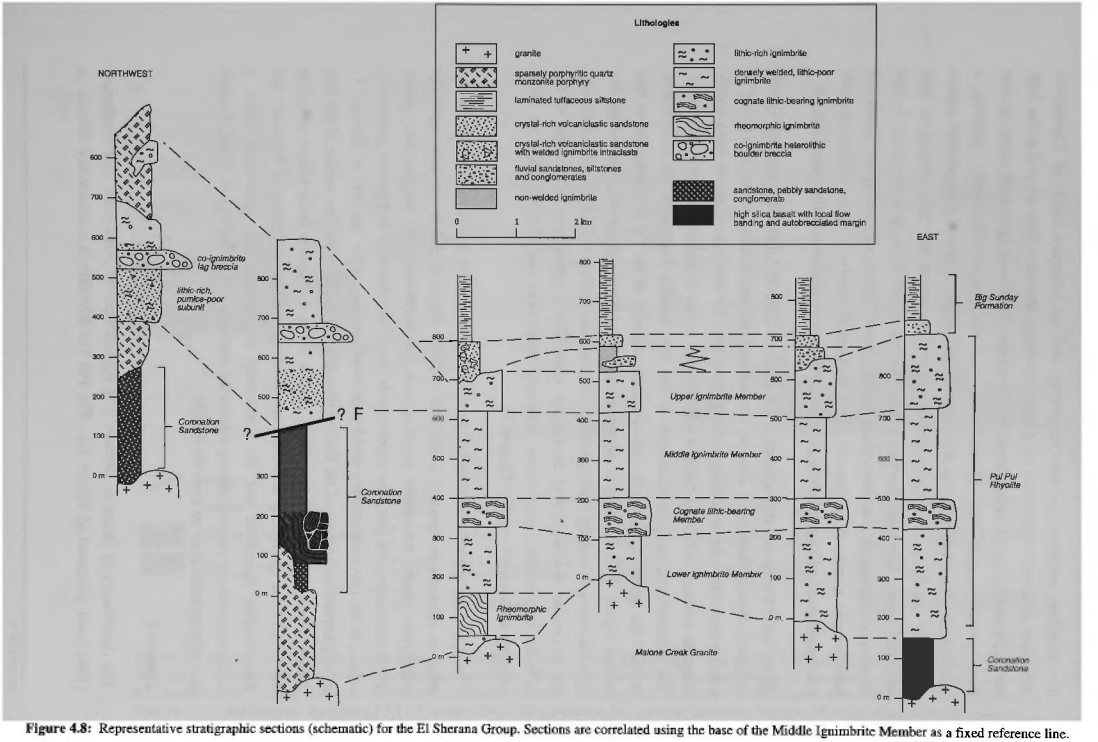

Figure 4.8: Representative stratigraphic sections (schematic) for the El Sherana Group. Sections are correlated using the base of the Middle Ignimbrite Member as a fixed reference line.

inferred by this abrupt lateral change in facies. Northwest of the fault, the basal units of the ignimbrite sequence are not recognised, and the basement block of Coronation Sandstone is directly overlain by the Upper Ignimbrite Member. This infers that the fault was activated prior to or synchronous with eruption of the basal ignimbrite units, so that they ponded against the exposed scarp or buttress unconformity, infilling a palaeodepression created on the downthrown fault block. A sparsely porphyritic quartz monzonite porphyry stock cross-cuts the fault, supporting the early timing of this structural event. Late-stage faulting is also evident in this area. Another fault further northwest displaces the basement block of Coronation Sandstone, the Upper Ignimbrite Member and a sparsely porphyritic quartz monzonite porphyry body, indicating fault movement postdated ignimbrite deposition and late-stage intrusion of the ignimbrite pile.

At the top of the ignimbrite sequence in the centre of Domain 1, laterally restricted fluvial epiclastic deposits interfinger with the non-welded ignimbrite along strike, and occur as small lenses within the underlying welded ignimbrite. The epiclastic deposits have highly irregular contacts, reflecting channel-style erosion of the underlying welded ignimbrite. The volcaniclastic turbidite succession of the Big Sunday Formation disconformably overlies the ignimbrites and fluviatile epiclastic deposits of the Pul Pul Rhyolite in this central region. This sequence is interpreted as a local lacustrine environment within the subaerial volcanic setting. Predominantly volcaniclastic detritus within the turbidites, and the occurrence of syn-eruptive crystal-rich volcaniclastic sandstones at the base of the turbidite succession, suggest that lacustrine deposition was contemporaneous with ongoing volcanic activity (see Chapter 3).

The ignimbrite sequence is intruded by co-magmatic rhyolite porphyries in the central area, an aphanitic to sparsely porphyritic rhyolite dome or sill in the east, sparsely porphyritic quartz monzonite porphyries in the northwest, and megacrystic quartz monzonite porphyries along the Palette Fault. Small rhyolite sills and dykes, genetically related to the intrusive sparsely porphyritic rhyolite dome in the east part of Domain 1, locally intrude ignimbrites of the Pul Pul Rhyolite and the turbidite succession of the Big Sunday Formation. The Malone Creek Granite forms a central circular pluton intruding the base of the ignimbrite sequence, cross-cutting the Lower Ignimbrite Member, the Rheomorphic Ignimbrite and the Coronation Sandstone. The ignimbrites show a concentric outcrop pattern, striking around the southern half of the Malone Creek Granite and dipping radially away from the margin.

Domain 2

The distribution of facies in Domain 2 is documented by Friedmann and Grotzinger (1994) and presented in Figure 4.1. The Pul Pul Rhyolite is considerably thinner in

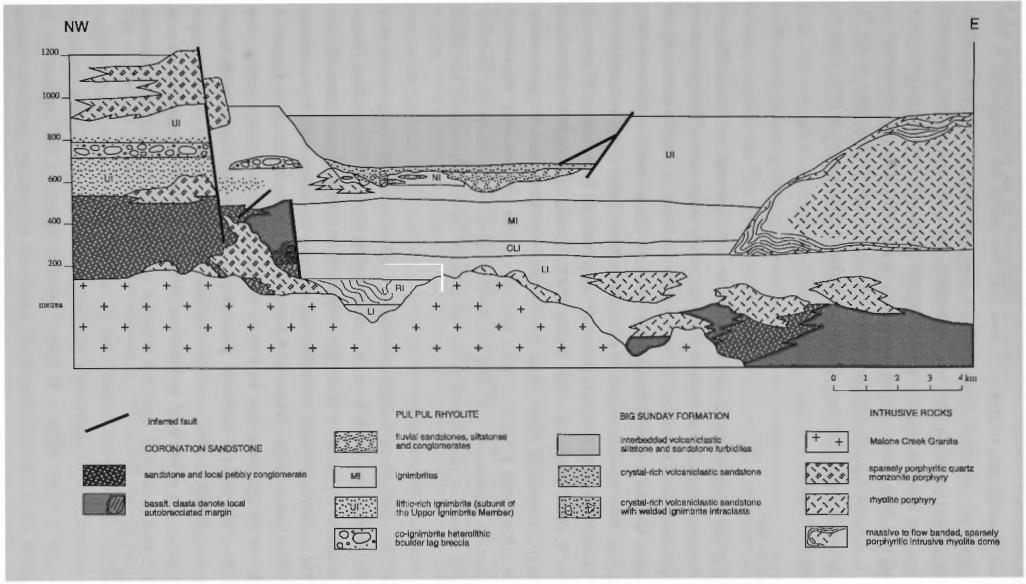

Figure 4.9 Schematic stratigraphic section through the El Sherana Group, along the southern margin of the Malone Creek Granite, showing the spatial relationship between primary volcanic, intrusive and sedimentary facies within the Pul Pul Rhyolite, structural complexities within the succession and the development of a local lacustrine environment within the volcanic landscape, represented by the Big Sunday Formation. LI = Lower Ignimbrite Member, RI = Rheomorphic Ignimbrite, CLI = Cognate lithic-bearing Member, MI = Middle Ignimbrite Member, UI = Upper Ignimbrite Member, NI = Non-welded Ignimbrite.

Domain 2, attaining a maximum thickness of only 190m at Monolith in the El Sherana-Stag Creek-Monolith area (Figure 4.7), and only two facies are recognised. A thin rhyolitic ignimbrite (60-100 m thick) overlies a major erosional surface which removed up to 100m of the Coronation Sandstone stratigraphy, and infills and mantles antecedent topography. The ignimbrite has a low lithic content, and contains smaller pumice clasts (1-15 cm) and lithic clasts (several centimetres in diameter) than the ignimbrites in Domain 1. A massive quartz-feldspar porphyry locally overlies the ignimbrite in the El Sherana-Stag Creek-Monolith area, attaining a maximum thickness of at least 130m in the vicinity of Monolith.

Proximity to vent

In terms of the facies model devised for subaerial silicic volcanic centres in Chapter 4.2.2, the facies association of Domain 1 would classify as proximal. The ignimbrites exhibit proximal characteristics such as extreme thickness, a rapid succession of emplacement without erosional breaks between units, dense welding and columnar jointing, high lithic contents and coarse lithic and pumice clasts. The associated facies include a co-ignimbrite lag breccia (a proximal vent pyroclastic flow feature; Wright and Walker 1977; Druitt and Sparks 1982; Walker 1985), abundant co-magmatic intrusions, high-energy, channelised fluvial deposits reflecting a texturally and compositionally immature volcaniclastic provenance and a (possible) caldera lake sequence, represented by the turbidite succession of the Big Sunday Formation, which developed co-evally with active volcanism (as indicated by the syn-eruptive crystal-rich volcanic sandstone facies).

Domain 2 is interpreted as a distal association of facies, although the presence of a porphyritic rhyolite lava infers a second eruption point in the El Sherana-Stag Creek-Monolith area, as rhyolite lavas do not generally travel far from their source vent (Walker 1973). The underlying rhyolitic ignimbrite may represent an outflow sheet that correlates with the thick ignimbrite pile in Domain 1. Its confinement to the northwest of Domain 1 suggests that the ignimbrite may have been sourced from this proximal region, and flowed down the regional northwest palaeoslope of the fluvial braidplain. It is not possible to rigorously test this correlation, because outcrop between the two domains is discontinuous, and geochemical comparisons cannot be made as all volcanic units in Domain 2 have undergone extensive alteration related to U(Au-PGE) mineralisation (Chapter 2.1.2).

4.3.2 Interpretation as an intracaldera setting

Given that Domain 1 contains a facies association consistent with deposition proximal to vent, the possibility that this succession represents a caldera sequence needs to be explored, as this is the most widely recognised type of modern silicic volcanic centre. The proximal features of the succession are consistent with an intracaldera setting as outlined by the facies model for subaerial silicic volcanic centres. However, only a remnant of the original system remains, and a well-defined caldera structure does not exist. Nor were any features identified that would conclusively indicate the presence of a caldera margin, such as an unequivocal ring dyke or ring fracture system, or intercalated collapse megabreccias. The marked decrease in the thickness of the ignimbrite succession from Domain 1 to Domain 2, however, could reflect syn-volcanic subsidence of the proximal ignimbrite succession within a caldera structure, which suggests that a caldera margin must lie between the two domains. A series of faults corresponds spatially to the marked change in thickness at the northwest margin of Domain 1 (near Dinner Creek). Most of the fault movement post-dates ignimbrite emplacement, but an early fault scarp is preserved near the base of the succession, against which the lower ignimbrite units have ponded (Figure 4.9). This fault is interpreted to be a preserved remnant of the early caldera margin that was later buried by the Upper Ignimbrite Member.

The Upper Ignimbrite Member grades into a co-ignimbrite lag breccia within 3 km of the proposed northwest caldera margin, and a basal lithic-rich subunit is also recorded in this vicinity, which lenses out away from the margin, to the south (Figure 4.8, 4.9). Lag breccias are typically found in proximal locations, and the lithic content and grainsize of ignimbrites and associated lithic breccias systematically decreases with distance from vent (e.g. Walker 1983; Druitt and Sparks 1982; Suzuki-Kamata and Kamata 1990). The coincidence of these features therefore suggests that the source of the Upper Ignimbrite Member may have been a ring vent, located at or near the northwest margin of Domain 1. Although a definitive ring dyke cannot be recognised, several sparsely porphyritic quartz monzonite porphyries are spatially associated with the faults at the northwest margin of the proximal ignimbrite succession, and may have used the faults as conduits during late-stage intrusion. These quartz monzonite porphyries could represent ring domes associated with the proposed caldera margin structure at this locality.

The absence of collapse megabreccias flanking a well-defined caldera fault scarp, suggests that caldera collapse did not fit the 'classic' model of cylindrical block subsidence (plate or piston collapse; Lipman 1997) epitomised by the Cainozoic centres of the western U.S.A. Instead of being formed in a single climactic large-volume eruption involving synchronous subsidence of an intracaldera block, the caldera may

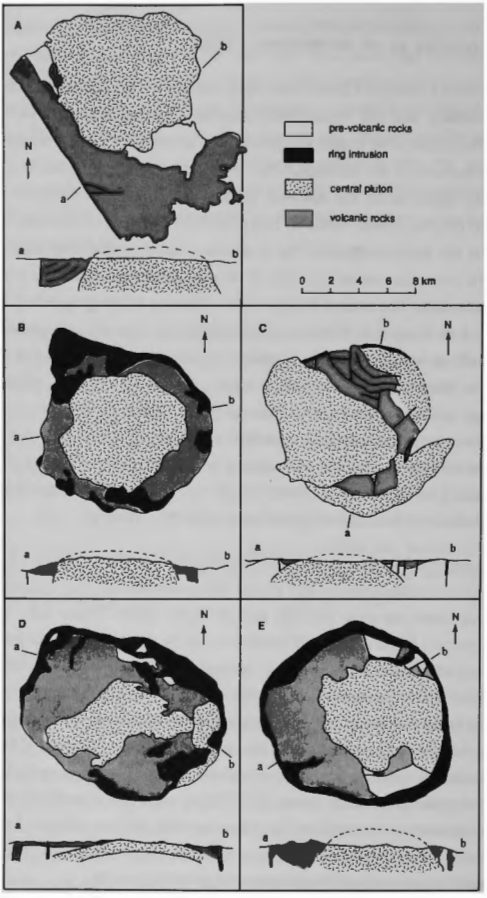

Figure 4.10: Comparison of the outcrop pattern of the Pul Pul Rhyolite and Malone Creek Granite volcano-plutonic complex, with four dome complexes interpreted to represent the roots of resurgent ash-flow calderas (reproduced from Smith and Bailey 1968): a) Pul Pul Rhyolite and Malone Creek Granite; b) Sande cauldron, Oslo region, Norway; c) Alnsjø cauldron, Oslo region, Norway; d) Liruei ring complex, northern Nigeria; and e) Ossipee cauldron, New Hampshire.

have developed incrementally, with stepwise collapse and/or downsagging resulting from a series of moderate- to small-volume eruptions (e.g. Walker 1984). In such caldera structures, a ring fracture system and steep marginal scarps are less likely to be developed, and catastrophic collapse of oversteepened caldera walls may not occur. The thick ignimbrite sequence of the Pul Pul Rhyolite has characteristics that are consistent with incremental caldera development. It contains several units of distinctive composition, separated by a short period of repose during which each flow unit had time to cool and weld (Chapter 2). This suggests that the succession was emplaced by a series of moderate- to small-volume eruptions, consistent with an incremental growth model. The preservation of a remnant fault scarp at the base of the succession suggests that the caldera structure formed by early partial collapse/subsidence, followed by later downsagging during and/or following emplacement of the Upper Ignimbrite Member, which drapes over and buries the pre-existing caldera margin structure. The occurrence of a fluvio-lacustrine successions at the top of the ignimbrite sequence, suggests that a topographic depression remained after the main series of eruptions ended, and was infilled with reworked volcaniclastic material.

Comparison with resurgent dome complexes

The spatial relationship between the Pul Pul Rhyolite and the Malone Creek Granite is highly suggestive of a resurgent dome structure. The ignimbrite sequence strikes around the southern margin of the circular pluton and dips radially away from the margin, suggesting domal uplift of the ignimbrite pile. This outcrop pattern is comparable to others that have been interpreted as deeply eroded cauldrons or roots of ash-flow calderas (Smith and Bailey 1968; Figure 4.10). Geochemical evidence indicates the Malone Creek Granite and Pul Pul Rhyolite form a geochemical suite derived from the same magmatic source, and the granite is interpreted to represent the fractionated residual magma remaining after eruption of the Pul Pul Rhyolite volcanic sequence (Chapter 2.5). It is postulated that after extraction of the ignimbrites, the residual magma fractionated significantly during final crystallisation at depth to produce the small circular stock of the Malone Creek Granite, which rose in the late stages of the caldera cycle to intrude and uplift its cogenetic volcanic pile.

Comparison with other Proterozoic caldera successions

Eroded remnants of other Proterozoic calderas have been described in the Great Bear Magmatic Zone of the northwestern Canadian Shield (Hildebrand 1984), the St. Francois Mountains, Missouri (Sides et al. 1981; Nusbaum 1987), the Tonto Basin, Arizona (Silver et al. 1986) and near Boston, Massachusetts (Thompson 1985). The Great Bear Magmatic Zone has been folded so that sections many kilometres thick, through several

cauldron complexes, are exposed on the individual fold limbs (Hildebrand 1984). The Black Bear and Clut Cauldrons both contain densely welded, lithic-rich ignimbrites, at least 1.5 km thick. The Moose Bay Tuff of the Black Bear Cauldron comprises one major ignimbrite sheet, and the White Eagle Tuff of the Clut Cauldron is a composite sheet, composed of several ignimbrites that range in composition from dacitic at the base to andesitic at the top. The structural margins of both cauldrons are well exposed. The margin of the Great Bear Cauldron is marked by a dramatic thickness change of the ignimbrite across a transcurrent fault, interpreted to be the main ring fault along which subsidence of the central block of the cauldron took place. The existence of several normal and reverse faults just inside the ring fracture suggests differential subsidence of the central block during collapse. The margin of the Clut Cauldron is a step-like feature with both fault contacts and buttress unconformities. In both cauldrons, the ignimbrites are intimately intercalated with caldera collapse mesobreccias, indicating that caldera collapse was synchronous with ignimbrite eruptions. In the Clut Cauldron, the mesobreccias form wedges flanking and thinning away from the structural margin, indicating that landsliding and avalanching of the cauldron walls accompanied eruption. In both cases, the topographic depression remaining after volcanism ended was filled by fluvio-lacustrine sedimentary rocks and the products of post-collapse intermediate volcanism (lavas and breccias). The Clut Cauldron is resurgent, and all intracauldron deposits were uplifted or domed during intrusion of the Calder Quartz Monzonite, which was emplaced more or less in the central part of the cauldron. A third cauldron, the Cornwall Cauldron, consists of 1-2 km of intracauldron facies ignimbrite overlain by a complex of dacite lava flows, intruded by a central granodiorite-monzogranite pluton, probably responsible for resurgence. It is interpreted to be a resurgent cauldron based on the extreme thickness of the ignimbrite succession, and the structural similarity of the complex to resurgent domes recorded in Cainozoic volcanic fields.

Sides et al. (1981) infer the existence of the Butler Hill caldera in the eastern St. Francois Mountains, based on six principal lines of evidence. These are: (1) the great thickness ($\geq$ 1 km) and uniformity of the Grassy Mountain ignimbrite; (2) the recognition of a downdropped block of Grassy Mountain ignimbrite and underlying Killarney formation on the eastern margin of the intruding Butler Hill granite, interpreted to have been downfaulted during caldera collapse; (3) flow direction orientations showing that the source of the Grassy Mountain ignimbrite was in the region now occupied by the Butler Hill granite; (4) the geochemical similarity of the Grassy Mountain ignimbrite and the Butler Hill granite; (5) structural evidence of resurgent doming of the Grassy Mountain ignimbrite and underlying Killarney formation, probably at the time that the Butler Hill granite was emplaced; and (6) the distribution of smaller granite plutons around the periphery of the Butler Hill granite, interpreted as ring plutons, perhaps the roots of

former ring domes. Sides et al. (1981) concluded that the present exposures of the volcanic-plutonic complex are of deeply eroded portions of the former Butler Hill caldera, and consequently direct evidence of the caldera, such as a preserved topographic wall, ring fractures and collapse breccias have been removed. The existence of a second caldera in the western St. Francois Mountains, is suggested by a > 3km thick volcanic succession, comprising ignimbrites, lava flows, minor intercalated volcaniclastic tuffaceous sediments and lahars, occupying a basinal structure to the west of the Butler Hill caldera (Sides et al. 1981; Nusbaum 1987). These rocks overlie older updomed rocks of the Butler Hill caldera along an zone of chaotic megabreccia and mesobreccia, arcuate faults and angular unconformity, which is strongly suggestive of a caldera boundary, and consequently interpreted as the topographic wall of the younger caldera. Several lava domes and a granite porphyry dyke, which may have intruded buried ring fractures, are spatially associated with this structure (Nusbaum 1987).

Thompson (1985) describes a megabreccia intruded by shallow-level granite, within a late Precambrian plutonic-volcanic terrain in southeastern New England. The megabreccia consists of ignimbrite containing accidental lithic fragments of older volcanic rocks, which occur as small clasts (a few centimetres to a few metres in size), intermediate-sized clasts (5-20 m), and a few larger blocks as much as 450 m long. The megabreccia is intruded by granite, and also occurs as xenoliths within the same granite body. Based on its similarity to elements found in deep levels of well-documented Cainozoic calderas, Thompson (1985) interpreted this facies association to represent a small remnant of the deeply eroded roots of much larger caldera structure, in which cauldron collapse and resurgence may have been important processes.

Silver et al. (1986) record a vast series of ash flow tuffs within the Red Rock group in the Tonto Basin-Mazatmal Mountains region of Arizona, that extend across > 3000 km^2, and are up to 1km in thickness. The abstract presents no detail about the internal characteristics of the ignimbrite succession, but based on the large volume of material represented, the authors interpret the succession as a great alkali-rhyolite caldera developed at 1700±6 Ma, which was intruded and reinflated by resurgent rhyolite at 1697±5 Ma.

These occurrences indicate that ash flow volcanism and caldera collapse have been significant processes in the geological history of volcanic regions since at least the Palaeoproterozoic. However, comparatively few caldera complexes are documented from pre-Tertiary terrains. This is probably because in ancient successions, primary caldera morphology can be overprinted and obscured by the effects of later deformation and deep erosion. The above examples illustrate that despite only partial preservation of the succession, caldera settings can be reconstructed in poorly preserved and tectonically

dismembered successions by interpreting the preserved facies associations. In each case, caldera structures are inferred from the association of large volumes of ignimbrite with distinctive components of caldera fill, such as late-stage intrusions interpreted as ring domes or plutons, or megabreccias, sometimes flanking well-exposed structural margins. Where only the deeply eroded roots of the caldera are preserved, evidence of resurgent doming of the caldera fill by a central granitoid pluton is used to infer the former existence of a caldera structure.

The Pul Pul Rhyolite in Domain 1 shares many common features with the Proterozoic calderas described above, and is interpreted as the remnants of an intracaldera succession based on similar criteria. These include: (1) the extreme thickness of the moderate to high grade ignimbrite succession, which is comparable to thicknesses recorded in other Proterozoic calderas (over 1-1.5 km); (2) the association of the ignimbrites with distinctive proximal facies such as co-ignimbrite lag breccias, abundant co-magmatic intrusions and immature fluvial deposits; and (3) their spatial relationship with a central pluton (Malone Creek Granite) which is highly suggestive of resurgence. The most notable difference between the Pul Pul Rhyolite and other Proterozoic calderas is the absence of collapse megabreccias flanking the proposed structural margin. As discussed above, this absence is considered to reflect a different collapse mechanism (i.e. incremental as opposed to catastrophic subsidence).

4.3.3 Volcanic history

The palaeovolcanology of the Pul Pul Rhyolite described below, is a synthesis of the information and discussions presented in Chapters 2, 3 and 4, and is outlined in terms of the history of caldera development.

- The precaldera landscape consisted of a terrestrial basin developed on older deformed, metamorphosed, uplifted and eroded Proterozoic basement rocks of the Pine Creek Geosyncline Sequence. A mature braidplain river system, that flowed down a northwest-facing palaeoslope, developed within the basin. The proposed caldera within the Pul Pul Rhyolite formed on an older pile of fluviatile sedimentary rocks, amygdaloidal basaltic lavas that extruded locally within the river valley, and small domes of rhyolite porphyry that either intruded the basalts as small hypabyssal stocks, and/or extruded as small lava domes (Coronation Sandstone). These rocks were eroded prior to the onset of ignimbrite eruptions. The rhyolite porphyries have an intimate spatial association with the overlying ignimbrites. Small volumes of porphyry have been incorporated into the ignimbrites as lithic clasts, and porphyry stocks also intrude the ignimbrites and the overlying lacustrine succession of the Big Sunday Formation. Their close association with the ignimbrite sequence infers they are part of

the same magma system and volcanic cycle, and the small domes within the underlying Coronation Sandstone may represent an effusive style of eruption occurring as a precursor to the main explosive eruptive events.

- Evidence of magma mingling within the basalts of the Coronation Sandstone suggests that the explosive eruptions that formed the thick ignimbrite succession of the Pul Pul Rhyolite may have been triggered by magma mixing. The injection of a basic magma into the silicic magma chamber could trigger explosive eruption by any or several of the following processes: (1) the addition of a volume of magma may cause an overall increase in the total magma chamber fluid pressure; (2) the basic magma may superheat the rhyolitic magma, inducing magma convection and uprising, and exsolution of volatiles, which would increase total fluid pressure in the magma chamber; (3) volatiles may exsolve from the uprising, high volatile basaltic magma and transfer by convection, diffusion and mixing to the low volatile rhyolitic magma, leading to fluid pressure build up in the magma chamber; and/or (4) heat transfer from the basic to rhyolitic magma may cause rapid cooling and crystallisation of the basic magma, leading to exsolution in the residual basic fluid, again building up the total chamber fluid pressure (Sparks et al. 1977; Huppert et al. 1982; Turner et al. 1983; Cas and Wright 1987).

- In many calderas, the eruption of voluminous ignimbrites is preceded by plinian eruptions from small intermediate stratovolcanoes. In the case of the Pul Pul Rhyolite, however, there are no preserved precursor fall deposits associated with the ignimbrite units. A series of eruptions resulted in the rapid emplacement of a thick stack of moderate to high grade welded layer 2b ignimbrite deposits. Large volumes of country rock were incorporated into the eruptions, and form local lithic concentration zones and co-ignimbrite lag breccias within the ignimbrite units. As discussed in Chapter 2.2.1, lithic-poor high-grade ignimbrite units within the succession are interpreted to have been derived from a high discharge-rate low fountaining eruption column, which provided a steady supply of material to dense, poorly expanded pyroclastic flows, with minimal cooling (Rheomorphic Ignimbrite and Middle Ignimbrite Member). The lower grade ignimbrite units are comparatively lithic-rich and exhibit a higher degree of crystal fragmentation, suggesting a more violent style of eruption, and the development of a higher (plinian) eruption column (Lower and Upper Ignimbrite Members and Cognate lithic-bearing Member). A thin, low grade, non-welded ignimbrite is preserved locally at the top of the ignimbrite succession. In contrast to the thick layer 2b welded ignimbrite units, the non-welded ignimbrite contains a range of facies, including a fine-grained basal layer (layer 2a) and fines-depleted layer 1 head deposits (ground layers) interlayered with layer 2b deposits.

- There is no evidence of large-scale catastrophic subsidence of the intra-caldera block, and the caldera is interpreted to have grown incrementally from a number of moderate-volume eruptions represented by the six separate units recognised in the ignimbrite succession. These eruptive episodes were not separated by significant periods of repose, although each unit cooled and welded separately prior to deposition of the overlying unit. A proposed caldera margin structure near Dinner Creek is marked by a dramatic thickness change in the ignimbrite succession, across a series of faults. These features are coincident with proximal co-ignimbrite lag breccias and lithic-rich, pumice-poor ignimbrite domains within the adjacent Upper Ignimbrite Member. Although a definitive ring dyke cannot be recognised, several sparsely porphyritic quartz monzonite porphyries are spatially associated with the faults at the northwest margin of the proximal ignimbrite succession, and may represent ring domes, that used the faults as conduits during late-stage intrusion. An early collapse scarp is identified, against which the lower ignimbrite units are abruptly terminated. The preservation of this early caldera margin, suggests that caldera subsidence could have involved early partial collapse/subsidence, followed by regional downsagging in the manner proposed by Walker (1984).

- A topographic depression remained after the bulk of the ignimbrite eruptions ended, and was filled by fluvio-lacustrine sedimentary rocks. The lacustrine deposits of the Big Sunday Formation are developed on what appears to be the surface of a subsided fault block. The depression may have resulted from a combination of fault subsidence, downsagging and erosion. High energy fluvial channels underlie the lacustrine sequence and erode into the underlying ignimbrites, indicating lake development was preceded by a period of erosion and epiclastic reworking. The volcaniclastic nature of the lacustrine deposits, and the presence of syn-eruptive crystal-rich deposits derived from subaerial pyroclastic flows which travelled beyond the lake shoreline, infer that pyroclastic eruption from a nearby volcanic centre was ongoing during development of the lake sequence (see Chapter 3).

- The emplacement of high-level intrusions post-dated explosive volcanism. A large, massive to flow-banded, aphyric to sparsely porphyritic rhyolite dome locally intrudes the top of the ignimbrite succession, and related late-stage rhyolite sills and dykes of smaller dimensions intrude the volcanic and overlying lacustrine succession. Sub-volcanic rhyolite and quartz monzonite porphyries also intrude the ignimbrite and lacustrine sequence.

- The Malone Creek Granite is interpreted to represent the residual magma remaining after eruption of the Pul Pul Rhyolite, which rose to intrude the centre of the volcanic pile during caldera resurgence. Emplacement of the pluton cause updoming of the sequence, resulting in patterns of radial dip away from the pluton margin.

CHAPTER 5

U-Pb zircon dating of the Pul Pul Rhyolite, and stratigraphic implications of results.

5.1 INTRODUCTION

U-Pb zircon geochronology was carried out on the volcanic and sub-volcanic intrusive association of the Pul Pul Rhyolite with the primary aim of determining the age of the El Sherana Group. In earlier studies its age was constrained indirectly, between 1885±2 Ma (conventional U-Pb ages of tuff horizons in the underlying South Alligator Group; Needham et al. 1988) and 1850-1860 Ma (an approximate age range assigned to the overlying Edith River Group and co-magmatic Grace Creek Granite by Needham et al. (1988), based on unpublished conventional U-Pb ages). Based on these constraints, Needham et al. (1988) assigned an approximate age of about 1860 Ma to the El Sherana Group. However, the Plum Tree Creek Volcanics of the Edith River Group have since been reanalysed using the SHRIMP U-Pb dating technique, and the new results indicate the volcanics have a crystallisation age of 1825±4 Ma (Kruse et al. 1994). This changes the minimum age constraint for the El Sherana Group significantly, and suggests that its estimated age of ~1860 Ma requires reassessment.

The data presented in this study provide a new stratigraphic age for the El Sherana Group. A revised stratigraphy of the Pine Creek Inlier sequence is proposed, incorporating this new result, as well as new age determinations and stratigraphic information for other units, obtained from recent publications. The tectonic implications of the revised stratigraphy are discussed.

This study also makes some important observations on the dating of volcanic rocks, particularly ignimbrites. Deriving a magmatic age for the Pul Pul Rhyolite presents a difficult dating prospect because the volcanic succession is dominated by ignimbrites that have incorporated large volumes of country rock as lithic clasts during explosive eruption and transportation. It is highly probable that these lithic-rich ignimbrites contain older zircon xenocrysts derived from the country rock as well as melt-precipitated grains. For

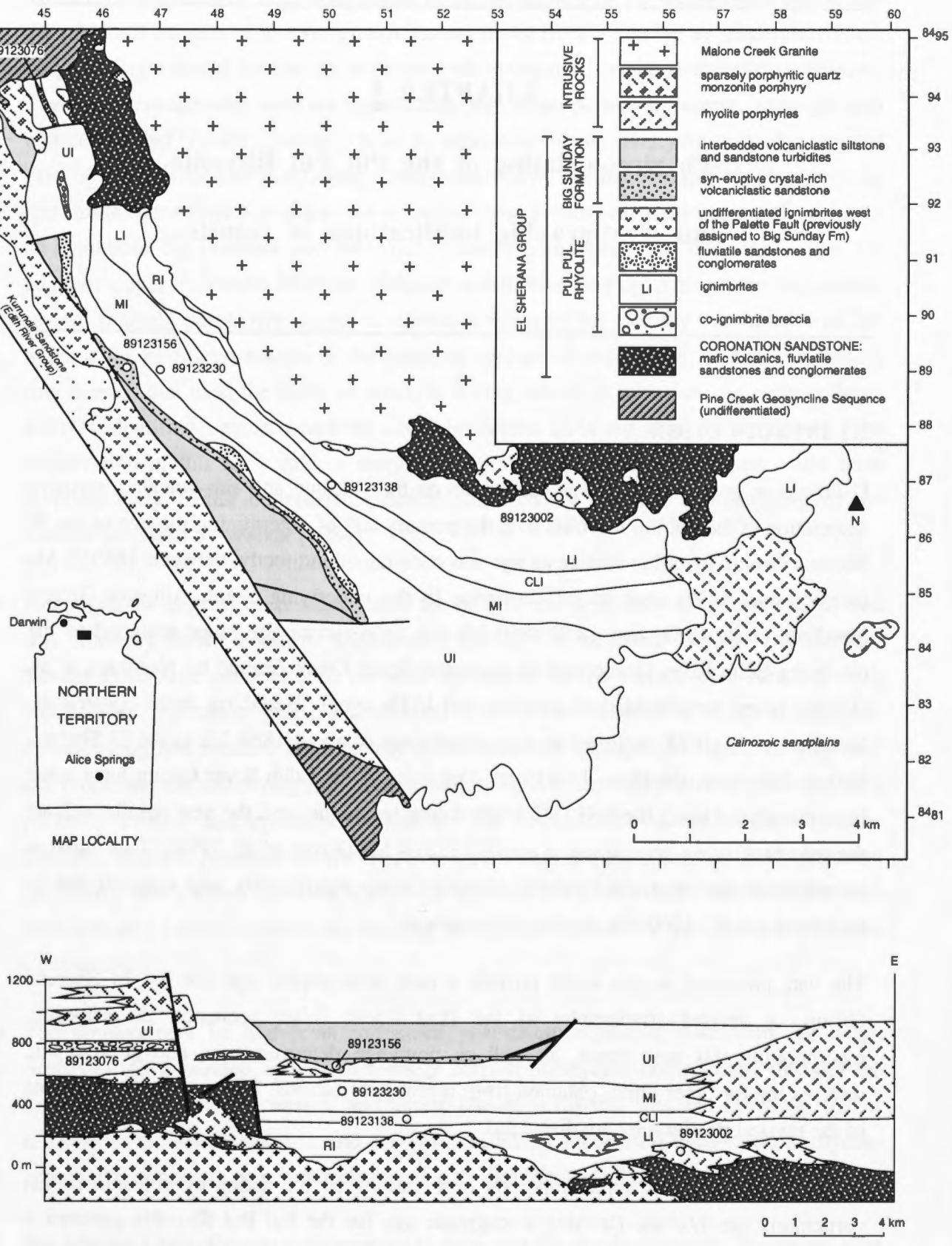

Figure 5.1: Simplified map and schematic stratigraphic section through the volcano-plutonic complex of the Pul Pul Rhyolite, and overlying volcaniclastic lacustrine succession of the Big Sunday Formation. The map shows the location of samples selected for zircon dating, and the cross section illustrates the spatial relationships between facies. LI = Lower Ignimbrite Member (lithic-rich ignimbrite), RI = Rheomorphic Ignimbrite (lithic-poor ignimbrite), CLI = Cognate lithic-bearing Member (lithic-rich ignimbrite), MI = Middle Ignimbrite Member (lithic-poor ignimbrite), UI = Upper Ignimbrite Member + Non-welded Ignimbrite (lithic-rich ignimbrites).

this reason a sampling strategy was devised incorporating both pyroclastic rocks with complex zircon populations, and non-fragmental volcanic rocks with comparatively simple zircon populations. The study illustrates the importance of applying a sound understanding of the nature of different types of volcanic deposits, and the geological relationships between volcanic facies to the sampling of volcanic and volcaniclastic rocks for geochronological analysis, the importance of careful scrutiny of zircon grain characteristics and the intricacies of data interpretation.

5.2 Sampling strategy

The felsic volcanic succession of the Pul Pul Rhyolite is dominated by welded rhyolitic ignimbrites that form a conformable sequence of up to 1km preserved thickness. The welded ignimbrites are subdivided into several regionally mappable units (Figure 5.1), some of which are lithic-rich (the Lower Ignimbrite Member, Cognate lithic-bearing Member, Upper Ignimbrite Member and Non-welded Ignimbrite) and others lithic-poor (Middle Ignimbrite Member and Rheomorphic Ignimbrite). The Upper Ignimbrite Member locally grades into a co-ignimbrite lag (boulder) breccia. The ignimbrites are intruded by coarse-grained rhyolite porphyries, a fine-grained rhyolite dome and associated sills and dykes, megacrystic and sparsely porphyritic monzonite porphyries, dolerite dykes and small dolerite bodies, and by the Malone Creek Granite. The top 150m of the ignimbrite succession is not welded and interfingers locally with laterally restricted fluvial epiclastic deposits. The overlying turbiditic sequence of the Big Sunday Formation erodes into the underlying ignimbrites and facies relationships suggest it represents the development of a local lacustrine environment within the subaerial volcanic setting.

Four samples from the Pul Pul Rhyolite and one from the overlying Big Sunday Formation were selected for dating, the locations and stratigraphic positions of which are shown in Figure 5.1. The selected samples include two ignimbrites and two coarse-grained rhyolite porphyries from the Pul Pul Rhyolite, and a syn-eruptive, crystal-rich volcaniclastic sandstone from the overlying Big Sunday Formation. The rationale behind the sampling program is outlined below.

5.2.1 Lithic-poor and lithic-rich ignimbrites

As well as crystals and pumice, the ignimbrites of the Pul Pul Rhyolite contain abundant lithic fragments, which is a common feature of pyroclastic flow deposits. The clasts are mainly country rock, which could comprise vent material explosively ejected during eruption (accessory lithics and xenocrysts) or loose material on the earth's surface picked up locally by the pyroclastic flow during transportation (accidental lithics and

xenocrysts). Although the most common lithic clast is basalt, which is unlikely to contain zircon, other clast types include coarse-grained rhyolite porphyry, quartz-rich sandstone, granite fragments, chert and metasedimentary basement clasts, all of which are potential sources of xenocrystic zircon.

The distribution of lithic clasts, and their composition and size, varies heterogeneously throughout the ignimbrite sequence. The larger lithic clasts (between 5 and 20 cm in diameter), concentrate to form lithic-rich horizons throughout the ignimbrite succession. An extreme example of lithic concentration occurs within the co-ignimbrite breccia associated with the Upper Ignimbrite Member, which contains boulders up to 2 m in diameter. Even where outsized lithic clasts are absent, the ignimbrites still contain a high proportion of sand- to gravel-sized lithic contaminant (up to 5 cm in diameter). These smaller lithic clasts comprise approximately 15% of the lithic-rich ignimbrite units. The Middle Ignimbrite Member however, contains a significantly lower proportion of lithic contaminant (about 4%).

The high degree of lithic contamination creates potential problems for dating the ignimbrite sequence. Zircons from two samples of ignimbrite were chosen for analysis. Sample 89123230 is from the relatively uncontaminated Middle Ignimbrite Member. Sample 89123138 is from the Cognate lithic-bearing Ignimbrite Member, the higher lithic content of which is likely to result in a higher proportion of xenocrystic zircons derived from the country rock. This sample is clearly less suitable for obtaining the crystallisation age of the ignimbrites, but was chosen to illustrate the effect of lithic contamination on the zircon population, and the extreme caution required when interpreting potentially ambiguous data from such contaminated samples.

5.2.2 Rhyolite porphyries

In addition to the ignimbrites, two samples of rhyolite porphyry were also selected for dating. Numerous small bodies of rhyolite porphyry intrude the Coronation Sandstone, the Pul Pul Rhyolite ignimbrites, and the overlying turbiditic sequence of the Big Sunday Formation (Figure 5.1). The ignimbrites also contain abundant lithic clasts of rhyolite porphyry. The fact that rhyolite porphyry is both incorporated into the ignimbrites as lithic clasts, and also intrudes the ignimbrite sequence indicates there were at least two generations of porphyry, one pre-dating and the other post-dating ignimbrite eruption. The porphyry clasts in the ignimbrites might have been derived from older porphyry bodies within the underlying Coronation Sandstone, which either intruded the pre-ignimbrite sequence, or extruded as small lava domes prior to ignimbrite eruption. Geochemically, the rhyolite porphyries have a highly evolved composition and plot as a high silica end member to the ignimbrite suite, suggesting the ignimbrites and porphyries

are related by crystal fractionation. Their intimate field and chemical association suggests that the ignimbrites and rhyolite porphyries are co-magmatic.

The rhyolite porphyries are not part of the eruptive sequence, and therefore cannot be used to directly date the Pul Pul Rhyolite volcanic sequence. They were selected for dating to provide maximum and minimum age constraints on the crystallisation age of the ignimbrites. Sample 89123076 was obtained from a large porphyry boulder within the co-ignimbrite breccia associated with the Upper Ignimbrite Member. The porphyry clast is older than the ignimbrite containing it, and therefore provides a maximum age for the ignimbrites. Sample 89123002, a rhyolite porphyry that intrudes the ignimbrite pile, was selected to constrain the minimum age of the ignimbrite sequence (Figure 5.1).

Coherent volcanic facies such as the rhyolite porphyries are not subjected to explosive volcanic activity, and are therefore largely free of lithic contamination. The zircon populations of the rhyolite porphyry samples are therefore expected to be less complicated by inheritance than the ignimbrite samples.

5.2.3 Syn-eruptive volcaniclastic sandstone

A crystal-rich volcaniclastic sandstone from the base of the Big Sunday Formation was also selected for analysis (sample 89123156). Thick, massive crystal-rich sandstones unconformably overlie the ignimbrite sequence and outcrop at the base of a lacustrine turbidite sequence. They are interpreted to be syn-eruptive, pyroclast-rich volcaniclastic deposits, formed when subaerial pyroclastic flows entered the lake, disintegrated and transformed into water-supported mass flows, which generated megaturbiditic sandstone beds (Chapter 3). A genetic association has been established between the syn-eruptive crystal-rich volcaniclastic sandstone and the underlying ignimbrites. They are interpreted to have the same eruptive origin, although their final deposition occurred in different environmental settings. This type of syn-eruptive subaqueous volcaniclastic deposit has also been identified in the Hill End Trough of New South Wales (Cas 1979, 1983, and Part 2 of this thesis), the Mt Read Volcanics of Tasmania (White and McPhie 1996, 1997) and other sedimentary basins (e.g. Niem 1977; Fiske 1963; Whitham 1989; Wright and Mutti 1981; Cole and Stanley 1994). Like ignimbrites, the deposits are voluminous and laterally extensive, forming thick massive beds that make excellent marker horizons (e.g. Cas 1979). They have good potential for zircon dating because of the large amount of juvenile volcanic debris they contain. For these reasons, the dating of this type of deposit has potential significance for both basin analysis and volcanological studies. The volcaniclastic sandstone was analysed to determine whether a crystallisation age could be established for this style of volcaniclastic deposit, which are primary in the sense that they are the direct product of eruptions, and deposited essentially during the

eruptive cycle. The work compliments a more detailed geochronological study addressing this issue in Chapter 8, in which similar deposits in the Merrions Formation and Turondale Formation of the Hill End Trough are analysed.

As with the ignimbrites, the sample is expected to be rich in xenocrystic zircon eroded from country rock and incorporated into the pyroclastic flow. The volcaniclastic sandstone contains a higher proportion of lithic fragments (20%) than the underlying ignimbrites. The source of this extra lithic contamination is considered to be the fluvial sandstones and conglomerates containing a large proportion of eroded basement material, which overlie the ignimbrite sequence. Some of this heterogeneous fluvial material may have been ingested by the pyroclastic flows as they travelled over the land surface prior to crossing the lake shoreline.

5.3 Choice of analytical technique

The two most widely practiced methods of U-Pb dating are by conventional isotope dilution mass spectrometry, and by SHRIMP (Sensitive High Resolution Ion Microprobe). Measurement by SHRIMP is applied in this study. It has an advantage over conventional U-Pb zircon dating in that small areas of zircon (between 20-30 μm in diameter) can be targeted for analysis, a necessary prerequisite for dating complex zircon populations that record a history of inheritance, magmatism, metamorphism and alteration. If a complex zircon population is analysed by conventional U-Pb techniques, the result would be a pattern of discordance representing an isotopic mixing line between various age components (e.g. Pidgeon and Aftalion 1978). The lower and upper Concordia intercepts of such mixing lines are likely to be of little geological value, because this interpretation simplistically treats the discordance trend as a two-component system (e.g. between inheritance and magmatic grains, or between magmatic grains and metamorphic overgrowths), when in fact the array is usually generated by mixing the isotopic compositions of zircons of several ages (Williams 1992). In addition, the effects of Pb-loss can be more evident in conventional analysis if abundant altered grains are incorporated into the analyses. Zircon grains that are clearly metamict or damaged can be readily avoided in SHRIMP analysis.

The SHRIMP analytical technique avoids the pitfalls of dating the complex, multi-component zircon populations, described above. Even single-grain conventional analysis is inappropriate in this regard, because although individual grains or parts of grains can be isolated and analysed separately as with SHRIMP, the technique is relatively time consuming and usually only ~ 6 grains are selected for analysis in a single sample. In multiple-age populations it is important to build up a large body of data from which the pattern of isotopic compositions can be established, in order to identify which grains

represent the magmatic age population, and which are inherited grains, or metamorphic grains, or grains altered by Pb-loss. This pattern cannot be established based on so few grains, and so it is possible for inherited grains to be mistakenly identified as magmatic grains.

5.4 ISOTOPIC TECHNIQUES

The analyses were made on the SHRIMP I and SHRIMP II ion microprobes at the Research School of Earth Sciences, Australian National University. Analytical techniques follow those described by Compston et al. (1984) and Williams and Claesson (1987). Zircons are mounted in epoxy resin, polished to expose their centres, and the mount is gold coated. U-Th-Pb isotopic compositions are measured on areas of zircon 20-40 μm in diameter, by focussing a primary beam of negative oxygen ions onto the sectioned crystal, then extracting the positive sputtered secondary ions emitted normally to the surface. These are accelerated to 10 keV and transferred to a double focussing mass spectrometer operated at a mass resolution of approximately 6000, to ensure there are no spectral interferences (Compston et al. 1984). Isotopic ratios are measured using an electron multiplier. Each analysis is the mean of seven scans through the mass stations of interest.

Pb/U ratios of unknown zircons were determined by normalising to interspersed analyses of a laboratory standard, (zircon standard SL13, SL3 or QGNG, for which radiogenic $^{206}Pb/^{238}U$ is taken to be 0.0928 (equivalent to an age of 572 Ma), 0.0894 (equivalent to an age of 552 Ma), and 0.33241 (equivalent to an age of 1850 Ma), respectively). Reproducibility of the Pb/U ratio of the standard varied between sessions, but was better than ±2.8% for each session. Radiogenic Pb compositions were determined by the subtraction of contemporaneous common Pb (using the model of Cumming and Richards 1975), the amount of common lead present being determined from the abundance of ^{204}Pb. All reported ages have been derived from $^{207}Pb/^{206}Pb$ ratios, and the U and Th decay constants recommended by the IUGS Subcommission on Geochronology (Steiger and Jäger 1977). Except for the data in Tables 5.1-5.5 (which report 1σ errors), age uncertainties are given at the 95% (tσ) confidence level.

5.5 ISOTOPIC DATA

Zircons from ignimbrite sample 89123138 were placed in two sample mounts and analysed over three sessions using SHRIMP I. Grains 1-8 and 17-25 were mounted with zircon standard SL13 (grain mount Z970) and grains 9-16 were mounted with zircon standard SL3 (grain mount Z969). The analyses from all three sessions were combined

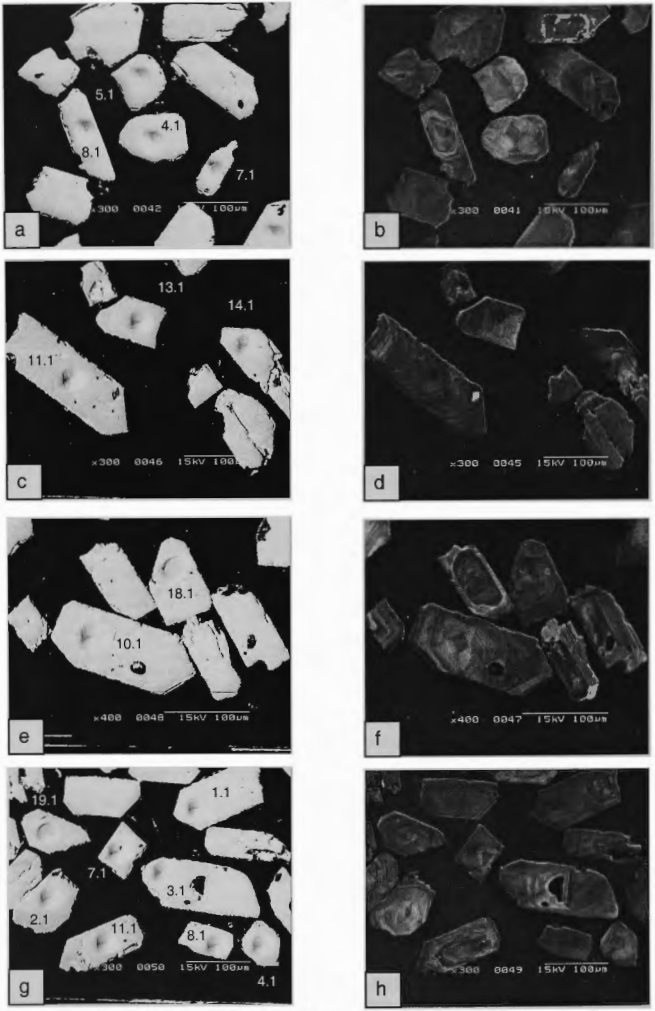

Figure 5.2: Backscattered electron (BE) and cathodoluminescence (CL) images of typical zircons from the rhyolite porphyries of the Pul Pul Rhyolite. Figures A and B are zircons from the intrusive porphyry (sample 89123002), and figures C-H are from the porphyry clast (sample 89123076). Note the grains are euhedral, and zoning is ubiquitous.

to obtain the weighted mean $^{207}Pb/^{206}Pb$ ages of the zircon populations. Zircons from rhyolite porphyry sample 89123002 were originally mounted with sample 89123138 and analysed over two sessions on SHRIMP I. 89123002 was later reanalysed on SHRIMP II with the remaining samples (89123230, 89123076 and 89123156). The four samples were placed on a single mount (grain mount Z245) with zircon standards SL13 and QGNG. Samples 89123230, 89123002 and 89123076 were analysed concurrently in a single session on SHRIMP II, permitting an inter-comparison of the relative ages of these samples. Sample 89123156 was analysed in a separate session on SHRIMP II together with four analyses of sample 89123230, allowing the data from both sessions to be compared. The reanalysis of sample 89123002 on SHRIMP II provides an extra measure of quality control to the data, through the comparison of ages derived for a single sample using different instruments and instrumental conditions.

5.5.1 Rhyolite porphyries

The two rhyolite porphyry samples contain morphologically similar zircons. Cathodoluminescence (CL) images and back scattered electron images of typical zircons from these rocks are presented in Figure 5.2. The zircons are euhedral, with prismatic faces dominated by 100, 010 and 110 forms. Some grains are terminated by 101 pyramids. Grains range from equant to elongate with aspect ratios mostly in the range of 2:1 to 3:1, but up to 4:1 in the largest grains. Grain lengths range between 50-200μm, and average about 100μm. The oscillatory growth zoning that is characteristic of crystallisation from a felsic melt is ubiquitous. Small silicate inclusions that are mostly rod-like, and rounded fluid inclusions are present.

89123002 - SHRIMP II analysis

Seventeen analyses of zircons from sample 89123002 were alternated with measurements of zircon standards SL13 and QGNG and unknown zircons from samples 89123076 and 89123230 over a single 48 hour session on SHRIMP II. The analyses of the SL13 standard for this session group as a single calibration run that follows the expected power law correlation between $^{206}Pb/^{238}U$ and UO/U. The error in reproducibility of $^{206}Pb/^{238}U$ for the standard was 2.8% (1 σ).

The ^{204}Pb-corrected analyses of sample 89123002 are slightly dispersed to the right of the Tera and Wasserburg (1974) concordia curve, indicating minor zero-age radiogenic Pb loss (Figure 5.3a). Common ^{206}Pb values range between 0.01%-0.4% (Table 5.1). The low common lead content of the zircons means that any uncertainty in its assumed composition will have little effect on the derivation of radiogenic Pb compositions.

Table 5.1: Ion microprobe analytical data for sample 89123002 (rhyolite porphyry intrusion)

Grain area	U (ppm)	Th (ppm)	Th/U	$^{206}Pb/^{204}Pb$	$f206^a$ (%)	$^{206}Pb/^{238}U$	$^{207}Pb/^{235}U$	$^{207}Pb/^{206}Pb$	Age[b] (Ma)	% Conc
Sessions 1 and 2: run using SHRIMP I, Grains 1-5 run with SL3 (grain mount Z969), grains 6-14 run with SL13 (grain mount Z970)										
1.1	151		0.63	18997	0.00	0.3229±.0092	5.015±.155	0.1126±.0010	1842±16	95
2.1	268		0.46	21195	0.00	0.3275±.0093	5.110±.151	0.1132±.0006	1851±10	97
3.1	192		0.59	18232	0.00	0.3120±.0088	4.819±.145	0.1120±.0008	1832±13	92
4.1	212		0.66	9355	0.00	0.3207±.0091	4.947±.155	0.1119±.0011	1830±18	95
5.1	95		0.89	16464	0.00	0.3401±.0033	5.251±.140	0.1120±.0026	1832±43	94
6.1	205		0.55	1317	0.01	0.3040±.0082	4.556±.158	0.1087±.0020	1777±34	98
7.1	154		0.96	974	0.02	0.3181±.0086	4.831±.173	0.1101±.0022	1802±38	101
8.1	307		0.62	4168	0.00	0.3342±.0089	5.099±.151	0.1107±.0011	1810±18	95
9.1	333		0.77	833	0.02	0.3187±.0085	4.838±.156	0.1101±.0017	1801±28	98
10.1	118		0.65	429	0.04	0.3193±.0088	4.868±.243	0.1106±.0042	1809±71	99
11.1	156		0.65	345	0.04	0.3211±.0087	4.747±.225	0.1072±.0038	1753±66	99
12.1	185		0.62	1837	0.01	0.3087±.0083	4.707±.146	0.1106±.0014	1809±23	95
13.1	191		0.60	3091	0.01	0.3235±.0087	5.012±.150	0.1124±.0011	1838±18	104
14.1	67		0.98	782	0.02	0.3366±.0096	4.830±.294	0.1041±.0052	1698±96	97
Session 3: grain mount Z2451, run using Shrimp II with zircon standard SL13										
1.1	53	45	0.862	7048	0.31	0.3109±.0093	4.732±.155	0.1115±.0010	1824±17	96
2.1	183	111	0.606	35549	0.08	0.3219±.0094	4.953±.149	0.1123±.0004	1836±6	98
3.1	129	82	0.636	36683	0.14	0.3140±.0092	4.781±.146	0.1116±.0005	1826±7	97
4.1	64	57	0.896	11441	0.16	0.3216±.0103	4.949±.169	0.1121±.0009	1833±13	97
5.1	61	58	0.942	8598	0.13	0.3151±.0094	4.867±.157	0.1116±.0009	1825±14	96
6.1	207	109	0.526	98328	0.01	0.3179±.0091	4.883±.143	0.1117±.0004	1827±6	97
7.1	147	119	0.810	4575	0.41	0.3121±.0093	4.809±.155	0.1119±.0009	1830±14	95
8.1	89	74	0.835	25025	0.18	0.3179±.0096	4.848±.155	0.1121±.0006	1833±9	97
9.1	287	145	0.506	166940	0.01	0.3199±.0092	4.921±.146	0.1121±.0005	1833±7	97
10.1	105	93	0.891	12716	0.15	0.3134±.0094	4.837±.155	0.1110±.0006	1815±10	96
11.1	216	125	0.582	71022	0.02	0.3197±.0092	4.925±.145	0.1120±.0004	1832±5	97
12.1	174	152	0.874	55248	0.06	0.3140±.0090	4.819±.144	0.1115±.0004	1824±6	96
13.1	143	113	0.796	41771	0.05	0.3233±.0103	4.948±.168	0.1112±.0004	1819±7	99
14.1	231	135	0.584	33288	0.05	0.3208±.0092	4.903±.144	0.1111±.0004	1818±5	98
15.1	122	78	0.641	21164	0.09	0.3225±.0093	4.943±.149	0.1117±.0005	1826±8	98
16.1	73	50	0.685	10435	0.25	0.3166±.0094	4.836±.157	0.1117±.0008	1827±12	97
17.1	124	83	0.670	27987	0.10	0.3195±.0093	4.880±.151	0.1119±.0005	1829±7	98

a Denotes the percentage of common ^{206}Pb in the total measured ^{206}Pb

b $^{207}Pb/^{206}Pb$ age

The gaussian summation of the individual analyses ($^{207}Pb/^{206}Pb$ ages) and uncertainties indicates all 17 analyses conform to a single population that closely approaches a normal distribution (Figure 5.4a). The weighted mean age of these analyses is 1827.4±4.2 Ma, with a χ^2 of 0.58.

89123002 - SHRIMP I analysis

Zircons from sample 89123002 were also analysed over two sessions on SHRIMP I. The analyses were carried out 5 years prior to reanalysis of the sample on SHRIMP II. The data from both machines can be compared to determine if similar results are obtained under different instrumental conditions using different instruments. The comparison provides a means of testing the accuracy of the SHRIMP analytical method and the reproducibility of results. Over two sessions on SHRIMP I, 14 analyses of sample 89123002 were obtained together with analyses of standard zircon SL3 (run with analyses 1.1-4.1) and SL13 (run with analyses 5.1-14.1), and unknown zircons from sample 89123138. For both sessions the standard analyses grouped as a single calibration run obeying the power law correlation between $^{206}Pb/^{238}U$ and UO/U. The error in reproducibility of $^{206}Pb/^{238}U$ was 2.8% for SL3 in the first session, and 2.6% for SL13 in the second session.

The analyses lie close to the Tera and Wasserburg (1974) Concordia curve (Figure 5.3b). The data exhibit a significantly greater degree of scatter than the data collected using SHRIMP II. The four analyses slightly below Concordia probably represent over-correction for common Pb. Imprecision in the $^{207}Pb/^{206}Pb$ ages obtained using SHRIMP I is approximately four times greater than the SHRIMP II analyses. Uncertainties in $^{207}Pb/^{206}Pb$ ratios are determined principally by counting statistics on the various masses, and so the larger errors reflect differences in primary beam strength, and sensitivity attainable by the two machines. SHRIMP II achieves a greater sensitivity of 60 counts per second per ppm of Pb, which compares with 15 cps/ppm of Pb achieved for SHRIMP I (Claoué-Long et al. 1995).

The weighted mean age of the 14 analyses is 1832±12 Ma with $\chi^2 = 1.12$. The tail on the gaussian histogram reflects the large uncertainty in the composition of grain 14 (Figure 5.4b). The reverse discordance of this grain (Figure 5.3b) suggests there may have been disturbance to the U-Pb systematics resulting in the incorporation of radiogenic Pb at some stage. There are no grounds to reject analysis 14.1 as an outlier however, as a χ^2 value of 1.12 indicates all analyses conform to a single population, and the large error on

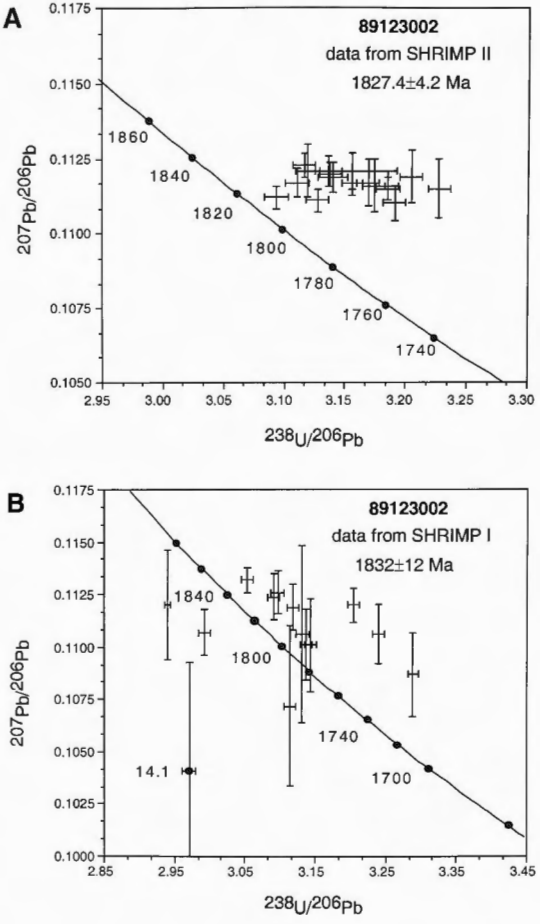

Figure 5.3: Terra and Wasserburg Concordia diagrams for zircons in sample 89123002, showing Pb compositions corrected for common Pb. The age derived from data collected by SHRIMP I is essentially indistinguishable from that the age obtained from data collected by SHRIMP II. However, analyses have greater 1σ errors, exhibit a greater degree of scatter and several grains are reverse discordant. The poorer data quality is reflected in the greater uncertainty of the final age.

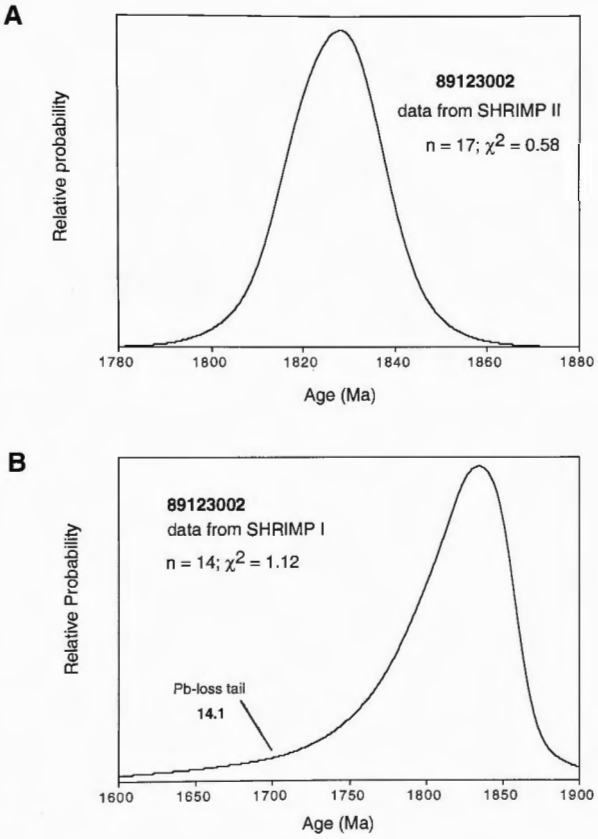

Figure 5.4: Histograms (gaussian summations) of $^{207}Pb/^{206}Pb$ ages for sample 89123002: (a) analyses collected by SHRIMP II show a close approach to a normal distribution; and (b) the tail of the distribution of analyses collected by SHRIMP I is mainly influenced by a single analysis with an abnormally large 1σ error (grain 14.1).

the analysis brings it within range of the other data. Rejecting the analysis makes no difference to the results, as the remaining 13 analyses yield the same weighted mean age of 1832±12 Ma with a negligibly lower χ^2 of 1.05.

The SHRIMP I result is within analytical uncertainty of 1827.4±4.2 Ma as measured by SHRIMP II, affirming the reproducibility of SHRIMP data obtained at different times, using different instruments with different machine conditions. Combination of these results produces a weighted mean age of 1827.3±3.5 Ma for sample 89123002.

89123076

Nineteen analyses of zircons from sample 89123076 (rhyolite porphyry clast) were produced from two SHRIMP II sessions (Table 5.2). In the first session, fifteen analyses were collected with analyses of SL13 and QGNG standards, and samples 89123002 and 89123230. The error in reproducibility of $^{206}Pb/^{238}U$ for SL13 for this session was 2.8% (1 σ). Four analyses were obtained in a second session with analyses of sample 89123156. The analyses of the standard SL13 for the second SHRIMP II session group as a single calibration run that follows the expected power law correlation between $^{206}Pb/^{238}U$ and UO/U. The error in reproducibility of $^{206}Pb/^{238}U$ for SL13 for this session was 2.3% (1σ).

All 15 analyses from the first session conform to a single population with a mean age of 1827.3±4.0 Ma (χ^2= 0.70). The four grains analysed in the second session yield a slightly older mean age of 1831±10 Ma (χ^2 = 0.49). A gaussian summation of the ages shows that the combined data from both sessions approach a normal distribution and therefore conform to a single population (Figure 5.5). The data are slightly dispersed to the right of Concordia, indicating minor zero-age radiogenic Pb loss (Figure 5.6).

The combined analyses (n=19) define a single population (χ^2 = 0.68) with a weighted mean age of 1828.1±3.5 Ma.

5.5.2 Ignimbrites

Zircon grains within the ignimbrite samples exhibit a wider diversity of morphologies than those within the rhyolite porphyries. Cathodoluminescence (CL) and backscattered electron (BE) images of typical zircons from the ignimbrites are presented in Figure 5.7. Many grains are morphologically similar to the zircons of the rhyolite porphyries. These are equant to elongate euhedral prismatic grains with aspect ratios ranging up to 3:1.

Table 5.2: Ion microprobe analytical data for sample 89123076 (rhyolite porphyry clast)

Grain area	U (ppm)	Th (ppm)	Th/U	$^{206}Pb/^{204}Pb$	$f206^{a}$ (%)	$^{206}Pb/^{238}U$	$^{207}Pb/^{235}U$	$^{207}Pb/^{206}Pb$	Age[b] (Ma)	% Conc
Session 1: grain mount Z2451, run using Shrimp II with zircon standard SL13										
1.1	293	145	0.495	56593	0.03	0.3175±.0091	4.873±.143	0.1117±.0003	1827±5	97
2.1	51	40	0.776	19417	0.05	0.3161±.0097	4.895±.164	0.1122±.0009	1835±15	96
3.1	104	79	0.763	24975	0.08	0.3211±.0093	4.927±.152	0.1114±.0006	1822±9	98
4.1	76	55	0.727	460830	0.03	0.3256±.0098	4.966±.157	0.1116±.0006	1824±9	99
5.1	81	54	0.668	37202	0.02	0.3208±.0094	4.900±.153	0.1109±.0007	1814±10	98
6.1	193	185	0.959	83402	0.02	0.3207±.0092	4.951±.146	0.1123±.0004	1836±6	97
7.1	153	105	0.689	3005	0.47	0.3094±.0093	4.741±.154	0.1118±.0017	1828±27	95
8.1	201	128	0.639	37397	0.05	0.3156±.0090	4.835±.142	0.1125±.0004	1839±6	96
9.1	234	161	0.688	10995	0.17	0.3118±.0089	4.780±.144	0.1116±.0004	1825±7	95
10.1	125	94	0.758	69735	0.00	0.3177±.0093	4.879±.148	0.1115±.0006	1824±10	97
11.1	137	108	0.793	18112	0.12	0.3175±.0094	4.887±.151	0.1116±.0005	1825±8	97
12.1	148	97	0.652	23397	0.09	0.3117±.0091	4.742±.152	0.1121±.0010	1833±16	96
13.1	199	117	0.586	35663	0.04	0.3227±.0092	4.941±.144	0.1114±.0004	1821±6	98
14.1	325	154	0.474	174820	0.01	0.3219±.0092	4.938±.144	0.1118±.0003	1829±4	98
15.1	341	181	0.531	61387	0.00	0.3197±.0091	4.898±.142	0.1114±.0003	1822±5	97
Session 2: grain mount Z2451, run using Shrimp II with zircon standard SL13										
17.1	298	195	0.655	14900	0.11	0.3233±.0078	4.992±.124	0.1121±.0004	1833±6	98
18.1	200	193	0.964	17700	0.08	0.3272±.0082	5.032±.132	0.1115±.0004	1823±7	100
19.1	239	241	1.007	90400	0.01	0.3155±.0075	4.879±.121	0.1121±.0004	1833±6	96
20.1	153	111	0.727	7600	0.26	0.3223±.0081	5.003±.136	0.1122±.0009	1835±13	97

a Denotes the percentage of common ^{206}Pb in the total measured ^{206}Pb

b $^{207}Pb/^{206}Pb$ age

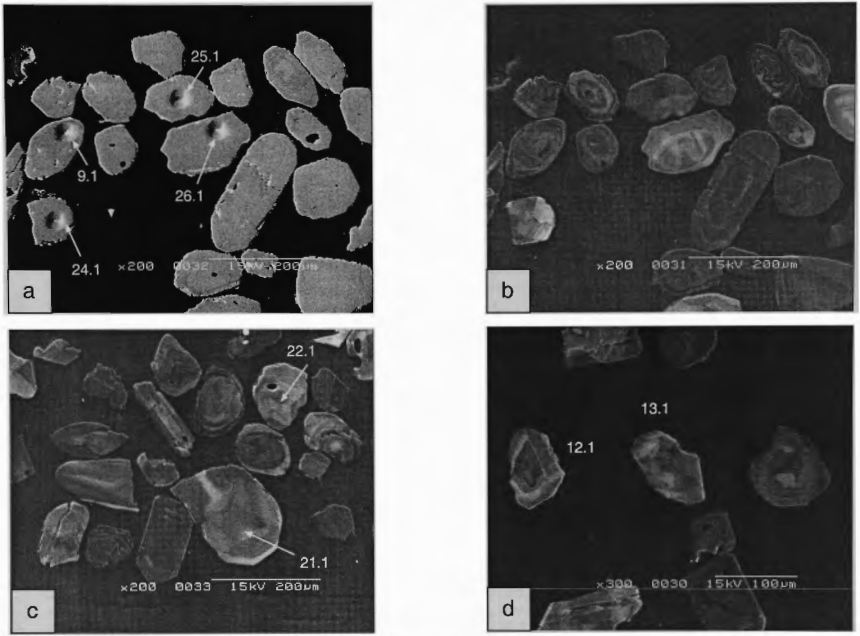

Figure 5.7: Backscattered electron (BE)and cathodoluminescence (CL) images of typical zircons from the ignimbrites of the Pul Pul Rhyolite. These grains were taken from sample 89123230. Grain 9 is an Archaean xenocryst. All other labelled grains belong to the 1828 Ma magmatic population. Note that zoning is ubiquitous, and that many grains contain cores. Also, many grains (eg grains 12.1, 26.1) are fragmented.

Grain lengths range between 50-150μm, and average ~ 100μm. Some grains are terminated with simple pyramids. Oscillatory zoning is ubiquitous. As expected, much of the zircon within the ignimbrites has been inherited; this component occurs as cores overgrown by younger zircon precipitated from the melt, as discrete older grains with a simple internal structure, and as complex grains containing cores and rims that are both older than zircon precipitated from the final melt. Xenocrystic zircons range from euhedral in shape, to rounded to subrounded equant grains with pitted surfaces, which are interpreted as detrital in origin. The detrital grains are slightly larger than the euhedral zircons, averaging 150μm in length. Rounded cores are present in both euhedral and rounded grains. Some cores exhibit oscillatory zoning, but most are internally structureless and generally have low CL, consistent with their high U concentrations. The selection of zircons for analysis was biased towards attaining a crystallisation age for the ignimbrites, so obvious cores and detrital grains were avoided. Despite this approach, a large number of xenocrystic grains were inadvertently analysed, indicating that inherited grains cannot always be optically distinguished from melt-precipitated zircons.

89123230 - lithic-poor ignimbrite

Thirty three analyses of thirty two zircons from sample 89123230 were measured in a single 48 hour session on SHRIMP II (Table 5.3). The analyses were interspersed with analyses of zircon standards SL13 and QGNG and unknown zircons from samples 89123076 and 89123002. The error in reproducibility of $^{206}Pb/^{238}U$ for SL13 for this session was 2.8%.

A gaussian histogram of the $^{207}Pb/^{206}Pb$ ages emphasises the polymodal distribution of the ages, and the large amount of inherited zircon in the sample (Figure 5.8a). Nine analyses with ages between 1900-2700 Ma, either indicating more than one inherited component, or a single inherited component with a multistage history. The two youngest ages (from analyses 1.1 and 2.1) are rejected as outliers resulting from Pb loss. The remaining 23 analyses cluster close to Concordia at about 1830 Ma (Figure 5.9). These analyses yield a χ^2 of 5.65 indicating the analyses do not conform to a single population. The distribution of these 23 analyses on a gaussian histogram shows that the three oldest grains are offset from the main population (Figure 5.8b). If these analyses are rejected as outliers, the remaining 20 grains closely approach a normal distribution, with a weighted mean age of 1828.6±5.1 Ma (χ^2 = 1.14). This is taken to be the crystallisation age of the ignimbrite. The three outliers give a weighted mean age of 1868±12 Ma, indicating a source of inheritance ~40 Ma older than the ignimbrites.

Table 5.3: Ion microprobe analytical data for sample 89123230 (lithic-poor ignimbrite)

Grain area	U (ppm)	Th (ppm)	Th/U	$^{206}Pb/^{204}Pb$	$f206^a$ (%)	$^{206}Pb/^{238}U$	$^{207}Pb/^{235}U$	$^{207}Pb/^{206}Pb$	Age[b] (Ma)	% Conc
Grain mount Z2451, run using Shrimp II with zircon standard SL13										
1.1	454	321	0.708	504	3.06	0.2356±.0066	3.283±.100	0.1019±.0007	1659±12	82
2.1	160	102	0.637	1236	1.47	0.2289±.0114	3.719±.205	0.1206±.0023	1964±34	68
3.1	1651	387	0.234	9288	0.17	0.3398±.0095	5.611±.159	0.1201±.0002	1957±2	96
4.1	399	626	1.566	26539	0.27	0.2880±.0082	4.406±.129	0.1130±.0007	1848±10	89
5.1	228	284	1.245	64977	0.02	0.3230±.0093	4.970±.146	0.1115±.0004	1824±6	98
6.1	133	96	0.721	13844	0.10	0.3258±.0111	5.131±.195	0.1142±.0005	1867±8	96
7.1	164	182	1.113	61576	0.05	0.3217±.0092	4.936±.146	0.1119±.0004	1830±7	98
8.1	45	31	0.694	13894	0.15	0.3199±.0100	4.902±.167	0.1118±.0009	1828±15	97
9.1	1092	361	0.331	4979	0.31	0.4425±.0125	9.956±.292	0.1634±.0002	2490±2	94
10.1	52	52	0.995	23121	0.11	0.3227±.0105	4.999±.172	0.1131±.0009	1849±13	97
11.1	103	101	0.978	12251	0.12	0.3217±.0094	4.892±.156	0.1112±.0008	1819±12	99
12.1	86	305	3.530	2942	0.62	0.2786±.0085	4.182±.141	0.1105±.0009	1807±15	88
13.1	67	67	1.013	16597	0.15	0.3159±.0097	4.804±.157	0.1111±.0008	1818±12	97
14.1	365	181	0.496	1754400	0.03	0.4598±.0130	10.352±.298	0.1639±.0003	2496±2	97
15.1	150	227	1.506	1000000	0.00	0.3240±.0094	5.035±.153	0.1126±.0004	1842±7	98
16.1	6	2	0.314	29308	2.82	0.5302±.0366	11.075±1.123	0.1838±.0094	2687±86	116
17.1	82	110	1.338	107180	0.12	0.3317±.0108	5.041±.174	0.1117±.0006	1827±9	101
18.1	83	71	0.860	13958	0.19	0.3164±.0097	4.836±.157	0.1120±.0006	1831±9	97
19.1	25	21	0.828	8517	0.20	0.3124±.0099	4.858±.167	0.1129±.0013	1846±20	95
20.1	305	51	0.170	869560	0.00	0.4177±.0119	8.746±.255	0.1505±.0010	2352±11	94
20.2	549	29	0.053	6967	0.23	0.4148±.0119	7.847±.233	0.1370±.0007	2189±9	101
21.1	64	81	1.270	10998	0.21	0.3187±.0097	4.832±.161	0.1109±.0008	1814±13	98
22.1	56	45	0.800	8422	0.12	0.2790±.0083	4.267±.137	0.1103±.0010	1805±16	87
23.1	54	68	1.264	17711	0.08	0.3273±.0104	5.079±.172	0.1124±.0008	1838±12	99
24.1	43	50	1.167	23402	0.00	0.3279±.0099	5.065±.162	0.1116±.0010	1825±16	99
25.1	215	149	0.694	653590	0.03	0.3580±.0103	6.069±.179	0.1231±.0003	2002±5	98
26.1	51	43	0.852	28612	0.31	0.3283±.0099	4.949±.165	0.1115±.0009	1824±14	102
27.1	55	58	1.062	11215	0.21	0.3085±.0093	4.657±.151	0.1105±.0007	1807±12	96
28.1	418	179	0.428	140850	0.02	0.3221±.0091	5.071±.146	0.1141±.0003	1866±3	96
29.1	52	61	1.168	5043	0.44	0.3260±.0100	5.008±.176	0.1126±.0011	1841±17	99
30.1	84	133	1.580	57971	0.01	0.3128±.0094	4.802±.151	0.1112±.0006	1818±10	95
31.1	297	80	0.271	2254	0.70	0.3498±.0100	5.880±.176	0.1226±.0005	1994±7	97
32.1	326	186	0.571	6156	0.28	0.2890±.0083	4.555±.136	0.1147±.0004	1874±6	87

a Denotes the percentage of common ^{206}Pb in the total measured ^{206}Pb

b $^{207}Pb/^{206}Pb$ age

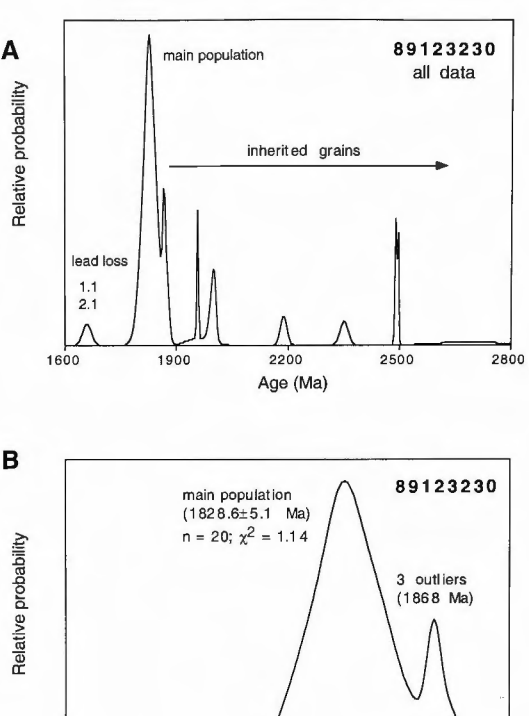

Figure 5.8: Histograms (gaussian summations) of $^{207}Pb/^{206}Pb$ ages for the zircons in sample 89123230: (a) displays all data, illustrating the wide range of inherited zircon ages. The small peak to the left of the main population is due to lead loss in grains 1.1 and 2.1; (b) shows the close approach to a normal distribution of the main population , except for the significant offset of 3 grains (grains 28.1, 6.1 and 32.1).

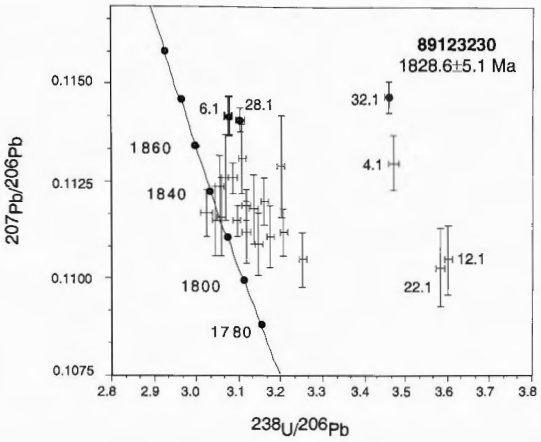

Figure 5.9: Terra and Wasserburg Concordia diagram for the main population of zircons in sample 89123230 (those between 1800 and 1900 Ma).

89123138 - lithic-rich ignimbrite

Twenty five zircons from sample 89123138 were analysed in three separate sessions on SHRIMP I (Table 5.4), with standard zircon SL13 (run with analyses 1.1-8.1 in the first session, and with analyses 17.1-25.1 in the third session) and SL3 (run with analyses 9.1-16.1 in the second session). For each session, the standard analyses grouped as a single calibration run obeying a power law correlation between $^{206}Pb/^{238}U$ and UO/U. The error in reproducibility of the standards ranged between 2.6% and 2.8% for the sessions.

A gaussian histogram shows a polymodal pattern of inheritance, as with sample 89123230 (Figure 5.10). Nine analyses with ages ranging between 1900-2600 Ma are of inherited origin. The remaining 16 analyses exhibit negligible discordance due to radiogenic Pb loss (Figure 5.11). These 16 analyses yield a weighted mean age of 1850±12 Ma. Their χ^2 of 1.54 is consistent conformation to a single statistical population, but the value is slightly high, suggesting complexities in the data, and the main peak of the gaussian curve appears to exhibit scatter in excess of a normal distribution.

Table 5.4: Ion microprobe analytical data for sample 89123138 (lithic-rich ignimbrite)

Grain area	U (ppm)	Th (ppm)	Th/U	$^{206}Pb/^{204}Pb$	$f206^{a}$ (%)	$^{206}Pb/^{238}U$	$^{207}Pb/^{235}U$	$^{207}Pb/^{206}Pb$	Age[b] (Ma)	% Conc
Session 1: grain mount Z970, run using Shrimp I with zircon standard SL13										
1.1	163	72	0.444	17161	0.11	0.3151±.0044	4.958±.092	0.11433±.00098	1869±13	94
2.1	72	85	1.178	8761	0.17	0.3105±.0055	4.714±.113	0.10995±.00157	1798±26	96
3.1	78	73	0.941	3355	0.19	0.2996±.0055	4.712±.125	0.11147±.00179	1823±29	90
4.1	61	70	1.141	20218	0.26	0.3118±.0062	4.731±.138	0.11151±.00134	1824±21	97
5.1	59	80	1.366	3080	0.46	0.2663±.0056	3.989±.144	0.10815±.00303	1768±52	85
6.1	105	70	0.663	8660	0.15	0.4708±.0077	10.890±.225	0.16822±.00120	2540±12	98
7.1	171	85	0.500	7087	0.41	0.3194±.0046	5.020±.102	0.11553±.00094	1888±14	95
8.1	128	131	1.017	29985	0.04	0.3000±.0054	4.678±.096	0.11287±.00087	1846±14	91
Session 2: grain mount Z969, run using Shrimp I with zircon standard SL3										
9.1	305	201	0.660	13581	0.05	0.3456±0.120	5.808±.209	0.12100±.00069	1971±10	97
10.1	589	118	0.201	49043	0.03	0.3003±.0171	5.109±.297	0.12403±.00048	2014±6	85
11.1	31	33	1.074	2517	0.73	0.4520±.0186	10.231±.575	0.16298±.00354	2486±37	96
12.1	1045	265	0.254	4412	0.37	0.4125±.0310	9.106±.729	0.15718±.00259	2425±28	90
13.1	1204	37	0.031	7741	0.21	0.3632±.0123	6.107±.212	0.12229±.00042	1989±6	100
14.1	49	40	0.827	14374	0.00	0.3231±.0108	5.061±.208	0.11037±.00282	1805±47	100
15.1	71	122	1.721	2536	0.56	0.3234±.0107	4.934±.228	0.10998±.00258	1799±43	100
16.1	136	86	0.632	48685	0.04	0.3117±.0101	4.838±.172	0.11333±.00108	1853±15	93
Session 3: grain mount Z970, run using Shrimp I with zircon standard SL13										
17.1	299	473	1.583	317	5.62	0.3025±.0120	4.641±.255	0.11125±.00374	1819±62	93
18.1	84	54	0.648	165	10.79	0.3332±.0166	5.275±.897	0.11483±.01796	1877±140	98
19.1	70	63	0.897	1408	1.27	0.3312±.0126	5.057±.304	0.11075±.00464	1811±68	101
20.1	521	139	0.267	9477	0.19	0.3519±.0125	5.735±.213	0.11819±.00086	1929±13	100
21.1	254	136	0.539	4692	0.38	0.3452±.0118	5.559±.208	0.11681±.00137	1907±21	100
22.1	276	265	0.960	8421	0.21	0.3313±.0130	5.160±.220	0.11295±.00139	1847±18	99
23.1	160	115	0.718	1944	0.92	0.3153±.0180	4.925±.323	0.11327±.00290	1852±33	95
24.1	349	369	1.056	2621	0.68	0.2969±.0109	4.508±.203	0.11012±.00238	1801±39	93
25.1	546	150	0.275	11379	0.16	0.3669±.0140	6.572±.267	0.12991±.00128	2096±17	96

a Denotes the percentage of common ^{206}Pb in the total measured ^{206}Pb

b $^{207}Pb/^{206}Pb$ age

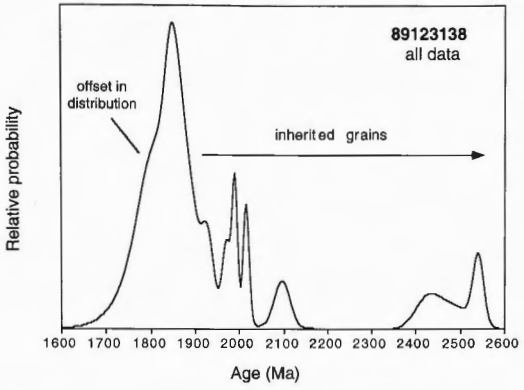

Figure 5.10: Histogram (gaussian summation) of $^{207}Pb/^{206}Pb$ ages for the zircons in sample 89123138, illustrating the wide range of ages for inherited grains. The main peak appears to exhibit scatter in excess of a normal distribution (there is a small bulge to the left of the main population).

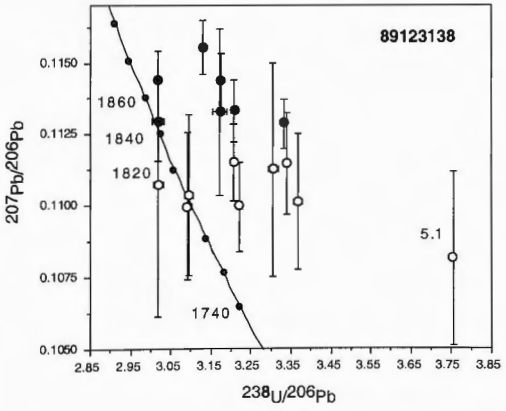

Figure 5.11: Terra and Wasserburg Concordia diagram for sample 89123138 (zircons <1900 Ma), showing Pb compositions corrected for common Pb. The open circles are zircons intertreted as belonging to the 1828 Ma magmatic population. The filled zircons are zircons interpreted as xenocrysts (see discussion, Chapter 5.6.1).

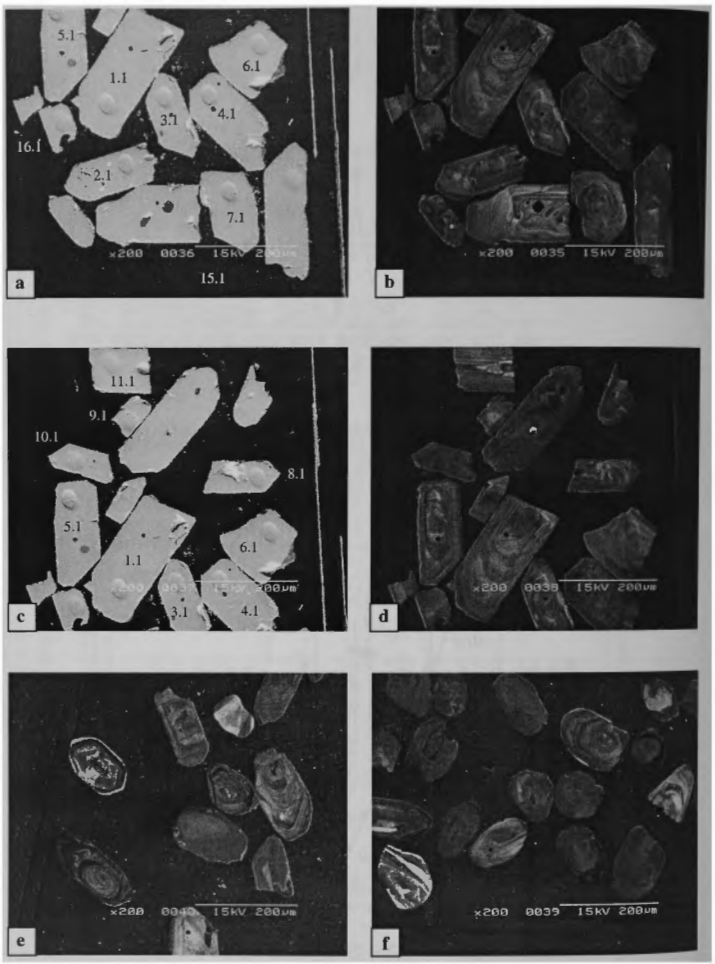

Figure 5.12: Backscattered electron (BE) and cathodoluminescence (CL) images of typical zircons from sample 89123156 (crystal-rich volcaniclastic sandstone). Note that the 1865 Ma zircons are euhedral and zoning is ubiquitous (figures 5.16a-d). Figures 5.16e-f show rounded xenocrysts that have obviously undergone detrital reworking at some stage in their history. These grains are interpreted to be derived from the metasedimentary basement to the Pul Pul Rhyolite volcanic succession.

Table 5.5: Ion microprobe analytical data for sample 89123156 (crystal-rich volcaniclastic sandstone)

Grain area	U (ppm)	Th (ppm)	Th/U	$^{206}Pb/^{204}Pb$	$f206^{a}$ (%)	$^{206}Pb/^{238}U$	$^{207}Pb/^{235}U$	$^{207}Pb/^{206}Pb$	Age[b] (Ma)	% Conc
Grain mount Z2451, run using Shrimp II with zircon standard SL13										
1.1	119	52	0.444	485400	0.02	0.3356±.0086	5.280±.139	0.1143±.0005	1868±7	100
2.1	118	63	0.536	100000	0.02	0.3244±.0083	5.097±.135	0.1140±.0005	1863±7	97
3.1	113	57	0.504	57700	0.06	0.3400±.0084	5.298±.138	0.1132±.0005	1851±8	102
4.1	252	149	0.590	63100	0.03	0.3290±.0078	5.135±.127	0.1132±.0004	1850±5	99
5.1	120	75	0.622	1000000	0.00	0.3237±.0079	5.025±.129	0.1126±.0005	1841±8	98
6.1	124	38	0.312	1000000	0.00	0.3544±.0086	5.864±.147	0.1194±.0005	1947±7	100
7.1	123	62	0.503	18800	0.38	0.3371±.0082	5.309±.139	0.1168±.0009	1907±13	100
8.1	181	112	0.619	25800	0.11	0.3416±.0082	5.335±.133	0.1137±.0004	1859±6	102
9.1	174	131	0.754	135100	0.05	0.3364±.0083	5.302±.136	0.1147±.0005	1874±8	100
10.1	501	229	0.458	42800	0.04	0.3143±.0074	5.005±.120	0.1155±.0003	1888±4	93
11.1	135	133	0.986	35700	0.08	0.3121±.0078	4.914±.130	0.1146±.0005	1874±8	93
12.1	165	145	0.876	117400	0.07	0.3215±.0080	5.040±.132	0.1141±.0005	1865±7	96
13.1	114	76	0.667	63300	0.02	0.3020±.0076	4.735±.130	0.1143±.0006	1868±9	91
14.1	331	129	0.390	119200	0.01	0.3497±.0084	5.899±.146	0.1223±.0003	1989±4	97
15.1	192	135	0.706	73000	0.03	0.3223±.0078	5.097±.128	0.1148±.0005	1877±7	96
16.1	221	94	0.425	96900	0.02	0.3089±.0076	4.858±.125	0.1141±.0005	1865±7	93
17.1	124	86	0.693	28900	0.05	0.3169±.0079	4.967±.133	0.1135±.0007	1856±11	95
18.1	238	106	0.448	36600	0.02	0.3076±.1005	5.179±1.697	0.1220±.0007	1985±9	87
18.2	212	90	0.428	43500	0.01	0.3031±.0074	5.110±.131	0.1220±.0007	1986±9	85
19.1	122	56	0.461	23700	0.13	0.3325±.0081	5.226±.137	0.1146±.0010	1873±8	99
20.1	216	125	0.582	71022	0.02	0.3187±.0092	4.925±.145	0.1120±.0004	1832±5	99

a Denotes the percentage of common ^{206}Pb in the total measured ^{206}Pb

b $^{207}Pb/^{206}Pb$ age

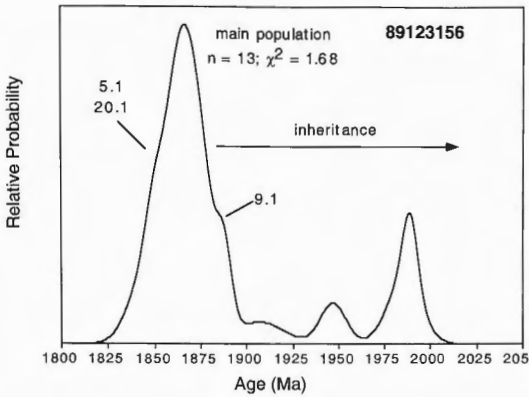

Figure 5.13: Histogram (gaussian summation) of $^{207}Pb/^{206}Pb$ ages for the zircons in sample 89123156, illustrating the wide range of ages for inherited grains. The main peak exhibits scatter in excess of a normal distribution. The small offset to the right of it reflects an offset in the composition of grain 9.1, which is rejected as an outlier. The small offset to the left of the main peak reflects an offset in the compositions of grains 5.1 and 15.1, which are slightly younger than the main population.

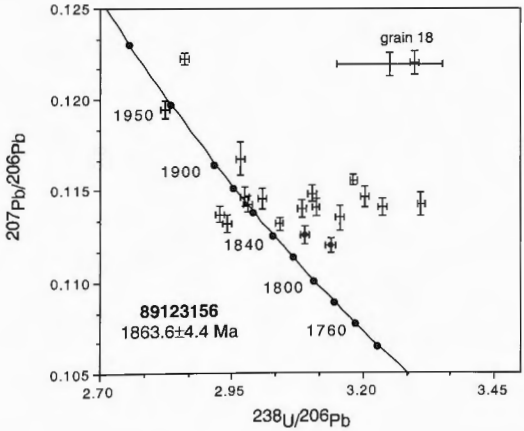

Figure 5.14: Terra and Wasserburg Concordia diagrams for zircons in sample 89123156, showing radiogenic Pb compositions.

5.6 DISCUSSION OF RESULTS

5.6.1 Obtaining a stratigraphic age for the Pul Pul Rhyolite

Figure 5.15 synthesises the results obtained for the five analysed samples. As expected, the two coherent rhyolite porphyry samples (89123002 and 89123076) which are free of lithic contamination contain zircons of uniform age, reflecting their relatively simple zircon populations. All grains analysed precipitated from the melt at the time of crystallisation of the porphyry bodies. The small amount of inherited zircon in these samples occurs as cores overgrown by magmatic rims, which could be readily detected and avoided during analysis. In contrast, the zircon populations of the lithic-contaminated samples have complex isotopic patterns that reflect a large inherited component of more than one age. It is important to note that inherited zircon dominates in the analyses, even though a deliberate attempt was made to target melt-precipitated grains. This is because many of the xenocrystic grains are of magmatic origin, and optically indistinguishable from the grains which precipitated from the melt at the time of crystallisation.

An independent geological control on the age of the ignimbrite sequence is established by the ages of the two rhyolite porphyry samples, which were selected on the basis of their stratigraphic context to constrain the maximum and minimum age of the ignimbrites. Together their ages tightly constrain the eruption of the ignimbrite sequence to lie between 1828.1±3.5 Ma and 1827.3±3.5 Ma.

Only the ignimbrite sample containing the least amount of xenolithic contamination (sample 89123230) yielded a well defined crystallisation age within the constraints imposed by the porphyry samples. In this lithic-poor ignimbrite, 60% of the 33 analysed grains date the crystallisation of this rock. The combined analyses of these grains indicate they crystallised at 1828.6±5.1 Ma. In contrast, inheritance is so pronounced in the zircon populations of the two samples with the highest degree of lithic contamination, that their crystallisation ages could not be determined. It is the presence of the youngest xenocrystic population that complicates the interpretation of the data in the most contaminated samples. The significantly older inherited grains (1900-2700 Ma) do not present a problem as they can be clearly identified as xenocrysts. The youngest xenocrystic zircon however, has an age of about 1865 Ma, which is only ~40 m.y. older than the melt-precipitated zircon. These xenocrysts did not present a problem when determining the crystallisation age of sample 89123230 (lithic-poor ignimbrite). Only three such xenocrysts were analysed, and were rejected as statistical outliers to the main crystallisation population of 20 grains.

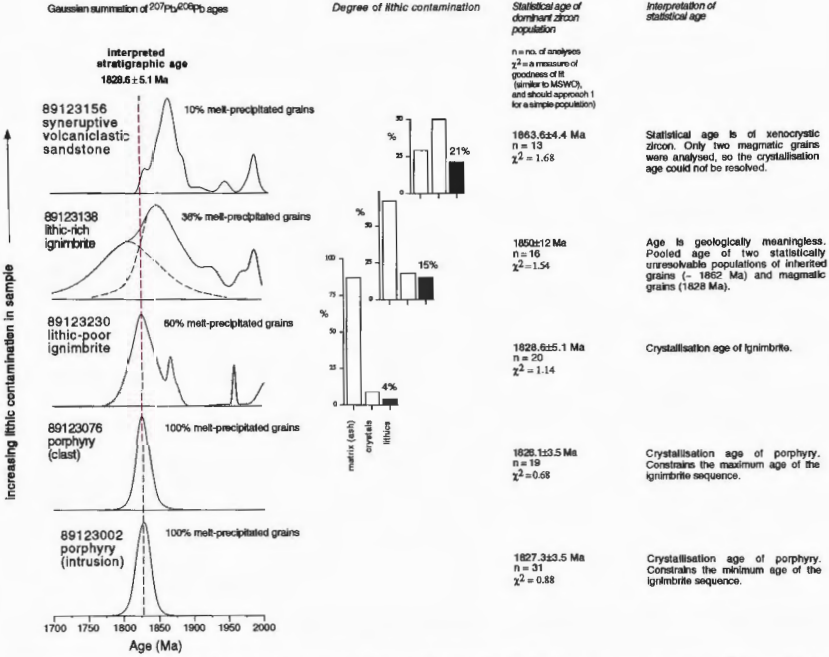

Figure 5.15: A summary of the data obtained for all samples analysed in this study. The left hand column compares histograms of the $^{207}Pb/^{206}Pb$ ages obtained for each sample, and illustrates how lithic contamination increases the complexity of the zircon populations (only ages less than 2000 Ma are plotted).

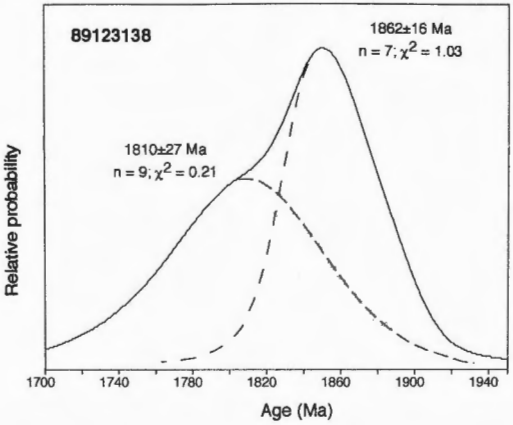

Figure 5.16: Histogram (gaussian summation) of $^{207}Pb/^{206}Pb$ ages for the youngest 16 zircons (<1900 Ma) in sample 89123138. The data show scatter in excess of a normal distribution, and can be deconvolved into two components with ages of 1810±27 Ma and 1862±16 Ma.

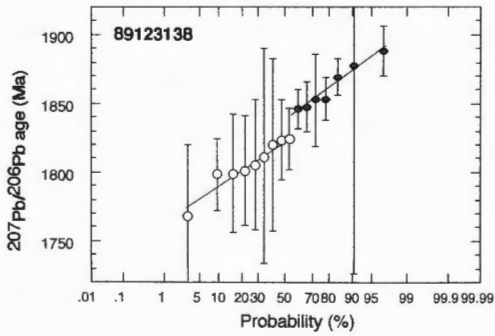

Figure 5.17 Probability graph of $^{207}Pb/^{206}Pb$ ages for the zircons in sample 89123138, showing 1σ errors for the analyses. Individual uncertainties are high for each sample, so all samples overlap to form a single statistical population. However, there is a step in the data which suggests there are two age populations within the data, which plot on the separate regression lines.

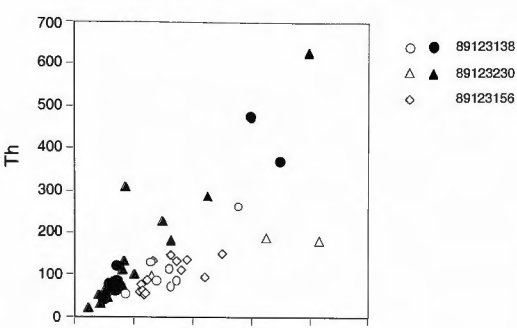

Figure 5.18: Graph of Th vs U values for zircons from all clastic samples, showing a distinctive compositional difference between the ~ 1828 Ma melt-precipitated grains (indicated by filled symbols) and the ~ 1864 Ma xenocrystics (indicated by open symbols). The melt-precipitated grains have lower U contents and therefore higher Th/U ratios. Optically, the low U content of the magmatic zircons is reflected by their higher cathodoluminescince.

In contrast, the presence of 1865 Ma xenocrysts greatly complicates the interpretation of analytical results in the case of the lithic-rich ignimbrite (sample 89123138). Taken at face value, the data for this sample suggest a crystallisation age of 1850±12 Ma. However, the maximum age of the ignimbrite is constrained independently by analyses of the rhyolite porphyries, to be no older than about 1828 Ma. A closer examination of the gaussian histogram indicates that the analyses comprising the main peak show scatter in excess of a normal distribution, suggesting it may represent more than one age population. The data appear to be skewed towards lower $^{207}Pb/^{206}Pb$ ages, with a slightly bimodal distribution (Figure 5.16). This bimodal distribution of ages is better illustrated on a probability plot of individual ages for each sample analysed (Figure 5.17). On this type of graph, a normal distribution is represented by a straight line, the slope of which is proportional to the standard deviation. The analyses divide into two populations as indicated by their conformity to separate lines on the probability graph, although the individual uncertainties of the analyses in both populations overlap. A bimodal population is also supported by the fact that the two proposed zircon populations can be clearly distinguished by their Th/U ratios (Figure 5.18). The older population has higher U, and therefore lower Th/U ratio than younger zircons. The higher U contents of the older grains is reflected optically by their lower CL.

An alternative way of interpreting the data for sample 89123138 is therefore to assume that the main peak represents zircons from two different age populations. Because the analyses are imprecise (1σ errors of individual analyses (measured on SHRIMP I) are about twice as large as those for sample 89123230, which was measured using SHRIMP II), these different age populations merge to form a complex statistical array. This can be deconvolved into two components which have ages of 1862±16 Ma (for the 7 oldest grains; $\chi^2 = 1.03$) and 1810±27 Ma (for the 9 youngest grains; $\chi^2 = 0.21$). The older component of the statistical population is indistinguishable from the age of a cluster of inherited grains in ignimbrite sample 89123230 (1868±12 Ma), and so these grains are also interpreted to be xenocrysts. The younger age of 1810±27 Ma is within analytical error of the crystallisation age of the ignimbrite sample 89123230 and the rhyolite porphyries (1828 Ma).

There are no strong statistical grounds for rejecting the age of 1850±12 Ma, and if sample 89123138 were analysed in isolation, the excess scatter in the gaussian distribution and slightly high χ^2 value of 1.54 may have been attributed to the poor precision of individual analyses, and the slight bias towards lower $^{207}Pb/^{206}Pb$ ages may have been attributed to Pb-loss. The statistical age of 1850±12 Ma might have been accepted as the crystallisation age of the ignimbrites. Taken in context with the other samples however, this age is known to be too old, and data were therefore interpreted in an entirely different manner. An accurate crystallisation age could not be obtained for this sample, as insufficient data were collected to resolve the age of the melt-precipitated zircons, and to deconvolve the two proposed age components with statistical confidence. The 1810±27 Ma 'crystallisation' age is derived from only 9 imprecise analyses, and the large error indicates the age is poorly defined.

The age characteristics of the volcaniclastic sandstone (89123156) with the highest degree of lithic contamination are even more significantly influenced by xenocrystic zircon. Two thirds of the zircons analysed combine to yield an age of 1863.6±4.4 Ma, the same age as the youngest xenocrystic population in the underlying ignimbrites. Only two of the analysed grains were identified as statistical outliers possibly belonging to a younger magmatic population, which may represent grains precipitated during crystallisation. If this sample had been analysed in isolation, the main zircon population would not have been recognised as xenocrystic, and the age of the Pul Pul Rhyolite would have been taken to be 1863.6±4.4 Ma.

In conclusion, the stratigraphic age of the Pul Pul Rhyolite has been obtained by interpreting analyses from several types of volcanic, subvolcanic and volcaniclastic facies

Sample No.	Rocktype	Crystallisation age (Ma)	Age of youngest inherited component	Other inheritance (approx. ages)
89123076	porphyry	1828.1±3.5 (n=19)		
89123002	porphyry	1827.3±3.5 (n=31)		
89123230	lithic-poor ignimbrite	1828.6±5.1 (n=20)	1868±12 (n=3)	**1960**,**1990**,2200, 2350,**2490**,2700
89123138	lithic-rich ignimbrite	1810±27 (n=9)	1862±16 (n=7)	**1910**,1930,1950, **1990**,2100,**2490**
89123156	volcaniclastic sandstone	~ 1835 (n=2)	1863.6±4.4 (n=13)	**1910**,**1960**,**1990**

Table 5.6: Summary of U-Pb zircon ages obtained for samples of the Pul Pul Rhyolite in this study. Bold type depicts xenocrystic populations that are common to more than one sample.

and considering the results of each sample in their geological context and in relation to the constraints placed on their age by the other analysed samples. The results (Figure 5.15) indicate that the ignimbrites and intrusive rhyolite porphyries are essentially co-magmatic and crystallised at 1828 Ma, and that the country rock incorporated into the ignimbrites and volcaniclastic sediment contained sources of more than one age, including a source rock ~ 40 Ma older than the Pul Pul Rhyolite sequence. The age of this inherited population is interpreted to be ~ 1865 Ma, the same as the age of the main compressional structural-metamorphic orogeny in the Pine Creek Inlier (Nimbuwah Event). The 1828.6±5.1 Ma stratigraphic age of the Pul Pul Rhyolite is derived from the youngest magmatic population in the lithic-poor ignimbrite. Ages for all samples are summarised in Table 5.6.

5.6.2 Implications for U-Pb dating of ignimbrites

Isotopic dating of volcanic rocks in sedimentary sequences has a wide variety of applications, as the data can provide direct numerical ages to complement stratigraphic, basin analysis and timescale studies. The primary eruptive products of silicic volcanic centres are pyroclastic fall deposits, ignimbrites and small-volume rhyolite lavas. Ignimbrites are the most voluminous of these volcanic products. They are laterally extensive, have good preservation potential and generally form the dominant component of ancient volcanic successions. For these reasons, they are likely to be a common target for the dating of volcanic complexes and stratigraphic sequences. However, of all the primary volcanic facies, ignimbrites present the most difficult dating prospect because

they are the products of violent and explosive volcanic activity, and the pyroclastic flow commonly assimilates large volumes of country rock during eruption and transportation. It is important to be aware that geochemical and geochronological analyses of ignimbrites are therefore subject to considerable error. Xenoliths can introduce inheritance into the zircon population. Inheritance is a widely recognised problem in U-Pb age-dating studies, as complex zircon populations with polymodal age distributions can be difficult to resolve. This geochronological study of the Pul Pul Rhyolite highlights this point by illustrating some of the problems that can be encountered in obtaining a crystallisation age for lithic-rich volcanic units. The results of this study have two important implications for the dating of ignimbrites and other facies which contain significant crustal contamination:

- Firstly, it is very important to minimise the degree of lithic contamination in samples selected for geochronological analysis. This study has shown that the crystallisation age of the samples can become more difficult to interpret as the degree of lithic contamination increases. The rhyolitic porphyries which contain no lithic clasts yield single concordant age populations which date the crystallisation age of these samples. A well defined magmatic age was also obtained for the ignimbrite sample with the least degree of lithic contamination, as most analyses combined to define the magmatic age population, and the comparatively few analyses of inherited grains were statistically resolved as outliers. By contrast, in the most contaminated samples zircon inheritance is so pronounced that the magmatic age could not be determined.

- Secondly, when interpreting the age of samples containing multiple age populations, the geochronological data cannot be considered in isolation from other data sets and available geological constraints. Without the independent geological constraints for the age of the volcanic sequence provided by the porphyry samples, the statistical ages obtained for the most lithic-rich clastic samples would have been misinterpreted.

Although it is important to be aware of lithic contamination and recognise that it may cause problems in dating ignimbrite samples, this need not exclude ignimbrites as potential targets for dating. As the distribution of lithic clasts in ignimbrites is usually heterogeneous, problems with inheritance can be largely avoided by careful sampling to minimise lithic contamination. Also, if the country rock comprises lithologies that are unlikely to contain zircons (e.g. mudstone, chert, basalt, quartzose sandstone, etc), its incorporation into the pyroclastic flow will not alter the zircon population.

5.7 STRATIGRAPHIC AND TECTONIC IMPLICATIONS OF RESULTS

Needham et al. (1988) subdivided the Pine Creek Inlier into a depositional period from about 2000-1880 Ma ('Pine Creek Geosyncline Sequence') and an orogenic period

lasting about 90 Ma (1870-1780 Ma) which they named the 'Top End Orogeny'. They suggested there was a continuum of deformation and igneous activity during this orogeny (Needham et al. 1988; Stuart-Smith et al. 1993; Figure 5.19a), with the peak of compressional deformation and metamorphism taking place during the Nimbuwah Event between 1870-1850 Ma. Granitoid intrusion associated with the Nimbuwah Event (the pre-orogenic to early syn-orogenic granitoid precursor to the Nimbuwah Complex) is dated at 1866±8 Ma (Page et al. 1980). Needham et al. (1988) suggested compressional deformation was closely followed by extensional block faulting, resulting in a shallow half graben in the east, which was filled by the El Sherana and Edith River Groups between about 1860-1850 Ma, and that granitoid plutons of the Cullen Supersuite (formerly Cullen Batholith, renamed by Wyborn et al. 1997) and other isolated plutons (including the Malone Creek Granite which intrudes the Pul Pul Rhyolite) later intruded the central domain of the Pine Creek Inlier between 1850-1780 Ma.

The above timing of events proposed by Needham et al. (1988) was based on estimated ages of ~1860 Ma for the El Sherana Group and ~1850 Ma for the Edith River Group, and an age range of 1850-1780 Ma for plutons of the Cullen Supersuite. These approximate ages were poorly constrained, and based on poorly defined isotopic data, some of which have never been published. The wide spread of ages estimating the timing of intrusion of the Cullen Supersuite was based on highly discordant conventional analyses (1860-1775 Ma) and Rb-Sr whole rock analyses (~1780 Ma) of individual plutons. Needham et al. (1988) present inconsistent information about the age of the Edith River Group, stating that 'the Plum Tree Creek Volcanics and Grace Creek Granite have igneous crystallisation ages of between 1870 and 1860 Ma' but that 'the Plum Tree Creek Volcanics were extruded ~1850 Ma ago'. They based this information on unpublished conventional U-Pb ages for the Plum Tree Creek Volcanics and Grace Creek Granite, which are given as 1858±25 Ma and 1863±5 Ma, respectively, in the Australian Geological Survey Organisation's OZCHRON database. The age of the El Sherana Group was indirectly constrained between 1885±2 Ma (conventional U-Pb ages of tuff horizons in the underlying South Alligator Group; Needham et al. 1988) and 1850-1860 Ma (unpublished conventional U-Pb analyses of the Edith River Group and co-magmatic Grace Creek Granite). A U-Pb age of 1890+18/-15 Ma for the Tollis Formation was considered the best direct estimate for the stratigraphic age of the El Sherana Group (Page and Williams 1988). At the time, the Tollis Formation was correlated with the Big Sunday Formation and considered part of the El Sherana Group (Figure 5.19a);. It has since been reinterpreted as correlating with the upper Burrell Creek Formation, and therefore forms part of the deformed metasedimentary basement to the El Sherana Group (Hein 1994; Kruse et al. 1994; Figure 5.19b).

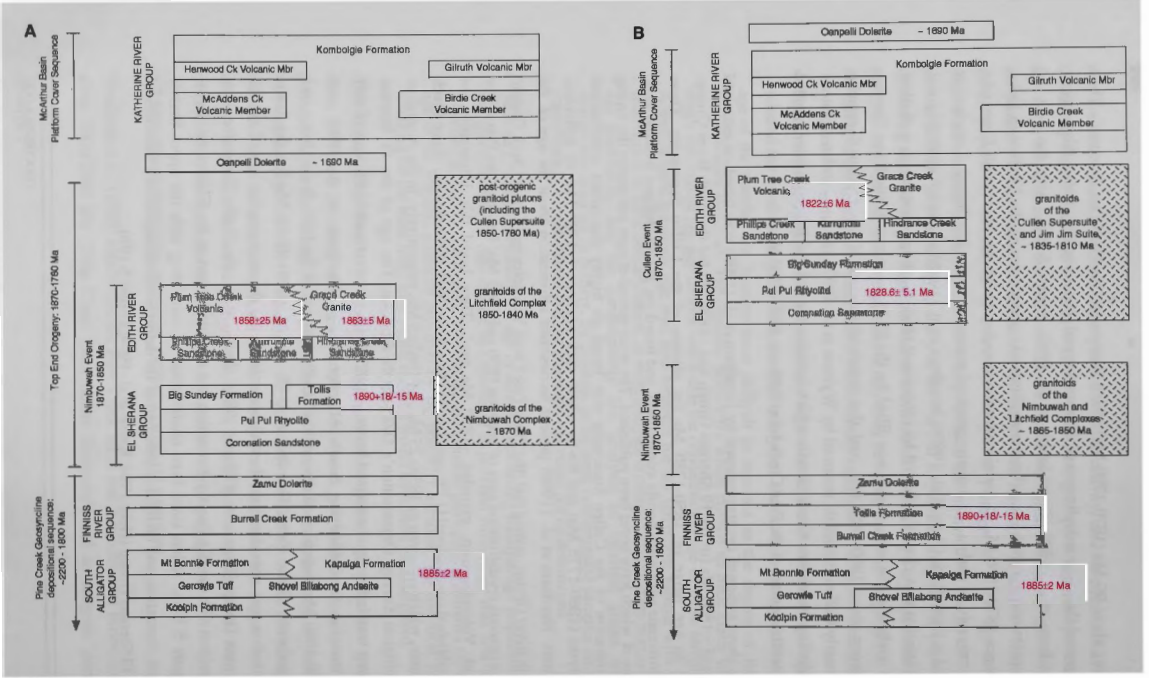

Figure 5.19: (a) Diagrammatic stratigraphy of the Pine Creek Inliercompiled from Needham et al. (1988) and Needham and Stuart-Smith (1985a), showing tectonic events and age determinations used by these authors; (b) Proposed modifications to the stratigraphy, based on new age determinations presented in this study, and published in Stuart-Smith et al. (1993) and Kruse et al(1994).

New (SHRIMP) isotopic ages are now available for the El Sherana and Edith River Groups and the Cullen Supersuite, which render the above poorly constrained age estimates obsolete (Table 5.7). Stuart-Smith et al. (1993) summarised isotopic data on granites of the Cullen Supersuite, and concluded that SHRIMP U-Pb ages ranging from 1835-1818 Ma are more precise and accurate than either Rb-Sr whole rock (~1780) or conventional U-Pb zircon ages (1860-1775 Ma). The Plum Tree Creek Volcanics of the Edith River Group have also been reanalysed using SHRIMP, and results indicate the volcanics have a crystallisation age of 1822±6 Ma (unpublished data from OZCHRON, quoted in Kruse et al. 1994). The discrepancy between SHRIMP and conventional U-Pb ages for these units reflects high discordance and the likely presence of inherited zircon in the conventional analyses. The present study provides a new stratigraphic age of 1828.6±5.1 Ma for the Pul Pul Rhyolite, El Sherana Group.

These results indicate that the stratigraphy of the Pine Creek Inlier, and the sequence of geological events proposed by Needham et al. (1988) require some modification, and a revised stratigraphy is presented in Figure 5.19b. Firstly, it is now clear that there are two main episodes of granitoid intrusion in the Pine Creek Inlier, instead of the continuum of igneous activity suggested by Needham et al. (1988). The first was related to the major compressional deformation event (Nimbuwah Event), and includes granitoid rocks of the Nimbuwah Complex (1866 Ma) and the Litchfield Complex (Allia and Waigat Suites, ~1850 Ma; Table 5.7). The next major event, involving intrusion of the Cullen Supersuite, occurred between about 1835-1820 Ma, about 40 million years after the Nimbuwah Event. Secondly, deposition of the El Sherana and Edith River Groups postdates the Nimbuwah Event by about 40 Ma, and magma generation therefore was not related to late-stage crustal extension associated with the release of compressional forces at the close of this event, as previously supposed. The new isotopic data suggest that the felsic volcanics of the El Sherana and Edith River Groups and the granitoids of the Cullen Supersuite were emplaced co-evally. Combined, these units define a major felsic magmatic event covering an area of at least 10 000 km^2 (Figure 5.20), which has been named the 'Cullen Event' (Jagodzinski and Wyborn 1995).

The volcanic and plutonic rocks of the Cullen Event have been divided into two groups on the basis of their chemistry; the Cullen Supersuite and the Jim Jim Suite (Wyborn et al. 1997). The Cullen Supersuite was intruded into the central part of the Pine Creek Inlier, and comprises all the plutons of the formerly named Cullen Batholith (Stuart-Smith et al. 1993). The Jim Jim Suite occurs in the eastern part of the Pine Creek Inlier, mainly along the western border of the McArthur Basin (Figure 5.20). It includes the felsic volcanic sequences of the El Sherana and Edith River Groups, the Grace Creek Granite and a number of small shallow level plutons (Malone Creek Granite

Geological Unit	Ion microprobe zircon age (Ma)	Conventional U-Pb zircon age (Ma)
Nimbuwah Complex		
Nimbuwah Complex (tonalite)		1866±8 Ma
Nimbuwah Complex (granite)		1866±7 Ma
Allia Suite		
Murra-Kamangee Granite		1850±2 Ma
Murra-Kamangee Granite		1840±5 Ma
Cullen Supersuite		
McMinns Bluff Granite	1835±6	1818±3
Allamber Springs Granite	1818±5	1826±18
(mafic phase)		
Allamber Springs Granite	1822±6	1826±32
Fingerpost Granodiorite	1823±3	1843±22
Umbrawarra Leucogranite	1825±7	1805±12
Burnside Granite	1800±5	1750+56
Shoobridge Granite		1775±16
Prices Springs Granite		1804±50
Margaret Granite		1860±45
Jim Jim Suite		
Pul Pul Rhyolite	1829±5	
Plum Tree Creek Volcanics	1822±6	1858±25
Grace Creek Granite		1863±5
Malone Creek Granite	1823±9 Ma	
Malone Creek Granite	1808±20 Ma	
Jim Jim Granite	1838±7 Ma	

Table 5.7: Summary of U-Pb ages for granitoids and volcanic rocks of the Pine Creek Inlier. Data for the Nimbuwah Complex are from Page et al. (1980), the Allia Suite from Page et al. (1985), the Cullen Supersuite from Stuart-Smith et al. (1993), the Plum Tree Creek Volcanics (SHRIMP) from Kruse et al. (1994). The age of the Pul Pul Rhyolite is from this study. All other ages are from unpublished data in the Australian Geological Survey Organisation's OZCHRON database. Shrimp ages for the Cullen Supersuite range between 1818-1835 Ma (the Burnside Granite is not considered, because Stuart-Smith et al. (1993) considered this age unlikely to define the magmatic crystallisation age).

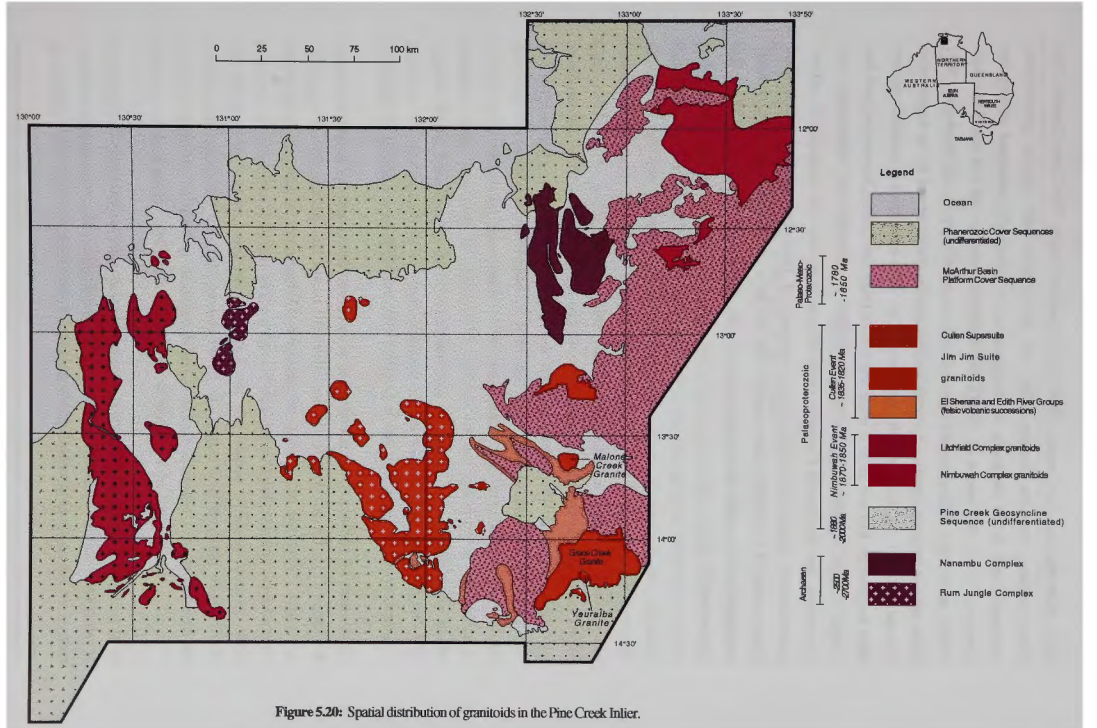

Figure 5.20: Spatial distribution of granitoids in the Pine Creek Inlier.

(1823-1808 Ma), Jim Jim Granite (1838 Ma), Nabarlek Granite, Tin Camp Granite, Eva Valley Granite, Yeuralba Granite). The two suites have very similar geochemical signatures, and differ markedly in composition to granitoids generated during the Nimbuwah Event (Wyborn et al. 1997). The Cullen Supersuite and Jim Jim Suite both classify as strongly differentiated I-(granodiorite) suites (Chappell and Stephens 1988) which have undergone significant chemical fractionation characterised by an exponential increase in Rb, U, Y, and Th with increasing SiO_2. They have been separated into two suites because the Jim Jim Suite is more fractionated than the Cullen Supersuite, and has a more A-type signature (which includes higher F contents) and mineralogy. By comparison, the Nimbuwah Complex granitoids are more mafic in composition and are predominantly restitic, with little or no evidence of fractionation. The geochemical characteristics of the Cullen Supersuite and Jim Jim Suite are documented in more detail in Appendix A5, with the geochemistry of the Nimbuwah Complex included for comparison.

CHAPTER 6

Introduction

6.1 Introduction and aims of the study

The Turondale Formation is a volcanogenic unit of Early Devonian age, which outcrops in the Silurian-Devonian Hill End Trough of central-western New South Wales, in the Palaeozoic Lachlan Fold Belt. It is one of two silicic volcanogenic formations in the submarine Hill End Trough succession, the better known of which is the Merrions Formation (formerly Merrions Tuff; Packham 1968a), which was studied in detail by Cas (1977, 1978, 1979, 1983a). Both formations contain a range of primary and resedimented volcanic facies. These include widespread subaqueous silicic lavas and/or lava cryptodomes in the Merrions Formation and compositionally equivalent porphyries intruding the Turondale Formation as sills, and thick massive deposits of crystal-rich volcaniclastic sandstone, interpreted to be syn-eruptive (i.e. emplaced as part of the eruption cycle. The work of Cas (1979, 1983a) on the syn-eruptive volcaniclastic deposits of the Merrions Formation is extensively referenced as a classic study of the behaviour of pyroclastic flows upon passage into a subaqueous environment. The Turondale Formation is studied as another example of this style of syn-eruptive deposit.

One major aim of this section of the thesis is to subdivide the Turondale Formation into its component lithofacies, and assess the characteristics of each facies to: (1) determine their origin and mode of deposition; (2) constrain the depositional setting; (3) assess the proximity of the deposits relative to the source of volcanic components; and (4) determine the composition, setting and eruptive style of the source volcanic centres. This information, combined with an assessment of the spatial and temporal relationships between the facies, is used to delineate potential source locations, and reconstruct the palaeogeographic setting and palaeovolcanological history of the succession.

The origin of syn-eruptive volcaniclastic deposits within the Turondale Formation is of particular interest, and the implications of deposit characteristics for the behaviour of pyroclastic flows upon passage into a subaqueous environment is explored as another

major aim. A study of similar deposits (CRVS) in the Big Sunday Formation (Pine Creek Inlier) is presented in Part 1 of the thesis, and the two studies provide complementary information on this style of syn-eruptive deposit. They illustrate two different types of depositional settings in which the deposits may occur. The CRVS of the Big Sunday Formation occurs in a restricted lacustrine setting within a predominantly subaerial volcanic landscape, whereas the Turondale Formation was deposited in an extensive deep marine basin. In the case of the Turondale Formation, the deposits are preserved throughout the entire extent of the basin, providing a regional, three dimensional and potential scale perspective on this style of deposit that is not available the Big Sunday Formation. This enables the deposits to be studied from a sedimentological perspective, supplying information that may assist in interpreting their origin, such as the size of the deposits, the frequency of their occurrence, lateral variations in their internal organisation, their context within the basin and the overall ratio of volcaniclastic to hemipelagic material in the sequence. These attributes are used to compare the thick volcaniclastic units of the Turondale and Merrions Formations with subaerial ignimbrites, and with epiclastic megaturbidites derived from basin margin collapse, to assess whether post-eruptive slumping and resedimentation is a likely mechanism for generating the sequence of thick, volcaniclastic mass flows.

Another aim of this study is to provide some numerical age control to the Hill End Trough sequence by obtaining U-Pb zircon ages for the Turondale and Merrions Formations (Chapter 8). The transported clastic fill of the Hill End Trough contains few *in situ*, age-diagnostic faunal assemblages, and direct biostratigraphic constraints on the age of the sequence are sparse. The U-Pb ages obtained for the Turondale and Merrions Formations provide information that can assist provenance studies, and correlation with volcanic events outside the Hill End Trough, within the well-constrained platform sequences of the adjacent highs. An interesting outcome of this study is that when the results are placed in the context of the limited fossil control available for the Early Devonian sequence, several problems become apparent with the existing Australian Phanerozoic time scale. The results are therefore discussed in conjunction with a recently published alternative version of the Phanerozoic time scale.

Another important aspect of the geochronological study is that it assesses whether volcaniclastic deposits such as occur in the Turondale and Merrions Formations are a suitable facies to target for isotopic dating. One of the main proposals of this thesis, and of previous authors (Cas and Wright 1987,1991; McPhie et al. 1993; White and McPhie 1997), is that these thick submarine volcaniclastic deposits have a genetic connection with active volcanism. They should correlate directly with large-volume explosive eruptions or result from resedimentation after only temporary storage, and are deposited essentially

during the eruptive cycle. If this is the case, the derived ages are very likely to be indistinguishable from, and to provide reasonable estimates of depositional age, because the zircons would be expected to have been derived from newly created volcanic products. This premise is tested by comparing the derived ages of the resedimented units, with crystallisation ages obtained for contemporary lavas and coevally emplaced sills within the succession.

6.2 GEOLOGICAL AND TECTONIC SETTING

6.2.1 The Lachlan Fold Belt: regional tectonic and palaeogeographic setting

The study area covers the exposed extent of the Turondale Formation, which outcrops extensively throughout the entire Hill End Trough as a folded, sheet-like body within the basin sequence. The Hill End Trough is located in the northeast of the Palaeozoic Lachlan Fold Belt; a 700 km wide orogenic belt that extends over a length of 1000 km from central New South Wales through Victoria and into Tasmania.

The Lachlan Fold Belt is one component of a larger orogenic system that formed along the eastern margin of Gondwanaland in the Palaeozoic, known as the Tasman Fold Belt. The Tasman Fold Belt is a composite orogenic belt occupying the eastern third of Australia from Tasmania to North Queensland. It comprises of several crustal segments which young progressively from west to east, formed by continental accretion onto the Precambrian craton (Scheibner 1987). From west to east, these distinct crustal entities are named the Kanmantoo Fold Belt, the Lachlan and Thomson Fold Belts and the New England Fold Belt (Figure 6.1). Major structural elements within the Lachlan Fold Belt are shown in Figure 6.2a.

The Lachlan Fold Belt consists of variably deformed, low to moderate metamorphic grade sequences of deep marine to continental sedimentary rocks, and mafic to felsic volcanic rocks of Cambrian to Carboniferous age. Granite plutons are voluminous and widespread, forming 30% of the present outcrop (Figure 6.2b; Chappell et al. 1988). The fold belt has a complex deformational history with inferred compressional events in the Late Ordovician-Early Silurian, Late Silurian, Early Devonian, Mid Devonian and mid-Early Carboniferous, and periods of extension in the Late Silurian, Early Devonian and Late Devonian (Gray 1997; Cas 1983b; Coney et al. 1990). These compressional and extensional events indicate nearly continuous long term orogenic activity during its Cambrian to Early Carboniferous tectonic history, and in this time marked changes in the palaeogeography occurred (Cas 1983b). No single comprehensive model has been widely accepted for the tectonic and palaeogeographic evolution of the Lachlan Fold

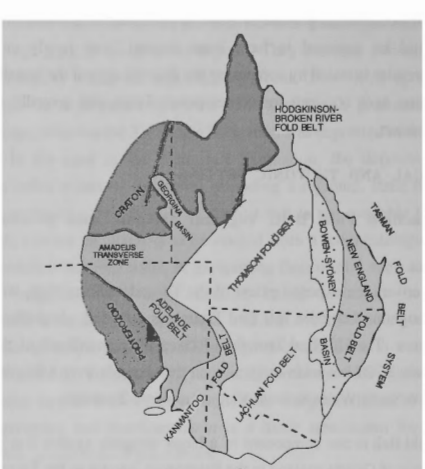

Figure 6.1: Schematic tectonic map of Australia showing the fold belts comprising the Phanerozoic Tasman Orogenic System on the eastern margin of the Australian continent. Modified after Scheibner (1989).

Belt. Current models are developed within a plate tectonics context. Many of the models agree that most aspects of the geology reflect the development of an active plate margin, requiring a major convergent plate boundary to the east of the Lachlan Fold Belt (Gray 1997). The following section summarises the palaeogeographic and tectonic history of the northern Lachlan fold belt (New South Wales).

The tectonic evolution of the Lachlan Fold Belt can be divided into discrete time slices which have unique facies associations and palaeogeographic and tectonic settings and are separated by periods of compressional deformation (Figure 6.3). They show progressive palaeogeographic changes from an open marine setting in the early Palaeozoic (Cambrian to Early Silurian), to a mixed continental and marine palaeogeography dominated by regionally extensive silicic magmatism in the Middle

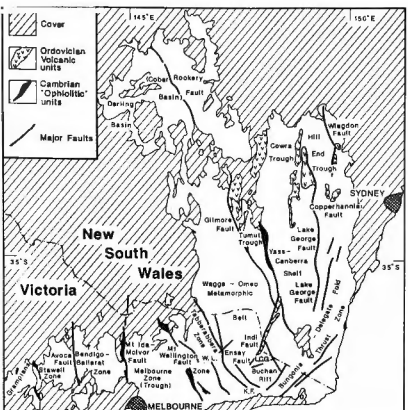

Figure 6.2a: Major faults, structural zones and sedimentary basins of the Lachlan Fold Belt in southeastern Australia, showing the location of the Hill End Trough in the extreme northeast (from Fergusson and Coney 1992).

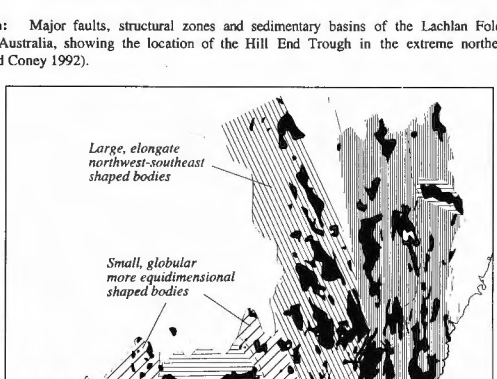

Figure 6.2b: Distribution of Late Devonian-Early Silurian granite plutons throughout the Lachlan Fold Belt (from Gray 1997). Gray (1997) subdivided the granites into five provinces (shown by the lined screens) on their shape and orientation. Dashed lines mark the 'basement terranes' of Chappell et al 1988, which were determined on the basis of geochemical variations within the plutons.

Silurian to Middle Devonian, to a dominantly continental palaeogeography with some extensional basins and bimodal magmatism in the Late Devonian to Middle Carboniferous, indicating progressive emergence of the orogen (Cas 1983b).

Cambrian

The Cambrian 'greenstone' successions of Victoria represent the oldest preserved rocks in the Lachlan Fold Belt. Cambrian boninites, andesites, tholeiites and intercalated marine sedimentary rocks outcrop as three fault-bounded 'greenstone belts' within three north-northwest trending zones; the Stavely, Heathcote and Mount Wellington Fault Zones. The greenstone belts are interpreted as recording submarine volcanism and associated volcaniclastic sedimentation that developed in an oceanic back-arc basin setting, adjacent to active volcanic arcs to the east or northeast (Crawford 1988). Further to the west deposition within shallow marine shelf environments of the Kanmantoo Trough and Adelaide Fold Belt occurred at this time.

Ordovician to Early Silurian

The Ordovician to Early Silurian history of the Lachlan Fold Belt can be divided into two main provinces: (1) the Late Ordovician Molong volcanic province (or Molong Volcanic Arc) in the north; a shallow marine basalt-volcaniclastics-limestone province that outcrops in several north-south trending belts in northern New South Wales, believed to be connected during the Ordovician (Packham 1969, 1987; Powell 1984; Wyborn 1992a, 1992b), and (2) the Early Ordovician Adaminaby Group; an extensive succession of quartz-rich turbidites, black shale and chert which occurs widely throughout much of Victoria and southern to central New South Wales (VandenBerg and Stewart 1992). The quartz turbidite succession has been interpreted as a giant terrigenous submarine fan, sourced from the western Gondwanan craton by the Delamerian Fold Belt in South Australia and western Tasmania (Cas et al. 1980; Cas 1983b; Gray and Webb 1995) and Ross Orogen in Antarctica (Cas and VandenBerg 1988; VandenBerg and Stewart 1992). The Molong volcanic province is set in the distal outreach of this submarine fan far from the inferred continental source, in a deep marine environment (Fergusson and Colquhoun 1996). The province appears to have consisted of shallow marine to emergent volcanic centres where episodic basaltic volcanism occurred. During periods of volcanic quiescence carbonates accumulated and the mafic volcanic piles were locally reworked to feed the adjacent marine basins (Powell 1976; Cas et al. 1980). The contact between the terrigenous turbidite fan and the overlying volcanic-derived detritus is sharp, with minor evidence of interdigitation (Wyborn 1992a), suggesting the fan was inundated by the growing volcanic centres, and quartz-rich turbidite sedimentation was starved from the area as local volcaniclastic

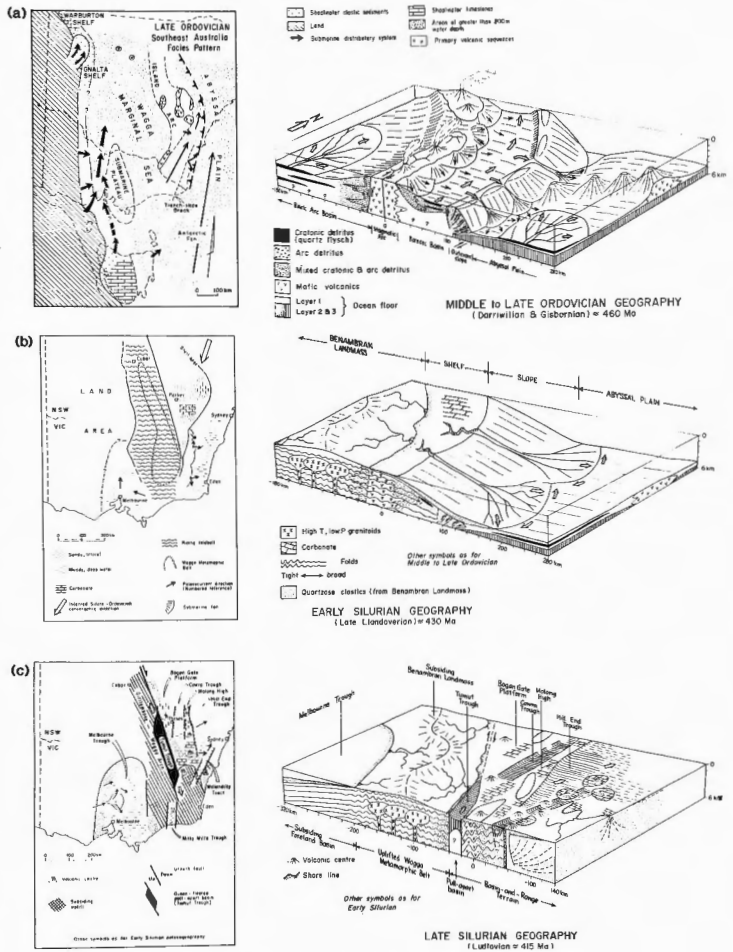

Figure 6.3: Facies distribution and palaeogeography of the Lachlan Fold Belt in the (a) Late Ordovician, (b) Early Silurian, (c) Late Silurian. Diagrams are taken from Powell (1983), who modified them from Cas et al (1980) and Cas (1983b).

sedimentation built up on the sea floor (Wyborn 1992a; Fergusson and Colquhoun 1996). The geochemistry of the Ordovician volcanism is controversial. Wyborn (1992a, 1992b) considers volcanism to be almost entirely shoshonitic, whereas other authors claim some of the volcanics have a calcalkaline affinity (Pemberton and Offler 1985; Pemberton 1990).

In summary, the palaeogeography for this period consists of an east-facing basaltic volcanic island chain in the northeast Lachlan Fold Belt, separated from the Gondwanan craton to the west by a marginal sea, with a large terrigenous submarine fan prograding from the western land mass (Figure 6.3a; Cas et al. 1980; Powell 1983). The Andaman-Nicobar system of the northeastern Indian Ocean is considered to be a reasonable modern analogue to the Late Ordovician palaeogeography (Cas et al. 1980; Powell 1983).

Most authors envisage an active convergent margin setting for the Late Ordovician (Figure 6.4; Oversby 1971; Scheibner 1973; Packham 1973, 1987; Powell 1983, 1984; Cas et al. 1980; Cas 1983b; Gray 1997). The Molong volcanic province is interpreted to be an east-facing island arc chain, possibly developed on a microcontinental basement (Molong Microcontinent; Scheibner 1987). A Marianas-type convergent plate boundary and west-dipping subduction zone is postulated along its eastern margin. The arc is separated from cratonic areas in the west by a marginal sea (Wagga Marginal Sea) in which backarc spreading took place. To the east of the arc there is a proposed forearc region in eastern Victoria and southeastern New South Wales, with possibly an accretionary complex around Bateman's Bay (Crook 1980).

There is some dispute about the existence of a subduction zone in the Ordovician. Wyborn (1992a, 1992b) questioned the existence of an arc in the Ordovician based on the dominant shoshonitic chemistry of the magmatism, absence of calcalkaline igneous rocks, and the broad as opposed to arcuate distribution of the volcanic centres. Wyborn (1992a, 1992b) suggested the Ordovician volcanics formed by partial melting of an enriched subcontinental lithosphere, triggered by heating associated with asthenospheric upwelling. VandenBerg and Stewart (1992) propose a passive margin setting with the Molong volcanic province possibly representing hot-spot volcanism, and Fergusson and Coney (1992) also linked the volcanics to several local volcanic centres within an abyssal plain. However, Fergusson and Colquhoun (1996) later supported an arc setting.

Benambran Orogeny

At the close of the Ordovician, the Benambran Orogeny caused widespread deformation

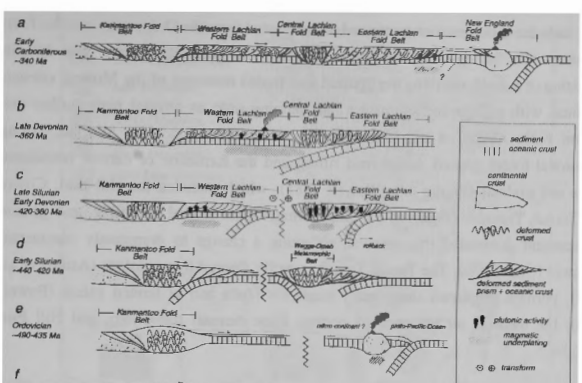

Figure 6.4: Recent model for the tectonic development of the Lachlan Fold Belt from the late Cambrian (*c.* 500 Ma) to the Early Carboniferous (*c.* 340 Ma), from Gray (1997).

in the Lachlan Fold Belt, in which significant north-south shortening produced mainly east-west trending folds devoid of cleavage (Packham 1969). The Benambran Orogeny corresponds with a major change the plate tectonic configuration. Powell (1983, 1984) and Scheibner (1985, 1987) suggested the Marianas-type convergent plate boundary changed into a Chilean-type boundary at this time, with closure of the Wagga Marginal Basin, which was folded and uplifted to form the Wagga Metamorphic Belt, then collided with the Molong Volcanic Arc and its microcontinental basement. In contrast, Packham (1987) considers the Benambran Orogeny to represent a change from subduction to sinistral strike-slip tectonics, with the Molong Volcanic Arc to splitting into a number of segments at this time.

Middle Silurian to Middle Devonian

Major changes in the palaeogeography occurred following the Benambran Orogeny (Cas 1983b), and the open marine setting of the Ordovician was replaced by a dominantly ensialic regime in the Silurian. During the Benambran Orogeny the Wagga Marginal Sea was folded, metamorphosed and intruded by granites to form the Wagga Metamorphic Belt, an uplifted land mass that divided the Lachlan Fold Belt into two contrasting regions (Powell 1983, 1984). In the Melbourne Trough to the west of the divide, deep

water turbidite sedimentation continued uninterrupted from the Ordovician into the Early Devonian. To the east, in the Early Silurian, the palaeogeography was simple, consisting of a shelf overlying the uplifted and folded remnants of the Molong volcanic province, with a slope and submarine fans passing onto an abyssal plain further east (Figure 6.3b; Crook et al. 1973; Powell 1983). In the Middle Silurian, strong extensional forces caused widespread rifting and the formation of narrow meridional horsts and grabens (Figure 6.3c; Powell 1983), which included the Hill End, Cowra and Tumut Troughs (Figure 6.5). Silicic magmatism related to rifting and granite emplacement dominated this interval, reflecting a change to dominantly continental basement (Cas 1983b). The Tumut Trough is partly floored by ophiolites (Ashley et al. 1979), perhaps emplaced along leaky transform faults and of limited extent (Powell 1983), but there is no evidence of oceanic crust beneath the Cowra and Hill End Troughs.

The troughs were infilled with deep water turbiditic sedimentation of alternating silicic volcanic, quartzose and lithic provenance, with thick mudstone intervals reflecting periods of volcanic quiescence and/or high sea-level. Deep water emplacement of silicic lavas occurred within the Hill End Trough (Cas 1978). Shallow water sedimentation occurred on the flanking ridges or highs and subaerial and subaqueous silicic volcanism provided most of the fill for the adjacent subsiding troughs (Cas 1983b). Carbonate platforms and volcaniclastic aprons fringed the highs. Marginal trough facies are typically proximal mass flow sequences (Colquhoun 1997) and include olistostromes and slump deposits (Crook and Powell 1976).

Bowning and Tabberabberan Orogenies

During the Late Silurian-Early Devonian the Bowning Orogeny caused widespread deformation, metamorphism and granite intrusion (Cas 1983b; Scheibner 1989; Fergusson and VandenBerg 1990) in the southern Lachlan Fold Belt. The northeast Lachlan Fold Belt was unaffected by the deformation, and sedimentation continued largely uninterrupted until the early Middle Devonian. A number of Silurian-Devonian disconformities on the Capertee High may have been caused by very mild deformation and/or sea-level fall related to the Bowning Orogeny in the south (Pemberton 1989, 1990; Pemberton et al. 1994; Colquhoun et al. 1996).

The Tabberabberan Orogeny represents renewed, more widespread compression in the Middle Devonian. Intense deformation in the southern Lachlan Fold brought the period of subaqueous horst and graben sedimentation and silicic magmatism of the Middle Silurian to Middle Devonian to a close. During the orogeny much of the Lachlan Fold Belt was cratonised and became emergent, resulting in an almost wholly continental

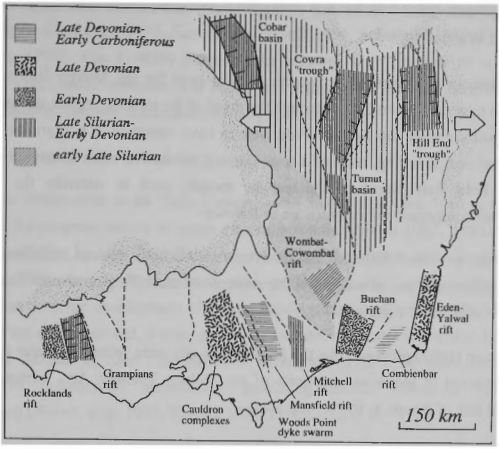

Figure 6.5: Map showing the timing and distribution of extensional elements within the Lachlan Fold Belt, from Gray (1997). Major E-W crustal extension occurred in the northeast portion of the fold belt (highlighted by the wider-spaced vertical slash pattern) in the Late Silurian to Early Devonian.

palaeogeography. The nature of this Middle Devonian deformation in the northeastern Lachlan Fold Belt has been interpreted in different ways. Powell et al. (1976) claimed the effects of this deformation are comparatively mild in the northeast, involving only uplift and broad folding or tilting, characterised by limb dips generally less than 30°, and low angle unconformities between Early and Late Devonian strata. Fergusson and Coney (1992) suggested that the Ordovician volcanic basement in the northeast acted as a rigid buttress and protected the overlying sediments from more significant deformation. However, there is new evidence suggesting that the main meridional regional deformation of the Hill End Trough occurred in the Middle Devonian. The metamorphic thermal maximum, which outlasted penetrative deformation in the Hill End Trough, has recently been estimated to have been about 370 Ma (Givetian) based on modelling of $^{40}Ar/^{39}Ar$ data (Packham 1999), and Glen and Watkins (1999) have recorded significant thrust deformation in the Middle Devonian. Although the nature of Middle Devonian deformation has been controversial, there is general consensus that the Middle Devonian represents a major change in the tectonic evolution in the eastern part of the Lachlan Fold Belt. It marks the boundary between mixed older marine volcanics

and clastic sedimentary rocks and younger largely non-marine continental deposition (Glen and Watkins 1999)

A large number of diverse plate tectonic models exist for the Middle Silurian-Middle Devonian interval (Figure 6.4). Although the detail of the tectonic regime differs in each model most consider the Lachlan Fold Belt to have occupied a backarc or intra-arc continental margin setting, west of a west-dipping subduction zone located in the New England Fold Belt. Some of the tectonic models used to describe the complex extensional-compressional tectonics are as follows:

(a) early arc evolution followed by arc-Proterozoic oceanic plateau collision, tectonic underplating and partial melting of the underplated crust (Fergusson and VandenBerg 1990; Collins and Vernon 1994);

(b) Packham (1987) proposed that the Silurian troughs were related to major strike slip displacement of individual segments of the Molong Volcanic Arc, forming on the frontal side of the arc as forearc regions;

(c) an intra-oceanic arc setting with multiple forearc basins (Crook 1980);

(d) a backarc setting behind a frontal arc located in the ancestral New England region, with oblique Marianas-type subduction accounting for a transtensional setting in the backarc (Scheibner 1973, 1987, 1989; Fergusson et al. 1986; Fergusson and Coney 1992); and

(e) a dextral transform plate margin setting similar to the Basin and Range Province of western North America (Cas 1983b; Powell 1983, 1984).

Late Devonian to Middle Carboniferous

The Late Devonian to Middle Carboniferous period commenced with a complete regression of the sea, and widespread quartz-rich mollassic ('red-bed') sedimentation which progressed diachronously from west to east. Facies environments were dominantly fluvial with a short-lived marine transgression in the northeast in the Frasnian (Webby 1972). Near the eastern edge of the Lachlan Fold Belt, a bimodal continental rift (the Eden-Comerong-Yalwal Rift; McIlveen 1974; Fergusson 1979) developed. A-type granitoids are associated with the rifting (Collins et al. 1982). A phase of Late Devonian, predominantly felsic to intermediate, magmatic activity is recorded in east-central Victoria.

During the Late Devonian to Early Carboniferous the New England Fold Belt was probably a developing westerly subducting continental margin arc. The proposed

tectonic setting of the Lachlan Fold Belt at this time is a foreland basin located west of the arc (Figure 6.4; Leitch 1975; Cas 1983b; Powell 1984; Scheibner 1989; Fergusson and Coney 1992). Cas (1983b) proposed the western U.S. margin as a modern analogue, with crustal extension and Basin and Range-style bimodal continental rift basins developing inboard of a continental magmatic arc.

Kanimblan Orogeny

Widespread deformation in the Early Carboniferous Kanimblan-Alice Springs Orogeny concluded the orogenic history of south eastern Australia (Powell 1983, 1984). At this time the northeast Lachlan Fold Belt was cratonised. Fergusson and Coney (1992) attributed deformation to high relative plate motions causing backarc deformation, synchronous with the development of a large subduction complex in the New England Orogen. Post-deformational, I-type granitoids intruded the eastern Lachlan Fold Belt during the Middle to Late Carboniferous (Scheibner 1989). A mild north-south compressive deformation immediately postdating granite intrusions has been documented (Powell et al. 1985; Kosaka 1994; Colquhoun et al. 1996).

6.2.2 The Hill End Trough: stratigraphy and setting

Tectonic and palaeogeographic setting

From the Early Silurian to the Middle Devonian, the Lachlan Fold Belt is considered to have occupied a backarc, or extensive rift zone, or intra-arc continental margin setting, west of a west-dipping subduction zone located in the New England Fold Belt (as discussed in Chapter 6.2.1). During this period, extension in the eastern Lachlan Fold Belt created a series of deep water basins or "troughs" flanked by shallow water to emergent, often volcanic platforms or "highs". At this time the Ordovician Molong Volcanic Arc split and formed the basement of two horsts (the western Molong and eastern Capertee Highs) which flanked the newly formed Hill End Trough (Packham 1960; Scheibner and Stevens 1974). On the Capertee and Molong Highs the dominant facies were shallow subaqueous to subaerial silicic volcanics, shallow marine clastics and shallow water carbonates (Pemberton et al. 1994). Coeval sedimentation in the Hill End Trough was characterised by deep water turbiditic sedimentation of alternating silicic volcanic, quartzose, and metasedimentary lithic provenance. The fill for the Hill End Trough is largely sourced from pyroclastic eruptions of silicic volcanic centres (Cas 1983a, 1983b; Cas and Jones 1979). Voluminous silicic pyroclastic activity dominated the Capertee High throughout the Lochkovian and Pragian. In contrast, the Molong High was volcanically quiet apart from some shoshonitic mafic volcanism, and extensive carbonate development occurred in platform areas. Thus the sediment fill for

the Hill End Trough is grossly asymmetrical, with a thick sediment wedge emanating from the Capertee High, and a lesser sediment contribution from the Molong High (Cas and Jones 1979). Thick hemipelagic mudstone intervals reflect periods of volcanic quiescence and/or high sea-level and there are no truly pelagic chemical and organic sediments. Local deep water silicic lavas and sills also occur throughout the trough fill (Cas 1978, 1979).

Modern analogues

The earliest models interpreted the tectonic setting of the Hill End Trough in terms of a geosynclinal framework (Packham 1968a; 1969). With the advent of plate tectonics theory, the tectonic setting was reinterpreted in terms of modern arc systems. The Hill End Trough and its flanking highs were compared generally to an interarc basin and its flanking volcanic ridges, such as occur in intraoceanic arc settings (Oversby 1971; Solomon and Griffiths 1972; Scheibner 1973). Two more detailed studies have compared the characteristics of the Hill End Trough with specific interarc basins, proposed as modern analogues to its palaeogeographic and tectonic setting. Cas and Jones (1979) compared the Hill End Trough to the Lau Basin and the Havre Trough. Both basins occur within the Tonga-Kermadec arc system, but the Lau Basin is wholly intraoceanic and the Havre Trough is ensialic, merging into a continental block (the New Zealand continental margin). Colquhoun (1997) proposed the Sumisu Rift, an asymmetric rift basin located on the Izu-Bonin Arc south of Japan, as a reasonable analogue. From the comparisons and contrasts made, both studies conclude that the Hill End Trough was an embryonic interarc basin in which rifting terminated prior to sea floor spreading. Both observed that the magmatic geochemistry of the Hill End Trough was more siliceous than intraoceanic arc geochemical signatures, and Cas and Jones (1979) also noted a higher alkali content. Cas and Jones (1979) concluded that this chemical difference indicates that the basement must have been at least partly continental in character, and not wholly intraoceanic in its tectonic setting. In contrast, Colquhoun (1997) considers an intraoceanic backarc basin to be an acceptable analogue, with the chemical difference indicating that the Hill End Trough is a more mature or evolved system.

The palaeogeography and facies distribution of all of the basins chosen for comparison are comparable to that of the Hill End Trough. The Lau Basin and Havre Trough are flanked by long narrow ridges; the Lau Ridge to the west, and the Tonga-Kermadec Ridge to the east. Both are submergent to periodically emergent volcanic chains with reef crusts. Volcanism is inactive on the western Lau Ridge, and the Tonga Ridge has active basaltic to dacitic volcanism. Mass flow emplaced volcanic and carbonate debris fill the Lau Basin. Like the Hill End Trough, it has an asymmetric sedimentation pattern

with most of the sediment derived from the volcanically active eastern flank. The geology of the Havre Trough is unknown, but believed to be comparable to the adjacent Lau Basin, apart from also receiving terrestrial and volcanic sediment from the New Zealand craton to the south.

In their study, Cas and Jones (1979) found that the facies distribution and palaeogeography of the Hill End Trough compared favourably with that of the southern Havre Trough, and that the wholly intraoceanic Lau Basin was a poor analogue. They noted many dissimilarities between the Lau Basin and the Hill End Trough. The Lau Basin is an order of magnitude larger. The clastic sedimentary fill is thin, only flanking the margins and constrained by numerous sub-basins, whereas coarse clastic sedimentation occurs throughout the Hill End Trough, reflecting a terrigenous provenance that is consistent with peri-continental influences. The two most significant differences are the nature of the basement in each basin, and the geochemical signature of the volcanics. The Lau basin has a basaltic basement overlain by pelagic carbonate whereas the Hill End Trough has no pelagic component and there is no indication of oceanic crustal basement. Volcanics on the highs flanking the Hill End Trough are alkali enriched compared to those of the Tonga Ridge flanking the Lau Basin. Lavas within the Hill End Trough also have high total alkalis and intermediate silica values, quite different in chemistry to the oceanic tholeiites of the Lau Basin.

The Lau Basin contracts southward, becoming the Havre Trough, which in turn terminates in the Bay of Plenty of the North Island of New Zealand and passes landward into the continental ensialic Central Volcanic Region (Cas and Jones 1979). The dimensions of the Havre Trough are closer than those of the Hill End Trough, and it is likely to receive more terrigenous clastic sediment from the adjacent continent. The volcanics become more alkali and silica enriched as the arc system changes from oceanic to continental in character. For these reasons, Cas and Jones (1979) considered the Havre Trough to be a closer analogue to the Hill End Trough than the Lau Basin. In addition, a region of continental silicic volcanism lies beyond the southern termination of both basins (Central volcanic Region of New Zealand, and the Canberra Magmatic Province in New South Wales), lending support to this analogue.

Based on their comparisons with the Havre Trough, Cas and Jones (1979) concluded that the Hill End Trough was an embryonic interarc basin generated by the extension of continental crust, with rifting terminating prior to developing a seafloor spreading stage.

Colquhoun (1997) compared the Hill End Trough to the Sumisu Rift, an intraoceanic arc rift segment for which the palaeogeography and facies distribution also compare well with the Hill End Trough. The Sumisu Rift is in an early stage of rifting and has not

developed a sea floor spreading stage. It is bound to the east by a frontal arc containing several active dacite to rhyolitic calderas, and to the west by a remnant arc containing more restricted volcanism. Volcanism commenced as tholeiitic basalt to sodic rhyolite, but became more silicic as rifting commenced. The Rift is filled with mass flow sequences with a wedge-like geometry, derived mainly from the more active eastern arc. Like the Hill End Trough, it contains thick hemipelagic mudstones reflecting periods of volcanic quiescence, and bimodal volcanics in the basin fill. Unlike the Hill End Trough, the bounding highs do not have a well developed shallow marine and siliciclastic carbonate sequence. Colquhoun (1997) attributes this to higher latitude conditions and a tectonic and eustatic balance less suitable for carbonate development and long lived shallow marine conditions.

The fill in the Sumisu Rift contains far less free quartz and more mafic to intermediate rock fragments than the volcaniclastics of the Hill End Trough. Colquhoun (1997) suggests this more siliceous chemistry reflects the eruptive history of the adjacent volcanic centres, which are becoming more silicic as rifting progresses. He concludes that the Hill End Trough was at a more mature stage of rift development than the Sumisu rift, although still in an embryonic stage prior to the commencement of sea-floor spreading. This contrasts with the model of Cas and Jones (1979), who concluded that the more siliceous and alkaline chemistry reflects a continental component to the magmatic source.

Stratigraphy

The Hill End Trough is a prominent, NNW-trending, palaeogeographic feature that runs through the centre of the Bathurst and Dubbo 1:250 000 mapsheets (Figure 6.6; Raymond et al. 1997; Morgan et al. 1999). It is separated from the Capertee High to the east by the Wiagdon Thrust (Packham 1960) and the Mudgee Thrust (Colquhoun et al. 1997), and flanked by the Molong High to the west. The trough contracts southward and terminates in the Rockley-Burraga area. The Late Carboniferous *Bathurst Granite* separates the Hill End Trough proper from the Hill End Trough South in the Rockley-Burraga region, which has a different lithological sequence. This may indicate a basement high existed in the area presently occupied by the granite, separating the two parts of the Hill End Trough (Glen and Watkins 1994). The Canberra Volcanic Province, a region of continental volcanics and coeval granites lies beyond the southern termination of the Hill End Trough. Silicic volcanism, including widespread ignimbritic eruptions, was continuous throughout the Middle Silurian and Early Devonian in this region (Cas and Jones 1979).

Flat-lying Permian-Triassic sediments of the Sydney Basin and undeformed Jurassic

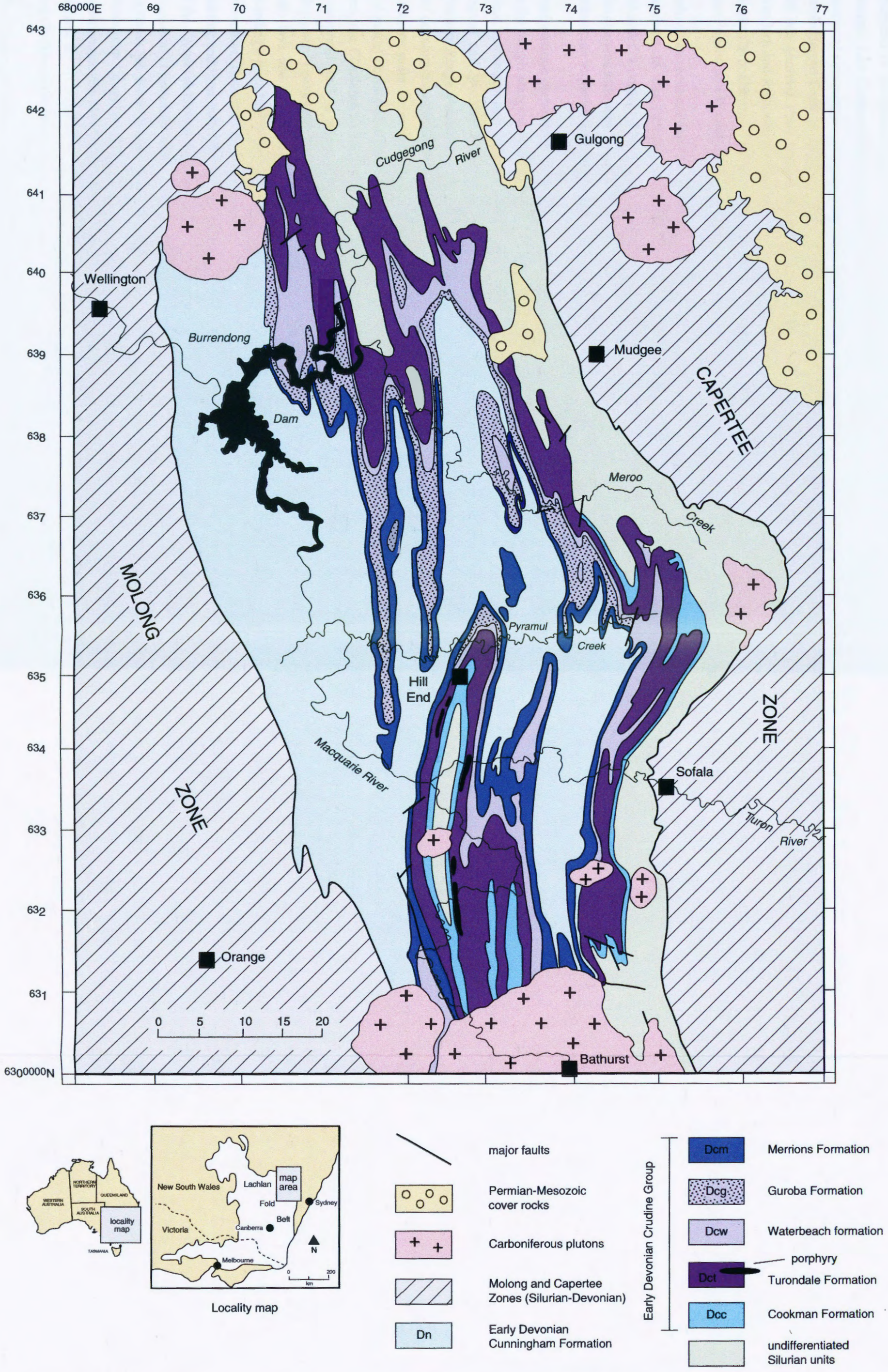

Figure 6.6: Simplified geological map of the Hill End Trough, showing the distribution of formations of the Crudine Group (adapted from Raymond et al. 1997 and Morgan et al. 1999).

sediments of the Great Australian Basin obscure the northern extent of the Hill End Trough. Late Carboniferous I-type granites, which include the *Bathurst Granite* and associated intrusions, and the *Wuuluman Granite,* intrude the trough sequence. Carboniferous Granites intruding the Capertee High have yielded Rb/Sr isotopic ages of 328 Ma (*Aarons Pass Granite*; Pemberton, 1990), and 319 Ma (*Gulgong Granite*; Evendern and Richards 1962, recalculated by Cas et al. 1976), which places them in the Middle Carboniferous. The *Bathurst Batholith* is considered to be Late Carboniferous in age (Pogson and Wyborn 1994).

Ordovician rocks are exposed at the margins of the Hill End Trough, and represent the basement to the Molong and Capertee Highs. Andesitic volcanics (e.g. *Sofala Volcanics, Coomber Formation, Burranah Formation*) dominate the Ordovician, which also contains sediments (quartz turbidites) of the Adaminaby Group. It is likely that this Ordovician sequence also forms the basement to the Hill End Trough.

Sedimentation commenced in the Middle Silurian with deposition of the *Mumbil Group* on the trough margins, characterised by widespread carbonate and shale deposition and silicic volcanism, and the turbiditic *Chesleigh Group* in the central trough (Figure 6.7; Pogson and Watkins 1998). Submarine to subaerial felsic eruptive centres of the *Mullions Range Volcanics* mark the western shelf edge, behind which thick carbonate reef developed on the Molong High. The eastern and southern Hill End Trough contains carbonate/shale facies (*Tanwarra Shale*) and thick silicic volcanic piles (*Bells Creek Volcanics*) developed along the margins of basement blocks. In the intervening trough area, the *Chesleigh Group* (formerly *Chesleigh Formation*; Colquhoun et al. 1997) is widespread, and is subdivided into a thick basal unit of slate and lithic sandstone (*Biraganbil Formation*) and an upper unit of volcaniclastic turbidites (mostly rhyolitic), latite lava and tuffaceous mudstones (*Piambong Formation*). Early Devonian sills, including a thick highly magnetic quartz monzodiorite to dolerite, intrude the *Piambong Formation.* Sediment movement indicators such as small slump, small-scale cross bedding and flute casts imply the sea-floor had a general easterly slope during deposition of the *Chesleigh Group* (Packham 1968a). The quartz-muscovite-lithic sediments in the *Biraganbil Formation* were probably derived from Ordovician sediments in the highlands of New South Wales and eastern Victoria, exposed as a result of the Benambran Orogeny (Packham 1968a). The overlying *Piambong Formation* contains quartz-muscovite-lithic sediments similar to the *Biraganbil Formation* interbedded with volcanic debris supplied by a source that probably lay to the west or southwest of Hill End (Packham 1968a).

The Chesleigh Group is overlain by the Early Devonian *Crudine Group*, which comprises about 2.5 km of turbiditic sandstone (mainly of silicic volcanic provenance)

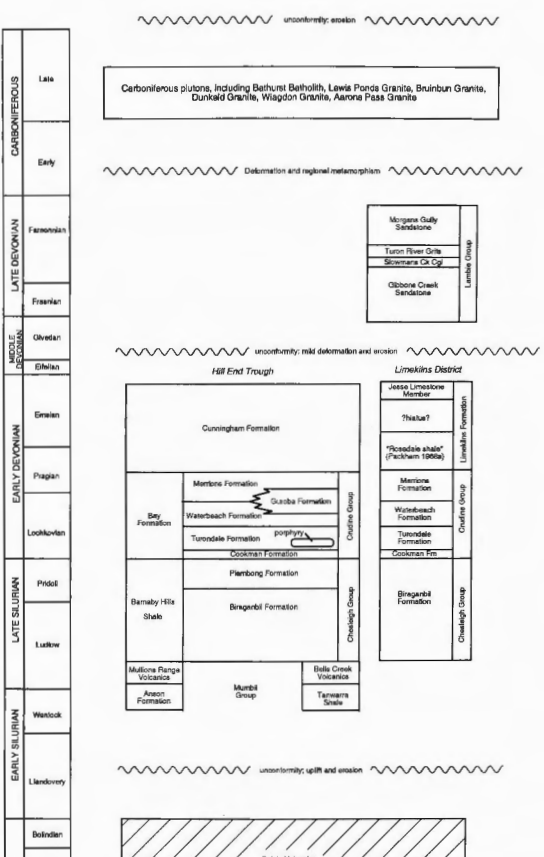

Figure 6.7: Stratigraphy of the Hill End Trough, based on Pogson and Watkins (1998) and Meakin and Morgan (19997).

and shale, with rare concordant volcanic horizons. The *Crudine Group* was originally defined by Packham (1968a) as comprising the *Turondale Formation* and overlying *Waterbeach Formation*, in the area north of the Bathurst Batholith. In present usage (Pogson and Watkins 1998; Meakin and Morgan 1999), the Crudine Group north of the Bathurst Batholith includes, in ascending stratigraphic order, the *Cookman Formation*, *Turondale Formation*, *Waterbeach Formation*, *Guroba Formation* and *Merrions Formation* (Figure 6.7). It also includes the *Bay Formation*, which represents the entire *Crudine Group* sequence along the western margin of the Hill End Trough

The *Cookman Formation* contains thinly interbedded fine to medium-grained quartz-rich sandstones and slate, with rare conglomerate and vitric tuffs. Because of its fine-grained quartzose nature it forms prominent resistant strike ridges and sheer cliff sections. The formation is 500-700 m thick and thins steadily north, pinching out so that the overlying *Turondale Formation* rests directly on the *Chesleigh Group*. Flute casts indicate a change in sea-floor slope from west to east following deposition of the *Chesleigh Group*, and the east-south-east palaeo-flow direction indicates the newly uplifted Capertee High sourced the sediments (Packham 1968a). This east direction of slope was maintained throughout the remaining depositional history of the Hill End Trough (Packham 1968a). The Cookman Formation has a multiple source terrain which included silicic volcanics, quartz-rich sediments, mafic volcanics and granite (Packham 1968a). From his studies of the Capertee High, Colquhoun (1997) postulated these sources to be the Silurian *Windamere* and *Dungaree Volcanics*, Early Ordovician *Adaminaby Group* and the Ordovician *Sofala Volcanics* and *Coomber Formation* respectively, while the source of the granite is unknown. The *Cookman Formation* contains non-age-diagnostic fragmentary plant material, but has been placed in the earliest Lochkovian based on the recent 1:100 000 scale mapping.

The 600-700m thick *Turondale Formation*, which is the focus of this thesis study, conformably overlies the *Cookman Formation*. It is defined by a compositional change from the quartz-rich sediments of the *Cookman Formation* to quartzo-feldspathic debris, indicating a renewal in volcanism on a large scale at this time. It is one of two silicic volcaniclastic formations in the *Crudine Group* (Figure 6.8), the better known of which is the *Merrions Formation* (formerly *Merrions Tuff*; Packham 1968a). These volcaniclastic units reflect periods of large-scale silicic volcanism on the margins of the Hill End Trough, which sourced the coeval volcaniclastic turbidites. The most notable feature of these turbidites is that many of the massive volcanogenic beds in both formations are abnormally thick (tens of metres) compared with normal turbidites (Cas 1979; Chapter 7, this study). These thick volcaniclastic turbidites are interpreted as the subaqueous, syn-eruptive equivalents of subaerial pyroclastic flows. The *Merrions*

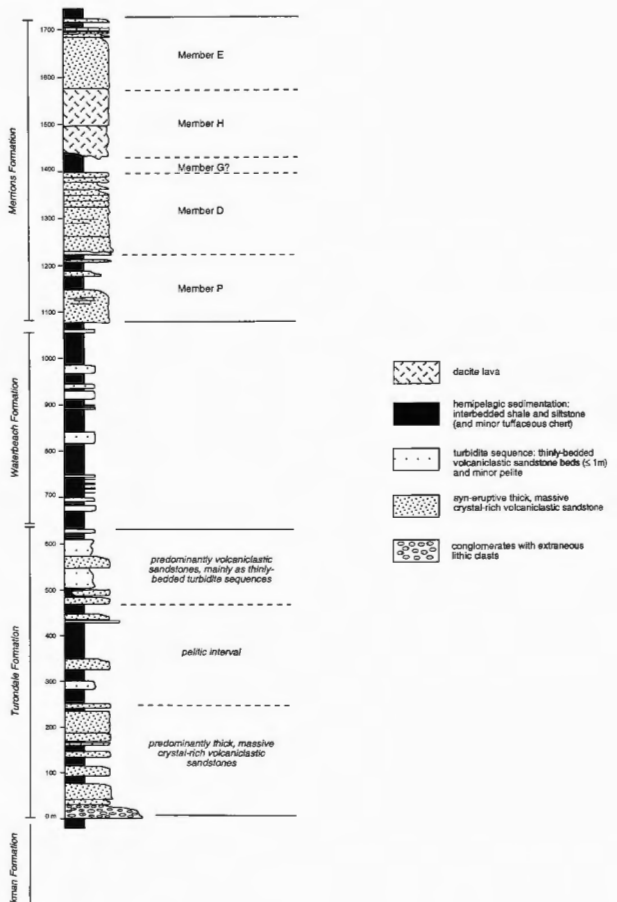

Figure 6.8: Type sections of the Turondale Formation (GR 745800 6338250), Waterbeach Formation (GR 743250 6338500) and Merrions Formation (Cas 1977; GR 7422500 6337500), showing the contrast between the silicic volcaniclastic formations, and the predominantly pelitic Waterbeach Formation, which represents ambient trough conditions with only minor clastic input. The threefold subdivision of the Turondale Formation recognised by Packham (1968a), and the subdivision of the Merrions Formation into lava, arenite and pelite members by Cas (1977), are also illustrated.

Formation had a multiple volcanic source, and with time the direction of dominant sediment influx shifted from the west through the south and southeast and finally to the east (Cas 1977). Active calderas on the Capertee High may have partly sourced the *Merrions Formation*. The *Turondale Formation* had a southeast source and was probably derived from an active volcanic source on the southern Capertee High (Chapter 7). At the same time that silicic volcanism was widespread on the flanking highs, porphyritic dacites of similar composition extruded within the trough as lavas during emplacement of the *Merrions Formation*. These porphyries also occur as sills within the underlying *Turondale Formation*.

The ~600m thick *Waterbeach Formation* outcrops between the two volcaniclastic formations. It comprises mainly shale and siltstone, and represents a thick interval of hemipelagic sedimentation throughout the trough, reflecting a long period of volcanic quiescence on the trough margins (Figure 6.8). Hemipelagic shale intervals also occur throughout the *Turondale* and *Merrions Formations*, and contacts between the three formations are conformable. In the type section of the *Waterbeach Formation* sandstone is a minor component and occurs in distinct packages throughout the thick shale interval. To the west and north of the type section, the *Waterbeach Formation* is divided into a thick basal shale/siltstone interval passing up into a thick sequence of turbiditic sandstones. The sandy zones may reflect periods of greater local tectonic activity that aided erosion and provided coarse detritus, or they may reflect eustatic or climatic changes (Packham 1968a).

In the northern Hill End Trough, The Guroba Formation outcrops between the Waterbeach and Merrions. The *Guroba Formation* was a local unit first defined by Dickson (1962), who correlated it with the *Merrions Formation* to the south. Following recent mapping in the northern Hill End Trough it was redefined to describe a massive to well-bedded quartzo-feldspathic sandstone facies between the *Waterbeach* and *Merrions Formations* (Meakin and Morgan 1999). The turbidites are compositionally similar to the *Merrions Formation*, but the beds are much thinner. The turbidites may represent distal equivalents to the thicker volcaniclastic turbidites of the *Merrions Formation*.

Along the western margin of the Hill End Trough the whole *Crudine Group* sequence is represented by the *Bay Formation*, a much thinner sequence of massive, fine to coarse-grained volcaniclastic sandstone interbedded with siltstone, and minor vitric tuff and chert (Pogson and Watkins 1998). In the Euchareena area and northward on the Molong High the mafic *Cuga Burga Volcanics* was extruded and extended into the Hill End Trough.

The *Cunningham Formation* represents the final fill of the Hill End Trough and it outcrops extensively throughout the region. Volcanism ceased following deposition of the Merrions Formation, and the *Cunningham Formation* comprises over 3000 m of thinly bedded slates, siltstones, quartzo-feldspathic and lithic sandstone and minor conglomerates. The sequence represents similar basin conditions to those that prevailed during deposition of the *Waterbeach Formation*, and there is no evidence of volcanism in the source region. On the eastern side of the Hill End Trough, east of the Wiagdon Thrust and northeast of Bathurst, the *Limekilns Formation* overlies the *Crudine Group* and is inferred to be laterally equivalent to the *Cunningham Formation*. The *Limekilns Formation* is a local marginal shelf sequence, consisting of thin bedded turbiditic siltstone and shale, and allochthonous limestone megaclasts (*Jesse Limestone Member*). The *Cunningham Formation* contains poorly preserved shelly fauna, possibly of late Pragian age (Wright 1994). Fossil evidence suggests the *Limekilns Formation* extends into the late Emsian *serotinus* Zone (Mawson and Talent 1992), suggesting deposition the *Cunningham Formation* extended from the Late Pragian to Late Emsian. The *Limekilns Formation* locally marks the trough margin to the east. A more extensive shelf sequence is developed farther north in the Cudgegong-Rylestone-Kandos district (*Kandos Group*), marking the site of the Capertee High.

Structure and metamorphism

The Hill End Trough opened along normal faults striking WNW and dipping NNE, which produced south dipping fault blocks (Pogson and Wyborn 1994). It opened from SSW to NNE during sinistral transtension along bounding meridional faults. The region was deformed by NNE-SSW dextral transpression, and the Hill End Trough closed by thrusting from NNE to SSW along the earlier meridional normal faults. As a result, the deep-water succession of the Hill End Trough has been overthrust onto the Capetee High on the east, along the Wiagdon Thrust (Packham 1999; Glen and Watkins 1999). The trough-fill passes without a disclocation of similar magnitude into the Molong High to the west. The principal compression direction rotated clockwise to produce E-W compression, which produced the strongest deformation in the area. Folding in the trough sequence is moderate to strong, and dominated by tight upright to steeply reclined, meridional F_2 folds with long planar limbs and angular hinges (Colquhoun et al. 1997). An S_2 axial plane slatey cleavage is well developed everywhere in the finer sediments, and in the coarser rocks in the central part of the trough (Packham 1968a). The cleavage fans on a regional scale, dipping to the west in the east and the east in the west, and is approximately vertical in the Hill End area. A weak earlier cleavage trending at 115° has been recorded at Hill End, and a crenulation cleavage post-dates the principal slaty cleavage (Seccombe and Hicks 1989). Packham (1968a) suggested that

the axis of the trough passed through the Hill End area, trending meridionally. Greenschist facies metamorphic assemblages are developed throughout the Hill End Trough. The highest grade of metamorphism is reached in the axial third of the trough (Packham 1999), where biotite is developed over a width of about 20 km (the regional biotite zone of Smith 1969). A secondary mineral assemblage of quartz-albite-chlorite-biotite is developed within the pelitic rocks (mainly slates and phyllites), felsic lavas and volcaniclastic sandstones within this biotite zone. Lower grade metamorphic rocks occur at the trough margins (actinolite zone of Smith 1969), and the secondary mineral assemblage consists of quartz-albite-chlorite-sericite-epidote-calcite. The overall effect of this metamorphism has been a partial recrystallisation of the grains and conversion of original clay minerals to micas with a well-developed parallel orientation. Quartz and feldspar grains show greater degrees of strain to the west, also indicative of a higher degree of metamorphism in this region.

The timing of regional deformation in the Hill End Trough has been contentious. For the past two decades, the prevailing view has been that the main D_2 deformation in the Hill End Trough is of Early Carboniferous age (e.g. Powell et al. 1976; Powell and Edgecombe 1978; Fergusson and Colquhoun 1996). However, Packham (1999) and Glen and Watkins (1999) have recently provided evidence for significant thrust deformation, and a metamorphic thermal maximum (post-dating deformation) in the Middle Devonian, suggesting the main D_2 event occurred at this earlier time.

6.3 THE TURONDALE FORMATION: PREVIOUS STUDIES

The Turondale Formation was first defined, described and mapped by Packham (1958), when he devised the stratigraphic system for the Hill End Trough fill based on his mapping in the Bathurst region (southern Hill End Trough). His mapping was incorporated into the first Bathurst 1:250000 mapsheet (SI55-8; Packham 1968b), and his stratigraphic system was largely retained when the Bathurst area was remapped on a 1:100000 scale by the New South Wales Geological Survey and Australian Geological Survey Organisation (AGSO) in recent years (Raymond et al. 1997). Packham (1968a) nominated the type section of the Turondale Formation to be the south bank of the Turon River, 2.5 km northeast of the village of Turondale and 6 km west of Sofala on the Bathurst 1:100000 mapsheet (Figure 6.6). It lies on the eastern limb of a syncline and overlies the type section of the Cookman Formation. To the west the type sections of the overlying Waterbeach and Merrions Formations are also situated along this stretch of the Turon River. Packham (1968a) also outlined stratigraphic variations within the Turondale Formation in the Euchareena-Hill End-Sofala area. To the north of this area, on the original Dubbo 1:250000 Mapsheet (SI55-4; Offenberg et al. 1971) the Crudine Group

Figure 6.9: Correlations for the Hill End Trough region, comparing local stratigraphic systems established in the northwest Hill End Trough, with the succession defined by Packham (1968a) for the Hill End-Sofala region to the south, and with the system of stratigraphic nomenclature presently in use, based on recent mapping (see also Figure 6.7). Note that the Crudine Group has been expanded to include the Cookman Formation and the Merrions Formation (formerly 'Merrions Tuff'), and that the Chesleigh Formation has been elevated to group status.

was undifferentiated apart from in the northwest Hill End Trough, north of Burrendong Dam, where it was subdivided into the Lana, Dunmoogin and Guroba Formations. The general geology and stratigraphy in this region were based on a series of Honours theses from the University of Sydney resulting from a mapping project that extended from Mudgee to Wellington. Each thesis in this project established a local stratigraphic nomenclature for the thesis area, then correlations were made between adjacent thesis areas, and with the southern area mapped by Packham (1968a; Figure 6.9). In this way, the Turondale Formation in the south was correlated with locally defined units in the northwest, namely the Lana Formation (Dickson 1962), Gulf Creek Formation (Shatwell 1962) and Molly's Creek Formation (Jessup 1967). The nomenclature established by Dickson (1962) was later applied to the Dubbo 1:250000 mapsheet (Offenberg et al. 1971) for the entire northwest region. Recent 1:100000 scale mapping by the New South Wales Geological Survey and AGSO concluded that the two-fold subdivision of the Crudine Group defined by Packham (1968a, 1968b) could be applied to the Dubbo 1:250000 mapsheet, and the undifferentiated Crudine Group underlying the Merrions

Formation was subdivided into the Waterbeach and Turondale Formations. In the northwest Hill End Trough, the Lana and Dunmoogin Formations were found to be junior synonyms for the Turondale and Waterbeach Formations respectively, and this local nomenclature has now been suppressed (Colquhoun et al. 1996, 1997; Meakin and Morgan 1999). The Guroba Formation, which was correlated with the Merrions Formation to the south (Shatwell 1962: Jessup 1967), is retained as a separate stratigraphic unit, and probably represents a lateral facies variant of part of the Merrions Formation, as both have predominantly volcaniclastic sources.

The Honours theses of Dickson (1962), Shatwell (1962) and Jessup (1967) contain detailed descriptions and stratigraphic logs of the Turondale Formation in the northwest region. These are referred to and used to supplement the new information presented in this study. The facies characteristics and associations of the Turondale Formation are similar to the Merrions Formation. Both are volcanogenic formations containing thick syn-eruptive, resedimented crystal-rich deposits sourced by large subaerial or shallow marine silicic volcanic eruptions on adjacent highs. The Merrions Formation was the subject of a detailed PhD study by Cas (1977, 1978, 1979, 1983a), and this work is referred to extensively for comparative purposes.

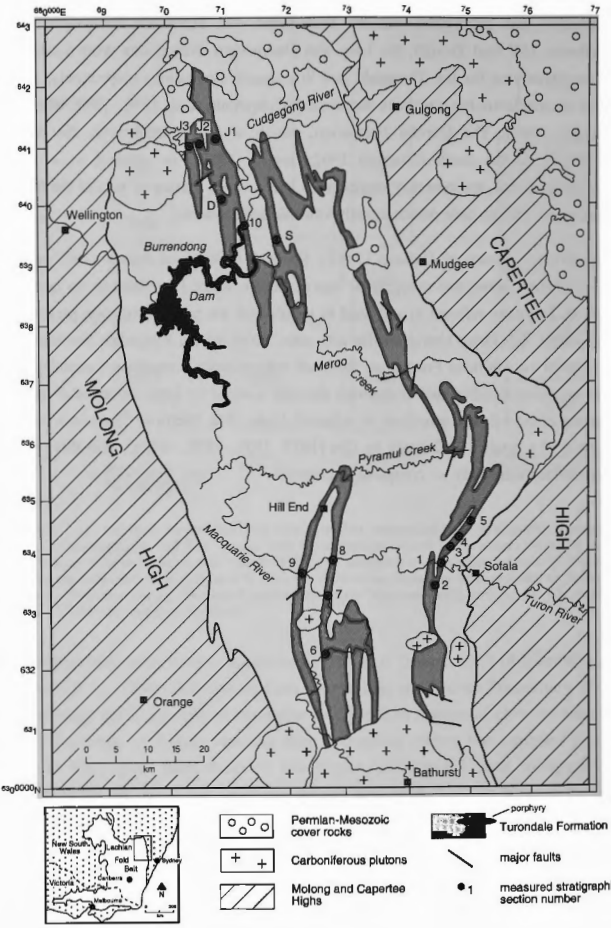

Figure 7.1: Distribution of the Turondale Formation in the Hill End Trough, and the location of measured stratigraphic sections.

CHAPTER 7

The Turondale Formation; facies analysis, provenance and palaeovolcanology.

7.1 FACIES OF THE TURONDALE FORMATION

The Turondale Formation comprises silicic volcaniclastic sandstones and breccias, chert, finely layered interbedded shales and siltstones, and minor polymictic volcaniclastic conglomerates. Dacitic porphyries of similar composition to regionally extensive silicic lavas in the overlying Merrions Formation locally intrude the formation. The Turondale Formation outcrops extensively throughout the Hill End Trough as a folded sheet-like body (Figure 7.1). The formation maintains a fairly constant thickness of 600-700m over its regional extent. The greatest variation in thickness occurs in the far northwest, where it varies from 950m to 420m over a relatively short distance strike distance of about 40 km (Jessup 1967). The only other significant anomaly in thickness occurs in the northeast between Pyramul Creek and Meroo Creek, where the formation thins locally to about 450m.

The base of the Turondale Formation is marked by an increase in the thickness of beds, and a compositional change from quartz-dominated detritus in the underlying Cookman Formation, to feldspathic volcaniclastic debris (Packham 1968a). In the southeast Hill End Trough (Sofala area) the contact is sharp, and the base is marked by thick, coarse-grained volcaniclastic sandstones, breccias and conglomerates. Elsewhere these basal coarse-grained beds are absent and the contact is taken to be the first appearance of a thick horizon of feldspathic sandstone of prominent and distinctive outcrop.

The upper boundary of the Turondale Formation represents a change from a sandstone-dominated facies to a shale-dominated facies in the Waterbeach Formation. The boundary is gradational over a distance of about 20m. The sandstones of the Turondale Formation become progressively thinner and finer in grainsize until they finally pass into siltstone bands

as the amount of shale increases. The shales and sandstones of the Waterbeach Formation are only partly derived from a volcanic source, and have a higher quartz and lithic content than those of the Turondale Formation (Packham 1968a).

The Turondale Formation comprises five main facies:

1. interbedded shale and siltstone
2. coherent dacite porphyry
3. polymictic volcaniclastic conglomerate
4. crystal-rich volcaniclastic sandstone (and breccia)
   - megaturbidite sub-facies
   - turbidite sub-facies
5. massive to laminated cherty tuffaceous sediments.

The descriptions and interpretations of facies in this chapter are based on stratigraphic sections measured throughout the Turondale Formation at the best available exposures. The raw data for these sections are included in Appendix B4. Outcrop is discontinuous throughout the Turondale Formation, but complete stratigraphic sections could be measured in some river beds and road cuttings. Fifteen measured sections, thirteen complete and two partial, form the basis for stratigraphic analysis (Figure 7.1). The sections provide good coverage of the southeast (Sofala area) and southwest (Hill End Anticline) Hill End Trough. Only one section was measured in the northwest (Mudgee-Wellington area), because five stratigraphic sections were already available for this area in the Honours theses of Dickson (1962), Shatwell (1962) and Jessup (1967). These sections contain only basic lithological information and do not exhibit important bedding features such as individual bed thicknesses within lithological intervals, graded bedding and other sedimentary structures. However, these features are described in detail in the text of the theses, enabling reasonable comparisons of the sections to be made with those measured in this study. There is no coverage of the northeastern margin of the Hill End Trough, due to poor exposure and complex folding in this area. Despite the lack of stratigraphic data for the northeast Hill End Trough, good coverage in the other three sub-areas allows comparisons to be made between them, and lateral and vertical facies variations within the Turondale Formation to be determined.

7.1.1 Interbedded shale and siltstone facies

Description Fine-grained sedimentary rocks comprise about one third of the Turondale Formation, occurring as thick pelite-dominated intervals, and as thin interbeds between crystal-rich volcaniclastic turbidites in sandstone-dominated intervals (Figure 7.2a,b). The facies comprises mainly shale and mudstone, interbedded with minor siltstone (generally < 1 cm thick) and thin sandstone (generally < 30 cm) beds. Thick shale intervals generally separate the siltstone, but cyclic repetition of siltstone and shale occurs locally, where the shale intervals between siltstone bands are only 1-3 cm thick. The thicker sandstone beds tend to group together in intervals that also have a higher proportion of siltstone. The metamorphosed and deformed shales have a well-developed cleavage that obscures any internal structure such as primary lamination. Bedding is locally defined by the thin siltstone beds that are distinctive in outcrop, as they weather out slightly more resistantly and are lighter in colour than the shales (Figure 7.2). Where shales and siltstones are interbedded, a strong cleavage may pervade the shales, whereas the siltstones still exhibit primary bedding features (Figure 7.2c).

The siltstones and sandstones have a volcanogenic composition. The siltstones comprise about 30-40% angular quartz and feldspar in roughly equal proportions and 60-70% matrix material, comprising a fine quartz-albite mosaic overprinted by sericite, chlorite, biotite and epidote. The shales have a similar composition to the siltstones, but contain only 10-20% angular quartz and feldspar disseminated throughout the matrix.

The siltstone beds are massive, planar or cross laminated, and are commonly graded. The beds have sharp, erosive bases, many of which exhibit scouring, and fine-scale flame and load structures. The beds pinch and swell and small scale slumps also occur (Figure 7.2d). These features are caused by interstratal flowage or squeezing of the more porous, waterlogged siltstone confined between more competent clay-rich shale beds.

Interpretation The shales are interpreted as representing the ambient hemipelagic marine sediment into which the other facies of the Turondale Formation were emplaced. Their recurrence throughout the ~ 5 km thick fill of the Hill End Trough (Packham 1968a) indicates a prolonged deep, quiet water (below storm wave base) depositional environment. The sharp, erosive basal contacts of the siltstones indicate lateral current transport, and they are interpreted to have been deposited under slightly higher energy conditions, from low-density turbidity currents or reworked bottom currents. This interpretation is consistent with the internal features of the beds (grading, planar or cross lamination). Intervals containing thicker

Figure 7.2a: A 20cm interval of interbedded shale and siltstone between thicker sandstone beds. Note also that a very thin layer of shale (<1cm) separates sandstone beds near the bottom of the photograph. This pattern is typical of the top ~ 100m of the Turondale Formation, which is dominated by fine- to medium-grained sandstone turbidites. Section 7, Wickett's Creek, GR 727000 6332150.

Figure 7.2b: A closer view of the interbedded shale and siltstone interval in Figure 7.2a, showing fine laminations in the siltstone interval.

Figure 7.2c: Shale and siltstone interbedded with thin sandstone beds. The shales are strongly cleaved, obliterating all primary structures, whereas the more resistant sandstone and siltstone beds preserve original bedding. The near-vertical cleavage in the shales is at a high angle to bedding. Section 5, Fairview Creek, GR 751500 6348600.

Figure 7.2d: Small slump structures in thin siltstone beds. Section 5, Fairview Creek, GR 751500 6348600.

volcaniclastic sandstone beds and a higher proportion of siltstone represent periods of increased influx of epiclastic sediments into this environment, perhaps in response to periods of higher rainfall or minor tectonic uplift in the source region. The fine sedimentary rocks are hemipelagic in character, composed of terrigenous, largely volcaniclastic material. There are no organic pelagic sediments within the sequence.

7.1.2 Turondale porphyry

Description A 250m thick dacite porphyry (informally named the Turondale porphyry in this thesis) represents the only primary igneous facies of the Turondale Formation. It is confined to the Hill End Anticline in the southwest Hill End Trough, where it outcrops as discontinuous bodies over a strike length of about 50 km (Figure 6.6). These bodies are broadly discordant within the Turondale Formation, occurring near the base of the formation to the south, and at a higher stratigraphic level to the north. They have a tabular form, with margins pinching out abruptly over a lateral distance of about 200 m. The base of the porphyry is sharp, and adjacent pelites are locally silicified, which may be a contact metamorphic effect. The top surface has intrusive characteristics. 10-20 m undulations cross cut the strike of the sedimentary turbidite sequence. On a smaller scale (< 1m) the upper surface is also irregular (Figure 7.3a) and cross cuts sedimentary features, and there is evidence of small-scale stoping of the country rock. Assimilated clasts of sandstone occur near the upper margin of the porphyry, and thin apophyses of porphyry protrude into the overlying sedimentary succession (Figure 7.3b).

The porphyry is coherent, internally massive and homogeneous, with a relatively high crystal content of 40% (Figure 7.4a). It contains Phenocrysts of euhedral plagioclase (87%) and quartz (12%) and accessory ilmenite and magnetite in a fine-grained crystalline (recrystallised?) mosaic of quartz and feldspar, and disseminated biotite, epidote and chlorite. Secondary minerals include biotite, epidote and minor chlorite and titanite.

Quartz phenocrysts range from 1 - 6 mm in diameter. They have a rounded subhedral form typical of volcanic quartz, and are commonly embayed (Figure 7.4a). Round embayments within crystals are infilled with fine-grained mosaics similar to the surrounding groundmass. The quartz exhibits straight extinction, and is clear and free of inclusions.

Plagioclase phenocrysts are generally smaller than quartz, ranging from 0.5-2 mm in length. The plagioclase crystals are euhedral and generally tabular, with marginal replacement by sericite giving some grains a ragged appearance. Some grains are subhedral with rounded corners indicating magmatic resorption, similar to the rounded quartz crystals. Phenocrysts

Figure 7.3a: Upper contact of the Turondale porphyry. Section 6, southern bank of the Macquarie River. GR 725700 6323300.

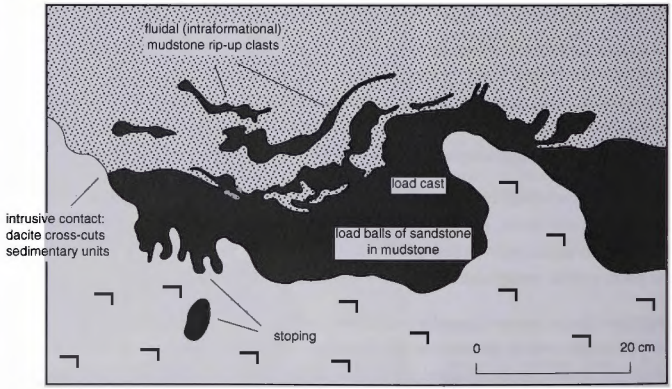

Figure 7.3b: A sketch of the upper contact of the Turondale porphyry, showing the porphyry cross-cutting bedding features in the clastic turbidite sequence, and small-scale stoping at the margin. Section 6, northern bank of the Macquarie River. GR 725700 6323300.

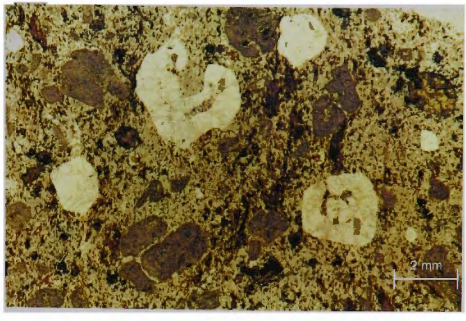

Figure 7.4a: Photomicrograph of the Turondale porphyry showing euhedral phenocrysts of quartz and plagioclase in a fine-grained granophyric groundmass. Quartz phenocrysts are commonly embayed and resorbed. Sample 95843132.

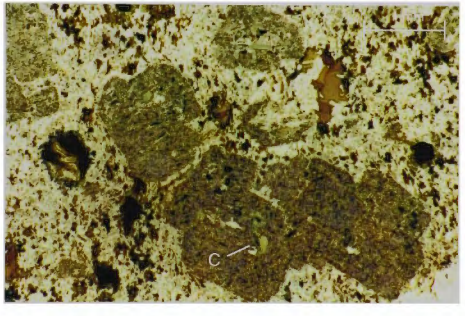

Figure 7.4b: A small glomeroporphyritic cluster of euhedral feldspar crystals. Te crystals contain small bleb-like inclusions of chlorite (C). Note also, anhedral biotite of metamorphic origin (Bt). Sample 95843132.

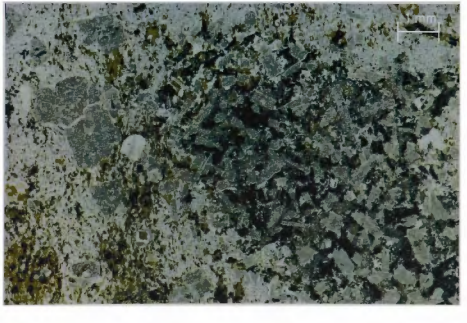

Figure 7.4c: Large glomeroporphyritic aggregate of plagioclase crystals, biotite, chlorite, epidote and opaques. Sample 95843132.

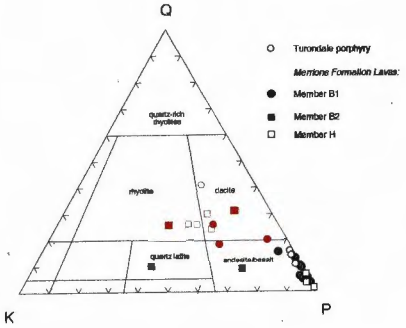

Figure 7.5: Classification of the Turondale and Merrions Formation porphyries (Streckeisen 1976). Black data points represent modal proportions of phenocrysts, and red data points represent CIPW normative proportions of quartz, plagioclase and K-feldspar, calculated from the geochemistry of the porphyries. The petrographic-based classification system of Streckeisen (1976) is generally based on modal mineral abundances. However, this presents a problem for porphyritic rocks, because minerals in the fine-grained groundmass are not included in modal calculations. In this case, porphyries classify as andesites based on modal analyses and as dacites based on normative compositions, indicating that quartz and K-feldspar concentrate in the groundmass, rather than occurring as phenocryst phases.

range from untwinned, to having well developed multiple twinning, with straight to undulose extinction. Only a few zoned crystals were recognised. The plagioclase is dusty in appearance due to clay, sericite and epidote alteration. The crystals contain bleb inclusions of chlorite, clinozoisite and epidote which are interpreted to have been volcanic glass originally (Figure 7.4b). Glomeroporphyritic aggregates of plagioclase are common. They range from small clusters of a few grains (1-6 mm in length), to large aggregates (> 1 cm in length) which may also contain coarse biotite, epidote, chlorite and ilmenite (Figures 7.4c).

The groundmass has a uniform mosaic texture of crystalline quartz and feldspar and disseminated secondary minerals (biotite, epidote, chlorite), which may represent a recrystallised metamorphic texture. Rare amygdales occur throughout the groundmass. They have a flattened oval shape and consist of equidimensional aggregates of epidote, quartz, biotite and minor chlorite.

Unit	Quartz%	Plag%	K-spar%	Misc%	Groundmass%
Turondale Porphyry	12	85.1	0.9	2	60.2
Merrions Formation Lavas					
Member B(1)	7.3	85.5	0.8	6.3	65.2
Member B(2)	9	53	33	4.7	68.0
Member H	3.5	81.8	0.2	14.6	61.9

Table 7.1: Average modal abundance of phenocrysts in the Turondale Porphyry and Merrions Formation lavas quoted in terms of percentage of the phenocryst population. The miscellaneous category refers to ilmenite in the Turondale Porphyry, and in the Merrions Formation Lavas, includes indistinguishable textural components of possible metamorphic origin, vesicles and amygdales. Data for the Merrions Formation are from Cas (1978).

A secondary mineral assemblage of biotite, epidote, chlorite and titanite formed during biotite-grade greenschist facies metamorphism. Biotite occurs as aggregates of anhedral to subhedral grains rather than as large euhedral crystals, indicating a metamorphic rather than primary origin (Figure 7.4b,c). Epidote (+/- biotite) pseudomorph equant to tabular grains that may represent a primary mafic phase (pyroxene or amphibole. The epidote infilling amygdales may have formed by the release of Ca 2^+ from original calcite during albitisation. The chlorite may represent original glassy material. Titanite forms reaction rims around ilmenite grains, or completely replaces the original crystals.

Comparison with porphyries in the Merrions Formation

Three conformable, coherent porphyritic lavas are recognised within the clastic sequence of the Merrions Formation (Cas 1977, 1978). Two of the porphyries (members B1 and H) are regionally extensive, and have a plagioclase-rich, quartz-poor phenocryst assemblage (Cas 1978). The third (member B2) is a small local body of K-feldspar-bearing rhyodacite. The porphyries classify as dacites based on their silica content (63-70% SiO_2), normative proportions of quartz, plagioclase and K-feldspar (Figure 7.5) and alkali and immobile element geochemical classification systems (Figure 7.6).

The modal abundance of quartz and plagioclase in the Turondale porphyry is almost identical to the regionally extensive porphyritic lavas of the Merrions Formation (Table 7.1). However, the Turondale porphyry is almost entirely devoid of amygdales, whereas vesicularity is estimated to have been as much as 10-15% in the Merrions Formation

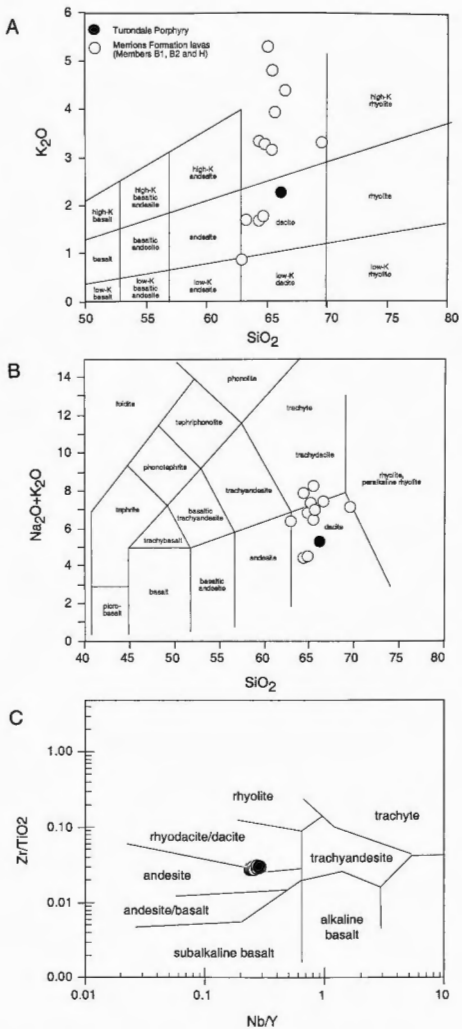

Figure 7.6: Classification of the Turondale porphyry and Merrions Formation lavas using: (a) the K_2O-SiO_2 geochemical system for volcanic rocks of Peccerillo and Taylor (1976), modified after Gill (1981); (b) the geochemical classification system for volcanic rocks of LeBas et al. (1986); and (c) a classification system based on immobile trace elements (Winchester and Floyd 1977).

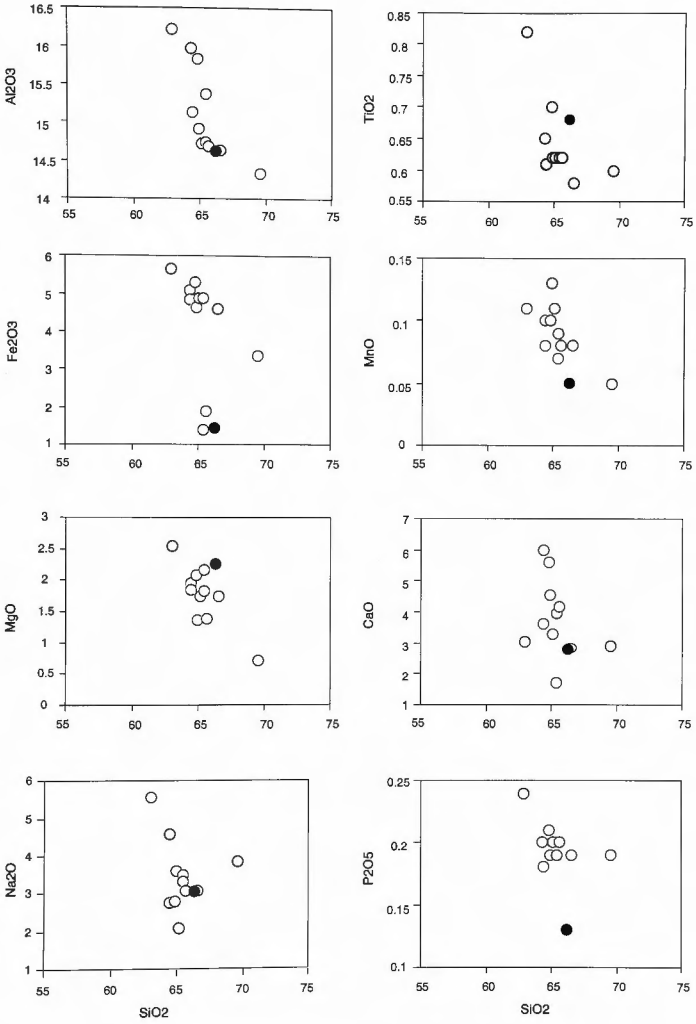

Figure 7.7a: Major element geochemistry of the Turondale Porphyry and Merrions Formation lavas.
● = Turondale Porphyry ○ = Merrions Formation lavas (Members B1, B2 and H)

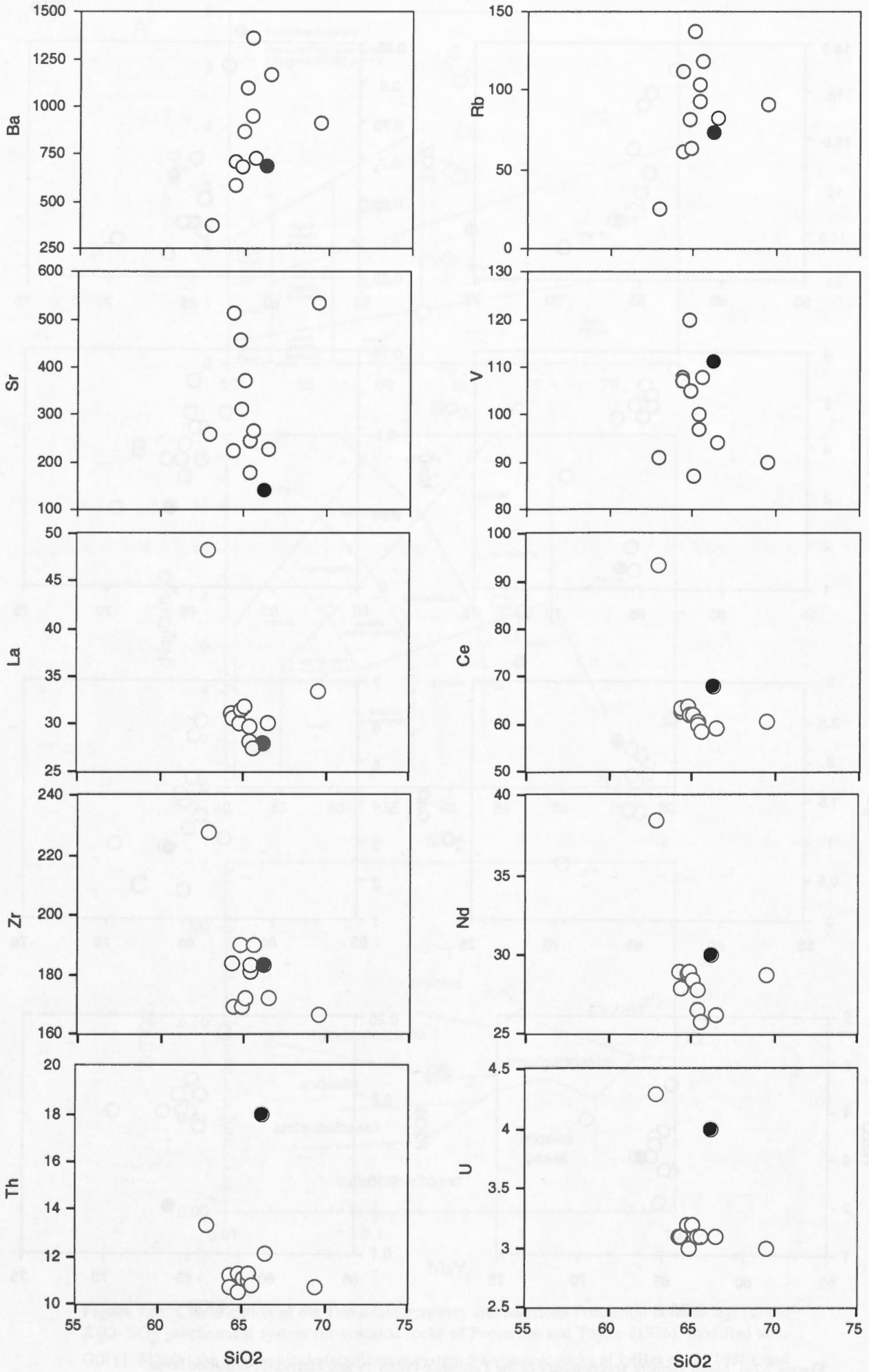

Figure 7.7b: Trace element geochemistry of the Turondale Porphyry and Merrions Formation lavas.

● = Turondale Porphyry ○ = Merrions Formation lavas (Members B1, B2 and H)

porphyries (Cas 1978). The porphyries of both formations form a reasonably coherent geochemical group for most elements, plotting in close association on variation diagrams (Figure 7.7). There is some scatter of K_2O, Na_2O and CaO, as alkali elements are highly mobile and prone to redistribution during devitrification, diagenesis and regional metamorphism (Vallance 1965; Lipman 1965). The Turondale porphyry has a notably lower P_2O_5, and slightly higher Fe, Ti, Th and U contents than most of the porphyries of the Merrions Formation, but as only one sample was analysed, this could be controlled by a local concentration of accessory phases such as apatite, magnetite/ilmenite zircon, rather than indicating a different initial magmatic chemistry.

Interpretation The porphyries in the Merrions Formation are considered to have been emplaced as lava flows (Cas 1978). Member B1 is interpreted as a lava flow because it has a topographic influence on the sedimentation patterns of overlying units. Volcaniclastic members within the formation (members D and E) drape over an axial high created by the very thick (~350m) B1 lava flow, and member H lava ponds against its northeastern margin (Cas 1977). Member H is interpreted as a lava flow or subaqueous lava dome complex because the top margin is locally quench fragmented, and the clasts are reworked into the overlying sediments. This suggests the porphyry was at least partly extrusive, and exposed to erosive action accompanying emplacement of the overlying sediment. The porphyry may have intruded into the shallow levels of the unconsolidated sediment pile, and been locally exposed by contemporary erosion (Cas 1978).

In contrast, field evidence suggests that the Turondale porphyry was emplaced as a sill. The porphyry is discordant within the Turondale Formation and the contacts have intrusive characteristics. There is no quench fragmentation and brecciation at the porphyry margins to suggest interaction with wet, unconsolidated sediments or water, as occurs in the Merrions Formation. The paucity of vesicles in the Turondale porphyry compared with the Merrions Formation lavas may relate to its intrusive character, having been emplaced in the sub-surface under a higher confining pressure than the Merrions Formation sea-floor lavas, and so suppressing exsolution.

The mineralogy and chemistry of the Turondale porphyry suggests a genetic association with the regionally extensive porphyries of the Merrions Formation. It have been derived from the same source as member B1 lava, which is most similar in composition, and has the closest spatial relationship with the Turondale porphyry. Member B1 is lobate in plan view, thinning north-westwards, and is thickest in the south where the Turondale porphyry is confined in outcrop (Figure 7.8). It is possible that these porphyries were emplaced coevally, with some

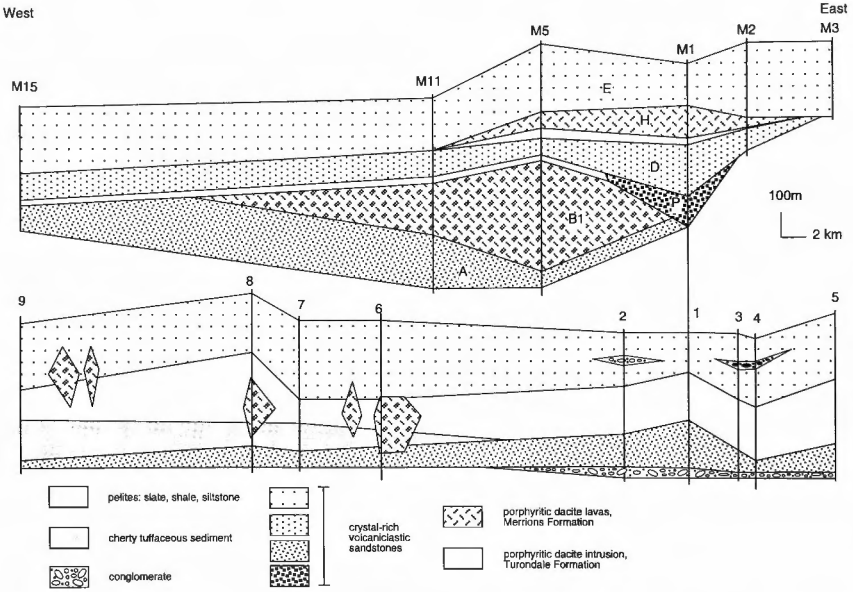

Figure 7.8: East-west (Sofala-Hill End) stratigraphic profile of the Merrions Formation and Turondale Formation, showing the spatial distribution and relative stratigraphic positions of the Merrions Formation lavas and the intrusive Turondale porphyry. Note that volcaniclastic Member D of the Merrions Formation thins over an axial high created by Member B1 lava flow, and Member H lava ponds within a depression along its eastern margin. Note also the broadly diachronous character of the Turondale porphyry. The correlation profile of the Merrions Formation is from Cas (1977). The thickness of the Waterbeach Formation is not accurately depicted except at section 1. For the location of measured stratigraphic sections for the Turondale Formation, see Figure 7.1.

of the magma intruding the Turondale Formation while the remainder extruded into the basin at the time the volcaniclastic sequence of the Merrions Formation was emplaced.

7.1.3 Polymictic volcaniclastic conglomerates

Description Polymictic cobble/pebble volcaniclastic conglomerates form a minor component of the Turondale Formation. In the southeast Hill End Trough (Sofala district), coarse conglomerate beds occur at the base of the formation. Their matrix ranges from fine-grained shale to volcaniclastic sandstone in composition. Sorting is poor and clasts range in size up to 60 cm in diameter, averaging 5-15 cm in diameter. The clast population consists mainly of acid volcanic rocks, limestone and shale. Rounded acid volcanic rocks include quartz-feldspar porphyry, welded ignimbrite, fine-grained volcaniclastic cherts and chlorite vitriclasts (Figure 7.9a,b). Limestone clasts are angular to sub-rounded in shape (Figure 7.9a-c). The limestones are recrystallised, and are commonly micritic lime mudstones which have a terrigenous sediment component (Figure 7.9d). They are fossiliferous but do not contain macrofossils that are age diagnostic, and no microfossils have been found. Fossils identified include *Favosites* sp., *Tryplasma* sp., corals and Pentamerid brachiopods (Packham 1968a). Shale intraclasts derived from contemporaneous basin sediments have a range of sizes, and dimensions of 1 x 3m have been recorded (Packham 1968a). The medium- to coarse-grained volcaniclastic sandstone matrix consists of angular quartz and feldspar crystal fragments and minor small lithic fragments, in the same modal proportion as the crystal-rich volcaniclastic sandstone facies described in Chapter 7.1.4.

South of the type section, conglomerate beds also occur locally near the top of the formation, interbedded with volcaniclastic sandstones and shales over an ~100 m thick interval (Figure 7.10). Part of this upper interval is well exposed in road cuttings on the Turon road, near Box Ridge Road (GR 430335). Like the basal conglomerates, they contain rounded pebbles and cobbles of acid volcanics, fossiliferous limestone, shale and also quartzite, in a medium-grained volcaniclastic sandstone matrix. Limestone and shale fragments have been flattened during deformation, to form lenses parallel to the cleavage plane. The clasts range in size from 2 cm to 20 cm, with an average diameter of about 5 cm. The largest recorded block of limestone measures 10x30 metres (Packham 1968a). Similar large allochthonous limestone blocks are recorded in the Hill End Trough sequence in the Limekilns area about 20 km to the southeast, where they are interpreted to have been shed from the adjacent carbonate platform of the Capertee High. Most of the conglomerate beds exhibit a high clast concentration (50-55%) and a close packing of clasts (Figure 7.11a), although some beds have an open framework configuration of clasts supported by a high proportion of matrix (~60%). They

Figure 7.9a: Conglomerate at the base of the type section (Turon River), showing clasts of fossiliferous limestone and abundant clasts of shale, in a matrix of volcaniclastic sandstone. Base of the type section, southern bank of the Turon River, GR 745600 6338500).

Figure 7.9b: Basal conglomerate exposed in Crudine Creek north of the type section, showing rounded black, porphyritic chlorite vitriclasts (below the hammer), and rounded clasts of fossiliferous limestone. Section 4, northern bank of the Turon River, GR 745600 6338500).

Figure 7.9c: Basal breccia exposed in Crudine Creek north of the type section, showing abundant angular limestone clasts and some rounded chlorite vitriclasts, in a matrix of volcaniclastic sandstone. Section 4, northern bank of the Turon River, GR 747600 6342200.

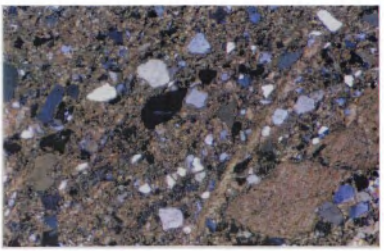

Figure 7.9d: Photomicrograph of a limestone clast, showing its micritic character (i.e. detrital grains in a limestone mud matrix). Sample 95843059.

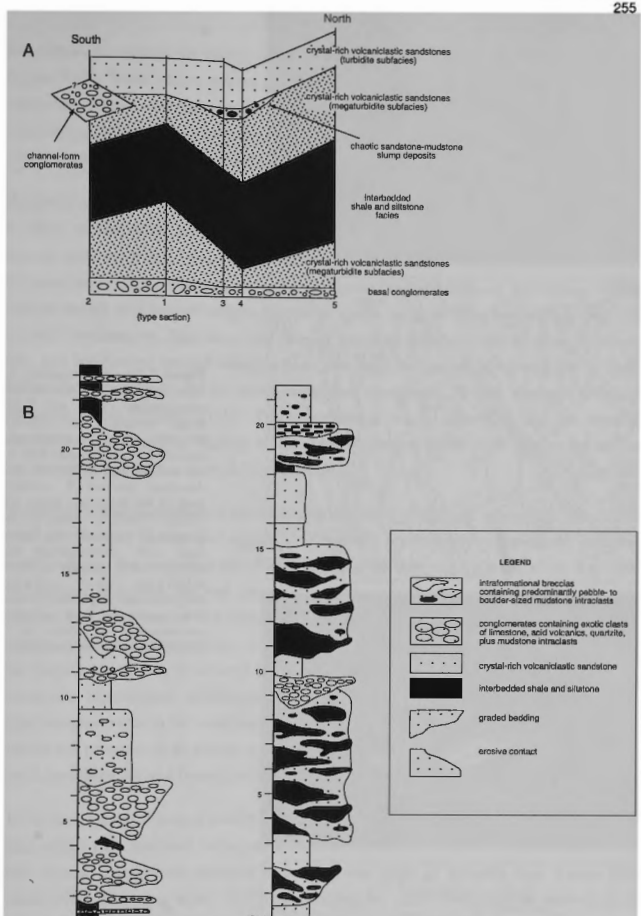

Figure 7.10: (a) Correlation profile for stratigraphic sections measured in the southeast region of the Hill End Trough, showing the approximate stratigraphic position conglomerate horizons in the Turondale Formation. (b) Measured sections through: (1) the channel-fill conglomerates near the top of the Turondale Formation, exposed in a road cutting on the Turon Road (section 2; GR 430335). Only part of this conglomeratic interval is exposed. Packham (1968a) estimates its full thickness to be over 100m; and (2) intraformational breccias (slump deposits) exposed at a similar stratigraphic level in sections 3 and 4 (GR 463413 and GR 473425).

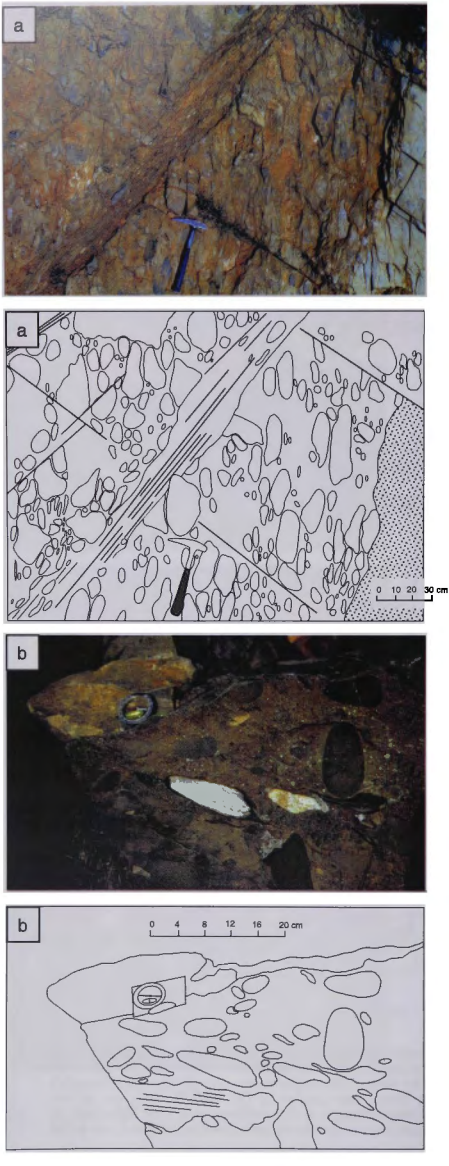

Figure 7.11: A comparison of: (a) proximal channel-fill conglomerates from the Turon Road cutting (GR 743000 6333500); with (b) conglomerates deposited in thin tabular beds on the western limb of the Hill End Anticline (Section 9, northern bank of the Macquarie River, GR 722250 6336500). Most of the channel-fill conglomerates have a high clast concentration and exhibit a close packing of clasts, whereas the tabular conglomerates, deposited by mass flow processes, have a lower concentration of clasts in a matrix-supported configuration.

have a lensoidal channel geometry, with bases clearly erosive into the underlying sediments (Figure 7.10). Some exhibit graded bedding. To the north of the type section, a slumped mudstone-sandstone intraformational breccia, about 15m thick, displaying chaotic bedding relationships between volcaniclastic sandstone and mudstone, occurs at a similar stratigraphic level to these conglomerate beds (Figure 7.10).

Elsewhere in the Hill End Trough, conglomerate beds are rare, and mainly occur as thin (< 10m) tabular beds distributed throughout the sequence. Some are intraformational breccias, containing only intraclasts of shale in a sandstone matrix (Figure 7.12). Others have the same exotic clast population as the conglomerates in the southeast, containing rounded clasts of mainly acid volcanic origin. Limestone clasts are generally less common. *Favosites* sp., and *Tryplasma* sp., have been identified in limestone pebbles in the Mudgee-Wellington area, and transported crinoid columns have also been recognised (Shatwell 1962; Jessup 1967). These conglomerates are matrix-supported, comprising 25-40% clasts in a shale or sandstone matrix (Figure 7.11b). The beds have a tabular geometry, and are internally massive and structureless, lacking sedimentary structures. Some beds grade upward into coarse sandstone which may be diffusely stratified.

Interpretation The association of the conglomerates with hemipelagic mudstones (interbedded shale and siltstone facies) and turbiditic sandstones (crystal-rich volcaniclastic sandstone facies) indicates that they were deposited in a relatively deep water, below storm wave base environment. However, the high degree of rounding and diverse composition of the clasts indicates they were eroded and reworked in a high energy, above wave base environment such as a shallow marine or fluvial setting, prior to resedimentation in a deep marine setting. The volcanic clasts may be derived from the same source region as volcanic detritus in the crystal-rich volcaniclastic sandstones (described in Chapter 7.1.4). Quartzite clasts in the upper conglomerates in the southeast are probably derived from Ordovician sediments, and indicate the presence of an emergent land mass in the source region. The limestone clasts would have been derived from carbonate shelf deposits flanking the trough margins.

The erosive, lensoidal beds of coarse clast-supported conglomerate outcropping in the Turon Road cutting may represent fractional sedimentary processes within channel environments. Such channel deposits are common in the proximal parts of turbidite fans (Lowe 1982; Walker 1984; Pickering et al. 1989), suggesting the upper conglomerate interval in the southeast is proximal to the source region. This is supported by the presence of large limestone blocks which would have been resedimented short distances downslope by gravitational processes (slump or slide). The conglomerates in the thick upper interval could

Figure 7.12a: Intraformational breccia in the upper Turondale Formation, exposed along the northern bank of the Cudgegong River. Section 10. GR 712800 6496400.

Figure 7.12b: A closer view of the above breccia, showing the extremely fluidal outlines and preserved delicate apophyses of the mudstone intraclasts. The light-coloured matrix comprises coarse volcaniclastic sandstone. Note also, that loading occurs at the base of the bed into the underlying mudstone, in the lower left hand corner of the photograph (L).

Figure 7.12c: Intraformational breccia in the upper Turondale Formation, exposed in the type section (GR 744800 6338350). This bed is thinner (about 1m thick) than the conglomerate beds illustrated in Figures 7.12a and b, and the clasts are smaller overall. The light-coloured volcaniclastic sandstone matrix grades from a coarse-grained sandstone at the base, to a medium-grained sandstone at the top of the bed.

have been dislodged from the shoreline by seismic activity, possibly related to volcanic eruptions in the source region. The chaotic mudstone-sandstone slump deposits which also occur at this stratigraphic level in the southeast may have a similar origin, representing local slope collapse in a proximal fan setting.

The massive to normally graded matrix-supported tabular conglomerate beds at the base of the Formation in the southeast, and randomly distributed throughout the sequence elsewhere, were emplaced by high density turbidity currents. Internally massive beds suggest high clast concentrations and grain interactions, whereas graded bedding reflects lower clast concentrations and fluid turbulence playing an important role in grain support (Lowe 1982; Pickering et al. 1989). Where the beds grade upward into pebble-free diffusely-stratified coarse sandstone, this upper interval represents fractional sedimentation due to increased fluid turbulence in a waning density current, and is analogous to Bouma division *b* in sands.

7.1.4 Crystal-rich volcaniclastic sandstones

Crystal-rich volcaniclastic sandstone (CRVS) is the most common facies in the Turondale Formation, comprising over half of the sequence. The sandstones are clast-supported grain aggregates of juvenile volcanic detritus (Figure 7.13a), which include angular sand-sized crystals and crystal fragments, devitrified volcanic glass fragments, rare tube pumice and pseudomorphed shards. The chief framework constituents consist of quartz and plagioclase in roughly equal proportions. K-feldspar only occurs in trace amounts as perthites. Accessory phases include large euhedral zircon crystals, ilmenite, magnetite and apatite. The sandstones have a minor lithic component which consists predominantly of exotic acid volcanic fragments and sedimentary intraclasts. A fine secondary matrix of quartz-albite±chlorite±epidote±clinozoisite±sericite±biotite fills the interstitial spaces.

The crystals show a complete range in grainsize from a maximum of 2 mm down to fine silt-sized grains, with an average grainsize of less than 1 mm. The sandstones have an immature texture. Grains are euhedral to angular, and show no signs of rounding by sedimentary processes. Some grains, particularly quartz, show rounding by magmatic corrosion, or by grain boundary modification during metamorphism (biotite grade). The framework of the sandstones is generally well sorted. Where poor sorting occurs, it is due to the local presence of pebble- to cobble- sized lithic fragments, which are particularly common in lithic breccias at the base of the thicker sedimentation units, or in thin horizons of mudstone intraclasts within sedimentation units.

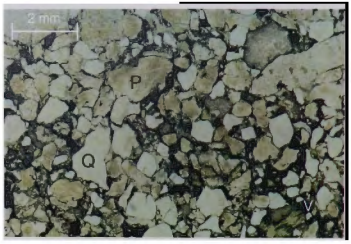

Figure 7.13a: Photomicrograph of the CRVS, showing the clast-supported framework of angular quartz (Q) and plagioclase (P) grains. Chlorite vitriclasts (V) occur in the bottom right hand corner of the photograph. Sample 95843002.

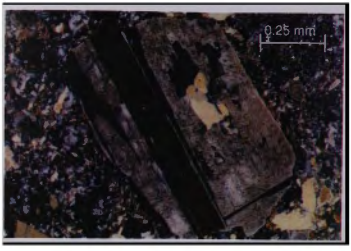

Figure 7.13b: Plagioclase crystal showing multiple twinning, and small bleb-like inclusions of quartz. Sample 95843086.

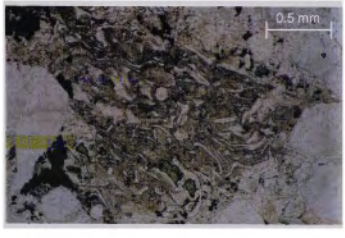

Figure 7.14a: Chloritised ignimbrite clast. Sample TUR 13.

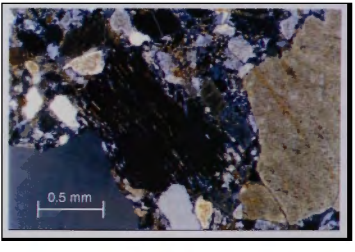

Figure 7.14b: Clast of tube pumice. Sample 95843086.

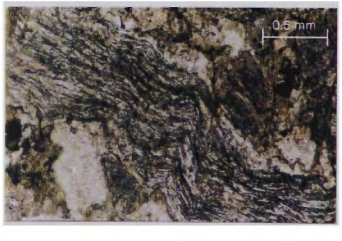

Figure 7.14c: Clast of tube pumice. Sample TUR 135.

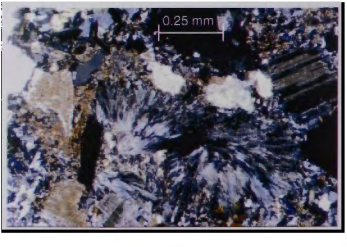

Figure 7.14d: Small clast exhibiting a spherulitic devitrification texture. Sample TUR 135.

Composition

Quartz: Quartz grains have a range of optical properties, from straight to undulose extinction, through to partial or complete recrystallisation with increasing metamorphic grade. However, even at the higher biotite facies metamorphic grade, a large proportion of quartz grains exhibit their original volcanic affinity. This is due to the fact that the large detrital grains have a random crystallographic orientation, and so show varying degrees of response to deformation. The proportion of crystals exhibiting undulose extinction decreases with higher metamorphic grade, as the polygonisation process releases strain in the grains. The volcanic quartz has straight extinction, is clear and generally free of inclusions apart from minor rutile. Crystals are monocrystalline, were originally bipyramidal and are generally fragmental in form. Rounding of grain corners and grain fracturing by magmatic resorption are common, and some grains exhibit resorption embayments. Some quartz grains contain chlorite inclusions interpreted to be altered volcanic glass, a feature also recognised in the plagioclase crystals of both the Turondale and Merrions Formations (Packham 1968a; Cas 1983a).

Feldspar: Only a small proportion of feldspars, about 15%, exhibit (multiple) twinning, and the twin planes are commonly diffusely defined. Where it is possible to use twinning as an indicator, the plagioclase is albite in composition (An_{8-11}). Some grains exhibit secondary glide lamellae, which are irregular and show a tendency to bunch up and bend wherever a crystal is slightly bent. No K-feldspar fragments have been observed in the volcaniclastic sandstones: some thin sections were etched and treated with sodium cobaltinitrate with negative results. On this basis, the abundant untwinned feldspars are identified as albite. Untwinned metamorphic albite was recognised and described by Middleton (1972), who concluded that the diffusion and eventual obliteration of twinning can be an effect of albitisation. The presence of calcite and Ca-Al silicates such as epidote and clinozoisite indicates the transfer of appreciable amounts of calcium. In some cases the calcite and Ca-Al silicates are seen replacing feldspar. This suggests the plagioclase was originally more basic, and that Ca^{2+} has been released and replaced by Na^{+} during albitisation.

Plagioclase grains are euhedral, subhedral or angular, with some grains preserving their original tabular or lath shape. The euhedral form, and an absence of zoning, indicate the feldspars have a volcanic rather than plutonic origin. Some grains contain inclusions of homogeneous chlorite or clinozoisite that are interpreted as altered glassy inclusions, as also observed in feldspars in the Turondale porphyry.

K-feldspar only occurs in trace amounts, as perthite and antiperthite (Figure 7.13b). Perthite unmixing increases with metamorphic grade, producing more inhomogenous grains. This relationship to metamorphic grade suggests the origin of the perthitic textures is metamorphic rather than igneous. An unusual feature of some feldspar grains is that they contain what appear to be quartz-bleb inclusions (Figure 7.13c). This feature is commonly associated with perthites, as the unmixing process may also release free silica to form these quartz inclusions.

As with quartz, the optical and textural properties of feldspar vary with increased strain and metamorphic grade. Many of the feldspars show features analogous to polygonisation and granulation, exhibiting undulose to patchy extinction, where the original grain is broken up into a number of differently oriented sub-grains, producing a checker board effect. The feldspar is always partly dusted with fine sericite and overprinted by small grains of epidote and to a lesser extent, chlorite and calcite. Both quartz and feldspar generally have sharp grain boundaries, but at higher metamorphic grades, recrystallisation and marginal replacement of grains by fine sericite and biotite gives grains an irregular, ragged appearance. Some plagioclase grains have reacted with the matrix, producing a myrmeckitic texture at the grain margins (Figure 7.13d).

Lithic fragments: The lithic component is only minor, but consists of a variety of different rock types. Pebble- to cobble-sized lithic clasts occur in breccias at the base of some of the thickest sandstone beds, and gravel-sized clasts from as small as 2 mm (only slightly larger than the crystal population) up to 20 cm are dispersed throughout the sandstones. There are two types of lithic clasts: intraclasts derived from contemporaneously deposited basin sediments and exotic clasts derived from the source area. Most of the exotic lithic fragments are igneous, although micritic limestones also occur throughout the succession.

Intraclasts: Fluidal mudstone intraclasts are the most common of the basin derived lithic clasts, occurring both as isolated clasts and concentrated in horizons, generally at the base of sandstone beds, but also occurring within beds. Their dark grey colour contrasts with the lighter grey sandstone host, making them distinctive in outcrop (Figure 7.12). In thin section the mudstones consist of a very fine granular mosaic of quartz, opaques and sericite. Other types of intraclasts consist of coarser granular quartz-sericite or quartz-biotite mosaics. These clasts have the same composition and texture as metamorphosed fine-grained sediments (siltstones, cherty sediments and volcaniclastic sandstones) that comprise much of the Turondale Formation.

Exotic clasts: Most of the exotic lithic fragments are igneous, and include acid volcanics, chlorite vitriclasts, and basic to intermediate rocks. Acid volcanic clasts are both porphyritic and holocrystalline in texture, and it is possible that the holocrystalline clasts are fragments of groundmass of porphyritic rocks. The porphyries contain phenocrysts of plagioclase and quartz, and where these are euhedral, it may be an indication that they are derived from a coherent igneous body such as a lava, or they may be fragments of pumice (Figure 7.14a). Other porphyritic fragments are clearly ignimbrites. They contain angular rather than euhedral crystal fragments in a finer grained cherty matrix, and many of these clasts contain shards pseudomorphed by chlorite (Figure 7.14b). Fine chert fragments, which may also contain pseudomorphed shard forms, are interpreted to be fragments of ignimbrite matrix. Some fragments of tube pumice (Figure 7.14c) and fragments exhibiting devitrification textures were detected (Figure 7.14d).

Basic rock fragments are far less common than acid volcanics. Most are fine-grained and contain needle-shaped laths of feldspar, generally with a flow-oriented trachytic texture. Some are coarser grained or porphyritic, and contain twinned lath-shaped feldspar grains. Glomeroporphyritic feldspar aggregates are common, and are probably derived from intrusive bodies or lavas.

Altered chlorite vitriclasts are common in sandstones of the Merrions Formation, where they are widespread, and may concentrate in horizons to form vitriclast boulder orthobreccias consisting of vitriclast boulders in a volcaniclastic sandstone matrix (Cas 1983a). Chloritic vitriclasts are present to a lesser degree in the Turondale Formation, and mainly occur as sand-sized fragments dispersed throughout the sandstones. These are occasionally visible in outcrop, but are more commonly detected microscopically (Figure 7.15a). These sand-sized homogeneous chlorite patches are interpreted to be reconstituted glassy volcanic fragments, and in some cases lath shaped feldspar crystals are embedded in the chlorite patches and shard forms are preserved in the chlorite matrix, supporting this origin (Figure 7.15b). They have irregular boundaries, and tend to have been squeezed into the interstices of the sandstone framework during compaction. Some are fragmental in shape and have possible bubble wall textures.

Larger vitriclast cobbles and boulders similar to those in the Merrions Formation only occur in the coarse sandstones, conglomerates and breccias at the base of the formation in the southeast Sofala district (Figure 7.15c,d). The vitriclast boulders are irregular, flattened tar-black chlorite bodies that have a random orientation within the coarse sandstone framework. In contrast to the host sandstones, the boulder-sized vitriclasts have an open framework

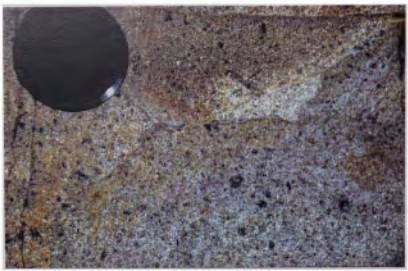

Figure 7.15a: Sand-sized chlorite vitriclasts (black), scattered through lighter coloured crystal-rich volcaniclastic sandstone, comprising mainly quartz and plagioclase crystals and crystal fragments. Section 10, south bank of the Cudgegong River. GR 713000 6496400).

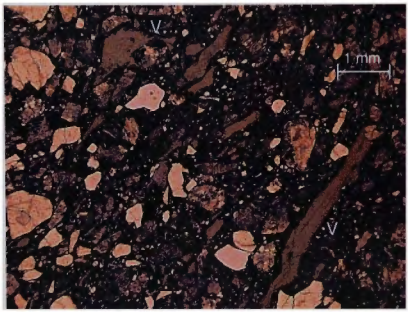

Figure 7.15b: Sand-sized chlorite vitriclasts in thin section (V). The clasts appear as elongate, ragged shreds, suggesting they were compacted during deposition, burial and deformation of the unit. Sample 89123059.

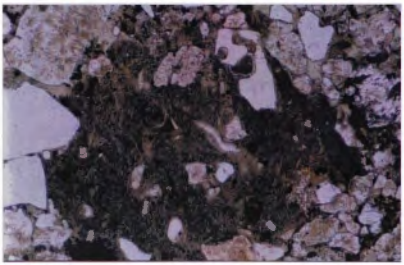

Figure 7.15c: Photomicrograph of a larger chlorite vitriclast, illustrating the porphyritic texture of the clasts. Sample TUR 73.

Figure 7.15d: Close-up of cobble-sized chlorite vitriclasts at the base of a thick megaturbidite bed. The porphyritic character of the vitriclasts is clearly illustrated. Type Section, south bank of the Turon River. GR 745600 6338500.

texture. They contain quartz and feldspar phenocrysts that are euhedral or rounded, and commonly embayed, set in a homogeneous fibrous chloritic groundmass, interpreted to be altered volcanic glass. These vitriclasts are interpreted as modified porphyritic volcanic rock fragments (Packham, 1968a; Cas, 1983a).

Limestone fragments, some containing crinoidal debris, tend to be concentrated as cobbles in conglomerate and breccia horizons (Chapter 2.2.5). However small round patches of polycrystalline calcite seen in thin section occur sporadically throughout the crystal-rich volcaniclastic sandstones, which may represent small limestone clasts.

Shards: Pseudomorphed shard forms are rarely preserved and only observed in the fine-grained siliceous sandstone to pelitic intervals at the top of thick graded sedimentation units where, if preserved, they are abundant (Figure 7.16). Their angular, cuspate forms are replaced by fine granular epidote. This suggests that much of the epidote in the matrix of the sandstones may replace original glassy ash (Packham 1968a; Cas 1983a).

Matrix: The matrix of the sandstones is a fine-grained mosaic of quartz and albite, and disseminated secondary minerals, consisting of epidote, clinozoisite, chlorite, sericite, biotite and calcite in varying proportions. The fine granular quartz and feldspar in the matrix may be primary in the chlorite grade rocks, but in the higher biotite grade, the matrix is clearly coarser due to recrystallisation, and it can be difficult to distinguish the matrix from recrystallised framework grains.

Epidote and chlorite are the most prominent secondary minerals in the matrix in chlorite grade metamorphic zones (eastern Hill End Trough). Chlorite is generally pale green in colour, fine-grained and has a ragged, platy appearance which contrasts with the large purple or brown fibrous patches that represent chlorite vitriclasts. Epidote is colourless, but can be weakly pleochroic (green-yellow), and is granular in form. Short prismatic crystals of clinozoisite are also abundant in the matrix. They are colourless, have high relief, and distinctive blue interference colours under crossed polars (Figure 7.17a). Authigenic calcite generally occurs as irregular patches replacing the matrix. Sericite is a minor component of the matrix, and more abundant in chlorite grade rocks. Some bright orange Fe-Mg clays occur in chlorite grade rocks (Figure 7.17b). As in the Turondale porphyry, ilmenite grains are commonly surrounded by a rim of titanite (Figure 7.17c). The titanite formed by Ca-releasing reaction between ilmenite and plagioclase. At higher metamorphic grades in the western Hill End Trough, biotite is the most abundant metamorphic mineral. It occurs as fine to coarse aggregates of anhedral to subhedral crystals that show a preferred orientation in

Figure 7.16: Abundant chloritised shards preserved in the fine-grained pelitic flow top of a crystal-rich volcaniclastic megaturbidite. Sample 95843005.

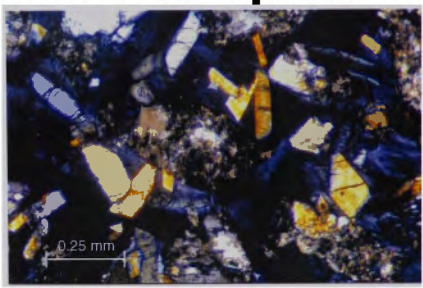

Figure 7.17a: Clinozoisite crystals in chlorite, overprinting the CRVS matrix. Sample 95843016.

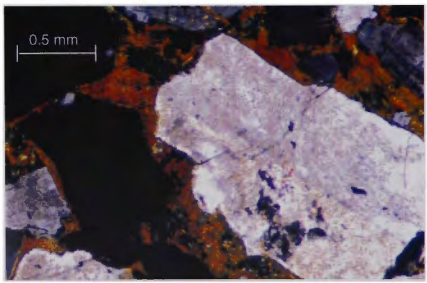

Figure 7.17b: Bright orange Fe-Mg clay overprinting the CRVS matrix. Sample 95843026.

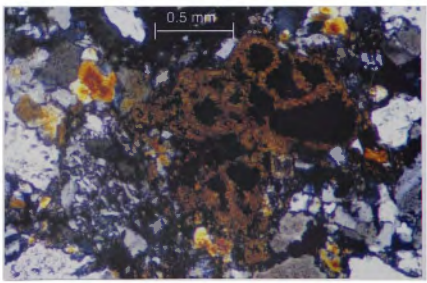

Figure 7.17c: Titanite reaction corona developed around ilmenite crystals (opaque). Sample 95843017.

Formation	bed thicknesses (m)			
	mean	median	maximum	beds over 1m
Turondale Formation	2.4	0.7	55	38%
Turondale Fm (beds < 4m)	0.95	0.6	-	-
Waterbeach Formation	0.6	0.4	4.5	11%
Guroba Formation	0.7	0.4	22	13%
Merrions Formation	30	-	~ 185	-

Table 7.2: A comparison of bedding thicknesses for formations of the Crudine Group. No data are available for the Cookman Formation. Data for the Merrions Formation are from Cas (1979).

some samples. The proportion of chlorite and calcite in the matrix decreases in the biotite zone where they may be converted to micas, but the amount of epidote remains constant.

Sedimentary structures

The CRVS can be divided into two sub-facies; turbidites and megaturbidites, based on the thickness of the beds. There is no precise formula for defining the size of megaturbidites; they are defined in general terms, as beds of exceptional thickness or volume relative to the host succession (Bouma 1987). A statistical evaluation of bedding thickness in the Turondale Formation suggests that any beds over four metres thick are anomalously large in size (Figure 7.18). On this basis, about 12% of beds can be classed as megaturbidites. Beds ≤ 4 m thick are taken to represent normal turbidite sedimentation for the formation.

To assess whether these beds are anomalously thick in the broader context of the Hill End Trough succession, they are compared with the thickness of sedimentation units in other formations of the Crudine Group (Table 7.2). Turbidites of the Waterbeach and Guroba Formations have a mean thickness of 60 and 70 cm, respectively (median 40 cm), with a low percentage of beds over 1m thick. Maximum bedding thickness is higher in the Guroba Formation (22 m), which contains some megaturbidites near the top of unit. The sandstone beds of the Turondale Formation have a higher average thickness (2.4 m; median 70 cm) with a considerably higher percentage of beds over 1m thick (36%), reflecting the presence of the megaturbidite beds (maximum thickness 55 m). If only the beds defined as 'normal'

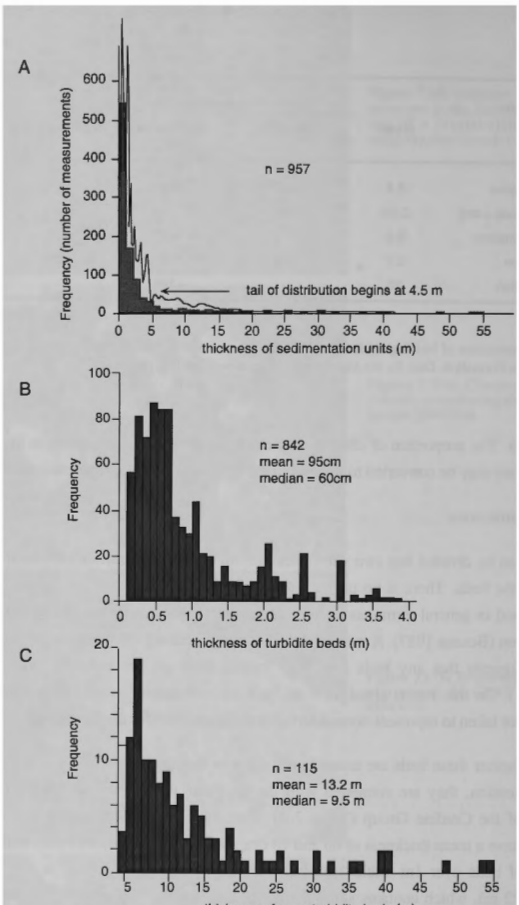

Figure 7.18: Frequency histograms of the thicknesses of sedimentation units of the Turondale Formation from nine measured stratigraphic sections. If the histogram representing all data is overlain by its gaussian distribution (Figure 7.18a) it becomes clear that the tail of the distribution begins at about 4.5m. On this basis, beds ≤ 4 m are considered to represent 'normal' turbidite sedimentation within the formation (Figure 7.18b), and beds over 4m thick are considered abnormal in size and assigned to the megaturbidite subfacies of the CRVS (Figure 7.18c). Note that since single sedimentation units cannot be linked from section to section, there will inevitably be duplication of data for some beds.

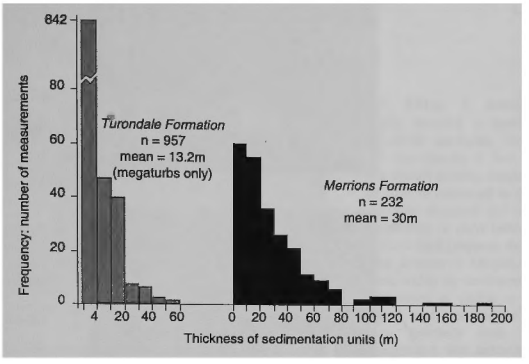

Figure 7.19: Frequency histograms comparing the thickness of sedimentation units of the Turondale and Merrions Formations. The number of turbidite beds in the Tuondale Formation (≤4m) is only schematically presented at this scale. It is clear that relatively thin sedimentation units (<1m) are only a minor component of the Merrions Formation, and the megaturbidites are considerably thicker and more abundant than in the Turondale Formation. Data for the Merrions Formation are from Cas (1979).

turbidites (under 4m thick) are considered, the mean thickness drops to 95 cm (median 60 cm), which is consistent with bedding thicknesses in the other formations (but still slightly higher). This suggests that the 4m is a reasonable value to use as the cutoff to distinguish megaturbidites from normal turbidites.

The character of sedimentation in the Merrions Formation is significantly different again, as the clastic component occurs predominantly in very thick sedimentation units, and there are very few 'normal' turbidite sandstone beds (Cas 1979; Figure 7.19). The beds are significantly thicker than the Turondale Formation, averaging 30m in thickness. This style of predominantly megaturbiditic sedimentation contrasts with the Turondale Formation, which comprises a mix of normal turbidite sedimentation, interspersed with deposition by megaturbidites over limited intervals. The sedimentary features of the two sub-facies of the Turondale Formation are described separately below.

Turbidite sub-facies: The thin-bedded volcaniclastic sandstones mainly range 10 to 60 cm, and most beds are less than one metre thick. Normal continuous-size grading from coarse- or medium-grained sandstone to mudstone or chert is a consistent feature of the thin beds, and

Figure 7.20: Measured section through a portion of the turbidite subfacies of the CRVS (section 9, Macquarie River, western limb of the Hill End Anticline) showing features typical of the sedimentation units, such as Bouma divisions, abundant load structures at the base of sandstone beds (Figure 7.20a,b,c) and the development of local intraformational conglomerates (Figure 7.20d). Mudstone intraclasts above the base of beds (Figure 7.20a) indicate the erosive power of the turbiditic flows.

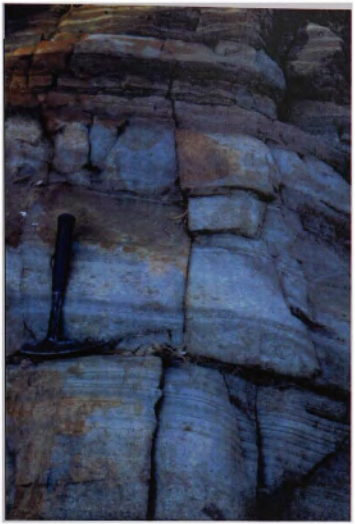

Figure 7.21a: A turbiditic sandstone sequence, showing a number of features typical of this sub-facies. The sandstone beds are all thin (mostly ≤ 1m), and commonly exhibit normal grading, ranging from massive at the base to laminated at the finer grained top (Bouma sequence *a,d* or *a,b,±d*). Very thin mudstone or chert intervals (some only millimetres thick) separate the sandstone beds (Bouma division *e*). Mudstone intraclasts are common within the sandstone beds. A thicker pelite horizon is visible at the top of the sequence, and consists of mudstone and siltstone interbeds with the occasional coarser-grained, thin sandstone bed. Section 8, northern bank of the Turon River. GR 726800 6338700).

Figure 7.21b: Turbiditic sandstone beds exhibiting top-absent Bouma sequences *a,e*, where the massive division *a* is commonly graded. The pelite horizons between sandstone beds are commonly very thin (≤ 1cm). Section 8, Turon River. GR 727500 6338700.

they exhibit Bouma sequence sedimentary structures (Figures 7.20, 7.21a,b). Small-scale cross laminations (division *c* of the Bouma sequence) are very rare, so the common Bouma pattern for the turbidites is *a, d, e* or *a, b, ± d, e*; a massive or graded coarse interval fining up into a parallel laminated interval, overlain by a pelitic division, which is commonly only a few millimetres thick. Top-absent Bouma sequences *a, e*, where the massive division *a* is graded, are also common throughout the succession (Figure 7.21b). Basal bedding planes are sharp and locally erosive, as indicated by the presence of scour structures (Figure 7.22a,b) and the common occurrence of pelite intraclasts at the base of the beds, derived from erosion of the underlying sediment (Figure 7.20a,d). Soft sediment deformation structures include abundant load casts, load balls and flame structures, and rare convolute laminations (Figure 7.20 b,c, 7.22c,d).

Megaturbidite sub-facies: The megabeds form thick, laterally extensive, massive beds that range in thickness between 4 and 55m. They are distinctive in outcrop, forming prominent generally north-south-trending strike ridges of disc-shaped tors. Individual sedimentation units are tabular in shape, but cannot be traced or correlated between sections regardless of thickness, because of the compositional homogeneity of all the volcaniclastic deposits. Similar thicker volcaniclastic megabeds (some > 100m thick) comprise most of the clastic component of the Merrions Formation (Cas 1979). The megabeds are generally coarser in grainsize than the normal-sized turbidites. Some beds have a basal volcaniclastic lithic breccia that grades upwards into massive crystal-rich volcaniclastic sandstone as the abundance and size of the lithic clasts decrease (coarse-fraction grading). The basal breccia comprises angular to rounded pebble- to cobble-sized clasts (mudstone intraclasts, chlorite vitriclasts, acid volcanic and fossiliferous limestone clasts) supported by a coarse-grained sandstone matrix. Above this coarse, graded base, the coarse- to medium-grained crystal-rich volcaniclastic sandstone forms a massive textural zone in which lithic clasts are less common. The massive sandstone lacks internal stratification apart from zones of diffuse lamination. Continuous-size grading is not conspicuous in outcrop, although based on thin section analysis, some of the beds appear to fine upward. Normal grading is common in the top few centimetres of the thick sedimentation units, where they fine-upward into laminated, fine-grained siliceous pelitic tops, some of which contain well-preserved shard pseudomorphs.

Character and setting of the source

The composition of the facies indicates its derivation from an active volcanic source terrain. The sandstones are composed almost entirely of texturally juvenile volcanic debris which consists of angular volcanic crystals and crystal fragments and rarely preserved tube pumice

Figure 7.22a: Amalgamated graded sandstone beds within the turbiditic sandstone sub-facies (Bouma divisions *a,b*). Scouring at the base of the bed indicate the turbiditic flows were highly erosive. Type section, southern bank of the Turon River. GR 244800 6338400.

Figure 7.22b: Amalgamated graded sandstone beds within the turbiditic sandstone sub-facies. The lower bed exhibits Bouma divisions *a*, *b* and *d*. A scour surface at the base of massive division *a* of the overlying bed has eroded into the lower bed, removing any pelitic interval that may have existed, and incorporating mudstone intraclasts into its base (M: right hand side of photograph). Section 7, Wickett's Creek GR 727000 6332150.

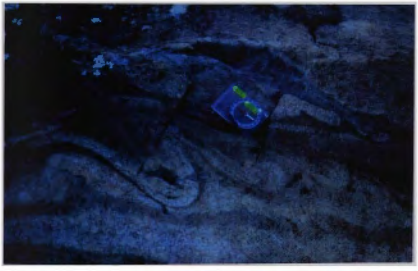

Figure 7.22c: Soft sediment deformation structures in turbiditic sandstones. Section 9, northern bank of the Macquarie River, GR 722000 6336450.

Figure 7.22d: Soft sediment deformation structures in turbiditic sandstones, forming folds in laminated fine grained sandstones. Section 7, Wickett's Creek. GR 726900 6332250.

and shards. The majority of lithic clasts are also derived from a volcanic terrain, and consist of chlorite vitriclasts, porphyritic acid volcanic and welded ignimbrite fragments. The abundance of angular euhedral and broken crystals and angular lithic fragments indicates the volcanic material erupted in a fragmental condition, and was therefore derived from explosive magmatic and/or phreatomagmatic eruptions. Depth constraints on pyroclastic eruptions imply that the source vents were shallow marine or subaerial, as vesiculation in silicic magmas is suppressed at deeper water levels (McBirney 1963). The occurrence of micritic crinoidal limestone clasts in the crystal-rich volcaniclastic sandstones and breccias, and the polymictic volcaniclastic conglomerates, suggests detritus passed through a shallow marine environment prior to deposition in deep water, which confirms that the source was above wave base.

The pyroclasts were not significantly abraded during transportation, and there was little admixture of foreign material, suggesting that pyroclastic debris was freshly erupted and rapidly deposited.

Mode of emplacement

Thin-bedded volcaniclastic beds are interpreted to be deposited from small-volume, low density turbidity currents. The continuous-size grading indicates deposition from a low density suspension (20% grains by volume; Lowe 1982). The massive to graded bases representing Bouma division Ta were deposited by direct suspension sedimentation from basal, high-density parts of turbidity current flows. The overlying Bouma divisions (*b-e*) are deposited from low-density turbidity currents. Division *b* was deposited by traction sedimentation as the current decelerated and sediment passed from suspended loads to bed loads. The overlying *d* division reflects suspension sedimentation of finer cherty material with some traction during deposition to produce fine lamination, and division *e* was formed by direct suspension sedimentation of the finest material (Middleton 1967; Walker 1984; Lowe 1982).

The megabeds are interpreted to be volcaniclastic megaturbidites, deposited from voluminous crystal-rich high-density turbidity currents. The transport of large amounts of coarse to gravelly sediment requires flows to have high particle concentrations (exceeding 20% grains by volume) in which grains can be supported by mechanisms such as hindered settling, dispersive pressure and matrix buoyancy lift, as well as flow turbulence (Lowe 1982). The volcaniclastic lithic breccias at the base of some beds form as the coarser material settles more rapidly through the suspended sediment load. Settling of the finer particles is hindered by

grain interaction in the high sediment concentration, and the bulk of the sand is deposited by direct suspension sedimentation, to form the overlying thick massive beds, in a similar manner to the massive to graded Bouma *a* beds in the thinner turbidites. Normal-size grading developed throughout some of the thick beds infers fluid turbulence may have played a significant role in grain support, retarding deposition of the finer size grades. However, most beds only exhibit coarse-tail grading, which indicates the sediment settled as a high concentration, non-turbulent suspension. The deposition of coarse massive sands is commonly attributed flow instability and the rapid dumping of material as the grains begin to settle, grain concentration in suspension decreases and grain suspension can no longer be supported by grain interactions (Middleton 1970; Lowe 1982). However Kneller and Branney (1995) propose a mechanism of gradual aggradation of sand beneath a sustained stable current. The principal grain support mechanisms are the same for both models. Deposition of the coarse-grained high-density suspended sediment load can leave a residual current containing finer material in low-density turbulent suspension which forms upward fining, laminated cherty mudstone at the top of many megaturbidite beds.

7.1.5 Massive to laminated cherty tuffaceous sediments

Description Fine-grained massive cherty siltstones and laminated cherty sandstones are spatially associated with the crystal-rich volcaniclastic sandstone facies. Both the megaturbidite and turbidite volcaniclastic sandstones commonly grade into finer-grained cherty rocks (Bouma divisions *d* and *e*). In the southeast, volcaniclastic megaturbidites are interbedded with thick intervals of massive fine-grained chert at the base of the formation, and the two facies have a complementary lateral relationship. Where the megaturbidite beds at the base of the formation thin towards the west (Hill End Anticline),they are overlain by thick intervals of massive fine cherts and planar-laminated cherty sandstones. This complementary pattern of thickness variation between the two facies is illustrated in Figure 7.8 The pattern suggests a genetic relationship between the two facies.

In outcrop, the very fine-grained, massive cherty siltstones are green-grey to black in colour, locally have ill-defined bedding and fracture conchoidally. The cherty sandstones are slightly coarser-grained, and commonly show very fine layering, on weathered surfaces. The cherts are composed of volcaniclastic material, consisting of fine-grained angular quartz and plagioclase grains disseminated throughout a fine quartz-albite matrix. The massive cherty siltstones contain fewer framework grains than the fine-grained sandstones. The matrix is secondary, and overprinted by sericite, chlorite, biotite and epidote, and may represent

devitrified volcanic glass. Epidote-pseudomorphed cuspate shard forms are preserved in some massive, cherty pelitic intervals.

Interpretation The cherts are interpreted to be of volcaniclastic origin. They cannot be true pelagic cherts, which precipitate from a siliceous 'gel', as they contain a large proportion of feldspar. The angular quartz and feldspar grains and the rare preservation of shards indicate the material is derived from pyroclastic eruptions, and the cherts represent silicified, fine compacted ashy sediments. The massive cherty rocks lack the strong tectonic cleavage present in the shales, indicating they were silicified prior to deformation of the succession.

The complementary lateral thickness variations of the volcaniclastic megaturbidites and cherts suggest that thick intervals of cherty sediments may be the distal equivalents of the coarser volcaniclastic megaturbidite beds, after mixing with water and extensive dilution has produced a low particle concentration ash-rich turbidity current (e.g. Wright and Mutti 1981). These ash turbidites are developed from fine-grained material that was elutriated from the megaturbidite flow fronts by surface shearing and erosion or ingestion of water at the base of the flow fronts, so generating an upper turbulent zone of mixing that would detach and travel further than the less fluidised body of the flow. The fine massive chert intervals would represent suspension settling of fine ash particles, and planar laminated fine cherty sandstones reflect traction sedimentation from low-density turbidity currents (Bouma division *b* or *d*).

7.2 Origin of the crystal-rich volcaniclastic megaturbidites

The thick intervals of amalgamated, thin-bedded volcanogenic turbidites that occur within the Turondale Formation, record denudation of the volcanic source region through normal sedimentary surface processes such as coastal fluvial erosion. In active volcanic terranes after major explosive eruptions, large volumes of loose, unconsolidated volcanic debris mantle the pre-existing topography, infilling valleys and disturbing pre-existing drainage patterns (Cas and Wright 1987; Smith 1991). In periods of repose between eruptions, drainage patterns are re-established and fluvial gullies rapidly incise the volcanic landscape. Erosion rates are high because of the high slopes and large volumes of highly erodible unconsolidated material. Rapid denudation of the volcanic landscape in the source region would have delivered a semi-continuous supply of immature volcaniclastic sediment to shelf margin systems, where it was then redeposited by mass-flow processes into the adjacent Hill End Trough.

The megaturbidites, however, are significantly thicker than the turbidite beds, and their origin cannot be explained by normal epiclastic surface processes. These single beds of juvenile

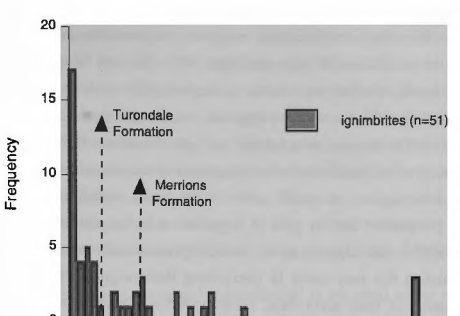

Figure 7.23: A comparison of average volume estimates for volcaniclastic beds of the Turondale and Merrions Formations with bulk volume estimates for some ignimbrites. Volume estimates for the Turondale and Merrions Formations are calculated using the average thickness of sedimentation units for each formation (13.2 m and 30 m, respectively), and an estimated unfolded surface area of 3415 km^2 for the Merrions Formation (Cas 1978). Bulk volume estimates for the ignimbrites are from Table 8.1 in Cas and Wright (1987). Seven ignimbrites with recorded volumes over 500km^3 (up to 3000 km^3) were not included due to the scale of the figure.

pyroclastic debris, tens of metres thick, represent particle mass flux rates that are orders of magnitude greater than those produced by the normal turbidity current surface processes described above, and are comparable with those of subaerial pyroclastic flow-forming eruptions (Figure 7.23). There is however, no evidence of a hot state of emplacement of the pyroclastic material, such as columnar jointing, welding textures (e.g. fiammé and plastically deformed shards) or devitrification textures (e.g. spherulites, perlites), which would favour transportation deposition in hot (>500°C) state. The pyroclastic debris was emplaced by high concentration turbidity currents, indicating the flows were cold and water-supported at the time of final deposition.

The possible origins of thick, massive submarine volcanogenic deposits emplaced at low temperatures have been discussed for similar deposits (CRVS) of the Proterozoic Big Sunday Formation, El Sherana Group, in Chapter 3.3. Such deposits could be fed directly from subaqueous eruptions or from subaerial pyroclastic flows that entered the sea and

transformed into cold, water-supported mass flows. Alternatively, the water-supported mass flows may be generated by post-eruptive slumping and remobilisation of unconsolidated pyroclastic debris. Deciding whether these massive volcaniclastic deposits are primary eruptive products can be difficult (Wright and Mutti 1981; Cas and Wright 1987, 1991). In the case of the Big Sunday Formation, evidence of heat retention within the CRVS was used to indicate syn-eruptive emplacement of the deposits. As the volcaniclastic megaturbidites of the Turondale Formation display no evidence of heat retention, it is more difficult to distinguish between syn- and post-eruptive emplacement of the juvenile debris. However, the beds are preserved throughout the entire extent of the basin, providing a regional, three dimensional scale perspective on this style of deposit that is not available the Big Sunday Formation. This enables the deposits to be studied from a sedimentological perspective, considering information that may assist in interpreting their origin such as the size of the deposits, the frequency of their occurrence, lateral variations in their internal organisation, their context within the basin and the overall ratio of volcaniclastic to hemipelagic material in the sequence. In the following section, these attributes are used to compare the volcaniclastic megaturbidites of the Turondale and Merrions Formations with epiclastic megaturbidites derived from basin margin collapse, to determine whether post-eruptive slumping and resedimentation is a likely mechanism for generating the sequence of thick, volcaniclastic mass flows, or whether a genesis related to contemporaneous passage of large-volume pyroclastic flows into the basin is a more likely origin.

7.2.1 Comparison with epiclastic megaturbidites

The term 'megaturbidites' refers to exceptionally thick, extensive, relatively homogeneous deposits from exceptionally large mass flows (Bouma 1987). These beds generally differ considerably in texture, composition and palaeocurrent direction from the sedimentary series in which they are found. They form very distinct sheet-like deposits that are not organised in facies associations resulting from long-lived channel-lobe turbidite systems (Mutti et al. 1984). The generation of epiclastic megaturbidites is attributed to shelf margin or slope collapse, triggered by exceptionally catastrophic events such as seismic activity, local overloading of the slope, or sediment instability related to sea level fluctuations, tsunamis and very large spring floods (Mutti et al. 1984). The tectonic stability of the region affects the size and frequency of triggering events such as strong earthquakes (Doyle 1987). Thus large scale deposits are more frequent in tectonically active basins like those of the Alps and Pyrenees, than in quiescent regions like the eastern United States and the Gulf of Mexico Basin, which commonly record only a single catastrophic event (Table 7.3). However, even in active basins recording multiple episodes of shelf collapse, these natural catastrophes are infrequent

events, and megaturbidites are isolated occurrences, randomly scattered throughout the stratigraphic succession and separated by thick pelagic or hemipelagic intervals representing 'normal' basin sedimentation. For example, the Eocene Hecho Group (south-central Pyrenean Basin) contains nine carbonate megabeds up to 200m thick, within an ~ 3 km thick normal siliciclastic turbidite succession of sandstones and mudstones. The recurring periodicity of megabed emplacement is calculated to be about 0.5 Ma (Seguret et al. 1984). In the Cretaceous North Pyrenean Basin about 20 megabeds are interbedded with 800m of hemipelagic sediments deposited over a period of about 20 Ma (Bourrouilh 1987). This infers a recurring periodicity of about 1.0 Ma. The great volume and thickness of the epiclastic megaturbidite deposits are attributed to long periods of primary accumulation of epiclastic debris between each catastrophic event (Seguret et al. 1984; Marjinac 1996).

In epiclastic marine sequences, the term 'megaturbidite' is not used *sensu stricto* to denote a bed deposited by a turbidity current. Instead it is applied in a much broader sense to describe an anomalously thick, widespread submarine sedimentary unit emplaced as a single mass movement event that may have involved several transport mechanisms. In most cases, only the upper part of such beds have been deposited by a true turbidity current, while the lower part is the product of more complex mass flows (Bouma 1987). Depositional units commonly exhibit a lateral and vertical continuum from slump-derived debris flows to turbidites. For example, Upper Cretaceous megaturbidites from the North Pyrenean Basin consist of a thick, chaotic, immature debris flow deposit at the base, in which the coarsest grains (up to boulder-sized) have a mudstone matrix-supported fabric. The debris flow becomes more organised upward and laterally, and passes into a mudflow in which winnowing of the muddy matrix occurs to form pockets of concentrated lithoclasts in clast-supported configuration. In turn this passes vertically and distally into a Bouma-type megaturbidite (Bourrouilh 1987). Megaturbidites in the Eocene Hecho Group in the Spanish south-central Pyrenees show similar characteristics, consisting of a largely clast-supported and poorly organised basal megabreccia, overlain by a better sorted, inverse graded megabreccia, then a Bouma-type megaturbidite (Figure 7.24; Labaume et al. 1987). Carbonate megabeds interfingering with proximal fan deltas of the Dalmatian Eocene-Miocene flysch basin (eastern Adriatic Sea) also commonly take the form of composite debrite-turbidite couplets (Marjinac 1996). These hydrodynamically graded sequences reflect the incorporation of water into the sediment gravity flows during transport, which allows winnowing of the mud matrix, the concentration of lithoclasts (i.e. their removal from the flow) and the emergence of a megaturbidite.

Deposit		T_{max}	V_{max}	$V_{average}$	Length	Area	Frequency of occurrence
volcaniclastic megaturbidites, Hill End Trough							
Turondale Formation, Hill End Trough		56m		45 km^3		3415km^{2*}	Amalgamated megaturbidite beds with
Merrions Formation, Hill End Trough		180m		100 km^3		3415km^{2*}	little or no intervening hemipelagic sediments
epiclastic megaturbidites							9 beds randomly distributed
Hecho Group, Pyrenees[1]:	debrite-turbidites	200m	155km^3	*37 km^3*	140km		throughout a ~ 3km thick succession.
	turbidite-portion only	42m	*13 km^3*	*4 km^3*			Recurring periodicity ~ 0.5 Ma
central Dalmatia (Croatia)[2]	debrite-turbidites	170m					random distribution of a small number
	megaturbidites	27m					of beds (10-49m thick) within a thick
	'reflected' turbidites	49m					flysch sequence
	composite turbidites	37m					
Cretaceous North Pyrenean Basin[3]	debrites	10-30m					~20 beds randomly interspersed with
	debrite-turbidites	≤ 18m					hemipelagic sediments. ~800m
	megaturbidites	≤ 5m					sequence deposited over about 20 m.y.
	Grand Barre Calcaire (MT)	63m	50km^3		95km		'Grand Barre Calcaire' (true mega-turbidite) is considerably thicker than the other megabeds
Upper Cretaceous-Tertiary Ligurian Flysch[4]		40m					4-40m megabeds randomly interleaved with pelagic seds
Vernasso 'complex layer', Eocene Friuli Flysch[5]		200m			22km		Occurrences of single megabeds, an
Missaglia Megabed, Lombardian Flysch, Southern Alps[6]		30m	20km^3				order of magnitude thicker than
normal debrite-turbidite, Mississippi Fan, west Florida[7]		25.5m					basin turbidites, each representing
Contessa, Marnoso-Arenacea Fm, Italy[8]		10-16m	30km^3		140km		an isolated catastrophic event within
Megalayer β, Herodotus Abyssal Plain, eastern Mediterranean Sea[9]		10m	10km^3		100km	1000km^2	
Balearic Abyssal Plain, Mediterranean Sea		4-8m	500km^3				the sedimentary basin.
Black Shell turbidite, Hatteras Abyssal Plain[11]		4m	> 100km^3		> 500km	44 000km^2	
debrite-turbidite, Exuma Sound, Bahamas[12]		2-3m	20km^3			6400km^2	

Table 7.3: Geometric characteristics of recorded epiclastic megaturbidites (debrite-turbidites) and the frequency of their occurrence. Data sources are: (1) Seguret et al. 1984, Labaume et al. 1987 (NB: volume estimates in italics are calculated using the formula in Table 7.4); (2) Marjinac 1996; (3) Bourrouilh 1987; (4) Mutti et al. 1984; (5) Gnaccolini 1968; (6) Galbiata 1969, Bernoulli et al. 1981; (7) Brooks et al. 1986; (8) Ricci Lucci and Valmori 1980; (9) Cita et al. 1984; (10) Rothwell et al. 1998; (11) Prince et al. 1987; and (12) Crevallo and Schlager 1980. The data are compared with volcaniclastic megaturbidites of the Turondale and Merrions Formations. * denotes the estimated unfolded surface area covered by the Merrions Formation (calculated by Cas 1977). A similar surface area is envisaged for the Turondale Formation.

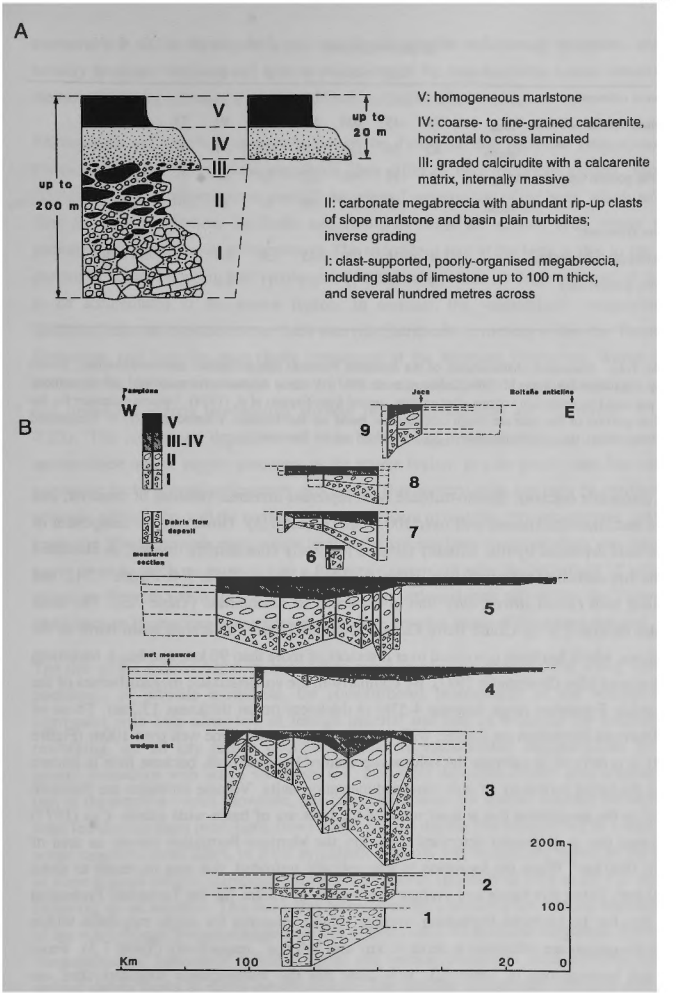

Figure 7.24: (a) Internal organisation of the south-Pyrenean carbonate megaturbidites (Hecho Group). It is clear that the term megaturbidite is not used *sensu stricto*, as only the upper internal divisions (III, IV and V) are the deposits of a true turbidity current. (b) Cross sections of the nine carbonate megabeds within the Hecho Group along the main axis of the basin, showing how the basal megabreccias can wedge out distally, resulting in the emergence of a true megaturbidite. Both figures are reproduced from Labaume et al. 1987.

		Megaturbidite unit								
		1	2	3	4	5	6	7	8	9
thickness estimates										
combined debrite-turbidite	t_{max}	85	45	200	130	143	80	75	62	80
	t_{mean}	85	38	134	110	116	30	39	47	64
turbidite portion only	t_{max}	0	10	42	22	13	6	19	15	10
	t_{mean}	0	6	16	16	10	6	10	13	5
volume estimates										
combined debrite-turbidite		4	38	100	45	155	0.8	7	6.5	6.4
turbidite portion only		0	1	12	6.5	13	1.6	1.8	1.8	.5

Table 7.4: Geometric characteristics of the Southern Pyrenean megaturbidites (debrite-turbidites), Hecho Group (data from Seguret et al. 1984; Labaume et al. 1987). Volume estimates for combined debrite-turbidite beds are based on minimum volume after erosion, quoted from Seguret et al. (1984). Volume estimates for the turbidite portion of the beds are rough calculations, based on the formula V(turbidite only) = V(combined debrite-turbidite). t_{mean}(turbidite only)/t_{mean}(combined debrite-turbidite).

The composite epiclastic debrite-turbidite beds represent immense volumes of material, and attain maximum thicknesses well over 100 metres (Table 7.3). However, the component of these beds deposited by true turbidity currents is usually considerably thinner, as illustrated by the nine carbonate megaturbidites within the Hecho Group (Table 7.4; Figure 7.24), and turbidite beds *(sensu stricto)* over 30m in thickness are uncommon (Table 7.3). The most notable exception is the Grand Barre Calcaire from the Upper Cretaceous basin north of the Pyrenees, which has been correlated over distances of more than 90 km, and has a maximum thickness of 63m (Bourrouilh 1987). By comparison, the volcaniclastic megaturbidites of the Turondale Formation range between 4-55m in thickness (mean thickness 13.2m). Those of the Merrions Formation are thicker, with many beds up to, and some well over 100m (Figure 7.19). It is difficult to estimate the volume represented by these beds, because little is known about the lateral continuity of individual sedimentation units. Volume estimates are therefore based on the assumption that at least some of the beds are of basin-wide extent. Cas (1977) estimated that in its present deformed condition, the Merrions Formation covers an area of about 1800 km^2. When the formation is schematically unfolded, this area increases to about 3400 km^2. Using this figure and average thicknesses of 13.2m for the Turondale Formation and 30m for the Merrions Formation, average volume estimates for single megabeds within these formations are calculated at about 45 km^3 and 100 km^3, respectively (Table 7.3). From the size comparisons in Table 7.3, it is clear that the volcaniclastic megaturbidites are

comparable in size to the megabeds generated by catastrophic sedimentary processes, and are actually greater in thickness and volume than many of the megaturbidites (*sensu stricto*) and the turbiditic components of composite debrite-turbidite beds.

Although the volcaniclastic megaturbidites of the Turondale and Merrions Formations are comparable in size to epiclastic megabeds, they differ in two important aspects, namely: (1) their frequency of occurrence; and (2) the internal organisation of the beds, which reflects their mode of deposition. Epiclastic megaturbidites occur as isolated beds within thick packages of 'normal' basin sedimentation. The anomalous size of the beds is due to the long periods of repose between their emplacement, which allow time for large volumes of debris to be accumulated in the source region. In contrast, the volcaniclastic megaturbidites dominate basin sedimentation over thick intervals (hundreds of metres) within the Turondale Formation, and form the main clastic component of the Merrions Formation. Within these intervals, the thick sedimentation units are commonly amalgamated, and hemipelagic pelite and turbidite horizons representing ambient basin sedimentation are subordinate (Figure 7.25). The continuous deposition of large volumes of material indicates rapid primary accumulation and/or supply processes in the source region, at a far greater rate than can be accounted for by normal sedimentary processes. This accumulation can only be attributed to volcanic aggradation, and the continuous replenishment of material through periodic volcanic eruptions. The large scale event which formed the volcaniclastic megaturbidites was repeated many times in quick succession, with a frequency consistent with the periodicity of volcanic eruptions from an active source region. Each large sedimentation unit within the Turondale and Merrions Formations may represent a separate eruptive phase of the source volcano.

The size of the sedimentation units and their rapid, successive emplacement, along with the abundance of juvenile pyroclasts, the compositional homogeneity of the volcaniclastic aggregates with little admixture of foreign material and lack of evidence for sedimentary reworking, are all key factors establishing that the volcaniclastic megaturbidites have a genetic connection with active volcanism (i.e. they were deposited shortly after eruption, as part of the eruptive cycle). However, this information does not discern whether the deposits were fed directly from pyroclastic flows which entered the sea and transformed in transit into water supported mass flows, or if the pyroclastic material was temporarily stored on the shelf or slope regions prior to slumping into the trough shortly (possibly as little as days or weeks) following initial eruption. This issue may be resolved by comparing the internal organisation of the volcaniclastic megaturbidites with that of slump-derived epiclastic megabeds. Epiclastic 'megaturbidites' commonly exhibit a lateral and vertical continuum from proximal slump-derived debris flows to distal megaturbidites. The initially viscous and cohesive mud-rich

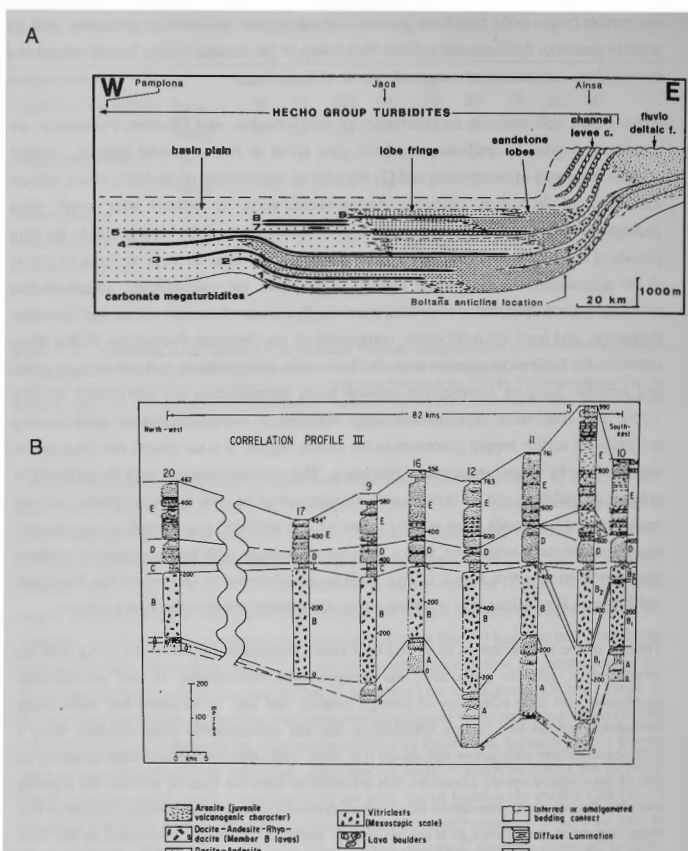

Figure 7.25: Correlation profiles comparing the distribution of: (a) the nine carbonate megaturbidites of the Eocene Hecho Group, south-central Pyrenean Basin (reproduced from Labaume et al. 1987); and (b) the volcaniclastic megaturbidites of the Merrions Formation, Hill End Trough (reproduced from Cas 1977). This figure highlights the high proportion of arenite to pelite, and the amalgamation of thick, massive megaturbidites in the Merrions Formation, which contrasts with the episodic, widely separated occurrences of megabeds within the Hecho Group.

deposits evolve hydrodynamically into slurry flows and turbidity currents, as water is ingested into the flows and mixes with the interstitial mud-fluid, reducing their viscosity and allowing fluid turbulence to develop (Hampton 1972). In contrast, the thick volcanogenic deposits of the Turondale and Merrions Formations do not exhibit any evidence of deposition by debris flow, even near points of sediment influx around the basin margins (Chapter 7.4.1). It could be argued that these deposits are all preserved in a deep marine basin some distance from their source, and their form in more proximal settings is unknown. However, similar volcaniclastic megabeds are deposited in proximal settings within the Bindook Volcanic Complex, which lies beyond the southern margin of the Hill End Trough. They occur in the Kowmung Volcaniclastics, within a broad, submarine volcaniclastic apron adjacent to, and fed by a subaerial volcanic edifice (Cas et al. 1981) and in the Devil's Pulpit Member of the Tangerang Formation, a shallow marine volcaniclastic sequence overlying low-energy shelf limestones (Simpson et al. 1997). As with the Turondale and Merrions Formations, these more proximal volcaniclastic megabeds exhibit features consistent with transportation by high concentration turbidity currents, and do not exhibit any evidence of initial deposition by slumping or cohesive debris flow mechanisms. They comprise massive non-graded to graded beds of predominantly sand-sized angular crystal fragments in a clast-supported configuration. This contrasts with the matrix-supported structure characteristic of debris flows. The beds are better sorted than debris flows, as they lack a volumetrically dominant fine-grained (mud-sized) matrix component.

It is clear that the slump-derived epiclastic megaturbidites are a poor analogue to the crystal-rich volcaniclastic megaturbidites of the Turondale and Merrions Formations (and of the Bindook Volcanic Complex). Although the final volcaniclastic deposits have high crystal-contents (mean crystal contents are 59% for the Turondale Formation and 63% for the Merrions Formation), they were presumably derived from initially more ash-rich pyroclastic deposits. By definition, ignimbrites are 'pumice and ash flow deposits' and therefore typically more ash-rich in character than the CRVS facies described in the Turondale and Merrions Formations. In most cases, ignimbrites are poorly sorted, massive deposits consisting of pumice lapilli and block sized pyroclasts (pumice, crystals and lithics) supported by an ash matrix in an matrix-supported configuration. Very few ignimbrites have greater than 60 wt% phenocrysts (Cas and Wright 1987), and usually only certain sub-facies such as ground layers are significantly fines-depleted to form crystal/lithic-rich aggregates. Similar CRVS facies recorded in the Big Sunday Formation (Chapter 3) and the Tyndall Group of the Mount Read Volcanics, western Tasmania (White and McPhie 1997) are estimated to contain approximately twice the crystal content of their subaerially-deposited

counterparts. It is reasonable to assume that the CRVS of the Turondale and Merrions Formations underwent a similar degree of crystal-enrichment during transportation, although they cannot be traced to their subaerial counterparts to allow a direct comparison of crystal contents. Phenocryst abundances in chlorite-altered vitriclasts, thought to be juvenile clasts, are significantly less than those in the crystal-rich volcaniclastic deposits (about 33% crystals, Section 7.3.2), supporting this assumption.

If the original ash-rich pyroclastic deposits had been briefly stored on the shelf prior to (penecontemporaneous) slumping into the basin, a proximal to distal, debris flow to turbidite flow transformation would be expected by analogy to the slump-derived epiclastic megabeds. The absence of such a flow transformation being preserved suggests much of the fine-ash component of the pyroclastic flows was removed prior to transportation into the deep-marine environment. This favours the model that these very thick, massive, crystal-rich volcaniclastic megaturbidites (that contain no pumice and are significantly depleted in ash, even in proximal settings), are directly fed from subaerial pyroclastic flows that entered the sea, as this scenario provides a mechanism for supplying huge volumes of juvenile, crystal-rich debris, and for the removal of significant volumes of ash and pumice during transportation (see below).

7.2.2 Models for flow transformation and crystal enrichment

Cas (1983a) proposed that the genesis of the crystal-rich megaturbidites of the Merrions Formation could have involved pyroclastic flows entering the sea, interacting explosively with seawater and disintegrating to generate cold water-supported turbidity currents. As a hot gas-particulate flow system enters the shoreline, seawater may be ingested into the vigorous, turbulent flow front, generating steam and triggering violent phreatic explosions. These secondary eruptions could produce rootless vents at the shoreline (e.g. Wright and Coward 1977; Walker 1979). The crystal enrichment that typically occurs in ignimbrites through the elutriation of fine ash from the eruption column and the resultant pyroclastic flows, would be further enhanced by the loss of pumice and ash through these secondary eruption columns. It is possible that through the ingestion of water, the hot gas comprising the interstitial medium of the initial pyroclastic flows rapidly cooled and collapsed, and the flows transformed in transit into cold, water-supported turbidity currents. Alternatively, the phreatic explosions may have completely disrupted the initial flows, producing thick, unstable, crystal-rich pyroclastic aggregates, which then slumped (contemporaneously) from the near-shore setting, to produce the cold state turbidity currents. More fine ash would then have been elutriated from the submarine volcaniclastic flows, either through ablation of the upper

surface of the flow front by shearing and erosion (e.g. surface transformations of Fisher 1983, 1984) or through fluidisation by the ingestion of water at the base of the flow front. These processes can generate dilute turbulent flows (ash turbidites) that form fine vitric deposits above the crystal-enriched deposits (e.g. the massive to laminated cherty tuffaceous sediments described in Chapter 7.2.5).

An alternative possibility is that the crystal-rich deposits were produced through the gravitational segregation of pyroclastic flows as they travelled over water. Pyroclastic flows with a bulk density less than sea water will continue to flow across the sea surface (e.g. Plateau ignimbrite, Kos, Stadlbauer et al. 1986; Allen 1998, Krakatau Ignimbrite; Mandeville et al. 1996; Carey et al. 1996). In the case of the 1883 Krakatau eruption, diminished deposition close to the source of the flows suggests the subaerially generated, highly turbulent pyroclastic flows initially travelled over the water (Sigurdsson et al. 1991a,b). As the flows continued to travel over the water, they would segregate into a highly deflated, basal flow enriched in the denser components (crystals and lithics), and an overriding lower concentration turbulent flow containing the low-density, fine-grained vitric components (pumice and ash). As the basal components of a flow becomes denser than seawater it would eventually submerge and sink through the water column, becoming separated from the overriding ash cloud, which would continue to travel over the water for long distances. Pumice and ash would be further sorted from crystals and lithics as they settle through the water column, with the lighter clasts remaining in suspension to be dispersed by currents (Carey et al. 1996; Mandeville et al. 1996). The elutriation of fine ash and pumice from the dense, basal component of the flow may be enhanced by phreatic explosions generated where the base of the hot flow is in contact with seawater, or where the flow begins to sink through the water column. Based on this scenario, the massive to laminated cherty tuffaceous sediments of the Turondale Formation could represent the distal equivalents of the crystal-rich megaturbidites, deposited by the overriding dilute, ash cloud, and dominated by very fine vitric dust that is now silicified. This scenario would allow more efficient sorting of fine/light pyroclasts and coarse/dense pyroclasts, as a larger surface area of the pyroclastic flows would be exposed to cold water.

7.3 PETROGRAPHY AND GEOCHEMISTRY

Modal point count analyses were carried out on 103 clastic samples (mainly crystal-rich volcaniclastic sandstones) and 5 samples of the Turondale porphyry, using conventional point counting techniques. The full results are in Appendix B3, and a summary of the analyses is presented in Table 7.5. The spacing of points was set to be approximately equal

to or larger than the diameter of the largest sand-sized grains in each sample. The limitations of thin-section size means that point count analyses only account for sand-sized and finer matrix fractions only. Outsized lithic clasts are therefore not included in modal estimates, so the results do not present a fair estimate of total lithic contents. Smaller, sand- to gravel-sized lithic clasts larger than the point spacing were only counted once, so that the relative volume of this finer lithic material is also slightly underestimated. However, this only occurred in a few coarser samples, and does not significantly affect the results. Secondary minerals (chlorite, epidote, clinozoisite, calcite, sericite, biotite) were counted only where they form large individual grains or grain aggregates overprinting the matrix. Where they visibly replace framework plagioclase, the primary grain mineralogy was recorded. Therefore the point count data only indicate the presence of secondary metamorphic minerals in a sample, and not their volumetric proportion. The counts for secondary minerals are added to the counts for undifferentiated matrix, to give the total matrix count. It is possible that some of the large chlorite and epidote grains and grain aggregates pseudomorph primary mafic mineral phases such as pyroxene or amphibole, but original crystal forms are rarely preserved. Alternatively, some chlorite and epidote may be replacing large glassy vitriclasts. Because preserved pseudomorphed crystal forms are rare, no attempt has been made to estimate the percentage of the original mafic framework component, and all epidote and chlorite has been included in the matrix tally. In the biotite-grade greenschist facies metamorphic rocks, it is possible that the proportion of matrix has been overestimated, as it can be difficult to distinguish the coarse recrystallised matrix from recrystallised framework grains.

Whole rock and trace element analyses were obtained for 17 volcaniclastic rocks of the Turondale Formation and one sample of the Turondale porphyry. In addition, 25 lava and volcaniclastic samples of the Merrions Formation collected by R.Cas (Cas 1977) were supplied by Macquarie University and reanalysed to obtain a full suite of trace element analyses. Major, trace and rare earth elements were analysed by the laboratories of the Australian Geological Survey Organisation, using a combination of XRF spectrometer techniques (Norrish and Chappell 1967), titrimetry (FeO) and ICP-MS (Induced Coupled Plasmatron Mass Spectrometer). The geochemical data are presented in Appendix B2.

7.3.1 Petrography

Modal analyses indicate that the CRVS contain roughly equal proportions of quartz (45%) and plagioclase (49%) with a minor lithic component (6%; Table 7.6). K-feldspar is rare, and occurs as perthites and antiperthites. It is possible that minor mafic phases (pyroxene and/or amphibole) occurred, which have been altered to chlorite, epidote and Fe-Ti oxides during

Table 7.5: Modal analyses (as percentage of total count) of volcaniclastic sandstones from the Turondale Formation. Note that the secondary minerals are added to the matrix to obtain the total matrix count.

Sample number	section	quartz	plagioclase	K-feldspar	Rock fragments	Matrix (total)	Secondary minerals
TUR11	1	23.4	22.4	0.6	5.4	47.6	11.2
TUR14	1	31.6	26.6	0.0	2.2	39.2	4.4
TURI5	1	28.4	23.0	0.0	2.6	46.0	8.0
TUR16	1	25.8	23.6	0.0	5.0	45.2	3.8
TUR18	1	27.4	14.2	1.0	4.0	53.4	12.2
TUR19	1	11.3	11.4	0.2	0.3	76.7	0.0
TUR22	1	35.8	31.6	0.8	5.4	25.6	11.4
TUR23	1	22.2	23.2	0.6	0.6	53.4	6.2
TUR28	1	35.0	15.4	0.8	5.0	43.8	9.4
TUR33	1	26.2	38.4	0.8	4.2	30.4	0.8
TUR35	1	18.6	37.8	1.9	2.9	38.6	18.1
TUR36	1	25.6	36.2	0.9	0.0	37.1	10.4
TUR40	1	26.4	41.0	1.8	4.4	26.0	13.8
TUR43	1	34.0	8.0	0.2	0.2	55.6	3.2
TUR44	1	17.0	15.4	0.0	0.0	66.4	15.0
TUR48	1	17.2	15.2	1.2	2.0	64.0	9.6
TUR51	1	35.2	30.8	1.6	6.4	26.0	1.8
TUR55	1	22.6	42.0	0.2	5.4	28.2	14.2
TUR61	1	33.6	31.6	0.4	0.0	32.0	14.8
TUR63	1	27.8	40.0	0.2	2.2	28.4	7.4
TUR65	1	32.8	30.6	0.0	1.4	34.2	19.2
TUR69	1	33.0	31.4	0.4	2.8	31.0	10.6
TUR70	1	18.0	43.0	0.0	1.2	37.4	22.6
TUR72	1	24.8	40.4	1.8	6.4	25.4	7.8
TUR73	1	34.5	35.2	0.4	5.7	22.5	5.3
TUR77	1	20.0	34.0	2.0	3.0	40.2	11.4
TUR80	1	21.8	47.2	0.2	5.4	25.4	7.6
TUR82	1	33.8	27.8	0.4	3.2	34.0	8.4
TUR159	2	20.8	18.8	3.0	16.4	40.0	20.4
95843089	3	28.6	29.8	0.6	3.0	36.2	7.6
95843090	3	36.8	24.0	0.0	3.0	36.6	17.6
95843091	3	31.4	29.2	0.0	0.0	37.6	11.8
95843092	3	25.2	37.2	0.4	2.4	33.6	6.4
95843093	3	28.2	25.0	0.6	3.0	41.4	9.4
TUR89	4	32.6	20.8	0.2	8.2	35.6	4.2
TUR90	4	17.2	44.0	0.2	2.2	35.8	9.8
TUR92	4	25.2	36.6	0.0	1.2	35.6	3.6
TUR93	4	28.6	29.0	0.0	5.6	35.4	2.0
TUR94	4	12.0	12.6	0.0	0.0	75.4	0.8
TUR95	4	22.0	24.6	0.4	2.4	49.6	5.2
TUR97	4	32.0	28.4	0.0	11.8	27.2	5.4
95843001	5	18.0	33.4	0.0	9.8	37.8	0.2
95843002	5	33.2	30.8	0.2	11.8	23.0	10.2
95843003	5	17.6	35.0	1.0	3.6	42.6	4.6
95843004	5	22.8	34.4	0.0	9.0	32.6	3.4
95843005	5	9.6	3.0	0.2	0.0	87.2	38.0
95843006	5	29.6	34.4	0.0	1.8	34.2	15.2
95843007	5	21.2	20.4	0.8	1.6	56.0	13.6
95843010	5	20.0	41.2	0.0	4.2	34.2	15.0
95843011	5	40.6	15.0	0.0	12.0	31.6	7.0

Sample number	section	quartz	plagioclase	K-feldspar	Rock fragments	Matrix (total)	Secondary minerals
95843012	5	49.4	6.8	0.0	20.0	23.2	14.6
95843013	5	29.0	9.8	0.0	3.5	56.8	12.8
95843014	5	18.8	36.6	0.0	6.8	36.6	11.4
95843015	5	15.8	43.4	0.0	4.4	35.4	13.8
95843016	5	17.2	43.2	0.0	4.4	34.8	3.0
95843017	5	20.4	40.4	0.0	0.6	37.6	3.8
95843018	5	25.6	32.0	0.0	1.6	39.8	2.6
95843019	5	24.8	34.2	0.0	0.6	39.0	4.4
95843021	5	33.4	27.6	0.0	8.0	30.4	5.2
95843022	5	26.8	32.0	0.0	5.8	34.6	11.0
95843023	5	15.4	19.8	0.0	0.4	64.4	3.6
95843024	5	25.8	30.4	0.0	3.2	40.4	9.0
95843025	5	20.8	30.2	0.0	3.2	45.2	58.0
95843026	5	29.2	31.8	0.0	8.6	29.4	8.2
95843027	5	27.0	39.6	0.0	4.8	28.2	4.2
95843028	5	28.2	30.2	0.0	5.0	35.6	23.4
95843029	5	22.0	37.8	0.0	2.6	37.2	13.6
95843030	5	13.2	6.6	0.0	1.8	77.8	7.6
95843031	5	49.3	40.4	0.0	10.4	45.0	6.0
95843032	5	34.4	30.2	0.0	4.2	30.8	16.8
95843034	5	28.0	23.0	0.0	25.4	23.6	4.8
TUR 113	8	16.6	31.2	0.6	0.2	51.2	13.8
TUR114	8	30.2	32.8	0.0	1.2	35.6	10.0
TUR115	8	33.2	40.6	0.8	0.8	24.6	13.8
TUR133	8	35.8	35.4	0.4	0.4	28.0	11.0
TUR134	8	33.8	34.2	4.4	0.0	27.6	23.8
TUR135	8	29.9	29.4	3.7	1.1	36.0	9.6
TUR136	8	24.2	24.8	6.8	1.8	42.2	22.2
TUR137	8	19.6	49.2	2.0	1.4	27.8	23.8
TUR140	8	26.0	24.2	0.0	2.4	47.0	17.9
TUR141	8	33.0	22.4	2.0	9.4	32.4	18.6
TUR142	8	21.2	22.4	0.8	4.0	50.6	13.6
95843082	9	15.4	21.7	0.5	0.0	62.4	8.8
95843083	9	6.0	5.4	0.6	0.0	88.0	9.0
95843085	9	21.3	27.3	1.0	6.2	43.5	23.1
TUR143	9	25.8	16.7	6.7	1.2	49.8	10.4
TUR144	9	13.3	12.5	1.3	1.2	71.7	12.6
TUR145	9	22.4	28.0	2.8	0.4	45.6	26.0
TUR146	9	21.2	30.4	1.8	3.2	43.4	16.0
TUR149	9	33.2	38.0	0.8	2.2	25.8	8.8
TUR150	9	42.8	30.8	1.4	1.2	23.8	18.1
TUR151	9	11.3	14.0	1.9	0.0	72.7	6.6
TUR152	9	14.6	18.2	2.4	0.0	64.8	7.8
TUR153	9	33.8	35.2	2.4	0.4	28.2	7.8
TUR154	9	17.6	38.5	0.4	0.0	42.5	10.0
TUR155	9	21.9	40.2	1.2	1.5	33.7	11.0
TUR156	9	23.9	31.8	1.8	4.3	37.8	15.2
TUR157	9	22.0	36.5	0.6	2.0	38.7	26.8
TUR158	9	29.4	14.8	0.6	2.8	52.2	16.6
95843100	10	31.8	25.2	0.6	1.6	40.6	27.6
95843097	10	31.4	6.0	4.4	2.4	55.6	3.6
95843101	10	23.0	19.6	0.6	4.6	51.4	25.1
95843099	10	28.6	37.2	0.4	0.0	33.4	30.6
	Average	25.7	28.4	0.8	3.7	41.2	11.8

Section	n	mean Q	±	mean F	±	mean L	±	matrix	±
mean for all data									
porphyry	5	12.6	1.9	87.4	1.9	0.4	0.8	60	2
clastics	103	**44.7**	10.2	**49.4**	11.6	**5.9**	5.4	**41.2**	14.5
Lateral variation: mean of each measured section									
Type Section (1)	28	45.8	11	49.2	10.9	4.98	3.1	39.8	13.7
Crudine Creek (3,4)	12	45.6	7.6	48.8	9.4	5.6	4.8	40	11.8
Fairview Creek (5)	30	43.4	12.2	47.7	14.5	8.9	7.2	54.3	14.6
Turon River (8)	11	43.6	6.7	52.9	8.8	3.4	4	36.6	9.3
Macquarie River (9)	17	43.5	7.8	53.7	8.3	2.8	3.2	48.5	17.5
Cudgegong River (10)	4	54	10.5	41.5	11.9	4.4	3.6	45.2	8.8
Vertical variation in mean, south east area									
Lower unit	5	46.1	11.4	47.1	10.7	6.7	4.8	44.1	15.7
Middle unit	18	49	13	45	12	6	3.9	44	15.2
Upper unit	9	43.7	9.9	49.2	12.6	7.1	6.4	37	12
Vertical variation in mean, west and northwest area									
Lower unit	18	49.5	12	48.3	14.4	2.2	1.7	43.3	12.8
Middle unit	10	42.7	6.9	55.9	8.3	1.4	1.6	44.3	18.8
Upper unit	43	46.6	7.8	46	8.1	7.4	3.5	43.8	6.6

Table 7.6: Summary of mean values of quartz, feldspar and lithics (recalculated as a percentage of the framework population), and matrix, for the clastic component of the Turondale Formation (the Turondale porphyry is also included for comparison). To test for lateral compositional variation, the means for each measured section are compared. To test for vertical compositional variation, the means for the basal volcaniclastic unit, middle pelitic unit and upper volcaniclastic unit are compared, for the combined southeast sections (1,3,4 and 5) and the remaining sections (8,9,10).

greenschist facies metamorphism. The lithic component consists largely of volcanic detritus, including chlorite vitriclasts, and acid ignimbrites and porphyries. Siltstone clasts are also common throughout the sequence but mainly occur in the coarser fraction as outsized intraclasts, which were not detected by point counting. Other sedimentary rock fragments are much less abundant, and include quartz-phyllosilicate aggregates, quartz sandstone, limestone and chert.

The volcaniclastic sandstones classify as feldsarenites (Folk 1980; Figure 7.26a), and it is clear from the composition of the grain assemblage and abundance of volcanic rock fragments, that the source of the clastic rocks is volcanic. The mineralogical assemblage

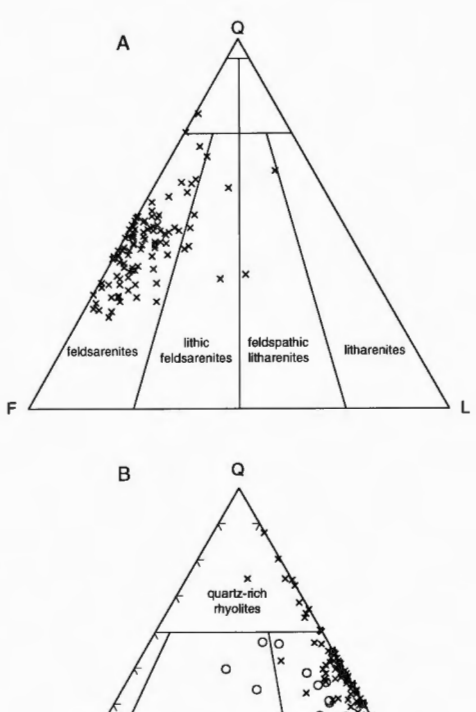

Figure 7.26: Petrographic-based classification of volcaniclastic sandstones of the Turondale Formation. Figure 7.25a is based on Folk (1980). Figure 7.25b is the quartz-orthoclase-plagioclase classification system of Streckeisen (1979) Crosses represent modal abundances and circles represent CIPW-normative compositions, plotted for comparison. The difference between normative and modal compositions reflects the presence of K-feldspar in the matrix of the volcaniclastic sandstones. This K-feldspar is included in CIPW-normative calculations, but not in modal analyses, as the matrix is too fine-grained to point count individual grain compositions.

indicates a dacitic composition for the source magma, based on the classification system of Streckeisen (1979; Figure 7.26b).

Because there are only two main components to the grain assemblage, the proportions of quartz and plagioclase vary sympathetically throughout the sequence (Figure 7.27). Although the ratio of quartz to plagioclase grains varies from bed to bed, there is no significant or systematic stratigraphic variation in the grain assemblage (Table 7.6; Figure 7.27). Sandstones at the base and the top of the formation have the same composition (Figure 7.28), although they are separated by a thick pelite interval (about 200 m thick), which must represent a significant hiatus in volcanic activity. The upper sandstone interval has a slightly higher average feldspar content (2%). This was also noted by Dickson (1962) in the northwest Hill End Trough. This compositional variation is not significant enough to indicate different sources for the basal and upper sandstone packages, and probably reflects separate eruptive phases of the same volcanic source, with a slight overall increase in the basicity of the source with time. No lateral variation in the mineralogy of the sandstones was detected (Figure 7.28, 7.29). Modal abundance of quartz and plagioclase in the Hill End Anticline (west) and northwest Hill End Trough, are within error of those in the type area (southeast).

The only other compositional difference between the basal and upper sandstone intervals is that the basal CRVS contain a higher proportion of outsized exotic lithic clasts, particularly in the southeast sections. This feature was not detected by point count analysis, which is limited to the sand-sized and finer matrix fractions only. The presence of these larger lithic clasts correlates with the overall coarser grainsize and greater bedding thickness of the basal sandstones (see Chapter 7.4.1). The clasts consist of: (1) acid volcanic rocks (ignimbrite and coherent porphyries) from the volcanic source region, which may be accessory or accidental in origin; (2) limestone fragments that were probably incorporated as accidental lithics into the parent pyroclastic flows as they traversed a shallow marine setting; and (3) shale intraclasts derived from contemporaneous basin sediments eroded by the derivative megaturbidites. For the finer lithic fraction (sand- to gravel-sized grains detectable by point counting), mean lithic contents are slightly lower for the Hill End Anticline and northwest Hill End Trough, than in the type area to the southeast (Figure 7.29).

Comparison with the Merrions Formation

In contrast to the compositionally uniform Turondale Formation, the CRVS of the Merrions Formation are subdivided into a number of stratigraphic members that have discrete compositional assemblages, reflecting derivation from several sources that were variously

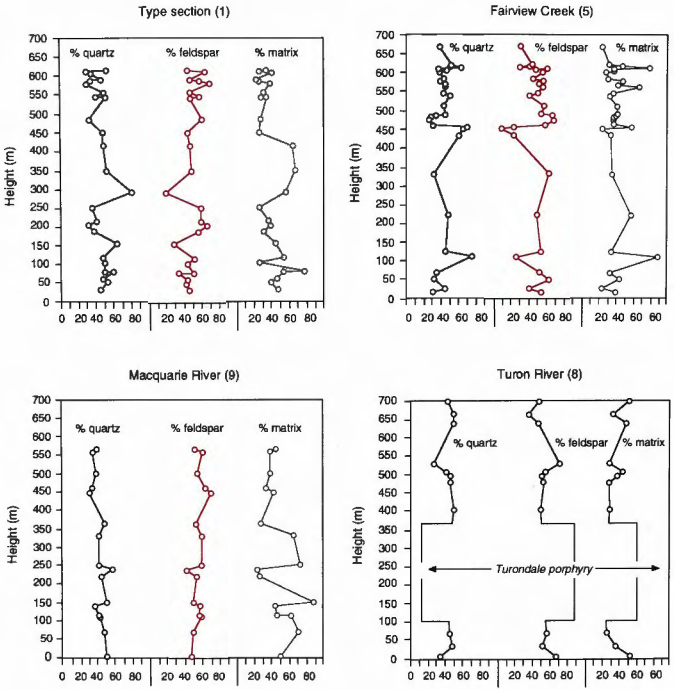

Figure 7.27: Stratigraphic variations in the percentage of quartz, feldspar and matrix in the CRVS of the Turondale Formation. The feldspar and quartz contents vary sympathetically, as they are the two main components of the grain assemblage. The mean composition of the Turondale porphyry is plotted on section 8, showing its markedly different composition to the clastic assemblage it intrudes.

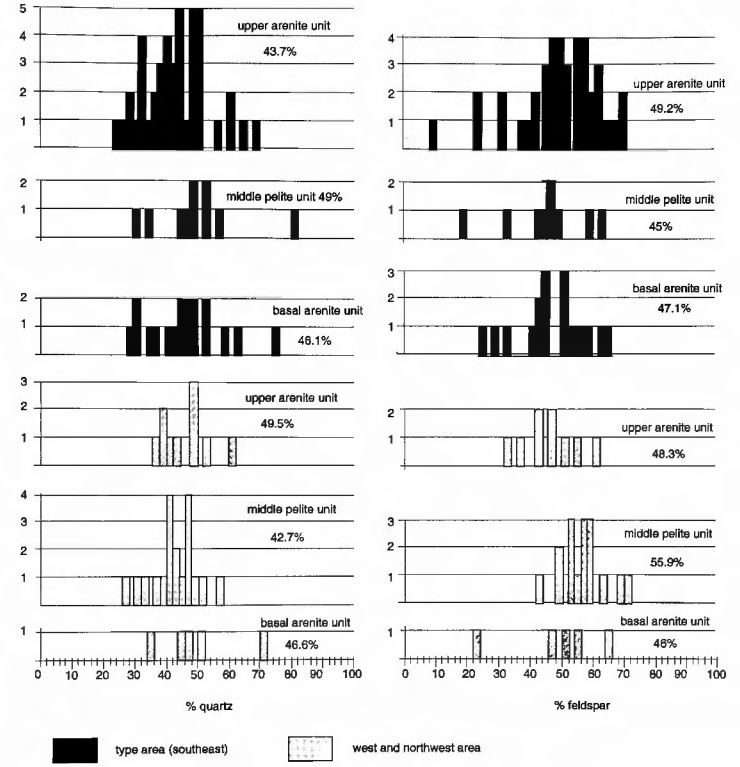

Figure 7.28: A graphic presentation of the data in Table 7.6, showing the lack of stratigraphic variation in the quartz and feldspar contents of the CRVS.

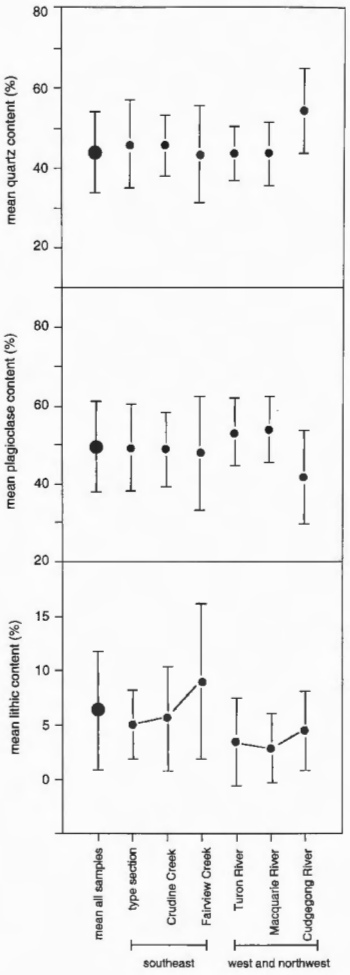

Figure 7.29: Mean quartz, plagioclase and lithic contents for measured sections, showing there is little lateral variation in the composition of the volcaniclastic sandstones

Unit	U-Pb zircon age[a]	Source direction	Stratigraphic member	Clastic assemblage[b]	Geochemical classification
Merrions Formation	407.1±6.9 Ma		E	1	andesite
	408.0±5.3 Ma		H	1	dacite
	407.8±6.6 Ma		D	3	rhyodacite-rhyolite
			M	1	andesite[c]
			L	1	andesite[c]
			B1	1	dacite
			B2	4	rhyodacite
	411.9±5.0 Ma		A	1	andesite
			P	2	andesite
			K	3	rhyodacite-rhyolite[c]
			F	2	andesite[c]
Turondale Formation			upper volcaniclastic unit	5	dacite
	413.4±6.6 Ma		lower volcaniclastic unit	4	dacite

a ages calibrated to QGNG standard (see Chapter 8)
b Clastic assemblage 1: high plagioclase-low quartz-little or no K-feldspar; Clastic assemblage 2: high plagioclase-moderate quartz-little or no K-feldspar; Clastic assemblage 3: quartz-K-feldspar-plagioclase; Clastic assemblage 4: high plagioclase-low quartz-variable range of K-feldspar; Clastic assemblage 5: plagioclase and quartz in equal proportion-little or no K-feldspar
c geochemical analyses are not available for these units; their composition is inferred by the similarity of their framework assemblages to units for which geochemical data are available.

Table 7.7: A summary of the petrographic and geochemical composition of volcaniclastic units within the volcanogenic Turondale and Merrions Formations of the Crudine Group, illustrating the temporal variation in the composition and direction of the source. Data for the Merrions Formation are from Cas (1977, 1978 and 1983).

active at different times (Cas 1977; 1983a). Three petrographically distinct clastic assemblages are recognised within the Merrions Formation:

1. quartz-poor (< 20%), plagioclase-rich, little or no K-feldspar (members E, L, M, A)
2. quartz-rich (≥ 20 %), plagioclase-rich, little or no K-feldspar (members P and F)
3. high quartz, plagioclase, K-feldspar (members D and K).

The CRVS of the Turondale Formation are most similar in composition to assemblage (2) of the Merrions Formation, which occurs in basal stratigraphic members P and F (Table 7.7). However, they have a significantly higher quartz content, indicating a more silicic magmatic composition (as discussed below), and are therefore unlikely to be derived from the same magmatic source.

7.3.2 Geochemistry

The volcanic and volcaniclastic suite of the Crudine Group shows a wide range of compositions from andesite to rhyolite, with silica ranging from 55-75% (Figure 7.30a). ASI (aluminium saturation index) ratios are mainly < 1.1, indicating the suite is metaluminous (Figure 7.30b). Aluminosilicates such as garnet and cordierite, which are characteristic of S-type or sediment-derived volcanics, are absent, and Cas (1977) recorded rare relict amphibole grains in the Merrions Formation porphyries. These features define the rocks as I-type based on the criteria of Chappell and White (1984). The suite shows some scatter of values for K_2O, with particularly high-K values for the porphyries of the Merrions Formation (Figure 7.31a). This scatter is likely to reflect mobility of K_2O during metamorphism. All units exhibit a high degree of scatter of Na_2O due to albitisation during greenschist facies metamorphism (Figure 7.32).

Classification

Based on their SiO_2 contents, the CRVS of the Turondale Formation classify as dacites in composition (Figure 7.31), which is consistent with their petrographic classification (Figure 7.26). Two of the sandstones analysed exhibit anomalously high silica, and are rhyolitic, rather than dacitic, in composition (SiO_2 ~75%). These samples represent rare quartz-lithic sandstones, which have a higher quartz content than the dacitic volcaniclastic sandstones that comprise most of the formation. In sample 95843097 the rhyolite composition reflects a greater mineralogical maturity. The sandstone contains more quartz (71%) and less feldspar and lithic fragments than most of the Turondale Formation arenites (average quartz content = 45%). Sample 95843086 has a higher quartz content than average (62%) and also contains a high proportion of quartz-rich volcaniclastic intraclasts, providing a silicic contaminant which alters the chemical composition. These samples are also strongly peraluminous (ASI from 1.35 - 1.5), reflecting a more sedimentary source than the metaluminous I-type volcaniclastics that dominate the formation (Figure 7.30b).

The volcaniclastic sandstones of the Merrions Formation fall within two distinct compositional ranges (Figure 7.31). The units containing essentially no K-feldspar, high plagioclase and moderate to low quartz contents (i.e. clastic assemblages 1 and 2), classify as andesites, with SiO_2 ranging from 55-60%. The K-feldspar-bearing units, with associated abundant quartz (i.e. clastic assemblage 3), are considerably more felsic in composition, and classify as rhyodacites to rhyolites (68-74% SiO_2). The Turondale porphyry and coherent porphyritic lavas of the Merrions Formation described in Section 7.1.2, classify as dacites

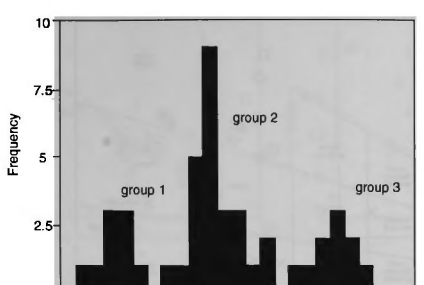

Figure 7.30a: Frequency histogram showing the silica range of the volcanogenic Turondale and Merrions Formations. Note that there is not a continuous spread in the composition as would occur in a fractionating intermediate calcalkaline suite. Instead, there appears to be three discrete compositional groupings within the silica range (labelled groups 1, 2 and 3). From the most mafic to most felsic, these correspond to: (1) andesitic volcaniclastic members of the Merrions Formation; (2) dacitic volcaniclastics of the Turondale Formation, plus the dacitic porphyries of the Merrions and Turondale Formations; and (3) rhyodacitic to rhyolitic volcaniclastic members of the Merrions Formation.

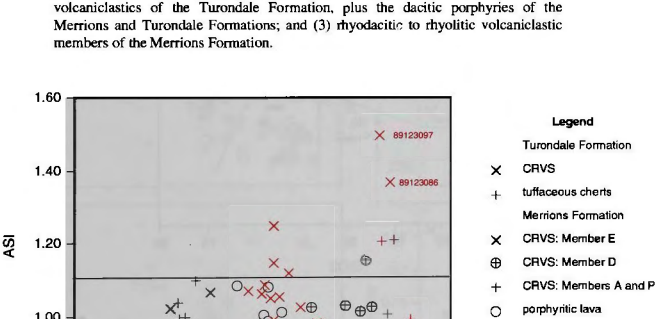

Figure 7.30b: ASI ratios showing that the suite of volcanogenic rocks within the Crudine Group is predominantly metaluminous to weakly peraluminous.

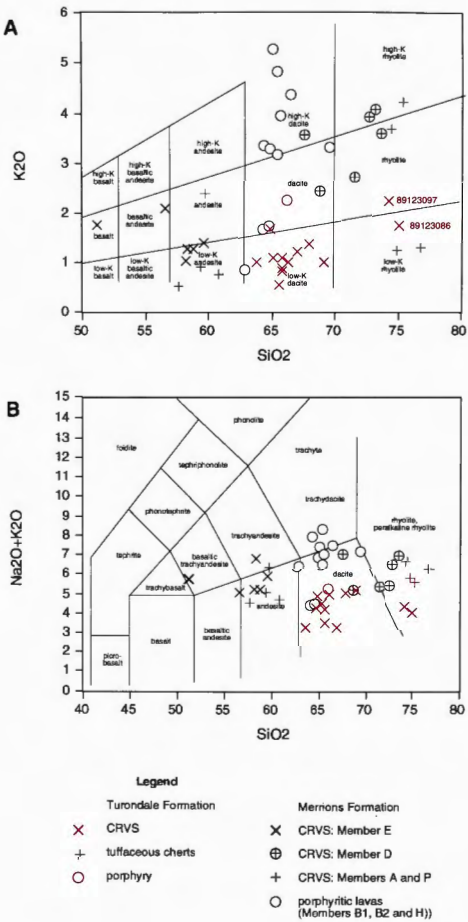

Figure 7.31: (a) Classification of CRVS of the Turondale and Merrions Formation using: a) the geochemical system of Peccerillo and Taylor (1976), modified after Gill (1981); and b) the geochemical system of LeBas et al. (1986).

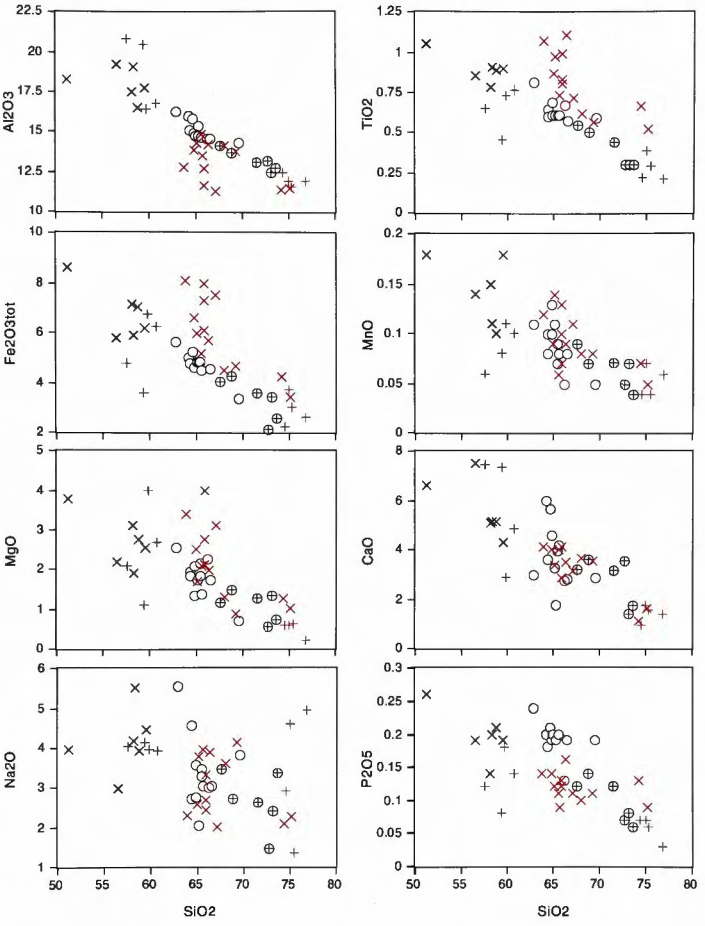

Figure 7.32a: Major element geochemistry of the Turondale and Merrions Formations. Legend is as for Figure 7.31. All x-axes have the same scale and represent percentages of SiO_2.

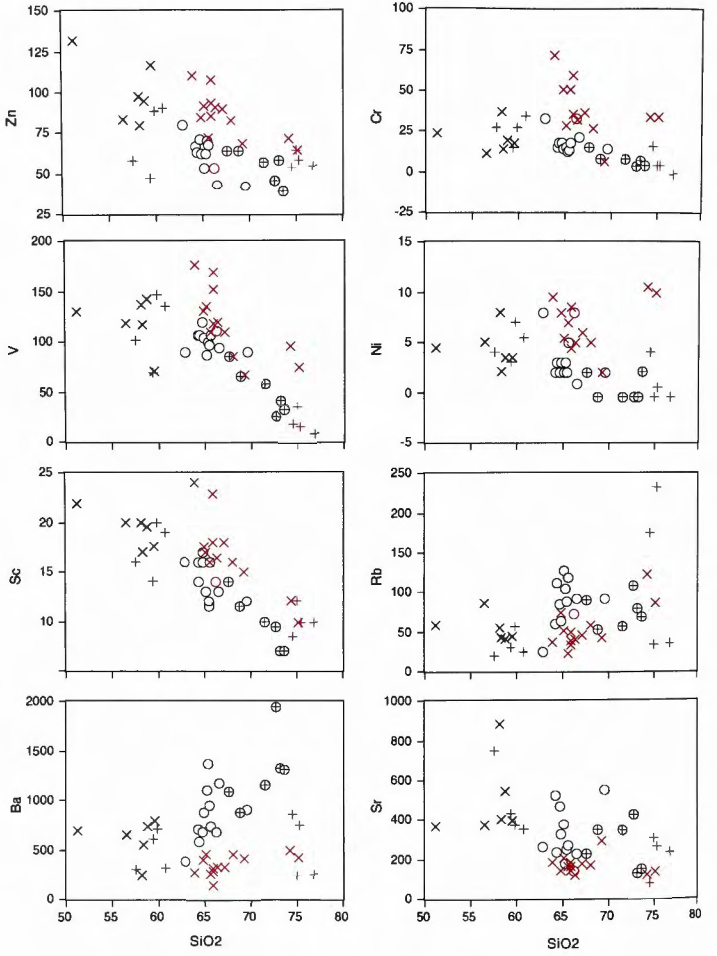

Figure 7.32b: Trace element geochemistry of the Turondale and Merrions Formations.

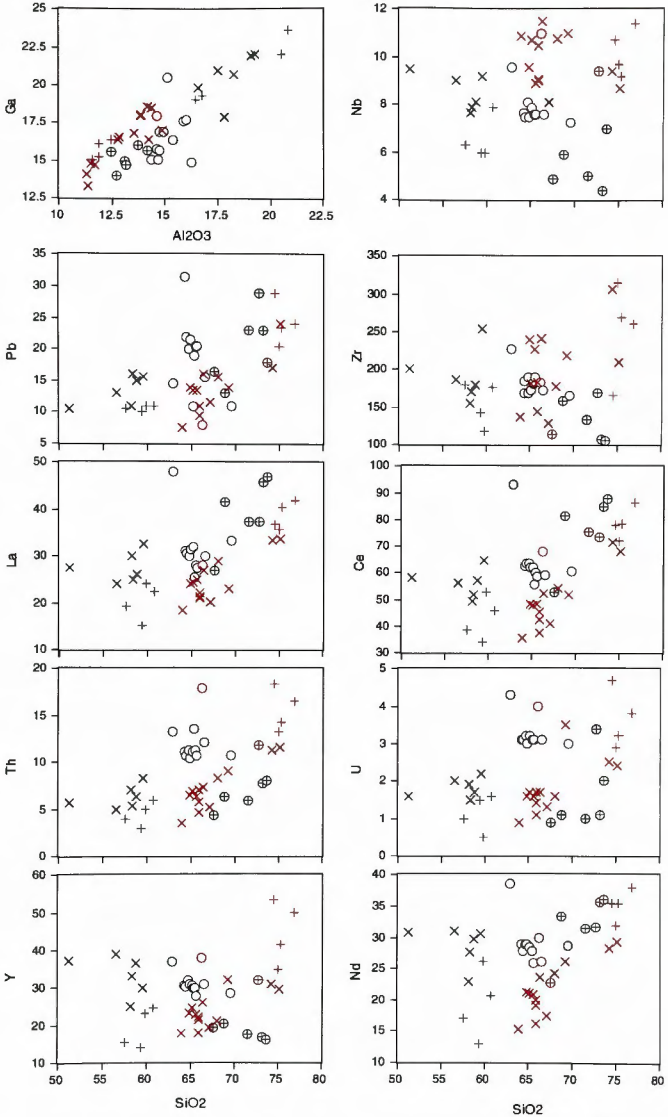

Figure 7.32b: cont'd.

(63-70% SiO_2). Although the lavas and CRVS of the Merrions Formation form a reasonably coherent geochemical suite spanning a wide range of SiO_2, the trends are not produced by differentiation of a single magmatic source. The lavas are enriched in K_2O, Rb, Th, U, Nb, Y and P_2O_5 relative to the CRVS, suggesting they were derived from a different magmatic source. Temporally, the volcaniclastics record a compositional trend from andesitic to rhyodacitic to andesitic, which is not consistent with magmatic differentiation, fractionation or restite unmixing of a single magmatic source. This implies that the volcaniclastic component of the Merrions Formation was derived from several sources, which is consistent with palaeogeographic evidence indicating a shift in the dominant source direction through time, from the west through to the south and southeast and finally the east (Cas 1977; Table 7.7).

Comparison of the Turondale and Merrions Formations

Variation diagrams indicate that the CRVS of the Turondale Formation are significantly enriched in high field strength elements (TiO_2, Nb) and transition elements (FeO_{tot}, MgO, Cr, Ni, V, Sc) relative to the suite of volcanic and volcaniclastic rocks comprising the Merrions Formation (Figure 7.32). They are also comparatively depleted in Al_2O_3, Ba, Sr, and rare earth elements (Figure 7.33), and have a higher Ga/Al ratio (7.32). The Turondale Formation volcaniclastics exhibit a flat HREE pattern, whereas the CRVS of the Merrions Formation exhibit some HREE depletion (Figure 7.33). Enrichment of the transition metals may be partly secondary, caused by chloritisation of volcanic glass in the matrix during greenschist facies metamorphism. However, Ti, Ni and rare earth elements are normally considered relatively immobile, so these trends must reflect primary differences in source composition. As the transition metals behave compatibly with the high field strength elements, this infers that their enrichment in the Turondale Formation is also likely to reflect primary differences in source composition. The high Mg, Fe and Ti contents combined with flat HREE patterns, suggest that the Turondale Formation originally contained mafic mineral phases such as igneous hornblende, that were altered to chlorite, epidote and Fe-Ti oxides during greenschist facies metamorphism. The high Ti and Nb contents and Ga/Al ratio of the Turondale Formation suggests the rocks were derived from partial melting of a continental basaltic (tholeiitic) source.

Estimating source composition

It is important to note that the geochemical compositions of the crystal-rich volcaniclastic sandstones do not reflect the original composition of their magmatic sources. One

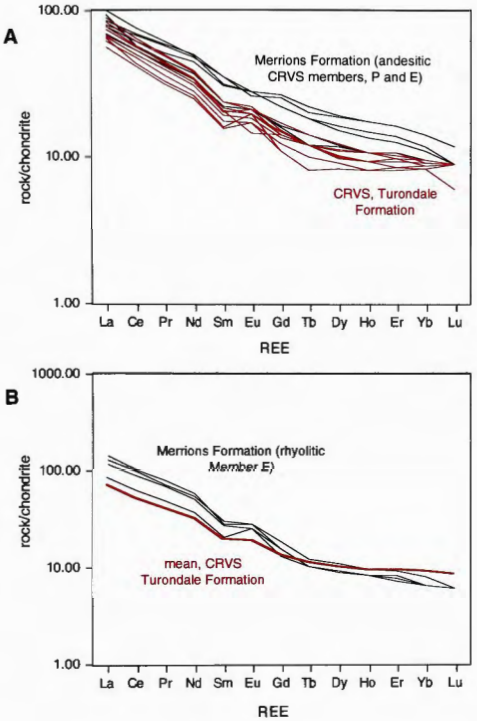

Figure 7.33: A comparison of rare earth elenent (REE) abundances in the CRVS of the Turondale Formation with: (a) andesitic members of the Merrions Formation; and (b) rhyolititc Members of the Merrions Formation. In both cases, the Turondale Formation contains lower REE concentrations and has a flat HREE pattern in contrast to sloping HREE patterns in the Merrions Formation.

consequence of crystal enrichment in the CRVS resulting from the preferential loss of vitric material during eruption and transportation, is that their composition will depart notably from that of the parent magma. The CRVS will be enriched in those chemical elements contained in higher proportion in the crystals, and depleted in those contained in higher proportion in the glass (e.g. Walker 1972). The overall geochemical effect is therefore analogous to removing the minimum melt component of the eruptive magma, and the original magmatic compositions would have been more evolved than the preserved feldspar-quartz-rich crystal aggregates would indicate from their geochemistry. Thus, for example, the andesitic CRVS of the Merrions Formation may have actually been derived from a dacitic source, and the dacitic CRVS of the Turondale Formation may have been derived from a rhyolitic source.

As discussed in Chapters 7.1.5 and 7.2.2, the fine-grained cherty tuffaceous sandstones and siltstones within the Turondale Formation are interpreted to represent the complementary glass-rich ash material from the same series of eruptions that produced the subaqueous crystal-rich volcaniclastic megaturbidites. They form the graded pelitic tops of megaturbidites, and a thick succession overlying the distal reaches of the basal megaturbidites that was deposited by ash turbidites developed from fine-grained material that was elutriated from the megaturbidite flow. Neither the crystal-enriched volcaniclastic deposits, or the complementary crystal-depleted ash, will have the same composition as the erupting magma.

Based on this model, the geochemical differences between the CRVS and complementary cherty rocks are considered to result from post-eruptive fractionation of the phenocryst and glass components of the original magma, with the fine vitric ash component being richer in SiO_2 (CRVS 64-70% SiO_2 c.f. cherty rocks 74-77% SiO_2; Figure 7.34). The composition of the source magma should therefore lie somewhere on a mixing line between the phenocryst-enriched volcaniclastics and the separated vitric fraction, represented by the now devitrified tuffaceous cherty rocks. The exact position of the original magmatic composition on this mixing line will depend on the amount of ash loss that occurred during eruption and transportation. In Figure 7.34, mixing trends representing the possible range of the original magmatic composition are constructed on variation diagrams using the average volcaniclastic and chert compositions as end members for bulk mixing calculations. Although there is a considerable degree of scatter in analyses of both the volcaniclastics and cherts, many element trends, particularly the compatible elements, follow the calculated mixing line as expected.

Based on visual estimates, crystals constitute up to about one third of the chlorite-altered vitriclasts thought to be juvenile clasts, that occur within the CRVS of the Turondale and

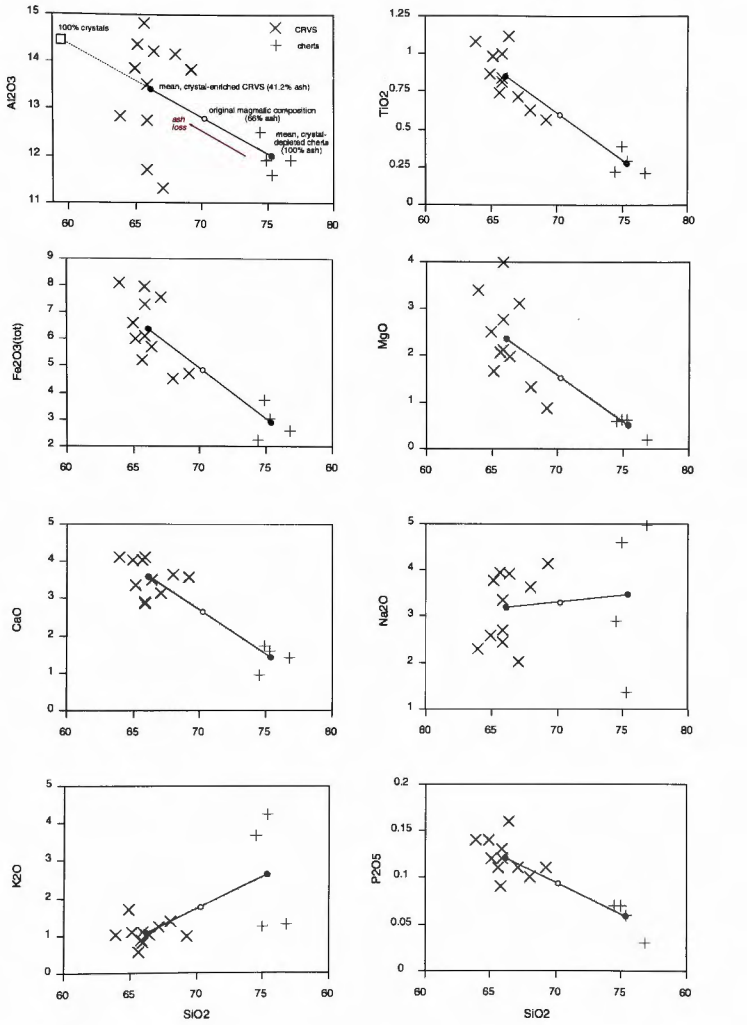

Figure 7.34: Variation diagrams showing mixing trends joining the average composition of the dacitic volcaniclastics and the rhyolitic cherts of the Turondale Formation. The open circle indicates the original magmatic composition, assuming 25% ash-loss in the CRVS, and is generated by bulk mixing calculations.

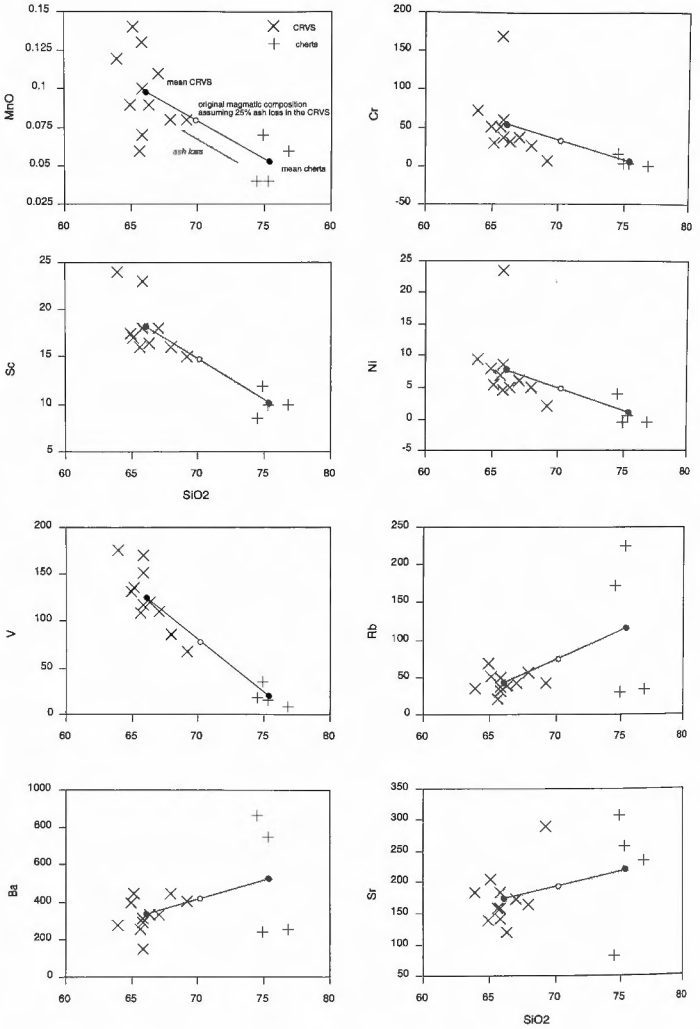

Figure 7.34: continued.

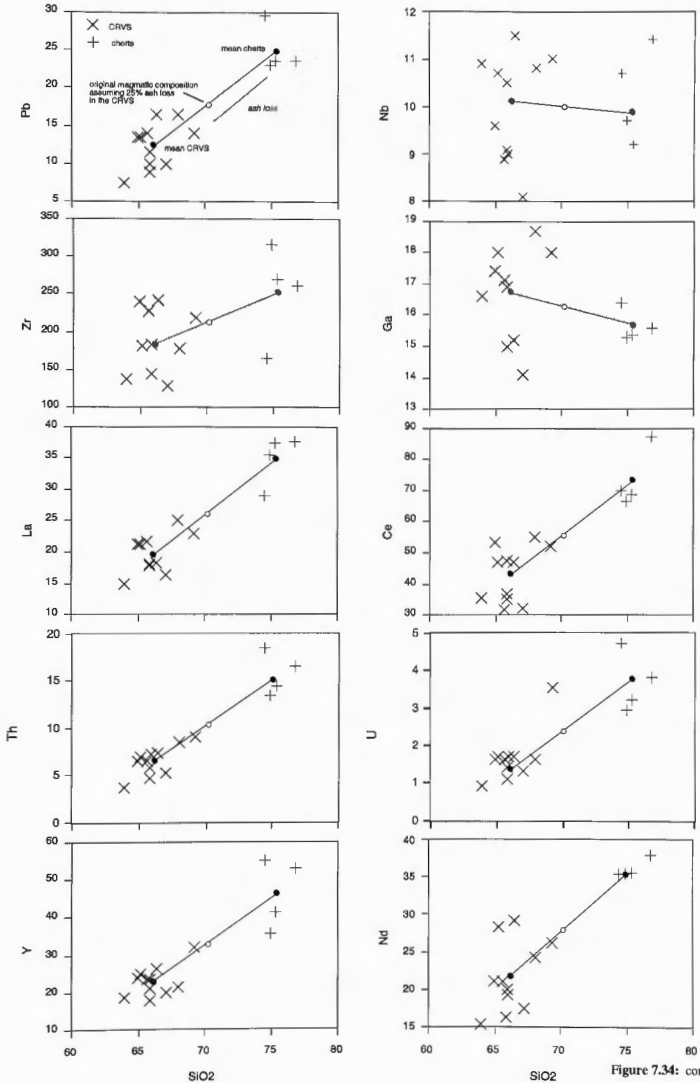

Figure 7.34: cont'd.

Merrions Formations (Cas 1983a). Using mean crystal contents of 58.8% for the Turondale Formation and 62.4% for the Merrions Formation (Figure 7.35), this implies that at least 25% ash loss occurred during transport and deposition of the CRVS in both formations. Assuming 25% ash loss, the SiO_2 content of the original magma sourcing the Turondale Formation is calculated as 70.1% (Figure 7.34), indicating on average, a 4% depletion in SiO_2 in the CRVS. For an ignimbrite and comagmatic pluton in the New England Batholith, Flood et al. (1980) showed that a 3.7% loss of SiO_2 is consistent with the loss of about 36% of the vitric fraction during eruption and transportation. The calculated silica difference resulting from ash loss is slightly higher for the Turondale Formation, but given the ball-park estimates involved in such calculations, the results of these two studies compare reasonably well.

The construction of mixing lines between the phenocryst-enriched and complementary glass-enriched fractionates from the same series of eruptions, allows the geochemical effect of ash loss to be quantified. The difference in composition between crystal-rich volcaniclastics and the cherty rocks reflects the partitioning of elements between the phenocrysts and the residual melt fraction of the parent magma just prior to eruption. Compatible elements such as Fe, Ti, Mg, Mn, Ni, Cr, V, Sc, which partition into ferromagnesian phenocryst phases (pyroxenes, amphiboles), are enriched in the volcaniclastics relative to the parent magma. The enrichment of Al and Ca reflects partitioning of these elements into plagioclase. Sr should also partition into plagioclase and concentrate in the volcaniclastics, but instead are depleted. However, these elements, along with Rb, Ba, K and Na, exhibit a very high degree of scatter in the cherts, probably reflecting their high mobility during metamorphism, and the trends may be unreliable. Incompatible elements (K, Na, Rb, Pb, Zr, Y, U, Th, Nd, La, Ce), which partition into the melt, are depleted in the CRVS following removal of the glass fraction. Most rare earth elements (REE) are also depleted in the CRVS relative to the cherty rocks (Figure 7.36). This indicates the REEs also partitioned into the melt, which, in turn, infers an absence of REE-rich minerals (e.g. allanite, monozite, titanite) in the phenocryst population (titanite is common, but secondary, replacing primary Fe-Ti oxides). The exception is Eu, which exhibits a small positive anomaly in the CRVS and a strong negative anomaly in the cherts. Eu^{2+} has a lower oxygen fugacity than the other REEs, and partitions into plagioclase, preferentially replacing Ca^{2+}, rather than concentrating in the melt. Eu is therefore concentrated in the CRVS and depleted in the cherts due to the separation of plagioclase crystals from the vitric fraction. The original magma probably had a small negative Eu anomaly.

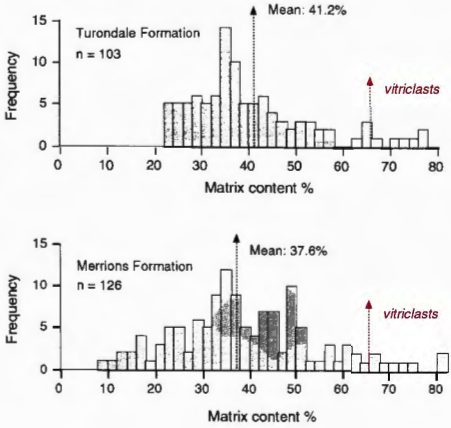

Figure 7.35.: Crystal/matrix proportions of the clastic rocks of the Merrions and Turondale Formations, with the approximate matrix content of altered juvenile vitriclasts plotted for comparison. The histogram for the Merrions Formation is from Cas (1983a). A crystal content of about 33% for the juvenile vitriclasts is based on visual estimate rather than modal analysis.

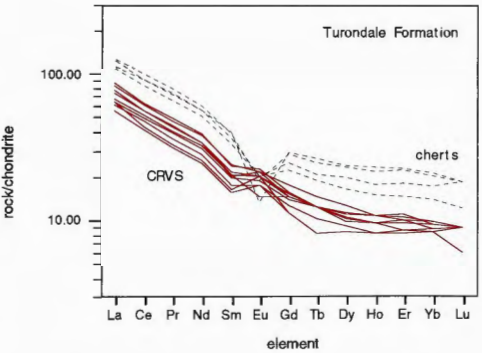

Figure 7.36.: Rare earth element (REE) abundances of the CRVS and cherty tuffaceous rocks of the Turondale Formation.

This study emphasises the problems of interpreting whole-rock geochemical analyses of pyroclastic flow deposits or other syn-eruptive volcaniclastic products that have been physically modified during eruption and deposition. However, it also shows how these problems may be overcome to enable the composition of the source magma to be constrained. The ability to constrain the possible range of the original magmatic composition (and to estimate the composition assuming a certain percentage of ash loss) is important for provenance studies, enabling geochemical matching of the modified syn-eruptive volcaniclastic deposit to suspected comagmatic plutons, or other unmodified to less modified volcanic products of the same source (e.g. Flood et al. 1980; Chapter 7.4.3).

7.4 PROVENANCE AND PALAEOVOLCANOLOGY

The following section discusses facies associations within the Turondale Formation, considering both vertical variation in the dominant facies type, and lateral variation in the spatial distribution of facies. The former reflects broad temporal changes in volcanic activity in the source region. The lateral distribution of facies, sand-to-shale ratios and lateral variations in the thickness and grainsize of beds within units, can be used with palaeocurrent indicators provided by sedimentary structures to determine the point of sediment influx into the Hill End Trough. This information is then used to outline potential sources for the Turondale Formation, and to reconstruct the volcanic history of its source region.

7.4.1 Facies relationships

Packham (1968a) subdivided the type section of the Turondale Formation into three units based on dominant lithology or facies type, which are referred to as the lower, middle and upper units in the following discussions. The lower and upper units comprise mainly volcaniclastic sandstones, and the middle unit represents a hemipelagic interval of mainly interbedded shale and siltstones. This broad three-fold subdivision of the type section can be recognised laterally throughout the Turondale Formation, and provides the basis for an internal first-order vertical stratigraphy. Lateral variations within and between units are illustrated in Figures 7.37-7.40 and described below.

Lower unit

The base of the Turondale Formation is marked by an increase in the thickness of beds, and a compositional change from quartz-dominated detritus in the underlying Cookman Formation, to feldspathic volcaniclastic debris (Packham 1968a). In the southeast Hill End Trough (Sofala area) the contact is sharp, and the base is marked by about 10-25m of conglomerates,

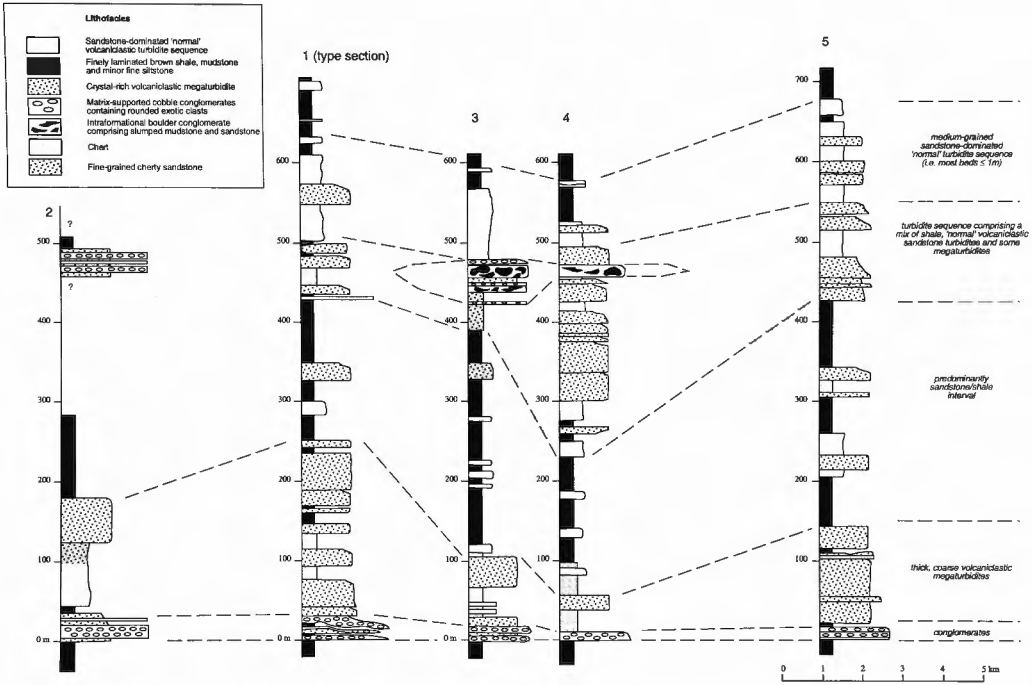

Figure 7.37: Correlation profile for stratigraphic sections measured in the southeastern region of the Hill End Trough (type area, Sofala region).

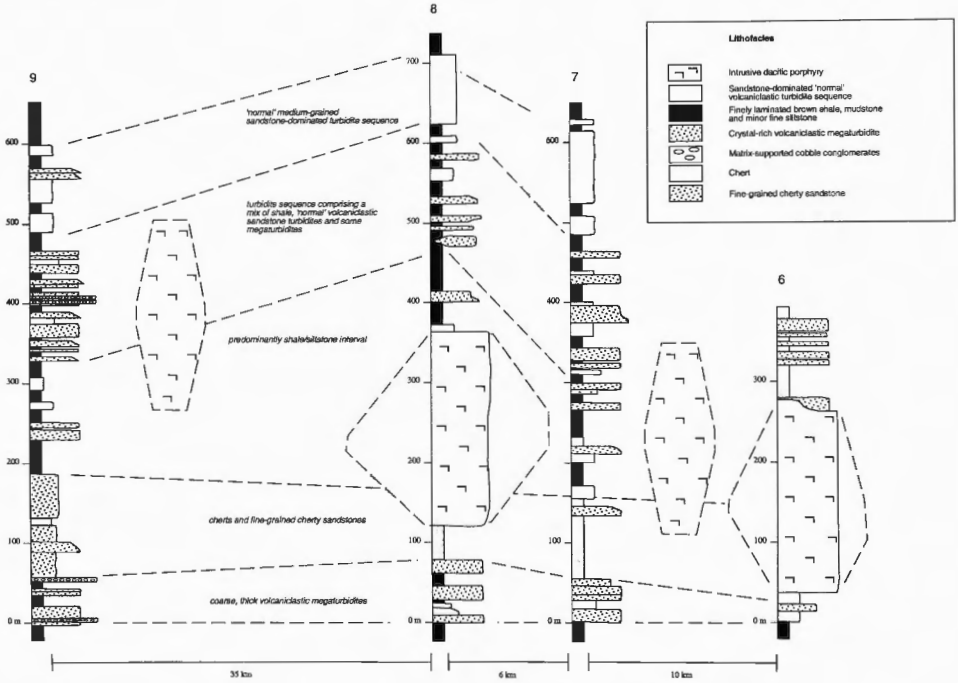

Figure 7.38: Correlation profile for stratigraphic sections measured in the southwestern region of the Hill End Trough, where the Turondale Formation folds around the axis of the Hill End Anticline. The sedimentary sequence shows stratigraphic continuity, apart from where it is intruded by lenses of porphyry.

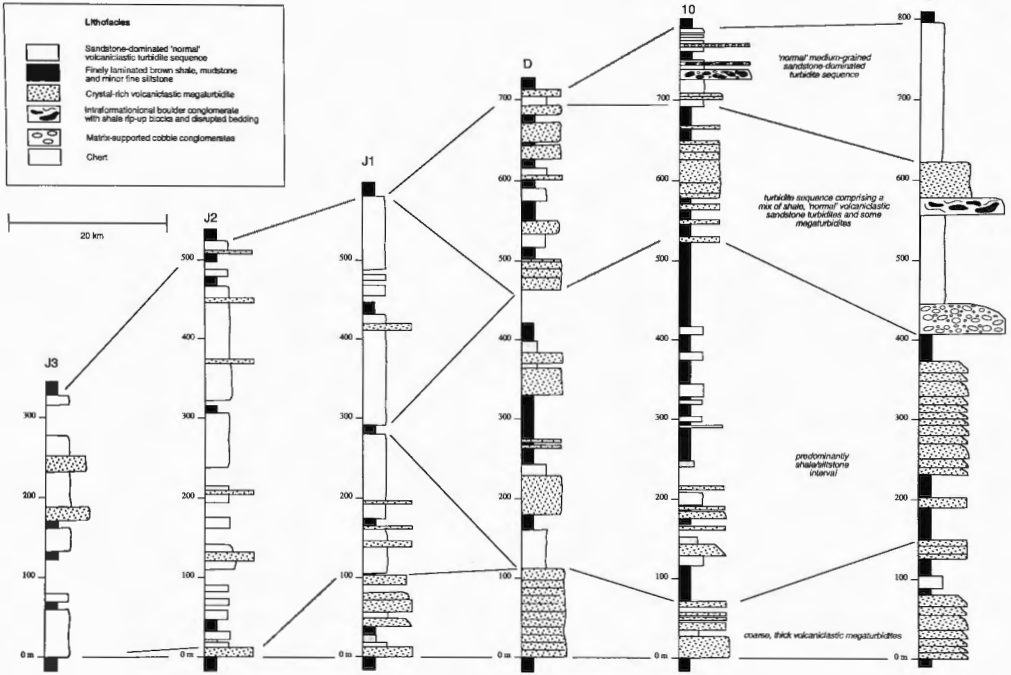

Figure 7.39: Correlation profile for stratigraphic sections measured in the northwestern region of the Hill End Trough. Sections from Dickson (1962; D), Shatwell (1962; S) and Jessup (1967; J1, J2 and J3) are included.

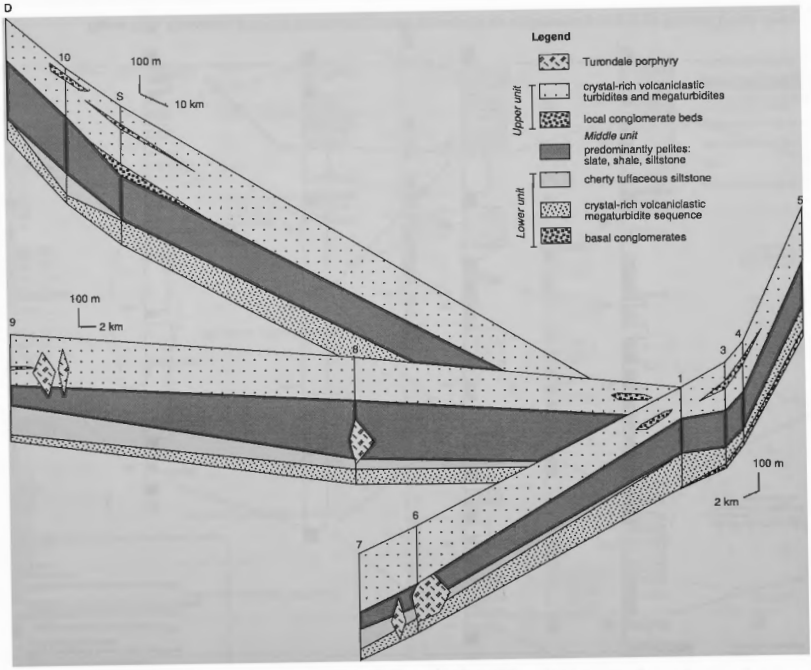

Figure 7.40: A schematic three dimensional depiction of the stratigraphy of the Turondale Formation, illustrating the lateral variation of units within the formation.

overlain by very thick (up to 55 m), coarse-grained volcaniclastic sandstones and breccias. These megabeds commonly grade from very coarse-grained volcaniclastic breccias at the base, into massive, coarse-medium-grained crystal-rich volcaniclastic sandstone, with small (cm-scale) intervals of laminated fine-grained cherty sandstone and/or mudstone at the top.

Elsewhere in the trough, these basal coarse-grained conglomerates and volcaniclastic breccias are not present, and the basal contact of the Turondale Formation is taken to be the first appearance of a thick horizon of feldspathic sandstone of prominent and distinctive outcrop (Packham 1968a). The volcaniclastic sandstone package within the lower unit thins to the northwest and west, with a wedge-like geometry (Figure 7.40). No megaturbidites are recognised in the northwest. Here the thick basal volcaniclastic sandstone package comprises amalgamated thin graded turbidite beds (1-3 m), which grade from coarse sandstone at the base to fine sandstone at the top, with some beds separated by shale partings (e.g. Dickson 1962; Shatwell 1962). To the southwest, the megaturbidites become thinner, finer-grained and less abundant. The percentage of megabeds decreases from 40% in the southeast to 25% in the southwest, and the average thickness of megabeds decreases from 18 to 11 m. The megabeds consist of coarse-grained sandstone, but the coarse basal breccias common at the base of the megabeds in the southeast are absent in the southwest, and the beds have a lower lithic content.

In sections measured around the Hill End Anticline in the southwest, the volcaniclastic sandstones are overlain by a thick westward-thickening interval of cherty tuffaceous sediments which includes thick horizons of massive fine-grained cherts, and laminated fine-grained cherty sandstones. The cherty sediments are interpreted to be distal derivatives of the underlying thick volcaniclastic megabeds. They represent the finer-grained material winnowed from the pyroclastic and derivative turbiditic flows, deposited by suspension settling through the water column, and from ash turbidites, generated from the more expanded and fluidised flow tops of poorly-fluidised high grain density megaturbidity currents.

The lateral facies association of proximal volcaniclastic megaturbidite sandstones in the southeast fining distally into fine-grained cherty sediments to the southwest, suggests a west-dipping slope direction, because the turbulent clouds would become better developed downslope, forming thicker deposits in the distal setting (c.f. Cole and DeCelles 1991). The coincidence of maximum bed thickness, maximum number of thick sedimentation units (megaturbidites), maximum grainsize and maximum lithic clast size and abundance along the

southeastern margin of the Hill End Trough also indicates dominant sediment influx from the southeast.

Middle unit

The middle unit is a regionally extensive, largely hemipelagic pelitic interval which is similar in character to the overlying Waterbeach Formation, comprising dominantly interbedded shale and siltstone facies with subordinate sandstone beds up to 1-2m thick. It is tabular in shape and maintains a fairly constant thickness of about 200m. The sand-to-shale ratio varies little from section to section, averaging about 75% shale. The number of sandstone beds generally increases upsection, prior to deposition of the sandstone-dominated turbidite sequence of the upper unit.

This predominantly pelitic interval pinches out in the far northwest and interfingers with a package of volcaniclastic sandstones localised adjacent to the northwestern margin of the Hill End Trough (Figure 7.39). Jessup (1967) noted a decreasing abundance of chlorite-altered vitriclasts in the volcaniclastic sandstones from west to east, and the occurrence of detrital hornblende confined to the western outcrops, and suggested that some contribution of tuffaceous material was probably derived from the west, and was likely to have been sourced by volcanics on the Molong High. The limited spatial distribution of the sandstone package also supports the input of some material from a local source in the northwest.

Upper unit

The upper unit is a volcaniclastic sandstone-dominated turbidite sequence, reminiscent of the lower unit. However, the sandstone beds are generally thinner and finer-grained, and contain fewer outsized lithic fragments than those in the lower unit, and there is a higher proportion of interbedded shales and siltstones. The upper unit contains fewer megaturbidite beds than the lower unit (about 10% of the sandstone beds are megaturbidites compared with 30% in the lower unit), and they are generally thinner (mean thickness 12m c.f. 18m). Most of these megabeds (80%) occur in the southeastern sections. Local thin intraformational breccia beds, and conglomerates derived from extrabasinal sources, are recorded at various stratigraphic levels throughout the unit.

In most sections, the top 100-200m of the formation is marked by an interval of "normal"-sized turbidites (mostly $\leq$ 1m thick), with minor interbedded pelite. Within this sandstone-dominated turbidite sequence, the thin turbidites are commonly amalgamated, or separated by only a few millimetres of pelitic sediment. These thinly-bedded sandstones at the top of the

formation comprise mainly juvenile volcaniclastic detritus, and have the same composition as the thick, megaturbiditic sandstone beds that occur within both the upper and lower units.

Sandstone-to-shale ratios are greatest in the southeast. The upper unit contains only 5-15% pelites in the southeastern sections, compared to 25-50% in the western and northwestern sections. The higher sand-to-shale ratios are coincident with megaturbidite thickness and frequency maxima in the southeast, and suggest sediment influx was from the southeast, as for the lower volcaniclastic unit. The occurrence of an ~100 m thick conglomerate sequence in the southeast (Figures 7.37, 7.40), containing large allochthonous limestone blocks and channelised clast-supported conglomerates, also suggests this area is proximal to a slope area, and perhaps the volcanic source region. Chaotic mudstone-sandstone slump deposits which occur at a similar stratigraphic level may represent local slope collapse in a proximal fan setting (Figure 7.37).

7.4.2 Sediment movement indicators

There is a lack of sedimentary structures providing palaeocurrent data in the clastic deposits of the Turondale Formation. Bouma *c* division cross-laminations, which are commonly used as current-direction indicators are largely absent, and the soles of beds which may contain flute marks and grooves are rarely exposed. The limited available evidence in all areas is consistent, however, and indicates a general westward direction of slope prior to, during and following deposition of the Turondale Formation, with sediment flow towards the west to northwest. In the Sofala area, flute casts on the base of overturned beds in Cheshire's Creek indicate a palaeoflow from the east-southeast during deposition of the underlying Cookman Formation (Packham 1968a). In the type section of the overlying Waterbeach Formation, and east of the Wiagdon Thrust (Sofala-Limekilns districts), flute casts and small-scale current bedding also indicate sediment flow to the west and west-northwest (Packham 1968a). In the northwest Hill End Trough, small-scale current bedding and slumps in siltstones in the Waterbeach and Turondale Formations indicate the seafloor sloped to the northwest and currents flowed down this slope from the southeast (Dickson 1962; Shatwell 1962). In the Hill End region, slump structures and cross-bedded ripple marks in the Turondale Formation indicate that the slope was from east to west (Packham 1968a). In summary, evidence from sedimentary structures in the Turondale Formation, and the underlying and overlying Cookman and Waterbeach Formations, all indicate sediment movement was from the southeast.

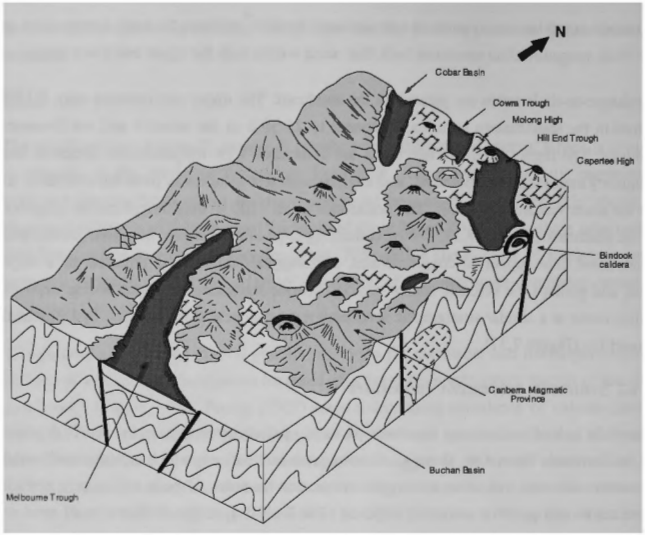

Figure 7.41: Schematic block diagram of the palaeogeography of the Lachlan Fold Belt during the Early Devonian, from Cas (1983b). The position of the Bindook Volcanic Complex at the southeastern margin of the Hill End Trough is illustrated, and active volcanism is depicted on the adjacent Capertee High (position of volcanic centres on the Capertee High is schematic).

7.4.3 Source area

Palaeocurrent indicators, and lithostratigraphic data such as sand-to-shale ratios, grainsize distribution, and variations in bedding thickness, all suggest derivation from a volcanic area somewhere south to east of Sofala. The Early Devonian was a period of extensive silicic magmatism in the northeastern Lachlan Fold Belt (Cas 1983b; Powell 1984), and potential sources for the Turondale Formation volcaniclastics exist on the adjacent Capertee High, and within the Canberra magmatic province lying beyond the southern apex of the Hill End Trough (Figure 7.41). The closest exposed source within the Canberra magmatic province is the Early Devonian Bindook Volcanic Complex, an extensive, largely subaerial silicic volcanic province filling the Wollondilly Basin east of Goulburn, considered to be

comagmatic with plutons of the Marulan Batholith (e.g. Simpson 1986; Simpson et al. 1997; Figure 7.42). The Bindook Volcanic Complex consists of an extensive pile of dacitic to rhyolitic pyroclastic rocks, quartzose and volcanogenic sedimentary rocks, and minor felsic lavas and subvolcanic intrusions. Mass-flow facies similar to those of the Merrions Formation have been documented from the southeastern margin of the Hill End Trough within the Kowmung Volcaniclastics (Cas et al. 1981). These are interpreted to be deposited within a broad, proximal submarine volcaniclastic apron, fed by the adjacent subaerial Bindook Complex. It is possible that this volcanic centre may have also sourced some of the more extensive members of the Merrions Formation, that were derived from the southeast. Members A and D of the Merrions Formation are both derived from a southeastern source. Member D shares a common framework assemblage with the lower volcaniclastic beds within the Kowmung Volcaniclastics (quartz, plagioclase and K-feldspar in roughly equal proportion), and may be their distal equivalent.

Some of the dacitic to rhyolitic ignimbrite and volcaniclastic members within the Bindook Complex have a mineralogy similar to the Turondale Formation volcaniclastics (Table 7.8), supporting its case as a potential source region. To test the hypothesis, the geochemical composition of the Turondale Formation volcaniclastics is compared with a suite of volcanics and granites from the Bindook Volcanic Complex and comagmatic Marulan Batholith (Figure 7.43). Also plotted are trend lines along which the original magmatic composition of the volcaniclastics should lie, as constructed theoretically in Chapter 7.3.2. If derived from the same source, these trend lines must intersect the chemical variation trends of the Marulan Batholith.

The variation diagrams in Figure 7.43 shows that the Turondale Formation does not conform with the trends of the Bindook-Marulan suite, showing enrichment in transition and high field strength elements and depletion in Al_2O_3, CaO, K_2O, Ba, Rb, Th, U and rare earth elements. These compositional differences are present in both the mafic and felsic end-members of the suites, and therefore must reflect different elemental abundances in their sources. High Al_2O_3, Ga, Na_2O contents and depletion of transition metals in the Merrions Formation andesites (relative to the Bindook-Marulan suite) are interpreted to be secondary trends resulting from sericitisation and albitisation. The four most altered samples were all collected from the same geographic locality (the type section) and have a highly sericitised matrix, confirming that these trends represent secondary alteration. The least altered samples plot more consistently with the Bindook-Marulan Suite, suggesting compatibility of the primary trends. It is therefore possible that some of the more voluminous members of the Merrions Formation were sourced from the Bindook Volcanic Complex.

Figure 7.42: Map of the Wellington-Bathurst-Goulbourn region, New South Wales, showing the distribution of exposed Early Devonian subaerial silicic volcanic complexes surrounding the Hill End Trough, and the distribution of the Turondale and Merrions Formations within the Hill End Trough.

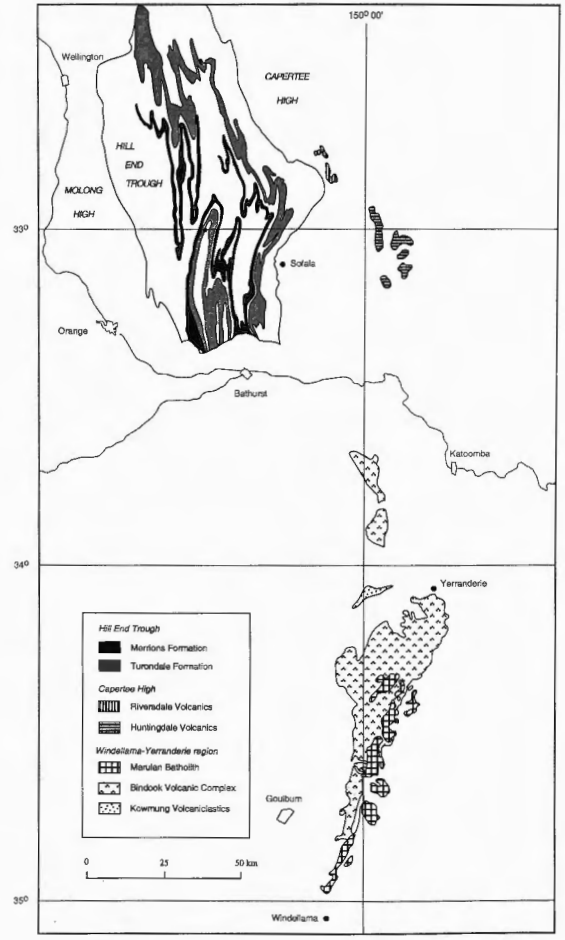

Stratigraphic Unit	Characteristic Lithofacies	Major crystal constituents	Geochemical Composition	Correlations
"Yerranderie Voicanics"	volcanic breccia & air-fall tuff	plagiociase, quartz	dacite-rhyodacite	
Barralier Ignimbrite	distinctive bluish-grey welded ignimbrite	plag.-quartz-hornblende-enstatite & minor augite, biotite & Fe-Ti oxides	dacite	
Joramin Ignimbrite	densely welded ignimbrite	plag-qtz-K-feldspar-biotite, minor hornblende	rhyolite	
"Wombeyan Voicanics"	rhyolitic tuff & rhyodacitic lava	quartz:plag in ratio of 3-2.	rhyolite	correlates with either Devil's Pulpit Member, Kerrilon Tuff Member or Joramin Ignimbrite and parts of Kowmung Volcaniclastics
Kowmung Volcaniclastics upper	"Merrions-like" thick, massive CRVS	quartz-plagioclase, minor K-feldspar, vitriclasts	dacite?	predates Barralier Ignimbrite, contemporaneous with, or postdates Wombeyan Volcs, probably lateral time-equivalent of the Tangerang Formation and Joramin Ignimbrite
Kowmung Volcaniclastics lower	"Merrions-like" thick, massive CRVS	quartz-plagioclase-K-feldspar in equal proportions	rhyolite?	
Tangerang Formation				
Kerrawarra & Came Dacite Members	extensive lavas high level sills, cryptodomes	quartz and plagiociase	dacites	
Kerrilon Tuff Member upper	multiple pyrociastic flows	lower quartz-feldspar ratio than lower unit	dacite	
Kerrilon Tuff Member lower	subaq? v'clastics non-welded igs phreatomag. air-fall	quartz-feldspar	rhyolite	
Devil's Pulpit Member	"Merrions-like" thick, massive CRVS	volcanic quartz, plag, minor K-feldspar & volcanic rock fragments	dacite?	

Table 7.8: Stratigraphy and composition of volcanic and volcaniclastic units within the Bindook Volcanic Complex (compiled from Simpson et al. 1997 and Cas et al. 1981).

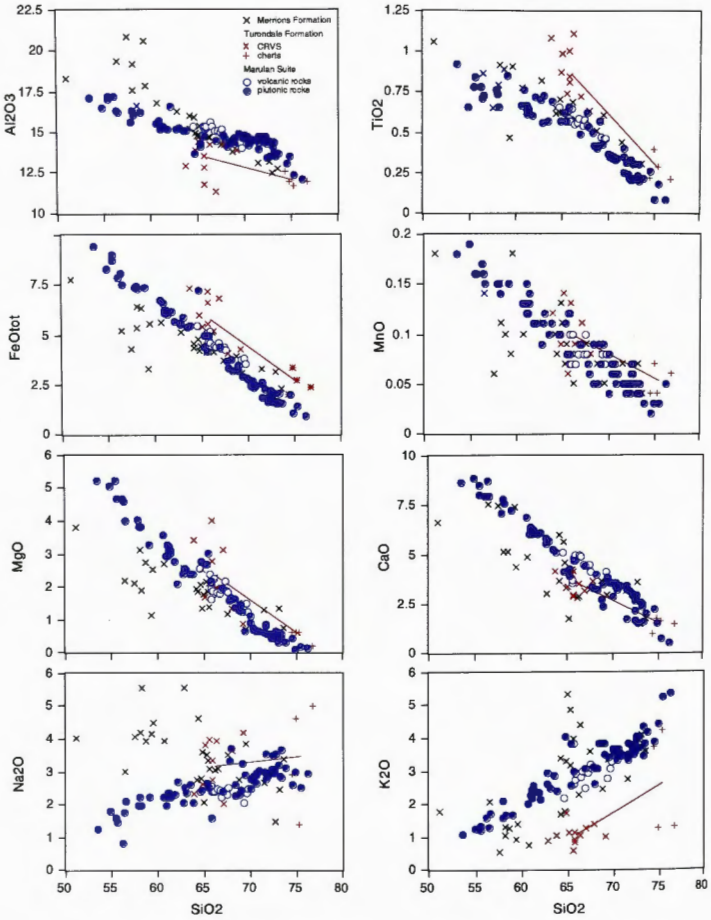

Figure 7.43: A comparison of the geochemistry of the Turondale and Merrions Formations with the Marulan Suite. Mixing lines between the Turondale Formation CRVS and cherts generated in Figure 7.34 are shown as red lines. Data for the Marulan Suite include unpublished analyses from Dr Paul Carr of Wollongong University, and analyses published in Simpson (1986).

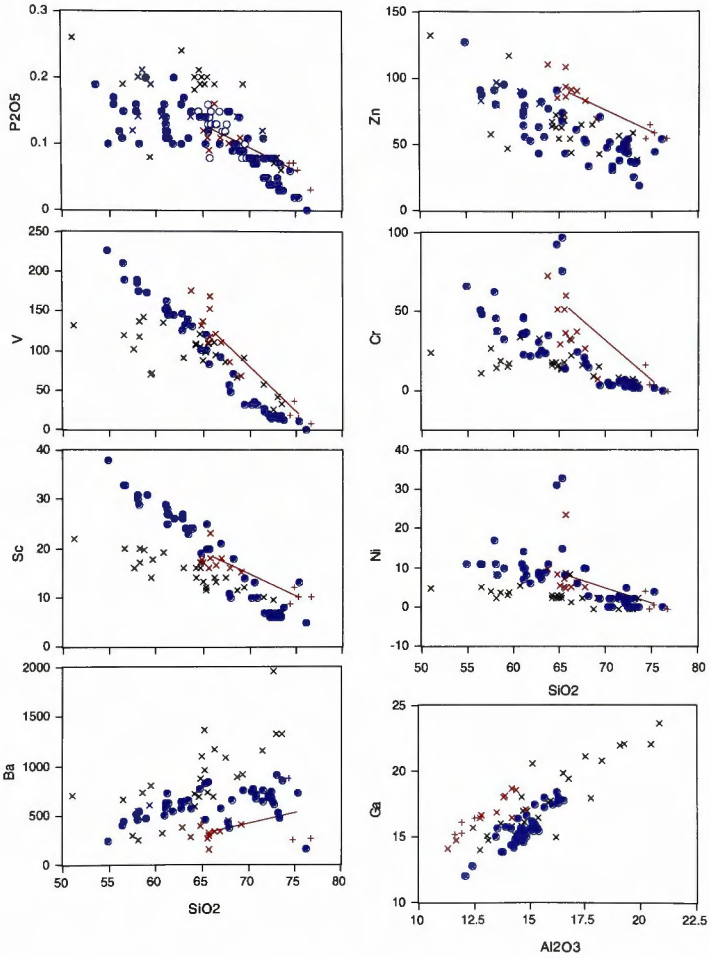

Figure 7.43: cont'd.

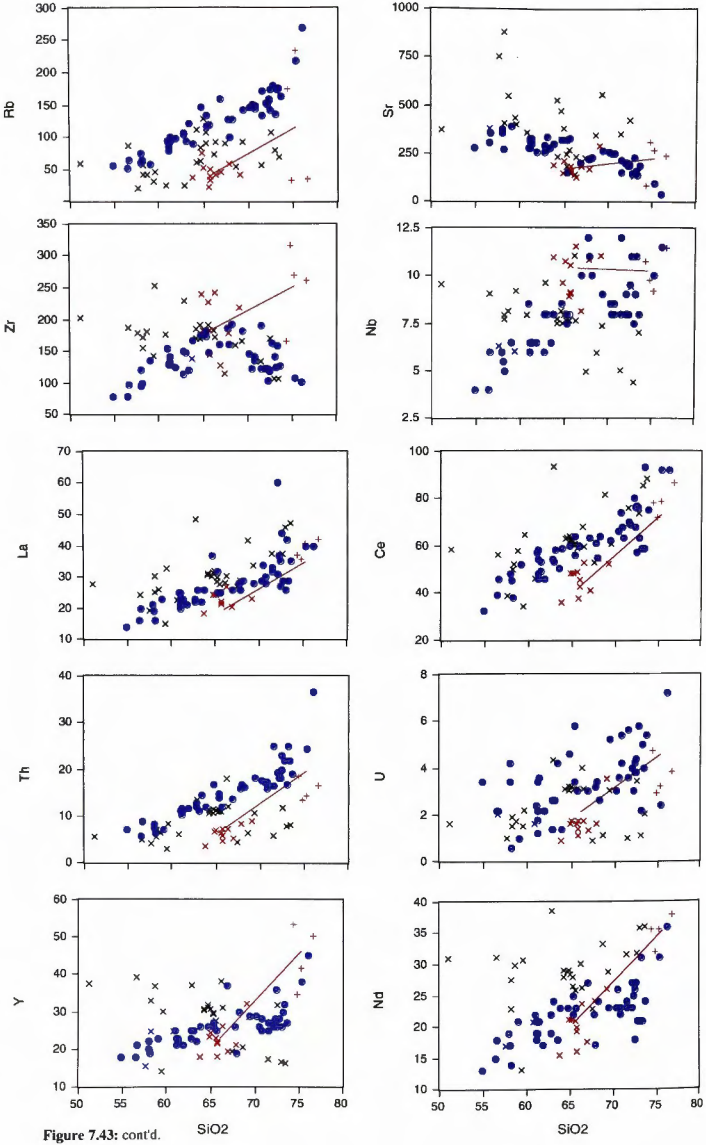

Figure 7.43: cont'd.

Voluminous silicic volcanism dominated the adjacent Capertee High during the Early Devonian, providing a potential source region more proximal to the point of sediment influx. Medium-scale calderas flanked by thick, extensive ignimbrite sheets, with associated epiclastic deposits, are recorded within the Riversdale Volcanics in the Cudgegong-Rylestone district (Colquhoun 1998). The Huntingdale Volcanics further south, in the Capertee Valley also consist of extensive ignimbrite sheets (Bracken 1977; Wright 1966). These units have a near identical mineralogy to the volcaniclastics of the Turondale Formation, suggesting they may be derived from the same magmatic source.

Modal analyses of rhyolitic ignimbrites of the Riversdale Volcanics (Appendix B2) indicate they contain roughly equal proportions of quartz (mean 50%) and plagioclase (mean 45%), with a minor lithic component (2%), comprising mainly porphyritic volcanic fragments. Minor Fe-Ti oxides and zircon are also present in most samples. The vitric component (matrix+pumice) comprises 85% of the rock, and the matrix consists of relic welded shards exhibiting a strong eutaxitic foliation. The Huntingdale Volcanics also contains quartz and plagioclase in roughly equal proportion and up to 10% opaques, in a vitric matrix (60-70%) comprising small black shards (Kennedy 1976). The Turondale Formation volcaniclastics contain the same framework minerals in similar modal abundance, averaging 45% quartz, 49% plagioclase, 6% lithics and minor Fe-Ti oxides, with a matrix component of 40%. The higher lithic content in the Turondale Formation is due to the presence of limestone clasts and intrabasinal siltstone clasts, incorporated as detritus passed through a shallow marine environment prior to final deposition in a deep marine basin.

The limited geochemical data available for the Riversdale Volcanics is compared with that of the Turondale Formation in Figures 7.44 and 7.45. No geochemical data are available for the Huntingdale Volcanics. Two dacitic samples plot within the same compositional field as the Turondale Formation for most elements (only TiO_2 is a poor match). There is also a good match in composition between the 'ash-rich' rhyolitic ignimbrites (85% matrix represents a high volcanic ash component) and the cherty tuffaceous sediments of the Turondale Formation. It is significant that the Riversdale Volcanics show the same enrichment of compatible elements (e.g. $FeO_{(tot)}$, MgO, Cr, V; Figure 7.44) and flat HREE pattern (Figure 7.45) as the Turondale Formation. This geochemical signature is distinctive, and differs notably from that of other volcanic suites assessed within in the area (c.f. Merrions Formation, Marulan-Bindook Suite), and suggests the Riversdale Volcanics were derived from a similar continental tholeiitic source as the Turondale Formation.

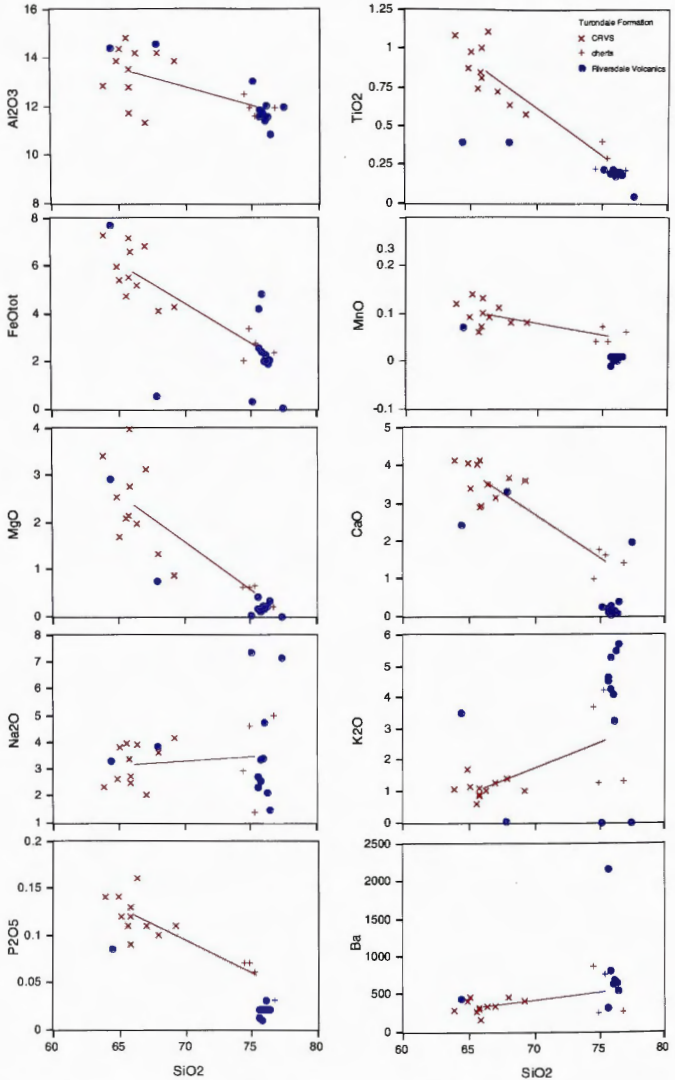

Figure 7.44: A comparison of the geochemistry of the Turondale Formation and the Riversdale Volcanics.

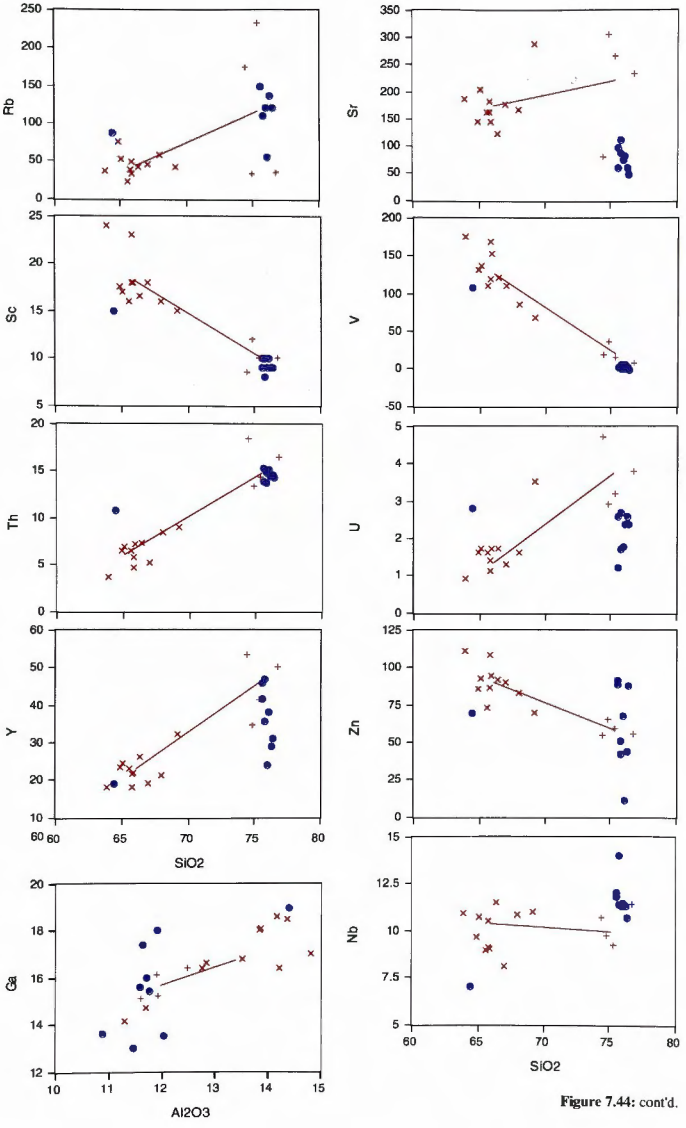

Figure 7.44: cont'd.

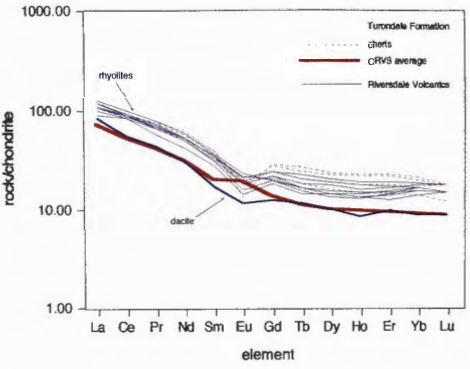

Figure 7.45: A comparison of rare earth element patterns of the Turondale Formation and Riversdale Volcanics, showing flat HREE patterns in both units.

Correlation of the Huntingdale Volcanics and Turondale Formation

Colquhoun (1995) assigned a general *sulcatus-kindlei* (early-mid Pragian) age to a marine fauna of brachiopods, corals, crinoids and conodonts recovered from small limestone lenses within the middle to upper parts of Riversdale Volcanics (Figure 7.46). The base of the Riversdale Volcanics is constrained to within or above the late Lochkovian *pesavis* Zone, by the occurrence of the conodont *Pandotinella exigua philipi* in the underlying Roxburgh Formation (Colquhoun 1995). The overlying Carwell Creek Formation is assigned a late Pragian to early Emsian (*pireneae to perbonus* Zone) age, based on conodont species recovered near its base (Colquhoun 1995). In the Capertee Valley, the upper limit of the Huntingdale Volcanics is also assigned a late Pragian to early Emsian *(pireneae to dehiscens)* age, by the occurrence of a *Spinella-Buchanathyris* brachiopod assemblage in the overlying Emu Swamp Formation (Wright 1967). The lower contact of the unit is not exposed and remains unconstrained biostratigraphically. These biostratigraphic constraints suggest the Riversdale Volcanics and Huntingdale Volcanics lie at a similar stratigraphic position, and are mainly Pragian in age (Figure 7.46).

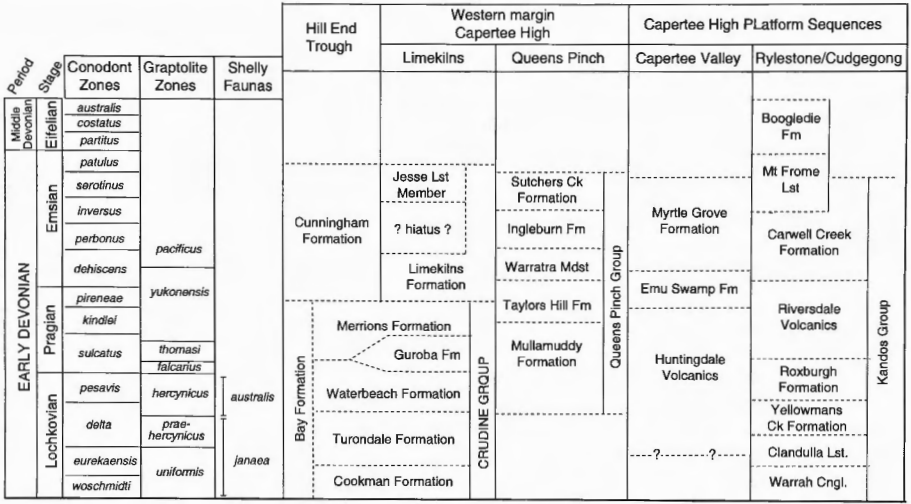

Figure 7.46: Stratigraphic correlations between the Hill End Trough and Captertee High, adapted from Colquhoun (1995) and Colquhoun et al. (1997).

The upper limit of the Turondale Formation is constrained to the late Lochkovian by a transported brachiopod fauna, in fine-grained volcanogenic sediments below the base of the Merrions Formation in the Limekilns district (Wright, in Packham 1969). Garratt and Wright (1988) correlate the fauna with their *australis* Assemblage Zone, which spans the *delta-pesavis* conodont zones (Figure 7.46). The exact stratigraphic position of the faunal assemblage within the Crudine Group is uncertain, and may lie anywhere within the Waterbeach Formation or upper Turondale Formation (Chapter 8.6).

Colquhoun (1998) speculatively places the base of the Riversdale Volcanics within the *sulcatus* Zone (Figure 7.46), but this boundary could be placed lower, within *pesavis* Zone, allowing some overlap in the possible biostratigraphic ranges of the Riversdale Volcanics and Turondale Formation. However, regardless of where this lower boundary is placed, the *sulcatus-kindlei* faunal assemblage within the middle to upper parts of Riversdale Volcanics suggests it is largely Pragian in age, whereas the Turondale Formation is confined to the Lochkovian. The Turondale Formation therefore appears to be older than the Riversdale Volcanics. It may, however, correlate temporally with the Huntingdale Volcanics. The base of the Huntingdale Volcanics is not exposed in the Capertee Valley, and it is possible this unit extends down into the Lochkovian and is coeval with the Turondale Formation. The 350 m thick Emu Swamp Formation in the Capertee Valley, is interpreted to represent rapid erosion of the underlying Huntingdale Volcanics (Kennedy 1976; Bracken 1977). To the north, the Riversdale Volcanics are overlain by similar immature volcaniclastic sandstones and conglomerates, but the reworked interval is much thinner (Colquhoun 1998). Colquhoun (1998) suggests this may indicate earlier cessation of volcanism in the Capertee Valley, and that silicic volcanism on the Capertee High was diachronous, commencing earlier and ending earlier in the Capertee Valley than in the Rylestone-Cudgegong district further north. The correlation between the Huntingdale Volcanics and Turondale Formation is supported by the palaeocurrent data and proximity trends in the latter, which indicate a source lying somewhere to the east of Sofala on the southern part of the Capertee High.

7.4.4 Palaeogeography

Depositional setting

In the Early Devonian, the eastern Lachlan Fold Belt was dominated by local marine basins comprising deep water troughs such as the Hill End Trough, and shallow to emergent areas, such as the Canberra-Yass magmatic province (Cas and Jones 1979; Cas 1983b; Powell 1984) and the Molong and Capertee Highs. The Hill End Trough developed on Ordovician

crust in the mid-Silurian, in response to strong extensional forces that caused widespread rifting in the region (Powell 1983). The trough contains deep water turbidite and hemipelagic mudstone facies, and there are no truly pelagic chemical and organic sediments. Pelitic intervals represent the ambient conditions of low energy sedimentation, involving the slow accumulation of fine-grained sediments supplied by normal erosion of the surrounding terrain. The lack of any tractional structures within shales and mudstones clearly indicates a low energy depositional environment dominated by suspension settling processes, uninterrupted by wave activity (i.e. the environment of deposition is below storm wave base). The persistent recurrence of these pelitic intervals throughout the 5 km thick fill of the Hill End Trough (Packham 1968a) indicates a prolonged deep, quiet depositional environment. There is a marked absence of demonstrably authochthonous shoalwater limestones or any other indications of shallow water deposition within the Hill End Trough (Cas and Jones 1979).

Palaeogeography and volcanic history

The base of the Early Devonian marks an important change in the palaeogeographic pattern of the region. Sediment movement indicators in the Late Silurian Chesleigh Group imply the sea-floor previously had a general easterly slope, and the volcanic centre supplying detritus to the Piambong Formation (upper Chesleigh Group) lay to the west or south-west of Hill End (Packham 1968a). Sedimentary structures within the overlying Early Devonian Cookman Formation indicate a reversal of dominant source direction from west to east, which was probably coincident with the emergence of an eastern land mass (Capertee High) during mild uplift related to the Bowning Orogeny (Packham 1968a). From this time onward, the Capertee High provided voluminous fill for the basin (Packham 1968a; Cas and Jones 1979), and the escalation of widespread volcanism on this shallow-marine to emergent land mass contributed to the volcaniclastic detritus in the Crudine Group.

During initial uplift, diverse rock types from a variety of Ordovician and Silurian sources were eroded off the emerging Capertee High, including silicic volcanic rocks, quartz-rich sedimentary rocks, mafic volcanics and possibly granite (Packham 1968a). This led to the deposition of the Cookman Formation, comprising up to 400m of interbedded slate and fine siltstone, interrupted periodically by turbidity currents carrying quartzose to quartz-lithic epiclastic sediments.

Following uplift, a transgressive system tract developed on the northern Capertee High (Colquhoun 1998; Figure 7.46), consisting of (in ascending order); wave dominated fan-

deltaic clastics (Warrah Conglomerate); biostromal to biohermal limestones (Clandulla Limestone); and a transgressive to regressive muddy, storm-influenced shelf deposit (Yellowmans Creek Formation). This transgressive sequence is overlain by a thick regressive unit of storm-dominated siliciclastics deposited in mid-shelf to nearshore settings (Roxburgh Formation). Evidence of intermittent (distal) silicic volcanism is recorded in the Clandulla Limestone and Yellowmans Creek Formation, and the upper Roxburgh Formation has a partial volcanic province (Colquhoun 1998). A major period of diachronous pyroclastic silicic volcanism commenced on the southern Capertee High with emplacement of the Huntingdale Volcanics, possibly synchronous with deposition of the Warrah Conglomerate and Clandulla Limestone. Volcanism later spread to the northern Capertee High to form the Riversdale Volcanics, overlying the Roxburgh Formation (Figure 7.46).

In the Hill End Trough, the influx of large volumes of coarse, juvenile volcaniclastic detritus in the Turondale Formation is probably related to the onset of dacitic to rhyolitic volcanism on the southern Capertee High (Figure 7.47a). The marked petrographic change from quartz-rich to plagioclase-rich detritus reflects the change from a mature to immature source terrain. Explosive magmatic and/or phreatomagmatic subaerial to shallow marine eruptions produced large volumes of juvenile pyroclasts, some of which may have been deposited subaerially by pyroclastic flows, to produce the thick ignimbrites of the Huntingdale Volcanics in the Capertee Valley (Figure 7.47a). The remainder may have accumulated rapidly on the shelf and slope areas on the western margin of the Capertee High, then slumped into the trough following a short storage period (possibly as little as days or weeks after initial eruption). The slumping may have been triggered by seismic shocks related to subsequent volcanic activity, or may have occurred in response to oversteepening of the thick, unstable volcaniclastic pile. Alternatively, and more likely, the material was transported into the marine basin by pyroclastic flows, which transformed into water-supported mass flows on entry into water. Large volumes of pumice and vitric ash were separated from the denser crystal component during transportation, removed in secondary eruption columns generated at the shoreline, and/or segregated by gravitational settling as the pyroclastic flows initially travelled for some distance over water before eventually sinking through the water column. As a result, the final deposits are significantly crystal-enriched compared with subaerially deposited pyroclastic flows, and all pumice has been removed by flotation or winnowed out in the secondary eruption columns.

The pattern of sedimentation in the Turondale Formation indicates there were two major eruptive phases of the source (represented by the lower and upper volcaniclastic units), separated by a significant period of repose, during which ambient sedimentation was

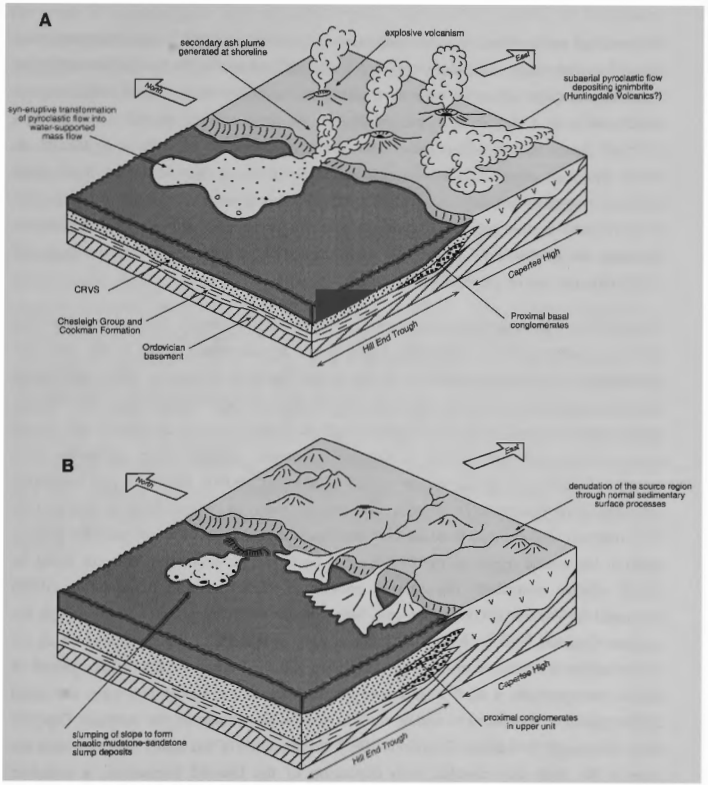

Figure 7.47: Palaeogeography of the Turondale Formation during: (a) deposition of the megaturbidite-dominated lower volcaniclastic unit; and (b) deposition of the 'normal' turbidite succession in the upper volcaniclastic unit.

re-established in the basin (middle pelagic unit). Under ambient conditions, a thick interval (200m) of hemipelagic shale and siltstone accumulated, interrupted sporadically by relatively small turbidity currents carrying volcaniclastic sediments eroded from the source region by fluvial and perhaps coastal erosion processes.

The proximal volcaniclastic boulder conglomerates, contain rounded ?penecontemporaneous volcanic and limestone clasts that were reworked in a littoral and/or fluvial environment prior to subsequent redeposition by mass-flow processes into deep water. These conglomerates could have been dislodged from the shoreline by violent volcanic eruptions, which also produced the succeeding syn-eruptive crystal-rich volcaniclastic deposits (e.g. Cas et al. 1981). Proximal chaotic mudstone-sandstone slump deposits may represent local slope collapse, triggered similarly, by volcanic-related seismic activity (Figure 7.47b). The conglomerates in the upper volcaniclastic unit are associated with large allochthonous limestone blocks that would have been resedimented short distances downslope from the littoral environment by gravitational processes.

The top of the Turondale Formation marks the end of the syn-eruptive style of sedimentation which produced the thick, crystal-rich volcaniclastic deposits characteristic of the unit. The thin-bedded volcanogenic turbidites at the top of the Turondale Formation reflect the waning and eventual cessation of active volcanism, and the onset of rapid denudation of the volcanic source region through normal sedimentary surface processes such as coastal and fluvial erosion. In the following period of volcanic quiescence, ambient basin conditions were resumed, resulting in the deposition of the hemipelagic shales, siltstones and sandstone turbidites of the Waterbeach Formation. The periodic influx of coarser detritus, separated by thick intervals of shale, may be related to eustatic sea level changes or reflect periodic tectonic uplift of the source region or the dynamics of basin margin submarine fans, or could be simply climate controlled, representing periods of higher rainfall. Colquhoun (1998) suggested the Waterbeach Formation correlates with the Yellowmans Creek Formation on the northern Capertee High, with both units representing an episode of transgression, which cut off the supply of coarse sediment to the deep basin and shelf areas. Following this period of marine transgression, a thick sequence of quartz-volcanolithic sandstones were deposited under regressive conditions in middle shelf to near shore settings on the northern Capertee High (Roxburgh Formation; Colquhoun 1995). Progradation of this sandy facies towards the edge of the high may correlate with deposition of the Guroba Formation, a turbiditic sandstone sequence overlying the Waterbeach Formation in the northern Hill End Trough. There is an influx of rhyolitic volcaniclastic detritus, deposited as relatively thick beds (up to 10m), towards the top of the Guroba Formation. This may correlate with emplacement of the

Riversdale Volcanics on the northern Capertee High, during a period of rhyolitic pyroclastic volcanism.

The thick, voluminous crystal-rich volcaniclastic deposits of the Merrions Formation mark the return of a syn-eruptive style of sedimentation, implying the renewal of widespread pyroclastic volcanism in volcanic terrains surrounding the trough. The volcaniclastic megabeds were derived from several sources which were variously active during different stages of deposition (Cas 1977). There was a shift in the dominant source direction through time, from the west through to the south and southeast and finally the east. The volcanic sources have never been identified, but it seems possible that the Bindook Volcanic Complex, which lies beyond the southeastern end of the Hill End Trough, contributed some detritus to the Merrions Formation (Member D?). Subaqueous volcanic centres also contributed to the Merrions Formation, producing thick regionally extensive lavas which blanketed the seafloor, influencing the basin floor topography. A peripheral hyaloclastite breccia locally flanks one possible lava dome complex (Member H lava), with angular lava clasts incorporated into the overlying volcaniclastic sandstones. This suggests the porphyry was at least partly extrusive, and exposed to erosive action accompanying emplacement of the overlying megaturbidites. The porphyry may have intruded into the shallow levels of the unconsolidated sediment pile, and been locally exposed by contemporary erosion (Cas 1978). Volcanism in the source regions ceased following deposition of the Merrions Formation. The overlying Cunningham Formation, which represents the final fill of the Hill End Trough, comprises over 3000 m of thinly bedded slates, siltstones, quartzo-feldspathic and lithic sandstone and minor conglomerates, representing normal clastic denudation of volcanic, and metasedimentary source terrains exposed around the margins of the Hill End Trough.

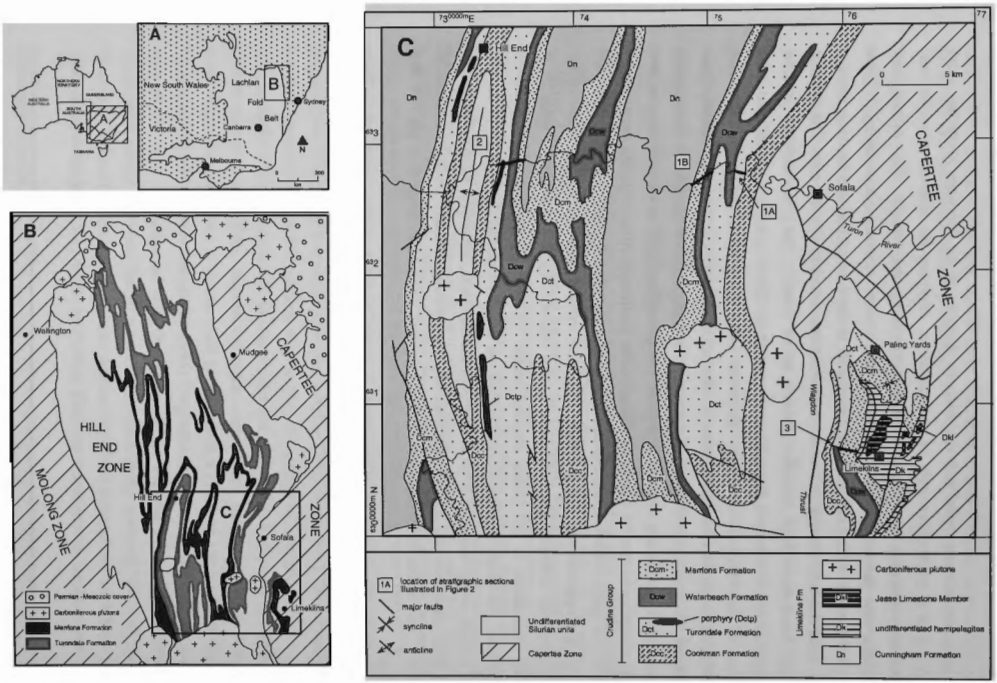

Figure 8.1: (a) Location map showing the study area in the northeastern Lachlan Fold Belt of southeastern Australia; (b) Outcrop distribution of the Turondale and Merrions Formations within the Hill End Trough. The Silurian-Devonian palaeogeographic elements (Molong High, Hill End Trough and Capertee High) coincide approximately with structural zones defined by Scheibner (1993); and (c) Simplified geological map of the Hill End-Sofala-Limekilns district (modified after Raymond et al. 1997) showing the geological setting of samples selected for U-Pb zircon analysis, and the location of the stratigraphic sections from which samples were obtained.

CHAPTER 8

U-Pb dating of silicic lavas, sills and syn-eruptive resedimented volcaniclastic deposits of the Early Devonian Crudine Group, Hill End Trough, New South Wales.

The following chapter takes the form of a paper in preparation, which has been submitted to the Australian Journal of Earth Sciences. The geochronological study was carried out in collaboration with Dr Lance Black of the Australian Geological Survey Organisation (AGSO). E.Jagodzinski devised the scope of the project, and determined which samples should be selected for analysis, based on previous fieldwork in the Hill End-Sofala district. The samples were collected and analysed by E.Jagodzinski and L.Black, with technical assistance provided by Mr Chris Foudoulis (of AGSO). L.Black processed the raw data to obtain the final ages of each sample, and wrote Section 8.5 of this Chapter, which presents the resultant isotopic data. E.Jagodzinski interpreted the results in terms of the biostratigraphic and lithostratigraphic context of the samples, based on personal field observations, and literature review as cited in the text. The remainder of the chapter, discussing the implications of the results for adjusting the numerical calibration of the Australian Phanerozoic Timescale, was largely written by E.Jagodzinski, with input from L.Black (mainly regarding the rationale for selection of the QGNG zircon standard).

8.1 INTRODUCTION

From the Late Silurian to the late Early Devonian, the palaeogeography of the Lachlan Fold Belt of southeastern Australia consisted of localised deep marine basins or 'troughs', separated by shallow marine environments with locally emergent land areas (Cas 1983a; Powell 1984). The Hill End Trough of central-western New South Wales was flanked to the west and east by the shallow marine to emergent platforms of the Molong and Capertee Highs (Packham 1960, 1969). Dominant facies on the bounding highs were mafic to silicic volcanics, shallow marine to subaerial siliciclastics and volcaniclastics, and thick, shallow-water carbonate sequences (reefal and associated

shoalwater limestones), flanked by derivative volcaniclastic, siliciclastic and carbonate debris-flow aprons (Pemberton et al. 1994). Beyond the southern apex of the trough, the Middle Silurian-Early Devonian Canberra Magmatic Province (Cas 1983a) contained similar shoalwater to emergent facies, dominated by silicic volcanics and volcaniclastics, mudstone and limestone (Crook et al. 1973; Cas and Jones 1979). Coeval sedimentation in the Hill End Trough was characterised by deep water turbiditic sedimentation of alternating silicic volcanic, quartzose and lithic provenance. Unlike the rock associations of the adjacent highs, there is a marked absence of demonstrably authochthonous shoalwater limestones or any other indication of shallow water deposition (Packham 1968; Cas and Jones 1979).

Because the transported clastic fill of the Hill End Trough contains few *in situ*, age-diagnostic faunal assemblages, direct biostratigraphic constraints on the age of the sequence are sparse, and the constituent formations are poorly constrained. Dating of the Hill End Trough sequence has relied largely on lithological correlation with the fossiliferous sequences of the adjacent Molong and Capertee Highs, which are biostratigraphically well-constrained by conodont species. The principal aim of this paper is to provide some numerical age control to the trough sequence by presenting U-Pb zircon ages for the Turondale and Merrions Formations, two widespread volcanogenic units within the Early Devonian Crudine Group. Prior to this study, the only direct isotopic constraint for the sequence was an imprecise whole-rock Rb-Sr isochron age of 395±32 Ma for the Merrions Formation (Cas et al. 1976).

Seven samples from the Turondale and Merrions Formations were selected for U-Pb dating by SHRIMP (Sensitive High Resolution Ion Microprobe), the locations and stratigraphic positions of which are presented in Figures 8.1 and 8.2 and Table 8.1. The selected samples include five syn-eruptive, crystal-rich volcaniclastic sandstones, one porphyritic lava within the Merrions Formation, and a porphyry of similar composition intruding the Turondale Formation. When the results are placed in the context of the limited fossil control available for the Early Devonian sequence, several problems become apparent with the existing Australian Phanerozoic Timescale. The results are therefore also discussed in conjunction with a recently published alternative version of the Phanerozoic time scale. In common with some other dating systems, Phanerozoic SHRIMP dating is critically dependent on the use of an appropriate standard. The new SHRIMP data are also discussed in terms of two different zircon standards, one of which yields significantly more consistency than the other.

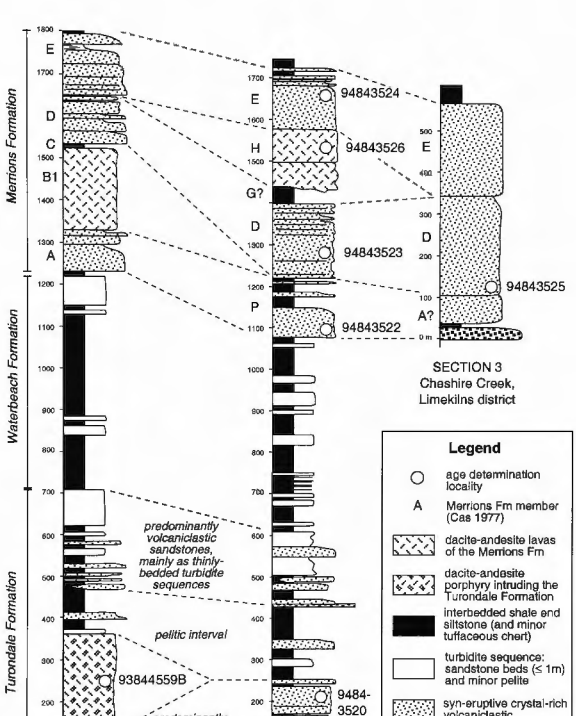

Figure 8.2: Measured stratigraphic sections showing the stratigraphic context of samples selected for U-Pb zircon analysis. Section locations are displayed in Figure 8.1. For the Merrions Formation, sections 1 and 2 are from Cas (1977), and section 3 from Voorhoeve (1986).

8.2 GEOLOGICAL SETTING

8.2.1 Regional Stratigraphy

Sedimentation in the Hill End Trough commenced at the start of the Late Silurian and continued uninterrupted to the end of the Early Devonian, when it was terminated by uplift associated with the Middle Devonian Tabberabberan Orogeny (Packham 1999; Glen and Watkins 1999). The Chesleigh Group is the basal unit of the deep-water Hill End Trough sequence. It contains no age-diagnostic fossils, but it has been assigned a late Ludlow to late Pridoli (late Silurian) age range on the basis of its stratigraphic position (Pogson and Watkins 1998). Along the eastern margin of the Hill End Trough, the Chesleigh Group conformably overlies the Bells Creek Volcanics which in turn conformably overlies the Tanwarra Shale, both shallow-water constituents of the underlying Mumbil Shelf. Pickett et al. (1996) have established a late Wenlock to earliest Ludlow age (*lundgreni-testis* to *nilssoni* graptolite Zones) for the latter.

The Chesleigh Group is overlain by the Crudine Group, which comprises about 2.5 km of turbiditic sandstone (mainly of silicic volcanic provenance) and shale, with rare concordant lavas. In present usage (Pogson and Watkins 1998), the Crudine Group in the Hill End-Sofala-Limekilns region includes the Cookman Formation, Turondale Formation, Waterbeach Formation and Merrions Formation (formerly Merrions Tuff; Packham 1968), in ascending stratigraphic order (Figure 8.3).

The Cunningham Formation, conformably overlying the Merrions Formation, represents the final fill of the Hill End Trough. It comprises over 3 km of thinly-bedded slates, siltstones, quartzo-feldspathic and lithic sandstones, and minor conglomerates. In the Limekilns district east of the Wiagdon Thrust (Figure 8.1), the Crudine Group is overlain by the Limekilns Formation (formerly Limekilns Group; Packham 1968), inferred to be laterally equivalent to the Cunningham Formation, and deposited in a proximal slope to base-of-slope setting marginal to the Capertee High. The Limekilns Formation comprises a comparatively thin shale sequence (about 200 m thick), in which condensed horizons enriched in shelly debris alternate with comparatively barren mudstone sequences, indicating a quiet, sub- storm wave-base environment characterised by slow hemipelagic deposition and sediment starvation over long periods (Colquhoun 1998). The sequence contains a fossiliferous limestone member (Jesse Limestone Member) containing allodapic limestones, mass-flow breccias with clasts of limestone and lesser silicic volcanics, isolated allochthonous limestone blocks and hemipelagic mudstone (Voorhoeve 1986; Wright and Chatterton 1988). The sequence at Limekilns is significant to the present study because it

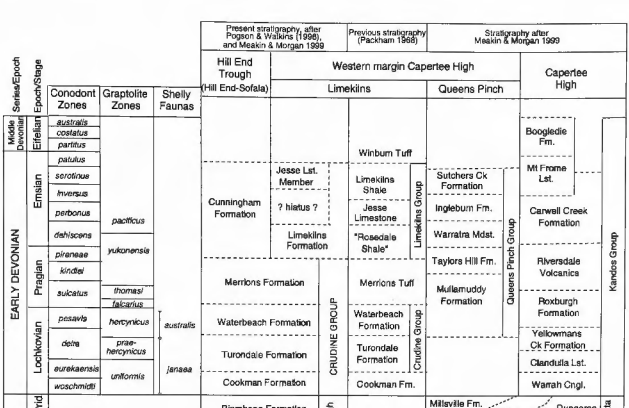

Figure 8.3: The stratigraphy of Early Devonian and some Silurian sequences of the Hill End Trough and adjacent Molong and Capertee Highs, showing biostratigraphic stages, the standard international conodont and graptolite zonation and the shelly faunal zonation of Garratt and Wright (1988) for the Early Devonian. The correlation of stratigraphic units between the trough and highs, and with Devonian biostratigraphic stages, is after Colquhoun (1995, 1998). Also shown is the previous stratigraphic scheme for the Limekilns district (Packham 1968), which was modified during the latest regional mapping program.

contains age-diagnostic fossils in a trough margin succession which appears to conformably overlie the Crudine Group.

The Hill End Trough succession has been folded into broad, generally upright north-south trending folds with axial-plane cleavage, and overthrust onto the Capertee High to the east along the Wiagdon Thrust (Packham 1999; Glen and Watkins 1999). The associated axial plane cleavage is typically only developed in finer sediments regionally, and in the coarser rocks in the axial region of the trough (Packham 1968). The sequence has been regionally metamorphosed to greenschist facies, which varies in intensity from biotite grade about the trough axis, to chlorite grade towards the margins (Smith 1969). Primary textures and structures are still well preserved in the lower chlorite grade rocks.

8.2.2 The Turondale and Merrions Formations

The Crudine Group contains two volcanogenic units, the Turondale and Merrions Formations, which record the influx of large volumes of volcaniclastic debris sourced from active volcanic terranes on the surrounding highs. These volcanogenic units are separated by the Waterbeach Formation, a ~600 m thick interval of ambient hemipelagic sediment comprising mainly shale and siltstone, which reflects an interval of volcanic quiescence in the source region (Packham 1968; Figure 8.2). Subaqueous volcanic centres also contributed to the Crudine Group. Dacite porphyries occur as regionally extensive submarine lavas within the Merrions Formation, and intrude the underlying Turondale Formation as sills.

The volcaniclastic component of the Merrions Formation and much of the Turondale Formation occurs as very thick (tens to hundreds of metres), massive, crystal-rich megaturbidites (Figure 8.2). The abundance of unabraded juvenile pyroclasts (crystals, crystal fragments and rarely preserved shards) within the volcaniclastic deposits indicates they have not been significantly reworked, and were probably emplaced synchronously with or shortly following eruption. Cas (1983b) proposed that the deposits originated from subaerial explosive volcanic eruptions, producing pyroclastic flows which fed into the sea. Upon entering the sea, the hot pyroclastic flows ingested and interacted explosively with water, transforming into water-supported mass-flows, which continued to travel underwater to their final setting, well below storm-wave base. Although their final emplacement was not by pyroclastic flows, the deposits are primary in the sense that they were deposited during the eruptive cycle. This style of deposit is becoming more widely recognised, and is categorised as a 'syn-eruptive volcaniclastic deposit', emphasising the genetic connection with active volcanism (e.g. McPhie et al. 1993).

Three conformable, coherent porphyry units are recognised within the clastic sequence of the Merrions Formation. Cas (1978) interpreted these units as subaqueous lava flows, because: (1) they have a topographic influence on the sedimentation patterns of overlying units; and (2) the upper margin of one unit is locally quench fragmented, and clasts are reworked into the overlying sediments, suggesting the porphyry was at least exposed during emplacement of the overlying sediment.
A dacite porphyry, of similar composition to the Merrions Formation lavas, outcrops within the Turondale Formation as discontinuous bodies around the nose of the Hill End Anticline (Figure 8.1). Unlike the porphyries of the Merrions Formation, which have features consistent with lava flows, those of the Turondale Formation are interpreted as post-sedimentation sills. The porphyry bodies are broadly discordant,

Sample number	Member	Rock type	Grid Reference	Geochemical classification	Framework constituents Q	P	Ks	maf.	L	Matrix/ G'mass
Merrions Formation										
94843524	E	volcaniclastic	417376	andesite	3	93	0	4	0	48%
96843526	H	porphyry lava	418375	dacite	3	95	2	0	0	64%
94843523	D	volcaniclastic	422376	rhyolite	41	38	19	0	2	17%
94843525	D	volcaniclastic	532172	rhyolite	34	42	22	0	3	25%
94843522	P	volcaniclastic	424375	andesite	12	88	0	0	0	53%
Turondale Formation										
93844559B		porphyry sill	271386	dacite	11	89	0	0	0	59%
94843520		volcaniclastic	453383	dacite	40	60	0	0	0	37%

Table 8.1. Modal analyses for samples analysed in this study. Maf. denotes a mafic phase (pyroxene or amphibole) pseudomorphed by chlorite±epidote. All samples contain accessory Fe-Ti oxides and zircon. The matrix/groundmass of all samples is recrystallised, and composed of secondary metamorphic minerals (quartz, albite, chlorite, sericite, epidote, biotite and clinozoisite).

occurring at several stratigraphic levels within the Turondale Formation, and their upper surfaces cross-cut the sedimentary sequence. There is also evidence of small-scale stoping near the upper margin of the porphyry, and thin apophyses of porphyry protrude into the overlying sediment.

8.3 SAMPLE SELECTION

Two samples were selected for analysis within the Turondale Formation. Sample 94843520 is a thick, crystal-rich volcaniclastic sandstone collected near the base of the type section, and sample 93844559B is from a dacite porphyry body intruding the base of the Turondale Formation, on the eastern limb of the Hill End Anticline (Figure 8.2).

The Merrions Formation has a complex internal stratigraphy, which Cas (1977) subdivided into informal members (members A to P), distinguished by gross lithological type (i.e. lava, arenite, pelite) and composition. The volcaniclastic component of the Merrions Formation was sampled at three stratigraphic levels of the type section (Figure 8.2), in order to assess whether this unit was deposited over a significant interval of geological time. The samples represent arenite members P (sample 94843522), D (94843523) and E (94843524). P is only found in the type section but is correlated with the more widespread basal arenite member A elsewhere (Cas 1977). D and E have a tabular, sheet-like form, and are the most widespread members of the Merrions Formation, occurring in the middle and at the top of the formation, respectively. Member H lava near the top of the type section was also

selected for analysis (96843526), in order to confirm the assumption that the resedimented volcaniclastic members were emplaced during the eruptive cycle and do not contain a significant component of reworked detritus, which would introduce inheritance into the zircon populations. The modal compositions of all samples selected for dating are presented in Table 8.1.

A fourth sample (94843525) was collected from a 600 m-thick volcaniclastic interval in the Limekilns district, east of the Wiagdon Thrust (Figure 8.1). This volcanogenic unit was originally mapped as the Winburn Tuff (Hawkins 1953; Packham 1968), and interpreted to overlie the Limekilns Formation (Figure 8.3). More recent mapping, however, has reinterpreted the sequence to lie on the inverted limb of an overturned syncline, placing the Winburn Tuff stratigraphically below the Limekilns Formation, and overlying the Waterbeach Formation (Voorhoeve 1986; Pogson and Watkins 1998). It has consequently been assigned to the Merrions Formation, and the term 'Winburn Tuff' has been suppressed. The sample was collected near the base of the volcaniclastic succession, from a distinctive 200 m thick interval which is rich in pink orthoclase (Figure 8.2). The sample contains 34% quartz, 22% K-feldspar and 42% plagioclase (Table 8.1). These framework constituents occur in similar abundance in sample 94843523, from Member D in the type section, and on this basis, these units are correlated. The sample site was selected because in this region there is fossil age control from units immediately above and below it, enabling the numerical ages obtained in this study to be tied to the regional biostratigraphy. The aim was also to test the structural and stratigraphic reinterpretation of the Limekilns sequence, by determining if the volcaniclastic unit is the same age as samples of the Merrions Formation collected from the type section. The Limekilns Formation ranges up to late Emsian in age (Wright and Chatterton 1988; Wright and Haas 1990). If the volcaniclastic 'Winburn Tuff' sequence overlies the Limekilns Formation as originally interpreted by Packham (1968), it will be significantly younger than the ages obtained for the type section of the Merrions Formation.

8.4 ISOTOPIC TECHNIQUES

The analyses were made on the SHRIMP I and SHRIMP II ion-microprobes at the Research School of Earth Sciences, Australian National University. Operation at a mass resolution in excess of 5000 at 1 % peak height ensured there were no significant spectral interferences (Compston et al. 1984). Variable discrimination between U and Pb was referenced to a $^{206}Pb/^{238}U$ ratio of 0.0928 (equivalent to an age of 572 Ma) for interspersed analyses of the SL 13 zircon standard, based on the power law relationship $^{206}Pb^{+}/U^{+} = a(U0^{+}/U^{+})^{2}$ (Claoué-Long et al. 1995). All of the analysed samples can be

calibrated against this standard. A $^{206}Pb/^{238}U$ value of 0.33241 was used, where appropriate, for calibration against the 1850 Ma-old QGNG standard (Daly et al. 1998).

The precision of the Pb/U ratios of the unknowns has been augmented by the uncertainty of the calibration of the appropriate standard during each relevant session. Th/U ratios were derived from the linear relationship $^{232}ThO/^{238}U = (0.03446.UO^+/U^+ + 0.868).ThO^+/UO^+$. Radiogenic Pb compositions were determined by the subtraction of contemporaneous common Pb (Cumming and Richards 1975), there being no detectable Pb in the Au coating that was used. All reported ages for the Palaeozoic zircons have been derived from ^{207}Pb-corrected $^{206}Pb/^{238}U$ ratios (Compston et al. 1984). Precambrian ages obtained for xenocrystic zircon have been derived from ^{204}Pb-corrected $^{207}Pb/^{206}Pb$ ratios. All ages have been calculated from the U and Th decay constants recommended by Steiger and Jäger (1977). Except for the data in Table 8.3 (which reports 1 sigma errors), age uncertainties are given at the 95 % (t σ) confidence level.

8.5 SL 13- CALIBRATED ISOTOPIC DATA

Initial assessment of the isotopic data is based on the SL 13 zircon standard, because all of the zircons were co-jointly analysed with it. However, as will be seen later, these data are not as consistent as those based on the QGNG standard.

8.5.1 The Merrions Formation, type section

Zircons from the stratigraphically oldest sample (94843522, from member P) were included in three of the sample mounts, as an "internal standard". This permits an inter-comparison of the relative ages of the samples on the same mount that is independent of the calibration assigned to the standard zircon (see below). It also provides an extra measure of quality control, through the comparison of ages derived for a single unit from different ion-microprobe mounts and using different instruments and instrumental conditions. An added advantage is that the intensive analyses should produce a more precise age for that reference sample (94843522).

All three volcaniclastic samples from the type section of the Merrions Formation contain morphologically similar zircons, which were set separately in a single ion-microprobe mount. These clear zircons are mostly euhedral, though some terminations are slightly rounded, a feature that appears to be slightly more common in the uppermost sample (94843524). Although prismatic faces are dominated by 100 and 010 forms, more complex facets are locally present. Normal and steep pyramids are about

equally common. Aspect ratios are mostly about 2:1, but range up to about 4:1 in the uppermost sample. Grain lengths (200 μm or less) are slightly smaller in the stratigraphically intermediate sample than the other two, which average about 250 μm. The prismatic zoning that is characteristic of igneous growth is ubiquitous (Figure 8.4a); sector zoning is neither as common nor as prominent. Silicate inclusions that are mostly rod-like, and rounded fluid inclusions are present in most grains. Although most grains have no obvious core, they are still relatively common. Both relatively large, luminescent cores (relatively low in U) and generally smaller poorly luminescent cores (relatively high in U) are present.

In the first mount, twenty four analyses of the jointly mounted SL 13 standard yield a 1.85 % calibration for the session in which these samples were dated. The appropriate reference line is shown on Figures 5 a, b and c. This calibration yields an age of 404.8±4.8 Ma (Figure 8.5a) for the volumetrically dominant, continuously zoned zircon in sample 94843524, from member E, near the top of the Merrions Formation. That age is derived from 18 of 20 analyses, which yield a χ^2 of 0.54. One of the outliers (analysis 208.1) represents a relatively rounded, ~530-Ma xenocrystic, grain with subdued zonation. It has distinctively low Th/U. No distinguishing morphological or chemical criteria could be found to explain the young age (~370 Ma) obtained for the other outlier, analysis 219.1, which presumably reflects a small component of recent radiogenic Pb loss.

All 20 ages obtained for sample 94843523, the intermediate-level representative (member D) of the Merrions Formation, are within error of each other (χ2 is 0.92) and a weighted mean crystallisation age of 405.5±4.6 Ma (Figure 8.5b).

The age distribution for sample 94843522, the lowermost representative (member P) of the Merrions Formation, is similarly simple. All 20 analyses conform to a single population (χ^2 is 0.89) with a mean age of 409.6±4.6 Ma (Figure 8.5c) for the crystallisation of the vast majority of zircon in this rock.

The second mount to contain zircons from Merrions Formation sample 94843522, also includes zircons from member H lava (sample 96843526) near the top of the type section. A small calibration change occurred at about the mid point of the analytical session, both calibrations being determined to 2.4 % precision. All 35 analyses of sample 94843522 from this session define a single population (χ^2 is 0.70) with a mean age of 410.7±5.0 Ma (Figure 8.5d).

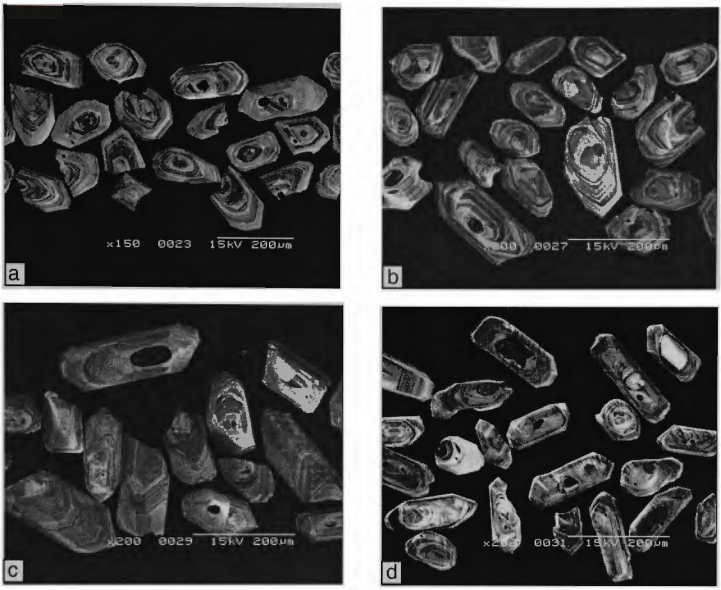

Figure 8.4: Cathodoluminescence (CL) image of typical continuously zoned zircons from: (a) the volcaniclastic components of the Merrions Formation. These grains were taken from 94843524, the uppermost of the analysed samples. Note the small, poorly luminescent cores in some of the extensively zoned grains; (b) the Merrions Formation lava (sample 96843526); (c) the volcaniclastic component of the Turondale Formation (sample 94843520); and (d) the porphyry within the Turondale Formation (sample 943844559B).

The accompanying zircon grains from the lava (sample 96843526) are clear and euhedral. Simple prisms are more common than more complex forms; normal and steep pyramids are about equally common. The grains are relatively squat, with aspect ratios ranging from about 2:1 to 2.5:1. Average length is about 250 µm. Although silicate and fluid inclusions are common, they are heterogeneously distributed. Most grains have continuous prismatic zoning (Figure 8.4b). However, some also contain anhedral cores, most of which are small, rounded and poorly luminescent.

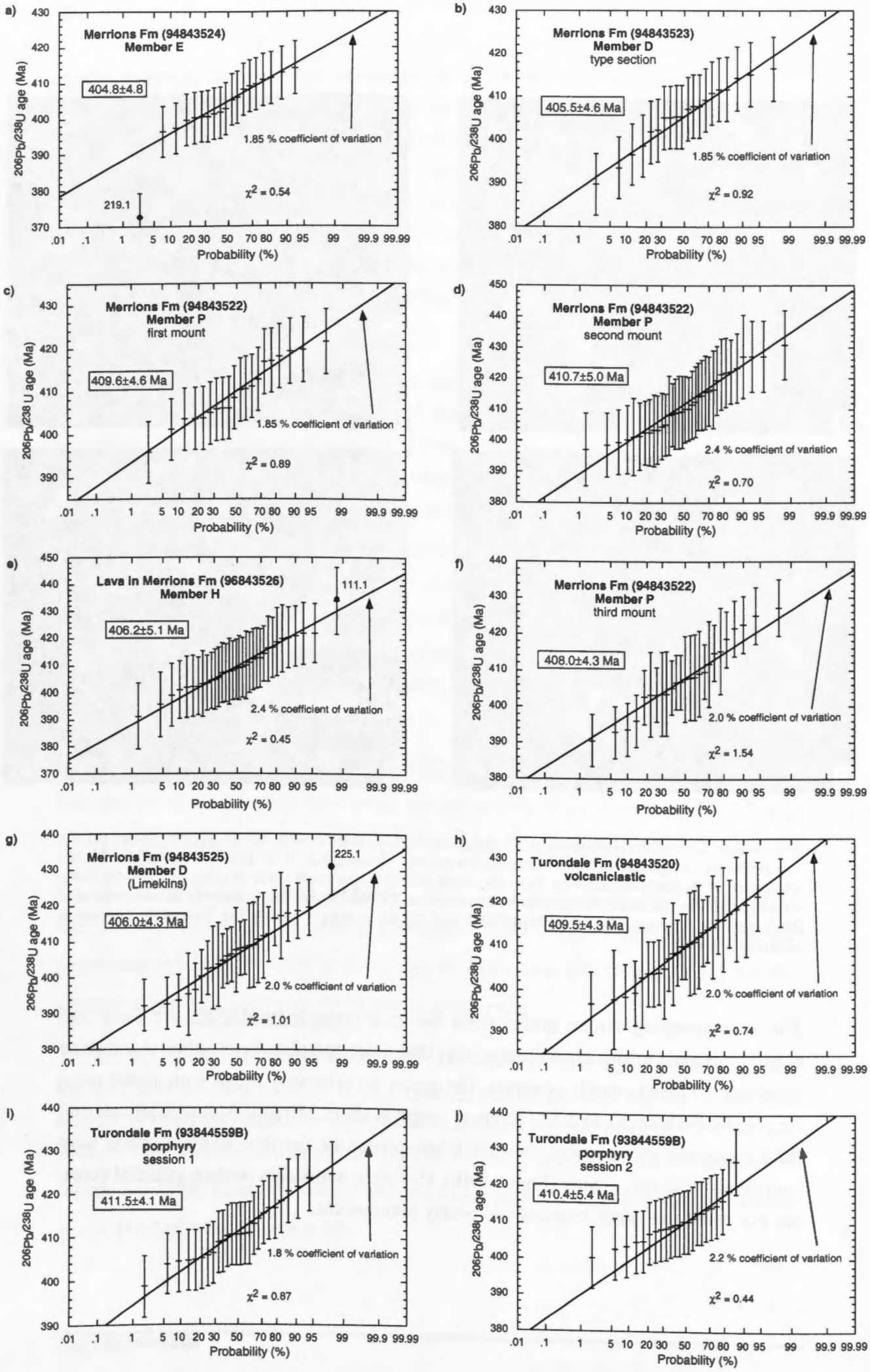
a)
Merrions Fm (94843524)
Member E
404.8±4.8
1.85 % coefficient of variation
219.1
χ² = 0.54
b)
Merrions Fm (94843523)
Member D
type section
405.5±4.6 Ma
1.85 % coefficient of variation
χ² = 0.92
c)
Merrions Fm (94843522)
Member P
first mount
409.6±4.6 Ma
1.85 % coefficient of variation
χ² = 0.89
d)
Merrions Fm (94843522)
Member P
second mount
410.7±5.0 Ma
2.4 % coefficient of variation
χ² = 0.70
e)
Lava in Merrions Fm (96843526)
Member H
111.1
406.2±5.1 Ma
2.4 % coefficient of variation
χ² = 0.45
f)
Merrions Fm (94843522)
Member P
third mount
408.0±4.3 Ma
2.0 % coefficient of variation
χ² = 1.54
g)
Merrions Fm (94843525)
Member D
(Limekilns)
225.1
406.0±4.3 Ma
2.0 % coefficient of variation
χ² = 1.01
h)
Turondale Fm (94843520)
volcaniclastic
409.5±4.3 Ma
2.0 % coefficient of variation
χ² = 0.74
i)
Turondale Fm (93844559B)
porphyry
session 1
411.5±4.1 Ma
1.8 % coefficient of variation
χ² = 0.87
j)
Turondale Fm (93844559B)
porphyry
session 2
410.4±5.4 Ma
2.2 % coefficient of variation
χ² = 0.44
206Pb/238U age (Ma)
Probability (%)
.01 .1 1 5 10 20 30 50 70 80 90 95 99 99.9 99.99

Thirty three of the 35 analyses of the lava represent a single population (χ^2 is 0.45) with an age of 406.2±5.1 Ma (Figure 8.5e) for zircon crystallisation. The most obvious outlier is a rounded ~1000 Ma core (131.1) with distinctively low Th/U. Although the deletion of this analysis alone yields a perfectly acceptable χ^2 of 0.55, the probability diagram (Figure 8.5e) identifies analysis 111.1 as another possible outlier. Its deletion is justified by cathodoluminescence (CL) evidence that it was produced by the inadvertent partial overlap of the ion-beam on a small, anhedral, poorly-luminescent core.

The third mount to include zircons from Merrions Formation sample 94843522 also contains zircons from volcaniclastic samples collected from the Merrions Formation in the Limekilns district (94843525) and from the type section of the Turondale Formation (94843520). Analyses of these were interspersed with 40 analyses of the SL 13 standard in two separate sessions on SHRIMP I. Near the end of the second of these sessions there was a change in the ionisation characteristics of the ion-microprobe, which required a referencing of the measured compositions of the unknown zircons to different values of $^{206}Pb/^{238}U$ and UO/U in the standard. Different calibrations were also found for the two analytical sessions. As each of the calibrations for the standard was determined to about 2.0%, this value has been used in the determination of the ages of the three concurrently analysed unknown zircon suites. The similar precision for each calibration allows the data for different sessions of each particular zircon suite to be presented on a single probability diagram (Figure 8.5f, g or h).

All 25 analyses of sample 94843522 on this mount (these are morphologically identical to previously described zircons from this rock) have indistinguishable $^{206}Pb/^{238}U$ (χ^2 is 1.54), which can be combined to yield a crystallisation age of 408.0±4.3 Ma (Figure 8.5f).

8.5.2 The Merrions Formation, Limekilns district

The analysed zircons from sample 94843525 are morphologically comparable with many of those studied in the preceding samples. They are clear, and mostly euhedral. Local embayments presumably are indicative of growth late in the magmatic crystallisation of the source rock. 100 and 010 prisms, and simple pyramids are dominant. Steep pyramids are also present, as are rare 001 prisms. Aspect ratios average about 2:1. Most grains contain fluid and rod-like silicate inclusions. Prismatic zonation is ubiquitous; sector zoning is much less common. Some grains contain

discordant, anhedral cores. The largest of these are strongly luminescent and zoned; smaller varieties are poorly luminescent.

The appropriate 2.0 % calibration for the standard has been applied to the analyses, as discussed above. Although the 26 analysed zircons from sample 94843525 fulfil one of the requirements of a simple population, with χ^2 being 1.34, the probability diagram (Figure 8.5g) suggests that the oldest of the analyses is an outlier. Its deletion yields a χ^2 of 1.01. Even though no independent criteria could be found to support this view, it is considered the more realistic of the two scenarios. This option yields a preferred crystallisation age of 406.0±4.3 Ma for these zircons, though the alternative age of 407.0±4.3 Ma is essentially the same.

8.5.3 The Turondale Formation

Sample 94843520 is a volcaniclastic rock from the Turondale Formation, sampled near the base of the type section. The zircons in this rock have euhedral form that is dominated by simple prisms and pyramids, though steep pyramids are relatively common. Aspect ratios are relatively constant, at about 2:1. Fluid and rod-like silicate inclusions are present in most grains, which are characteristically clear. CL (Figure 8.4c) shows that most of the grains consist of uninterrupted prismatic zones that would have formed during a single igneous event. Sector zoning is locally developed. Some grains also contain discordant cores, some of which have high luminosity and are zoned, and smaller, poorly-luminescent varieties. Neither core type was selected for analysis.

This rock was analysed in the same two analytical sessions in which sample 94843525 of the Merrions Formation was dated, and has therefore also been assigned a calibration uncertainty of 2.0 %. All 27 zircons from this Turondale Formation sample have mutually indistinguishable 206Pb/238U ages (χ^2 is 0.74), which combine to yield a mean crystallisation age of 409.5±4.3 Ma (Figure 8.5h) for the vast majority of zircon in this rock.

Sample 93844559B was collected from the intrusive porphyry that cuts volcaniclastic rocks at the base of the Turondale Formation in the Hill End Anticline. The zircons in this rock are primarily euhedral, and are dominated by simple prismatic and pyramidal faces (according to Bossière et al. (1996) such forms are typical of high-temperature, relatively alkali-rich magmas); however, steeper pyramids occur on some crystals (Figure 8.4d). The aspect ratio of the grains ranges from about 2:1 to 4:1. Fluid and silicate inclusions are common. Some grains have distinctly embayed margins.

CL identifies the widespread occurrence of prismatic zonation, and the presence of discordant, anhedral cores, some of which have been dated. Although the latter are clearly exotic, most of the zoned zircon in this rock is cogenetic.

Dating was accomplished in two separate analytical sessions, on different ion-microprobes. In the first session, utilising SHRIMP I, all 26 analyses of the SL 13 standard yield a 1.8 % reproducibility. Except for a 2500 Ma core, the remaining 27 206Pb/238U ages of the Turondale zircons are within error (χ^2 is 0.87) of a mean value of 411.5±4.1 Ma (Figure 8.5i).

In the second session (on SHRIMP II), 22 analyses of the standard yield a 2.2 % reproducibility. Twenty three of the Turondale porphyry ages are within error (χ^2 is 0.44) of a mean value of 410.4±5.4 Ma (Figure 8.5j). The three exceptions, with ages of about 460 Ma, 580 Ma and 1450 Ma, all reflect the presence of inherited components.

Because the results of the two sessions are within error of each other, they can be combined to give a preferred age of 411.1±3.2 Ma for the crystallisation of the porphyritic magma.

8.5.4 Significance of the isotopic ages

The ages obtained above for the lava from the Merrions Formation and the porphyry from the Turondale Formation can potentially be assigned to the crystallisation of those rocks. In other words, they have the ability to provide direct stratigraphic information. In contrast, all of the other dated rocks are secondary resedimented volcaniclastic deposits. Strictly, the ages derived for them will be only maximum values for their time of deposition. In practice, those ages are very likely to be indistinguishable from, and to provide reasonable estimates of depositional age, because those zircons would be expected to have been derived from newly created volcanic products.

Table 8.2 reveals that there is only a limited range in the ages derived above. Indeed, on the basis of the quoted errors, it is not possible to statistically discriminate between any of the ages. However, those precision limits incorporate a component to allow for the uncertainty of the calibration, so that the ages can be justifiably compared with samples dated during different analytical sessions. This extra component of uncertainty is not required for ages that have been calibrated against a common set of standard analyses (ie., jointly analysed samples) and are being compared with each other.

From all of the data presented above, it is possible to demonstrate the existence of only one likely age difference, even without the precision limits of the mean ages being

Table 8.2: Summary of U-Pb zircon ages obtained in this study.

Location	Member	Sample No.	Rock type	IP Mount	Age (Ma) calibrated to SL 13	Age (Ma) calibrated to QGNG	No of analyses
Merrions Formation							
type section (upper)	E	94843524	volcaniclastic	1	404.8±4.8	407.1±6.9	18
type section	H	96843526	porphyry lava	2	406.2±5.1	408.0±5.3	33
type section (intermediate)	D	94843523	volcaniclastic	1	405.5±4.6	407.8±6.6	20
Limekilns (section 3)	D	94843525	volcaniclastic	3	406.0±4.3	409.9±6.6	25
type section (lower)	P	94843522	volcaniclastic	3	408.0±4.3		25
type section (lower)	P	94843522	volcaniclastic	1	409.6±4.6		20
type section (lower)	P	94843522	volcaniclastic	2	410.7±5.0	411.9±5.0	35
Turondale Formation							
section 2		93844559B	porphyry sill	4	411.1±3.2		49
type section		94843520	volcaniclastic	3	409.5±4.3	413.4±6.6	27

augmented by uncertainty related to the calibration of the standard. That age difference applies to the session in which the three samples of the Merrions Formation itself were analysed. Without the augmented uncertainties, the ages (with one sigma precision) for the three samples are 409.6±1.6.Ma (lower), 405.5±1.6 Ma (intermediate) and 404.5±1.7 Ma (upper). The difference between the ages for the upper and lower parts generates a Student's t value of 2.18, which is significant for 36 degrees of freedom (n-2) at slightly more than the 95 % confidence level (for which t is 2.03). It is therefore probable that the apparent age differences are real, and that the zircon ages from the lower part of the Merrions Formation are older (by about 5 million years) than those derived from the youngest dated unit.

8.6 REGIONAL BIOSTRATIGRAPHY

Fossils are generally rare in the Crudine Group in the Hill End Trough and are confined to those in transported limestone blocks and rare non-age diagnostic plant stems (Packham 1968). Bischoff and Fergusson (1982) describe conodonts ranging in age from late Wenlock to middle Lochovian (early *delta* Zone) in allochthonous limestone blocks within a limestone-mudstone breccia facies at Palmers Oakey. This unit correlates with undifferentiated lower Crudine Group (Turondale and Waterbeach Formations; Raymond et al. 1997; Glen and Watkins 1999), so the conodont fauna provide a maximum age for the overlying Merrions Formation. Age-diagnostic fossils have also been found in the Crudine Group and the overlying Limekilns Formation in the Limekilns district, east of the Wiagdon Thrust. Fossils occur in three units in the Limekilns sequence: (1) in sediments underlying the Merrions Formation; (2) at the base of the Limekilns Formation; and (3) throughout the Jesse Limestone Member.

1. Wright (in Packham 1969) recorded a transported brachiopod fauna in fine-grained volcanogenic sediments below the base of the Merrions Formation at Paling Yards, about 8 km north of Limekilns (Figure 8.1). Garratt and Wright (1988) correlated the fauna with their 'late' Lochkovian *australis* assemblage zone (Figure 8.3). Unfortunately, the exact stratigraphic position of the faunal assemblage within the Crudine Group is uncertain. Packham (1969) initially described the fauna as located near the top of the (undifferentiated) Crudine Group, which originally comprised only the Turondale and Waterbeach Formations (Figure 8.3). Subsequent publications have assumed from this description, that the fauna lay at the top of the Waterbeach Formation (e.g. Strusz 1972; Garratt and Wright 1988). However, based on the most recent mapping of the area (Raymond et al. 1997), the Turondale Formation is immediately overlain by the Merrions Formation at Paling Yards (Figure 8.1). Interpreting the nature of the contact between the two formations is hampered by poor outcrop and structural complexity. If the Waterbeach Formation

has been removed by faulting or erosion, the brachiopod fauna would lie at the top of the Turondale Formation. The possibility exists, however, that the Waterbeach Formation is present in condensed form, but could not be distinguished from fine-grained sediments of the upper Turondale Formation (Watkins pers. comm. 1998), in which case the fauna may also lie at any stratigraphic level within the Waterbeach Formation. Regardless of its precise stratigraphic position, the faunal assemblage constrains the upper limit of the Turondale Formation and the lower limit of the Merrions Formation to the 'late' Lochkovian.

2. Fossils are scattered at different levels in the basal unit of the Limekilns Formation (formerly the "Rosedale Shale" of Packham 1968), which conformably overlies the Merrions Formation. The basal shales yield a mostly pelagic fauna, comprising graptolites, tentaculitids, hyolithids and conulariids, and plant fragments (Wright and Haas 1990). Benthic faunas comprising mostly brachiopods with some corals, rare bivalves and trilobites, are also present. The occurrence of the tentaculitid (dacryocanarid) *Nowakia acuaria*, a well known Pragian index fossil (Wright and Haas 1990), indicates a Pragian to early Emsian age for the base of the Limekilns Formation (Lütke 1979).

3. The Jesse Limestone Member contains mass-flow breccias representing slump-transported platform carbonate material that was redeposited in fans on the flank of the Capertee High. The unit is well constrained to the Emsian. Conodonts from the matrix of the breccias are of the late Emsian *serotinus* Zone (Mawson et al. 1990; Mawson and Talent 1992).

   The conodont data from the Jesse Limestone Member do not conflict with the faunal data from the base of the Limekilns Formation. However, they infer that the Limekilns Formation encompasses a considerable time period (Figure 8.3). The assignment of the Jesse Limestone Member to the late Emsian (*serotinus* Zone) implies that the underlying 200 m condensed shale sequence could possibly span the Pragian, and all of the Emsian *dehiscens, perbonus and inversus* conodont zones. Alternatively, as the sequence contains no trace of early Emsian faunas, a hiatus during this period may be inferred.

According to the biostratigraphic constraints described above, the allowable biostratigraphic range of the Merrions Formation spans from the middle Lochkovian to the early Emsian (i.e. late *delta* to *dehiscens* conodont Zones; Figure 8.6). The *australis* zone brachiopod fauna constrains the upper limit of the Turondale Formation to the top of the Lochkovian *pesavis* Zone. Graptolites in the Tanwarra Shale, assigned a late Wenlock to earliest Ludlow age, provide the only fossil control for the base of the

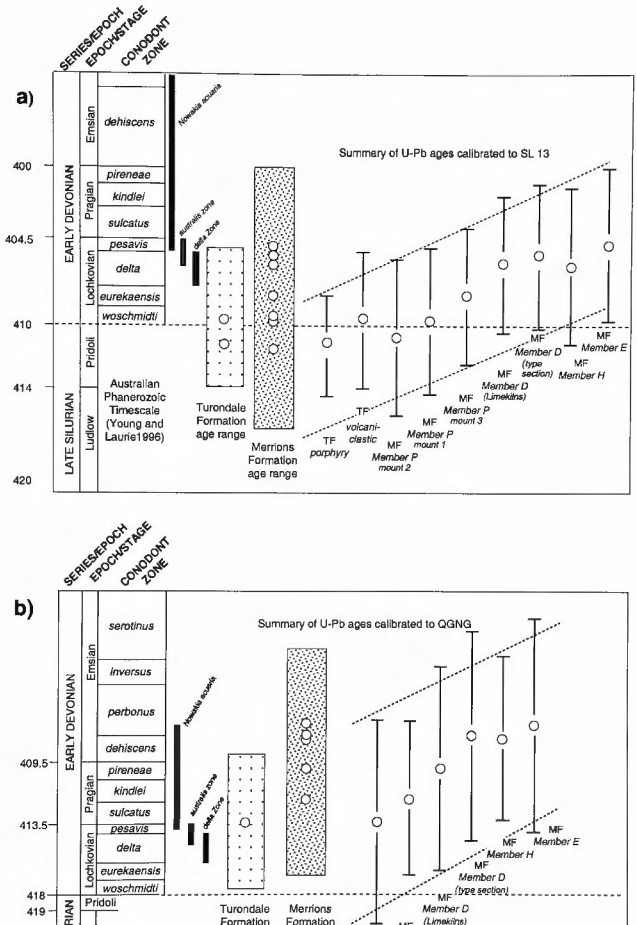

Figure 8.6: Graphic presentation of the: (a) SL 13-calibrated data plotted against the Australian Phanerozoic Timescale; and (b) QGNG-calibrated data plotted against the recently published time scale of Tucker et al. (1998). Faunal zones constraining the allowable biostratigraphic range of the samples, as discussed in the text, are also illustrated.

Turondale Formation. However, Colquhoun (1998), suggested that the Turondale Formation is probably equivalent to the lower Kandos Group on the adjacent Capertee High, which would infer that the unit is of Lochkovian age.

8.7 DISCUSSION

8.7.1 Consequences of the SL 13-calibrated dataset

Figure 8.6a shows that the ages obtained for the Turondale and Merrions Formations are broadly consistent with the historical assignment of the Crudine Group to the Early Devonian (Packham 1968). The samples selected for analysis span almost the entire Group, excluding only the basal, non-volcanic Cookman Formation. The envelope of analytical errors encompassing the derived ages straddles the Silurian-Devonian boundary at 410 Ma, as defined on both the Australian Phanerozoic Timescale (Young and Laurie 1996), and the IUGS global stratigraphic chart (Cowie and Bassett 1989). Within this envelope of analytical uncertainty, Early Devonian Lochkovian ages were consistently reproduced, spanning a limited range of about 6 Ma (404.8-411.1 Ma).

It is not possible to statistically discriminate between ages obtained for the Turondale and Merrions Formations. The age of 409.5±4.3 Ma for sample 94843520 from the base of the Turondale Formation lies within the range of ages derived for sample 94843522 at the base of the Merrions Formation (408±4.3, 409.6±4.6 and 410.7±5.0 Ma). However, about 900 metres of predominantly hemipelagic sediment, representing over half of the Turondale Formation and the entire Waterbeach Formation, was deposited in the intervening period. If only data obtained from the same sample mount are compared, the mean for the bases of the Turondale and Merrions Formations are 409.5 Ma and 408.0 Ma, respectively. Although statistically indistinguishable, these ages are nevertheless in the correct sense, and when considered with the analytical uncertainties, would allow up to several millions of years for the deposition of the Waterbeach Formation and remainder of the Turondale Formation.

Figure 8.6a identifies a conflict between the isotopic data and the biochronological framework provided by the Limekilns sequence. Fossil control from contiguous units indicates a mostly Pragian age for the Merrions Formation. In contrast, isotopic ages derived for the Merrions Formation consistently yield Lochkovian, not Pragian, ages (as defined above). The stratigraphically oldest sample of the Merrions Formation yielded ages ranging between 410.7±5.0 and 408.0±4.3 Ma, placing the base of the Merrions Formation close to the base of the Lochkovian (410 Ma) on the current Australian Phanerozoic Timescale (Young and Laurie 1996). This discrepancy between

the existing biochronological constraints and the new isotopic data suggests that the numerical calibration of the Silurian-Devonian boundary requires some revision.

The numerical age of 410 Ma presently used for the Silurian-Devonian boundary on the Australian Phanerozoic Timescale is deduced indirectly from measured ages at widely separated stratigraphic levels, which lack precise biostratigraphic control. The age is presently based on isotopic dating of Late Silurian - Early Devonian volcanic sequences in the Yass district, New South Wales (Young 1995). Owen and Wyborn (1979) produced a Rb/Sr age of 406±5 Ma from the Boggy Plain Granite, inferred on similar geochemical characteristics to be comagmatic with the Mountain Creek Volcanics, which underlie fossiliferous limestones of late Pragian *pireneae* age. Earliest Devonian strata of the Bowning Group, containing the conodont *Icriodus woschmidti* underlie and are separated from the volcanics by an unconformity representing the Early Devonian Bowning event of southeastern Australia. Owen and Wyborn (1979) estimated that the unconformity represents a break in sedimentation of about 4 million years, in order to accommodate the entire Ludlovian of the underlying Yass Basin sequence above the biostratigraphically constrained earliest Ludlow date of 421±2 Ma for the Laidlaw Volcanics (Wyborn et al. 1982). On this basis, they estimated a numerical age of 410 Ma for the Silurian-Devonian Boundary, interpolating from the oldest 406 Ma age for the granites that intrude the Mountain Creek Volcanics.

This estimated age of the Silurian-Devonian boundary is incompatible with the isotopic ages presented above for the Crudine Group. In addition, the results for the Merrions Formation suggest that the base of the *delta* Zone in the middle Lochkovian is no younger than about 410 Ma. These inconsistencies necessitate a reassessment of the core assumptions reached above.

8.7.2 A preferred interpretation

It is clear from the preceding discussion that the ages obtained in this study are inconsistent with those assigned by Young and Laurie (1996) to the appropriate part of the Australian Phanerozoic Timescale, an issue that was also identified by Young (1997), largely on the basis of the new data presented above. This inconsistency could be a consequence of either or both of two issues; namely: (1) whether or not the chronological ties to the time scale are correct; and (2) whether the new data accurately depicts the crystallisation ages of the dated rocks. The evidence presented below suggests that both issues are relevant.

Data assessment based on calibration to the QGNG standard

Most readers would be aware of a lack of consensus on which isotopic ages are best used as benchmarks in the derivation of the Phanerozoic time scale, and this has led to widely differing estimates of the age and duration of its component Periods (e.g., Harland et al. 1982, 1990; Fordham 1992; Gradstein and Ogg 1996; Tucker et al. 1998). Although this divergence of opinion has arisen from a variety of factors, it primarily results from different assessments of the most appropriate isotopic ages to use for numerically constraining key biostratigraphic horizons. Each isotopic dating scheme has its own strengths and weaknesses, and it requires judicious assessment of all available data (acquired from a variety of sources over the past several decades) to assemble a meaningful time scale. It is not only the relative robustness of the different chronometers that is important. Other considerations include achieving a balance between accuracy and precision, and even assessing the effects of uncertainty in the decay constants of the relevant radioactive isotopes. Naturally, due to advances in technology and knowledge, recently acquired ages are generally more reliable.

Over recent years, U-Pb zircon geochronology has played a pivotal role in numerically constraining geological time, and it has therefore been extensively used in the definition of the different time scales. The most recently published, authoritative division of Devonian time is that of Tucker et al. (1998), which is based not only on previously obtained data, but on six new and precise isotope dilution U-Pb zircon ages. Although the Tucker et al. (1998) time scale will almost certainly require adjustment as more information becomes available, it currently represents a benchmark with which the ages produced in this study should be compared.

Another vital issue that must be addressed before meaningful comparisons can be made with an established time scale is whether the ages in question can be justifiably compared with each other. As an example, the change in the recommended decay constants of some parent isotopes (Steiger and Jäger 1977) would lead, if uncorrected, to non-agreement between genuinely concordant ages that were published before and after that time. The current data are susceptible to a different effect of this type, namely the choice of the particular SHRIMP standard that was used for age calculation.

Ages derived from ^{207}Pb are unsuitable for the ion-microprobe dating of Phanerozoic zircon, because that isotope and its parent ^{235}U were so depleted by then that they are not capable of being measured with sufficient precision. Consequently, the $^{207}Pb/^{206}Pb$ dating technique, which is extensively used for Precambrian dating, is replaced by the $^{206}Pb/^{238}U$ technique for the dating of Phanerozoic rocks by ion microprobe. However,

unlike the Pb isotopes, which are not significantly fractionated during the SHRIMP sputtering process, there is a dramatic change in Pb/U in the secondary ion beam compared with that in the target zircon. This is compensated for by comparing the relative proportion of those ions in the zircon being dated with that in a zircon (known as the standard) of independently determined age. Until now, at least most SHRIMP ages that have been used as tie points for the time scale (eg., Compston and Williams 1992; Compston et al. 1992; Claoué-Long et al. 1991; Claoué-Long et al. 1995; Roberts et al. 1996) have been calibrated against a Late Neoproterozoic zircon (SL 13) from Sri Lanka that yields an isotope dilution age of 572 Ma. In common with those studies, all of the analyses reported above have also been calibrated against SL 13. Several years ago the near exhaustion of SL 13 led to the introduction of two new zircon standards in the ANU SHRIMP laboratory. Fortunately, one of these, an 1850 Ma-old zircon known as QGNG was used as a backup standard for the last batch of analyses performed in this study.

Recent comparative studies (Black et al. 1997; Black in press) have revealed a small, but often significant inconsistency between SHRIMP analyses of those two standards, even though their ages have been independently documented by isotope dilution U-Pb zircon studies. Those studies indicate that, on average, SL 13-derived SHRIMP U-Pb ages are approximately 1.5 % younger than those derived from QGNG. A difference of similar magnitude (1-2 %) and sense has also been reported by Tucker and McKerrow (1995) between SL 13-calibrated SHRIMP ages and isotope dilution zircon ages. These observations indicate that it is inappropriate to compare SL 13-derived ages with the most recently reported Devonian time scale (Tucker et al. 1998), and that QGNG-derived SHRIMP ages would be much better suited for that task.

If the offset between SHRIMP U-Pb ages derived from the two standards was constant, the SL-13 derived data could be adjusted upwards by that fixed percentage to convert to QGNG-referenced ages. Unfortunately, the accumulated comparisons of Black et al. (1997) and Black (in press) indicate that the offset is variable, ranging from about 0 % to 3 %. It is therefore believed that an upward adjustment of all SL 13-derived ages by 1.5 % would be an unreliable means of making the newly acquired data congruent with QGNG-calibrated data. An alternative (yet imperfect) approach is used for that purpose.

As stated above, the QGNG standard was in use by the time of the last dating session (labelled as the second mount in Table 8.3 and text), when both it and SL 13 were jointly analysed. The two unknowns analysed at that time, volcaniclastic sample 94843522 from the base of the Merrions type section, and sample 96843526 (lava from the same section) can therefore be directly calibrated against QGNG. This exercise yields slightly (but not significantly) older mean ages than those calibrated against

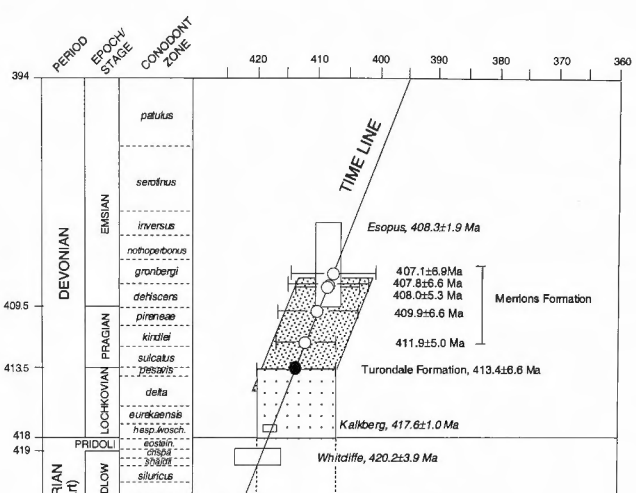

Figure 8.7: Time scale for the Late Silurian and Early Devonian, showing pre-existing tie-points in italics (from Tucker et al. 1998) with the ages from this paper plotted for comparison. Each tie point on the time line has an assigned uncertainty represented by a rectangle, defined by the precision of the isotopic age (2σerror) on the horizontal axis, and the sample's allowable biostratigraphic range on the vertical axis. The possible biostratigraphic range of the Turondale Formation is denoted by dashed lines. Lithostratigraphic constraints, based on calibrations with units on the Capertee High (after Colquhoun 1998), further confine the likely age range of the Turondale Formation (denoted by wide stipple). The duration of Lochkovian conodont Zones follows Fordham (1992). All other conodont Zone calibrations follow Tucker et al. (1998).

SL 13, of 411.9±5.0 Ma and 408.0±5.3 Ma, respectively. As described above, sample 94843522 was also set in two of the other mounts, where it served as an "internal standard". It is therefore possible to adjust all ages on each of those mounts by the amount that the sample 94843522 age is different from 411.9 Ma, which indirectly normalises those ages to the QGNG standard. That procedure yields the ages listed in Table 8.2, which are linked to an age of 411.9± 5.0 Ma for the base of the Merrions Formation. The ages determined for the "internal standard" have an uncertainty of their own, which is combined in quadrature with that determined for the unknowns for the QGNG cross-calibrated results. It is not possible to derive a QGNG-based age for

sample 93844559B, because it was analysed before QGNG was trialed as a standard and before sample 94843522 had been collected.

Time scale calibrations

According to the biostratigraphic (and lithostratigraphic) constraints described earlier, the volcaniclastic sample from the Turondale Formation is of Lochkovian age, and the allowable biostratigraphic range of the Merrions Formation spans from the middle Lochkovian to the early Emsian (i.e. late *delta* to *dehiscens* conodont Zones; Figure 8.6). The QGNG-based ages would therefore indicate that 413.4±6.6 Ma (Turondale volcaniclastic) should be a Lochkovian age, and the 407.1±6.9 Ma for the top of the Merrions Formation should provide a tie point close to the Pragian-Emsian boundary. These ages are well within error of the Tucker et al. (1998) estimates of 413.5 Ma and 409.5 Ma for the base and top of the Pragian, respectively (Figure 8.6b). There is therefore no discrepancy between the ages obtained in this study when based on the QGNG standard and the most recently published Devonian time scale. Indeed, the estimates of Lochkovian time derived above might make a useful addition to that time scale, which currently has no tie points between early Lochkovian and early Emsian times (Figure 8.7).

8.8 CONCLUSIONS

1. U-Pb zircon ages were obtained for two samples of the Turondale Formation and five of the Merrions Formation. The samples from the Turondale Formation include a volcaniclastic sandstone at the base of the unit, and a porphyry sill intruding the basal volcaniclastic sequence. The Merrions Formation was sampled at four stratigraphic levels of the type section. From base to top, the samples represent basal arenite member P, arenite member D, which occupies an intermediate stratigraphic position within the formation, a dacitic lava (member H) and upper arenite member E (Cas 1977). When the ages are recalibrated against zircon standard QGNG, an age of 413.4±6.6 Ma is obtained for the base of the Turondale Formation, and ages ranging between 411.9±5.0 Ma and 407.1±6.9 Ma are obtained for the Merrions Formation.

2. A sample was also collected at Limekilns, from a unit originally mapped as the Winburn Tuff, interpreted to overlie the Limekilns Formation. The derived age of 409.9±6.6 Ma confirms more recent mapping, which recognised that the unit underlies the Limekilns Formation, and forms part of the Merrions Formation (Voorhoeve 1986; Pogson and Watkins 1998). The age of the unit is within the range of ages quoted above for the type sequence of the Merrions Formation, and

well within error of member D (407.8±6.8 Ma), which is compositionally similar to the analysed sample.

3. The Limekilns sample is significant because there is fossil age control from units above and below the Merrions Formation in this area, enabling the numerical ages presented in this paper to be tied to the regional biostratigraphy. Based on these biostratigraphic constraints, the Turondale Formation is confined to the Lochkovian stage (approximately delta Zone, based on data from Bischoff and Fergusson 1982, and Garratt and Wright 1988), and the allowable biostratigraphic range of the Merrions Formation spans from the late Lochkovian to the early Emsian (late *delta* to *dehiscens* conodont Zones).

4. The choice of SHRIMP standard used for age calibration can have a significant effect on isotopic data. Data normalised against the commonly used SL 13 zircon standard yield ages that are younger, and variably offset by 0-3%, from ages derived from QGNG (Black in press), and from isotope dilution zircon ages (Tucker and McKerrow 1995). These observations indicate that QGNG-derived SHRIMP ages are better suited than SL 13 for the task of numerical time scale calibration.

5. The new isotopic data presented in this paper support a revision of the Australian Phanerozoic Timescale, suggesting that the numerical calibration of the Silurian-Devonian Period boundary, and the Lochkovian-Pragian and Pragian-Emsian Stage boundaries require downward adjustment. The new ages are well within error of the division of Devonian time proposed by Tucker et al. (1998), which places the Silurian-Devonian boundary at 418 Ma, and estimates ages of 413.5 Ma and 409.5 Ma for the base and top of the Pragian, respectively.

6. The estimates of late Lochkovian time and the age of the Pragian-Emsian boundary derived from this study might make a useful addition to that time scale, which currently has no tie points between early Lochkovian and early Emsian times.

Table 8.3: U-Th-Pb isotopic compositions of the analysed zircons.

Grain area	U (ppm)	Th (ppm)	Th/U	$^{206}Pb/^{204}Pb$	f_{206} (%)	$^{206}Pb/^{238}U$	$^{207}Pb/^{235}U$	$^{207}Pb/^{206}Pb$	Age (Ma)
Merrions Formation, Type Section (upper) 94843524									
201.1	289	259	0.898	1000000	0.22	0.0657±.0012	0.481±.013	0.0531±.0009	411±7
202.1	185	107	0.574	11300	0.00	0.0645±.0012	0.495±.013	0.0556±.0009	403±7
203.1	208	157	0.753	9123	0.00	0.0640±.0012	0.484±.013	0.0549±.0010	400±7
204.1	149	113	0.761	10900	0.00	0.0634±.0012	0.482±.014	0.0552±.0012	396±7
205.1	212	127	0.598	13600	0.01	0.0650±.0012	0.500±.013	0.0558±.0010	405±7
206.1	198	122	0.614	35800	0.09	0.0653±.0012	0.489±.013	0.0543±.0009	408±7
207.1	189	106	0.559	1000000	0.03	0.0655±.0012	0.493±.013	0.0546±.0009	409±7
208.1	344	45	0.131	13700	0.01	0.0854±.0016	0.681±.014	0.0578±.0004	529±9
209.1	186	119	0.642	7912	0.06	0.0655±.0012	0.489±.013	0.0541±.0010	410±7
210.1	183	131	0.714	1000000	0.00	0.0644±.0012	0.505±.014	0.0569±.0010	401±7
211.1	297	158	0.531	6804	0.11	0.0659±.0012	0.497±.012	0.0547±.0007	411±7
212.1	117	65	0.560	17600	0.20	0.0642±.0012	0.490±.015	0.0554±.0012	401±7
213.1	211	113	0.537	4230	0.02	0.0664±.0012	0.510±.013	0.0557±.0009	414±7
214.1	120	79	0.654	10730	0.10	0.0641±.0012	0.486±.016	0.0549±.0013	401±7
215.1	125	77	0.616	10260	0.12	0.0640±.0012	0.484±.015	0.0548±.0012	400±7
216.1	219	132	0.600	1000000	0.00	0.0651±.0012	0.503±.013	0.0561±.0009	406±7
217.1	235	235	1.000	3123	0.49	0.0662±.0012	0.504±.016	0.0553±.0013	413±7
218.1	281	166	0.590	1000000	0.15	0.0636±.0012	0.484±.012	0.0552±.0009	398±7
219.1	201	152	0.756	1000000	0.00	0.0596±.0011	0.457±.014	0.0556±.0012	373±7
220.1	245	99	0.405	12530	0.28	0.0642±.0012	0.478±.012	0.0539±.0008	402±7

f_{206} is the proportion of common ^{206}Pb to total ^{206} Pb expressed as a percentage. The Palaeozoic ages are derived from ^{207}Pb-corrected $^{206}Pb/^{238}U$ ratios. Precambrian ages are derived from ^{204}Pb-corrected $^{207}Pb/^{206}Pb$ ratios.

Grain area	U (ppm)	Th (ppm)	Th/U	$^{206}Pb/^{204}Pb$	f_{206} (%)	$^{206}Pb/^{238}U$	$^{207}Pb/^{235}U$	$^{207}Pb/^{206}Pb$	Age (Ma)
Merrions Formation, Type Section (intermediate) 94843523									
101.1	175	94	0.540	54400	0.19	0.0663±.0012	0.494±.013	0.0541±.0009	414±7
102.1	182	93	0.508	1000000	0.00	0.0659±.0012	0.497±.013	0.0547±.0008	412±7
103.1	126	61	0.488	1000000	0.00	0.0645±.0012	0.503±.014	0.0566±.0010	402±7
104.1	315	118	0.374	1000000	0.10	0.0630±.0012	0.477±.011	0.0549±.0006	394±7
105.1	110	80	0.721	10700	0.41	0.0621±.0012	0.445±.016	0.0520±.0015	390±7
106.1	150	88	0.586	47000	0.14	0.0659±.0012	0.492±.014	0.0541±.0011	412±7
107.1	149	71	0.478	1000000	0.02	0.0665±.0012	0.506±.014	0.0552±.0009	415±7
108.1	177	90	0.509	48500	0.03	0.0653±.0012	0.503±.013	0.0559±.0009	407±7
109.1	287	184	0.640	8833	0.00	0.0667±.0012	0.503±.012	0.0547±.0008	416±7
110.1	110	60	0.543	7730	0.10	0.0634±.0012	0.473±.014	0.0541±.0012	397±7
111.1	149	71	0.474	1000000	0.00	0.0656±.0012	0.507±.013	0.0560±.0009	409±7
112.1	100	53	0.528	145000	0.00	0.0649±.0012	0.497±.015	0.0555±.0012	405±7
113.1	162	82	0.509	5956	0.06	0.0644±.0012	0.492±.013	0.0554±.0009	402±7
114.1	191	92	0.483	1000000	0.07	0.0653±.0012	0.495±.013	0.0550±.0009	408±7
115.1	226	101	0.448	11300	0.00	0.0654±.0012	0.509±.012	0.0564±.0008	408±7
116.1	235	111	0.474	1000000	0.07	0.0649±.0012	0.496±.012	0.0554±.0008	405±7
117.1	179	137	0.769	1000000	0.00	0.0640±.0012	0.503±.015	0.0570±.0012	399±7
118.1	149	108	0.723	27000	0.18	0.0657±.0012	0.487±.016	0.0537±.0013	411±7
119.1	207	103	0.499	15800	0.04	0.0649±.0012	0.493±.013	0.0551±.0009	405±7
120.1	217	156	0.718	1000000	0.00	0.0650±.0012	0.513±.014	0.0572±.0010	405±7
Merrions Formation, Type Section (lower, first mount) 94843522									
1.1	167	91	0.544	9025	0.00	0.0658±.0012	0.502±.013	0.0554±.0009	410±7
2.1	315	208	0.661	1000000	0.02	0.0658±.0012	0.497±.012	0.0548±.0007	411±7
3.1	171	124	0.727	1000000	0.09	0.0651±.0012	0.495±.014	0.0552±.0011	406±7
4.1	150	86	0.571	1000000	0.06	0.0646±.0012	0.488±.013	0.0548±.0010	404±7

Grain area	U (ppm)	Th (ppm)	Th/U	$^{206}Pb/^{204}Pb$	f_{206} (%)	$^{206}Pb/^{238}U$	$^{207}Pb/^{235}U$	$^{207}Pb/^{206}Pb$	Age (Ma)
5.1	239	131	0.548	20500	0.07	0.0650±.0012	0.497±.012	0.0555±.0008	406±7
6.1	128	67	0.524	30500	0.06	0.0633±.0012	0.482±.014	0.0552±.0011	396±7
7.1	163	82	0.502	31500	0.40	0.0675±.0012	0.500±.014	0.0537±.0009	422±8
8.1	154	92	0.598	69900	0.00	0.0672±.0012	0.536±.015	0.0578±.0010	418±8
9.1	189	103	0.547	89900	0.00	0.0647±.0012	0.498±.013	0.0558±.0009	404±7
10.1	194	96	0.494	1000000	0.06	0.0667±.0012	0.498±.013	0.0542±.0008	417±7
11.1	226	132	0.584	12130	0.00	0.0673±.0012	0.517±.013	0.0557±.0009	419±8
12.1	315	181	0.575	1000000	0.03	0.0672±.0012	0.505±.012	0.0544±.0007	420±8
13.1	191	96	0.505	1000000	0.00	0.0652±.0012	0.511±.013	0.0569±.0009	406±7
14.1	289	163	0.563	47300	0.05	0.0654±.0012	0.489±.012	0.0542±.0007	408±7
15.1	310	217	0.701	1000000	0.00	0.0647±.0012	0.481±.012	0.0538±.0008	405±7
16.1	187	105	0.563	5433	0.08	0.0657±.0012	0.484±.013	0.0534±.0010	411±7
17.1	259	133	0.512	12190	0.00	0.0662±.0012	0.514±.013	0.0563±.0008	413±7
18.1	195	100	0.512	21820	0.15	0.0668±.0012	0.496±.013	0.0539±.0009	417±7
19.1	126	79	0.624	10400	0.00	0.0648±.0012	0.505±.016	0.0566±.0013	404±7
20.1	139	75	0.538	24500	0.00	0.0643±.0012	0.494±.015	0.0557±.0012	401±7
Merrions Formation, Type Section (lower, second mount) 94843522									
1.1	168	86	0.513	17400	0.28	0.0642±.0018	0.477±.023	0.0538±.0020	401±10
2.1	208	118	0.568	24700	0.00	0.0679±.0018	0.511±.022	0.0546±.0017	423±11
3.1	201	124	0.617	7842	0.31	0.0689±.0019	0.496±.021	0.0522±.0015	430±11
4.1	433	249	0.575	10220	0.19	0.0658±.0017	0.497±.018	0.0549±.0012	410±10
5.1	272	164	0.603	18600	0.21	0.0684±.0019	0.502±.022	0.0532±.0016	427±11
6.1	318	170	0.537	13500	0.17	0.0645±.0017	0.491±.018	0.0552±.0012	402±10
7.1	246	126	0.516	33600	0.23	0.0660±.0019	0.492±.023	0.0540±.0018	412±11
8.1	272	207	0.760	18200	0.00	0.0687±.0019	0.538±.022	0.0568±.0015	427±11
9.1	158	100	0.636	1000000	0.08	0.0685±.0022	0.520±.029	0.0551±.0023	427±13
10.1	391	210	0.538	23400	0.09	0.0676±.0019	0.508±.019	0.0545±.0012	421±11
11.1	160	107	0.674	100000	0.00	0.0648±.0019	0.511±.027	0.0572±.0022	403±11

Grain area	U (ppm)	Th (ppm)	Th/U	$^{206}Pb/^{204}Pb$	f_{206} (%)	$^{206}Pb/^{238}U$	$^{207}Pb/^{235}U$	$^{207}Pb/^{206}Pb$	Age (Ma)
12.1	202	115	0.573	1000000	0.13	0.0655±.0019	0.486±.023	0.0538±.0018	409±11
13.1	254	125	0.492	10500	0.00	0.0647±.0018	0.510±.021	0.0572±.0016	402±10
14.1	183	104	0.567	8105	0.00	0.0656±.0019	0.514±.026	0.0568±.0022	408±11
15.1	222	124	0.558	100000	0.00	0.0673±.0019	0.519±.024	0.0559±.0019	419±11
16.1	213	128	0.605	25300	0.04	0.0667±.0018	0.511±.022	0.0555±.0017	415±11
17.1	416	302	0.726	28200	0.28	0.0675±.0019	0.492±.020	0.0529±.0014	421±11
18.1	162	85	0.525	4842	0.33	0.0640±.0018	0.479±.026	0.0543±.0023	400±11
19.1	141	76	0.541	1000000	0.31	0.0651±.0021	0.461±.024	0.0514±.0020	408±12
20.1	241	126	0.523	7522	0.21	0.0647±.0018	0.483±.022	0.0541±.0018	404±10
21.1	211	127	0.604	6099	0.10	0.0636±.0019	0.489±.028	0.0558±.0025	397±11
22.1	201	109	0.547	1000000	0.02	0.0640±.0017	0.487±.023	0.0552±.0020	399±10
23.1	183	103	0.565	1000000	0.17	0.0664±.0019	0.492±.027	0.0538±.0024	414±11
24.1	211	106	0.502	94800	0.04	0.0655±.0019	0.492±.030	0.0545±.0027	409±11
25.1	214	123	0.578	1000000	0.26	0.0660±.0018	0.502±.023	0.0552±.0019	411±10
26.1	227	128	0.563	9920	0.04	0.0659±.0018	0.517±.029	0.0569±.0026	410±10
27.1	124	59	0.480	9312	0.15	0.0668±.0021	0.513±.030	0.0557±.0026	416±12
28.1	151	84	0.557	9473	0.47	0.0663±.0018	0.485±.028	0.0531±.0026	414±10
29.1	253	180	0.713	1000000	0.36	0.0646±.0016	0.463±.020	0.0520±.0017	405±9
30.1	226	166	0.734	5193	0.22	0.0645±.0018	0.482±.029	0.0542±.0027	403±10
31.1	277	197	0.712	26900	0.46	0.0652±.0017	0.470±.022	0.0523±.0019	408±10
32.1	160	89	0.559	11070	0.21	0.0641±.0020	0.473±.031	0.0535±.0028	401±12
33.1	282	160	0.568	100000	0.08	0.0676±.0017	0.497±.022	0.0533±.0018	422±10
34.1	280	230	0.822	7535	0.25	0.0637±.0017	0.476±.024	0.0541±.0021	398±10
35.1	142	70	0.492	1000000	0.00	0.0669±.0020	0.538±.032	0.0583±.0029	415±11
Merrions Formation, Type Section (lower, third mount) 94843522									
101.1	217	117	0.540	3978	0.28	0.0671±.0013	0.501±.016	0.0542±.0012	419±8
102.1	325	255	0.785	114000	0.26	0.0675±.0013	0.498±.016	0.0535±.0013	422±8
103.1	192	107	0.560	109000	0.32	0.0651±.0012	0.479±.016	0.0534±.0014	407±8

Grain area	U (ppm)	Th (ppm)	Th/U	$^{206}Pb/^{204}Pb$	f_{206} (%)	$^{206}Pb/^{238}U$	$^{207}Pb/^{235}U$	$^{207}Pb/^{206}Pb$	Age (Ma)
104.1	174	103	0.593	1000000	0.14	0.0634±.0012	0.487±.017	0.0557±.0015	396±7
105.1	249	166	0.668	4091	0.01	0.0665±.0013	0.509±.015	0.0555±.0012	415±8
106.1	167	88	0.525	2863	0.02	0.0651±.0012	0.509±.016	0.0567±.0013	405±7
107.1	216	170	0.785	5261	0.13	0.0630±.0012	0.476±.017	0.0548±.0015	394±7
108.1	190	103	0.541	1000000	0.00	0.0646±.0012	0.487±.016	0.0547±.0013	403±7
109.1	207	151	0.727	6519	0.57	0.0643±.0012	0.468±.018	0.0528±.0016	403±7
110.1	258	163	0.630	3309	0.00	0.0679±.0013	0.527±.015	0.0563±.0010	423±8
111.1	170	92	0.540	3329	0.28	0.0652±.0012	0.495±.016	0.0551±.0012	407±8
113.1	130	78	0.598	2341	0.12	0.0630±.0012	0.491±.017	0.0565±.0015	393±7
114.1	320	158	0.494	13600	0.10	0.0656±.0012	0.489±.012	0.0541±.0008	410±8
115.1	223	143	0.639	8864	0.32	0.0624±.0012	0.467±.014	0.0542±.0012	391±7
116.1	232	136	0.584	6161	0.33	0.0665±.0020	0.493±.019	0.0538±.0011	415±12
117.1	273	153	0.561	4929	0.23	0.0646±.0019	0.482±.018	0.0542±.0010	404±12
118.1	189	108	0.572	3394	0.37	0.0653±.0019	0.477±.019	0.0529±.0012	409±12
119.1	159	100	0.633	1000000	0.33	0.0645±.0019	0.475±.021	0.0534±.0015	403±12
120.1	239	118	0.496	58900	0.40	0.0645±.0019	0.475±.018	0.0534±.0011	404±12
121.1	307	243	0.792	1000000	0.12	0.0659±.0019	0.488±.019	0.0537±.0012	412±12
122.1	180	108	0.602	1738	0.25	0.0654±.0019	0.492±.020	0.0546±.0013	408±12
123.1	232	154	0.664	110000	0.10	0.0653±.0019	0.489±.019	0.0543±.0012	408±12
124.1	246	130	0.529	5475	0.20	0.0652±.0019	0.479±.018	0.0533±.0011	408±12
125.1	143	84	0.589	2461	0.12	0.0681±.0013	0.510±.018	0.0543±.0014	425±8
126.1	188	103	0.546	3799	0.23	0.0685±.0013	0.512±.016	0.0542±.0012	427±8
Merrions Formation, Type Section (lava) 96843526									
101.1	134	84	0.628	11840	0.14	0.0650±.0018	0.493±.030	0.0550±.0028	405±11
102.1	139	118	0.853	1000000	0.00	0.0659±.0022	0.515±.094	0.0567±.0100	410±12
103.1	113	69	0.614	1000000	0.08	0.0625±.0020	0.457±.029	0.0530±.0027	391±12
104.1	212	126	0.593	24900	0.21	0.0641±.0018	0.474±.022	0.0536±.0018	401±10
105.1	156	88	0.566	1000000	0.00	0.0654±.0020	0.505±.032	0.0560±.0030	407±12

Grain area	U (ppm)	Th (ppm)	Th/U	$^{206}Pb/^{204}Pb$	f_{206} (%)	$^{206}Pb/^{238}U$	$^{207}Pb/^{235}U$	$^{207}Pb/^{206}Pb$	Age (Ma)
106.1	182	101	0.557	10400	0.24	0.0648±.0019	0.482±.023	0.0539±.0019	404±11
107.1	155	94	0.608	4578	0.15	0.0654±.0018	0.487±.022	0.0540±.0017	408±10
108.1	188	105	0.561	1000000	0.00	0.0676±.0019	0.517±.026	0.0555±.0022	421±11
109.1	160	98	0.613	3356	0.00	0.0654±.0018	0.514±.025	0.0570±.0021	407±10
110.1	271	237	0.874	100000	0.04	0.0643±.0019	0.472±.025	0.0533±.0022	402±11
111.1	157	90	0.574	56300	0.06	0.0698±.0021	0.539±.032	0.0560±.0027	434±12
112.1	212	159	0.752	100000	0.11	0.0644±.0019	0.493±.024	0.0555±.0020	402±11
113.1	362	419	1.159	8325	0.68	0.0671±.0019	0.445±.026	0.0481±.0023	421±11
114.1	166	113	0.680	3190	0.54	0.0672±.0021	0.522±.030	0.0563±.0026	418±12
115.1	250	236	0.944	25300	0.20	0.0676±.0018	0.498±.025	0.0534±.0021	422±11
116.1	203	144	0.708	3266	0.56	0.0665±.0019	0.466±.024	0.0509±.0020	416±11
117.1	178	106	0.597	1000000	0.05	0.0661±.0019	0.502±.024	0.0551±.0019	412±11
118.1	120	64	0.535	1000000	0.00	0.0674±.0021	0.518±.031	0.0558±.0027	419±12
119.1	166	98	0.589	3229	0.26	0.0640±.0019	0.502±.028	0.0568±.0024	399±11
120.1	142	85	0.602	100000	0.66	0.0644±.0020	0.471±.028	0.0530±.0025	403±12
121.1	217	178	0.823	6660	0.00	0.0667±.0017	0.532±.024	0.0579±.0020	414±10
122.1	235	156	0.665	6578	0.01	0.0661±.0018	0.494±.023	0.0542±.0019	412±10
123.1	188	134	0.716	8971	0.00	0.0657±.0018	0.506±.026	0.0559±.0022	409±10
124.1	172	102	0.592	100000	0.00	0.0653±.0017	0.499±.024	0.0554±.0020	407±10
125.1	183	126	0.689	1966	0.23	0.0671±.0019	0.476±.035	0.0514±.0033	420±11
126.1	229	144	0.631	10600	0.23	0.0647±.0017	0.484±.024	0.0543±.0021	404±10
127.1	169	152	0.899	9462	0.00	0.0664±.0019	0.535±.033	0.0584±.0030	412±11
128.1	160	116	0.729	1000000	0.20	0.0643±.0017	0.474±.024	0.0535±.0021	402±10
129.1	163	133	0.815	1000000	0.00	0.0635±.0020	0.503±.029	0.0575±.0026	395±12
130.1	208	113	0.542	7016	0.33	0.0646±.0017	0.488±.023	0.0548±.0020	403±10
131.1	352	124	0.352	76700	0.01	0.1721±.0045	1.650±.050	0.0695±.0009	914±25
132.1	207	158	0.762	3251	0.07	0.0656±.0020	0.497±.027	0.0550±.0023	409±11
133.1	123	69	0.564	111000	0.11	0.0667±.0020	0.499±.028	0.0543±.0024	416±11
134.1	135	82	0.607	116000	0.04	0.0661±.0019	0.523±.034	0.0574±.0031	411±11
135.1	220	183	0.835	7420	0.00	0.0654±.0018	0.500±.032	0.0554±.0030	408±10

Grain area	U (ppm)	Th (ppm)	Th/U	$^{206}Pb/^{204}Pb$	f_{206} (%)	$^{206}Pb/^{238}U$	$^{207}Pb/^{235}U$	$^{207}Pb/^{206}Pb$	Age (Ma)
					Merrions Formation, Limekilns 94843525				
201.1	95	56	0.586	32200	0.17	0.0655±.0013	0.507±.021	0.0561±.0019	408±8
202.1	204	119	0.583	874	2.41	0.0661±.0013	0.511±.018	0.0560±.0015	412±8
203.1	126	60	0.478	1000000	0.42	0.0666±.0013	0.488±.017	0.0531±.0014	417±8
204.1	203	98	0.483	9580	0.00	0.0673±.0013	0.529±.016	0.0570±.0012	419±8
205.1	123	81	0.664	2675	0.39	0.0647±.0012	0.485±.019	0.0543±.0017	405±7
206.1	148	94	0.637	65200	0.33	0.0653±.0012	0.488±.018	0.0541±.0015	408±8
207.1	156	85	0.546	2023	0.23	0.0636±.0012	0.489±.017	0.0558±.0015	397±7
208.1	237	187	0.786	1000000	0.19	0.0640±.0012	0.469±.016	0.0532±.0015	400±7
209.1	132	79	0.599	4788	0.16	0.0672±.0013	0.499±.017	0.0539±.0014	420±8
210.1	91	48	0.523	2822	0.52	0.0648±.0012	0.469±.019	0.0524±.0018	406±8
211.1	124	68	0.549	1439	0.94	0.0650±.0012	0.489±.017	0.0545±.0015	406±8
212.1	237	110	0.463	4870	0.93	0.0627±.0012	0.451±.013	0.0523±.0011	393±7
213.1	222	159	0.714	4750	0.19	0.0629±.0012	0.466±.015	0.0537±.0012	394±7
214.1	199	103	0.519	5731	0.27	0.0627±.0012	0.461±.014	0.0533±.0011	392±7
215.1	230	166	0.722	7750	0.20	0.0644±.0012	0.483±.015	0.0544±.0012	403±7
216.1	163	92	0.566	16200	0.50	0.0666±.0020	0.473±.020	0.0515±.0014	417±12
217.1	169	128	0.756	3521	0.29	0.0646±.0019	0.488±.021	0.0548±.0015	404±12
218.1	214	127	0.594	3274	0.13	0.0655±.0019	0.488±.019	0.0540±.0012	409±12
219.1	150	116	0.772	19500	0.47	0.0659±.0019	0.486±.022	0.0536±.0016	412±12
220.1	212	122	0.574	28500	0.18	0.0657±.0019	0.489±.019	0.0540±.0012	411±12
221.1	128	70	0.551	2833	0.53	0.0643±.0019	0.461±.020	0.0520±.0015	403±12
222.1	165	92	0.559	5034	0.11	0.0655±.0019	0.501±.020	0.0554±.0013	409±12
223.1	157	68	0.433	1000000	0.06	0.0654±.0019	0.503±.019	0.0558±.0012	408±12
224.1	176	133	0.759	77600	0.21	0.0633±.0019	0.485±.021	0.0555±.0015	395±11
225.1	142	123	0.869	10370	0.19	0.0692±.0013	0.525±.021	0.0550±.0018	431±8
226.1	147	95	0.646	2014	0.52	0.0670±.0013	0.501±.018	0.0543±.0016	418±8

Grain area	U (ppm)	Th (ppm)	Th/U	$^{206}Pb/^{204}Pb$	f_{206} (%)	$^{206}Pb/^{238}U$	$^{207}Pb/^{235}U$	$^{207}Pb/^{206}Pb$	Age (Ma)
Turondale Formation (volcaniclastic sandstone) 94843520									
1.1	145	71	0.487	2801	0.31	0.0678±.0013	0.537±.018	0.0574±.0014	422±8
2.1	225	113	0.503	2438	0.16	0.0668±.0013	0.509±.015	0.0553±.0012	416±8
3.1	214	109	0.508	15900	0.29	0.0662±.0013	0.489±.015	0.0536±.0012	414±8
4.1	158	82	0.520	1000000	0.30	0.0646±.0012	0.474±.016	0.0532±.0014	404±7
5.1	213	106	0.498	5208	0.21	0.0678±.0013	0.509±.015	0.0545±.0011	423±8
6.1	126	58	0.462	18900	0.42	0.0670±.0013	0.510±.017	0.0552±.0014	418±8
7.1	116	58	0.499	2216	0.23	0.0657±.0013	0.490±.018	0.0541±.0015	410±8
8.1	227	121	0.531	3915	0.09	0.0655±.0012	0.491±.015	0.0544±.0011	409±8
9.1	203	100	0.494	2057	0.27	0.0637±.0012	0.475±.016	0.0541±.0013	399±7
10.1	238	128	0.537	13400	0.00	0.0648±.0012	0.509±.016	0.0569±.0012	404±7
11.1	218	123	0.566	3300	0.27	0.0662±.0013	0.485±.014	0.0531±.0011	414±8
12.1	141	78	0.558	18600	0.82	0.0653±.0012	0.444±.016	0.0494±.0014	410±8
13.1	158	78	0.490	1323	0.75	0.0652±.0012	0.486±.015	0.0541±.0012	408±8
14.1	199	97	0.490	3254	0.29	0.0647±.0012	0.480±.014	0.0539±.0010	404±7
15.1	215	119	0.554	1000000	0.15	0.0635±.0012	0.474±.014	0.0542±.0010	397±7
16.1	138	59	0.425	3968	0.16	0.0640±.0012	0.487±.014	0.0552±.0011	399±7
17.1	182	90	0.494	2994	0.48	0.0660±.0020	0.482±.019	0.0530±.0012	413±12
18.1	173	85	0.490	6185	0.29	0.0666±.0020	0.490±.019	0.0533±.0011	417±12
19.1	207	101	0.486	9455	0.30	0.0670±.0020	0.491±.018	0.0531±.0011	419±12
20.1	194	94	0.486	4422	0.26	0.0658±.0019	0.482±.018	0.0531±.0011	411±12
21.1	196	96	0.492	1916	0.41	0.0663±.0020	0.482±.019	0.0527±.0012	415±12
22.1	111	51	0.460	9736	0.33	0.0672±.0020	0.497±.021	0.0536±.0015	420±12
23.1	162	76	0.467	10030	0.23	0.0654±.0019	0.486±.019	0.0539±.0012	409±12
24.1	156	80	0.510	3463	0.72	0.0657±.0019	0.476±.019	0.0526±.0013	411±12
25.1	146	78	0.535	6743	0.40	0.0644±.0019	0.471±.020	0.0530±.0014	403±12
26.1	196	95	0.484	6987	0.16	0.0636±.0019	0.474±.018	0.0540±.0011	398±11
27.1	199	127	0.639	3552	0.25	0.0648±.0019	0.480±.020	0.0537±.0014	405±12

Grain area	U (ppm)	Th (ppm)	Th/U	$^{206}Pb/^{204}Pb$	f_{206} (%)	$^{206}Pb/^{238}U$	$^{207}Pb/^{235}U$	$^{207}Pb/^{206}Pb$	Age (Ma)
porphyry in Turondale Formation (session 1) 93844559B									
1.1	204	87	0.425	3452	0.98	0.0656±.0012	0.487±.016	0.0538±.0013	410±7
2.1	473	261	0.552	5135	0.46	0.0670±.0012	0.501±.013	0.0542±.0009	419±7
3.1	260	117	0.450	1043	0.64	0.0658±.0012	0.505±.015	0.0556±.0012	411±7
4.1	259	162	0.624	1944	0.95	0.0657±.0012	0.483±.016	0.0533±.0013	411±7
5.1	250	121	0.486	2157	0.87	0.0666±.0012	0.504±.015	0.0549±.0012	416±7
6.1	136	62	0.459	586	1.38	0.0677±.0012	0.542±.019	0.0581±.0016	421±7
7.1	264	150	0.566	835	1.21	0.0663±.0012	0.489±.015	0.0535±.0012	415±7
8.1	206	114	0.555	699	1.26	0.0658±.0012	0.494±.016	0.0545±.0014	411±7
9.1	350	178	0.508	2227	0.77	0.0657±.0012	0.485±.013	0.0535±.0010	411±7
10.1	331	159	0.481	1753	0.88	0.0637±.0012	0.474±.013	0.0540±.0010	399±7
11.1	204	101	0.495	1289	1.57	0.0646±.0012	0.476±.015	0.0534±.0013	404±7
12.1	165	98	0.594	494	1.89	0.0666±.0012	0.481±.019	0.0524±.0018	417±7
13.1	200	88	0.439	2929	0.63	0.0682±.0012	0.527±.016	0.0560±.0012	425±7
14.1	317	168	0.529	2332	0.30	0.0656±.0012	0.499±.014	0.0552±.0010	409±7
15.1	228	105	0.459	10270	0.63	0.0646±.0012	0.467±.014	0.0525±.0012	405±7
16.1	216	120	0.557	3981	1.21	0.0660±.0012	0.477±.017	0.0524±.0014	413±7
17.1	315	172	0.544	6374	0.30	0.0669±.0012	0.511±.015	0.0554±.0012	417±7
18.1	266	141	0.531	20000	0.09	0.3929±.0072	8.835±.174	0.1631±.0009	2488±9
19.1	201	103	0.512	83200	0.46	0.0678±.0012	0.532±.016	0.0569±.0012	422±7
20.1	186	117	0.627	2355	0.00	0.0660±.0012	0.556±.017	0.0611±.0014	409±7
21.1	163	73	0.449	1419	1.06	0.0683±.0012	0.552±.018	0.0586±.0014	424±7
22.1	348	229	0.657	2364	0.96	0.0648±.0012	0.488±.014	0.0545±.0011	405±7
23.1	287	167	0.582	55100	0.67	0.0647±.0012	0.488±.014	0.0548±.0011	404±7
24.1	202	113	0.558	2597	1.43	0.0650±.0012	0.493±.016	0.0550±.0014	406±7
25.1	367	230	0.628	3814	0.34	0.0658±.0012	0.493±.012	0.0544±.0008	411±7
26.1	282	153	0.540	3440	0.67	0.0650±.0012	0.484±.013	0.0540±.0009	407±7
35.2	309	214	0.691	2532	0.15	0.0648±.0012	0.496±.015	0.0555±.0012	405±7

Grain area	U (ppm)	Th (ppm)	Th/U	$^{206}Pb/^{204}Pb$	f_{206} (%)	$^{206}Pb/^{238}U$	$^{207}Pb/^{235}U$	$^{207}Pb/^{206}Pb$	Age (Ma)
porphyry in Turondale Formation (session 2) 93844559B									
2.2	398	238	0.597	18000	0.10	0.0652±.0014	0.491±.012	0.0547±.0003	407±9
3.2	229	110	0.478	17300	0.04	0.0646±.0014	0.500±.012	0.0562±.0004	403±9
4.2	199	115	0.577	1000000	1.76	0.0726±.0016	0.461±.012	0.0461±.0005	456±10
7.2	247	131	0.532	12700	0.14	0.0646±.0014	0.489±.012	0.0548±.0004	404±9
9.2	191	97	0.505	2468	0.62	0.0650±.0014	0.507±.012	0.0566±.0004	405±9
10.2	285	131	0.458	70700	0.14	0.0661±.0015	0.496±.012	0.0543±.0003	413±9
11.2	296	158	0.535	15200	0.20	0.0656±.0014	0.489±.012	0.0541±.0003	410±9
12.2	185	105	0.566	1000000	0.16	0.0655±.0014	0.486±.012	0.0538±.0005	410±9
14.2	222	112	0.504	31300	0.04	0.0641±.0014	0.490±.012	0.0554±.0004	400±9
15.2	309	185	0.597	46500	0.21	0.0658±.0015	0.489±.012	0.0539±.0003	412±9
16.2	258	197	0.764	24600	0.00	0.0672±.0015	0.513±.013	0.0553±.0005	419±9
17.2	283	173	0.612	24100	0.49	0.0651±.0014	0.465±.011	0.0518±.0004	408±9
22.2	333	228	0.685	58700	0.18	0.0663±.0015	0.492±.012	0.0538±.0004	415±9
27.1	308	23	0.073	40100	0.04	0.0933±.0020	0.764±.018	0.0594±.0003	580±13
28.1	269	155	0.576	13140	0.21	0.0661±.0015	0.490±.012	0.0538±.0004	413±9
29.1	191	96	0.503	32050	0.16	0.0647±.0014	0.481±.012	0.0539±.0004	405±9
30.1	349	179	0.514	18270	0.15	0.0663±.0015	0.495±.012	0.0542±.0003	414±9
31.1	370	217	0.586	10500	0.04	0.0654±.0014	0.498±.012	0.0553±.0003	408±9
32.1	232	113	0.485	45900	0.00	0.0655±.0014	0.499±.012	0.0552±.0003	409±9
33.1	407	277	0.681	58500	0.00	0.0658±.0015	0.503±.012	0.0555±.0003	411±9
34.1	392	209	0.535	1000000	0.00	0.0658±.0015	0.502±.012	0.0554±.0003	411±9
35.1	271	150	0.555	410000	0.04	0.0667±.0015	0.506±.012	0.0550±.0004	416±9
36.1	282	134	0.474	45500	0.18	0.0664±.0015	0.493±.012	0.0539±.0003	415±9
37.1	92	20	0.217	35500	0.05	0.2140±.0047	2.672±.062	0.0905±.0004	1437±9
38.1	315	163	0.519	12880	0.14	0.0655±.0014	0.491±.012	0.0544±.0003	409±9
39.1	234	132	0.563	1000000	0.00	0.0686±.0015	0.530±.013	0.0560±.0004	427±9

CHAPTER 9

Conclusions and discussion of salient issues.

9.1 THE EL SHERANA GROUP, PINE CREEK INLIER

The El Sherana Group is a succession of fluvial and lacustrine sedimentary rocks and bimodal volcanics outcropping in a NW-trending faulted belt in the South Alligator Valley area of the Proterozoic Pine Creek Inlier, Northern Territory, Australia. It unconformably overlies a basement of older Proterozoic metasedimentary rocks that were deposited in an intracratonic basin between about 2000-1880 Ma, then deformed and metamorphosed to lower greenschist grade during a major period of compressional deformation at about 1870 Ma (Nimbuwah Event). The El Sherana Group is divided, in ascending stratigraphic order, into the Scinto Breccia, Coronation Sandstone, Pul Pul Rhyolite and Big Sunday Formation. The Scinto Breccia is a siliceous phosphatic saprolite, developed locally on carbonate rocks during a period of weathering and regolith development along the unconformity dividing the El Sherana Group and underlying deformed and metamorphosed basement rocks. The Coronation Sandstone consists of coarse fluviatile sedimentary rocks (predominantly polymictic conglomerate, sandstone and minor shale derived by the erosion of underlying metasedimentary basement) and contemporaneous felsic and mafic volcanics. The Pul Pul Rhyolite represents a major period of silicic volcanism during deposition of the El Sherana Group. It contains an association of volcanic, volcaniclastic and intrusive facies dominated by welded ignimbrites, which are thickest (over 1km thick) at the southeastern end of the South Alligator Valley, thinning to under 200m to the northwest. In the southeast the Pul Pul Rhyolite is overlain by the Big Sunday Formation, a succession of volcaniclastic turbidites interpreted to represent a local lacustrine environment in the predominantly subaerial palaeo-landscape. The El Sherana Group is overlain by the Edith River Group, which contains the Kurrundie Sandstone (fluviatile sandstones and conglomerates) and Plum Tree Creek Volcanics (rhyodacitic ignimbrite). A disconformity separates each formation within the El Sherana and Edith River Groups from the underlying units.

9.1.1 Summary of the main palaeogeographic findings

- The Pul Pul Rhyolite and Big Sunday Formation of the El Sherana Group are disconformably bound between subaerial braidplain sandstones and conglomerates of the Coronation Sandstone (El Sherana Group) below, and Kurrundie Sandstone (Edith River Group) above. The volcanic succession of the Pul Pul Rhyolite is therefore interpreted to have accumulated in a mainly subaerial terrestrial environment. The turbidite succession of the Big Sunday Formation records subaqueous sedimentation in relatively quiet water. However, the presence of subaerial units both directly above and below the turbidite succession, and its restricted distribution, suggests that the formation is non-marine, and probably lacustrine.

- By comparing its facies architecture with a caldera-based facies model for ancient silicic volcanic centres, the Pul Pul Rhyolite can be divided into two distinct domains representing a medial to distal (i.e. extracaldera) facies association and a proximal (i.e. intracaldera) facies association. The distal facies association (up to 200m thick), is recognised where the Pul Pul Rhyolite folds around the base of the Mt Callanan Basin and outcrops in the South Alligator Valley northwest of Coronation Hill. The proximal facies association occurs where the formation abruptly thickens (to over 1 km thick) about 4km southeast of Coronation Hill, and outcrops around the southern margin of the Malone Creek Granite.

- The distal facies association consists of a relatively thin ignimbrite (60 to 100m thick in the South Alligator Valley) which infills and mantles antecedent topography. The ignimbrite contains smaller pumice (1-15cm) and lithic clasts (several centimetres) than its proximal counterparts, and has a low lithic content. A massive quartz-feldspar porphyry locally overlies the ignimbrite in the South Alligator Valley, attaining a maximum thickness of at least 130m in the vicinity of Monolith (uranium prospect), suggesting an eruption point at this location.

- The proximal facies association is characterised by a thick succession of moderate to high grade welded rhyolitic ignimbrites, that exhibit dense welding and columnar jointing, have high lithic contents and contain coarse lithic (up to 20 cm) and pumice clasts (up to 100cm). The welded ignimbrites were emplaced in rapid succession without significant erosional breaks between units, and form a conformable sequence with a preserved thickness of about 1km. The welded ignimbrites are subdivided into five units that are informally termed (in ascending stratigraphic order), the Lower Ignimbrite Member, Rheomorphic Ignimbrite, Cognate lithic-bearing Member, Middle Ignimbrite Member and Upper Ignimbrite Member. The Upper Ignimbrite

Member locally grades into a lithic-rich lens interpreted as a co-ignimbrite lag breccia. The top 150m of the ignimbrite succession is unwelded and interfingers locally with compositionally-related volcaniclastic fluvial and lacustrine deposits. The ignimbrites are intruded by rhyolite porphyries, massive to flow-banded, aphyric to sparsely-porphyritic rhyolite domes, sills and dykes, megacrystic and sparsely porphyritic quartz monzonite porphyries, dolerite dykes and small dolerite bodies, and by the Malone Creek Granite.

- A caldera margin lies between the proximal and distal facies associations, marked by a series of faults that correspond spatially to a significant change in thickness of the ignimbrite succession. Most of the fault movement post-dated ignimbrite emplacement, but a syn-depositional fault, interpreted as an early collapse scarp, is also preserved. This scarp is considered to be a preserved remnant of the early caldera margin, that was later buried by the Upper Ignimbrite Member. Sparsely-porphyritic quartz monzonite porphyry intrusions at this locality may correspond to a ring dyke associated with this fracture system. The quartz monzonite porphyries are highly altered and silicified and laced with a network of fine quartz veinlets and fractures with hematite and chlorite alteration. These features may represent hydrothermal alteration and brecciation associated with faulting.

- The caldera is interpreted to have developed incrementally. Partial collapse of the caldera in the early stages of eruption is suggested by the remnant fault scarp described above. The caldera structure then continued to grow by regional downsagging of the area, and/or incremental collapse accompanying episodic eruptions during deposition of the Upper Ignimbrite Member. Co-ignimbrite lag breccias within the Upper Ignimbrite Member may coincide with one late-stage episode of caldera collapse.

- The Big Sunday Formation turbidite succession may represent a small caldera lake that developed within a topographic depression after the bulk of ignimbrite eruptions had ceased. However, the emplacement of syn-eruptive, crystal-rich volcaniclastic sandstones derived from pyroclastic flows that entered the lake, indicates that subaerial volcanism continued to be active during deposition of the lacustrine succession.

9.1.2 Summary of geochronological results and their implications

- Deriving a magmatic age for the Pul Pul Rhyolite presented a difficult dating prospect because the volcanic succession is dominated by ignimbrites that have incorporated large volumes of country rock as lithic clasts during explosive eruption and

transportation, which provide an obvious source of inheritance of xenocrysts to the zircon population. For this reason a sampling strategy was devised incorporating both pyroclastic rocks expected to have complex zircon populations, and non-fragmental volcanic rocks containing no lithic contaminant, which were expected to have comparatively simple, first cycle zircon populations.

- Four samples of the Pul Pul Rhyolite were selected for U-Pb zircon dating by sensitive high resolution ion microprobe (SHRIMP). The samples from the Pul Pul Rhyolite include a rhyolite porphyry clast from a co-ignimbrite breccia within the Upper Ignimbrite Member, and a rhyolite porphyry intruding the main ignimbrite sequence, selected to provide maximum and minimum constraints on the crystallisation age of the ignimbrites. A lithic-poor ignimbrite from the Middle Ignimbrite Member, and a lithic-rich ignimbrite from the Lower Ignimbrite Member were also analysed in an attempt to directly date the eruptive sequence.

- An age of 1827±3.5 Ma was obtained for the intrusive rhyolite porphyry (sample 89123002), and 1828.1±3.5 Ma was obtained for the porphyry clast extracted from the co-ignimbrite breccia (sample 89123076). Together these ages tightly constrain the eruption of the ignimbrite sequence at approximately 1828 Ma. The Middle Ignimbrite Member (sample 89123230), which contained only minor lithic contamination, yielded a crystallisation age of 1828.6±5.1 Ma, in accord with the independent controls supplied by the porphyry samples. The results support geochemical evidence that the ignimbrites and rhyolite porphyries are co-magmatic. The stratigraphic age of the Pul Pul Rhyolite is taken to be 1828.6±5.1 Ma.

- An accurate crystallisation age could not be obtained for the Lower Ignimbrite Member (sample 89123138), which contains a large amount of lithic contamination. The main statistical population yielded an age of 1850±12 Ma, which does not accord with the age constraints supplied by the rhyolite porphyry samples. An alternative interpretation of the data is therefore proposed, which yields a result more consistent with these independent age constraints. The analyses comprising the main statistical population are interpreted to represent zircons from two age populations. The older grains yield an age of 1862±16, and are interpreted as xenocrysts. The younger 1810±27 Ma zircons are interpreted to have precipitated from the melt at or near the time of eruption. This age is within analytical error of the crystallisation age of ignimbrite sample 89123230 and the rhyolite porphyries (1828 Ma), but the large error indicates the age is poorly defined.

- A syn-eruptive crystal-rich volcaniclastic sandstone of the Big Sunday Formation, genetically related to Pul Pul Rhyolite ignimbrites (i.e. from the same volcanic source), was also selected for analysis. This sample contained a higher degree of lithic contaminant than the underlying ignimbrites of the Pul Pul Rhyolite. Two thirds of the zircons analysed combine to yield an age of 1863.6±4.4 Ma, which is the same age as the youngest xenocrystic population in the underlying ignimbrites. Only two of the analysed grains were identified as statistical outliers possibly belonging to a younger magmatic population, which may represent grains precipitated during crystallisation. If this sample had been analysed in isolation, the main zircon population would not have been recognised as xenocrystic, and the age of the Pul Pul Rhyolite would have been taken to be 1863.6±4.4 Ma.

- Zircon xenocrysts in all samples analysed yield a similar range of ages in the range 1865-2700 Ma, with a significant cluster of data close to 1865 Ma, and others at 1910 Ma, 1960 Ma, 1990 Ma and 2400 Ma. This pattern is a clear indication that there are inherited components of more than one age or that, if there is only a single inherited component, it has a multistage history. The 1865 Ma xenocrysts may have been derived from unexposed plutons emplaced before or during the main compressional structural-metamorphic orogeny in the Pine Creek Inlier (Nimbuwah Event) at 1850-1870 Ma.

- The new age of 1828.6±5.1 Ma for the Pul Pul Rhyolite obtained from this study indicates that the El Sherana Group is about 30 m.y. younger than previously estimated. A new SHRIMP age determination of 1822±6 Ma for the overlying Edith River Group is also about 30 m.y. younger than unpublished conventional age determinations for this unit. These results indicate that deposition of the El Sherana and Edith River Groups postdated the Nimbuwah Event by about 40 m.y., and was not related to late-stage crustal extension at the close of this event, as previously supposed.

- The El Sherana and Edith River Groups have been grouped with a number of small plutons of similar age and composition that occur in the eastern part of the Pine Creek Inlier (mainly along the western border of Arnhem Land), to form the Jim Jim Suite (Wyborn et al. 1997). The component plutons of the Jim Jim Suite include the Nabarlek Granite, Tin Camp Granite, Jim Jim Granite (1838±7 Ma), Malone Creek Granite (intrudes the Pul Pul Rhyolite; 1823±9 Ma), Grace Creek Granite (co-magamtic intrusive equivalent of the Plum Tree Creek Volcanics, Edith River Group), Eva Valley Granite and Yeuralba Granite. Ages available for the components of the Jim Jim Suite fall within a range of SHRIMP U-Pb available for the Cullen

Supersuite (1818-1835 Ma), suggesting they were emplaced coevally. The emplacement of these suites is defined as the 'Cullen Event' (Jagodzinski and Wyborn (1995).

- It is now clear that there are two main magmatic episodes in the Pine Creek Inlier. The first was related to the major compressional deformation event (Nimbuwah Event) and occurred between 1870-1850 Ma. It includes granitoid rocks of the Nimbuwah Complex (1866 Ma) and the Litchfield Complex (Allia and Waigat Suites, ~1850 Ma). The next major event (Cullen Event) was the intrusion of the Cullen Supersuite and Jim Jim Suite (containing the El Sherana and Edith River Groups) from about 1830-1810 Ma.

9.2 THE CRUDINE GROUP, HILL END TROUGH

The Turondale Formation is the oldest of two volcanogenic formations within the Early Devonian Crudine Group of the Hill End Trough, northeastern Lachlan Fold Belt, the better known of which is the Merrions Formation (formerly Merrions Tuff), studied in detail by Cas (1977a 1977b, 1978, 1979, 1983a). The host environment for the Crudine Group was a relatively deep, quiet marine basin known as the Hill End Trough, which is represented by a regionally extensive sequence of hemipelagic shales and interbedded turbidites. This passes laterally into contemporaneous shallow-water sediments of the Molong and Capertee Highs, which flank the Hill End Trough to the west and east. North of the Bathurst Batholith, the Crudine Group comprises, in stratigraphic order, the Cookman Formation (slate and thinly interbedded quartz sandstones), Turondale Formation (volcaniclastic turbidites and megaturbidites), Waterbeach Formation (thick shale sequence with interbedded siltstone), Guroba Formation (a sandstone-dominated unit present only in the northern Hill End Trough) and Merrions Formation (volcaniclastic megaturbidites and silicic lavas). It also includes the Bay Formation, which represents the whole Crudine Group sequence along the western margin of the Hill End Trough. The Turondale and Merrions Formations are two prominent volcanogenic formations within the predominantly sedimentary Hill End Trough succession, which reflect periods of large-scale silicic volcanism on the adjacent highs and within the trough itself. They contain a range of primary and resedimented volcanic facies, including widespread subaqueous silicic lavas and/or lava cryptodomes in the Merrions Formation and their compositionally equivalent porphyries intruding the Turondale Formation as sills, and thick sequences of syn-eruptive, resedimented crystal-rich volcaniclastic sandstone. The work of Cas (1979, 1983a) on the syn-eruptive volcaniclastic deposits of the Merrions Formation is extensively referenced as a classic study of the behaviour of pyroclastic

flows upon passage into a subaqueous environment. The Turondale Formation was studied as another example of this style of resedimented deposit.

9.2.1 Summary of the main palaeogeographic findings (Turondale Formation)

- The Turondale Formation consists of shale, volcaniclastics including crystal-rich volcaniclastic sandstone (turbidites and megaturbidites), normally graded volcaniclastic breccia/sandstone (megaturbidites), polymictic volcaniclastic conglomerates and cherty tuffaceous sandstones and siltstones, and minor amounts of intrusive coherent porphyry. 'Normal' basin sedimentation is represented by thick, hemipelagic shale intervals, which contain discrete interbedded siltstone and fine sandstone beds deposited by fine-grained, small-volume turbidity currents. This 'shale and interbedded siltstone' facies represents ambient deep-water sedimentation, below the influence of storm wave activity.

- Ambient sedimentation was periodically interrupted by the emplacement of the various volcaniclastic mass-flow facies listed above. The detritus of the volcaniclastic facies was largely derived from penecontemporaneous subaerial to shallow marine explosive volcanic eruptions.

- The conglomerates reflect mechanical reworking of the component clasts (predominantly silicic volcanic and limestone clasts) in littoral and/or fluvial environments, prior to downslope resedimentation into the adjacent deep marine basin by mass-flow. Near the southeastern margin of the Hill End Trough (south of Sofala), conglomerates near the top of the Turondale Formation exhibit channel geometries, suggesting a local feeder-channel environment emanating from a point source on the basin margin, proximal to this area. These conglomerates are associated with large allochthonous limestone blocks which would have been resedimented short distances downslope from the littoral environment by gravitational processes. Chaotic mudstone/volcaniclastic sandstone slump deposits (intraformational breccias) which occur at the same stratigraphic level as the polymictic channel-fill conglomerates, are interpreted to be derived from local slope collapse at the basin margins.

- The thickly bedded crystal-rich volcaniclastic sandstones and normally graded volcaniclastic breccia/sandstones are composed of unabraded juvenile pyroclasts (mainly crystals and crystal fragments), emplaced as cold, water-supported mass-flows (megaturbidites). These single beds of juvenile pyroclastic debris, tens of metres thick, are orders of magnitude larger than those produced by normal turbidity currents , and are comparable in thickness and volume to

ignimbrites. However, they contrast with ignimbrites in terms of their facies profile and textural characteristics, and are crystal-enriched relative to most ignimbrites (see Section 9.3.3). The abundance of juvenile pyroclasts and extreme thickness of the beds suggests they are essentially syn-eruptive, and related to the contemporaneous entry of pyroclastic flows into basin margins, and transformation into water-supported megaturbidites of pyroclastic debris. They may have been derived either from flow transformation as the pyroclastic flows ingested water upon entering the sea, or from post-eruptive slumping of unreworked pyroclastic debris ponded at the shoreline shortly (possibly as little as days or weeks) following initial eruption. The former scenario is preferred, as it provides a mechanism for the removal of large volumes of fine volcanic ash and pumice, and subsequent concentration of crystals in the volc aniclastic megaturbidites. Ash and pumice are elutriated through secondary eruption columns generated by phreatic explosions, and/or through gravitational segregation as the pyroclastic flows initially travelled across the sea surface, with further separation of fines from coarser fractions also occurring in the derivative megaturbidites. Distally associated tuffaceous cherts and cherty sandstones are interpreted to represent suspension settling and reworking of the separated ash component of the parent pyroclastic flows.

- Intervals dominated by thinly-bedded crystal-rich volcaniclastic turbidites are interpreted to result from temporary sediment over-supply in the source region, following large-scale volcanic eruptions. Immediately following a period of active volcanism, alluvial/fluvial depositional systems would become choked with freshly erupted volcaniclastic debris, resulting in rapid deltaic progradation at the shoreline, and the subsequent generation of the small-volume, low concentration mass-flows at the unstable delta front.

- Coherent dacite porphyries locally intrude the Turondale Formation as thick sills. The porphyries are similar in composition to lavas within the Merrions Formation, suggesting a genetic association. They have an absence of vesicles compared with the Merrions seafloor lavas, which may be related to their intrusive character, having been emplaced in the sub-surface under a higher confining pressure, so suppressing exsolution.

- The pattern of sedimentation in the Turondale Formation indicates there were two major influxes of volcaniclastic detritus, separated by a significant hiatus during which ambient, predominantly hemipelagic sedimentation was re-established in the basin. Volcaniclastic sandstones at the base and the top of the formation have the same composition, indicating they represent two eruptive phases of the same volcanic

source, or similar magmatic sources, separated by a significant period of repose. A syn-eruptive style of sedimentation dominates the basal volcaniclastic package, which is characterised by abundant thick, crystal-rich volcaniclastic megaturbidites. The upper volcaniclastic package is an upward thinning and fining sequence. The thicker beds at the base of the upper unit are essentially syn-eruptive, and mark the onset of the second eruptive phase of the volcanic source. The overlying thinner and finer grained turbidites reflect reworking and resedimentation of the freshly erupted debris as temporarily over-supplied alluvial/fluvial/deltaic depositional systems in the source region returned to a more normal state.

- The coincidence of bedding thickness and grainsize maxima, maximum number of thick sedimentation units, maximum lithic clast size and abundance and highest sand-to-shale ratios in the southeast Sofala district, suggests sediment derivation from a volcanic area to the south or southeast of Sofala, probably located on the adjacent Capertee High. This is supported by palaeocurrent indicators in the Turondale Formation and contiguous units, which suggest the basin floor sloped from east to west, with dominant sediment influx from the southeast. The Huntingdale Volcanics outcropping in the Capertee Valley about 30 km east of Sofala, may represent the source region for the volcaniclastic component of the Turondale Formation. This unit contains thick, extensive ignimbrite sheets that are compositionally similar to the volcaniclastic sandstones, and may represent material from the same volcanic source deposited by pyroclastic flows in a more proximal, subaerial setting.

9.2.2 Summary of geochronological results and their implications

- Two samples of the Turondale Formation and five of the Merrions Formation were selected for U-Pb zircon dating by sensitive high resolution ion microprobe (SHRIMP). The samples from the Turondale Formation include a syn-eruptive crystal-rich volcaniclastic sandstone at the base of the unit collected from the type section (on the Turon River about 6km west of Sofala), and a dacitic, porphyritic sill intruding the basal volcaniclastic sequence on the eastern limb of the Hill End Anticline. Three syn-eruptive crystal-rich volcaniclastic sandstones and one dacitic lava were collected from the type section of the Merrions Formation, which lies along the southern bank of the Turon River about 9km west of Sofala. In stratigraphic order from base to top, the samples represent volcaniclastic member P, volcaniclastic member D, member H lava and volcaniclastic member E of the Merrions Formation (Cas 1977). A second sample of volcaniclastic member D was also collected in the Limekilns district, a local, relatively shallow marine sequence where there is fossil age control from units above and below the Merrions Formation.

- The choice of SHRIMP standard used for age calibration has a significant effect on isotopic data. Data calibrated against the commonly used SL 13 zircon standard yield ages that are younger, and variably offset by 0-3%, from ages derived from QGNG (Black in prep.), and from isotope dilution zircon ages (Tucker and McKerrow 1995). These observations indicate that QGNG-derived SHRIMP ages are better suited for the task of numerical time scale calibration.

- When the data are calibrated against the preferred zircon standard QGNG, an age of 413.4±6.6 Ma is obtained for the volcaniclastic sandstone at the base of the Turondale Formation, and ages of 411.9±5.0 Ma (member P), 409.9±6.6 Ma (member D, Limekilns), 407.8±6.6 Ma (member D, type section), 408.0±5.3 Ma (member H) and 407.1±6.9 Ma (member E) are obtained for the Merrions Formation. The porphyry intruding the Turondale Formation could not be calibrated against the QGNG standard, but yielded an age of 411.1±3.2 Ma when calibrated against zircon standard SL 13.

- Ages obtained for the two samples of member D collected from Limekilns (409.9± 4.3 Ma) and from the type section (407.8±4.6 Ma) are well within error of each other, confirming the correlation of the volcaniclastic sequences between the two areas. The volcaniclastic sequence sampled at Limekilns was originally mapped as the Winburn Tuff and interpreted to overlie the Limekilns Formation (formerly Limekilns Group), which in turn overlies the Merrions Formation (Hawkins 1953; Packham 1968). The derived age of 409.9±4.3 Ma confirms more recent mapping, which recognised that the unit underlies the Limekilns Formation, and is part of the Merrions Formation (Voorhoeve 1986; Pogson and Watkins 1998). The Limekilns Formation ranges from late Pragian to late Emsian in age (Wright and Chatterton 1988; Wright and Haas 1990), so if the volcaniclastic sequence overlies the Limekilns Formation as originally interpreted, it would have yielded a significantly younger age than the type sequence of the Merrions Formation.

- In the Limekilns district, there is fossil age control from units above and below the Merrions Formation, enabling the numerical ages obtained in this study to be tied to the regional biostratigraphy. A transported brachiopod fauna is recorded in fine volcanogenic sediments below the base of the Merrions Formation, which Garrett and Wright (1988) correlate with their 'late' Lochkovian *australis* assemblage zone. The exact stratigraphic position of the faunal assemblage is uncertain, and it may lie near the top of the Turondale Formation or at any stratigraphic level within the Waterbeach Formation, the former being more likely based on the description of the host lithology. Regardless of its precise stratigraphic position, the faunal assemblage

constrains the upper limit of the Turondale Formation and the lower limit of the Merrions Formation to the late Lochkovian. Middle Lochovian (early *delta* Zone) conodonts in allochthonous limestone blocks within undifferentiated lower Crudine Group (Turondale and Waterbeach Formations) at Palmers Oakey (Bischoff and Fergusson 1982), similarly constrain the base of the overlying Merrions Formation to the late Lochkovian. Shales at the base of the Limekilns Formation, which conformably overlies the Merrions Formation, yield a mostly pelagic fauna, which includes the tentaculitid *Nowakia acuaria*, a well known Pragian index fossil (Wright and Haas 1990). This indicates a Pragian to early Emsian age for the base of the Limekilns Formation.

- When the new ages are placed in the context of the regional biostratigraphy, several problems become apparent with the existing Australian Phanerozoic time scale. According to the biostratigraphic constraints described above, the allowable biostratigraphic range of the Merrions Formation spans from the middle Lochkovian to the early Emsian (i.e. late *delta-dehiscens* conodont Zones). In contrast, isotopic ages derived for the Merrions Formation consistently yield Lochkovian, not Pragian, ages. The stratigraphically oldest sample (member P) yielded an age of 411.9±5.0 Ma, placing the base of the Merrions Formation close to the base of the Lochkovian (410 Ma) on the current Australian Phanerozoic Timescale (Young and Laurie 1996). This discrepancy between the existing biochronological constraints and the new isotopic data suggests that the numerical calibration of the Silurian-Devonian Period boundary, and the Lochkovian-Pragian and Pragian-Emsian Stage boundaries require downward adjustment. The new ages are well within error of the division of Devonian time proposed by Tucker et al. (1998), which places the Silurian-Devonian boundary at 418 Ma, and estimates ages of 413.5 Ma and 409.5 Ma for the base and top of the Pragian, respectively. The estimates of late Lochkovian time and the age of the Pragian-Emsian boundary derived from this study might make a useful addition to that time scale, which currently has no tie points between early Lochkovian and early Emsian times.

9.3 INTERACTION BETWEEN PYROCLASTIC FLOWS AND WATER

9.3.1 Conclusions from literature review

- Most juvenile pyroclastic material emplaced in subaqueous environments appears to have been transported and deposited by water-supported mass-flow or fall processes (Cas and Wright (1991). The inability of most pyroclastic flows to maintain their integrity as hot gas-particulate systems when they cross the land-sea interface relates to dynamic boundary conditions that favour: (1) disruption of the pyroclastic flow

through phreatic explosions and subsequent downslope resedimentation of the unconsolidated pile as a water-supported slurry of pyroclastic debris; and/or (2) the ingestion of water and subsequent transformation into water-supported mass flows.

- Primary pyroclastic flow and welding in subaqueous environments appear to be feasible only in special circumstances where the flow is prevented from interacting with surrounding water, as in the following situations:

a) Shallow marine near-shore settings

(1) where thick pyroclastic flows are deposited in shallow tidal flats or a shallow shelf environment causing displacement of the shoreline seawards, and resulting in near-shore zones of emergence. Under these circumstances the creation of temporary subaerial conditions enables the deposits to weld. (e.g. Capel Curig Formation and Pitts Head Tuff (Wales), Mweelrea Group (Ireland), Koura Formation (Japan)).

(2) where agglutination and primary or secondary rheomorphism has occurred during transport of pyroclastic flows in subaerial settings prior to their encroachment into water. Agglutinated material entering water in a hot, viscous state may be insulated by film boiling. However, the rheomorphic flows may also undergo disruption by quench, phreatic and autoclastic fragmentation (e.g. Garth Tuff (Capel Curig Formation), Pitts Head Tuff; McArthur 1995).

(3) where large-volume, fast moving pyroclastic flows enter the sea at a high topography shoreline (e.g. 1883 eruption of Krakatau). In this case the pyroclastic flows were plausibly projected straight onto the shallow seafloor surrounding the volcano without coming into contact with seawater, as the collapsing eruption column swamped the surrounding area. Tsunamis were generated during the eruption, suggesting that large volumes of seawater were displaced during deposition. Shoaling occurred and local temporary islands formed.

b: Below storm wave base settings

(4) where wholly or partly submerged calderas are infilled by rapidly emplaced material. Very high accumulation rates and subsidence possibly synchronous with eruption enables material to form very thick ponded intracaldera deposits without interacting significantly with water. (e.g. Vandever Mountain Tuff, Mineral King (USA), Monarch Rhyolite, Sierra Nevada (USA), Lower Rhyolitic Tuff Formation (Wales), Cader Rhwydog Tuff? (Wales).

(5) where high eruption discharge rates and rapid emplacement of material near a subaqueous vent assist flow insulation and heat retention (e.g. thin welded ignimbrites in close proximity to subaqueous fissures in deep-water turbidite successions, northern Anatolia, Turkey and southern Vosges, France). NB: only the interior portions of these subaqueous ignimbrite sheets show evidence of welding. The margins and distal facies are non-welded crystal-rich deposits which contain abundant bioclasts, indicating mixing with water and flow transformation during flowage.

(6) where a sudden influx of sediment related to large volume eruptions enters a deep-water basin and considerably reduces water depth, creating temporary shallow water to emergent conditions (e.g. Tyndall Group, Mt Read Volcanics (Tasmania). In this case a pyroclast-rich delta was rapidly constructed, creating local shallow marine to emergent conditions that allowed pyroclastic flows to deposit thin layers of primary welded ignimbrite.

- From the above, it can be concluded that welding and other evidence of heat retention in subaqueous deposits can generally be used as an indicator of proximity to vent and/or shoreline in facies analysis studies of ancient subaqueous volcanic successions.

9.3.2 Implications of the present study

This thesis considers the likely processes and deposits arising from the interaction between pyroclastic flows and water, through the study of a distinctive facies found in subaqueous settings; very thick, massive, crystal-rich volcaniclastic sandstones (CRVS), that are composed of large volumes of unmodified dense/coarse juvenile pyroclasts (crystals and crystal fragments), but contain no pumice and are significantly depleted in fine ash. Examples of this style of deposit have been recorded in the Merrions Formation of the Hill End Trough, New South Wales (Cas 1979, 1983a), the Kowmung Volcaniclastics and Tangerang Formation of the Bindook Volcanic Complex which lies beyond the southern margin of the Hill End Trough (Cas et al. 1981; Simpson et al. 1997), and the Tyndall Group of the Mt Read Volcanics, Tasmania (White and McPhie 1996, 1997). The above authors propose that the CRVS facies is a category of syn-eruptive volcaniclastic deposits, generated by complex interaction between subaerial pyroclasts flows and the sea. This interaction may have involved submergence of the subaerial flow and transformation into cold, water-supported mass flows, and/or sedimentation from the bases of subaerial flows that were travelling across the sea surface, as well as the generation of secondary phreatic explosions as the hot pyroclastic flows come into contact with cold water. This model provides a mechanism for the removal of significant volumes of ash (and pumice), by: (1) elutriation through secondary

eruption columns resulting from the phreatic explosions; (2) through gravitational segregation of the dense crystal/lithic and light ash/pumice components of pyroclastic flows as they travelled across water; and 3) elutriation of fine ash from the head and body of the derivative megaturbidites.

By studying two examples of this facies, preserved within a restricted lacustrine setting in the Big Sunday Formation of the Pine Creek Inlier, and within a deep-marine basin in the Turondale Formation of the Hill End Trough, New South Wales, the following conclusions supporting and refining this general model, could be made.

- The CRVS of the Big Sunday Formation, El Sherana Group were derived from pyroclastic flows undergoing primary agglutination and welding as they reached the shoreline. As a result, these pyroclastic flows contained both agglutinated and particulate domains, which behaved in a different manner as they encountered water. The agglutinated component of the flow may have been partially insulated through film boiling, and survived the transition beyond the shoreline relatively intact, experiencing only partial disruption through: (1) ductile stretching induced by flow shear; (2) brittle disaggregation during flow as large clasts were rafted, flexed and collided; and (3) quenching upon contact with water. The agglutinated component of the flow is represented in the final deposits by fluidally-shaped welded ignimbrite intraclasts that display evidence of ductile shear and brittle disaggregation at clast margins, and evidence of insitu quenching at the site of final deposition (internal fracturing exhibiting jigsaw-fitted textures). The particulate component of the flows underwent complete disruption at the shoreline, through phreatic explosions and/or ingestion of water and transformation into water-supported mass flows. The flow transformation process involved significant loss of pumice and ash. Only small local, diffusely-bound domains of pumice- and ash-rich non-welded ignimbrite remain intact within the predominantly crystal-rich facies. The different behaviour of the particulate and agglutinated components of the same flows strongly supports models that predict the explosive disintegration and transformation of pyroclastic flows upon encountering water, because it suggests that only the coherent domains may be insulated through film boiling and survive relatively intact.

- A comparison between basin-wide, voluminous crystal-rich volcaniclastic megaturbidites of the Turondale and Merrions Formations and slump-derived epiclastic megaturbidites shows that although the two types of deposits are comparable in size, they differ in: (1) their frequency of occurrence; and (2) their internal facies profile. Whereas epiclastic megabeds are isolated occurrences within thick packages of 'normal' basin sedimentation, the volcaniclastic megaturbidites

dominate basin sedimentation over thick intervals. This indicates a rapid accumulation of detritus or supply event in the source region. The size of the beds, the abundance of juvenile pyroclasts and their frequency of occurrence are consistent with the continuous replenishment of source material through periodic pyroclastic flow-forming eruptions, and are key factors in establishing that volcaniclastic megaturbidite deposits of this sort have a genetic connection with active volcanism (ie they are essentially syn-eruptive).

This information, however, does not establish whether the deposits were fed directly from pyroclastic flows which entered the sea and transformed in transit into water-supported mass flows, or if the pyroclastic material was briefly stored prior to redeposition (by slumping). This issue may be resolved by comparing the internal organisation of the volcaniclastic megaturbidites with that of slump-derived epiclastic megabeds. Epiclastic 'megaturbidites' commonly exhibit a lateral and vertical continuum from proximal slump-derived debris flows to distal megaturbidites, as the initially viscous and cohesive mud-rich deposits evolve hydrodynamically away from the source, by the ingestion of water into the flows. In contrast, the thick volcanogenic deposits of the Turondale and Merrions Formations do not exhibit evidence of deposition by debris flow, even near points of sediment influx around the basin margins. Similar volcaniclastic megabeds deposited in more proximal, shallow-marine settings within the Bindook Volcanic Complex, also do not display any evidence of initial deposition by slumping or cohesive debris flow mechanisms. If the presumably initially ash-rich pyroclastic deposits had been temporarily stored on the shelf prior to (penecontemporaneous) slumping into the basin, a proximal to distal, debris flow to turbidite flow transformation would be expected by analogy to the slump-derived epiclastic megabeds. The absence of such a flow transformation suggests much of the fine-ash component of the pyroclastic flows was removed prior to transportation into the deep-marine environment. This favours the model that these very thick, massive, crystal-rich volcaniclastic megaturbidites (that contain no pumice and are significantly depleted in ash), are directly fed from subaerial pyroclastic flows that entered the sea, as this scenario (described above) provides a mechanism for the removal of significant volumes of ash (and pumice).

9.3.3 The character of syn-eruptive, water-supported mass-flow deposits

Both subaerial and subaqueous volcaniclastic successions have been studied in the course of this thesis, enabling the general and granulometric characteristics of subaerially-deposited ignimbrites to be compared with their subaqueously-deposited volcaniclastic derivatives. Both types of deposits display the distinctive texture and facies characteristics of mass flow deposition such as poor sorting, massive, graded or diffusely stratified

bedding, sharp basal contacts and tabular bed geometries. Voluminous syn-eruptive volcaniclastic deposits in subaqueous settings are generated by the same pyroclastic processes, and are therefore as compositionally uniform as primary pyroclastic flow deposits, reflecting a homogeneous source consisting of large volumes of texturally unmodified pyroclasts. However, differences in the physical properties of the transportation medium result in different lithofacies characteristics, though their constituent components are similar. Water acts as a more efficient sorting medium than air due to its greater viscosity (Fiske and Cashman 1987). As a result, subaqueous deposits tend to be better sorted than their subaerial counterparts (Fiske and Matsuda 1964; Yamada 1984; Stix 1991), and density grading is commonly well developed. Vertical sections through these deposits are characterised by a lower, very thick massive to graded unit overlain by a thinner unit that is finer-grained and stratified, and may comprise several graded beds. Lithofacies and textures of these deposits are similar to those found in volcaniclastic megaturbidites (Figure 9.1). In the case of pumice-bearing deposits, the low density of pumice means that coarse pumice particles are deposited together with finer non-vesicular particles. This results in much poorer sorting of deposits in terms of grainsize, although they are well sorted in terms of hydraulic equivalence.

The effectiveness of water as a density-sorting medium also suggests greater potential for depletion of pumice and vitric ash in the subaqueous environment, and as a result, many subaqueous volcaniclastic mass-flow deposits are crystal enriched (e.g. Cas 1983a; Yamada 1984; Cas et al. 1990; Stix 1991; Kano et al. 1996). In subaqueous eruption columns, coarse pumice blocks and fine ash ascend rapidly through the plume by buoyancy and thermal convection, and are separated from the plume and dispersed (Kano et al. 1996). The coarse pumice will either fall out in the later stages of eruption, resulting in an upward-coarsening deposit, or float off to form rafts on the water surface, where they can remain buoyant for sufficient time to disperse away. The fine vitric ash component remains in suspension in the water column, and is also dispersed by thermal convection in the eruption column and/or surface currents. Pumice and fine ash will also be elutriated by hydraulic sorting in the derivative turbulent, water-logged mass-flow and remain in suspension in the water column. The elutriated ash can be dispersed by surface currents, or eventually settle out of suspension and form a massive to laminated ash cap overlying the main crystal-enriched deposit. The fractionation and sorting that occurs in the subaqueous environment is likely to be further enhanced if the pyroclastic flows are derived from subaerial eruptions, and transgress the land/water interface. In this case, crystal enrichment is enhanced by phreatic eruptions at the land/water interface, and/or segregation of pyroclastic flows that initially travel across water before sinking through the water column (Walker 1979; Cas 1983 Carey et al. 1996).

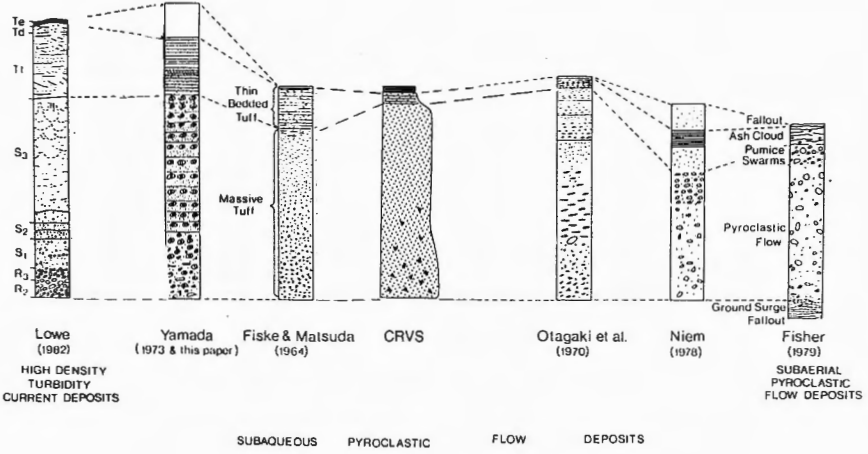

Figure 9.1: Comparison of the vertical lithofacies sequence of some subaqueous volcaniclastic mass flow deposits with high-density turbidity currents and subaerial pyroclastic flow deposits (from Yamada 1984). A typical CRVS deposit is included in the centre of the figure for comparison.

Most subaqueous volcaniclastic mass-flow deposits described in the literature contain abundant pumice and a high ash matrix component (e.g. Ohanepecosh Formation, Washington, Fiske 1963; Tokiwa Formation, Japan, Fiske and Matsuda 1964; Onikobe Basin deposits, Japan, Yamada 1973; Ouachita Basin deposits, U.S.A., Niem 1977; distal deposits of Mineral King, U.S.A., Busby-Spera 1986; Shinjima Pumice, Japan, Kano et al. 1996; deposits of the 1883 Krakatau eruption, Carey et al. 1996; Mandeville et al. 1996). However, as more examples of CRVS deposits are documented (Cas 1983a; Cas et al. 1981; Simpson et al. 1997; White and McPhie 1996, 1997; the present study), this facies is emerging as a common variant of this style of deposit, in which extremely efficient pumice and ash depletion has resulted from the interaction of subaerial pyroclastic flows and the sea, resulting in more extreme crystal enrichment (Figure 9.1).

9.3.4 Geochemical implications and applications

One of the outcomes of studying crystal-rich volcaniclastic sandstone facies has been an assessment of how magmatic compositions are modified through the loss of pumice and ash during the eruption and transportation of pyroclastic flows and associated syn-eruptive volcaniclastic mass flows. As predicted by Walker (1972), chemical modification by pumice- and ash-loss reflects the partitioning of elements between the phenocrysts and the residual melt fraction of the parent magma (which forms the vitric fraction of the ash flow) just prior to eruption. The post-eruptive removal of the vitric component, and subsequent concentration of crystals, creates a disparity in the silica contents of the parent magma and the modified volcanic/volcaniclastic product. Except where quartz is an abundant phenocryst (as in the CRVS of the Big Sunday Formation), the crystal-enriched deposits will have a lower SiO_2 content than the parent magma. Bulk mixing calculations for the Turondale Formation suggest that a 4% loss of SiO_2 is consistent with 25% ash loss during eruption and transportation. This result is slightly higher, but comparable to similar calculations for an ignimbrite and comagmatic pluton in the New England Batholith, which suggest a 3.7% loss of SiO_2 is consistent with about 36% ash loss (Flood et al. 1980). The behaviour of other elements will depend on the phenocryst phases present, but in general compatible elements such as Fe, Ti, Mg, Mn, Ni, Cr, V, Sc, Al, Ca, Sr and Eu, which partition into early phenocryst phases (pyroxenes, amphiboles, plagioclase), are enriched in ignimbrites and syn-eruptive volcaniclastic products relative to the parent magma. Conversely, incompatible elements (K, Na, Rb, Pb, Zr, Y, U, Th), which partition into the melt, are depleted following removal of the vitric fraction. Unless REE-rich minerals (e.g. allanite, monozite, titanite) are ubiquitous, rare earth elements (with the exception of Eu, which partitions into plagioclase) will also partition into the melt, and be depleted following removal of the vitric fraction.

The potential application of this knowledge to provenance studies was illustrated in Chapter 7.4.3. If chemical modification through pumice- and ash-loss can be quantified, it should be possible to predict the composition of the source magma. This enables geochemical matching of modified pyroclastic or syn-eruptive volcaniclastic deposits to suspected comagmatic plutons or other unmodified (or less modified) volcanic products of the same source. For example, in the case of the Turondale Formation, the possible composition range of the source magma was constrained by constructing tie lines between phenocryst-enriched and complementary glass-enriched fractionates from the same series of eruptions (represented by the crystal-rich volcaniclastic sandstones and associated cherty tuffaceous sediments, respectively). The predicted compositional range was then compared with time-equivalent volcanic and plutonic rocks identified as possible sources of the Turondale Formation. Units that differed significantly from the predicted compositional range were rejected as a potential source (e.g. the Bindook Volcanic Complex), whereas those that displayed a compatible chemistry (e.g. the Riversdale and Huntingdale Volcanics of the adjacent Capertee High) were investigated further. The same principals can be applied to constraining the source composition of ignimbrites, which also undergo significant pumice and ash loss during eruption and transportation, as has been demonstrated by Flood et al. (1980).

This knowledge can also potentially be applied to the interpretation of facies in high grade metamorphic terranes, where determining metamorphic precursors can be difficult due to the obliteration of primary textures and structural features. This can be illustrated by considering the Potosi gneiss of the upper-amphibolite to granulite grade Broken Hill Block of New South Wales. The Potosi gneiss is a garnet-biotite-rich quartzofeldspathic gneiss that forms a homogeneous mappable unit throughout the Broken Hill Block, ranging in thickness from about 20 m to 150 m. There has been much speculation over its origin, and its precursor has been variously described as igneous, volcanic and sedimentary. For instance, it has been described as an ignimbrite, although possibly a lava flow (Laing et al. 1984), a subaqueous volcaniclastic or lava mass flow (Willis et al. 1983) and a granite (Gustafson et al. 1950; Nutman and Ehlers 1998). Wright et al. (1993) critically evaluated these interpretations, and concluded that they were rarely supported by adequate field data or descriptions, or valid volcanological criteria. Applying a more rigorous facies analysis approach, Wright et al. (1993) found no unequivocal evidence for primary volcanic units in the Potosi gneiss. They favoured a sedimentary origin based on interbedding with obvious sedimentary psammites, and often gradational relationships to psammopelite, and interpreted the gneiss as an 'immature arkosic sandstone, rapidly deposited as a progradation wedge or delta of muddy sand'. They noted that the Potosi gneiss does not possess a volcanic chemical signature, but one which is similar to immature clastic sediments, arkoses and greywackes. They suggested

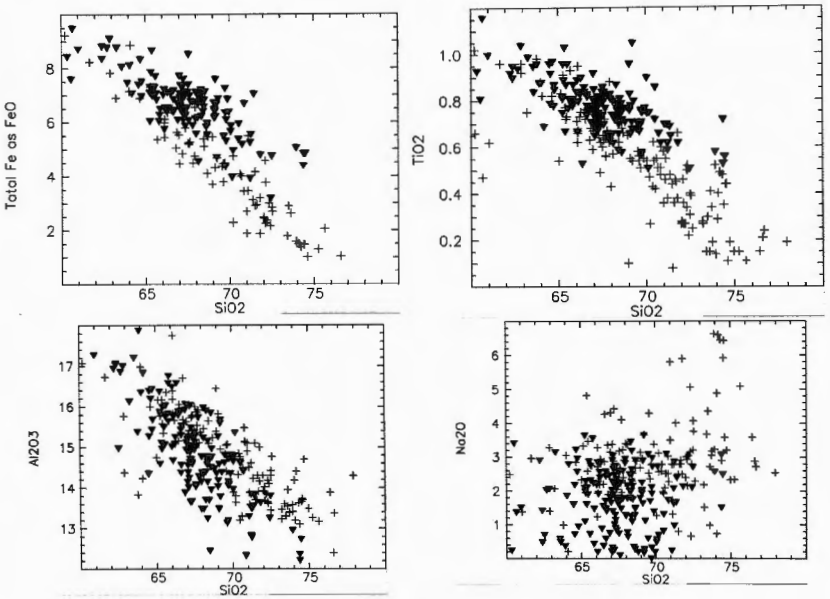

Figure 9.2: Select variation diagrams comparing the geochemistry of the Potosi gneiss (triangles) with the Alma and Rasp Ridge Gneisses (crosses), which are believed to have a granitoid precursor (i.e. their chemistry should approximate original magmatic compositions). Unpublished data supplied by L.Wyborn.

the Potosi gneiss may have been derived by erosion and redeposition of granite dominated felsic crystalline basement, although they admitted they could not prove the rock did not comprise a significant proportion of volcanic detritus. In fact, north of Yanco Glen, near the andalusite/sillimanite transition, volcanic quartz and feldspar can be identified within lower grade rocks (Page and Laing 1992; Stevens et al. 1998), suggesting there was indeed a contemporaneous(?) volcanic influence in the source.

Chemically, the Potosi gneiss does not conform to a normal igneous rock (as recognised by Stanton 1976; Stevens et al. 1988; Wright et al. 1993). When compared to the time-equivalent (~1690 Ma) Rasp Ridge and Alma 'granitic' gneisses (used to represent the primary magmatic composition), the Potosi gneiss exhibits a modified geochemical signature consistent with trends produced by ash-loss. This includes enrichment of the early fractionating elements such as Fe, Ti and Ca, and depletion of elements that concentrate in the minimum melt, such as Na and K (Figure 9.2). By geochemical analogy, the possibility should be considered that the precursor of the Potosi gneiss was a 'Merrions-like' syn-eruptive crystal-rich volcaniclastic deposit generated by cold, water-supported mass flows resulting from interaction of large-volume subaerial pyroclastic flows and the sea. This interpretation is consistent with the limited field data and petrographic information available for the Potosi gneiss; ie. its occurrence as a large-volume thick, massive homogeneous unit, its interelationship with sedimentary psammites and psammopelites, the recognition of irregular metasedimentary rip-up clasts in lower grade rocks at Yanco Glen (Figure 9.3a,b), and the preservation of volcanic quartz and feldspar in these lower grade rocks (Figure 9.3c,d). Rip-up clasts are common in turbidite successions (Chapter 7), and their occurrence is consistent with interpretation of the surrounding Potosi gneiss as a subaqueous mass flow deposit.

9.4 THE APPLICATION OF VOLCANIC FACIES ANALYSIS TO THE FIELD OF GEOCHRONOLOGY: DISCUSSION

One of the most significant outcomes of this study is that it illustrates the importance of applying a sound understanding of volcanic processes and facies to the field of geochronology, using in particular U-Pb methods applied to the dating of zircon crystals and grains. It is widely recognised that isotopic dating of volcanic rocks in sedimentary sequences has a variety of applications, as the data can provide direct numerical ages to complement stratigraphic, basin analysis and timescale studies. However, commonly little thought is given to selecting samples for analysis beyond broadly identifying a deposit as 'volcanic'. Often more information is required about the origins of a deposit in order to make a correct geological interpretation of the geochronological results. When analysing volcanic rocks to obtain stratigraphic ages for volcano-sedimentary sequences, questions

Figure 9.3 a,b: Field photographs of lower grade metamorphic equivalents of the Potosi gneiss at Yanco Glen, showing what appear to be (meta)pelite clasts. These clasts bear a strong resemblance to rip-up clasts in turbidite deposits. Photographs supplied by B. Stephens.

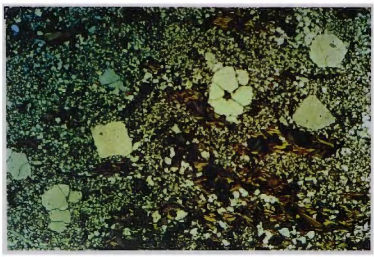

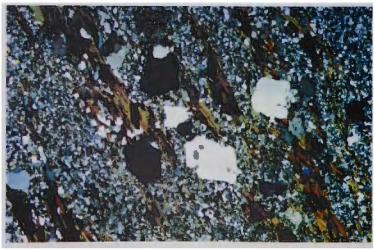

Figure 9.3 c,d: Photomicrographs of the lower grade metamorphic equivalents of the Potosi gneiss at Yanco Glen, showing what appear to be volcanic quartz grains. Photographs supplied by B. Stephens.

should be raised such as: (1) is there unequivocal evidence that the deposit is extrusive, or could it be intrusive? (2) is it a coherent or fragmental volcanic facies? (3) is it a primary or secondary (reworked) deposit? Common mistakes that are made for example, include sampling an intrusive sill that is thought to be a lava flow or sampling a reworked tuffaceous sediment and calling it a tuff, which infers the deposit is of primary volcanic origin. In both these cases, misinterpreting (or not interpreting) the origin of the facies can lead to misinterpretation of the geological significance of the age obtained.

This study involved dating a range of primary and syn-eruptive resedimented volcanic facies in both subaerial and submarine ancient successions, and specifically illustrates some of the pitfalls that may be encountered in analysing fragmental facies, which may have incorporated a lithic component during eruption and transportation. The following section expands on this work, and evaluates the suitability of different coherent and fragmental volcanic facies for U-Pb dating, based on: (1) their composition; (2) the likelihood of the facies to be affected by xenolithic and xenocrystic contamination; and (3) which facies provide the best stratigraphic markers within volcanic and sedimentary successions (based on their distribution, and preservation and recognition potential).

9.4.1 Composition

When selecting samples for U-Pb zircon analysis, it is important to be aware that all volcanic and intrusive rocks can be contaminated by xenocrysts inherited from the protolith during partial melting. In most igneous rocks, the zircon is dominantly melt-precipitated, with only a comparatively small component inherited from the protolith. There are, however, some exceptions and the relative proportions of the components vary widely (Williams 1992). In some cases, inheritance can completely dominate the zircon population. This is common in relatively mafic magmas (basalts and some andesites) and also in S-type granites. S-type granites and volcanics are considered to be derived from source rocks dominated by sedimentary material (Chappell and White 1974, 1984, 1992), and therefore can be expected to be rich in protolith zircon inherited from that sediment. In contrast, I-type granites derived from infracrustal sources, should contain lower abundances of protolith zircon. For example, Williams (1992) observed that S-type granites from the Berridale and adjacent Kosciusko Batholiths contained a far greater abundance of inherited zircon than associated I-type granites.

Chappell et al. (1999) have proposed a subdivision of I-type granites (and volcanics) into two groups, formed at high and low temperatures. High temperature I-type granites form from completely or largely molten magmas produced by partial melting of mafic source rocks. Only minute amounts of protolith zircon (if any) will be present in these magmas, because the melt is initially undersaturated in Zr (at compositions below about 66% SiO_2).

Low-temperature I-type granites result from the partial melting of quartzofeldspathic rocks such as older tonalites, formed under conditions in which the melt was saturated in Zr. A greater amount of protolith zircon is therefore expected to be present in these lower-temperature melts.

It can be concluded from the above, that composition is a factor that should be taken into consideration when selecting volcanic rocks for U-Pb dating. Problems arising from zircon inheritance are most likely to be encountered in igneous rocks of mafic to intermediate composition, and those with S-type compositions.

9.4.2 Crustal Contamination

In addition to xenocrystic zircon inherited from the protolith, pyroclastic deposits commonly contain large volumes of country rock assimilated during eruption and deposition. Accessory xenoliths and xenocrysts derived from erosion of the vent are explosively ejected during eruption, and accidental xenoliths and xenocrysts are picked up locally by pyroclastic flows and surges as they travel across the landscape. Lithic clasts are dispersed and carried significant distances from vent, and occur within the distal reaches of pyroclastic deposits, although clast size generally decreases with increasing distance from vent. The vertical distribution of lithic clasts is usually heterogeneous, and can vary as a function of supply (e.g. a vertical increase in lithic abundance is common, reflecting an increased rate of vent wall erosion during eruption) or in response to current fluctuations, which affect the erosive capacity of pyroclastic flows and surges. Branney et al. (1992) observed that lithic contents in high grade ignimbrites may be far smaller than in lower grade ignimbrites. They interpreted high grade ignimbrites to result from less-violent, high discharge-rate 'boil over' eruptions, which would incorporate lesser amounts of lithic ejecta than highly explosive pyroclastic eruptions. The resultant pyroclastic flows would have less momentum than flows derived from high eruption columns, reducing the incorporation of accidental lithics during transport. Boundary layer accretion along conduit walls and at the base of the hot proximal flows would also reduce incorporation of lithics during eruption and transport.

In contrast to pyroclastic deposits, coherent rocks (ie lavas) are the product of non-explosive eruptions, and incorporate very few xenoliths and xenocrysts during eruption and transportation. Therefore most xenocrysts in coherent rocks are derived from the source, and not from the country rock outcropping near vent at the surface.

9.4.3 Volcanic facies as stratigraphic markers

Facies architecture of subaerial silicic volcanic sequences

In subaerial settings, the primary eruptive products of silicic volcanic centres are pyroclastic fall, flow and surge deposits, and small-volume rhyolite lavas (Figure 9.4a). Ignimbrites are the most voluminous of these volcanic products, forming thick intracaldera fill deposits (100's of metres to over 1km thick) and thinner outflow sheets (up to tens of metres thick) in distal environments beyond the caldera margins. They are laterally extensive, due to the ability of pumice flows to travel over large distances, often over sloping ground and surmounting topographic barriers. The maximum distance travelled by ignimbrites is in the range of tens of kms, with some large volume ignimbrites (e.g. Fish Canyon Tuff) travelling over 100 km (Cas and Wright 1987). Pyroclastic fall deposits are also widely dispersed, but generally form considerably thinner deposits (cms to < 1m thick in distal settings, and no greater than 10-25m near vent). Unconsolidated pyroclastic fall and surge deposits and non-welded ignimbrites in subaerial settings are highly susceptible to erosion and therefore have poor preservation potential in ancient successions, unless they are capped by welded ignimbrite shortly after deposition. Coherent facies are usually comparatively small volume flows that are limited in aerial extent and confined to near-vent settings (Cas and Wright 1987).

Facies architecture of submarine silicic volcanic sequences

The facies architecture of submarine volcanic sequences differs markedly from subaerial settings (Figure 9.4b), reflecting the different eruption styles and depositional processes prevalent in the two environments. Explosive volcanism is normally constrained to water depths of less than 1 km, and significant vesiculation of silicic magma should only occur in water depths of several hundred metres or less (McBirney 1963). As a result, primary pyroclastic deposits play a less significant role in deep marine successions than in subaerial environments. Intrabasinal eruption centres are dominated by lava domes, laterally extensive lava flows (as in the Merrions Formation, Hill End Trough), largely intrusive high-level cryptodomes that may or may not breach the sediment surface, and related breccia sequences (autobreccia, hyaloclastite breccia and redeposited equivalents; Cas 1992, McPhie 1992). The timing of emplacement of coherent facies can be difficult to determine (this is also applicable to subaerial settings). Positive identification of syn-sedimentary emplacement requires evidence of extrusion or partial extrusion, or sub-surface emplacement into unconsolidated, wet sediments. This evidence includes: (1) hyaloclastite breccias and peperitic textures (quench fragmentation) at facies margins, initiated by contact of hot lava with water or water-saturated sediments;

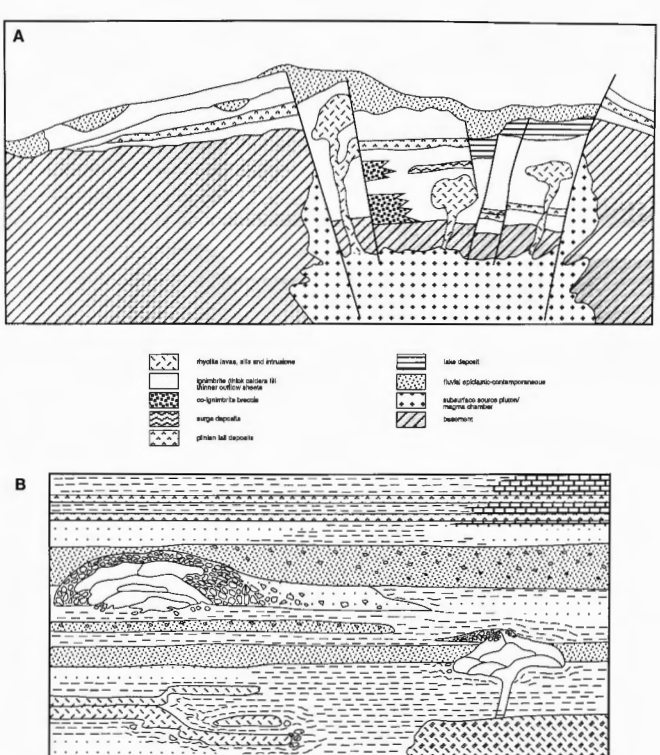

Figure 9.4: Schematic facies architecture of: (a) subaerial volcanic sequences (based on Cas and Wright 1987); and (b) submarine volcanic sequences (based on McPhie et al. 1993).

(2) resedimentation of hyaloclastite to form mass-flow emplaced, coeval volcaniclastic deposits flanking dome margins, and reworking of lava clasts and discrete crystals into coeval sediments (extrusive facies); (3) deformation or destruction of bedding in the unconsolidated host sequence; and (4) modification of seafloor topography. If these features are absent, it may be impossible to distinguish syn-sedimentary lavas, sills and cryptodomes from post-depositional sills.

Because of depth constraints on explosive volcanism, pyroclastic debris in deep marine successions is likely to be derived from extrabasinal subaerial or shallow marine basin margin volcanic centres. As concluded in Chapter 9.3, pyroclastic flows are unlikely to travel considerable distances under water, and subaqueous surge deposits have not been reported in the literature. However, large volumes of juvenile pyroclastic debris sourced by contemporaneous pyroclastic eruptions may be emplaced by syn-eruptive water-supported mass flows that were fed directly from subaerial pyroclastic flows that entered the sea, or generated by penecontemporaneous slumping and resedimentation of unconsolidated pyroclastic debris piled up at shorelines. These form thick, massive pumiceous and/or crystal-rich volcaniclastic deposits that are widely distributed throughout the basin (e.g. the crystal-rich volcaniclastic megaturbidites of the Big Sunday Formation, Turondale Formation and Merrions Formation, described in Chapters 3 and 7). Water-settled distal ash layers representing pyroclastic fallout have been identified in submarine successions, and thin clay beds interpreted as bentonites (clay altered volcanic ashes) interspersed through Phanerozoic marine sequences have been successfully targeted for radiometric dating (e.g. Claoué-Long et al. 1991; Riley et al. 1994; Black in prep.). Air-fall ashes have a better preservation potential in submarine and lacustrine successions than in subaerial and shallow-marine successions, because they are less susceptible to erosion and reworking in below storm-wave-base settings. However, it can be difficult to distinguish primary air-fall ashes from reworked tuffaceous sediments (e.g. Cas 1992). This is particularly the case for bentonite clay beds, in which original sedimentary textures that may aid interpretation of the facies origin are completely obliterated.

Potential of facies as marker beds

In both subaerial and submarine volcanic successions, the best framework for correlations is provided by volcanic facies that are strictly extrusive, produced in large volumes, erupted infrequently and rapidly emplaced, and have a wide distribution (McPhie 1992). Facies that have a genetic connection with large magnitude explosive eruptions best fit these criteria. In subaerial settings, these include pyroclastic flow, fall and surge deposits, with welded ignimbrites having the best preservation potential and generally forming the dominant component of ancient volcanic successions. In submarine

settings, water-settled ash layers (including bentonites) and mass-flow-emplaced pumiceous or crystal-rich volcaniclastic facies provide the best stratigraphic markers. In contrast, coherent lavas and syn-sedimentary intrusions may have limited value for correlation purposes because of their restricted distribution and random spatial and temporal occurrence in both subaerial and subaqueous successions (they can occur at many localities within the succession, and are not obviously confined to a discrete stratigraphic position). They can also pose a problem for dating stratigraphic sequences because their timing of emplacement may be difficult to determine (ie syn-depositional vs post-depositional).

9.4.4 Conclusions

The above discussion reveals a conflict that may arise in choosing the best volcanic facies for U-Pb dating. Whereas pyroclastic rocks or syn-eruptive pumiceous and/or crystal-rich volcaniclastic facies provide the best stratigraphic markers in subaerial and submarine successions, they are the most likely facies to contain significant crustal contamination. This can introduce a significant inherited component into the zircon population, which may cause problems in resolving the crystallisation age of the sample (as was illustrated when dating the lithic-rich ignimbrite succession of the Pul Pul Rhyolite; Chapter 5). Conversely, coherent facies such as lavas and syn-sedimentary sills and intrusions are less affected by crustal lithic contamination (although they may still contain xenocrysts derived from the magmatic source), and generally should have comparatively simple zircon populations. However, they have limited value for correlation purposes and can be difficult to distinguish from post-depositional intrusions. Therefore no volcanic facies can be singled out as ideally suitable for isotopic dating studies.

An accurate interpretation of geochronological results requires: (1) an awareness of the potential difficulties inherent in dating each type of facies; and (2) careful elucidation of eruptive and emplacement processes of volcanic facies selected for dating. If crustal contamination is likely to introduce significant inheritance in the zircon population, or if the origin of the facies is equivocal (e.g. if there is a problem determining the timing of emplacement of coherent bodies, or distinguishing primary from reworked tuffaceous units), then information independently constraining the age of the facies is required to ensure the correct age interpretation.

This approach proved very effective in the two geochronological studies undertaken in this thesis (presented in Chapters 5 and 8). In each case, obtaining a stratigraphic age for the selected units (the Pul Pul Rhyolite in Chapter 5, and the Turondale and Merrions Formations in Chapter 6) presented a potentially difficult dating prospect. Ambiguous results were avoided by selecting several different volcanic facies for isotopic analysis,

and cross-referencing the results. In the first study, lithic-contaminated ignimbrites represented the only lithofacies that could provide direct stratigraphic information on the Pul Pul Rhyolite, El Sherana Group. All other (coherent) volcanic facies appeared to be intrusive. The ignimbrites were expected to be rich in inherited zircon due to their high degree of crustal contamination. To avoid possible problems in interpreting their complex zircon populations, two coherent rhyolite porphyries, expected to have comparatively simple zircon populations, were also selected for dating to provide independent maximum and minimum age constraints on the crystallisation age of the ignimbrites.

In the second study, syn-eruptive crystal-rich volcaniclastic sandstones (CRVS) of the Turondale and Merrions Formations were targeted for isotopic dating. Because they classify as secondary deposits, the ages derived for this facies should be strictly interpreted as maximum values for their time of deposition. For this reason, an independent check on the results was established by also selecting coherent facies for analysis; a lava within the Merrions Formation, and sills within the Turondale Formation interpreted to be coevally emplaced with the lava. These coherent facies had less value as a stratigraphic marker than the volcaniclastic facies because of the more restricted lateral extent of the lava, and the post-depositional timing of emplacement of the Turondale porphyry. However, the ages obtained for the facies could be unequivocally assigned to the crystallisation of those rocks. An additional check on the ages obtained for volcaniclastic samples was provided by biostratigraphic constraints, which assigned a general Early Devonian age to the Crudine Group, and more specifically, a Lochkovian age to the Turondale Formation and a Pragian age to the Merrions Formation.

A further corollary of the second study is that it confirms that these thick resedimented volcaniclastic deposits, which make excellent marker beds and time markers, are also suitable for isotopic dating. Although the deposits are resedimented and transported into subaqueous settings by secondary mass-flow processes, they are primary in the sense that they are deposited as part of the eruptive cycle, and contain juvenile pyroclasts derived from newly created volcanic products. The ages obtained for the resedimented CRVS compare favourably with the crystallisation age obtained for a lava within the Merrions Formation succession, confirming that this provide can reasonable estimates of depositional age.

This is an important outcome, with implication for basin analysis studies. Isotopic dating of prominent volcanogenic marker beds provides direct numerical ages for stratigraphic packages, which can be used for inter- and intra-basin correlations of sedimentary sequences, estimating rates of sedimentation, subsidence, sea-level change, etc, and establishing a tectonostratigraphy by relating the sedimentary sequence to tectonic and thermal events. The conclusion that this facies is suitable for isotopic dating should be

tempered with caution, however, as it is fragmental in origin, and therefore, like primary pyroclastic deposits, is prone to crustal contamination. This is illustrated by the results obtained from dating a similar CRVS in the Big Sunday Formation (analysed as part of the first study of the El Sherana Group). In this case, the CRVS are genetically related underlying ignimbrites of the Pul Pul Rhyolite, and so also contain a large amount of primary lithic contamination (i.e. incorporated into the flow during eruption and transportation over the subaerial land surface). In addition, they incorporated an additional source of lithics, identified as fluvial epiclastic sediments eroded by the parent pyroclastic flow before it entered the lake (Chapter 4). As a result of this extra lithic contamination, the zircon population was overwhelmed by xenocrystic grains (21 of 23 grains analysed were xenocrysts), and the age obtained for the facies provided the age of the xenocrystic population, and not the depositional age. The important difference between the CRVS of the Turondale and Merrions Formations, and the CRVS of the Big Sunday Formation, is that the former contained predominantly siltstone and limestone lithic clasts which were unlikely to contain zircon, whereas the latter contained abundant clasts of rhyolite porphyry, quartz-rich sandstone, granite fragments, chert and metasedimentary basement clasts, all of which are potential sources of zircon.

REFERENCES

Allen, J.R.L. 1970. *Physical processes of sedimentation: an introduction.* Allen and Unwin: London 248 pp.

Allen, S.R. 1998. Volcanology of the Kos Plateau Tuff, Greece: the product of an explosive eruption in an archipelago. PhD thesis, Monash University, Melbourne (unpublished).

Allen, S.R. and Cas, R.A.F. 1998. Lateral variation within coarse co-ignimbrite lithic breccias of the Kos Plateau Tuff, Greece. *Bulletin of Volcanology* **59**: 356-377.

Aramaki, S. 1984. Formation of the Aira caldera, southern Kyushu, ~22 000 years ago. *Journal of Geophysical Research* **89**: 8485-8501.

Ashley, P.M., Brown, P.F., Franklin, B.J., Ray, A.S. and Scheibner, E. 1979. Field and geochemical characteristics of the Coolac Ophiolite suite and its possible origin in a marginal sea. *Journal of the Geological Society of Australia* **25**: 1-22.

Bacon, C.R. 1983. Eruptive history of Mount Mazama and Crater Lake caldera, Cascade Range, U.S.A. *Journal of Volcanology and Geothermal Research* **18**: 57-115.

Bailes, A.H. 1980. Origin of Early Proterozoic volcaniclastic turbidites, south margin of the Kisseynew sedimentary gneiss belt, File Lake Manitoba. *Precambrian Research* **12**: 197-225.

Bailey, R.A., Dalrymple, G.B. and Lanphere, M.A. 1976. Volcanism, structure and geochronology of Long Valley Caldera, Mono County, California. *Journal of Geophysical Research* **81**: 725-744.

Bernoulli, D., Bischel, M., Bolli, H.M., Haring, M.O., Hochuli, P.A. and Kleboth, P. 1981. The Missaglia Megabed, a catastrophic deposit in the Upper Cretaceous Bermago Flysch, northern Italy. *Eclogae Geologicae Helvetiae* **74**: 421-442.

Bischoff, G.C.O. and Fergusson, C.L. 1982. Conodont distributions, and ages of Silurian and Devonian limestones in the Palmers Oakey district, N.S.W. *Journal of the Geological Society of Australia* **29**: 469-476.

Black, L.P. in press. The role of the zircon standard in the derivation of SHRIMP U-Pb ages. Submitted to *Chemical Geology (Isotope Geoscience).*

Black, L.P., Seymour, D.B., Corbett, K.B., Cox, S.E., Streit, J.E., Bottrill, R.S., Calver, C.R., Everard, J.L., Green, G.R., McClenaghan, M.P., Pemberton, J., Taheri, J. and Turner, N. J. 1997. Dating Tasmania's oldest geological events. *Australian Geological Survey Organisation Record* 1997/15 57 pp.

Bossière, G., Bonkoungou, I., Peucat, J.-J. and Pupin, J.-P. 1996. Origin and age of Palaeoproterozoic conglomerates and sandstones of the Tarkwaian Group in Burkina Faso, West Africa. *Precambrian Research* **80**: 153-172.

Bouma, A.H. 1962. *Sedimentology of some flysch deposits: a graphic approach to facies interpretation.* Elsevier: Amsterdam 168 pp.

Bouma, A.H. 1987. Megaturbidite: An Acceptable Term? *Geo-Marine Letters* 7: 63-67.

Bourrouilh, R. 1987. Evolutionary Mass-flow-megaturbidites in an Interplate Basin: Examples of the North Pyrenean Basin. *Geo-Marine Letters* **7**: 69-81.

Bracken, A.J. 1977. The pre-Permian Stratigraphy and Structure of the Capertee Valley. BA (Hons) Thesis, Macquarie University, Sydney (unpublished).

Branney, M.J. 1995. Downsag and extension at calderas. New perspectives on collapse geometries from ice-melt, mining, and volcanic subsidence. *Bulletin of Volcanology* **57**: 303-318.

Branney, M.J. and Kokelaar, B.P. 1992. A reappraisal of ignimbrite emplacement: progressive aggradation and changes from particulate to non-particulate flow during emplacement of high-grade ignimbrite. *Bulletin of Volcanology* **54**: 504-520.

Branney, M. J. and Kokelaar, B.P. 1994. Volcanotectonic faulting, soft state deformation, and rheomorphism of tuffs during development of a piecemeal caldera, English Lake District. *Geological Society of America Bulletin* **106**: 507-530.

Branney, M.J., Kokelaar, B.P. and McConnell, B.J. 1992. The Bad Step Tuff: a lava-like rheomorphic ignimbrite in a calc-alkaline piecemeal caldera, English Lake District. *Bulletin of Volcanology* **54**: 187-199.

Briggs, N.D. 1976. Welding and crystallisation zonation in Whakamaru Ignimbrite, Central North Island, New Zealand. *New Zealand Journal of Geology and Geophysics* **19**: 463-501.

Brooks, G.R., Doyle, L.J. and McNeillie, J.L. 1986. A massive carbonate gravity-flow deposit intercalated in the lower Mississippi Fan. *In:* Bouma, A.H., Coleman, Y.M. and Meyer, A.A. (eds) *Initial Reports of the Deep Sea Drilling Project* **96**, pp. 541-546. U.S. Government Printing Office: Washington, D.C.

Bryan, R. 1962. Lower Proterozoic basic intrusive rocks of the Katherine-Darwin area, Northern Territory. *Bureau of Mineral Resources Geology and Geophysics Australia Record* 1962/7 46 pp.

Bryan, S.E., Cas, R.A.F. and Martí, J. 1998. Lithic breccias in intermediate volume phonolitic ignimbrites, Tenerife (Canary Islands): constraints on pyroclastic flow depositional processes. *Journal of Volcanology and Geothermal Research* **81**: 269-296.

Buesch, D.C. 1992. Incorporation and redistribution of locally derived lithic fragments within a pyroclastic flow. *Geological Society of America Bulletin* **104**: 1193-1207.

Busby-Spera, C. 1984. Large-volume rhyolite ash-flow eruptions and submarine caldera collapse in the lower Mesozoic Sierra Nevada, California. *Journal of Geophysical Research* **89**: 8417-8427.

Busby-Spera, C.J. 1986. Depositional features of rhyolitic and andesitic volcaniclastic rocks of the Mineral King submarine caldera complex, Sierra Nevada, California. *Journal of Volcanology and Geothermal Research* **27**: 43-76.

Carey, S., Sigurdsson, H., Mandeville, C. and Bronto, S. 1996. Pyroclastic flows and surges over water: an example from the 1883 Krakatau eruption. *Bulletin of Volcanology* **57**: 493-511.

Carey, S.N. 1991. Transport and deposition of tephra by pyroclastic flows and surges. *In:* Fisher R.V. and Smith, G.A. (eds) *Sedimentation in volcanic settings,* pp. 39-57. Society of Economic Palaeontologists and Mineralogists Special Publication: Tulsa, Oklahoma **45**.

Carey, S.N. and Sigurdsson, H. 1980. The Roseau Ash: deep-sea tephra deposits from a major eruption on Dominica, Lesser Antilles arc. *Journal of Volcanology and Geothermal Research* **7**: 67-86.

Cas, R.A.F. 1977. Basin characteristics of the Early Devonian part of the Hill End Trough based on a stratigraphic analysis of the Merrions Tuff. *Journal of the Geological Society of Australia* **24**: 381-401.

Cas, R.A.F. 1978. Silicic lavas in Palaeozoic flysch-like deposits in New South Wales, Australia: Behaviour of deep subaqueous silicic flows. *Geological Society of America Bulletin* **89**: 1708-1714.

Cas, R.A.F. 1979. Mass-flow arenites from a Palaeozoic interarc basin, New South Wales, Australia: mode and environment of emplacement. *Journal of Sedimentary Petrology* **49**: 29-44.

Cas, R.A.F. 1983a. Submarine 'crystal-tuffs': their origin using a Lower Devonian example from southeastern Australia. *Geological Magazine* **120**: 471-486.

Cas, R.A.F. 1983b. A review of the facies patterns, palaeogeographic development and tectonic context of the Palaeozoic Lachlan Fold Belt of southeastern Australia. *Geological Society of Australia Special Publication* **10** 120 pp.

Cas, R.A.F. 1992. Submarine volcanism: eruption styles, products, and relevance to understanding the host-rock successions to volcanic-hosted massive sulfide deposits. *Economic Geology* **87**: 511-541.

Cas, R.A.F. and Jones, J.G. 1979. Paleozoic interarc basin in eastern Australia and a modern New Zealand analogue. *New Zealand Journal of Geology and Geophysics* **22**: 71-85.

Cas, R.A.F. and VandenBerg A.H.M. 1988. Ordovician. *In:* Douglas, J.G. and Ferguson, J.A. (eds) *Geology of Victoria,* pp. 63-101. Victorian Division, Geological Society of Australia: Melbourne.

Cas, R.A.F. and Wright, J.V. 1987. *Volcanic successions: modern and ancient. A geological approach to processes, products and successions.* Allen and Unwin: London 528 pp.

Cas, R.A.F. and Wright, J.V. 1991. Subaqueous pyroclastic flows and ignimbrites: an assessment. *Bulletin of Volcanology* **53**: 357-380.

Cas, R.A.F., Flood, R.H. and Shaw, S.E. 1976. Hill End Trough: new radiometric ages. *Search* **7**: 205-207.

Cas, R.A.F., Powell, C. McA. and Crook, K.A.W. 1980. Ordovician palaeogeography of the Lachlan Fold Belt; modern analogue and tectonic constraints. *Journal of the Geological Society of Australia* **27**: 19-31.

Cas, R.A.F., Powell, C.McA., Fergusson, C.L., Jones, J.G., Roots, W.D. and Fergusson, J. 1981. The Lower Devonian Kowmung Volcaniclastics: a deep water succession of mass flow origin, northeastern Lachlan Fold Belt, N.S.W. *Journal of the Geological Society of Australia* **28**: 271-288.

Chapin, C.E. and Lowell, G.R. 1979. Primary and secondary flow structures in ash-flow tuffs of the Gribbles run palaeovalley, Central Colorado. *In:* Chapin, C.E. and Elston, W.E. (eds) *Ash Flow Tuffs*, pp. 137-154. Geological Society of America Special Paper **180**.

Chappell, B.W. 1999. Aluminium saturation in I- and S-type granites and the characterization of fractionated haplogranites. *In:* Sial, A.N., Stephens, W.E. and Ferreira, V.P. (eds) *Granites; crustal evolution and associated mineralization*, pp. 535-551. Lithos **46**.

Chappell, B.W. and Stevens, W.E. 1988. Origin of infracrustal (I-type) granite magmas. *Transactions of the Royal Society of Edinburgh: Earth Sciences* **79**: 71-86.

Chappell, B.W. and White, A.J.R. 1984. I-type and S-type granites in the Lachlan Fold Belt, southeastern Australia. *In:* Xu Kequin and Tu Guangchi (eds) *Geology of granites and their metallogenic relations*, pp. 87-101. Proceedings of the International Symposium, Nanjing University, Nanjing, China. Science Press: Beijing.

Chappell, B.W. and White, A.J.R. 1974. Two contrasting granite types. *Pacific Geology* **8**: 173-174.

Chappell, B.W. and White, A.J.R. 1992. I- and S-type granites in the Lachlan Fold Belt. *Royal Society of Edinburgh Transactions* **83**: 1-26.

Chappell, B.W., White, A.J.R. and Hine, R. 1988. Granite provinces and basement terranes in the Lachlan Fold Belt, southeastern Australia. *Australian Journal of Earth Sciences* **35**: 505-524.

Christiansen, R.L. 1979. Cooling units and composite sheets in relation to caldera structure. *In:* Chapin, C.E. and Elston, W.E. (eds) *Ash Flow Tuffs*, pp. 29-42. Geological Society of America Special Paper **180**.

Christiansen, R.L., Lipman, P.W., Carr, W.J., Byers, F.M., Orkild, P.P. and Sargent, K.A. 1977. Timber Mountain - Oasis Valley caldera complex of southern Nevada. *Geological Society of America Bulletin* **88**: 943-959.

Cita, M.B., Beghi, C., Camerlenghi, A., Kastens, K.A., McCoy, F.W., Nosetto, A., Parisi, E., Scolari, F. and Tomadin, L. 1984. Turbidites and megaturbidites from the Herodotus abyssal Plain (eastern Mediterranean) unrelated to seismic events. *Marine Geology* **55**: 79-101.

Claoué-Long, J.C., Zhang Zichao, Ma Guogan,. and Du Shaohua. 1991. The age of the Permian-Triassic Boundary. *Earth and Planetary Science Letters* **105**: 182-190.

Claoué-Long, J.C., Compston, W.C., Roberts, L. and Fanning, C.M. 1995. Two Carboniferous ages: A comparison of SHRIMP zircon dating with conventional zircon

ages and $^{40}Ar/^{39}Ar$ analysis. *In:* Berggren, W.A., Kent, D.V., Aubry, M.P. and Hardenbol, J. (eds) *Geochronology, Time Scales and Global Stratigraphic Correlation,* pp. 3-21. Society of Economic Palaeontologists and Mineralogists Special Publication: Tulsa, Oklahoma **54**.

Cole, P.D. and Scarpati, C. 1993. A facies interpretation of the eruption and emplacement mechanisms of the upper part of the Neapolitian Yellow Tuff, Campi Flegrei, southern Italy. *Bulletin of Volcanology* **55**: 311-326.

Cole, P.D., Guest, J.E. and Duncan, A.M. 1993. The emplacement of intermediate volume ignimbrites: A case study from Roccamonfina Volcano, Southern Italy. *Bulletin of Volcanology* **55**: 467-480.

Cole, R.B. and DeCelles, P.G. 1991. Subaerial to submarine transitions in early Miocene pyroclastic flow deposits, southern San Joaquin basin, California. *Geological Society of America Bulletin* **103**: 221-235.

Cole, R.B. and Stanley, R.G. 1994. Sedimentology of subaqueous volcaniclastic sediment gravity flows in the Neogene Santa Maria Basin, California. *Sedimentology* **41**: 37-54.

Collins, B.D. and Dunne, T. 1986. Erosion of tephra from the 1980 eruption of Mount St Helens. *Geological Society of America Bulletin* **97**: 896-905.

Collins, W.J. and Vernon, R.H. 1992. Palaeozoic arc growth, deformation and migration across the Lachlan Fold Belt, southeastern Australia. *In:* Fergusson, C.L. and Glen, R.A. (eds) *The Palaeozoic Eastern Margin of Gondwanaland: Tectonics of the Lachlan Fold Belt, Southeastern Australia and Related Orogens,* pp. 381-400. Tectonophysics **214**.

Collins, W.J., Beams, S.D., White, A.J.R. and Chappell, B.W. 1982. Nature and origin of A-type granites with particular reference to southeastern Australia. *Contributions to Mineralogy and Petrology* **80**: 189-200.

Colquhoun, G.P. 1995. Early Devonian conodont faunas from the Capertee High, NE Lachlan Fold Belt, southeastern Australia. *Courier Forschungsinstitut Senckenberg* **185**: 347-369.

Colquhoun, G.P. 1996. The Early Devonian of the Capertee High, Northeastern Lachlan Fold Belt: stratigraphy, correlations, and palaeogeography. *Geological Society of Australia Abstracts* **41**: 93.

Colquhoun, G.P. 1998. Early Devonian stratigraphy, conodont faunas and palaeogeography of the Capertee High, Mudgee-Capertee Region, Central New South Wales. PhD thesis, University of Wollongong, Wollongong (unpublished).

Colquhoun, G.P., Meakin, N.S., Krynen, J., Watkins, J.J., Henderson, G.A.M. and Jagodzinski, E.A. 1996. The Mudgee 1:100 000 Sheet: stratigraphy, structure and mineralisation. *Geological Society of Australia Abstracts* **41**: 94.

Colquhoun, G.P., Meakin, N.S., Krynen, J., Watkins, J.J., Henderson, G.A.M. and Jagodzinski, E.A. 1997. Stratigraphy, structure and mineralisation of the Mudgee 1:100,000 Geological Sheet. *Quarterly Notes of the Geological Survey of New South Wales* **102**: 1-14.

Compston, W. and Williams, I.S. 1992. Ion-probe ages for the British Ordovician and Silurian stratotypes. *In:* Webby, B.D. and Laurie, J.R. (eds) *Global perspectives on Ordovician Geology*, pp 59-67. Balkema: Rotterdam.

Compston, W., Williams, I.S. and Meyer, C. 1984. U-Pb geochronology of zircons from lunar breccia 73217 using a sensitive high mass-resolution ion-microprobe. On: Boynton-William V. and Schubert, G. (eds) *Proceedings of the 14th Lunar Science Conference*, pp. B525-534. Journal of Geophysical Research **89**.

Compston, W., Williams, I.S., Kirschvinsk, J.L., Zichao, Z. and Guogan, M. 1992. Zircon U-Pb ages for the Early Cambrian time-scale. *Journal of the Geological Society of London* **149**: 171-184.

Coney, P.J., Edwards, A., Hine, R., Morrison, F. and Windrum, D. 1990. The regional tectonics of the Tasman orogenic system, eastern Australia. *Journal of Structural Geology* **12**: 519-543.

Cowie, J.W. and Bassett, M.G. 1989. IUGS 1989 Global Stratigraphic Chart with geochronometric and magnetostratigraphic calibration. *Supplement to Episodes* **12 (2)**.

Crawford, A.J. 1988. Cambrian. *In:* Douglas, J.G. and Ferguson, J.A. (eds) *Geology of Victoria*, pp. 37-62. Victorian Division, Geological Society of Australia: Melbourne.

Crevallo, P.D. and Schlager, W. 1980. Carbonate debris sheets and turbidites, Exuma Sound, Bahamas. *Journal of Sedimentary Petrology* **50**: 1121-1148.

Crook, K.A.W. 1980. Fore-arc evolution in the Tasman Geosyncline. *Journal of the Geological Society of Australia* **27**: 215-232.

Crook, K.A.W. and Powell, C.McA. 1976. The evolution of the southeastern part of the Tasman Geosyncline. *International Geological Congress, 25, Field Excursion Guide* 17A 122 pp.

Crook, K.A.W., Bein, J., Hughes, R.J. and Scott, P.A. 1973. Ordovician and Silurian history of the south-eastern part of the Lachlan geosyncline. *Journal of the Geological Society of Australia* **20**: 113-137.

Cumming, G.L. and Richards, J.R. 1975. Ore lead isotope ratios in a continuously changing earth. *Earth and Planetary Science Letters* **28**: 155-171.

Daly, S.J., Fanning, C.M. and Fairclough, M.C. 1998. Tectonic evolution and exploration potential of the Gawler Craton, South Australia. *AGSO Journal of Australian Geology and Geophysics* **17**: 145-168.

Dewey, J.F. 1963. The lower Palaeozoic stratigraphy of central Murrisk, County Mayo, Ireland, and the evolution of the South Mayo Trough. *Quarterly Journal of the Geological Society of London* **119**: 313-343.

Dickson, T.W. 1962. The geology of the parishes of Guroba and Merinda. B.Sc. Hons. thesis, University of Sydney, Sydney (unpublished).

Dimroth, E. and Demarcke, J. 1978. Petrography and mechanism of eruption of the Archaean Dalembert tuff, Rouyn-Noranda, Quebec, Canada. *Canadian Journal of Earth Sciences* **15**: 1712-1723.

Doyle, L.J. 1987. Anomalously Large Marine Sedimentary Units Deposited in a Single Mass Wasting Event. *Geo-Marine Letters* 7: 59-61.

Druitt, T.H. 1992. Emplacement of the 18 May 1980 lateral blast deposit ENE of Mount St Helens, Washington. *Bulletin of Volcanology* **54**: 554-572.

Druitt, T.H. 1995. Settling behaviour of concentrated dispersions and some volcanological applications. *Journal of Volcanology and Geothermal Research* **65**: 27-39.

Druitt, T.H. and Sparks, R.S. J. 1982. A proximal breccia facies on Santorini volcano, Greece. *Journal of Volcanology and Geothermal Research* **13**: 147-171.

Eby, G.N. 1990. The A-type granitoids: a review of their occurrence and chemical characteristics and speculations on their petrogenesis. *Lithos* **26**: 115-134.

Eichelberger, J.C. and Koch, F.G. 1979. Lithic fragments in the Bandalier Tuff, Jemez Mountains, New Mexico. *Journal of Volcanology and Geothermal Research* **5**: 115-134.

Elston, W.E. 1984. Mid-Tertiary ash flow tuff cauldrons, southwestern New Mexico. *Journal of Geophysical Research* **89**: 8733-8750.

Etheridge, M.A., Rutland, R.W.R. and Wyborn, L.A.I. 1987. Orogenesis and tectonic processes in the early to middle Proterozoic of Northern Australia. *In:* Kröner, A. (ed) *Proterozoic Lithospheric Evolution,* pp. 131-147. American Geophysical Union Geodynamics Series **17**.

Evendern, J.F. and Richards, J.R. 1962. Potassium-argon ages in eastern Australia. *Journal of the Geological Society of Australia* **9**: 1-49.

Ferguson, J. and Goleby, A.B. 1980. *Uranium in the Pine Creek Geosyncline.* International Atomic Energy Agency: Vienna 760 pp.

Fergusson, C.L. 1979. Pre-cleavage folds in the mid-Palaeozoic sequence near Capertee, New South Wales. *Journal and Proceedings of the Royal Society of New South Wales* **112**: 125-132.

Fergusson, C.L. and Colquhoun, G.P. 1996. Early Palaeozoic quartz turbidite fan and volcaniclastic apron, Mudgee district, northeastern Lachlan Fold Belt, New South Wales. *Australian Journal of Earth Sciences* **46**: 497-507.

Fergusson, C.L. and Coney, P.J. 1992. Convergence and intraplate deformation in the Lachlan Fold Belt of southeastern Australia. *In:* Fergusson, C.L. and Glen, R.A. (eds) *The Palaeozoic Eastern Margin of Gondwanaland: Tectonics of the Lachlan Fold Belt, Southeastern Australia and Related Orogens,* pp. 417-439. Tectonophysics **214**.

Fergusson, C.L. and VandenBerg, A.H.M. 1990. Middle Palaeozoic thrusting in the eastern Lachlan Fold Belt, southeastern Australia. *Journal of Structural Geology* **12**: 577-589.

Fergusson, C.L., Gray, D.R. and Cas, R.A.F. 1986. Overthrust terranes in the Lachlan Fold Belt, southeastern Australia. *Geology* **14**: 519-522.

Fisher, R.V. 1966. Mechanism of deposition from pyroclastic flows. *American Journal of Science* **264**: 350-363.

Fisher, R.V. 1983. Flow transformation in sediment gravity flows. *Geology* **11**: 273-274.

Fisher, R.V. 1984. Submarine volcaniclastic rocks. *In:* Kokelaar, B.P. and Howells, M.F. (eds), *Marginal basin geology: volcanic and associated sedimentary and tectonic processes in modern and ancient marginal basins,* pp. 5-27. Geological Society of London Special Publication **16**.

Fiske, R.S. 1963. Subaqueous pyroclastic flows in the Ohanapecosh Formation, Washington. *Geological Society of America Bulletin* **74**: 391-406.

Fiske, R.S. and Matsuda,T. 1964. Submarine equivalents of ash flows in the Tokiwa Formation, Japan. *American Journal of Science* **262**: 76-106.

Fiske, R.S. and Cashman, K.V. 1987. Partitioning of tephra in submarine eruption columns. *Geological Society of America Abstracts with Programs* **19**: 664.

Flood, R.H., Shaw, S.E. and Chappell, B.W. 1980. Mineralogical and chemical matching of plutonic and associated volcanic units, New England Batholith, Australia. *Chemical Geology* **29**: 163-170.

Folk, R.L. 1980. *Petrology of Sedimentary Rocks*. Hemphills: Austin.

Fordham, B.G. 1992. Chronometric calibration of mid-Ordovician to Tournasian conodont zones: a compilation from recent graphic-correlation and isotope studies. *Geological Magazine* **129**: 709-721.

Francis, E.H. and Howells, M.F. 1973. Transgressive welded ash-flow tuffs among Ordovician sediments of N.E. Snowdonia. *Journal of the Geological Society of London* **140**: 165-183.

Fridrich, C. J., Smith, R.P., DeWitt, E. and McKee, E.H. 1991. Structural, eruptive and intrusive evolution of the Grizzly Peak caldera, Sawatch Range, Colorado. *Geological Society of America Bulletin* **103**: 1160-1177.

Friedmann, S.J. and Grotzinger, J.P. 1994. Sedimentology, stratigraphy and tectonic implications of a paleo-Proterozoic continental extensional basin: the El Sherana - Edith River groups, Northern Territory, Australia. *Canadian Journal of Earth Sciences* **31**: 748-764.

Fritz, W.J. and Stillman, C.J. 1996. A subaqueous welded tuff from the Ordovician of County Waterford, Ireland. *Journal of Volcanology and Geothermal Research* **70**: 91-106.

Galbiata, B. 1969. Stratigrafia e tettonica delle colline di Montevecchiae Lissolo (Brianza orientale). *Atti del'Instituto Geologico della Universita di Pavia* **20**: 102-119.

Garratt, M.J. and Wright, A.J. 1988. Late Silurian to Early Devonian biostratigraphy of Southeastern Australia. *In:* McMillan, N.J., Embry, A.F. and Glass D.J. (eds) *Devonian of the World,* pp. 647-662. Canadian Society of Petroleum Geologists Memoir **14**.

Gill, J.B. 1978. Role of trace element partition coefficients in models of andesite genesis. *Geochimica et Cosmochimica Acta* **42**: 709-724.

Glen, R.A. and Watkins, J.J. 1994. The Orange 1:100,000 sheet: A preliminary account of stratigraphy, structure and tectonics, and implications for mineralisation. *Quarterly Notes of the Geological Survey of New South Wales* **95**: 1-17.

Glen, R.A. and Watkins, J.J. 1999. Implication of Middle Devonian deformation of the eastern part of the Hill End Trough, Lachlan Orogen, New South Wales. *Australian Journal of Earth Sciences* **46**: 35-52.

Gnaccolini, M. 1968. Sull'origine del "conglomerato pseudocretaceo" di Vernasso (Cividale del Friuli). *Rivista Italiana di Palaeontogia e Stratigrafia* **74**: 1233-1254.

Gradstein, F.M. and Ogg, J. 1996. A Phanerozoic Timescale. *Episodes* **19**: 3-5.

Gray, C.M. and Webb, J.A. 1995. Provenance of Palaeozoic turbidites in the Lachlan Orogenic Belt: strontium isotopic evidence. *Australian Journal of Earth Sciences* **42**: 95-105.

Gray, D.R. 1997. Tectonics of the southeastern Australian Lachlan Fold Belt: structural and thermal aspects. *In:* Burg, J.P. and Ford, M. (eds) *Orogeny through time,* pp. 149-177. Geological Society Special Publication **121**.

Gustafson, J.K., Burrell, H.C. and Garretty, M.D. 1950. Geology of the Broken Hill ore deposits, Broken Hill, NSW, Australia. *Geological Society of America Bulletin* **61**: 1369-1437.

Hampton, M.A. 1972. The role of subaqueous debris flow in generating turbidity currents. *Journal of Sedimentary Petrology* **42**: 775-793.

Hampton, M.A. 1975. Competence of fine-grained debris flows. *Journal of Sedimentary Petrology* **45**: 834-844.

Harland, W.B., Cox, A.V., Llewellyn, P.G., Pickten, C.A.G., Smith, A.G. and Walters, R. 1982. *A Geologic Time Scale.* University Press: Cambridge 131 pp.

Harland, W.B., Cox, A.V., Craig, L.E., Smith, A.G. and Smith, D.G. 1990. *A Geologic Time Scale 1989.* University Press: Cambridge 265 pp.

Hawkins, L.V. 1953. The geology of the Sofala-Wattle Flat-Limekilns districts. MSc Qual thesis, University of Sydney, Sydney (unpublished).

Hein, K.K. 1994. The structure and geochemistry of gold mineralisation in the Mount Todd Goldfield, Pine Creek Inlier, Northern Territory. PhD thesis, University of Tasmania, Hobart (unpublished).

Hildebrand, R.S. 1984. Folded cauldrons of the Early Proterozoic Labine Group, northwestern Canadian Shield. *Journal of Geophysical Research* **89**: 8429-8440.

Hildreth, W. 1979. The Bishop Tuff: evidence for the origin of compositional zonation in silicic magma chambers. *In:* Chapin C.E. and Elston W.E. (eds) *Ash flow tuffs,* pp. 43-75. Geological Society of America Special Paper **180**.

Hildreth, W. 1981. Gradients in magma chambers: implications for lithospheric magmatism. *Journal of Geophysical Research* **18**: 10153-10192.

Hildreth, W. 1983. The compositionally zoned eruption of the Valley of Ten Thousand Smokes, Katmai National Park, Alaska. *Journal of Volcanology and Geothermal Research* **18**: 1-56.

Howells, M.F., Leveridge, B.E., Addison, R., Evans, C.D.R. and Nutt, M.J.C. 1979. The Capel Curig Volcanic Formation Snowdonia, North Wales; variations in ash-flow tuffs related to emplacement environment. *In:* Harris, A.L., Holland, C.H. and Leake, B.E., (eds) *Caledonides of the British Isles – reviewed,* pp. 611-618. Geological Society of London Special Publication **8**.

Howells, M.F., Campbell, S.D.G. and Reedman, A.J. 1985. Isolated pods of subaqueous welded ash-flow tuff: a distal facies of the Capel Curig Volcanic Formation (Ordovician), North Wales. *Geological Magazine* **122**: 175-180.

Huppert, H.E., Sparks, R.S.J. and Turner, J.S. 1982. Effects of volatiles on mixing in calc-alkaline magma systems. *Nature* **297**: 554-557.

Jagodzinski, E.A. and Wyborn L.A.I. 1995. The Cullen Event: a major felsic magmatic episode in the Proterozoic Pine Creek Inlier of Northern Australia. *Abstracts for Precambrian '95, an International conference on Tectonics and Metallogeny of Early/Mid Precambrian Orogenic Belts, Montreal, Canada, August* 1995: p199.

Jessup, A. 1967. The geology of the Belara-Mt. Bodangora district, east of Wellington N.S.W. B.Sc. (Hons) thesis, University of Sydney, Sydney (unpublished).

Johnson, A.M. 1970. *Physical processes in geology.* Freeman, Cooper: San Francisco.

Johnston, J.D. 1984. Structural evolution of the Pine Creek Inlier and mineralisation therein, N.T. Australia. PhD thesis, Monash University, Melbourne (unpublished).

Kano, K. 1990. An ash-flow tuff emplaced in shallow water, Early Miocene Koura Formation southwest Japan. *Journal of Volcanology and Geothermal Research* **40**: 1-9.

Kano, K. 1996. A Miocene coarse volcaniclastic mass-flow deposit in the Shimane Peninsula, SW Japan: product of a deep submarine eruption? *Bulletin of Volcanology* **58**: 131-143.

Kano, K., Yamamoto T. and Ono, K. 1996. Subaqueous eruption and emplacement of the Shinjima Pumice, Shinjima (Moeshima) Island, Kagoshima Bay, SW Japan. *Journal of Volcanology and Geothermal Research* **71**: 187-206.

Kennedy, A.B. 1976. The geology of the Capertee Valley. BSc (Hons) thesis, Australian National University, Canberra (unpublished).

Kneller, B.C. and Branney, M.J. 1995. Sustained high-density turbidity currents and the deposition of thick massive sands. *Sedimentology* **42**: 607-616.

Kokelaar, P. 1986. Magma-water interactions in subaqueous and emergent basaltic volcanism. *Bulletin of Volcanology* **48**: 275-289.

Kokelaar, P. and Busby, C. 1992. Subaqueous explosive eruption and welding of pyroclastic deposits. *Science* **257**: 96-201.

Kosaka, K. 1995. Brittle deformation of the Bathurst Batholith: a coeval behaviour with megakinking in the Lachlan Fold Belt, southeastern Australia. *Journal and Proceedings of the Royal Society of New South Wales* **127**: 135-146.

Kruse, P.D., Sweet, I.P., Stuart-Smith, P.G., Wygralak, A.S., Pieters, P.E. and Crick, I.H. 1994. *Katherine SD53-9, 1: 250 000 geological map series explanatory notes.* Northern Territory Geological Survey Department of Mines and Energy: Darwin 69 pp.

Labaume, P., Mutti E. and Seguret, M. 1987. Megaturbidites: A depositional model from the Eocene of the SW-Pyrenean Foreland Basin, Spain. *Geo-Marine Letters* 7: 91-101.

Laing, W.P., Sun S.S. and Nesbitt, R.W. 1984. Acid volcanic precursor to Potosi Gneiss at Broken Hill and its implications for ore genesis. *In:* Binns, R.A. (ed) *Geoscience in the development of natural resources,* pp. 318-321. Geological Society of Australia Abstracts **12**.

Le Bas, M.J., Le Maitre, R.W., Streckeisen, A. and Zanettin, B. 1986. A chemical classification of volcanic rocks based on the total alkali - silica diagram. *Journal of Petrology* **27**: 745-750.

Leitch, E.C., 1975. Plate tectonic interpretation of the Palaeozoic history of the New England Fold Belt. *Geological Society of America Bulletin* **86**: 141-144.

Lipman, P.W. 1965. Chemical comparison of glassy and crystalline rocks. *Geological Survey of America Bulletin* **78**: 1282-1288.

Lipman, P.W. 1975. Evolution of the Platoro Caldera Complex and related volcanic rocks, southeastern San Juan Mountains, Colorado. *United States Geological Survey Professional Paper* No. **852** 128 pp.

Lipman, P.W. 1976. Caldera-collapse breccias in the western San Juan Mountains, Colorado. *Geological Society of America Bulletin* **87**: 1397-1410.

Lipman, P.W. 1984. The roots of ash flow calderas in western North America: windows into the tops of granitic batholiths. *Journal of Geophysical Research* **89**: 8801-8841.

Lipman, P.W. 1997. Subsidence of ash-flow calderas: relation to caldera size and magma-chamber geometry. *Bulletin of Volcanology* **59**: 198-218.

Lipman, P.W., Christiansen, R.L. and O'Connor, J.T. 1966. A compositionally zoned ash-flow sheet in southern Nevada. *United States Geological Survey Professional Paper* **524-F**: F1-F47.

Lowe, D.R. 1982. Sediment gravity flows: II. Depositional models with special reference to the deposits of high-density turbidity currents. *Journal of Sedimentary Petrology* **52**: 279-297.

Lowe, D.R. 1988. Suspended-load fallout rate as an independent variable in the analysis of current structures. *Sedimentology* **35**: 765-776.

Lütke, F. 1979. Biostratigraphical significance of Devonian dacryoconarids. *Special Papers in Palaeontology* **23**: 281-289.

Mahood, G. 1980. Geological evolution of a Pleistocene rhyolitic centre - Sierra La Primavera, Jalisco, Mexico. *Journal of Volcanology and Geothermal Research* **8**: 199-230.

Mahood, G. 1981. A summary of the geology and petrology of the Sierra La Primavera, Jalisco, Mexico. *Journal of Geophysical Research* **86**: 10137-10152.

Mandeville, C., Carey, S. and Sigurdsson, H. 1996. Sedimentology of the 1883 Krakatau submarine pyroclastic flow deposits. *Bulletin of Volcanology* **57**: 512-529.

Marjinac, T. 1996. Deposition of megabeds (megaturbidites) and sea-level change in a proximal part of the Eocene-Miocene flysch of central Dalmatia (Croatia). *Geology* **24**: 543-546.

Mawson, R. and Talent, J.A. 1992. Molong platform and Hill End Trough (NSW) in the Early Devonian: a pattern of platform exposure and reciprocal carbonate sedimentation offshore. *Geological Society of Australia Abstracts* **32**: 180.

Mawson, R., Talent, J.A., Engelbretsen, M.J. and Brock, G.A. 1990. Mid Palaeozoic conodont data as fundamental chronological underpinning for analysis of allochthoneity of terranes in Eastern Australia. *Geological Society of Australia Abstracts* **25**: 50.

McArthur, A.N. 1995. Eruption, emplacement and environmental context of the Ordovician Garth Tuff, Capel Curig Formation, North Wales. PhD thesis, Monash University, Melbourne (unpublished).

McBirney, A.R. 1963. Factors governing the nature of submarine volcanism. *Bulletin Volcanologique* **26**: 455-469.

McIlveen, G.R. 1974. The Eden-Comerong-Yalwal rift zone and the contained mineralisation. *Geological Survey of New South Wales Record* **16**: 245-277.

McPhie, J. 1983. Outflow ignimbrite sheets from Late Carboniferous calderas, Currabubula Formation, New South Wales, Australia. *Geological Magazine* **120**: 487-503.

McPhie, J. 1988. Proximal and distal facies associations of subaerial silicic caldera volcanoes. *Geological Society of Australia Abstracts* **21**: 278-279.

McPhie, J. 1992. Facies architecture of mineralised submarine volcanic sequences: Cambrian, Mount Reid Volcanics, western Tasmania. *Economic Geology* **87**: 587-596.

McPhie, J., Doyle, M. and Allen, R. 1993. *Volcanic textures. A guide to the interpretation of textures in volcanic rocks.* University of Tasmania, Centre for Ore Deposits and Exploration Studies: Launceston, Tasmania, Australia 196 pp.

Meakin, N.S. and Morgan, E.J. (compilers) 1999. *Dubbo 1:250 000 Geological Sheet SI/55-4 Second Edition Explanatory Notes.* Geological Survey of New South Wales: Sydney.

Mernagh, T.P., Wyborn, L.A.I. and Jagodzinski, E.A. 1998. 'Unconformity-related' U±Au±platinum-group-element deposits. *AGSO Journal of Australian Geology and Geophysics* **17**: 197-205.

Middleton, G.V. 1967. Experiments on density and turbidity currents III. Deposition of sediment. *Canadian Journal of Earth Sciences* **4**: 475-505.

Middleton, G.V. 1970. Experimental studies related to problems of flysch sedimentation. *In:* Lajoie, J. (ed) *Flysch Sedimentology in North America,* pp. 253-272. Geological Association of Canada Special Paper **7**.

Middleton, G.V. 1972. Albite of secondary origin in Charny Sandstones, Quebec. *Journal of Sedimentary Petrology* **42**: 341-349.

Middleton, G.V. and Hampton, M.A. 1976. Subaqueous sediment transport and deposition by sediment gravity flows. *In:* Stanley, D.J. and Swift D.P.J. (eds) *Marine sediment transport and environmental management,* pp. 197-218. Wiley: New York.

Mills, A.A. 1984. Pillow lavas and the Liedenfrost effect. *Journal of the Geological Society of London* **141**: 183-186.

Millsteed, B.D. 1985. The geology of an area to the northeast of Cudgegong, N.S.W. – with particular reference to the petrology and environments of deposition of the Carwell Creek beds. BSc (Hons) Thesis, University of Wollongong, Wollongong (unpublished).

Moore, J.G., Phillips, R.L., Grigg, R.W., Peterson, D.W. and Swanson, D.A. 1973. Flow of lava into the sea, 1969-1971, Kilauea volcano, Hawaii. *Geological Society of America Bulletin* **84**: 537-546.

Morgan, E.J., Cameron, R.G., Colquhoun, G.P., Meakin, N.S., Raymond, O.L., Scott, M.M., Watkins, J.J., Barron, L.M., Henderson, G.A.M., Krynen, J.P., Pogson, D.J., Warren, A.Y.E., Wyborn, D., Yoo, E.K., Glen, R.A. and Jagodzinski, E.A. 1999. *Dubbo 1:250 000 Geological Sheet SI/55-4 (Second Edition).* Geological Survey of New South Wales: Sydney and Australian Geological Survey Organisation: Canberra.

Mutti E., Ricci Lucci, F., Seguret, M. and Zanzucci, G. 1984. Seismoturbidites: a new group of resedimented deposits. *Marine Geology* **55**: 103-116.

Needham, R.S. 1988. *Geology and Mineralisation of the South Alligator Valley Mineral Field 1: 75 000 Geological Map.* Bureau of Mineral Resources Geology and Geophysics Australia: Canberra.

Needham, R.S. and Stuart-Smith, P.G. 1985a. Revised stratigraphic nomenclature and correlation of Early Proterozoic rocks of the Darwin-Katherine region, Northern Territory. *BMR Journal of Australian Geology and Geophysics* **10**: 121-131.

Needham, R.S. and Stuart-Smith, P.G. 1985b. Stratigraphy and tectonics of the Early to Middle Proterozoic transition, Katherine-El Sherana area, Northern Territory. *Australian Journal of Earth Sciences* **32**: 219-230.

Needham, R.S., Crick, I.H. and Stuart-Smith, P.G. 1980 Regional Geology of the Pine Creek Geosyncline. *In:* Ferguson, J. and Goleby, A.B. (eds) *Uranium in the Pine Creek Geosyncline,* pp. 273-285. International Atomic Energy Agency: Vienna.

Needham, R.S., Stuart-Smith, P.G. and Page, R.W. 1988. Tectonic evolution of the Pine Creek Inlier, Northern Territory. *Precambrian Research* **40/41**: 543-564.

Nelson, C.H., Meyer, A.W., Thor, D. and Larsen, M. 1986. Crater Lake, Oregon: A restricted basin with base-of-slope aprons of non-channelized turbidites. *Geology* **14**: 238-241.

Niem, A.R. 1971. Stratigraphy and origin of tuffs in the Stanley Group (Mississippian), Ouachita Mountains, Oklahoma and Arkansas. PhD thesis, University of Wisconsin, Madison, WI (unpublished).

Niem, A.R. 1977. Mississippian pyroclastic flow and air-fall deposits in the deep-marine Ouachita flysch basin, Oklahoma and Arkansas. *Geological Society of America Bulletin* **88**: 49-61.

Noble, D.C. 1967. Sodium, potassium and ferrous iron contents of some secondarily hydrated natural silicic glasses. *American Mineralogist* **52**: 230-285.

Norrish, K. and Chappell, B.W. 1977. X-ray fluorescence spectrometry. *In:* Zussman, J. (ed) *Physical methods in determinative mineralogy,* pp. 201-272. Academic Press: London.

Nusbaum, R.L. 1987. Recognition of a Proterozoic cauldron boundary in southeastern Missouri. Southeastern *Geology* **27**: 219-227.

Nutman, A.P. and Ehlers, K. 1998. Archaean crust near Broken Hill? *Australian Journal of Earth Sciences* **45**: 687-694.

Offenberg, A.C., Rose, D.M. and Packham, G.H. 1971. *Dubbo 1:250 000 Geological Sheet SI55-4.* Geological Survey of New South Wales: Sydney.

Orth, K., Cas, R.A.F. and Wright, J.V. 1989. Facies analysis and facies associations in the recognition of volcanic centres in silicic terranes: an example from the Early Devonian of Australia. *Australian Journal of Earth Sciences* **36**: 167-188.

Orton, G.J. 1989. Misbehavior of pyroclastic flows at the land-sea interface: a tale from Wales. *Geological Society of Australia Abstracts* **25**: 35.

Oversby, B. 1971. Palaeozoic plate tectonics in the southern Tasman Geosyncline. *Nature* **234**: 45-47.

Owen, M. and Wyborn, D. 1979. Geology and geochemistry of the Tantangara and Brindabella area. *Bureau of Mineral Resources Geology and Geophysics Australia Bulletin* **204** 52 pp.

Packham, G.H. 1958. Stratigraphic studies in the older Palaeozoic rocks of the Tasman Geosyncline in central-western New South Wales. PhD thesis, University of Sydney, Sydney (unpublished).

Packham, G.H. 1960. Sedimentary history of part of the Tasman Geosyncline in Southeastern Australia. *Report of the International Geological Congress XXI, part XII Regional Palaeogeography, Copenhagen*: 74-83.

Packham, G.H. 1968a. The lower and middle Palaeozoic stratigraphy and sedimentary tectonics of the Sofala-Hill End-Euchareena region, N.S.W. *Proceedings of the Linnean Society of New South Wales* **93**: 111-163.

Packham, G.H. 1968b. *Bathurst 1:250 000 Geol. Series Sheet SI55-8*. Geological Survey of New South Wales: Sydney.

Packham, G.H. (ed.), 1969. The Geology of New South Wales. *Journal of the Geological Society of Australia* **16** 654 pp.

Packham, G.H. 1973. A speculative Phanerozoic history of the southwest Pacific. *In:* Coleman, P. J. (ed) *The western Pacific island arcs, marginal seas, geochemistry,* pp. 369-388. University of Western Australia Press: Perth.

Packham, G.H. 1987. The eastern Lachlan Fold Belt of southeastern Australia: a possible Late Ordovician to Early Devonian sinistral strike slip regime. *In:* Leitch, E.C. and Scheibner, E. (eds) *Terrane Accretion and Orogenic Belts,* pp. 67-82. American Geophysical Union, Geodynamic Series **19**.

Packham, G.H. 1999. Radiometric evidence for Middle Devonian inversion of the Hill End Trough, northeast Lachlan Fold Belt. *Australian Journal of Earth Sciences* **46**: 23-33.

Page, R.W. and Laing, W.P. 1992. Felsic Metavolcanics related to the Broken Hill pb-Zn-Ag orebody, Australia: geology, depositional age, and timing of high-grade metamorphism. *Economic Geology* **87**: 2138-2168.

Page, R.W. and Williams, I.S. 1988. Age of the Barramundi Orogeny in Northern Australia by means of ion microprobe and conventional U-Pb zircon studies. *Precambrian Research* **40/41**: 21-36.

Page, R.W., Compston, W. and Needham, R.S. 1980. Geochronology and evolution of the late-Archaean basement and Proterozoic rocks in the Alligator Rivers Uranium Fields, Northern Territory, Australia. *In:* Ferguson, J. and Goleby, A.B. (eds) *Uranium in the Pine Creek Geosyncline,* pp. 39-68. International Atomic Energy Agency: Vienna.

Peccerillo, A. and Taylor, S.R. 1976. Geochemistry of Eocene calc-alkaline volcanic rocks from the Kastamonu area, northern Turkey. *Contributions to Mineralogy and Petrology* **58**: 63-81.

Pemberton, J.W. 1989. The Ordovician-Silurian stratigraphy of the Cudgegong-Mudgee district, New South Wales. *Proceedings of the Linnean Society of New South Wales* **111**: 169-200.

Pemberton, J.W. 1990. The stratigraphy of the Ordovician-Silurian rocks of the Cudgegong-Mudgee district and the petrography and geochemistry of the volcanic rocks. PhD thesis, University of Wollongong, Wollongong (unpublished).

Pemberton, J.W. and Offler, R. 1985. Significance of clinopyroxene compositions from the Cudgegong Volcanics and Toolamanang Volcanics, Cudgegong-Mudgee district, New South Wales, Australia. *Mineralogical Magazine* **49**: 591-599.

Pemberton, J.W., Colquhoun, G.P., Wright, A. J., Booth, A.N., Campbell, J.C., Cook, A.G. and Millsteed, B.D. 1994. Stratigraphy and depositional environments of the

northern Capertee High. *Proceedings of the Linnean Society of New South Wales* **114**: 105-134.

Pickering, K.T., Hiscott, R.N. and Hein, F.J. 1989. *Deep Marine Environments: Clastic Sedimentation and Tectonics.* Unwin Hyman: London 416 pp.

Pickett, J.W., Sherwin, L. and Watkins, J.J., 1996. The age of the Tanwarra Shale. *Quarterly Notes of the Geological Survey of New South Wales* **100**: 1-8.

Pidgeon, R.T. and Aftalion, M. 1978. Cogenetic and inherited zircon U-Pb systems in granites: Palaeozoic granites of Scotland and England. *In:* Bowes, D.R. and Leake, B.E. (eds) *Crustal evolution in northwestern Britain and adjacent regions,* pp. 201-272. Geological Journal Special Issue **10**.

Pierson, T.C. and Scott, K.M. 1995. Downstream dilution of a lahar: transition from debris flow to hyperconcentrated streamflow. *Water Resource Research* **21**: 1511-1524.

Pierson, T.C., Janda, R.J., Umbal, J.V. and Daag, A.S. 1992. Immediate and long-term hazards from lahars and excess sedimentation in rivers draining Mt Pinatubo, Philippines. *United States Geological Survey Water Resources Investigative Report* **92-4039**: 1-35.

Pogson, D.J. and Watkins, J.J. 1998. *Bathurst geological sheet SI/55-8 Explanatory notes.* Geological Survey of New South Wales, Department of Mineral Resources: Sydney 430 pp.

Pogson, D.J. and Wyborn, D. 1994. Excursion Guide, Bathurst 1:250 000 *Geological Sheet. Geological Survey of New South Wales Report GS 1994/139 (unpublished).*

Powell, C.McA. 1976. A critical appraisal of the tectonic history of the Hill End Trough and its margins. *Australian Society of Exploration Geophysicists Bulletin* **7**: 14-18.

Powell, C.McA. 1983. Tectonic relationship between the Late Ordovician and Late Silurian palaeogeographies of southeastern Australia. *Journal of the Geological Society of Australia* **30**: 353-373.

Powell, C.McA. 1984. Ordovician to earliest Silurian: Marginal sea and island arc; Silurian to mid-Devonian: dextral transtensional margin; Late Devonian and Early Carboniferous: Continental magmatic arc along the eastern edge of the Lachlan Fold Belt. *In:* Veevers, J. J. (ed) Phanerozoic *Earth History of Australia,* pp. 290-340. Clarendon Press: Oxford.

Powell, C.McA. and Edgecombe, D.R. 1978. Mid-Devonian movements in the northeastern Lachlan Fold Belt. *Journal of the Geological Society of Australia* **25**: 165-184.

Powell, C.McA., Edgecombe, D.R., Henry, N.M. and Jones, J.G. 1976. Timing of regional deformation of the Hill End Trough: a reassessment. *Journal of the Geological Society of Australia* **23**: 407-421.

Powell, C.McA., Cole, J.P. and Cudahy, T.J. 1985. Megakinking in the Lachlan Fold Belt, Australia. *Journal of Structural Geology* **7**: 281-300.

Prince, C.M., Elmore, R.D., Ehrlich, R. and Pilkey, O.H. 1987. Areal and Lateral changes in a major trailing margin turbidite - the Black Shell Turbidite. *Geo-Marine Letters* **7**: 103-112.

Pudsey, C.J. 1984. Fluvial to marine transition in the Ordovician of Ireland - a humid-region fandelta? *Journal of Geology* **19**: 143-172.

Rawlings, D.J. 1994. Characterisation and correlation of volcanism in the McArthur Basin and Transitional Domain. *In:* Hallenstein, C.P. (ed) *Australian Mining Looks north – the challenges and the choices,* pp. 157-160. AusIMM Publication Series **5/94**: Melbourne.

Raymond, O.L., Pogson, D.J., Wyborn, D., Hawley, S.P., Henderson, G.A.M., Krynen, J., Meakin, N.S., Moffitt, R.S., Morgan, E.J., Scott, M.M., Spackman, J.M., Stuart-Smith, P.G., Wallace, D., Warren, A.Y.E., Watkins, J.J. and Glen, R.A. 1997. *Bathurst Second Edition (1:250 000 scale geological map SI/55-8).* Geological Survey of New South Wales: Sydney and Australian Geological Survey Organisation: Canberra.

Reading, H.G. (ed.) 1996. *Sedimentary environments: processes, facies and stratigraphy.* Blackwell Scientific: Oxford.

Ricci Lucci, F. and Valmori, E. 1980. Basin-wide turbidites in a Miocene, over-supplied deep-sea plain: a geometrical analysis. *Sedimentology* **27**: 241-270.

Riley, N.J., Claoué-Long, J., Higgins, A.C., Owens, B., Spears, A., Taylor, L. and Varker, W.J. 1994. Geochronomerty and geochemistry of the European Mid-Carboniferous boundary global stratotype proposal, Stonehead Beck, North Yorkshire, UK. *In:* Streel, M, and Paproth, E. (eds) *Carboniferous biostratigraphy,* pp. 275-289. Annales de la Societe Geologique de Belgique **16**: Belgium.

Rix, P. 1968. *Millingimbi, Northern Territory SD/53-2 1: 2500 000 Geological Map and Commentary.* Bureau of Mineral Resources, Geology and Geophysics, Australia: Canberra.

Roberts, J., Claoué-Long, J.C. and Foster, C.B. 1996. SHRIMP zircon dating of the Permian System of Eastern Australia. *Australian Journal of Earth Sciences* **43**: 401-421.

Roobol, M.J., Smith, A.L. and Wright, J.V. 1987. Lithic breccias in pyroclastic flow deposits on St Kitts, West Indies. *Bulletin of Volcanology* **49**: 384-388.

Rothwell, R.G., Thomson, J. and Kahler, G. 1998. Low-sea-level emplacement of a very large Late Pleistocene 'megaturbidite' in the western Mediterranean Sea. *Nature* **392**: 377-380.

Scandone, R. 1990. Chaotic collapse of calderas. *Journal of Volcanology and Geothermal Research* **42**: 285-302.

Scheibner, E. 1973. A plate tectonic model of the Palaeozoic tectonic history of New South Wales. *Journal of the Geological Society of Australia* **20**: 405-426.

Scheibner, E. 1985. Suspect terranes in the Tasman Fold Belt System, Eastern Australia. *In:* Howell, D.G. (ed) *Tectonostratigraphic Terranes of the Circum-Pacific Region,* pp. 493-514. Circum-Pacific Council Energy Mineral Resources, Earth Science Series **1**.

Scheibner, E. 1987. Paleozoic development of eastern Australia in relation to the Pacific region. *In:* Monger, J.W.H. and Francheteau, J. J. (eds) *Circum-Pacific Orogenic Belts and Evolution of the Pacific Ocean Basin,* pp. 133-165. American Geophysical Union Geodynamic Series **18**.

Scheibner, E. 1989. The tectonics of New South Wales in the second decade of application of the plate tectonics paradigm. *Journal and Proceedings of the Royal Society of New South Wales* **122**: 35-74.

Scheibner, E. and Stevens, B.P.J. 1974. The Lachlan River Lineament and its relationship to metallic deposits. *Quarterly Notes of the Geological Survey of New South Wales* **14**: 8-18.

Schmid, R. 1981. Descriptive nomenclature and classification of pyroclastic deposits and fragments: recommendations of the IUGS Subcommission on the Systematics of Igneous Rocks. *Geology* **9**: 41-43.

Schmincke, H.-U. and Swanson, D.A. 1967. Laminar viscous flowage structures in ash-flow tuffs from Gran Canaria, Canary Islands. *Journal of Geology* **75**: 641-664.

Schneider, J.-L., Fourquin, C. and Paicheler, J.-C. 1992. Two examples of subaqueously welded ash-flow tuffs: the Visean of southern Vosges (France) and the Upper Cretaceous of northern Anatolia (Turkey). *Journal of Volcanology and Geothermal Research* **49**: 365-383.

Scott, R.B. 1971. Alkali exchange during devitrification and hydration of glasses in ignimbrite cooling units. *Journal of Geology* **79**: 100-109.

Seccombe, P.K. and Hicks, M.N. 1989. The Hill End goldfield, NSW Australia - Early metamorphic deposition of auriferous veins. *Mineralogy and Petrology* **40**: 259-273.

Seguret, M., Labaume, P. and Madariaga, R. 1984. Eocene seismicity in the Pyrenees from megaturbidites of the South Pyrenean Basin (Spain). *Marine Geology* **55**: 117-131.

Self, S. and Wright, J.V. 1983. Large waveforms from the Fish Canyon Tuff, Colorado. *Geology* **11**: 443-446.

Self, S., Goff, F., Gardner, J.N., Wright, J.V. and Kite, K.M. 1986. Explosive rhyolitic volcanism in the Jemez Mountains: Vent locations, caldera development and relation to regional structure. *Journal of Geophysical Research* **91**: 1779-1798.

Shatwell, D.O. 1962. The geology of the parishes of Merinda, Rouse, Wiadere and Piambong, near Mudgee, N.S.W. B.Sc. (Hons) thesis, University of Sydney, Sydney (unpublished).

Sides, J.R., Bickford, M.E., Shuster, R.D. and Nusbaum, R.L. 1981. Calderas in the Precambrian terrane of the St. Francois Mountains, southeastern Missouri. *Journal of Geophysical Research* **86**: 10349-10364.

Sigurdsson, H., Carey, S., Mandeville, C. and Bronto, S. 1991. Pyroclastic flows of the Krakatau eruption. *EOS* **36**: 377-381.

Silver, L.T., Conway, C.M. and Ludwig, K.R. 1986. Implications of a precise chronology for early Proterozoic crustal evolution and caldera formation in the Tonto Basin-Mazatazal Mountains region, Arizona. *Geological Society of America Abstracts with Programs* **18 no. 5**: 413.

Simpson, C.J. 1986. Volcanic-plutonic associations within the Bindook Volcanic Complex, Goodmans Ford-Bullio area, New South Wales. *Australian Journal of Earth Sciences* **33**: 475-489.

Simpson, C.J., Carr, P.F. and Jones, B.G. 1997. Evolution of the Bindook Volcanic Complex, Wollondilly Basin, eastern Lachlan Fold Belt. *Australian Journal of Earth Sciences* **44**: 711-726.

Smith, G.A. 1986. Coarse-grained non-marine volcaniclastic sediment: terminology and depositonal processes. *Geological Society of America Bulletin* **97**: 1-10.

Smith, G.A. 1987. The influence of explosive volcanism on fluvial sedimentation: the Deschutes Formation (Neogene) in Central Oregon. *Journal of Sedimentary Petrology* **57**: 613-629.

Smith, R.C.M. 1991. Landscape response to a major ignimbrite eruption, Taupo Volcanic Center, New Zealand. *In:* Fisher R.V. and Smith, G.A. (eds) *Sedimentation in volcanic settings,* pp 123-137. Society of Economic Palaeontologists and Mineralogists Special Publication: Tulsa, Oklahoma **45**.

Smith, R.E. 1969. Zones of progressive regional burial metamorphism in part of the Tasman Geosyncline, eastern Australia. *Journal of Petrology* **10:** 144-163

Smith, R.L. 1960. Zones and zonal variations in welded ash flows, 149-159. *United States Geological Survey Professional Paper* **354-F**.

Smith R.L. and Bailey, R.A. 1968. Resurgent cauldrons. *In:* Coats, R.R., Hay, R.L. and Anderson, C.A. (eds) *Studies in volcanology (Howell Williams volume),* pp. 153-210. Geological Society of America Memoir **116**.

Solomon, M. and Griffiths, J.R. 1972. Tectonic evolution of the Tasman Orogenic Zone, eastern Australia. *Nature* **237**: 3-6.

Sparks, R.S.J. 1976. Grain size variations in ignimbrites and implications for the transport of pyroclastic flows. *Sedimentology* **23**: 147-188.

Sparks, R.S.J. and Walker, G.P.L. 1977. The significance of vitric-enriched air-fall ashes associated with crystal-enriched ignimbrites. *Journal of Volcanology and Geothermal Research* **2**: 329-341.

Sparks, R.S.J., Self, S. and Walker, G.P.L. 1973. Products of ignimbrite eruptions. *Geology* **1**: 115-118.

Sparks, R.S.J., Sigurdsson, H. and Wilson, L. 1977. Magma mixing; a mechanism for triggering acid explosive eruptions. *Nature* **267**: 315-318.

Sparks, R.S.J., Sigurdsson, H. and Carey, S.N. 1980a. The entrance of pyroclastic flows into the sea. I. Oceanographic and geological evidence from Dominica, Lesser Antilles. *Journal of Volcanology and Geothermal Research* **7**: 87-96.

Sparks, R.S.J., Sigurdsson, H. and Carey, S.N. 1980b. The entrance of pyroclastic flows into the sea. II. Theoretical considerations on subaqueous emplacement and welding. *Journal of Volcanology and Geothermal Research* **7**: 97-105.

Stadlbauer, E., Bohla, M. and Keller, J. 1986. The Kos-Plateau-Tuff (Greece): A major ignimbrite eruption that crossed the open sea. *IAVCEI (1986). New Zealand, 1-9 February 1986, Abstracts*: 75.

Stanton, R.I. 1976. Petrochemical studies of the ore environment at Broken Hill, New South Wales: 4 - Environmental synthesis. *Institute of Mining and Metallurgy Transactions Section B* **85**: B221-B223.

Stanton, W.I. 1960. The lower Palaeozoic rocks of southwest Murrisk, Ireland. *Journal of the Geological Society of London* **116**: 269-296.

Stauffer, P.H. 1967. Grain-flow deposits and their implications, Santa Ynez Mountains, California. *Journal of Sedimentary Petrology* **37**: 487-508.

Steiger, R.H. and Jäger, E. 1977. Subcommission of geochronology: Convention on the use of decay constants in geo- and cosmochronology. *Earth and Planetary Science Letters* **36**: 359-362.

Steven, T.A. and Lipman, P.W. 1976. Calderas of the San Juan volcanic field, south-western Colorado. *United States Geological Survey Professional Paper* **958** 35 pp.

Stevens, B.P., Wyborn, L.A.I. and Jagodzinski, E.A. 1998. The origin of the Hores Gneiss at Broken Hill, N.S.W. and its role in mineralisation. *Geological Society of Australia Abstracts* **49**: 431.

Stewart, J.R. 1965. Middle Proterozoic Volcanic Rocks in the Katherine-Darwin Area, Northern Territory. *Bureau of Mineral Resources Geology and Geophysics Australia Report* **90** 24 pp.

Stix, J. 1991. Subaqueous, intermediate to silicic-composition explosive volcanism: a review. *Earth-Science Reviews* **31**: 21-53.

Streckeisen, A. 1976. To each plutonic rock its proper name. *Earth-Science Reviews* **12**: 1-33.

Streckeisen, A. 1979. Classification and nomenclature of volcanic rocks, lamprophyres, carbonatites, and melilitic rocks: Recommendations and suggestions of the IUGS Subcommission on the Systematics of Igneous Rocks. *Geology* 7: 331-335.

Strusz, D.L. 1972. Correlation of the Lower Devonian rocks of Australasia. *Journal of the Geological Society of Australia* **18**: 427-455.

Stuart-Smith, P.G. and Ferguson, J. 1978. The Oenpelli Dolerite - a Precambrian continental tholeiitic suite from the Northern Territory, Australia. *BMR Journal of Australian Geology and Geophysics* **3**: 125-133.

Stuart-Smith, P.G., Needham, R.S. and Bagas, L. 1988. Stow Region, Northern Territory (Sheet 5470) *1: 100 000 Geological Map and Commentary*. Bureau of Mineral Resources Geology and Geophysics Australia: Canberra 67 pp.

Stuart-Smith, P.G., Needham, R.S., Page, R.W. and Wyborn, L.A.I. 1993. Geology and Mineral Deposits of the Cullen Mineral Field, Northern Territory. *Australian Geological Survey Organisation Bulletin* **229**: 145 pp.

Tassé, N., Lajoie, J. and Dimroth, E. 1978. The anatomy and interpretation of an Archaean volcaniclastic sequence, Noranda region, Quebec. *Canadian Journal of Earth Sciences* **15**: 874-888.

Tera, F. and Wasserburg, G.J. 1974. U-Th-Pb systematics on lunar rocks and inferences about lunar evolution and the age of the moon. *Proceedings of the Fifth Lunar Conference (Supplement 5, Geochimica et Cosmochimica Acta)* **2**: 1571-1599.

Thompson, M.D. 1985. Evidence for a late Precambrian caldera in Boston, Massachusetts. *Geology* **13**: 641-643.

Tucker, R.D. and McKerrow, W.S. 1995. Early Palaeozoic chronology: a review in light of new U-Pb zircon ages from Newfoundland and Britain. *Canadian Journal of Earth Sciences* **32**: 368-379.

Tucker, R.D., Bradley, D.C., VerStraeten, C.A., Harris, A.G., Ebert, J.R. and McCutcheon, S.R. 1998. New U-Pb zircon ages and the duration and division of Devonian time. *Earth and Planetary Science Letters* **158**: 175-186.

Turner, J.S., Huppert, H.E. and Sparks, R.S.J. 1983. An experimental investigation of volatile exsolution in evolving magma chambers. *Journal of Volcanology and Geothermal Research* **16**: 263-278.

Valenta, R.K. 1991. Structural controls on mineralisation of the Coronation Hill Deposit and surrounding area. *Bureau of Mineral Resources Geology and Geophysics Australia Record* 1991/107 220 pp.

Vallance, T.G. 1965. On the chemistry of pillow lavas and the origin of spilites. *Mineralogical Magazine, Tilley Volume*: 471-481.

VandenBerg, A.H.M. and Stewart, I.R. 1992. Ordovician terranes of the southeastern Lachlan Fold Belt: stratigraphy, structure and palaeogeographic reconstruction. *In:* Fergusson, C.L. and Glen, R.A. (eds) *The Palaeozoic Eastern Margin of Gondwanaland: Tectonics of the Lachlan Fold Belt, Southeastern Australia and Related Orogens,* pp. 159-176. Tectonophysics **214**.

Vessell, R.K. and Davies, D.K. 1981. Non-marine sedimentation in an active fore arc basin. *In:* Ethridge, F.G. and Flores, R.M. (eds) *Recent and ancient non-marine depositional environments: models for exploration,* pp. 31-45. Society of Economic Palaeontologists and Mineralogists Special Publication: Tulsa, Oklahoma **31**.

Voorhoeve, W.J.H. 1986. Problems in fold belt geology in the Wattle Flat-Limekilns district: with an emphasis on stratigraphy and structure. BSc (Hons) thesis, Australian National University, Canberra (unpublished).

Walker, G.P.L. 1972. Crystal concentration in ignimbrites. *Contributions to Mineralogy and Petrology* **36**: 135-146.

Walker, G.P.L. 1973. Lengths of lava flows. *Philosophical Transactions of the Royal Society of London Series* A **274**: 107-118.

Walker, G.P.L. 1979. A volcanic ash generated explosions where ignimbrite entered the sea. *Nature* **281**: 642-646.

Walker, G.P.L. 1983. Ignimbrite types and ignimbrite problems. *Journal of Volcanology and Geothermal Research* **17**: 65-88.

Walker, G.P.L. 1984. Downsag calderas, ring faults, caldera sizes and incremental caldera growth. *Journal of Geophysical Research* 89: 8407-8416.

Walker, G.P.L. 1985. Origin of coarse lithic breccias near ignimbrite source vents. *Journal of Volcanology and Geothermal Research* 25: 157-171.

Walker, G.P.L., Wilson, C.J.N. and Froggatt, P.C. 1980. Fines-depleted ignimbrite in New Zealand - the product of a turbulent pyroclastic flow. *Geology* **8**: 245-249.

Walker, G.P.L., Self, S. and Froggatt, P.C. 1981. The ground layer of the Taupo Ignimbrite: a striking example of sedimentation from a pyroclastic flow. *Journal of Volcanology and Geothermal Research* **10**: 1-11.

Walker, R.G. (ed.) 1984. *Facies Models*, 2nd edition. Geological Association of Canada Reprint Series 1: Waterloo, Ontario, Canada.

Walker, R.G. 1984. Turbidites and associated clastic deposits. *In:* Walker, R.G (ed) *Facies Models* (2nd edition) pp. 171-188. Geological Association of Canada, Geoscience Canada Reprint Series 1: Waterloo, Ontario, Canada.

Walpole, B.P. Crohn, P.W., Dunn, P.R. and Randal, M.A. 1968. Geology of the Katherine-Darwin region, Northern Territory. *Bureau of Mineral Resources Geology and Geophysics Australia Bulletin* **82** 272 pp.

Warren, R.G. and Kamprad, J.L. 1990. Mineralogical, petrographic and geochemical studies in the South Alligator Region, Pine Creek Inlier, N.T. *Bureau of Mineral Resources Geology and Geophysics Australia Record* 1990/54 114 pp.

Webby, B.D. 1972. Devonian geological history of the Lachlan Geosyncline. *Journal of the Geological Society of Australia* **19**: 99-123.

White, M.J. and McPhie, J. 1996. Stratigraphy, volcanology and sedimentology of the Cambrian Tyndall Group, Mount Read Volcanics, western Tasmania. *Australian Journal of Earth Sciences* **43**: 147-159.

White, M.J. and McPhie, J. 1997. A submarine welded ignimbrite-crystal-rich sandstone facies association in the Cambrian Tyndall Group, western Tasmania, Australia. *Journal of Volcanology and Geothermal Research* **76**: 277-295.

Whitham, A.G. 1989. The behaviour of subaerially produced pyroclastic flows in a subaqueous environment: evidence from the Roseau eruption, Dominica, West Indies. *Marine Geology* **86**: 27-40.

Williams, I.S. 1992. Some observations on the use of zircon U-Pb geochronology in the study of granitic rocks. *Transactions of the Royal Society of Edinburgh: Earth Sciences* **83**: 447-458.

Williams, I.S. and Claesson, S. 1987. Isotopic evidence for the Precambrian provenance and Caledonian metamorphism of high grade paragneisses from the Seve Nappes, Scandinavian Caledonides, II. Ion microprobe zircon U-Th-Pb. *Contributions to Mineralogy and Petrology* **97**: 205-217.

Wilson, C.J.N. 1985. The Taupo eruption, New Zealand II. The Taupo Ignimbrite. *Philosophical Transactions of the Royal Society of London* **A314**: 229-310.

Wilson, C.J.N. and Walker, G.P.L. 1982. Ignimbrite depositional facies: the anatomy of a pyroclastic flow. *Journal of the Geological Society of London* **139**: 581-592.

Wilson, C.J.N., Rogan, A.M., Smith, I.E.M., Northey, D. J., Nairn, I.A. and Houghton, B.F. 1984. Caldera volcanoes of the Taupo Volcanic Zone, New Zealand. *Journal of Geophysical Research* **89**: 8463-8484.

Winchester, J.A. and Floyd, P.A. 1977. Geochemical discrimination of different magma series and their differentiation products using immobile elements. *Chemical Geology* **20**: 325-343.

Wohletz, K.H. 1986. Explosive magma-water interactions: Thermodynamics, explosion mechanisms, and field studies. *Bulletin of Volcanology* **48**: 245-264.

Wright, A.J. 1966. Studies in the Devonian of the Mudgee district, N.S.W. PhD thesis, University of Sydney, Sydney (unpublished).

Wright, A.J. 1967. Devonian of the Capertee Geanticline, N.S.W., Australia. *In*: Oswald, D.H. (ed) *International Symposium on the Devonian System, Volume II,* pp. 117-121. Alberta Society of Petroleum Geologists, Calgary.

Wright, A.J. 1994. Shelly fossils from the Cunningham Formation. *Department of Geology, University of Wollongong; Wollongong* (unpublished report).

Wright, A.J. and Chatterton, B.D.E. 1988. Early Devonian trilobites from the Jesse Limestone, New South Wales, Australia. *Journal of Palaeontology* **62**: 93-103.

Wright, A.J. and Haas, W. 1990. A new Early Devonian spinose phacopid trilobite from Limekilns, New South Wales: morphology, affinities, taphonomy and palaeoenvironment. *Records of the Australian Museum* **42**: 137-147.

Wright, J.V. 1981. The Rio Caliente Ignimbrite: analysis of a compound intraplinian ignimbrite from a major late Quaternary Mexican eruption. *Bulletin Volcanologique* **44**: 189-212.

Wright, J.V. and Coward, M.P. 1977. Rootless vents in welded ash-flow tuffs from Northern Snowdonia, North Wales. *Geological Magazine* **114**: 133-140.

Wright, J.V. and Mutti, E. 1981. The Dali Ash, Island of Rhodes, Greece: a problem in interpreting submarine volcanigenic sediments. *Bulletin Volcanologique* **44**: 153-167.

Wright, J.V. and Walker, G.P.L. 1977. The ignimbrite source problem: significance of a co-ignimbrite lag-fall deposit. *Geology* **5**: 729-732.

Wright, J.V. and Walker, G.P.L. 1981. Eruption, transport and deposition of ignimbrite: a case study from Mexico. *Journal of Volcanology and Geothermal Research* **9**: 111-131.

Wright, J.V., Haydon, R.C. and McConachy, G.W. 1993. *Sedimentary analysis and implications for Pb-Zn Mineralisation at Broken Hill, Australia.* James Cook University of North Queensland. Economic Geology Research Unit. Contributions **48**: 91pp.

Wyborn, D. 1992a. Stratigraphy and geochemistry of Ordovician volcanics from the Lachlan Fold Belt in central New South Wales. *In:* Webby, B.D. and Laurie, J.R. (eds) *Global Perspectives on Ordovician Geology,* pp. 495-497. Balkema: Rotterdam.

Wyborn, D. 1992b. The tectonic significance of Ordovician magmatism in the eastern Lachlan Fold Belt. *In:* Fergusson, C.L. and Glen, R.A. (eds) *The Palaeozoic Eastern Margin of Gondwanaland: Tectonics of the Lachlan Fold Belt, Southeastern Australia and Related Orogens,* pp. 177-192. Tectonophysics **214**.

Wyborn, D., Owen, M., Compston, W. and McDougall, I. 1982. The Laidlaw Volcanics: a Late Silurian point on the geological time scale. *Earth and Planetary Science Letters* **59**: 90-100.

Wyborn, L.A.I., Jagodzinski, E.A., Bastrakova, I. and Budd, A. 1997. The metallogenic potential of Australian Proterozoic Granites: Pine Creek Inlier. *Australian Geological Survey Organisation Commercial in Confidence Report.*

Wyborn, L.A.I., Valenta, R.K., Needham, R.S., Jagodzinski, E.A. Whitaker, A. and Morse, M.P. 1990. A review of the geological, geophysical and geochemical data of the Kakadu Conservation Zone as a basis for assessing the resource potential. Confidential contractors report to the Resource Assessment Commission Inquiry on the Kakadu Conservation Zone 291 pp.

Yamada, E. 1973. Subaqueous pumice flow deposits in the Onikobe Caldera, Miyagi Prefecture, Japan. *Journal of the Geological Society of Japan* **79**: 585-597.

Yamada, E. 1984. Subaqueous pyroclastic flows: their development and their deposits. *In:* Kokelaar, B.P. and Howells, M.F. (eds), *Marginal basin geology: volcanic and associated sedimentary and tectonic processes in modern and ancient marginal basins,* pp. 29-36. Geological Society of London Special Publication **16**.

Yamazaki, T., Kato, I., Muroi, I. and Abe, M. 1973. Textural analysis and flow mechanisms of the Donzurobo subaqueous pyroclastic flow deposits. *Bulletin of Volcanology* **37**: 231-244.

Yokoyama, I. 1983. Gravimetric studies and drilling results at the four calderas in Japan. *In:* Shimozuru, D. and Yokoyama, I. (eds) *Arc volcanism: physics and tectonics,* pp. 29-41. Proceedings of the 1981 IAVCEI Symposium, DiReidel Publishing Company: Dordrecht, Netherlands.

Yokoyama, I. 1987. A quantitative consideration of several calderas for study of their formation. *Geofisca International* **26**: 487-498.

Young, G.C. 1995. Timescales 4. Devonian. Biostratigraphic charts and explanatory notes. Second Series. *Australian Geological Survey Organisation Record* 1995/33 47 pp.

Young, G.C. 1997. Revision of the age of the Silurian-Devonian boundary on the AGSO Phanerozoic Timescale. *Australian Geological Survey Organisation Professional Opinion* 1997/001.

Young, G.C. and Laurie, J.R. (eds) 1996. *An Australian Phanerozoic Timescale.* Oxford University Press: Melbourne 279 pp.

APPENDIX A1

SAMPLE LOCALITIES

PINE CREEK

Appendix A1 contains a list of grid references for samples collected during this study. All grid references refer to the Stow 1:100 000 mapsheet (map number 8470). Samples are assigned to the facies and subunits outlined in the main text of the thesis (Chapters 2, 3 and 4). Thin sections are available for all samples, and a note is made of those for which point count analyses, geochemical data and SHRIMP U-Pb isotopic data are available (marked in columns 'pet', 'chem' and 'chron', respectively). Thin sections, hand specimens and rock powders (for geochemical analysis) are stored at the Australian Geological Survey Organisation (AGSO) rock store. All samples are registered with AGSO's corporate databases (SITES (sample locations); OZROXS (sample descriptions); OZCHEM (geochemical analyses); and OZCHRON (geochronology)).

APPENDIX A1
SAMPLE LOCALITIES
PINE CREEK

Sample	Stratunit	Facies	Mbr	Easting	Northing	pet	chem	chron
89123001	Coronation Sst	amgdaloidal basalt lava		254100	8487400		x	
89123002	Coronation Sst	rhyolite porphyry		253200	8487400	x	x	x
89123004	Coronation Sst	basalt lava		254300	8487000		x	
89123006	Coronation Sst	sandstone		253200	8487400		x	
89123008	Coronation Sst	high-Si basalt		254000	8487700			
89123009	Coronation Sst	high-Si basalt		253400	8487100		x	
89123011	Coronation Sst	basalt lava, flow banded		253400	8486900			
89123013	Coronation Sst	basalt; magma mingling		252700	8487100			
89123014	Coronation Sst	basalt lava, flow banded		252500	8487500		x	
89123015	Coronation Sst	rhyolite porphyry		253500	8487400			
89123017A	Coronation Sst	basalt; magma mingling		252500	8487300		x	
89123017B	Coronation Sst	rhyolite; magma mingling		252500	8487300		x	
89123018	Coronation Sst	basalt lava		252400	8487500		x	
89123019	Coronation Sst	basalt lava, flow banded		253200	8487500			
89123020	Pul Pul Rhyolite	rhyolite sill		247600	8487800			
89123021	Pul Pul Rhyolite	ignimbrite	NI	247800	8487900		x	
89123022	Pul Pul Rhyolite	medium-grained sandstone (fluvial)		247900	8487900		x	
89123023	Pul Pul Rhyolite	ignimbrite	UI	248000	8488000			
89123024B	Pul Pul Rhyolite	ignimbrite	MI	248300	8488200	x		
89123025	Big Sunday Fm	f.g. tuffaceous siltstone		248600	8484800		x	
89123026	Pul Pul Rhyolite	dolerite intrusion		248000	8488400		x	
89123027	Big Sunday Fm	dolerite intrusion		247800	8487100		x	
89123028	Pul Pul Rhyolite	medium-grained sst (fluvial)		248200	8487600	x	x	
89123029	Pul Pul Rhyolite	coarse-grained sandstone (fluvial)		248300	8487700	x	x	
89123033	Pul Pul Rhyolite	ignimbrite	NI	247800	8487900	x		
89123034	Big Sunday Fm	CRVS crystal-rich domain		248000	8487500			
89123035	Big Sunday Fm	CRVS crystal-rich domain		247900	8487600	x	x	
89123036	Pul Pul Rhyolite	conglomerate (fluvial)		248300	8487600	x		
89123038	Big Sunday Fm	dolerite intrusion		247700	8487200		x	
89123041	Pul Pul Rhyolite	ignimbrite	UI	247200	8488400			
89123043	Pul Pul Rhyolite	ignimbrite	UI	248400	8487700	x		
89123045	Pul Pul Rhyolite	fine-grained sandstone (fluvial)		248200	8487600		x	
89123046	Pul Pul Rhyolite	layered sandstone (fluvial)		246500	8489100			
89123047	Pul Pul Rhyolite	ignimbrite	MI	246500	8490700	x		
89123048	Pul Pul Rhyolite	ignimbrite	MI	246400	8490300	x		
89123052	Pul Pul Rhyolite	ignimbrite	CLI	247600	8489600	x		
89123055	Pul Pul Rhyolite	ignimbrite	MI	246400	8490300		x	
89123056	Pul Pul Rhyolite	medium-grained sandstone (fluvial)		247700	8488200	x		
89123057	Pul Pul Rhyolite	dolerite		245100	8493500		x	
89123058	Pul Pul Rhyolite	ignimbrite	UI	245200	8493400	x	x	
89123059	Pul Pul Rhyolite	sparsely porphyritic qtz monz porph		246087	8491833		x	
89123062	Pul Pul Rhyolite	ignimbrite	MI	249100	8487300	x	x	
89123063	Pul Pul Rhyolite	ignimbrite	NI	247800	8487900		x	
89123064	Pul Pul Rhyolite	ignimbrite	NI	247900	8487900	x		
89123065	Pul Pul Rhyolite	dolerite intrusion		249200	8488000			
89123068	Big Sunday Fm	CRVS crystal-rich domain		249500	8486400	x		
89123072	Pul Pul Rhyolite	dolerite intrusion		249800	8486400		x	
89123073	Pul Pul Rhyolite	sparsely porphyritic qtz monz po		244900	8493100		x	
89123076	Pul Pul Rhyolite	co-ignimbrite lag breccia		245100	8493500	x		x

Sample	Stratunit	Facies	Mbr	Easting	Northing	pet	chem	chron
89123077	Big Sunday Fm	CRVS pumice-bearing domain		246700	8488700	x	x	
89123079	Big Sunday Fm	CRVS pumice-bearing domain		246700	8488700	x	x	
89123080	Big Sunday Fm	qtz-rich conglomerate turbidite		246700	8488900			
89123081	Big Sunday Fm	qtz-rich conglomerate turbidite		246700	8488900		x	
89123082	Pul Pul Rhyolite	ignimbrite	MI	246800	8489100	x	x	
89123083	Pul Pul Rhyolite	ignimbrite	UI	245500	8491500		x	
89123084	Coronation Sst	high-Si basalt		246300	8492100		x	
89123085	Coronation Sst	sandstone		246200	8492400			
89123086	Coronation Sst	high-Si basalt		245900	8492200		x	
89123087	Pul Pul Rhyolite	ignimbrite	UI	245000	8491400	x	x	
89123088	Pul Pul Rhyolite	sparsely porphyritic qtz monz porph		244400	8493800		x	
89123089	Pul Pul Rhyolite	ignimbrite	UI	244250	8493500		x	
89123090	Pul Pul Rhyolite	ignimbrite	RI	247100	8490600	x	x	
89123092	Pul Pul Rhyolite	dolerite		245000	8494000			
89123094	Pul Pul Rhyolite	ignimbrite	UI	244200	8493800			
89123095	Pul Pul Rhyolite	sparsely porphyritic qtz monz porph		244200	8493600	x		
89123096	Pul Pul Rhyolite	ignimbrite	RI	247800	8490000	x		
89123097	Pul Pul Rhyolite	ignimbrite	RI	248100	8489600	x	x	
89123098	Pul Pul Rhyolite	ignimbrite	MI	247200	8488800			
89123099	Pul Pul Rhyolite	sandstone (fluvial)		246900	8489000			
89123101	Pul Pul Rhyolite	rhyolite dome/sill		263500	8486900		x	
89123102	Pul Pul Rhyolite	rhyolite porphyry		264300	8491200	x	x	
89123103	Pul Pul Rhyolite	dolerite intrusion		264500	8491100		x	
89123104	Pul Pul Rhyolite	ignimbrite	LI	258200	8487800	x	x	
89123105	Pul Pul Rhyolite	dolerite intrusion		257900	8486900		x	
89123106	Pul Pul Rhyolite	ignimbrite	LI	258600	8486500	x	x	
89123107	Pul Pul Rhyolite	ignimbrite	LI	258700	8486900	x	x	
89123108	Pul Pul Rhyolite	rhyolite dome/sill		259800	8484400		x	
89123109	Pul Pul Rhyolite	rhyolite dome/sill		258300	8484900		x	
89123111	Pul Pul Rhyolite	rhyolite dome/sill		257800	8484700		x	
89123113	Pul Pul Rhyolite	dolerite		256700	8484500			
89123114	Pul Pul Rhyolite	rhyolite dome/sill		256700	8484400		x	
89123115	Pul Pul Rhyolite	dolerite		256800	8486100		x	
89123117	Coronation Sst	basalt lava		255600	8487300		x	
89123120	Coronation Sst	dolerite		255600	8487800			
89123123	Pul Pul Rhyolite	rhyolite porphyry		255400	8487200	x	x	
89123125	Pul Pul Rhyolite	ignimbrite	MI	256400	8485100	x		
89123129	Pul Pul Rhyolite	ignimbrite	UI	251200	8485000		x	
89123132	Pul Pul Rhyolite	ignimbrite	LI	252500	8485800	x	x	
89123133	Pul Pul Rhyolite	rhyolite porphyry		252600	8486000		x	
89123134	Pul Pul Rhyolite	ignimbrite	LI	252700	8486100	x	x	
89123135	Pul Pul Rhyolite	ignimbrite	CLI	252400	8485200	x		
89123136	Pul Pul Rhyolite	ignimbrite	LI	250000	8487600	x	x	
89123137	Pul Pul Rhyolite	ignimbrite	LI	250000	8487600	x	x	
89123138	Pul Pul Rhyolite	ignimbrite	CLI	255400	8487200	x	x	x
89123139	Pul Pul Rhyolite	ignimbrite	MI	249900	8486900	x	x	
89123140	Pul Pul Rhyolite	sandstone (fluvial)		250100	8486300			
89123141	Pul Pul Rhyolite	ignimbrite	MI	249500	8487100	x		
89123142	Pul Pul Rhyolite	sandstone (fluvial)		250000	8486000		x	
89123143	Pul Pul Rhyolite	sandstone (fluvial)		250000	8486100		x	

Sample	Stratunit	Facies	Mbr	Easting	Northing	pet	chem	chron
89123144	Pul Pul Rhyolite	medium-grained sandstone (fluvial)		249900	8486000		x	
89123145	Big Sunday Fm	CRVS crystal-rich domain		249900	8486000		x	
89123146	Pul Pul Rhyolite	ignimbrite	UI	250200	8484300		x	
89123147	Pul Pul Rhyolite	ignimbrite	UI	249900	8484400		x	
89123148	Pul Pul Rhyolite	ignimbrite	UI	249600	8484500		x	
89123149	Big Sunday Fm	rhyolite sill		249800	8486000		x	
89123152	Pul Pul Rhyolite	ignimbrite	UI	246800	8489000	x	x	
89123153	Pul Pul Rhyolite	ignimbrite	UI	246800	8449100	x	x	
89123154	Big Sunday Fm	CRVS crystal-rich domain		246800	8489000	x	x	
89123155	Big Sunday Fm	rhyolite porphyry		246800	8489000	x	x	
89123156	Big Sunday Fm	CRVS crystal-rich domain		246800	8489000	x	x	x
89123157	Big Sunday Fm	CRVS crystal-rich domain		246800	8489000		x	
89123158	Big Sunday Fm	CRVS: welded ignimbrite clast		246800	8489000	x		
89123172	Pul Pul Rhyolite	ignimbrite	UI	246300	8489800		x	
89123173	Pul Pul Rhyolite	ignimbrite	UI	246300	8489700	x	x	
89123174	Pul Pul Rhyolite	ignimbrite	UI	245400	8491500		x	
89123178	Pul Pul Rhyolite	sandstone (fluvial)		247000	8488500	x		
89123179	Pul Pul Rhyolite	ignimbrite	RI	247100	8490600	x		
89123180	Pul Pul Rhyolite	ignimbrite	CLI	248000	8488750	x		
89123182	Pul Pul Rhyolite	co-ignimbrite lag breccia		245300	8492400		x	
89123185	Pul Pul Rhyolite	ignimbrite	NI	249600	8487500	x		
89123186	Pul Pul Rhyolite	ignimbrite	UI	249300	8488000			
89123188	Big Sunday Fm	"normal"-sized turbidite		247800	8487250	x		
89123189	Big Sunday Fm	"normal"-sized turbidite		247800	8487250	x		
89123191	Pul Pul Rhyolite	ignimbrite	CLI	248300	8488400	x		
89123192	Big Sunday Fm	CRVS: welded ignimbrite clast		246650	8488650	x		
89123193	Pul Pul Rhyolite	ignimbrite: pumice clasts		245000	8492500			
89123194	Big Sunday Fm	CRVS: basal shear zone		246700	8488750	x		
89123195	Big Sunday Fm	CRVS pumice-bearing domain		246700	8488700	x		
89123196	Pul Pul Rhyolite	co-ignimbrite lag breccia		245100	8493500	x		
89123197	Big Sunday Fm	contact: CRVS and UI		246700	8488750			
89123198	Pul Pul Rhyolite	fine-grained sandstone (fluvial)		246700	8488750	x		
89123199	Pul Pul Rhyolite	ignimbrite	NI	247650	8487750	x		
89123201	Pul Pul Rhyolite	ignimbrite	NI	247800	8487900			
89123202	Pul Pul Rhyolite	rhyolite porph clast in co-ig breccia		245100	8493500		x	see 3076
89123203	Pul Pul Rhyolite	ignimbrite	UI	245000	8494000	x		
89123204	Pul Pul Rhyolite	ignimbrite	UI	245100	8492500	x		
89123205	Pul Pul Rhyolite	ignimbrite	UI	245100	8491500	x		
89123208	Coronation Sst	sandstone		245500	8494000			
89123210	Pul Pul Rhyolite	ignimbrite	NI	247750	8487850	x		
89123211	Pul Pul Rhyolite	ignimbrite	NI	247750	8487850			
89123212	Pul Pul Rhyolite	ignimbrite	NI	247750	8487850			
89123213	Pul Pul Rhyolite	ignimbrite	NI	247750	8487850			
89123214	Pul Pul Rhyolite	ignimbrite	NI	247750	8487850	x		
89123215	Pul Pul Rhyolite	siltstone (fluvial)		247500	8488000	x		
89123216	Pul Pul Rhyolite	siltstone (fluvial)		249900	8485850	x		
89123225	Pul Pul Rhyolite	fine-grained sandstone (fluvial)		248000	8487550	x		
89123228	Pul Pul Rhyolite	dolerite-bearing cngl (fluvial)		245450	8490550	x		
89123229	Pul Pul Rhyolite	porphyry- bearing cngl (fluvial)		250550	8485000	x		
89123230	Pul Pul Rhyolite	ignimbrite	MI	247200	8488800			x

APPENDIX A2

GEOCHEMICAL ANALYSES

PINE CREEK INLIER

ANALYTICAL METHODS:

Approximately 100 samples representative of each of the primary igneous and some volaniclastic units were collected from the study area for geochemical analysis. Major and trace elements were analysed by the laboratories of the Australian Geological Survey Organisation. All major elements and most trace elements were analysed by X-ray fluorescence, using Li-borate glass discs and pressed powder pellets respectively (Norrish and Chappell 1967). Li, Be, Co, and Ag were determined by atomic absorption spectrophotometry and FeO concentrations were determined by titration.

Representative ignimbrites (marked hand picked in the tables) were jaw-crushed and the rock chips hand-picked to remove lithic fragments, in order to assess the effects of lithic contamination. The chemistry of 13 samples (marked contaminated in the tables) were considered to be significantly affected by lithic contamination, and these samples were removed from the dataset prior to plotting magmatic trends in Chapter 2.

Sample	8912-3097	8912-3104A	8912-3104B	8912-3106	8912-3108A	8912-3108B	8912-3107	8912-3132A	8912-3132B
Number	Lower lg.	Lower lg.	Lower lg.	Lower lg.	Lower lg.	Lower lg.	Lower lg.	Lower lg.	Lower lg.
Unit	248100	258200	258200	258800	258600	258800	258700	252500	252500
Easting	8489600	8487800	8487800	8486500	8486500	8486500	8486900	8485800	8485800
Northing		contaminated	hand picked			hand picked	contaminated	contaminated	hand picked
SiO2	74.44	72.55	74.9	74.84	73.5	74.18	71.88	71.89	73.39
TiO2	0.15	0.25	0.18	0.2	0.24	0.2	0.28	0.29	0.19
Al2O3	12.57	11.34	10.91	12.28	12.32	12.5	11.9	12.81	12.61
Fe2O3tot	2.48	2.98	2.5	2.89	3.02	2.74	3.12	3.06	2.35
Fe2O3	0.76	1.55	1.48	2.53	1.93	1.9	1.6	1.63	1.44
FeO	1.55	1.2	0.94	0.32	0.98	0.76	1.37	1.29	0.82
MnO		0.06	0.05	0.03	0.06	0.05	0.05	0.05	0.04
MgO	1.04	0.84	0.68	0.43	0.7	0.52	0.95	1.11	0.85
CaO	0.11	2.08	1.6	0.17	0.86	0.33	1.59	0.96	0.72
Na2O	2.52	2.04	1.99	1.99	3.2	3.4	2.87	3.15	2.96
K2O	5.44	4.52	4.64	5.31	4.82	5.07	4.77	5.07	5.62
P2O5	0.03	0.06	0.04	0.04	0.06	0.04	0.08	0.07	0.04
rest	1.38	3.4	2.66	2.03	1.74	1.11	2.48	1.49	1.3
L.O.I.	0.21	0.21	0.24	0.2	0.21	0.26	0.24	0.24	0.26
TOTAL	100.24	100.1	100.29	100.15	100.42	100.32	100.06	100.05	100.04
Ba	195	246	252	320	295	313	347	271	285
Li	18	11	9	9	12	12	12	15	10
Rb	249	226	221	285	200	210	212	216	240
Sr	45	53	50	41	51	51	58	62	57
Pb	28	22	21	21	18	18	21	26	28
Th	57	45	48	56	52	55	47	50	55
U	14	11	12	9	6	6	12	11	12
Zr	203	210	203	259	243	253	246	253	249
Nb	24	19	17	22	21	21	19	22	22
Y	51	42	38	44	44	44	40	45	49
La	63	65	59	63	76	70	66	74	74
Ce	124	119	131	109	144	128	135	146	142
Nd	56	53	56	51	61	56	54	61	59
Sc	3	7	5	5	8	4	7	6	6
V	9	21	16	13	14	11	17	25	13
Cr	12	24	16	15	21	11	39	37	14
Mn	315	604	405	244	521	391	464	478	323
Co	4	8	5	5	5	5	5	6	5
Ni	4	6	5	4	7	4	10	11	7
Cu	7	-1	-1	-1	-1	2	-1	6	6
Zn	46	49	41	53	70	54	68	80	53
Sn	4	-2	3	4	-2	-2	-2	2	-2
Ga	20	17	15	17	17	16	17	21	17
Ag	2	3	2	3	3	1	1	2	2
Ge	4	2.5	3	3	3	3	4	4	4
Quartz	35.92	36.71	40.05	40.33	32.92	32.18	31.17	29.1	31.02
Corundum	2.36			2.97	0.59	0.86		0.51	0.39
Zircon	0.04	0.04	0.04	0.05	0.05	0.05	0.05	0.05	0.05
Orthoclase	32.24	26.8	27.51	31.49	27.38	30.04	28.27	30.04	33.3
Albite	21.32	17.26	16.84	16.84	27.08	28.77	24.29	28.65	25.05
Anorthite	0.41	8.39	7.1	0.68	3.97	1.48	5.45	4.4	3.41
Diopside		1.36	0.56				1.69		
Di(CaMg)		0.6	0.23				0.77		
Hedenbergite		0.76	0.33				0.92		
Hypersthene	5.29	4.44	4.1	4.13	4.95	4.23	4.76	5.92	4.1
Enstatite	2.59	1.81	1.59	1.07	1.74	1.3	2.01	2.76	1.62
Ferrosilite	2.7	2.63	2.52	3.06	3.2	2.93	2.75	3.15	2.48
Magnetite	0.72	0.84	0.73	0.84	0.88	0.8	0.91	0.89	0.68
Chromite		0.01					0.01	0.01	
Ilmenite	0.28	0.47	0.34	0.38	0.46	0.38	0.53	0.55	0.36
Apatite	0.08	0.14	0.1	0.1	0.14	0.1	0.19	0.17	0.1
Diff. Index	89.49	80.77	84.4	88.66	87.38	90.99	83.73	85.79	89.37
Colour Index	6.3	7.12	5.74	5.35	6.29	5.41	7.9	7.37	5.15
Pf	21.74	25.68	23.94	17.52	31.05	30.25	29.74	31.05	29.45
Norm Plag	1.91	32.72	29.65	3.87	12.79	4.88	18.35	14.17	11.98
100An/(An+Ab)	1.91	32.72	29.65	3.87	12.79	4.88	18.35	14.17	11.98
Ab	21.32	17.26	16.84	16.84	27.08	28.77	24.29	28.65	25.05
Q	37.31	37.85	41.1	41.35	34.17	33.24	32.4	30.64	32.07
Qt	3.9	3.3	3.05	3.11	3.7	3.17	3.53	4.37	3.05
Ne	11.58	9.36	9.13	9.13	14.88	15.59	13.16	14.45	13.58
Q	47.07	45.75	48.81	49.06	48.57	48.41	43.52	42.85	43.54
mg number	50.91	41.9	40.19	26.95	38.47	31.93	42.96	47.28	40.63

Sample Number	8912-3134	8912-3135	8912-3137A	8912-3137B	8912-3090A	8912-3090B	8912-3138A	8912-3138B	8912-3055
Unit	Lower lg.	Lower lg.	Lower lg.	Lower lg.	Rheo. lg.	Rheo. lg.	Cognate lg	Cognate lg.	Middle lg.
Easting	252700	250000	250000	250000	247100	247100	249900	249900	246400
Northing	8486100	8487600	8487600	8487600	8490600	8490600	8487000	8487000	8490300
	contaminated		contaminated	hand picked	contaminated	hand picked		hand picked	
SiO2	71.64	68.66	71.73	73.42	71.55	72.34	67.91	71.55	71.37
TiO2	0.37	0.45	0.28	0.2	0.28	0.24	0.44	0.38	0.28
Al2O3	12.57	12.44	12.77	12.48	12.99	12.91	12.72	12.84	13.34
Fe2O3tot	3.23	4.98	3.27	2.37	3.08	2.7	4.57	3.29	2.82
Fe2O3	1.8	1.5	0.9	0.98	1.37	1.22	2.15	1.76	1.24
FeO	1.29	3.13	2.13	1.25	1.54	1.33	2.18	1.36	1.42
MnO	0.05	0.09	0.08	0.04	0.06	0.05	0.08	0.04	0.03
MgO	1.37	1.73	1.17	0.81	0.86	0.7	2.22	1.22	0.78
CaO	0.79	2.35	0.91	0.83	0.71	0.83	1.02	0.42	0.7
Na2O	3.49	3.78	3.21	3.18	3.11	3.09	2.82	2.81	3.2
K2O	4.3	3.56	4.83	5.31	5.64	5.86	4.95	5.87	5.85
P2O5	0.08	0.13	0.07	0.05	0.07	0.07	0.14	0.11	0.08
rest	1.95	1.97	1.56	1.35	1.46	1.24	3.1	1.67	1.44
L.O.I.	0.23	0.21	0.23	0.27	0.23	0.3	0.28	0.3	0.28
TOTAL	99.93	100	99.85	99.95	99.87	99.98	100.01	100.15	100.01
Ba	244	280	275	274	317	387	613	737	482
Li	13	16	11	9	11	8	15	10	6
Rb	172	192	240	249	150	237	178	207	230
Sr	54	118	89	85	50	67	85	73	84
Pb	22	23	39	32	20	30	25	30	34
Th	50	35	48	52	47	55	42	47	54
U	13	10	11	12	12	13	9	10	12
Zr	243	230	221	224	242	304	342	385	349
Nb	24	22	19	24	19	20	17	17	22
Y	49	44	46	42	41	41	36	37	42
La	70	71	61	63	87	95	104	107	114
Ce	130	129	119	123	129	173	197	202	206
Nd	57	56	49	50	57	71	76	77	81
Sc	8	4	12	7			12	7	7
V	23	17	53	25	8	6	31	19	13
Cr	35	25	107	41	20	9	54	24	28
Mn	493	390	785	535	44	11	703	387	269
Co	8	13	8	8	427	450	9	7	3
Ni	10	24	23	10	5	4	15	11	7
Cu	1	8	8	12	10	5	-1	-1	1
Zn	90	91	90	140	1	15	174	114	40
Sn	9	3	4	6	69	49	-2	-2	-2
Ga	20	20	19	18	294	781	18	13	19
Ag	2	2	2	2	17	19	2	2	2
Ge	4	4	4	4	2	2	3	3	3
Quartz	29.81	24.29	29.4	31.06	27.68	28.34	25.17	28.89	26.5
Corundum	0.89		0.72	0.46	0.59	0.45	1.13	1.08	0.6
Zircon	0.05	0.05	0.04	0.05	0.06	0.06	0.07	0.08	0.07
Orthoclase	25.48	21.11	28.64	31.48	33.42	34.72	29.32	34.77	34.86
Albite	29.53	31.99	27.18	26.74	26.32	28.15	23.86	23.78	27.08
Anorthite	3.48	8.41	4.18	2.9	3.19	2.79	4.33	1.56	3.11
Diopside		3.76							
Di(CaMg)		1.84							
Hedenbergite		1.92							
Hypersthene	6.63	7.62	6.33	4.5	5.35	4.56	10.23	6.29	4.79
Enstatite	3.41	3.46	2.91	2.02	2.14	1.74	5.53	3.04	1.94
Ferrosilite	3.22	4.16	3.41	2.48	3.21	2.82	4.7	3.25	2.85
Magnetite	0.94	1.45	0.96	0.69	0.9	0.78	1.33	0.98	0.82
Chromite	0.01	0.01	0.02	0.01			0.01	0.01	0.01
Ilmenite	0.7	0.85	0.53	0.38	0.53	0.46	0.84	0.72	0.53
Apatite	0.19	0.31	0.17	0.12	0.17	0.17	0.34	0.28	0.2
Diff. Index	84.82	77.39	85.2	89.27	87.42	89.21	78.36	87.24	88.24
Colour Index	6.28	13.69	7.84	5.58	6.78	5.8	12.41	7.97	5.15
Pl	33.01	38.4	31.33	29.64	29.51	28.94	28.19	25.35	30.16
Norm Plag	10.54	16.7	13.29	9.79	10.82	9.86	15.36	6.22	10.29
100An/(An+Ab)	10.54	16.7	13.29	9.79	10.82	9.86	15.36	8.22	10.29
Ab	29.53	31.99	27.16	26.74	26.32	26.15	23.86	23.78	27.08
Q	31.56	28.27	31.05	32.22	29.06	29.5	27.9	30.34	27.73
Cl	4.87	5.64	4.66	3.33	3.96	3.4	7.51	4.84	3.56
Ne	16.01	17.34	14.72	14.49	14.26	14.17	12.93	12.89	14.68
Ip	45.09	40.92	43.49	44.47	41.11	41.48	38.83	41.23	40.13
mg number	51.19	46.24	46.99	45.84	40.86	39.11	54.58	47.85	40.86

Sample Number	8912-3062A	8912-3062B	8912-3062C	8912-3082	8912-3139A	8912-3139B	8912-3139C	8912-3058a	8912-3058b
Unit	Middle Ig.	Middle Ig.	Middle Ig.	Middle Ig.	Middle Ig.	Middle Ig.	Middle Ig.	Upper Ig.	Upper Ig.
Easting	249100	249100	249100	246800	249900	249900	249900	245200	245200
Northing	8467300	8467300 hand picked	8467300 hand picked	8469100	8486900	8486900 hand picked	8486900 hand picked	8493400	8493400 hand picked
SiO2	69.61	69.5	69.99	70.19	71.15	70.94	70.91	73.57	75.37
TiO2	0.35	0.34	0.35	0.34	0.32	0.29	0.31	0.29	0.26
Al2O3	13.4	13.35	13.45	12.92	13.32	13.21	13.28	11.79	11.74
Fe2O3tot	3.48	3.49	3.59	3.23	3.08	3.11	3.15	3.24	2.38
Fe2O3	1.97	2.09	1.89	1.84	1.98	2.15	1.99	1.14	0.88
FeO	1.36	1.28	1.53	1.43	0.99	0.88	1.04	1.89	1.33
MnO	0.06	0.06	0.06	0.05	0.05	0.04	0.05	0.08	0.07
MgO	0.63	0.6	0.68	0.59	0.61	0.61	0.67	1.38	1
CaO	1.26	1.23	1.32	1.75	0.61	0.79	0.9	1.11	0.84
Na2O	3.16	3.14	3.13	2.89	3.51	3.52	3.59	2.52	2.42
K2O	5.71	5.73	5.71	5.41	5.87	5.71	5.56	4.07	4.41
P2O5	0.1	0.1	0.1	0.1	0.09	0.09	0.09	0.08	0.07
rest	1.86	1.94	1.79	2.49	1.37	1.47	1.5	1.66	1.27
L.O.I.	0.3	0.29	0.28	0.27	0.29	0.28	0.26	0.21	0.27
TOTAL	99.79	99.63	100.26	100.07	100.16	99.99	100.15	99.79	99.93
Ba	461	458	445	472	447	442	429	340	378
Li	7	3	7	10	7	7	8	24	20
Rb	236	236	234	212	230	230	227	180	190
Sr	71	71	69	59	85	83	84	92	87
Pb	35	36	35	19	23	24	22	77	66
Th	53	52	52	50	54	53	54	48	50
U	11	11	12	11	12	11.5	12	12	13
Zr	417	423	413	389	360	361	356	186	190
Nb	20	20	20	19	21	20	20	20	19
Y	40	40	40	35	41	42	42	41	39
La	138	139	127	129	112	111	112	47	49
Ce	241	242	225	223	198	204	202	100	98
Nd	91	91	86	84	74	80	78	47	44
Sc	10	10	10	10	7	8	7	7	8
V	10	10	13	11	10	11	14	29	28
Cr	15	15	16	21	18	14	19	63	55
Mn	550	538	547	410	432	433	492	686	579
Co	4	4	3	3	5	5	5	8	9
Ni	5	4	5	6	5	6	6	17	14
Cu	-1	-1	-1	-1	-1	-1	-1	17	15
Zn	106	104	105	39	84	85	93	111	93
Sn	4	3	4	-2	-2	-2	-2	-2	-2
Ga	20	19	19	16	18	17	18	16	16
Ag	2	2	2	2	2	2	2	2	2
Ge	3	3	4	3	4	4	3	3	3
Quartz	24.32	24.33	24.85	27.11	25.09	24.69	24.55	37.44	40.09
Corundum					0.09			1.35	1.58
Zircon	0.08	0.09	0.08	0.08	0.07	0.07	0.07	0.04	0.04
Orthoclase	33.83	33.95	33.83	32.05	33.6	33.83	32.94	24.12	26.13
Albite	26.74	26.57	26.49	24.45	29.7	29.79	30.38	21.32	20.46
Anorthite	5.49	5.39	5.78	8.27	3.57	3.44	3.67	5.11	3.84
Diopside	0.21	0.16	0.23	1.62		0.03	0.26		
Di(CaMg)	0.07	0.08	0.08	0.55		0.01	0.11		
Hedenbergite	0.14	0.12	0.15	1.07		0.02	0.16		
Hypersthene	5.02	4.99	5.21	3.91	4.64	4.69	4.74	6.85	4.91
Enstatite	1.54	1.47	1.81	1.22	1.52	1.52	1.62	3.44	2.49
Ferrosilite	3.46	3.52	3.6	2.7	3.12	3.18	3.12	3.41	2.42
Magnetite	1.01	1.01	1.04	0.94	0.9	0.9	0.92	0.95	0.69
Chromite								0.01	0.01
Ilmenite	0.68	0.65	0.86	0.65	0.61	0.55	0.59	0.55	0.49
Apatite	0.24	0.24	0.24	0.24	0.22	0.22	0.22	0.19	0.17
Diff. Index	84.89	84.86	84.97	83.82	86.38	86.31	87.88	82.86	86.7
Colour Index	6.91	6.83	7.15	7.12	6.15	6.17	6.54	6.36	6.11
Pl	32.23	31.96	32.25	30.73	33.27	33.23	34.05	26.43	24.32
Norm Plag	17.04	16.87	17.87	20.42	10.73	10.36	10.79	19.33	15.8
100An/(An+Ab)	17.04	16.87	17.87	20.42	10.73	10.36	10.79	19.33	15.8
Ab	26.74	26.57	26.49	24.45	29.7	29.79	30.38	21.32	20.46
Q	25.57	25.56	25.95	28.09	26.26	25.87	25.75	39.24	41.39
Ol	3.77	3.75	3.91	2.94	3.48	3.51	3.54	5.04	3.61
Ne	14.49	14.4	14.35	13.25	16.1	16.14	16.46	11.58	11.1
Q	37.81	37.74	36.08	39.29	39.86	39.51	39.86	49.01	50.78
mg number	30.94	29.85	31.27	31.14	32.9	32.71	34.52	51.32	51.21

Sample	8912-3058c	8912-3083	8912-3087	8912-3089	8912-3129	8912-3146	8912-3147A	8912-3147B	8912-3148
Number	Upper lg.	Upper lg.	Upper lg.	Upper lg.	Upper lg.	Upper lg.	Upper lg.	Upper lg.	Upper lg.
Elnfi	245200	245500	245000	244250	251200	250200	249900	8484400	249600
Easting	8493400	8491500	8491400	8493500	8485000	8484300	8484400	hand picked	8484500
Northing	hand picked								
						contaminated	contaminated		contaminated
SiO2	76.71	71.09	66.56	72.03	72.6	70.74	71.53	73.3	69.95
TiO2	0.22	0.34	0.55	0.28	0.17	0.26	0.22	0.16	0.33
Al2O3	11.06	12.85	12.99	11.86	12.82	12.69	12.49	12.28	12.87
Fe2O3tot	2.25	3.61	5.25	1.3	2.24	3.15	2.88	2.42	3.41
Fe2O3	0.65	1.98	2.06	1.35	1.48	1.19	1.22	1.21	0.98
FeO	1.26	1.47	2.87	0.05	0.7	1.76	1.49	1.09	2.19
MnO	0.05	0.05	0.1	0.88	0.06	0.06	0.05	0.03	0.06
MgO	0.98	0.92	2.17	1.99	0.77	1.44	0.79	0.63	1.2
CaO	0.61	0.96	2.83	3.48	0.71	1.09	1.89	1.08	1.6
Na2O	2.43	3.23	2.58	3.59	2.8	2.56	2.71	2.7	2.71
K2O	4.47	5.27	4.59	0.08	5.35	4.95	4.68	4.92	4.51
P2O5	0.06	0.1	0.17	0.2	0.03	0.08	0.05	0.04	0.08
rest	1.13	1.77	2.07	2.79	2.87	2.9	2.82	2.15	3.08
L.O.I.	0.24	0.26	0.32	99.86	0.19	0.2	0.2	0.2	0.22
TOTAL	100.09	100.29	99.86	317	100.14	99.93	99.94	99.79	99.96
Ba	381	490	652	11	114	187	198	206	249
Li	17	14	22	150	6	15	16	13	17
Rb	186	193	154	50	243	252	250	249	276
Sr	86	74	177	20	23	32	47	44	58
Pb	51	29	32	47	17	13	21	18	18
Th	50	47	39	12	57	51	53	54	48
U	12	10	9	242	14	12	11	12	11
Zr	181	354	314	19	279	253	260	257	242
Nb	17	18	17	41	23	22	23	22	23
Y	36	36	37	67	46	46	46	44	47
La	48	126	87	129	84	73	79	80	73
Ce	92	217	159	57	158	140	154	155	138
Nd	39	84	63	16	67	57	66	65	58
Sc	5	9	13	6	5	7	7	5	6
V	19	14	47	20	8	20	17	12	25
Cr	37	24	91	44	6	31	24	16	50
Mn	467	437	923	427	507	529	450	289	515
Co	7	5	13	5	2	6	7	5	8
Ni	12	8	26	10	2	9	10	7	13
Cu	5	-1	7	1	2	1	7	8	8
Zn	85	61	127	69	17	69	62	51	72
Sn	4	4	2	2	-2	6	3	3	5
Ga	13	19	18	17	20	20	20	18	21
Ag	2	2	2	2	2	2	2	2	1
Ge	3	4	4	3	3	3	3	4	3
Quartz	41.89	27.16	23.19	32.11	33.2	30.98	31.71	34.33	29.78
Corundum	1.22	0.26			1.49	1.28		0.6	0.4
Zircon	0.04	0.07	0.08	0.05	0.06	0.05	0.05	0.05	0.05
Orthoclase	26.49	31.22	27.18	21.27	31.77	29.41	27.75	29.17	26.76
Albite	20.56	27.33	21.83	29.28	22	21.66	22.93	22.85	22.93
Anorthite	2.76	4.27	10.26	8.2	3.37	4.95	5.04	5.17	8.5
Diopside			2.39	2.72			0.06		
Di(CaMg)			1.29	1.27			0.03		
Hedenbergite			1.11	1.45			0.04		
Hypersthene	4.77	6	9.56	3.7	4.31	6.9	4.98	4.16	8.5
Enstatite	2.44	2.29	4.81	1.6	1.92	3.59	1.95	1.57	2.99
Ferrosilite	2.33	3.71	4.75	2.1	2.4	3.32	3.03	2.59	3.51
Magnetite	0.68	1.05	1.53	0.82	0.65	0.92	0.84	0.7	1
Chromite	0.01	0.01	0.02	0.01		0.01	0.01		0.01
Ilmenite	0.42	0.65	1.04	0.53	0.32	0.49	0.42	0.3	0.63
Apatite	0.15	0.24	0.41	0.19	0.07	0.19	0.12	0.1	0.19
Diff. Index	88.74	85.71	72.2	82.86	86.96	82.06	82.39	86.35	79.47
Colour Index	5.85	7.7	14.55	7.78	5.31	8.32	8.32	5.17	8.13
Pl	23.32	31.6	32.11	35.47	25.37	26.61	30.97	28.02	31.43
Norm Plag	11.84	13.5	32.01	17.47	13.27	18.59	25.95	16.45	27.03
100An/(An+Ab)	11.84	13.5	32.01	17.47	13.27	18.59	25.95	16.45	27.03
Ab	20.56	27.33	21.83	29.28	22	21.66	22.93	22.85	22.93
Q	42.95	28.89	25.71	33.07	34.31	32.81	32.98	35.39	31.47
Ol	3.51	4.47	7.04	2.74	3.19	5.07	3.71	3.1	4.8
Ne	11.14	14.81	11.83	15.87	11.92	11.74	12.43	12.38	12.43
Q	52.36	41.21	35.71	46.46	44.39	42.73	43.46	45.85	41.97
mg number	51.88	38.88	50.57	43.75	46	53.12	40.46	39.18	46.53

Sample	8912-3152A	8912-3152B	8912-3153	8912-3172	8912-3173	8912-3174	8912-3182	8912-3021A	8912-3021B
Number	Upper lg.	Upper lg.	Upper lg.	Upper lg.	Upper lg.	Upper lg.	Co-ig. brecc.	Non-weld	Non-weld
Unit	246800	246800	246800	246300	246300	245400	245300	247800	247800
Easting	8489000	8489000 hand picked	8449100	8489800 contaminated	8489700 contaminated	8491500	8492400	8487900 contaminated	8487900 hand picked
SiO2	73.27	73.81	73.16	70.91	72.09	72.77	74.22	72.71	75.23
TiO2	0.29	0.29	0.29	0.28	0.31	0.31	0.13	0.28	0.28
Al2O3	12.31	12.16	12.36	11.84	12.18	12.32	12.17	12.13	11.85
Fe2O3tot	3.07	2.52	2.82	3.08	2.49	3.12	2.19	3.12	2.35
Fe2O3	1.55	1.63	0.95	1.28	1.12	1.25	1.3	1.56	1.11
FeO	1.37	0.8	1.68	1.62	1.23	1.68	0.8	1.4	1.12
MnO	0.08	0.05	0.08		0.05	0.06	0.05		0.04
MgO	0.76	0.61	0.96	1.82	0.79	1.11	0.94	1.04	0.77
CaO	0.97	0.7	0.63	1.41	1.83	1.14	0.67	1.3	0.76
Na2O	3.27	3.15	2.38	1.65	2.52	2.81	1.88	2.84	2.97
K2O	4.84	4.84	5.16	4.84	5.13	4.59	5	4.67	4.6
P2O5	0.08	0.07	0.06	0.07	0.08	0.1	0.03	0.07	0.06
rest	1.11	1.24	2.1	4.08	2.56	1.7	2.7	1.77	1.17
L.O.I.	0.25	0.28	0.24	0.26	0.24	0.26	0.23	0.23	0.25
TOTAL	100.13	99.73	100.07	100.17	99.93	100.1	100.12	100.06	100.25
Ba	335	353	356	433	458	414	393	330	333
Li	15	15	18	35	22	22	17	16	14
Rb	190	203	269	260	234	196	225	197	192
Sr	64	63	65	42	69	83	18	64	61
Pb	36	38	20	60	24	38	12	29	30
Th	48	50	49	47	49	48	51	50	48
U	13	13	11	12	12	13	12	12	12
Zr	286	299	275	256	257	256	238	236	233
Nb	20	21	20	19	20	20	22	20	20
Y	40	41	37	40	41	41	49	40	38
La	57	60	90	76	71	75	88	69	56
Ce	165	149	166	145	134	139	166	130	111
Nd	66	59	66	57	56	56	69	52	46
Sc	7	5	7	9	7	7	4	8	6
V	16	11	18	15	21	27	6	21	16
Cr	28	27	43	36	43	59	7	41	38
Mn	470	370	497	905	424	573	492	563	381
Co	6	4	8	9	4	8	3	6	5
Ni	9	8	10	13	12	14	4	10	9
Cu	47	2	5	23	-1	-1	-1	-1	-1
Zn	93	83	80	123	59	129	119	104	77
Sn	3	-2	5	8	2	3	3	3	-2
Ga	18	16	17	18	17	17	18	19	14
Ag	2	1	2	2	2	2	2	2	2
Ge	3	4	3	3	3	4	3	3	4
Quartz	31.17	33.09	35.52	35.56	32.3	33.44	40.17	32.58	36.58
Corundum	0.07	0.47	1.84	1.41		0.83	2.46	0.15	0.71
Zircon	0.06	0.06	0.06	0.05	0.05	0.05	0.05	0.05	0.05
Orthoclase	28.68	29.27	30.6	28.7	30.41	27.2	29.63	27.67	27.26
Albite	27.87	26.65	20.14	13.96	21.32	23.78	15.91	24.03	25.13
Anorthite	4.4	3.13	2.72	6.67	6.72	5.14	3.24	6.1	3.46
Diopside					0.63				
Di(CaMg)					0.4				
Hedenbergite					0.43				
Hypersthene	5.08	4.04	5.33	7.81	4.01	5.96	4.75	5.84	4.25
Enstatite	1.89	1.52	2.44	4.53	1.78	2.76	2.34	2.59	1.92
Ferrosilite	3.18	2.52	2.88	3.28	2.22	3.2	2.41	3.25	2.33
Magnetite	0.69	0.73	0.82	0.9	0.73	0.91	0.64	0.91	0.69
Chromite	0.01	0.01	0.01	0.1	0.01	0.01		0.01	0.01
Ilmenite	0.55	0.55	0.55	0.53	0.59	0.59	0.25	0.53	0.53
Apatite	0.19	0.17	0.19	0.17	0.19	0.24	0.07	0.17	0.19
Diff. Index	87.51	89.02	86.26	78.25	84.03	84.42	85.71	84.28	88.97
Colour Index	6.53	5.33	6.71	9.25	8.16	7.47	5.63	7.29	5.47
Pl	32.07	29.79	22.86	20.63	28.04	28.92	19.15	30.14	28.59
Norm Plag	13.73	10.51	11.9	32.33	23.98	17.78	16.92	20.26	12.09
100An/(An+Ab)	13.73	10.51	11.9	32.33	23.96	17.78	16.92	20.26	12.09
Ab	27.67	26.85	20.14	13.96	21.32	23.78	15.91	24.03	25.13
Q	32.48	34.12	36.91	37.69	33.34	35	41.42	34.09	37.88
Ol	3.78	3.01	3.94	5.71	2.97	4.41	3.5	4.32	3.14
Ne	15	14.45	10.92	7.57	11.56	12.89	8.62	13.02	13.62
Q	45.13	48.33	48.14	44.08	43.1	45.89	48.71	45.1	49.19
mg number	37.96	37.48	48.27	59.39	44.02	46.85	51.53	45.24	44.74

Sample Number	8912-3063	8912-3157	8912-3002	8912-3102	8912-3123	8912-3133	8912-3155	8912-3059	8912-3088
Unit	Non-weld	Ignimbrite clast in CRWS	rhyolite porphyry	rhyolite porphyry	rhyolite porphyry	rhyolite porphyry	rhyolite porphyry	sparsely po qtz monz po.	sparsely po qtz monz po.
Easting	247800	248800	253200	284300	255400	252600	246800	246087	244400
Northing	8487900 contaminated	8489000	8487400	8491200	8487200	8486000	8489000	8491833	8493800
SiO2	70.74	71.35	75.93	75.37	75.78	76.35	75.78	66.32	63.71
TiO2	0.34	0.42	0.11	0.05	0.1	0.1	0.11	0.51	0.57
Al2O3	13.39	12.08	12.02	11.93	11.51	11.43	11.81	14.72	15.31
Fe2O3tot	3.25	3.76	1.69	1.77	2.07	2.57	1.37	4.75	5.24
Fe2O3	1.22	1.65	0.65	0.68	1.04	1.41	0.79	1.22	1.84
FeO	1.83	1.9	0.94	0.98	0.93	1.04	0.52	3.16	3.08
MnO	0.08		0.03	0.02	0.03	0.02	0.04		0.13
MgO	1.05	1.45	0.39	0.41	0.72	0.49	0.38	0.68	0.93
CaO	1.45	0.89	0.21	0.75	0.04	0.03	0.69	1.08	1.39
Na2O	2.43	1.49	2.16	1.41	1.1	2.77	2.44	2.89	3.28
K2O	5.4	5.52	5.89	8.8	7.51	5.39	5.8	6.88	6.66
P2O5	0.09	0.12	0.01	0.01	0.01	0.01	0.01	0.14	0.17
rest	1.78	1.92	1.31	1.44	1.31	0.8	1.56	2.02	2.61
L.O.I.	0.28	0.31	0.26	0.26	0.27	0.22	0.21	0.35	0.37
TOTAL	100.06	100.16	99.71	100.11	100.35	100.06	100.14	99.61	100.05
Ba	394	977	1383	247	411	386	329	703	674
Li	29	31	40	21	21	6	7	15	7
Rb	239	243	110	582	293	206	233	144	168
Sr	103	83	256	21	60	47	28	100	95
Pb	63	31	19	9	16	10	15	26	18
Th	52	42	3	85	38	40	49	52	46
U	13	10	2	23	4	5	10	10	8
Zr	305	300	137	193	179	185	195	666	793
Nb	21	18	7	49	20	17	23	19	17
Y	43	38	26	94	57	35	53	37	33
La	91	89	32	52	74	22	67	233	241
Ce	170	155	57	120	144	57	134	399	410
Nd	69	62	29	62	61	23	63	139	144
Sc	9	9	25	-1	3	2	3	16	18
V	28	31	165	-2	7	7	-2	9	6
Cr	34	61	253	-1	-1	2	-1	10	6
Mn	498	569	1609	150	278	152	258	507	1189
Co	6	11	42	3	2	2	3	3	4
Ni	10	16	66	-1	1	-1	1	3	3
Cu	7	2	20	-1	1	-1	3	8	33
Zn	80	84	218	31	40	32	16	23	73
Sn	8	-2	-2	6	-2	-2	-2	-2	-2
Ga	20	15	19	25	17	17	17	18	18
Ag	2	2	3	2	2	1	2	2	3
Ge	4	3	2	3	4	3	3	3	3
Quartz	29.85	32.07	39.61	37.85	36.31	37.44	36.8	18.83	12.57
Corundum	1.05	1.12	9.93	0.84	1.45	0.96	0.24	1.05	0.49
Zircon	0.06	0.06	0.04	0.04	0.04	0.04	0.04	0.14	0.16
Orthoclase	32	38.62	33.75	40.41	44.49	31.93	34.37	39.41	39.54
Albite	20.56	12.61	18.28	11.93	9.31	23.44	20.65	24.45	27.75
Anorthite	8.75	3.92	1.09	3.73	0.26	0.2	3.46	4.88	6
Diopside									
Di(CaMg)									
Hedenbergite									
Hypersthene	5.92	7.37	2.81	3.02	4.06	4.06	2.42	6.29	7.88
Enstatite	2.62	3.81	0.97	1.02	1.79	1.22	0.95	1.84	2.32
Ferrosilite	3.31	3.76	1.83	2	2.29	2.84	1.47	4.64	5.36
Magnetite	0.95	1.1	0.49	0.51	0.6	0.75	0.4	1.38	1.52
Chromite	0.01	0.01							
Ilmenite	0.65	0.8	0.21	0.09	0.19	0.19	0.21	0.97	1.06
Apatite	0.22	0.3	0.03	0.02	0.03	0.03	0.02	0.34	0.41
Diff. Index	82.41	83.3	91.63	90.19	92.12	92.81	91.61	82.69	79.86
Colour Index	7.52	9.28	3.51	3.63	4.87	4.99	3.03	8.75	10.28
PI	27.31	16.52	19.37	15.66	9.57	23.64	24.1	29.12	33.75
Norm Plag	24.71	23.7	5.83	23.82	2.73	0.84	14.34	16.02	17.77
100An/(An+Ab)	24.71	23.7	5.83	23.82	2.73	0.84	14.34	16.02	17.77
Ab	20.56	12.61	18.28	11.93	9.31	23.44	20.65	24.45	27.75
Q	31.36	34	40.32	38.61	39.37	38.45	37.22	20.36	14.48
Or	4.39	5.43	2.1	2.26	3.02	3.05	1.8	4.74	5.76
Ne	11.14	6.63	9.91	6.47	5.04	12.7	11.19	13.25	15.04
Q	40.8	39.78	48.69	44.07	43.64	49.19	46.87	31.58	27.2
mg number	44.41	48.83	36.29	36.46	46.22	32.1	40.75	25.58	30.52

Sample Number	8912-3073	8112-0139	8812-8006	8812-6007	8912-3149	8912-3101	8912-3108	8912-3109	8912-3111
Unit	sparsely po qtz monz po.	megacrystic qtz monz po.	megacrystic qtz monz po.	megacrystic qtz monz po.	rhyolite dyke	flow bded rhy. dome	flow bded rhy. dome	rhyolite dome/sill	rhyolite dome/sill
Easting	244900				249800	283500	259800	258300	257800
Northing	6493100				6486000	6488900	6484400	6484900	6484700
SiO2	63.55	53.51	64.25	64.09	76.77	75.58	74.55	77.99	75.29
TiO2	0.58	1.19	0.5	0.5	0.09	0.09	0.09	0.08	0.1
Al2O3	15.14	13.97	15.86	15.61	11.25	12.12	12.29	11.87	11.86
Fe2O3tot	5.2				1.02	1.7	1.84		2.49
Fe2O3	1.09	7.99	1.14	1.52	0.32	0.84	0.76	1.02	0.89
FeO	3.7	2.06	3.06	2.86	0.63	0.77	0.79	0.38	1.44
MnO	0.06	0.14	0.09	0.09	0.05	0.02	0.04	0.02	0.07
MgO	1.42	5.43	1.17	0.95	0.32	0.23	0.21	0.16	0.13
CaO	1.18	5.96	0.7	1.24	1.33	0.52	1.24	0.03	0.45
Na2O	2.55	0.95	3	3.2	4.53	2.59	2.6	1.43	2.45
K2O	6.83	5.89	7.57	7.16	2.81	5.96	5.27	4.91	4.82
P2O5	0.17	0.16	0.12	0.12	0.01	0.01	0.01	0	0.01
rest	3.15	0.45	0.5	0.45	1.61	1.14	2.2	1.88	2.22
L.O.I.	0.29	2.38	2.12	2.52	0.27	0.22	0.17		0.12
TOTAL	99.71	100.08	100.08	100.15	99.99	100.09	100.22	99.79	99.85
Ba	825	1179	1947	1314	151	62	73	142	73
Li	16	20	18	13	8	9	9	9	3
Rb	172	176	183	194	104	300	261	264	261
Sr	78	98	165	109	13	13	15	12	7
Pb	20	34	57	18	474	23	11	54	52
Th	46	47	34	39	53	56	49	52	52
U	6	7	5.5	6	12	14	10	13	13
Zr	795	709	614	706	197	215	185	225	234
Nb	17	20	17	19	27	30	23	28	24
Y	33	37	26	32	55	63	54	64	64
La	226	342	201	236	75	85	77	233	81
Ce	385	614	342	398	151	129	147	434	151
Nd	133	190	121	138	66	61	65	165	67
Sc	18	16	13	14	2	2	5	-1	2
V	5	8	5	9	-2	-2	-2	-2	-2
Cr	9	23	96	10	-1	-1	-1	-1	1
Mn	734	_	752	766	408	151	376	193	540
Co	3	_	_	_	4	2	0	2	2
Ni	3	7	27	5	1	-1	-1	-1	-1
Cu	7	5	7	4	8	3	1	3	-1
Zn	22	127	108	84	18	35	50	31	29
Sn	2	2	<2	<2	-2	6	3	-2	0
Ga	17	20	18	19	15	22	20	23	22
Ag	3	1	2	2	2	2	1	1	2
Ge	2	_	1.5	1.5	3	3	3	3	3
Quartz	16.11	2.84	12.54	11.96	38.78	35.33	35.4	49.76	40.11
Corundum	1.77		1.56	0.48		0.46	0.05	4.11	1.8
Zircon	0.18	0.14	0.12	0.14	0.04	0.04	0.04	0.05	_
Orthoclase	40.43	34.87	44.8	42.5	16.65	35.34	31.24	29.12	28.58
Albite	21.58	8.04	25.39	27.08	38.33	21.92	22	12.1	20.73
Anorthite	4.83	16.44	3.25	5.76	2.03	2.54	6.11	0.19	2.17
Diopside		10.2			3.8				
Di(CaMg)		8.16			1.72				
Hedenbergite		4.04			2.08				
Hypersthene	8.29	18.72	7.5	6.91		2.43	4.31	1.93	3.17
Enstatite	3.54	10.68	2.91	2.37		0.57	1.92	0.4	0.32
Ferrosilite	4.75	8.04	4.59	4.54		1.85	2.4	1.53	2.84
Magnetite	1.51	2.98	1.32	1.31	0.3	0.49	0.65	0.42	0.72
Chromite			0.02						
Ilmenite	1.1	2.26	0.95	0.95	0.17	0.17	0.32	0.15	0.19
Apatite	0.41	0.36	0.31	0.3	0.02	0.02	0.07		0.02
Diff. Index	78.12	45.75	82.73	81.54	91.76	92.59	86	91	89.42
Colour Index	11.31	34.17	9.79	9.17	4.29	3.09	5.31	2.54	4.08
PI	26.41	24.48	28.64	32.83	40.37	24.45	25.37	12.29	22.9
Norm Plag	18.31	87.16	11.36	17.53	5.04	10.37	13.27	1.56	9.47
100An/(An+Ab)	18.31	87.16	11.36	17.53	5.04	10.37	13.27	1.56	9.47
Ab	21.58	6.04	25.39	27.08	38.33	21.92	22	12.1	20.73
Q	16.25	7.86	14.45	13.7	38.78	35.93	34.31	50.25	40.85
Cl	6.15	13.89	5.56	5.17		1.83	3.19	1.46	2.42
Ne	11.69	4.36	13.76	14.68	20.78	11.86	11.92	8.56	11.24
Q	28.13	11.54	26.06	26.1	54.34	45.97	44.39	55.79	50.35
mg number	40.32	56.67	38.94	34.33	43.71	25.14	46	21.54	11.44

		Pul Pul Rhyolite: fluvial deposits							
Sample Number	8912-3114	8912-3022a	8912-3022b	8912-3028	8912-3029	8912-3045	8912-3142	8912-3143	8912-3144
Unit	rhyolite dome/sill	medium sandstone	medium sandstone	medium sandstone	coarse sandstone	fine sandstone	medium sandstone	coarse sandstone	medium sandstone
Easting	256700	247900	247900	248200	248300	248200	250000	250000	249900
Northing	8484400	8487900	8487900	8487600	8487700	8487600	8486000	8486100	8486000
SiO2	76.08	75.38	76.1	74.16	72.8	70.42	80.29	71.8	69.83
TiO2	0.08	0.27	0.3	0.31	0.4	0.53	0.29	0.5	0.47
Al2O3	11.97	10.4	10.63	9.98	10.55	12.81	7.02	9.13	11.85
Fe2O3tot	1.76	2.82	2.82	3.17	3056	4.28	2.92	4.79	4.14
Fe2O3	1.29	1.13	1.02	1.18	1.95	3.02	1.06	1.6	
FeO	0.44	1.34	1.62	1.79	1.45	2.53	2.2	3.36	2.29
MnO	0.02	0.05	0.05	0.07	0.06	0.08	0.07	0.1	0.08
MgO	0.27	1.39	1.32	1.91	1.63	1.21	1.83	3.47	1.35
CaO	0.01	0.92	0.26	1.28	2.48	1.44	0.95	1.58	2.38
Na2O	2.22	2.08	2.06	1.96	1.71	2.54	0.9	1.26	1.93
K2O	6.36	3.82	4.39	3.63	3.89	4.33	3.06	2.91	4.51
P2O5	0.01	0.07	0.09	0.09	0.14	0.11	0.1	0.18	0.12
rest	1.28	2.7	1.76	3.01	2.73	2.27	2.53	4.4	3.59
L.O.I.	0.22	0.23	0.31	0.23	0.31	0.24	0.22	0.25	0.23
TOTAL	100.25	99.78	99.91	99.6	100.1	99.98	99.94	100	100.23
Ba	161	383	478	523	1063	474	584	888	540
Li	12	11	23	21	24	23	16	29	16
Rb	211	187	200	197	169	211	110	103	215
Sr	10	53	61	55	118	98	58	64	90
Pb	8	19	26	17	28	36	14	13	47
Th	51	38	38	33	33	39	19	21	38
U	12	10	9	9	9	10	6	7	11
Zr	220	191	203	196	198	220	144	162	217
Nb	27	15	16	13	14	17	8	10	17
Y	50	32	33	31	34	37	17	31	38
La	100	50	54	53	50	57	25	38	50
Ce	195	96	97	97	102	112	51	71	104
Nd	80	41	42	43	48	19	33	45	45
Sc	1	6	8	8	9	10	7	12	10
V	-2	22	23	30	51	48	29	63	43
Cr	1	47	53	60	103	62	85	141	86
Mn	157	475	458	612	523	727	579	973	703
Co	5	6	6	8	10	9	9	15	12
Ni	-1	14	14	17	27	20	19	40	25
Cu	-1	-1	6	-1	3	2	2	1	17
Zn	50	80	91	121	136	128	70	136	101
Sn	5	3	-2	3	-2	-2	5	-2	-2
Ga	17	15	16	14	14	17	10	14	17
Ag	1	2	2	2	2	2	2	2	2
Ge	3	3	3	3	3	3	3	4	3
Quartz	37.44	43.49	43.16	41.9	39.25	32.42	57.37	42.91	32.72
Corundum	1.41	1.28	2.16	0.64		1.51	0.67	1.38	
Zircon	0.04	0.04	0.04	0.04	0.04	0.04	0.03	0.03	0.04
Orthoclase	37.67	22.85	26.02	21.53	23.05	25.67	18.13	17.24	28.74
Albite	18.79	17.6	17.43	18.58	14.47	21.49	7.82	10.66	16.33
Anorthite	0.02	4.23	0.84	5.92	9.61	6.59	4.23	6.88	10.32
Diopside					1.74				0.73
Di(CaMg)					0.99				0.35
Hedenbergite					0.75				0.38
Hypersthene	2.83	6.13	6.14	8.03	8.77	7.23	7.58	13.53	7.15
Enstatite	0.67	3.46	3.29	4.76	3.81	3.01	4.58	8.64	3.2
Ferrosilite	1.98	2.67	2.65	3.28	3.18	4.22	3.03	4.89	3.95
Magnetite	0.52	0.76	0.82	0.93	1.04	1.25	0.85	1.4	1.21
Chromite		0.01	0.01	0.01	0.02	0.01	0.01	0.03	0.02
Ilmenite	0.15	0.51	0.57	0.59	0.78	1.01	0.55	0.95	0.89
Apatite	0.03	0.17	0.23	0.22	0.34	0.26	0.24	0.43	0.29
Diff. Index	93.89	83.74	87.05	80.01	76.77	79.59	83.11	70.81	75.79
Colour Index	3.3	7.42		9.58	10.33	9.5	9	15.91	10.01
Pt	18.81	21.83		22.51	24.08	28.08	11.85	17.52	28.65
Norm Plag	0.12	19.37		26.31	39.91	23.46	35.74	39.16	38.73
100An/(An+Ab)	0.12								
Ab	18.79	17.6		16.58	14.47	21.49	7.62	10.66	16.33
Q	38.09	45.13		44.08	41.05	34.28	59.42	46.61	34.58
Or	1.99	4.49		5.88	4.97	5.37	5.53	9.83	5.29
Ne	10.18	9.54		8.99	7.84	11.65	4.13	5.76	8.85
Q	46.7	53.19		51.86	47.68	44.13	62.91	51.49	42.06
mg number	27.31	56.78		59.87	53.12	41.18	60.76	64.18	44.64

	Big Sunday Formation							
Sample	8912-	8912-	8912-	8912-	8912-	8912-	8912-	8912-
Number	3081	3025	3035	3077	3079	3145	3154	3156
Unit	qtz-rich turbidite	tuffaceous siltstone	crystal-rich	pumice-bearing	pumice-bearing	crystal-rich	crystal-rich	crystal-rich
Easting	246700	248600	247900	246700	246700	249900	246800	246800
Northing	8488900	8484800	8487600	8488700	8488700	8488000	8489000	8489000
SiO2	76.85	74.8	72.95	72.82	73.16	62.09	76.17	76.63
TiO2	0.42	0.17	0.61	0.32	0.34	0.41	0.53	0.58
Al2O3	7.73	12.28	8.89	11.84	10.98	6.35	8.51	8.53
Fe2O3tot	3.56	2.07	6.23	3.1	3.09	3.24	4.14	4.67
Fe2O3	0.48	1.03	1.34	0.92	1.04	0.87	1.31	1.43
FeO	2.29	0.94	4.4	1.96	1.98	2.13	2.55	2.92
MnO	0.1	0.05	0.09	0.12	0.1	0.08		0.08
MgO	2.81	0.36	2.08	1.5	1.06	1.25	2.07	2.05
CaO	1.25	1.22	2.46	0.97	1.87	1.16	0.98	1.1
Na2O	1	2.73	1.48	2.01	2.18	0.59	1.1	1.03
K2O	2.72	3.51	1.81	4.51	4.17	2.83	3.83	3.45
P2O5	0.16	0.03	0.12	0.09	0.11	0.1	0.12	0.13
rest	3.64	2.87	3.57	2.86	2.9	2.36	2.71	2.18
L.O.I.	0.25	0.18	0.2	0.26	0.24	0.2	0.27	0.26
TOTAL	100.08	99.77	99.98	99.98	99.98	100.42	100.22	100.37
Ba	654	119	490	564	627	598	798	643
Li	50	9	26	20	23	16	27	39
Rb	115	210	87	242	203	100	153	119
Sr	48	31	55	66	87	59	61	81
Pb	15	26	177	21	27	15	16	28
Th	15	53	16	41	39	14	18	20
U	5	12	5	10	10	4	5	5
Zr	143	195	157	246	221	167	191	205
Nb	7	22	8	17	17	8	9	9
Y	20	44	24	35	34	17	23	22
La	36	54	33	60	50	32	34	32
Ce	70	111	53	113	104	54	61	64
Nd	30	50	24	49	43	24	26	29
Sc	10	4	15	8	9	8	8	10
V	50	7	72	24	28	36	52	50
Cr	118	12	67	56	67	57	73	85
Mn	915	428	813	1161	955	491	699	696
Co	14	11	14	7	8	10	14	14
Ni	31	4	21	16	18	18	24	26
Cu	8	4	40	4	4	2	2	8
Zn	73	44	87	68	68	55	97	115
Sn	-2	18	12	16	15	7	10	13
Ga	10	3	8	4	5	2	2	2
Ag	2	2	2	2	2	1	2	2
Ge	3	3	3	2	2	3	3	3
Quartz	52.67	41.13	46.44	38.17	37.84	62.15	48.28	50.13
Corundum	1.15	1.81	0.24	1.83		0.34	0.97	1.32
Zircon	0.03	0.04	0.03	0.05	0.04	0.03	0.04	0.04
Orthoclase	16.12	20.82	10.73	26.75	24.72	16.76	22.69	20.43
Albite	8.46	23.1	12.52	17.01	18.45	4.99	9.31	8.72
Anorthite	5.34	5.9	11.57	4.4	7.62	5.38	4.31	4.81
Diopside					0.78			
Di(CaMg)					0.38			
Hedenbergite					0.4			
Hypersthene	10.12	3.11	11.38	6.89	5.42	6.28	8.28	9.69
Enstatite	8.5	0.9	5.13	3.74	2.48	3.11	3.11	5.11
Ferrosilite	3.62	2.21	6.25	3.25	2.96	3.17	3.17	4.59
Magnetite	1.05	0.6	1.82	0.9	0.9	0.95	0.95	1.37
Chromite	0.03		0.01	0.01	0.01	0.01	0.01	0.02
Ilmenite	0.8	0.32	1.16	0.61	0.65	0.78	0.78	1.1
Apatite	0.39	0.07	0.29	0.22	0.26	0.24	0.24	0.32
Diff. Index	77.25	85.05	89.69	81.92	81.01	83.91	83.91	79.28
Colour Index	12	4.03	14.47	8.53	7.78	8.02	8.02	12.18
Pl	13.81	29	24.1	21.41	26.27	10.37	10.37	13.52
Norm Plag 100An/(An+Ab)	38.71	20.34	48.03	20.54	29.77	51.87	51.87	35.54
Ab	8.46	23.1	12.52	17.01	18.45	4.99	4.99	8.72
Q	55.44	41.9	49.4	40.03	39.25	63.81	63.81	52.7
Or	7.35	2.33	8.42	5.13	4.01	4.63	4.63	7.12
Ne	4.59	12.52	8.79	9.22	10	2.71	2.71	4.72
Q	59.32	52.48	55.14	47.82	47.7	66.09	66.09	58.69
mg number	84.31	30.05	45.01	54.51	45.92	48.87	48.87	52.05

	Coronation Sandstone									
Sample Number	8912-3001	8912-3004	8912-3009	8912-3014	8912-3017a	8912-3018	8912-3084	8912-3088	8912-3117a	8912-3117b
Facies	basalt	basalt	high-Si bit (mingling)	high-Si bit (mingling)	high-Si bit (mingling)	high-Si bit (mingling)	high-Si bit (mingling)	high-Si bit (mingling)	basalt	rhy. mingling with basalt
Easting	254100	254300	253400	252500	252500	252400	246300	245900	Core Sat 255600	255600
Northing	8487400	8487000	8487100	8487500	8487300	8487500	8492100	8492200	8487300	8487300
SiO2	49.44	56.46	62.15	61.38	55.45	61.86	64.19	63.61	54.35	75.03
TiO2	1.32	1.41	0.5	0.68	0.71	0.52	0.64	0.69	1.46	0.5
Al2O3	14.85	14.68	13.21	14.46	16.6	14.16	12.17	12.82	15.06	9.85
Fe2O3tot	11.9	10.66	5.21	6.14	7.65	6.49	5.25	4.89	10.81	4.04
Fe2O3	3.89	4.91	1.42	3.05	4.04	3.7	2.69	2.15	6.55	2.44
FeO	7.21	5.17	4.31	2.78	3.25	2.51	2.3	2.47	3.83	1.44
MnO	0.19	0.14	0.12	0.1	0.07	0.09	0.08	0.1	0.12	0.03
MgO	7.21	3.01	4.51	3.84	5.27	3.59	3.35	3.95	3.41	1.38
CaO	6.52	4.71	3.63	5.17	5.49	5.1	3.01	2.59	3.86	1.9
Na2O	2.42	2.78	2.64	2.77	2.91	2.75	1.48	1.98	2.84	1.57
K2O	2.44	3.13	4.69	4.11	2.23	3.96	7.28	5.88	4.18	3.73
P2O5	0.42	0.84	0.28	0.36	0.32	0.3	0.62	0.58	0.88	0.28
treat	3.79	2.45	2.04	1.05	3.23	1.1	1.68	3.03	3.19	0.33
LOI	0.38	2.46	0.57	0.43	0.97	0.41	0.43	0.41	0.4	1.48
TOTAL	100.08	100.17	100.01	100.18	99.94	100.15	99.93	100.26	100.13	99.96
Ba	1363	2086	2291	1499	917	1382	1564	1400	1575	1106
Li	40	32	21	12	32	11	18	30	27	14
Rb	110	88	210	142	99	134	280	253	168	113
Sr	256	355	320	430	405	409	267	307	281	201
Pb	19	28	58	41	24	33	20	40	17	29
Th	3	16	47	30	34	31	40	37	17	17
U	2	5	11	7	8	8	12	12	4	4.5
Zr	137	246	198	220	238	206	316	303	255	161
Nb	7	13	11	13	13	12	14	13	13	12
Y	26	32	24	26	31	26	29	26	35	27
La	32	64	98	73	59	67	83	70	66	53
Ce	57	129	162	134	125	132	156	136	136	91
Nd	29	59	64	57	56	54	70	62	64	37
Sc	25	20	18	19	22	18	16	15	21	11
V	165	196	97	107	99	94	82	100	211	53
Cr	253	6	417	200	310	255	129	110	4	68
Mn	1509	1162	1110	878	630	828	737	883	1091	285
Co	42	24	20	20	27	21	15	14	24	8
Ni	86	4	57	32	61	49	30	29	5	26
Cu	20	15	3	33	-1	13	-1	2	1	5
Zn	218	205	275	85	141	99	177	236	194	36
Sn	-2	-2	3	-2	2	-2	3	-2	-2	-2
Ga	19	20	15	18	22	17	3	3	21	12
Ag	3	3	2	2	3	2			3	2
Ge	2	2	2	2	3	1			4	3.5
Quartz	_	11.16	13.41	12.63	7.51	14.01	16.73	17.54	6	
Zircon	0.03	0.05	0.04	0.04	0.05	0.04	0.06	0.06	0.05	
Orthoclase	14.46	18.53	27.44	24.34	13.22	23.45	43.19	34.85	24.77	
Albite	20.48	23.52	22.34	23.44	24.62	23.27	12.52	16.75	24.03	
Anorthite	22.43	18.38	10.55	14.91	25.54	14.62	4.99	8.7	13.9	
Diopside	6.24	0.13	5.18	7.3	_	7.58	5.21	0.67		
Di(CaMg)	3.95	0.06	3.44	4.69	_	4.61	3.39	0.47		
Hedenbergite	2.28	0.07	1.74	2.62	_	2.97	1.82	0.2		
Hypersthene	21.13	17.66	15.27	12.15	20.86	11.86	10.97	14.21	18.78	
Enstatite	12.71	7.47	9.68	7.41	13.13	6.82	6.79	9.62	8.49	
Ferrosilite	8.42	10.19	5.61	4.75	7.77	5.04	4.18	4.58	10.28	
Olivine	4.15									
Forsterite	2.4									
Fayalite	1.75									
Magnetite	3.49	3.13	1.82	1.8	2.24	1.9	1.54	1.44	3.18	
Chromite	0.05	_	0.09	0.04	0.07	0.05	0.03	0.02		
Ilmenite	2.51	2.68	0.95	1.29	1.35	1.18	1.22	1.31	2.77	
Apatite	1	2.03	0.68	0.86	0.76	0.72	1.5	1.41	2.12	
Diff. Index	34.94	53.21	63.2	60.41	45.35	60.74	72.44	69.14	54.8	
Colour Index	37.57	23.61	23.31	22.59	24.55	22.57	18.98	17.65	24.73	
Fl	42.91	41.91	32.68	38.35	50.16	37.89	17.52	25.46	37.93	
Norm Plag	52.27	49.87	32.07	38.88	50.19	38.59	28.5	34.18	36.64	
Fe#An/(An+Ab	52.27	49.87	32.07	38.88	50.19	38.59	28.5	34.18	36.64	
Ab	20.48	23.52	22.34	23.44	24.62	23.27	12.52	16.75	24.03	
Q	5.72	15.71	17.58	15.92	13.2	17.2	19.71	21.46	10.89	
Or	19.56	13.1	11.1	8.86	15.2	8.67	7.99	10.26	13.89	
Ne	11.1	12.75	12.11	12.7	13.95	12.61	6.79	9.08	13.02	
Cl	15.1	26.49	27.81	26.66	24.48	27.89	25.45	29.14	21.89	
mg number	58.99	41.15	64.26	56.76	63.03	57.8	61.25	66.64	43.86	

Sample	8912-3026	8912-3027	8912-3038	8912-3057	8912-3072	8912-3103	8912-3105	8912-3115	8912-3136b
Number									
Facies	dolerite intrusion	dolerite intrusion	dolerite intrusion	dolerite intrusion	dolerite intrusion	dolerite intrusion	dolerite intrusion	dolerite intrusion	xenolith in Lower lg.
Easting	248000	247800	247700	246100	249800	264500	257900	256800	258000
Northing	8488400	8487100	8487200	8493500	8488400	8491100	8486900	8486100	8487600
SiO2	48.04	48.84	51.24	46.55	50.95	50.28	51.23	43.7	51.81
TiO2	2.38	1.72	1.54	1.77	0.96	1.16	1.49	1.82	1.28
Al2O3	12.97	14.32	14.99	14.83	14.71	12.73	13.3	13.84	17.38
Fe2O3tot	16.26	12.81	11.37	15.17	9.95	9.49	11.89	14.74	9.87
Fe2O3	4.85	4.01	3.47	5	0.89	3.22	4.02	3.43	2.32
FeO	10.27	7.92	7.11	9.15	8.24	5.64	7.08	10.16	6.79
MnO	0.22	0.13	0.15	0.21	0.15	7.48	0.16	0.21	0.12
MgO	5.34	5.36	4.45	7.76	8.04	7.48	3.33	5.96	4.16
CaO	8.08	7.45	6.8	5.66	6.6	4.4	6.03	7.29	3.8
Na2O	2.27	1.96	3.05	2.21	1.83	2.44	3.97	2.34	5.13
K2O	1.62	1.64	2.35	1.71	2.39	2.4	1.38	0.88	3.64
P2O5	0.21	0.58	0.68	0.51	0.49	0.41	0.21	0.22	0.47
resat	3.05	5.69	3.71	4.21	4.23	9.02	7.75	10.08	2.61
L.O.I.	0.23	0.35	0.39	0.34	0.43	0.33	0.26	0.21	0.35
TOTAL	99.73	99.97	99.93	99.71	99.84	99.72	100.21	99.96	99.86
Be	323	1019	1271	785	1120	610	392	169	225
Li	38	47	38	37	26	193	19	11	44
Rb	76	51	81	110	98	87	45	133	482
Sr	224	329	520	284	307	320	93	49	125
Pb	18	16	12	17	16	20	18	8	9
Th	2	7	10	4	13	6	9	28	10
U	1	2	2	1	2	2	2	4	5
Zr	125	171	227	190	180	145	341	127	171
Nb	12	10	12	8	9	11	15	6	16
Y	29	36	36	36	23	29	52	29	45
La	17	43	59	27	58	48	45	10	65
Ce	42	94	121	63	123	93	87	26	129
Nd	20	49	57	36	56	44	46	16	57
Sc	38	28	24	30	29	30	32	40	30
V	442	181	182	213	173	196	136	187	166
Cr	29	244	194	305	626	199	135	126	511
Mn	1775	1217	1182	1712	1310	1965	1419	1918	1071
Co	51	35	36	49	34	31	31	4	29
Ni	36	58	37	124	114	56	14	59	76
Cu	72	29	21	37	12	37	115	59	-1
Zn	194	137	126	214	199	412	276	255	199
Sn	-2	-2	-2	-2	-2	-2	-2	-2	-2
Ga	23	20	20	23	18	16	23	12	31
Ag	4	3	3	3	4	3	4	1	3
Ge	4	3	3	4	3	4	4	3	5
Quartz	0.37	4.82	2.11	_	3.85	3.51	3.28	_	_
Zircon	0.03	0.03	0.05	0.04	0.04	0.03	0.07	0.03	0.03
Orthoclase	10.79	9.71	13.92	10.15	14.16	14.22	8.17	4.07	21.7
Albite	19.21	16.58	25.81	18.7	13.79	20.65	33.59	19.8	34.69
Anorthite	19.75	25.39	20.25	24.92	25.77	16.34	14.36	25.22	13.5
Diopside	15.89	6.74	7.91	0.12	3.39	2.5	11.98	7.91	1.97
Di(CaMg)	8.03	3.76	4.29	0.07	2.35	1.75	5.41	4.32	1.1
Hedenbergite	7.86	2.99	3.62	0.05	1.04	0.75	6.57	3.59	0.87
Hypersthene	20.33	22.21	17.93	26.4	28.52	26.6	13.85	21.87	
Enstatite	9.58	11.61	9.1	14.88	18.94	17.82	5.79	11.2	
Ferrosilite	10.75	10.59	8.83	11.53		8.78	8.06	10.67	
Olivine				5.74				2.36	13.84
Forsterite				3.1				1.15	6.9
Fayalite				2.64	9.58			1.21	6.94
Magnetite	4.81	3.75	3.34	4.44	2.92	2.79	3.48	4.32	2.89
Chromite	0.01	0.05	0.04	0.07	0.13	0.04	0.03	0.03	0.11
Ilmenite	4.52	3.27	2.92	3.36	1.82	2.2	2.83	3.46	2.43
Apatite	0.5	1.38	1.63	1.22	1.17	0.98	0.5	0.52	1.12
Diff. Index	30.36	31.12	41.83	28.85	31.6	38.37	45.04	29.87	56.38
Colour Index	45.84	36.02	32.24	40.13		34.35	32.17	40.18	21.26
Pl	38.96	41.96	46.06	43.62		36.98	47.96	45.02	48.18
Norm Plag	50.7	60.49	43.97	57.13		44.18	29.95	56.02	28.01
100An/(An+Ab	50.7	60.49	43.97	57.13		44.18	29.95	56.02	23.72
Ab	19.21	16.58	25.81	18.7		20.65	33.59	19.8	43.41
Q	5.69	10.71	6.84	7.08		10.84	6.85	5.78	_
Or	15.02	16.32	13.19	25.07		19.27	10.28	18.45	13.84
Ne	10.41	8.99	13.99	10.14		11.19	18.21	10.73	23.53
Q	14.48	18.31	18.66	15.64		20.29	22.23	14.85	15.89
mg number	44.84	50.87	49.2	55.88		66.12	40.95	50.02	51.07

APPENDIX A3

PETROGRAPHIC ANALYSES

PINE CREEK INLIER

Quantitative point counts of selected samples of the Pul Pul Rhyolite and Big Sunday Formation are documented in this Appendix. The number of grains counted for each sample is given (n). Other abbreviations are as follows:

- Crystals: Qv = volcanic quartz; Qm = metamorphic quartz; Qgl = composite quartz grains (glomeroporphyritic aggregates); Ks = K-feldspar; Kp = perthite; Km = microcline; Pl = plagioclase (grains exhibiting multiple twinning); F(gl) = glomeroporphyritic aggregates of feldspar (K-feldspar±plagioclase); Mt = opaques (magnetite or ilmenite); Zr = zircon; Fl - fluorite;

- Secondary minerals: Ch = chlorite; Ep = epidote; Ser = sericite; Ca = calcite;

- Lithic clasts: Lms = metasedimentary basement clasts, usually highly strained or unstrained composite quartz grains (quartzite?), and minor composite quartz-sericite aggregates; Lgn = highly strained metasedimentary basement clasts (gneiss and mylonite); Lss = sandstone; Ls = metasiltstone; Lch = fine-grained microgranular cherty mosaics which display no remnant volcanic textures or phenocrysts (interpreted to represent groundmass/matrix of volcanic clasts); Lv = undifferentiated volcanic clasts, including vitriclasts; Lpo = volcanic clasts containing euhedral phenocrysts (interpreted to be porphyries, pumice and/or juvenile vitriclasts); Lig = volcanic clasts exhibiting compacted shards and/or angular crystal fragments indicative of a pyroclastic origin (interpreted to be ignimbrite clasts); Lrh = layered rhyolite clasts (cognate lithic clasts); Ltr = clasts exhibiting a subtrachytic texture; Lalt = altered mafic(?) volcanic clasts; Ld = mafic volcanic clasts (dolerite and basalt);

- Others: Mat = matrix/groundmass; Pu = pumice; Pu2 = Fe-rich pumice (in the Middle Ignimbrite Member).

Total quartz (Q%), feldspar (F%), lithic (L%), pumice (P%) and matrix/groundmass (M%) contents, recalculated as a percentage of total count, are also presented. Total matrix/groundmass contents include secondary mineral counts.

Sample No.	Facies	%Q	%F	%L	%M	%P	crystals Qv	Qm	Ks	Kp	Km	Pl	Fgl	Mt	Zr	Fl	secondary Ch	Ep	Ca	lithic clasts Lms	Lgn	Lss	Ls	Lch	Lv	Lpo	Lig	Lrh	Ltr	Lalt	Ld	Mat	Pu	Pu2	n
PUL PUL RHYOLITE																																			
Lower Ignimbrite Member																																			
89123137	2b	7.6	5.2	24.4	62.3		62	16	40			8	4	3						40		68								65	71	623			1000
89123104	2b	14.2	9.2	17.0	42.6	16.9	62	80	74	11		7		1	1	3	13		6	55		6			23	24	22		4		36	403	169		1000
89123106	2bL	8.5	6.0	9.3	60.4	14.9	55	47	61	3		6	2	10			4	2	3	58		1	1			7	2			1	42	716	179		1200
89123136	2b	6.1	4.5	14.9	74.5		48	13	34			9	2				1			58		11			4		2				74	744			1000
89123132	2bL	3.8	1.7	41.8	41.9	10.7	18	9	10	2				1			17	3	13	11	5	2			35	174	13				60	268	77		718
89123134a	2b	8.0	5.0	14.1	39.3	35.3	55	17	46			11	3	3		2	7			22	1	3			28	15	18	14		4	64	483	424		1200
89123134b	2b	2.8	3.7	58.9	27.9	6.0	8	4	12			4		3			2	1		4	3				6	120				122	114	26		433
89123107	2b	12.6	6.9	8.2	39.1	29.7	83	58	48	6	1	12	9	37		7	34	2	12	30		3			13	3	3			2	36	375	327		1100
																				0															
Cognate Lithic-bearing Ignimbrite																				0															
89123138	2b	5.1	7.6	47.4	33.1	5.2	38	17	59	1		6	2	5			10	4		39						8		335	6		39	284	47		900
89123180	2b	5.8	7.0	24.6	46.0	15.8	36	22	60	2		6	2	8			5	2		32		2			10		151			51	453	158		1000
89123191	2b	5.4	6.9	38.4	45.6	3.3	29	20	49	10		3		3				29	1	51		2		2	30		182			79	380	30		900
89123135	2b	5.1	7.1	10.2	52.3	25.4	40	21	28	1		49	7				14	8	4	50	3			1			155	1		67	601	150		1200
89123052	2b	4.3	8.2	26.4	47.8	11.2	31	21	60			37	1	2		2	13	1		63	2	1			12	1	222	6		34	557	134		1200
																				0															
Rheomorphic Ignimbrite																				0															
89123090	2b	2.5	5.7	4.8	86.6		20	5	40			17		6			2			5					4	1			24	12	864			1000
89123179a	2b	1.8	0.6	0.6	96.4		6	3				3		3						1										2	482			500
89123096	2b	5.0	4.1	4.3	64.8	21.5	34	16	17			17	7	2						8		14								21	649	215		1000
89123097	2b	1.8	1.6	3.6	31.6	61.4	6	3	2				6							0	14									4	158	307		500
																				0															
Middle Ignimbrite Member																				0															
89123047	2b	2.9	7.3	1.2	64.5	23.6	25	9	72			16		5		7	15			13										1	752	285		1200
89123139	2b	2.3	5.4	3.2	58.1	30.5	16	11	42	1		21	1	7			5			17					1					20	692	366		1200
89123024B	2b	3.8	7.5	2.7	64.2	21.3	34	13	58			29	3	5		1	16			17						2				13	753	256		1200
89123048	2b	3.6	5.6	3.4	56.3	30.8	26	18	49			17	2	3						23			2	3						13	579	372		1207
89123141	2b	2.4	4.1	5.2	54.0	33.9	18	8	32			9		4		1	10	2	8	6				2						44	519	339		1000
89123125	2b	3.3	6.0	3.6	62.6	22.0	22	11	62	1		14	3	5		5	8			22	3				1					10	613	176	44	1000
89123062	2b	2.1	6.5	1.5	61.3	28.4	18	7	53			21	4	2		4	22	4		9				2	1					6	706	239	102	1200
89123082	2b	4.8	4.9	8.4	50.4	31.4	32	16	43	1		5		1			3	4	1	27						13				44	496	224	90	1000
89123230A	2b	3.2	8.9	3.6	48.3	35.5	26	6	70	5		14		5						19					4					13	483	196	159	1000
89123230B	2b	3.8	6.7	1.6	45.3	42.4	43	5	67	2		14		2		1	1			10		1	2							7	558	306	218	1237
																				0															
Upper Ignimbrite Member																				0															
89123058	Lconc.	9.7	6.5	20.3	63.5		66	30	43	11		10								68	3	15	3	14		3				95	629			990
89123203	Lconc.	5.9	8.2	18.8	44.1	23.9	71	41	102	8		13	11		1					42	3		25	10		11				183	717	389		1627
89123204	Pconc	4.0	8.8	4.8	50.9	31.7	45	40	147	7		31								36				1		2				57	1089	665		2100
89123205	Pconc	5.6	8.3	9.7	51.3	24.8	39	30	85			7	7							29	10		3	10		14				50	611	295		1190
89123043	2b	8.7	9.7	6.9	47.2	26.1	80	7	72	2		16	7	14			2			32	3				6					26	470	162	99	1000
89123152a	2b	9.1	8.8	5.0	54.5	22.6	115	40	105	10		4	29	1			16	41	2	52	2				7					24	867	384		1700
89123152b	2b	6.9	7.5	10.1	50.4	24.1	48	21	52	5		13	5	10			7	10	3	37	6				1	3	3			5	46	484	241		1000
89123089	2b	15.3	9.3	19.5	55.3		58	34	43	7		5	1	3			6			36						10				55	18	326			600
89123173	2b	10.5	4.5	28.5	43.6	11.4	84	36	21	10		10	2	5		1	7	16	2	19	1	2	3	1	16					19	221	390	109		955
89123153	2b	12.1	6.8	12.1	58.8	8.8	61	36	36	4		14		4			7	6		33	1		20		16	2				10	15	165	70		800
89123087	2b	8.0	12.4	46.4	26.9	6.4	30	18	80	4		15						3	2	19	11	2	255	1	22	2	10			7	42	210	67		800
																				0															

Sample No.	Facies	%Q	%F	%L	%M	%P	crystals Qv	Qm	Ks	Kp	Km	Pl	Fgl	Mt	Zr	Fl	secondery Ch	Ep	Ca	lithic clasts Lms	Lgn	Lss	Ls	Lch	Lv	Lpo	Llg	Lrh	Ltr	Lalt	Ld	Mat	Pu	Pu2	n
PUL PUL RHYOLITE																				0															
Co-ignimbrite breccia																				0															
89123198C		4.4	5.3	21.8	68.4		41	29	78			1	6	2						42		22		6		38					241	1094			1600
89123076E		12.2	4.6	32.8	48.0	4.5	47	32	16	6	2	6		2			3	2		31	20	33	4		13					55	57	284	29		550
Non-welded ignimbrite																				0															
89123185	2b	11.8	5.2	13.8	68.7		68	23	30	5		4	1	4			6	27	10	26	1			7	29						44	489			774
89123064	2b	8.6	7.0	4.6	79.1		55	24	50	3		8	2	5			29	13	6	12		1			21						7	664			900
89123033A	2b	9.9	5.9	2.6	81.7		113	34	67	2		17	2							27		1	4	2							4	1217			1490
89123199AIg	2b	9.5	8.7	3.2	80.4		119	33	69	12		19	1	2						31		3	1	5	1						7	1206			1500
89123199BIg	2b	9.5	7.4	10.6	72.6		68	37	62	4		12	3							45			1	8	15	3					45	797			1100
89123210	Loonc	24.7	12.4	18.3	44.6		148	99	75	33		11	5							93		3	4	9	6	1					67	446			1000
89123214	Loonc	19.2	11.2	8.8	60.8		123	69	75	22		14	1							48		4		1		3					32	608			1000
89123033B	Loonc	29.0	14.0	28.9	28.1		171	90	92	8		26								166	14	4		12							64	283			900
89123199AIith	Loonc	25.4	12.8	28.8	33.0		95	32	37	9		12	6							97		3	1	6	3	2					32	165			500
89123199Blith	Loonc	6.0	6.7	63.1	22.2		29	10	13	2		2	16							129		19	1	12	1						147	109			490
Intrusions							Qv	Qgl																											
89123002	rhy po#	11.8	14.6		73.7		101	5	43	60		9	19	0																		663			900
89123102	rhy po	20.3	24.9		54.7		105	73	195	3		0	15	4																		480			875
89123123	rhy po	24.2	25.1		49.6		215	3	206	9		0	11	10																		446			900
89123155	rhy po	12.0	16.3		70.7		90	8	54	0		14	66	5																		583			820
89123095	spqm*	0.0	10.9	0.3	88.5				51			54	4	3										3								885			1000
88126007	mqm**	0.0	49.4	0.0	50.6				33			35	98				13															157			336

rhy po = rhyolite porphyry
* spqm = sparsely porphyritic quartz monzonite porphyry
** mqm = megacrystic quartz monzonite porphyry

Sample No.	Facies	Qt%	Pt%	Lt%	Mat%	crystals Qv	Qm	Ks	Kp	Km	Pl	Fgl	Mt	Zr	secondary Ch	Ep	Ser	Ca	lithic clasts Lms	Lgn	Lss	La	Lch	Lv	Lpo	Ld	Mat	n
PUL PUL RHYOLITE																												
secondary volcaniclastic facies (fluvial deposits)																												
89123028	medium sandstone	13.8	10.6	21.0	54.4	28	41	39	1		1	12	1						51	2		12	4	5		31	272	500
89123029A	coarse sandstone	23.8	8.0	44.6	23.6	54	136	40	4		16	4							240			1	4	8	7	97	189	800
89123036	coarse conglomerate	16.3	3.3	61.4	19.0	40	88	14	5		4		3				5		176		13	1	5	8	7	220	111	700
89123056	medium sandstone	27.2	14.8	19.4	38.4	65	71	55	6		5	8	1						72	2			3	5	5	10	192	500
89123178A	med-coarse sandstone	16.6	8.8	26.3	44.8	77	56	41	14		8	7	13						128			17	5	20	4	52	358	800
89123178B	fine sandstone	27.3	13.3	24.3	34.1	130	88	73	19		5	9	8	1					143			5	1	22		23	273	800
89123178C	medium sandstone	34.6	10.9	14.8	35.9	154	123	45	18		24		5	2					65			2		13		18	311	800
89123198	fine sandstone	32.6	18.1	23.1	25.8	117	144	95	24	2	19	5	3						142		1		2	27		13	206	800
89123215	siltstone	26.9	14.1	9.1	49.9	105	110	76	21		16								58		2		9			4	399	800
89123216	siltstone	21.4	11.9	7.4	56.9	135	36	52	20		22	1	20						44					10		5	455	800
89123225	fine sandstone	20.3	14.6	13.4	51.4	119	43	65	20		27	5	3						81		1	2	9	4		10	411	800
89123228	coarse conglomerate	17.0	4.4	52.7	25.8	33	83	17	4		4						19		79			1		6	4	208	127	565
89123229	coarse conglomerate	4.4	3.8	70.9	21.0	18	4	16			3								5			2		129	190	32	106	505
88126005	conglomerate	35.2	8.5	32.6	23.8	205	94	57	3		9	3							201		50		16			10	202	850
BIG SUNDAY FORMATION																												
89123194	basal shear zone	26.2	11.6	10.1	50.2	163	119	71	25		19								79				12	2		8	502	1000
89123154	crystal-rich domain	38.8	24.4	15.0	21.8	105	89	74	32		16			1					65				8			2	108	500
89123156	crystal-rich domain	34.4	15.5	21.2	28.6	241	103	111	15		27	3		2					142				14	7		48	286	1000
89123035	crystal-rich domain	31.5	8.7	27.3	32.4	126	188	55	20		11	1	1						188	4		2	21			58	324	1000
89123068	crystal-rich domain	30.5	17.1	19.8	32.5	189	118	89	43		32	7	1						114		1		12	55		16	325	1000
89123192A	crystal-rich domain	28.7	14.9	22.0	34.3	131	70	49	28		20	7		1					105				8	14		27	240	700
89123077	pumice-bearing domain	18.5	12.9	9.1	59.5	128	57	37	52		34	6							83				2			8	595	1000
89123079	pumice-bearing domain	18.2	12.8	14.1	54.8	112	70	55	42		23	9							106				7	17		11	548	1000
89123195A	pumice-bearing domain	32.1	17.0	12.4	38.5	192	129	110	29		23								68	2			21	27		5	385	992
89123195B	pumice-bearing domain	22.3	11.4	8.5	57.4	137	92	86	21		10			3					55	1			12			10	589	1026
89123158	ignimbrite clast	10.1	3.9	13.4	72.4	102	40	27	19		8			1					97			1	17			73	1015	1400
89123192B	ignimbrite clast	8.0	6.4	14.3	71.3	90	30	52	31		12	2							97				7	8		103	1074	1506
88123080	qtz-rich coarse cgl turbidite	6.3	1.3	70.6	19.9	27	31	4	1		4						7		110		17	8	6	5		348	132	700
89123081	qtz-rich cgl turbidite	22.4	11.0	47.0	19.6	87	92	46	25		16	1					1		255			3	6	11	3	98	156	800
89123188	normal turbidite	36.5	29.8	7.5	26.2	231			93	21	36	29			2	4	27	6 23	30	7			6	1		1	115	632
89123189	normal turbidite	27.6	24.5	1.6	46.5	221			148	6	4	38		1		13	7	18 38	6	1			4			2	260	767

APPENDIX A4

MEASURED SECTIONS

PINE CREEK

The raw data for 4 measured sections are included in Appendix A4. Measured section locations are illustrated in Figure A4.1.

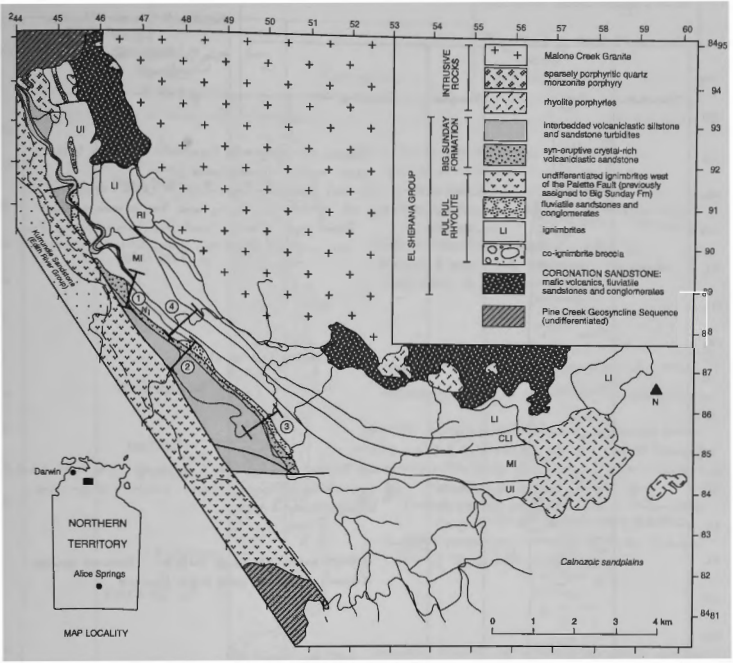

Figure A4.1: Location of measured stratigraphic sections in Appendix A4. LI = Lower Ignimbrite Member (lithic-rich ignimbrite), RI = Rheomorphic Ignimbrite (lithic-poor ignimbrite), CLI = Cognate lithic-bearing Member (lithic-rich ignimbrite), MI = Middle Ignimbrite Member (lithic-poor ignimbrite), UI = Upper Ignimbrite Member + Non-welded Ignimbrite (lithic-rich ignimbrites). Grid references for measured sections are as follows:

1: Big Sunday Formation CRVS:246800 8488800 - 246700 8488600.

2a: Big Sunday Formation turbidites: 247950 8487400 - 247950 8487300.

2b: Big Sunday Formation turbidites: 247850 8487400 - 247800 8487200.

3: Big Sunday Formation turbidites: 250000 8485950 - 249500 8485600.

4. Non-welded ignimbrite: 249000 8488000 - 247600 8487800.

Section 1: South Alligator River
Big Sunday Formation
CRUS
p 1 of 3

m	Structure	log	Samples	Description
50				
48				blocks of ignimbrite (welded) overlying contact 3cm inverse graded base (sheer)
46			8912 3212	contact between ignimbrite & CRUS: erosional
44			8912 3211	top of ignimbrite: TS to look for a non-welded flow top. Fiamme look compacted to top of pic so welded flow top probably preserved
42			8912 3197	
40				
38				welded ignimbrite
36				
34				
32				
30			* 8912 3213	small fluvial channel ~ 3 m thick. Contains blocks of ignimbrite at base, cross stratification, fine laminations at top.
28				
26				lithics more abundant (~10%). Fiamme smaller (6cm) & fewer very large fiamme.
24				
22				welded ignimbrite
20				
18				
16	140/40 to 230			
14				
12				
10				lithics up to 3cm
8				
6				large wispy fiamme in fine siliceous groundmass hematite altered (red)
4				
2	140°/44° to 230°		*photo	1cm lithics
0			* 8912 3152	

Section I: South Alligator River

Big Sunday Formation
CRUS
p 2 of 3

m	Structure/ Samples	log	Description
92			
90			0.5 m thick CRUS tongue cuts down into pumice-ash-rich domain. cross-cutting. Compaction layering of pumice clasts. fine material is winnowed from pumiceous ash-rich domains.
88	89123195 *		
86	89123077 *		diffuse boundaries between CRUS & pumice & ash-rich domains. boundaries between 2 domains are irregular
84			
82	89123079 *		
80			coarser turbidite, reverse graded, qtz-rich
78	89123080 *		reverse-grading ⇒ grainflow, loading at base
76			qtz-rich conglomeratic turbidite. erosional contact with welded ignimbrite. Load casts at basal contact with CRUS ⇒ underlying beds unconsolidated at time of deposition. Higher qtz (cuspate, milky pebbles) content than CRUS higher lithics (especially dacite)
74	100°/30° to 190° 89123088 *		rhyolite porph gry intruding CRUS. contains clast of CRUS near contact.
72		F	
		F	
	89123155 *		
70			irregular fluidal ig intrusions in CRUS. ave size = 20×30cm. grainsize of CRUS coarser than underlying unit
68	89123156 89123157 * 89123158		loading at base. concentration of lithics at base 1.5-2m relief on basal contact
66			large welded ig clast 80×40cm
64			cngl
62			5cm scour at base
60	89123154 *		diffuse laminae
58			cgl lenses in CRUS 5-10cm ig. lithics at base
56			welded ig clast 60×30cm
54			CRUS: massive, structureless, clast-supported, angular fragments, contains chlorite.
52			
50			

Section 1: South Alligator River

Big Sunday Formation
CRUS
p3 of 3

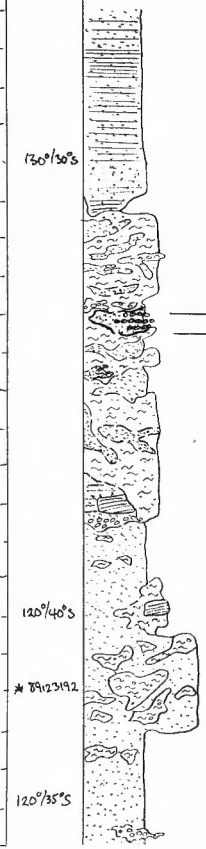

diffuse to planar laminated CRUS, fining upward. planar laminae 1-5mm

CRUS, base is irregular ± loading into underlying pumice & ash-rich domain 1m thick

pebble concentration becomes random and diffuse up section

↑ reverse grading, rounded pebbles up to 3cm at top of bed

1m

= thin pebble layer in CRUS

diffuse mix of CRUS & pumice & ash-rich domains. Pu & ash-rich material is dominant. base of unit is irregular.

large block of v. fine-grained, laminated siltstone. diffuse layering in CRUS. base of unit is erosional. Thin len of pebbles concentrated at base.

irregular, fluidal welded ignimbrite clasts in CRUS. Max clast size 65x30cm.

Soft-sediment redeposition of gravel pod

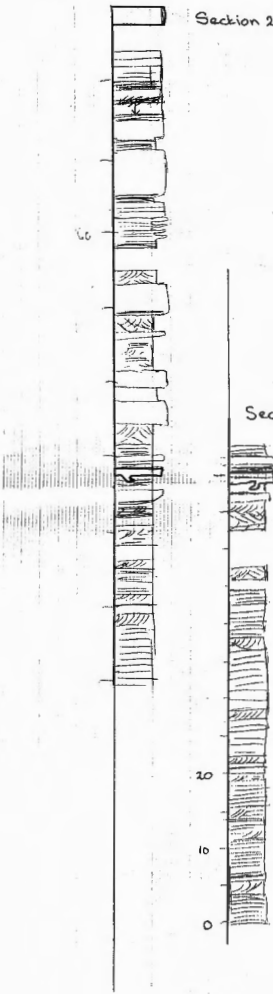

Correlation between sections 2a & 2b

Section 2a = base of turbidite sequence
section 2b begins higher in the sequence

Section 2a: side creek to South Alligator River
Big Sandy Fm turbidites
pg of 3

m	structure	grainsize clay	silt	vf	f	m	c	vc	granule mm	sample TS	Description
											No outcrop for 1m
24											massive unit, diffuse laminae. ~4 totally massive beds. ~12-15cm thick. Rest is diffusely laminated
											16cm of planar laminae.
22											1.2m diffusely layered material, as opposed to very fine, obvious // laminations. cm-scale laminae.
											50cm massive bed.
20											2-3mm thick planar laminae and cross beds.
											massive bed, 50 cem thick.
18											low angle cross stratification. Climbing ripples?
16											
14											fine planar laminations. cross beds, trough structures
											occasional massive interval, 2-6 cm thick
12											
10											
8											
6											fine planar laminations
											predominance of trough cross beds in the section:
4											
										photo	fine planar laminae 2cm - mms in width
2											
											planar laminations.
0m											

Section 2a: side section to South Alligator River

Big Sandy Fm turbidites

p2 of 3

m	structure	grainsize log	sample TS	Description
50				
48				no outcrop for 6m
				cross beds & planar laminae.
46				no outcrop.
44				
42				massive, diffusely laminated
40				
38	120°/34°			cross beds & planar laminae 
36				massive, diffusely laminated
34				
32			*	89123025
30				⇐ base of section 2b correlates with this point.
28				10cm delicate fine laminae & x beds
26				massive, diffusely laminated

Section 2a: side creek to South Alligator River

Big Sunday Fm turbidites

m	structure log	grainsize f m c g p c b	Sample	Description
62	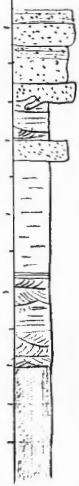			many thin, massive sst beds.
				massive medium grained sst
				massive sst, laminated at top.
60			*photo	massive bed with loading at base
				diffuse laminae
59				planar & cross laminae
				massive, medium-grained sst
57				massive, diffusely laminated interval
55				cross laminae & planar laminae
53				no outcrop.

m	Structure	grainsize clay .01 .5 v f s 2 mud 100 mm	Sample # S	Description.	Section 4b: South Alligator River, Waterfall Section Big sandy Fm turbidites p 1 of 4
44				diffuse-planar laminations and low angle cross laminations	
42				bands of low angle cross laminae & planar lamination at the top of more massive interval with diffuse laminations.	
40				massive interval, tuffaceous siltstone.	
				cross lamination.	
38				planar laminations.	
36				fine, massive tuffaceous siltstone with diffuse lamination throughout	
34					
32					
30					

Section 2a: South Alligator River Waterfall Section
Big Sunday Fm turbidites
P2 of 4

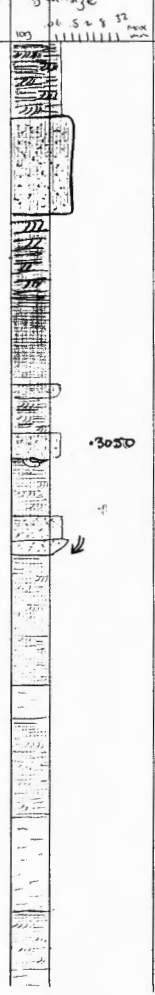

Section 2a: South Alligator River Waterfall Section
Big Sunday Fm turbidite
P 3 of 4

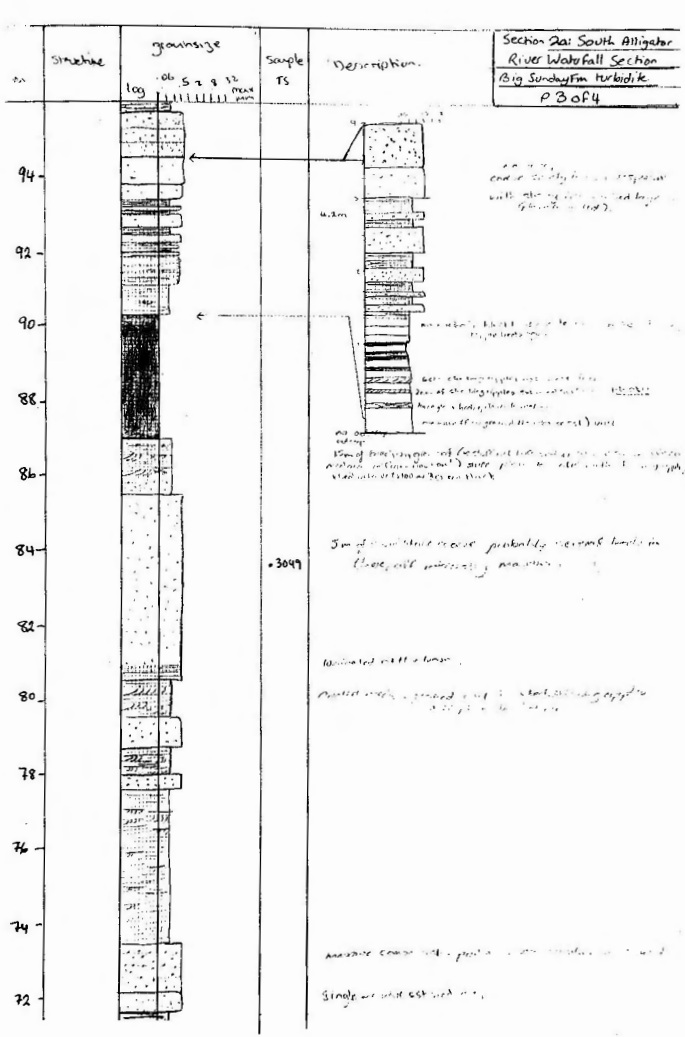

Section 2b: South Alligator River Waterfall Section
'Big Sunday Fm
P4 of 4

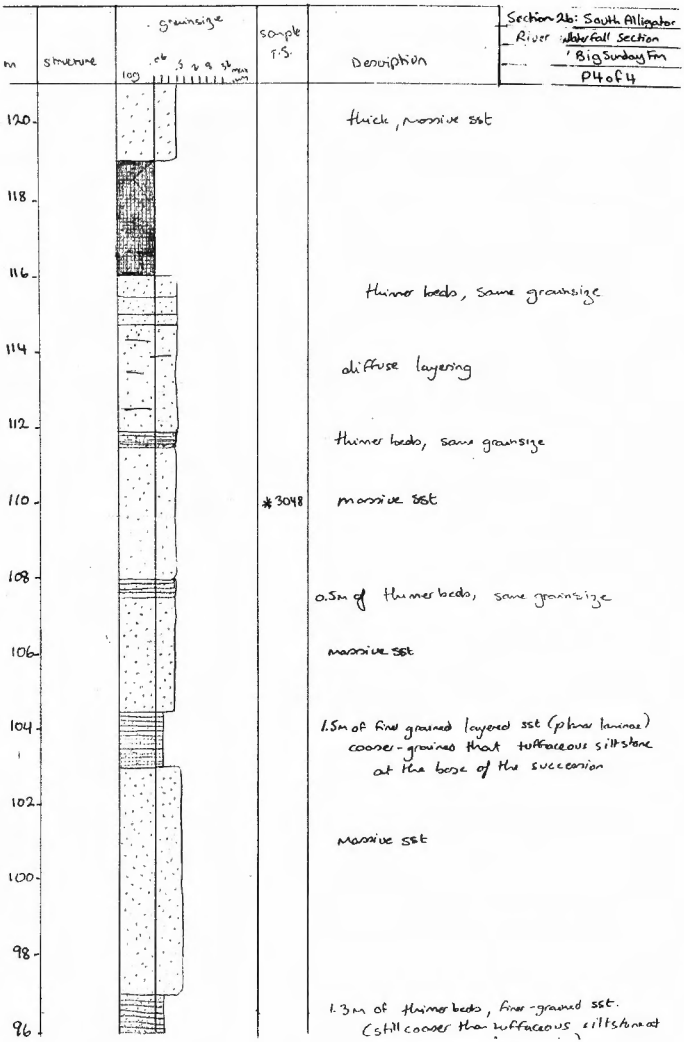

Location: Section B: tributary to South Alligator River

Pul Pul Rhyolite / Big Sunday Formation

1 of 4

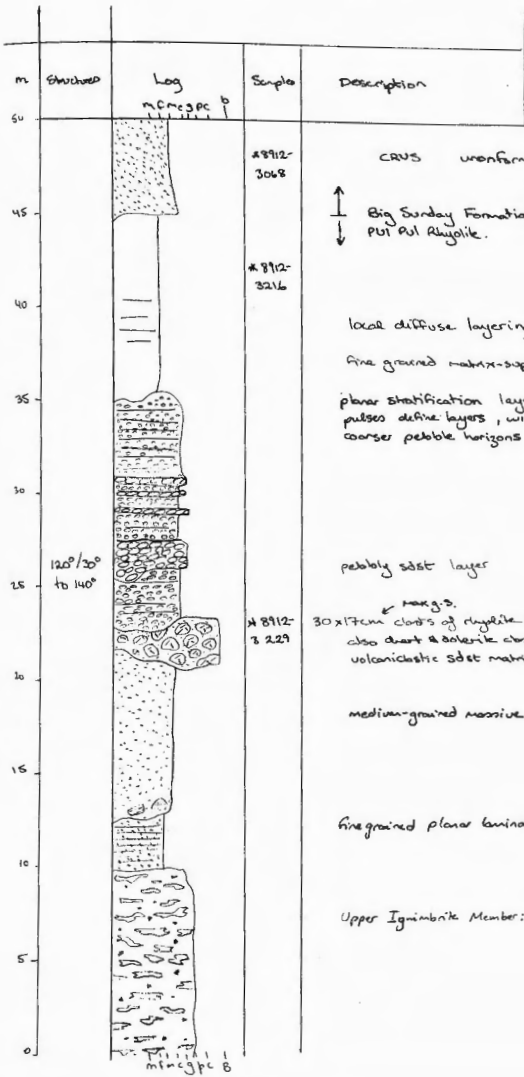

Location: Section 3. tributary to South Alligator River.

Big Sunday Formation p2of4

m	Structure	Log (m f m c g p c b)	Samples	Description
65				
64				planar laminations
63				sparsely porphyritic, flow banded rhyolite sill/dyke.
				'scabby' cross laminations (low angle)
62				massive bed, lithic clasts siltstone, some g.s. as laminated interval
61				
60				
59				Felsic sill (rhyolite, sparsely porphyritic). Flow banded.
58				exhumed ripples on top surface, layering slightly undulose
	120°/30°			parallel laminae, finely layered
57				
56				
55				
				no outcrop for ~6m.
				fining upward, diffuse - to planar laminated flow top.
50				CRUS massive

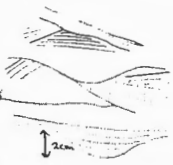

Location: Section 3
tributary to South
Alligator River
BJ Sunday Formation
p 3 of 4

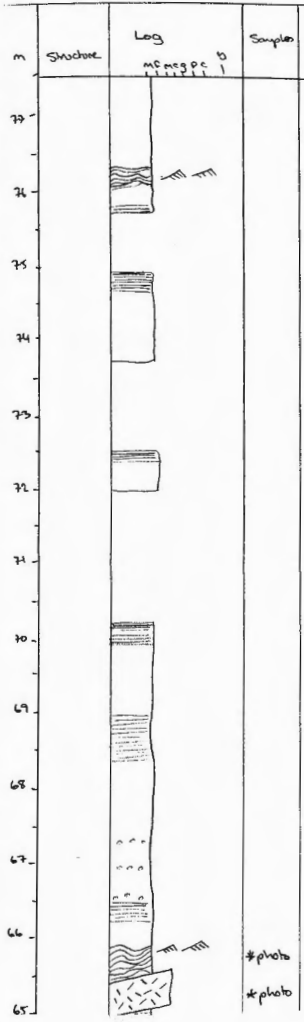

Location: Section 3. tributary to South Alligator River

Big Sunday Formation

m	Structure	Log	Samples	Description
93		Mcrigocco		
				mainly planar lamination, occasional cross laminations.
90				
87				change in scale
86				
85				
84				exhumed ripple pavement.
				planar laminations cross beds.
83				
82				
81				
80				
79				
78				

Section 4: Tributary to Sth Alliggator River

Non-welded ignimbrite p1 of 2

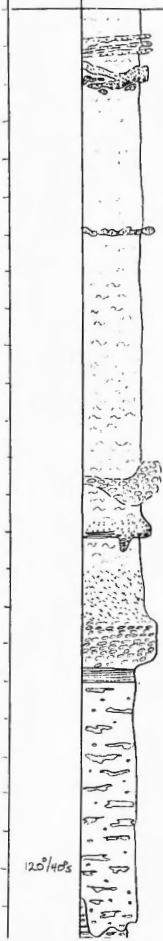

several diffuse boards of crystal-enriched material

diffuse crystal and pebble rich layers

crystal rich layer

layer 2b crystal rich ignimbrite

upper ignimbrite interior

10% lithics dolerite 2.5-20cm

dolerite rich layer

15% fiamme (flattened pumice)

contact deepens over columnar joints

middle ignimbrite interior

Section 4: Tahutong to South Alligator River
Non-welded ignimbrite
p2 of 2

98
96
94
92
90
88
86
84
82
80
78
76
75
74
73
72
71
70
69
68
67
66

crystal-rich volcaniclastic sandstone, + big sandy lenses

Flow banded rhyolite sill

unwelded 2b ignimbrite

Diffuse, irregular layers of crystal rich, coarse sand sandstone & conglomerate, interbedded with matrix supported, unwelded

coarse, clast rich, crystal-rich [illegible] sandstone (rocks at irregular base, interbedded with unwelded

APPENDIX A5

THE CULLEN EVENT: A GEOCHEMICAL DESCRIPTION OF THE CULLEN SUPERSUITE AND JIM JIM SUITE

The following Appendix includes a copy of the abstract "The Cullen Event: a major felsic magmatic episode in the Proterozoic Pine Creek Inlier of northern Australia" (Jagodzinski and Wyborn 1995), which defines and describes the tectonic setting of the ~1830 Ma post-orogenic 'Cullen Event'. This is followed by a geochemical description and comparison of the Cullen Supersuite and Jim Jim Suites. Geochemical variation diagrams of the older, syn-orogenic Nimbuwah Suite are also included for comparison.

11:00

THE CULLEN EVENT: A MAJOR FELSIC MAGMATIC EPISODE IN THE PROTEROZOIC PINE CREEK INLIER OF NORTHERN AUSTRALIA.

E.A. Jagodzinski*, Australian Geological Survey Org., P.O. Box 378, Canberra, ACT 2601, Australia and **L.A.I. Wyborn**, Australian Geological Survey Org., P.O. Box 378, Canberra, ACT 2601, Australia.

Based on new geochronological and geochemical data, volcanic and plutonic suites of the Cullen Batholith, El Sherana and Edith River Groups, are now considered to represent a single large-scale felsic magmatic event (the Cullen Event) covering a roughly circular area of at least 20 000 km2. The tectonic setting, geochemical signature and associated metallogenic styles of the Cullen Event are consistent with intracontinental rifting, with magmas derived from partial melting of a pre-existing lower crustal igneous source. The units overlie and intrude older basin sediments (~2100-1880 Ma) of the Pine Creek Inlier, which were affected by a major high T, low P compressional orogenic event (1870-1850 Ma). Previously considered to be synorogenic, the 1830-1820 Ma Cullen Event is now known to clearly postdate the thermal effects of this event by at least 40 Ma, and is associated with an unrelated extensional tectonic event. Volcanics are subaerial, proximal ignimbrites, and interbed with braidplain and lacustrine sediments. They infill rift valleys which formed on the older basin sediments during reactivation of pre-existing basement structures .

Magmatism is bimodal, consistent with extensional magmatism, and the geochemical signature is quite different to felsic arc magmas in modern subduction zones in either an island arc or continental margin environment. The granites are predominantly I- (granodiorite) type, and compared with granites associated with Phanerozoic subduction zones, they have much higher SiO_2, K, Th and U values. Multi-element, primordial-mantle-normalised abundance diagrams are Sr-depleted and Y-undepleted. This, as well as flat HREE patterns and negative Eu anomalies, indicate plagioclase stability and the absence of garnet/hornblende phases in the source region. This suggests a lower crustal, underplated source for magmas of the Cullen Event, supported by Sm-Nd model source ages for volcanics of the El Sherana Group, which range between 2000 and 2400 Ma, suggesting the source of the magmas had an extended crustal prehistory. In contrast, the Sr-undepleted, Y-depleted signature typical of granites from modern subduction settings, reflect melts derived from a deeper, higher pressure garnet-rich source, such as the upper mantle region above the subducting slab.

The Cullen Batholith is chemically fractionated, with large chemical variations both within and between individual plutons. Fractionation is controlled by mineral phases such as hornblende, muscovite, apatite, zircon and allanite, and is characterised by exponentially increasing Rb, Y and U, and decreasing K/Rb, with increasing SiO_2. Associated greisens, aplites and pegmatites indicate late stage magmatic fluid saturation. Associated Au and base metals can occur some distance from the granite, and their distribution reflects host rock interaction with ore-bearing magmatic fluids. It is probable that vapour/brine separation occurs in the ore-bearing magmatic fluids, with Au and Cu preferentially carried in a sulphur-enriched phase, and precipitating in reductant-bearing units, while Pb and Zn are transported in chloride-enriched brines that react with carbonate hosts. In addition, the most fractionated leucogranites concentrate U, Sn and W, to form vein-hosted deposits within and near the granites. These styles of mineralisation also contrast with Phanerozoic skarn-type porphyry copper (± Au, ± Mo) systems, which are associated with subduction-related granites of markedly different chemistry and morphology.

Geochemistry of the Cullen Supersuite and Jim Jim Suite

The volcanic and plutonic rocks of the Cullen Event have been divided into two groups on the basis of their chemistry; the Cullen Supersuite and the Jim Jim Suite (Wyborn et al. 1997). The Cullen Supersuite was intruded into the central part of the Pine Creek Inlier, and comprises all the plutons of the Cullen Batholith. There are no comagmatic volcanic equivalents to this suite. The Jim Jim Suite occurs in the eastern part of the Pine Creek Inlier, mainly along the western border of the McArthur Basin. The Jim Jim Suite includes the felsic volcanic sequences of the El Sherana and Edith River Groups, the Grace Creek Granite and a number of small shallow level plutons (Malone Creek Granite, Jim Jim Granite, Nabarlek Granite, Tin Camp Granite, Eva Valley Granite, Yeuralba Granite). The Cullen Supersuite and Jim Jim Suite are interpreted to have been emplaced coevally during the Cullen Event. The two suites have very similar geochemical signatures, and have been separated based on the more A-type signature and mineralogy of the Jim Jim Suite. This difference in chemistry between the suites can be attributed to melting of source rocks with different chemical characteristics.

Both the Cullen Supersuite (Stuart-Smith et al. 1993) and the Jim Jim Suite comprise predominantly felsic rocks with minor coeval doleritic magmas. The dominant silica range is from 63-79% in both suites (Figure A5.1). The Cullen Supersuite is metaluminous to weakly peraluminous, and the Jim Jim Suite progress from metaluminous to strongly peraluminous (Figure A5.2), and both suites have less than 1% normative corundum. These features define the rocks as I-type or 'infracrustal', derived from sources that have never undergone surficial weathering, based on the criteria of Chappell and White (1984). They are identified as I-(granodiorite) suites based on the classification system of Chappell and Stephens (1988). Most samples are classified as granite to adamellite, or their volcanic equivalents, rhyolite and rhyodacite (Figure A5.3), and plot in the strongly differentiated field (Figure A5.4). The Cullen Supersuite straddles the boundary between A-type and normal granites, and the Jim Jim Suite plots in the A-type field as defined by Eby (1990) for Palaeozoic granites (Figure A5.5).

The Cullen Supersuite has undergone significant chemical fractionation, and large chemical variations occur both within and between individual plutons. Fractionation is controlled by mineral phases present in each pluton, particularly hornblende, biotite, muscovite, apatite, zircon and allanite (Stuart-Smith et al. 1993). Associated greisens, pegmatities and aplites indicate a late stage release of magmatic fluid, which is consistent with a fractionating system. Chemical fractionation is characterised by an exponential increase in Rb, U, Y, and a weak increase in Th with increasing SiO_2 (Figures A5.6, A5.7, A5.8, A5.9). There is a late strong exponential increase in Rb/Sr (Figure A5.10).

Significant chemical fractionation also occurs in the Jim Jim Suite, but fractionation is suppressed in the earlier stages of crystallisation, possibly because the more mafic phases contain a restite component which needs to be separated from the melt before fractionation can commence. The granites begin to fractionate at about 74% SiO_2, and once they start fractionating the SiO_2 level remains fairly constant. The Jim Jim Suite is more enriched in high field strength elements (Zr, Ce; Figures A5.11, A5.12) and incompatible elements (Rb, U, Th, Y) than the Cullen Supersuite, and once fractionation commences, the exponential rise in Rb, U, Y, Th and Rb/Sr is more rapid and pronounced. Nb also rises exponentially with increasing SiO_2 (Figure A5.13). The Jim Jim Suite has a higher Ga/Al ratio than the Cullen Supersuite (Figure A5.5). The K/Rb ratio of both suites decreases with increasing SiO_2 (Figure A5.14). As shown in the spidergrams in Figure A5.15, the Jim Jim Suite is more fractionated than the Cullen Supersuite. Biotite is the dominant ferromagnesian mineral, and hornblende is only recorded in the more mafic plutons. This contrasts with the Cullen Supersuite in which hornblende is a dominant ferromagnesian phase. The granites have high F values and fluorite is commonly recorded in the granites and volcanic rocks.

The mineralogical and geochemical features described above indicate that the Jim Jim Suite has a more A-type signature than the Cullen Supersuite, suggesting that the Jim Jim Suite was sourced by a refractory residue from which a previous melt phase had been extracted. The previous melt phase is represented by the 1866 Ma granitoids of the Nimbuwah Suite, an I-granodiorite restite suite which also outcrops along the eastern margin of the Pine Creek Inlier (Wyborn et al. 1997). In contrast, the Cullen Supersuite is the first melt component to be extracted from the protolith in the central Pine Creek Inlier.

A-type suites are generated by the partial melting of the felsic granulite residue that remains in the lower crust after production of a previous felsic melt (Collins et al. 1982; Clemens et al. 1986). The first melt to be extracted is a minimum or near minimum melt formed under hydrous conditions at relatively low temperatures (< 850°C). The release of volatiles by the breakdown of biotite and amphibole initiates partial melting of quartz-K-feldspar-plagioclase, which according to the restite model of White and Chappell (1977) produces an I-type magma consisting of unmelted residual material (restite) and felsic melt (the Nimbuwah Suite is classified as an I-granodiorite restite suite; Wyborn et al. 1997). The residue remaining in the lower crust after production of a minimum melt magma is a granulite, consisting of quartz+K-feldspar+plagioclase+orthopyroxene ±clinopyroxene. If amphibole±biotite remain, they are F-rich (Munoz and Ludington 1974). Cl-rich amphibole±biotite are removed in the first melt. Other residuals include zircon±sphene±apatite (Collins et al. 1982) and monazite±allanite (Miller and Mittlefehldt 1982). Due to removal of H_2O by the minimum melt, the residue is anhydrous.

Formation of a second melt from this residue must occur at higher temperatures, and the main volatile components are F and Cl rather than H_2O.

- F and Cl complexing in the melt produces a melt framework which favours the retention of high field strength cations and incompatible elements, explaining their strong enrichment in the Jim Jim Suite compared with the Cullen Supersuite. It also explains the presence of fluorite as a common accessory mineral. The higher Ga/Al ratio of the Jim Jim Suite is a diagnostic feature of A-type granites, and reflects preferential retention of anorthite in the in the source region, because Ga is excluded from the anorthite structure relative to Al (Goodman 1972). Also, Ga is partitioned into the melt more readily than Al by forming GaF^{3-}_6 complexes (Collins et al. 1982).

Legend: Cullen Supersuite

- + Hornblende dominated
- × Biotite dominated
- ✳ Hornblende/biotite
- □ Zoned hornblende dom
- ◇ Zoned biotite dom
- ○ Saunders Suite
- △ Burnside Suite
- ▽ Tennysons Suite

Legend: Jim Jim Suite

- △ Malone Creek Granite
- ◇ Jim Jim Granite
- ○ Grace Creek Granite
- □ Nabarlek Granite
- ✡ Tin Camp Granite
- × Pul Pul Rhyolite
- + Edith River Group

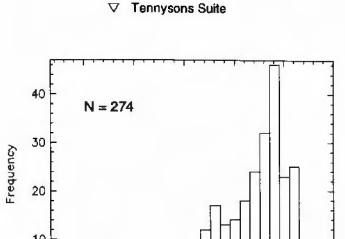

Figure A5.1a: Frequency histogram of the Cullen Supersuite

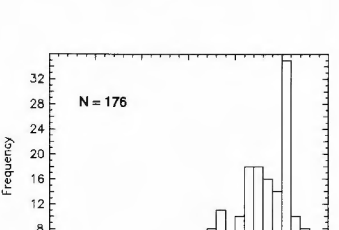

Figure A5.1b: Frequency histogram of the Jim Jim Suite

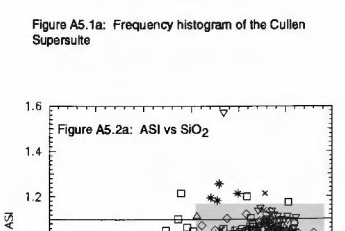

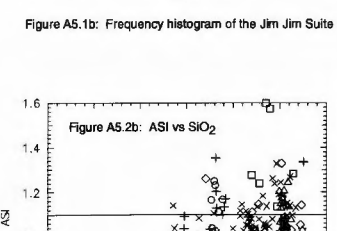

Figures A5.1-A5.16: Geochemical classification and fractionation plots. The figures to the left of the page (A Figures) represent the Cullen Supersuite, and the figures to the right of the page (B Figures) represent the Jim Jim Suite. The legends at the top of this page are for all figures. All figures are reproduced from Wyborn et al. 1997.

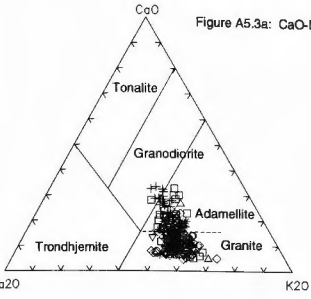

Figure A5.3a: CaO-Na_2O-K_2O

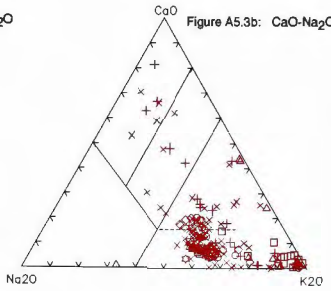

Figure A5.3b: CaO-Na_2O-I

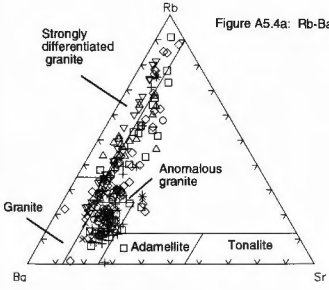

Figure A5.4a: Rb-Ba-Sr

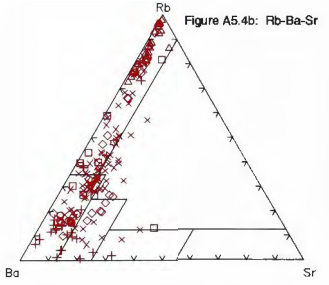

Figure A5.4b: Rb-Ba-Sr

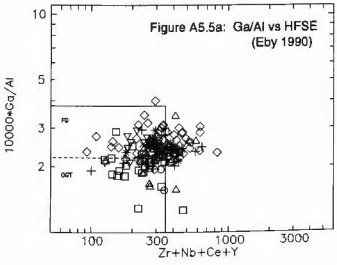

Figure A5.5a: Ga/Al vs HFSE (Eby 1990)

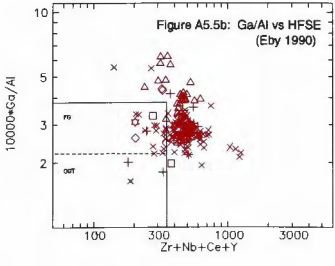

Figure A5.5b: Ga/Al vs HFSE (Eby 1990)

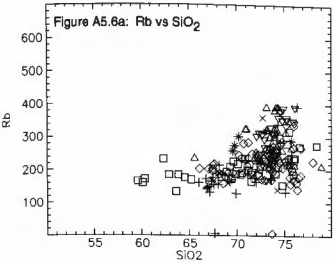
Figure A5.6a: Rb vs SiO2
Rb
SiO2

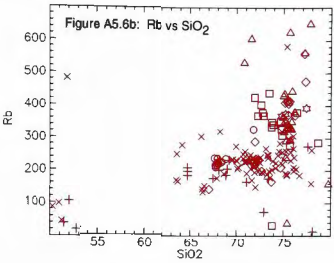
Figure A5.6b: Rb vs SiO2
Rb
SiO2

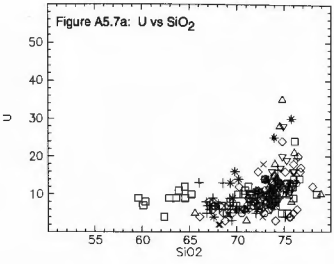
Figure A5.7a: U vs SiO2
U
SiO2

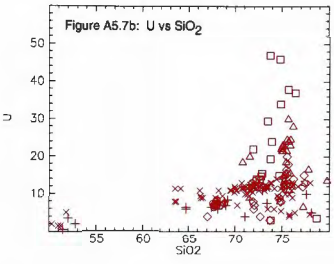
Figure A5.7b: U vs SiO2
U
SiO2

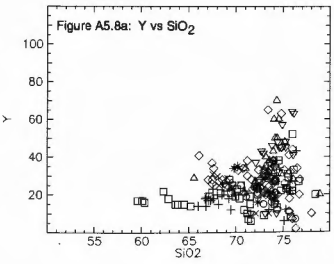
Figure A5.8a: Y vs SiO2
Y
SiO2

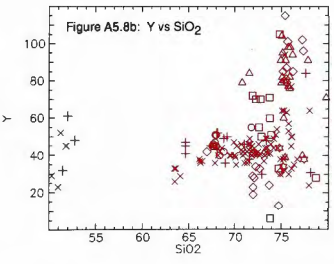
Figure A5.8b: Y vs SiO2
Y
SiO2

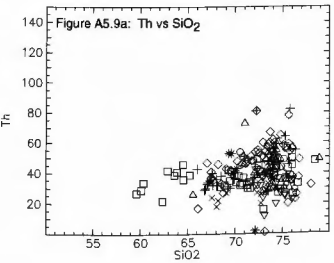
Figure A5.9a: Th vs SiO2
Th
SiO2

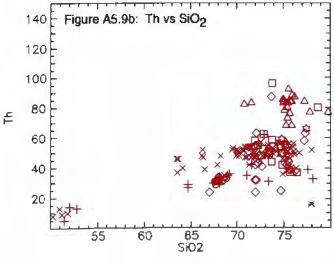
Figure A5.9b: Th vs SiO2
Th
SiO2

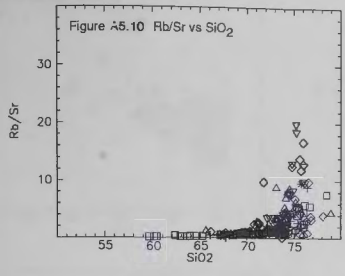
Figure A5.10 Rb/Sr vs SiO2
Rb/Sr
SiO2

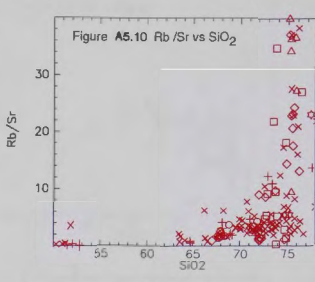
Figure A5.10 Rb /Sr vs SiO2
Rb/Sr
SiO2

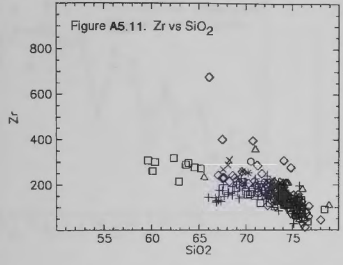
Figure A5.11. Zr vs SiO2
Zr
SiO2

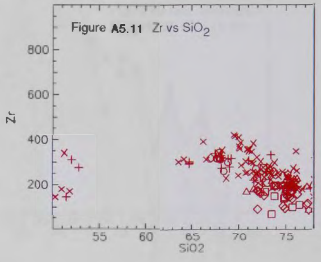
Figure A5.11 Zr vs SiO2
Zr
SiO2

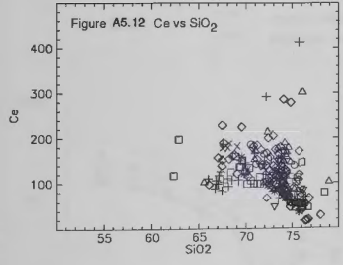
Figure A5.12 Ce vs SiO2
Ce
SiO2

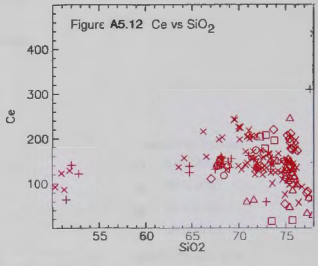
Figure A5.12 Ce vs SiO2
Ce
SiO2

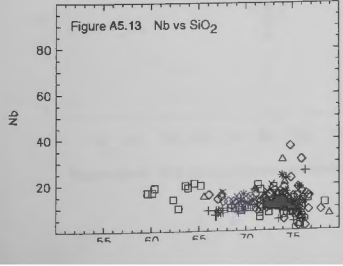
Figure A5.13 Nb vs SiO2
Nb

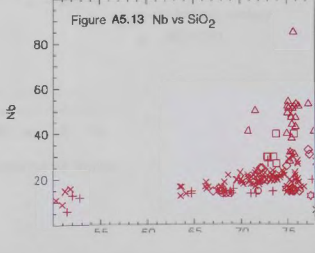
Figure A5.13 Nb vs SiO2
Nb

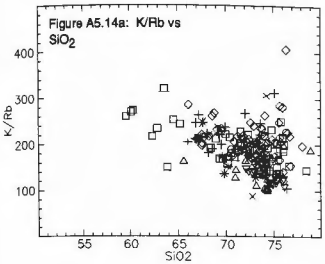

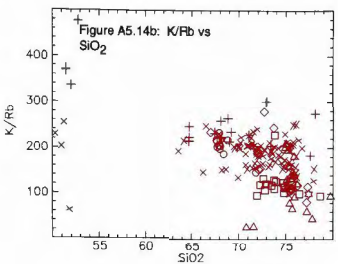

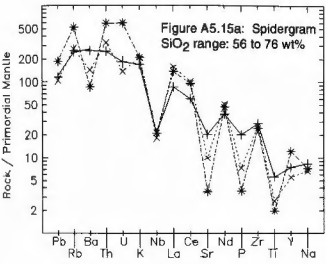

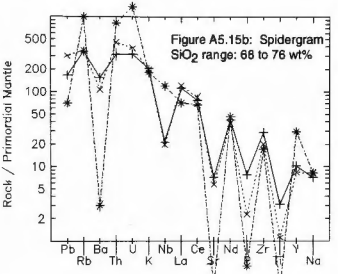

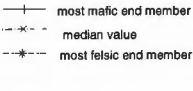

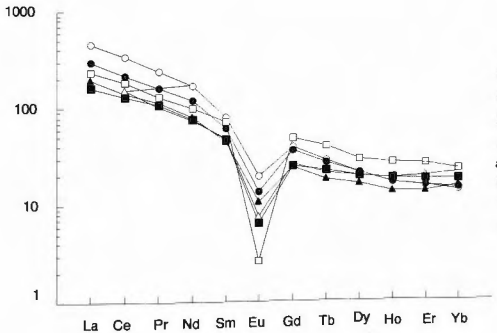

Figure A5.16: REE data for representative samples of the Pul Pul Rhyolite.

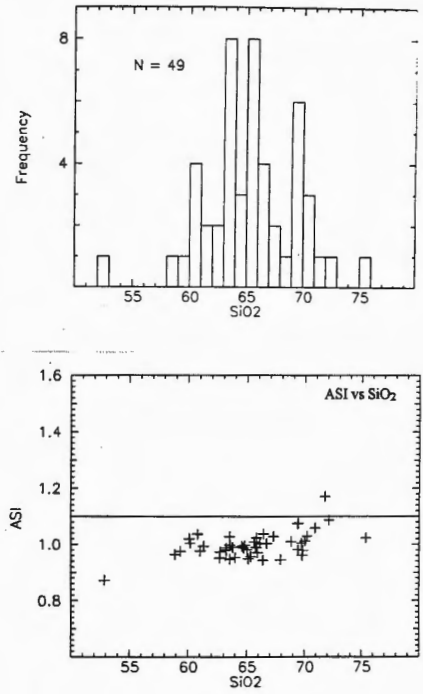

Figure A5.17: Geochemical variation diagrams for the ~ 1860 Ma syn-orogenic Nimbuwah Suite, included for comparison with the ~1830 Ma post-orogenic Cullen Supersuite and Jim Jim Suite.

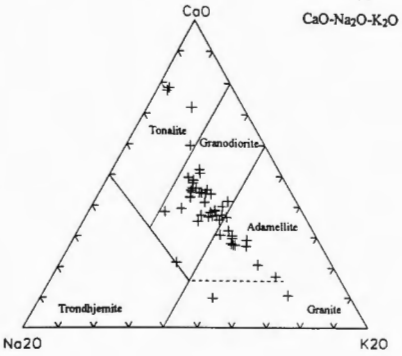
CaO
CaO-Na2O-K2O
Tonalite
Granodiorite
Adamellite
Trondhjemite
Granite
Na20
K20

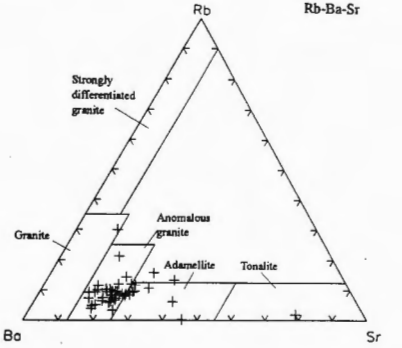
Rb
Rb-Ba-Sr
Strongly differentiated granite
Granite
Anomalous granite
Adamellite
Tonalite
Ba
Sr

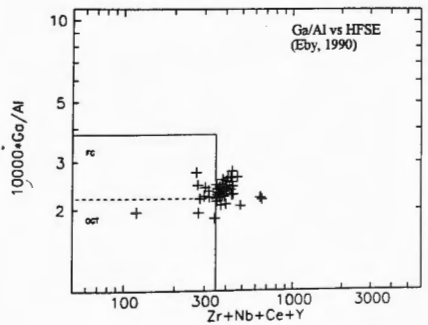
Ga/Al vs HFSE
(Eby, 1990)
10000*Ga/Al
10
5
3
2
rg
ogt
100
300
1000
3000
Zr+Nb+Ce+Y

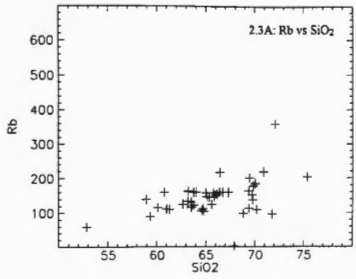
2.3A: Rb vs SiO2
Rb
SiO2

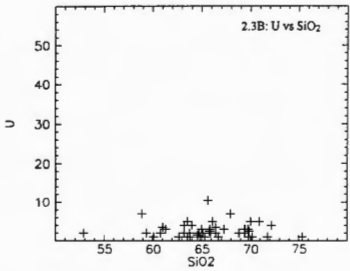
2.3B: U vs SiO2
U
SiO2

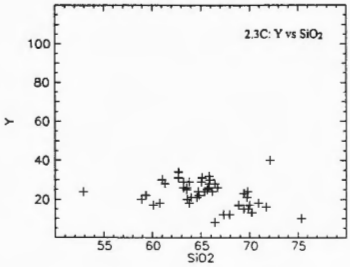
2.3C: Y vs SiO2
Y
SiO2

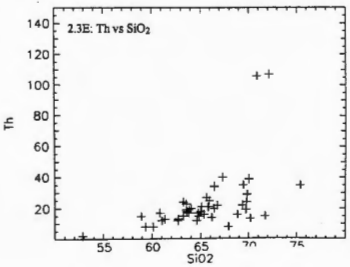
2.3E: Th vs SiO2
Th
SiO2

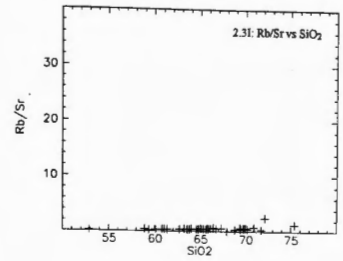
2.3I: Rb/Sr vs SiO2
Rb/Sr
30
20
10
55
60
65
70
75
SiO2

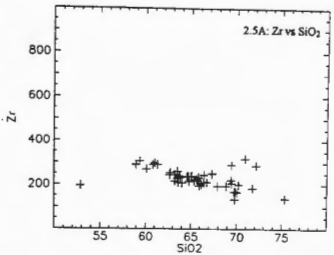
2.5A: Zr vs SiO2
Zr
800
600
400
200
55
60
65
70
75
SiO2

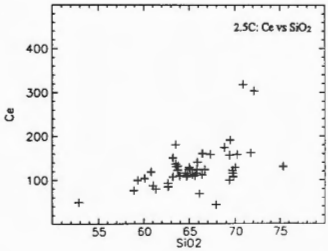
2.5C: Ce vs SiO2
Ce
400
300
200
100
55
60
65
70
75
SiO2

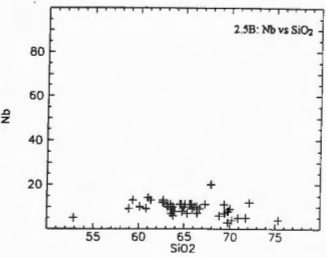
2.5B: Nb vs SiO2
Nb
80
60
40
20
55
60
65
70
75
SiO2

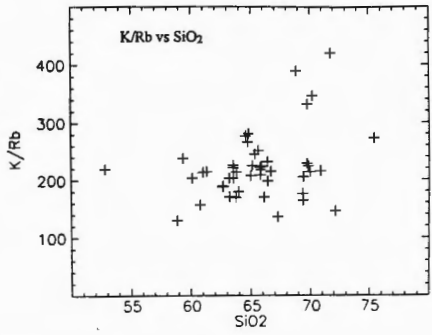
K/Rb vs SiO2
K/Rb
400
300
200
100
55
60
65
70
75
SiO2

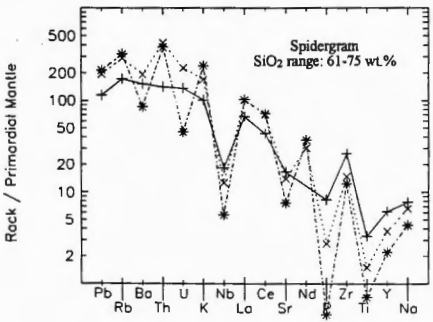
Spidergram
SiO2 range: 61-75 wt.%
Rock / Primordial Mantle
500
200
100
50
20
10
5
2
Pb
Rb
Ba
Th
U
K
Nb
La
Ce
Sr
Nd
P
Zr
Ti
Y
Na

APPENDIX B1

SAMPLE LOCALITIES

HILL END TROUGH

Appendix B1 contains a list of samples collected during this study, with brief lithological descriptions. Thin sections are available for all samples, and a note is made of those for which point count analyses, geochemical data and SHRIMP U-Pb isotopic data are available (marked in columns 'pet', 'chem' and 'chron', respectively). Thin sections, hand specimens and rock powders (for geochemical analysis) of samples collected by E. Jagodzinski are stored at the Australian Geological Survey Organisation (AGSO) rock store. All samples are registered with AGSO's corporate databases (SITES (sample locations); OZROXS (sample descriptions); OZCHEM (geochemical analyses); and OZCHRON (geochronology data)).

Sample locations are plotted on measured sections in Appendix B4. Section numbers for each sample are included in this appendix for cross reference.

APPENDIX B1

SAMPLE LOCALITIES

HILL END TROUGH

Sample	Section	Formation	Mbr	pet	chem	chron	Description
Samples stored at AGSO (originator E.Jagodzinski)							
TUR3	1	Turondale Fm					interbedded coarse & fine CRVS: coarse
TUR4	1	Turondale Fm					interbedded coarse & fine CRVS: fine
TUR5	1	Turondale Fm					medium-grained CRVS, loading at base
TUR6	1	Turondale Fm					graded CRVS, coarse lithic base
TUR7	1	Turondale Fm					graded CRVS: finer, medium-grained top
TUR8	1	Turondale Fm					coarse-grained CRVS
TUR9	1	Turondale Fm					conglomerate with abundant siltstone clasts
TUR11	1	Turondale Fm		x			thick, coarse-grained CRVS: lithic base
TUR12	1	Turondale Fm					conglomerate with abundant siltstone clasts
TUR13	1	Turondale Fm					thick, coarse CRVS: near base, contains lithics
TUR14	1	Turondale Fm		x			thick, coarse CRVS: centre of bed, fewer lithics
TUR15	1	Turondale Fm		x			thick, coarse CRVS: centre of bed, fewer lithics
TUR16	1	Turondale Fm		x			thick, coarse CRVS: centre of bed, fewer lithics
TUR17	1	Turondale Fm					thick, coarse CRVS: centre of bed, fewer lithics
TUR18	1	Turondale Fm		x			thick, coarse CRVS: graded flow top, coarse
TUR19	1	Turondale Fm		x			thick, coarse CRVS: graded flow top, medium
TUR20	1	Turondale Fm					thick, coarse-grained CRVS: graded flow top, fine
TUR21	1	Turondale Fm					f.g. laminated 'cherty' tuffaceous siltstone
TUR22	1	Turondale Fm		x			coarse-grained CRVS: centre of bed, coarse
TUR23	1	Turondale Fm		x			coarse-grained CRVS: graded flow top, medium
TUR24	1	Turondale Fm					coarse-grained CRVS: graded flow top, fine
TUR25	1	Turondale Fm					f.g. laminated 'cherty' tuffaceous siltstone
TUR26	1	Turondale Fm					medium-grained CRVS: centre of bed
TUR27	1	Turondale Fm					medium CRVS: top contact with f.g. chert
TUR28	1	Turondale Fm		x			coarse-grained CRVS: lithic base
TUR29	1	Turondale Fm					coarse CRVS: top of bed, coarse-grained-grained
TUR30	1	Turondale Fm					coarse CRVS: centre of bed, coarse-grained
TUR31	1	Turondale Fm					coarse CRVS (interbedded with conglomerate)
TUR32	1	Turondale Fm					coarse-grained CRVS
TUR33	1	Turondale Fm		x			coarse-grained CRVS
TUR34	1	Turondale Fm					coarse-grained CRVS
TUR35	1	Turondale Fm		x			coarse-grained CRVS
TUR36	1	Turondale Fm		x			coarse-grained CRVS
TUR37	1	Turondale Fm					coarse-grained CRVS
TUR38	1	Turondale Fm					coarse-grained CRVS
TUR39	1	Turondale Fm					coarse-grained CRVS
TUR40	1	Turondale Fm		x			coarse-grained CRVS: centre of bed
TUR42	1	Turondale Fm					fine-grained sandstone
TUR43	1	Turondale Fm		x			fine-grained sandstone
TUR44	1	Turondale Fm		x			coarse-grained CRVS
TUR45	1	Turondale Fm					coarse-grained CRVS
TUR46	1	Turondale Fm					layered siltstone
TUR47	1	Turondale Fm					thin coarse CRVS
TUR48	1	Turondale Fm		x			thin medium-grained sandstone
TUR49	1	Turondale Fm					thin medium-grained sandstone
TUR50	1	Turondale Fm					coarse-grained CRVS
TUR51	1	Turondale Fm		x			coarse-grained CRVS: base of bed
TUR52	1	Turondale Fm					coarse-grained CRVS: centre of bed
TUR53	1	Turondale Fm					f.g. laminated 'cherty' tuffaceous siltstone

Sample	Section	Formation	Mbr	pet	chem	chron	Description
TUR54	1	Turondale Fm					f.g. laminated 'cherty' tuffaceous siltstone
TUR55	1	Turondale Fm		x			coarse-grained CRVS
TUR56	1	Turondale Fm					coarse-grained CRVS
TUR57	1	Turondale Fm					medium CRVS: centre of bed
TUR58	1	Turondale Fm					medium CRVS: graded, fine laminated flow top
TUR59	1	Turondale Fm					medium CRVS: centre of bed
TUR60	1	Turondale Fm					medium CRVS: graded, fine laminated flow top
TUR61	1	Turondale Fm		x			medium CRVS: centre of bed
TUR62	1	Turondale Fm					medium CRVS: graded, fine laminated flow top
TUR63	1	Turondale Fm		x			medium CRVS: centre of bed
TUR64	1	Turondale Fm					medium CRVS: graded, fine laminated flow top
TUR65	1	Turondale Fm		x			medium CRVS: centre of bed
TUR66	1	Turondale Fm					medium CRVS: graded, fine laminated flow top
TUR67	1	Turondale Fm					medium CRVS: centre of bed
TUR68	1	Turondale Fm					medium CRVS: graded, fine laminated flow top
TUR69	1	Turondale Fm		x			medium-grained CRVS
TUR70	1	Turondale Fm		x			medium-grained CRVS
TUR71	1	Turondale Fm					fine 'cherty' laminated interval: tuffaceous?
TUR72	1	Turondale Fm		x			coarse-grained CRVS
TUR73	1	Turondale Fm		x			coarse-grained CRVS
TUR74	1	Turondale Fm					fine-grained laminated sandstone
TUR75	1	Turondale Fm					medium CRVS, diffuse laminae
TUR76	1	Turondale Fm					planar laminated fine sediment
TUR77	1	Turondale Fm		x			medium-grained CRVS
TUR78	1	Turondale Fm					medium-grained CRVS
TUR79	1	Turondale Fm					medium-fine CRVS, graded flow top
TUR80	1	Turondale Fm		x			coarse sdst: basal scour contact with underlying sdst
TUR81	1	Turondale Fm					upper fine laminated interval of coarse CRVS turbidite
TUR82	1	Turondale Fm		x			coarse CRVS
TUR83	1	Turondale Fm					laminated fine sandstone
TUR84	1	Turondale Fm					diffuse laminated medium-grained CRVS
TUR85	1	Turondale Fm					siltstone
TUR86	1	Turondale Fm					coarse CRVS: centre of bed
TUR87	1	Turondale Fm					coarse CRVS:upward fining flow top
TUR88	1	Turondale Fm					medium-grained CRVS
TUR89	4	Turondale Fm		x			medium-grained CRVS
TUR90	4	Turondale Fm		x			coarse-grained CRVS
TUR91	4	Turondale Fm					fine-medium laminated CRVS
TUR92	4	Turondale Fm		x			medium-grained CRVS
TUR93	4	Turondale Fm		x			coarse, thick CRVS: centre of bed
TUR94	4	Turondale Fm		x			coarse, thick CRVS: fine laminated flow top
TUR95	4	Turondale Fm		x			coarse, thick CRVS: centre of bed
TUR96	4	Turondale Fm					coarse, thick CRVS: fine laminated flow top
TUR97	4	Turondale Fm		x			coarse, thick CRVS: centre of bed
TUR98	4	Turondale Fm					coarse, thick CRVS: fine laminated flow top
TUR99	4	Turondale Fm					coarse CRVS with boulder sized siltstone clasts
TUR100	4	Turondale Fm					contact; coarse CRVS and overlying pelite interval
TUR101	4	Turondale Fm					medium CRVS contact with laminated siltstone
TUR102	4	Turondale Fm					coarse CRVS with slumped siltstone
TUR103	4	Turondale Fm					coarse CRVS with slumped siltstone
TUR104	4	Turondale Fm					coarse CRVS with slumped siltstone
TUR105	2	Turondale Fm					coarse-grained CRVS
TUR106	2	Turondale Fm					polymictic volcaniclastic conglomerate
TUR107	2	Turondale Fm					coarse-grained CRVS
TUR108	2	Turondale Fm					coarse CRVS with lithics: base of bed
TUR109	2	Turondale Fm					coarse CRVS with lithics: centre of bed
TUR110	2	Turondale Fm					coarse CRVS with lithics: centre of bed

Sample	Section	Formation	Mbr	pet	chem	chron	Description
TUR111	2	Turondale Fm					coarse CRVS with lithics: centre of bed
TUR112	2	Turondale Fm					coarse CRVS with lithics: top of bed
TUR113	8	Turondale Fm		x			coarse-grained CRVS
TUR114	8	Turondale Fm		x			coarse-grained CRVS
TUR115	8	Turondale Fm		x			coarse-grained CRVS
TUR133	8	Turondale Fm		x			coarse-grained CRVS
TUR134	8	Turondale Fm		x			coarse-grained CRVS
TUR135	8	Turondale Fm		x			coarse-grained CRVS
TUR136	8	Turondale Fm		x			coarse-grained CRVS
TUR137	8	Turondale Fm		x			coarse-grained CRVS
TUR138	8	Turondale Fm					fine-grained massive CRVS
TUR139	8	Turondale Fm					coarse-grained thin CRVS
TUR140	8	Turondale Fm		x			coarse-grained thin CRVS
TUR141	8	Turondale Fm		x			coarse thin CRVS showing fining upward flow top
TUR142	8	Turondale Fm		x			medium-grained CRVS
TUR143	9	Turondale Fm		x			coarse-grained CRVS
TUR144	9	Turondale Fm		x			cherty tuffaceous sandstone
TUR145	9	Turondale Fm		x			coarse-grained CRVS
TUR146	9	Turondale Fm		x			medium-grained CRVS
TUR147	9	Turondale Fm					fine-grained chert
TUR148	9	Turondale Fm		x			medium-grained CRVS
TUR149	9	Turondale Fm		x			coarse-grained thin CRVS
TUR150	9	Turondale Fm		x			coarse-grained CRVS
TUR151	9	Turondale Fm		x			fine-medium thick CRVS
TUR152	9	Turondale Fm		x			coarse-grained CRVS with vitriclasts
TUR153	9	Turondale Fm		x			coarse-grained CRVS
TUR154	9	Turondale Fm		x			coarse-grained CRVS
TUR155	9	Turondale Fm		x			coarse-grained CRVS
TUR156	9	Turondale Fm		x			coarse-grained CRVS
TUR157	9	Turondale Fm		x			coarse-grained CRVS
TUR158	9	Turondale Fm		x			coarse-grained CRVS
TUR159	2	Turondale Fm		x			polymictic volcaniclastic conglomerate
WAT1	8	Waterbeach Fm		x			medium-grained sandstone
WAT2	8	Waterbeach Fm		x			medium-grained sandstone
WAT3	8	Waterbeach Fm					medium-grained sandstone
WAT4	8	Waterbeach Fm					medium-grained sandstone
WAT5	8	Waterbeach Fm					medium-grained sandstone
WAT6	8	Waterbeach Fm					medium-grained sandstone
WAT7	8	Waterbeach Fm					medium-grained sandstone
WAT8	8	Waterbeach Fm					medium-grained sandstone
95843001	5	Turondale Fm		x			conglomerate
95843002	5	Turondale Fm		x			very coarse-grained CRVS
95843003	5	Turondale Fm		x			intraformational breccia
95843004	5	Turondale Fm		x			coarse-grained CRVS
95843005	5	Turondale Fm		x			fine-grained CRVS
95843006	5	Turondale Fm		x			coarse-grained CRVS
95843007	5	Turondale Fm		x			coarse-grained CRVS
95843009	5	Turondale Fm					fine-grained cherty tuffaceous siltstone
95843010	5	Turondale Fm		x			coarse-grained CRVS
95843011	5	Turondale Fm		x			coarse-grained CRVS
95843012	5	Turondale Fm		x			coarse-grained CRVS
95843013	5	Turondale Fm		x			medium-grained CRVS
95843014	5	Turondale Fm		x			very coarse-grained CRVS: base of bed
95843015	5	Turondale Fm		x			coarse-grained CRVS: centre of bed
95843016	5	Turondale Fm		x			coarse-grained CRVS: top of bed
95843017	5	Turondale Fm		x			medium CRVS: fine graded laminated flow top
95843018	5	Turondale Fm		x			coarse-grained CRVS

Sample	Section	Formation	Mbr	pet	chem	chron	Description
95843019	5	Turondale Fm		x			medium-grained thin CRVS
95843020	5	Turondale Fm					coarse basal CRVS with siltstone lithics
95843021	5	Turondale Fm		x			coarse-grained CRVS: top of unit
95843022	5	Turondale Fm		x			coarse-grained CRVS with lithics
95843023	5	Turondale Fm		x			interbedded sandstone/siltstone sequence
95843024	5	Turondale Fm		x			coarse-grained CRVS
95843025	5	Turondale Fm		x			coarse-grained CRVS
95843026	5	Turondale Fm		x			coarse-grained CRVS
95843027	5	Turondale Fm		x			coarse-grained CRVS: centre of bed
95843028	5	Turondale Fm		x			coarse-grained CRVS: centre of bed
95843029	5	Turondale Fm		x			medium-grained CRVS: finer flow top
95843030	5	Turondale Fm		x			cherty tuffaceous siltstone
95843031	5	Turondale Fm		x			coarse-grained CRVS
95843032	5	Turondale Fm		x			coarse-grained CRVS
95843033	5	Turondale Fm		x			sandstone/siltstone interbeds
95843034	5	Turondale Fm		x			medium-grained CRVS
95843039	G1	Guroba Fm			x		medium-grained CRVS
95843043	G1	Guroba Fm					coarse-grained sandstone
95843045	G1	Guroba Fm			x		medium-grained sandstone
95843046	G1	Guroba Fm					coarse-grained sandstone
95843050	G1	Guroba Fm					medium-grained sandstone
95843052	G1	Guroba Fm					coarse-grained CRVS
95843053	G1	Guroba Fm					coarse-grained CRVS
95843057	G1	Guroba Fm					fine-grained chert
95843058	G1	Guroba Fm					coarse-grained CRVS
95843059	G1	Guroba Fm					coarse-grained CRVS
95843060	G2	Guroba Fm			x		coarse-grained CRVS
95843061	G2	Guroba Fm			x		medium-grained sandstone
95843062	G2	Guroba Fm			x		coarse sandstone: base of unit
95843063	G2	Guroba Fm			x		coarse sandstone: top of unit
95843064	G2	Guroba Fm			x		fine-grained sandstone
95843065	G2	Guroba Fm			x		medium-grained sandstone
95843068	G2	Guroba Fm			x		medium-grained sandstone
95843069	G2	Guroba Fm			x		coarse-grained lithic conglomerate
95843072	G2	Guroba Fm					medium-grained layered sandstone
95843073	G2	Guroba Fm			x		coarse-grained CRVS
95843074	G2	Guroba Fm			x		coarse-grained CRVS
95843081	3	Turondale Fm			x		acid volcanic porphyry clast
95843082	9	Turondale Fm		x	x		fine-grained cherty tuffaceous siltstone
95843083	9	Turondale Fm		x	x		fine-grained cherty tuffaceous siltstone
95843084	9	Turondale Fm			x		medium-grained CRVS
95843085	9	Turondale Fm		x	x		medium-grained CRVS
95843086	9	Turondale Fm			x		medium-grained CRVS
95843087	9	Cookman Fm			x		fine-grained cherty tuffaceous siltstone
95843088	9	Cookman Fm			x		fine-grained cherty tuffaceous siltstone
95843089	3	Turondale Fm		x	x		medium-grained CRVS
95843090	3	Turondale Fm		x	x		medium-grained CRVS
95843091	3	Turondale Fm		x	x		medium-grained CRVS
95843092	3	Turondale Fm		x	x		medium-grained CRVS
95843093	3	Turondale Fm			x		medium-grained CRVS
95843094	4	Turondale Fm			x		fine-grained cherty tuffaceous siltstone
95843095	10	Turondale Fm			x		dolerite intrusion
95843096	10	Turondale Fm			x		dolerite intrusion
95843097	10	Turondale Fm		x	x		medium-coarse CRVS
95843098	10	Turondale Fm			x		fine-grained CRVS
95843099	10	Turondale Fm		x	x		medium-coarse CRVS
95843100	10	Turondale Fm		x	x		medium-coarse CRVS

Sample	Section	Formation	Mbr	pet	chem	chron	Description
95843101	10	Turondale Fm		x	x		medium-coarse CRVS
95843103		Riversdale V.			x		ignimbrite: GR 774825 6357406
95843104		Riversdale V.			x		ignimbrite: GR 768626 6361753
95843105		Riversdale V.			x		ignimbrite: GR769395 6360388
95843106		Riversdale V.			x		ignimbrite: GR 769085 6360349
95843107		Riversdale V.			x		ignimbrite: GR 769843 6361078
95843108		Riversdale V.			x		ignimbrite: GR 766118 6363249
95843109	M8	Merrions Fm	E		x		coarse-grained CRVS
95843110	M16	Merrions Fm	A		x		coarse-grained CRVS
95843111	M16	Merrions Fm	H		x		lava
95843112	M16	Merrions Fm	E		x		coarse-grained CRVS
95843113	M16	Merrions Fm	D		x		coarse-grained CRVS
95843114	M16	Merrions Fm	D		x		coarse-grained CRVS
95843115	6	Turondale Fm		x			Turondale porphyry
95843116	8	Turondale Fm		x			Turondale porphyry
95843132	6	Turondale Fm		x			Turondale porphyry
95843129	6	Turondale Fm		x			Turondale porphyry
95308499B	8	Turondale Fm		x	x	x	Turondale porphyry
94843520	1	Turondale Fm			x	x	coarse-grained CRVS
94843521	1	Turondale Fm					loose boulder of CRVS containing vitriclasts
94843522	M1	Merrions Fm	P	x	x	x	coarse-grained CRVS
94843523	M1	Merrions Fm	D	x	x	x	coarse-grained CRVS
94843524	M1	Merrions Fm	E	x	x	x	coarse-grained CRVS
94843525	M0	Merrions Fm	D		x		coarse-grained CRVS
94843526	M1	Merrions Fm	H		x	x	coarse-grained CRVS
*Samples/analyses from other collections:**							
MU4642	M20	Merrions Fm	B1		x		lava
MU4644	M20	Merrions Fm	B2		x		lava
MU4647	M1	Merrions Fm	H		x		lava
MU4653	M10	Merrions Fm	B1		x		lava
MU4654	M9	Merrions Fm	B1		x		lava
MU4655	M5	Merrions Fm	H		x		lava
MU4656	M6	Merrions Fm	H		x		lava
MU4657	M13	Merrions Fm	H		x		lava
MU4658	M21	Merrions Fm	H		x		lava
MU4659	M1	Merrions Fm	P		x		coarse-grained CRVS
MU4660	M1	Merrions Fm	E		x		coarse-grained CRVS
MU4661	M1	Merrions Fm	D		x		coarse-grained CRVS
MU4662	M9	Merrions Fm	D		x		coarse-grained CRVS
MU4663	M1	Merrions Fm	D		x		coarse-grained CRVS
MUGC0088		Riversdale V.			x		ignimbrite
Milsteed 1		Riversdale V.			x		ignimbrite: GR 766800 6365400
Milsteed 2		Riversdale V.			x		ignimbrite: GR 767900 6365400
Milsteed 3		Riversdale V.			x		ignimbrite: GR 767100 6369000

* samples prefixed by MU are from the PhD collection of R.Cas, stored at Macquarie University
samples prefixed by MUGC refer to analyses supplied by G.Colquhoun, NSW Geological Survey
other samples of Riversdale Volcanics refer to geochemical analyses from Milsteed 1985, supplied by G.Colquhoun.

APPENDIX B2

GEOCHEMICAL ANALYSES

HILL END TROUGH

SAMPLE		95843520	95843084	95843085	95843086	95843089	95843090	95843091	95843092	95843093	95843097	95843099
UNIT		Turondale Formation	Turondale Formation	Turondale Formation	Turondale Formation	Turondale Formation	Turondale Formation	Turondale Formation	Turondale Formation	Turondale Formation	Turondale Formation	Turondale Formation
SECTION		1	9	9	9	3	3	3	3	3	10	10
FACIES		CRMS	CRMS	CRMS	CRMS	CRMS	CRMS	CRMS	CRMS	CRMS	CRMS	CRMS
MEMBER												
SiO2	XRF	69.2	66.36	65.13	75.13	63.87	67.06	65.83	67.97	65.85	74.28	65.6
TiO2	XRF	0.57	1.11	0.98	0.53	1.08	0.72	0.84	0.63	1	0.67	0.74
Al2O3	XRF	13.84	14.21	14.37	11.53	12.84	11.31	13.51	14.18	12.76	11.38	14.63
Fe2O3tot	XRF	4.73	5.73	6	3.48	8.1	7.55	6.12	4.54	7.96	4.29	5.23
Fe2O3	XRF	1.43	1.7	1.29	0.96	1.93	1.68	1.72	1.46	1.78	1.22	1.71
FeO	XRF	2.97	3.63	4.24	2.27	5.55	5.27	3.96	2.77	5.56	2.76	3.17
MnO	XRF	0.08	0.09	0.14	0.05	0.12	0.11	0.07	0.08	0.13	0.07	0.06
MgO	XRF	0.87	1.97	1.68	1.04	3.4	3.12	2.13	1.32	2.76	1.26	2.08
CaO	XRF	3.58	3.49	3.37	1.83	4.11	3.14	4.1	3.65	2.87	1.11	4.02
Na2O	XRF	4.19	3.91	3.78	2.29	2.3	2.03	3.34	3.62	2.71	2.1	3.85
K2O	XRF	1.01	1.02	1.11	1.77	1.03	1.24	0.89	1.39	0.83	2.27	0.56
P2O5	XRF	0.11	0.16	0.12	0.09	0.14	0.11	0.09	0.1	0.13	0.13	0.11
LOI		1.81	2.32	3.8	2.59	3.68	4.06	3.58	2.84	3.72	2.22	2.47
rest		0.16	0.14	0.18	0.14	0.16	0.15	0.15	0.15	0.18	0.18	0.14
TOTAL		99.78	100.11	100.19	100.02	100.11	100.03	100.21	100.16	100.28	99.85	99.44
Ag	ICPMS	2	-0.1	-0.1	-0.1	-0.1	-0.1	-0.1	-0.1	-0.1	-0.1	-0.1
As	ICPMS	3	5	7.4	7.2	3.4	3.2	4.3	5.9	7.6	6.8	2.1
Ba	XRF	406	330	449	430	274	332	290	446	315	489	254
Be	ICPMS	4	1.7	1.7	1.6	1.1	1.2	1.5	1.8	1.4	1.6	1.6
Bi	ICPMS	-2	0.2	0.1	0.3	-0.1	-0.1	-0.1	0.2	0.1	0.2	0.2
Co	ICPMS	52	52.5	47.8	68.2	35.3	40.6	37.3	54.4	42.6	71.6	48.4
Cr	XRF	7	32	29	34	72	37	36	27	50	34	51
Cs	ICPMS	-3	2.4	2.6	4.2	0.8	1.1	1.9	3.4	2.1	6.6	0.9
Cu	XRF	4	3	2	3	3	3	3	3	3	12	5
Dy	ICPMS	0	4.2	3.7	4.7	2.8	3.1	2.8	3.4	3.3	4.9	3.5
Er	ICPMS	-1	2.4	2.3	2.9	1.8	1.9	1.8	1.9	2.1	2.9	2.2
Eu	ICPMS	0	1.6	1.5	1.3	1.3	1.3	1.5	1.7	1.4	1.3	1.6
F	XRF	0	443	200	463	-200	-200	-200	338	-200	387	202
Ga	ICPMS	18	16.4	18.5	14.8	16.6	14.1	16.8	18.6	16.4	13.3	17
Ge	ICPMS	2	1.4	1.5	1.5	1.4	1.2	1.4	1.5	1.7	1.5	1.7
Gd	ICPMS	0	4.7	3.9	5	3	3.4	3	4.2	3.7	5.3	3.9
Hf	ICPMS	6	0	0	0	0	0	0	0	0	0	0
Ho	ICPMS	764	0.8	0.8	1	0.6	0.6	0.6	0.7	0.7	1	0.7
La	ICPMS	23	26.8	24.3	33.7	19.4	20.2	21.1	28.8	21.3	33.4	25.1
Li	ICPMS	16	21.6	30.5	24.5	26	27.5	28	29	54.5	35	23
Lu	ICPMS	0	0.3	0.3	0.4	0.3	0.3	0.3	0.2	0.3	0.4	0.3
Mo	ICPMS	-2	0.1	0.1	-0.1	0.3	0.3	-0.1	-0.1	0.1	-0.1	-0.1
Nb	ICPMS	11	11.5	10.7	8.7	10.9	8.1	9.1	10.8	10.5	9.4	8.9
Nd	ICPMS	26	23.6	21.1	29.2	15.3	17.5	16.1	24.1	19.2	26.3	20.9
Ni	XRF	2	5	5.5	10	9.5	6	4.5	5	8.5	10.5	7
Pb	ICPMS	14	16	13.5	24	7.5	11.5	9.5	15.5	9.5	17	13.5
Pr	ICPMS	7	6.1	5.6	8	4	4.6	4.2	6.3	5	7.6	5.5
Rb	ICPMS	42	41	52	86	37	46	39	58	33	121	23
S	XRF	200	50	180	190	470	150	110	200	180	140	50
Sb	ICPMS	0	0.6	0.6	0.4	0.2	0.2	0.4	0.5	0.2	0.5	1.2
Sc	XRF	15	19.5	17	10	24	18	18	16	23	12	16
Sm	ICPMS	0	4.8	4.1	5.6	3.1	3.5	3.2	4.7	3.9	5.7	4
Sn	ICPMS	4	2.5	2	2.5	1.5	1.5	1.5	2	2.5	2.5	2
Sr	ICPMS	289	123	205	132	187	177	162	167	182	118	162
Ta	ICPMS	-2	0.8	0.7	0.7	0.6	0.6	0.6	0.7	0.6	0.7	0.7
Tb	ICPMS	0	0.7	0.6	0.8	0.4	0.5	0.4	0.6	0.6	0.8	0.6
Th	ICPMS	9	7.3	6.9	11.8	3.6	5.2	4.6	8.4	5.8	11.3	6.4
U	ICPMS	3.5	1.7	1.7	2.4	0.9	1.3	1.1	1.6	1.4	2.5	1.6
V	XRF	68	120	136	76	176	110.5	118	86	169	95.5	109.5
W	ICPMS	13	1.2	1.1	1.1	0.8	0.8	0.8	1.1	1.1	1.2	0.9
Y	ICPMS	32	26	24.4	29.3	17.9	19.2	17.9	21.1	21.4	30.9	22.8
Yb	ICPMS	0	2	2.1	2.6	1.8	1.9	1.8	2	2.6	3	1.9
Zn	XRF	69	91	92	65	111	90	86	83	108	72	73
Zr	XRF	219	241	182	209	137	128	144	178	144	307	227
Quartz		31.97	29.14	28.46	50.12	31.33	37.6	30.63	31.77	34.97	49.02	28.74
Corundum			0.72	1.02	3.14	0.72	1.1	0	0.31	2.35	3.74	0.65
Zircon		0.04	0.05	0.04	0.04	0.03	0.03	0.03	0.04	0.03	0.06	0.05
Ortoclase		5.92	6.04	6.59	10.51	5.95	7.28	5.23	8.22	4.79	13.42	3.31
Albite		34.73	32.54	31.69	19.41	16.98	16.9	28.01	30.55	22.36	17.71	33.3
Anorthite		15.98	15.91	15.99	7.39	19.13	14.77	19.04	17.41	13.21	4.61	19.21
Spodumene		0.04	0.06	0.08	0.07	0.07	0.07	0.08	0.08	0.15	0.09	0.06
Diopside		0.86	0	0				0.54	0	0	0	0
Diopside (CaMg)		0.68	0	0				0.47	0	0	0	0
Hedenbergite		0.19	0	0				0.07	0	0	0	0
Hypersthene		2.42	5.06	5.55	3.06	10.02	10.01	5.91	3.67	8.81	3.63	5.52
Enstatite		1.83	4.83	4.15	2.59	8.26	7.64	5.04	3.28	6.7	3.13	5.16
Ferrosilite		0.59	0.23	1.4	0.46	1.76	2.37	0.87	0.39	2.1	0.5	0.36
Magnetite		6.8	8.2	8.65	5.07	11.49	10.79	8.82	6.58	11.29	6.22	7.58
Chromite		0	0.01	0.01	0.01	0.02	0.01	0.01	0.01	0.01	0.01	0.01
Hematite								0	0	0	0	0
Ilmenite		1.07	2.07	1.84	1.01	2	1.34	1.58	1.19	1.85	1.27	1.4
Apatite		0.26	0.37	0.28	0.22	0.32	0.26	0.21	0.24	0.3	0.31	0.26
Fluorite		0	0.06	0	0.08	0	0	0	0.05	0	0.06	0.02
Pyrite		0.04	0.01	0.03	0.04	0.09	0.03	0.02	0.04	0.03	0.03	0.01

SAMPLE	95843100	95843101	93844559B	95843082	95843083	95843094	95843098	95843087	95843088	95843110	94843522	MU4659
UNIT	Turondale Formation	Turondale Formation	Turondale Formation	Turondale Formation	Turondale Formation	Turondale Formation	Turondale Formation	Cookman Formation	Cookman Formation	Merrions Formation	Merrions Formation	Merrions Formation
SECTION	10	10	8	9	9	4	10	9	9	M16	M1	M1
FACIES	CRVS	CRVS	porphyry	chert	chert	chert	chert	chert	chert	CRVS	CRVS	CRVS
MEMBER										Member A	Member P	Member P
SiO2	64.9	65.86	66.23	74.92	76.77	75.33	74.45	74.7	76.66	60.77	59.44	57.61
TiO2	0.87	0.81	0.58	0.39	0.21	0.29	0.22	0.18	0.39	0.77	0.46	0.65
Al2O3	13.87	11.71	14.62	11.91	11.92	11.61	12.49	13.45	11.23	16.76	20.5	20.85
Fe2O3tot	5.62	7.31		3.75	2.62	3.05	2.26	2.15	3.2	6.25	3.61	4.76
Fe2O3	2.02	1.38	1.43	1.25	0.73	-1.03	0.64	0.77	1.03	2.17	1.09	1.53
FeO	4.14	5.34	3.81	2.25	1.7	3.87	1.45	1.24	1.95	3.87	2.27	2.91
MnO	0.09	0.1	0.05	0.07	0.06	0.04	0.04	0.04	0.04	0.1	0.08	0.06
MgO	2.52	3.98	2.25	0.62	0.2	0.63	0.6	0.37	1.01	2.7	1.11	2.09
CaO	4.04	2.9	2.76	1.74	1.41	1.61	0.96	0.74	0.63	4.86	7.36	7.45
Na2O	2.59	2.46	3.01	4.59	4.96	1.37	2.91	6.02	0.41	3.93	4.13	4.03
K2O	1.7	1.1	2.26	1.24	1.3	4.23	3.69	1.32	4.19	0.75	0.89	0.51
P2O5	0.14	0.12	1.21	0.07	0.03	0.06	0.07	0.05	0.08	0.14	0.08	0.12
LOI	2.47	3.47	2.55	1	0.73	2.06	1.85	1.03	2.33	3.01	2.49	1.97
rest	0.19	0.15		0.17	0.15	0.21	0.15	0.14	0.16	0.17	0.19	0.22
TOTAL	99.54	99.38	99.97	100.22	100.17	100.06	99.53	100.06	100.11	99.8	100.09	100
Ag	-0.1	-0.1		-0.1	-0.1	-0.1	-0.1	-0.1	-0.1	-0.1	3	0.1
Ars	8.7	12.4	8	3.8	1.5	4.1	0.3	1.9	10.7	7.6	1.5	5.7
Ba	394	149	681	240	257	747	861	448	786	318	606	293
Be	1.4	1.3		2.1	2.5	2.2	2.6	2.2	3.1	1.6	4	1.9
Bi	0.2	0.1		0.3	0.4	0.3	0.5	0.4	0.8	0.1	-2	-0.1
Ce	48.1	45.4	68	71.9	86.3	78.3	77.7	65.5	63.6	45.7	34	38.3
Cr	51	169	33	4	-1	4	16	9	40	34	15	27
Cs	6.6	5.5		0.6	0.4	13.4	5.5	3.5	10.9	1.2	6	1.7
Cu	3	7	15	3	2	4	5	3	7	10	4	6
Dy	3.8	3.7		5.5	7.7	6.5	8	6.3	5.3	4	9	2.7
Er	2.3	2.2		3.2	4.8	3.9	5	3.7	3.1	2.4	-1	1.6
Eu	1.5	1.1		1.5	1.4	1.5	1	1.4	0.9	1.6	0	2
F	-200	425		-200	-200	430	699	469	984	219	0	-200
Ga	18.1	14.7	18	16.1	15.2	15.1	16.4	16.1	20	19.3	22	23.6
Ge	1.7	1.7		1.8	1.6	1.6	1.8	1.9	2	1.3	1.5	1.5
Gd	4.1	3.9		5.9	7.7	6.7	7.9	6.5	5.6	4.4	0	3.1
Hf	0	0		0	0	0	0	0	0	0	3	0
Ho	0.8	0.8		1.1	1.6	1.3	1.7	1.3	1.1	0.8	807	0.5
La	24.2	22.1	28	35.6	41.8	40.5	36.9	32.1	34.3	22.5	15	19.3
Li	38	48.5		22	15	28.5	33	23.5	56	35.5	24	37
Lu	0.3	0.3		0.4	0.6	0.6	0.6	0.5	0.4	0.3	0	0.2
Mo	0.3	0.2		0.1	0.3	-0.1	-0.1	0.2	-0.1	-0.1	-2	0.2
Nb	9.6	9	11	9.7	11.4	9.2	10.7	8.7	11.2	7.9	6	8.3
Nd	21.2	19.9	30	31.9	37.9	35.4	35.5	30.2	28.7	20.7	13	16.9
Ni	8	23.5	8	-0.5	-0.5	0.5	4	0.5	14.5	5.5	3	4
Pb	14	11	6	20.5	24	23.5	29	24.5	35	11	10	10.5
Pr	5.6	5.2		8.4	10.1	9.5	9.3	8.1	7.7	5.3	6	4.4
Rb	75	49	73	33	35	233	174	44	197	25	31	20
S	60	70	200	150	160	140	750	40	50	120	90	10
Sb	0.8	0.5		1.1	0.7	1.4	0.3	0.8	0.2	0.9	0	0.9
Sc	17.5	18	14	12	10	10	8.5	7.5	8	19	14	16
Sm	4.3	4.1		6.6	7.9	7.2	8	6.8	5.9	4.4	0	3.3
Sn	2	2	5	3	4	3.5	5.5	4.5	6	2	3	1
Sr	145	144	139	305	233	265	81	266	48	355	432	751
Ta	0.6	0.6		0.8	1	0.7	1	0.9	0.8	0.7	-2	0.6
Tb	0.6	0.6		0.9	1.2	1	1.3	1	0.9	0.6	0	0.4
Th	6.5	7.1	18	13.3	16.5	14.3	18.4	13.3	11.2	6	3	4
U	1.6	1.7	4	2.9	3.8	3.2	4.7	3.3	2.5	1.6	1.5	1
V	131	152	111	36	8.5	15.5	19	11.5	53	135	69	102
Y	23.2	21.9	38	34.6	50	41.4	53.3	30.7	34.8	24.6	14	15.4
Yb	2.1	2.1		3	4.3	3.7	4.5	3.4	3	2.1	0	1.4
Zn	85	94	54	65	55	59	54	56	70	90	47	58
Zr	240	183	183	315	261	269	165	171	111	176	143	179
Quartz	30.33	33.75	32.55	38.11	38.95	44.29	40.85	32.45	55.63	20.49	14.73	12.93
Corundum	0.67	1.46	5.12	0	0	1.94	2.21	0.94	5.2	0.88		0.27
Zircon	0.05	0	0.04	0.06	0.05	0.05	0.03	0.03	0.02	0.04	0.03	0.04
Orthoclase	9.93	6.41	13.63	7.23	7.61	24.62	22.06	7.8	24.89	4.41	5.27	3.99
Albite	21.59	20.46	25.92	38.25	41.48	11.38	24.84	50.8	3.48	33.02	34.97	33.75
Anorthite	19.01	13.23	6.1	8.09	6.34	7.48	4.13	3.18	2.15	23.25	34.8	36.16
Spodumene	0.1	0.13	0	0.06	0.04	0.08	0.09	0.06	0.15	0.1	0.06	0.1
Diopside	0	0	0	0.11	0.45	0	0	0	0	0	1.22	0
Diopside (Ca	0	0	0	0.09	0.2	0	0	0	0	0	1.04	0
Hedenbergite	0	0	0	0.02	0.25	0	0	0	0	0	0.18	0
Hypersthene	7	12.27	10.46	1.94	0.95	5.25	1.87	1.19	2.87	7.12	2.74	5.58
Enstatite	6.18	9.75	5.7	1.48	0.4	1.54	1.51	0.92	2.52	6.68	2.28	5.15
Ferrosilite	0.82	2.52	4.76	0.46	0.55	3.71	0.36	0.27	0.35	0.44	0.45	0.43
Magnetite	9.49	10.45	2.13	5.36	3.76	4.34	3.29	3.11	4.66	9.03	5.45	6.85
Chromite	0.01	0.04	0.01	0	0	0	0	0	0.01	0.01	0	0.01
Haematite	0	0	0	0	0	0	0	0	0	0	0	0
Ilmenite	1.63	1.51	1.31	0.73	0.39	0.54	0.42	0.34	0.74	1.45	0.87	1.22
Apatite	0.33	0.28	2.95	0.17	0.07	0.14	0.17	0.16	0.2	0.33	0.19	0.28
Fluorite	0	0.07	0	0	0	0.08	0.14	0.09	0.2	0	0	0
Pyrite	0.01	0.01	0	0.03	0.03	0.03	0.14	0.01	0.01	0.02	0.02	0

SAMPLE	94843523	95843113	95843114	MU4661	MU4662	MU4663	94843524	95843109	MU4660	95843112	95843111	MU4642
UNIT	Marrions Formation	Marrions Formation	Marrions Formation	Marrions Formation	Marrions Formation	Marrions Formation	Marrions Formation	Marrions Formation	Marrions Formation	Marrions Formation	Marrions Formation	Marrions Formation
SECTION	M1	M16	M16	M1	M9	M1	M1	M8	M1	M16	M16	M20
FACIES	CRMS	CRMS	CRMS	CRMS	CRMS	CRMS	CRMS	CRMS	CRMS	CRMS	lava	lava
MEMBER	Member D	Member D	Member D	Member D	Member D	Member D	Member E	Member E	Member E	Member E	Member H	Member B1
SiO2	73.88	72.69	68.77	67.53	71.53	73.12	56.53	58.75	58.3	51.2	55.36	62.91
TiO2	0.3	0.3	0.51	0.56	0.44	0.3	0.86	0.89	0.91	1.05	0.62	0.82
Al2O3	12.72	13.14	13.71	14.17	13.09	12.45	19.28	16.55	19.1	18.28	14.74	16.23
Fe2O3tot	2.55	2.14	4.34	4.12	3.61	3.47	5.77	7.04	5.9	8.59	4.87	5.67
FeO0	0.76	1.26	1.61	1.25	1.17	0.78	2.59	2.24	2	3.1	1.38	1.45
FeO	1.61	0.79	2.28	2.58	2.2	2.42	2.77	4.32	3.51	4.94	3.14	3.8
MnO	0.04	0.05	0.07	0.09	0.07	0.07	0.14	0.1	0.11	0.18	0.07	0.11
MgO	0.76	0.57	1.5	1.15	1.27	1.34	2.2	2.75	1.9	3.78	2.15	2.55
CaO	1.74	3.58	3.63	3.24	3.16	1.43	7.5	5.12	5.12	6.63	1.74	3.02
Na2O	3.35	1.47	2.74	3.48	2.63	2.42	2.98	3.93	5.51	3.98	3.48	5.54
K2O	3.59	3.93	2.45	3.56	2.73	4.08	2.07	1.26	1.27	1.75	4.64	0.87
P2O5	0.06	0.07	0.14	0.12	0.12	0.08	0.19	0.21	0.2	0.26	0.19	0.24
LOI	1.05	1.25	1.64	2.02	1.35	1.28	2.61	3.4	1.88	3.9	1.39	2.22
resi	0.23	0.33	0.2	0.23	0.24	0.23	0.22	0.24	0.19	0.22		0.17
TOTAL	99.79	99.43	99.45	99.98	100	100	100.04	99.76	100	99.27	99.34	99.93
Ag	2	-0.1	-0.1	0.2	0.4	0.5	3	-0.1	0.3	-0.1		0.3
As	2	1.8	4.1	2.5	4.4	4.4	5.5	6.4	9.3	4.7	5	7.3
Ba	1317	1948	877	1086	1155	1324	654	728	548	697	1365	376
Be	3	2.7	1.4	1.2	1.3	1.1	4	1.7	1.7	2.4	2	1.9
Bi	-2	0.4	-0.1	-0.1	-0.1	-0.1	-2	0.2	0.1	0.1		0.3
Ce	88	73.3	81.4	52.6	78.4	85.1	55	57.4	52	58.3	60.5	93.4
Cr	4	3	9	16	8	7	11	19	14	24	13	33
Cs	-3	1.8	2	1.3	2.7	1.4	8	2.3	1.6	2	5	0.7
Cu	2	2	3	5	4	3	8	7	4	3	11	24
Dy	6	5.2	3.7	3	3.1	3	0	5.3	5.5	6.5	5	6.1
Er	-1	3	2	1.8	1.7	1.6	-1	3.6	3.1	3.6	3	3.6
Eu	0	1.7	2.1	1.9	1.9	2.1	0	2	2.1	2.1	1	1.9
F	0	559	359	-200	232	237	0	254	254	335	676	207
Ga	14	14.7	16	15.7	15	15.6	22	19.8	21.9	20.7	16.1	14.9
Gd	1.5	1.6	1.5	2	1.6	1.1	1.5	1.7	1.6	1.5	2	1.7
Ge	0	6	4.8	3.5	4.1	4.1	0	6.9	6.1	7.2	5	6.7
Hf	3	0	0	0	0	0	5	0	0	0	0	0
Ho	396	1.1	0.7	0.6	0.6	0.6	1394	1.3	1.1	1.3	1	1.2
La	47	37.4	41.5	26.8	37.5	45.9	24	26	25	27.6	29.1	48.2
Li	10	7.5	13	10	15	14.5	16	35.5	20	16.5	32	23.5
Lu	0	0.4	0.2	0.2	0.2	0.2	0	0.4	0.3	0.4	0	0.5
Mo	-2	-0.1	0.1	0.6	0.7	0.5	-2	0.2	0.4	0.5	1	5
Nb	7	9.4	5.9	4.9	5	4.4	9	9.1	7.9	9.6	8	9.6
Nd	36	31.7	33.2	22.8	31.4	35.7	31	29.7	27.5	30.8	26.5	36.5
Ni	2	-0.5	-0.5	2	-0.5	-0.5	5	3.5	2	4.5	3	8
Pb	18	25	13	16.5	23	23	13	15	16	10.5	18.5	14.5
Pr	7	8.5	9	6.1	8.5	10	6	7.2	6.5	7.4	7	10.5
Rb	89	107	53	90	67	79	86	41	42	58	106	25
S	70	80	130	130	70	10	70	390	50	290	450	610
Sb	0	0.4	0.4	0.3	0.4	0.3	0	0.8	0.6	0.2	0	0.7
Sc	7	9.5	11.5	14	10	7	20	19.5	17	22	11.5	16
Sm	0	6.5	5.9	4.1	5.3	5.6	0	7	6.2	7.1	6	7.5
Sn	3	3	1.5	1	1	1	5	2.5	2	2.5	2	2.5
Sr	149	423	345	223	347	128	376	547	405	368	182	263
Ta	-2	0.9	0.5	0.8	0.9	0.8	-2	0.5	0.6	0.6	1	1.1
Tb	0	0.9	0.6	0.5	0.5	0.5	0	1	0.9	1.1	1	1
Th	8	11.8	6.4	4.4	5.9	7.8	5	5.4	5.4	5.6	11	13.3
U	2	3.4	1.1	0.9	1	1.1	2	1.7	1.5	1.6	3.1	4.3
V	32	25.5	66.5	86	58	41	119	142.5	117	130.5	100	91
Y	16	31.8	20.3	19.2	17.3	16.6	39	36.5	32.9	37.3	29.3	37
Yb	0	2.8	1.7	1.4	1.4	1.4	0	3.1	2.6	3.1	3	3.4
Zn	39	45	65	65	57	59	83	95	80	132	63	81
Zr	106	169	158	114	134	107	187	180	171	201	181	228
Quartz	35.2	41.18	33.7	25.44	36.79	37.47	12.94	16.02	7.9	2.84	19.55	16.89
Corundum	0.18	0.06	0.23	0	0.24	1.54	0	0	0	0	1.04	1.16
Zircon	0.02	0.03	0.03	0.02	0.03	0.02	0.04	0.04	0.03	0.04	0.04	0.05
Orthoclase	21.18	23.56	14.48	20.95	16.02	23.86	12.23	7.39	7.39	10.3	28.3	5.06
Albite	28.26	12.6	23.15	29.27	22.07	20.24	25.14	32.95	45.79	33.46	29.1	46.06
Anorthite	8.63	17.85	17.26	12.49	15.11	6.77	33.03	23.58	23.22	26.69	7.35	13.38
Spodumene	0.03	0.02	0.03	0.03	0.04	0.04	0.04	0.1	0.05	0.04	0.08	0.06
Diopside	0	0	0	2.45	0	0	2.45	0.5	0.58	3.63	0	0
Diopside (Cal	0	0	0	2.11	0	0	2.45	0.45	0.56	3.47	0	0
Hedenbergite	0	0	0	0.34	0	0		0.04	0.03	0.16	0	0
Hypersthene	2.3	1.44	3.73	2.23	3.57	4.49	4.33	7.28	4.62	8.16	6.02	7.23
Enstatite	1.89	1.44	3.73	1.88	3.14	3.3	4.33	6.58	4.39	7.75	5.29	6.24
Ferrosilite	0.41	0	0	0.35	0.43	1.19	0	0.7	0.23	0.41	0.73	0.98
Magnetite	3.69	1.63	6.04	5.96	5.2	4.98	6.84	10.14	8.42	12.4	7	8.1
Chromite	0	0	0	0	0	0	0	0	0	0.01	0	0.01
Haematite	0	0.91	0.18	0	0	0	1.05	0	0	0	0	0
Ilmenite	0.57	0.56	0.97	1.08	0.83	0.56	1.63	1.67	1.7	1.98	1.16	1.53
Apatite	0.15	0.17	0.34	0.29	0.29	0.19	0.45	0.5	0.47	0.62	0.46	0.56
Fluorite		0.11	0.05	0	0.03	0.04		0	0	0	0.11	0
Pyrite	0.01	0.01	0.02	0.02	0.01	0	0.01	0.07	0.01	0.05	0.08	0.11

SAMPLE UNIT	MU4653 Merrions Formation	MU4654 Merrions Formation	MU4644 Merrions Formation	95843526 Merrions Formation	MU4647 Merrions Formation	MU4655 Merrions Formation	MU4656 Merrions Formation	MU4657 Merrions Formation	MU4658 Merrions Formation	95843039 Guroba Formation	95843045 Guroba Formation	95843060 Guroba Formation
SECTION	M10	M9	M20	M1	M1	M5	M6	M13	M21	G1	G1	G2
FACIES	lava	lava	lava	lava	lava	lava	lava	lava	lava	sandstone	sandstone	sandstone
MEMBER	Member B1	Member B1	Member B2	Member H	Member H	Member H	Member H	Member H	Member H			
SiO2	64.34	65.38	65.07	65.6	64.75	66.45	64.3	64.84	69.48	71.02	70.06	70.05
TiO2	0.61	0.62	0.62	0.62	0.7	0.58	0.65	0.62	0.6	0.85	0.69	0.8
Al2O3	15.13	15.37	14.73	14.89	15.84	14.63	15.97	14.81	14.34	11.9	13.2	11.63
Fe2O3tot	4.85	4.88	4.88	4.55	5.29	4.6	5.08	4.85	3.38	4.57	5.73	4.49
Fe2O3	1.97	2.04	1.76	1.87	1.9	1.49	1.84	1.74	1.15	0.84	1.2	1.12
FeO	2.59	2.56	2.81	2.41	3.05	2.8	2.92	2.62	2.01	3.36	4.06	3.03
MnO	0.08	0.09	0.11	0.08	0.1	0.08	0.1	0.13	0.05	0.07	0.05	0.09
MgO	1.85	1.83	1.74	1.37	2.07	1.74	1.94	1.35	0.7	1.44	1.75	1.22
CaO	3.62	3.95	3.3	4.18	5.63	2.83	5.98	4.55	2.91	2.31	1.15	3.2
Na2O	4.58	3.31	2.07	3.05	2.78	3.05	2.72	3.58	3.81	2.67	2.58	2.78
K2O	3.35	3.16	5.3	3.95	1.76	4.39	1.68	3.3	3.33	1.86	2.05	2.77
P2O5	0.18	0.19	0.2	0.2	0.21	0.19	0.2	0.19	0.19	0.1	0.14	0.12
LOI	1.43	1.2	0.25	1.85	1	1.52	1.46	1.59	1.18	3.61	3.05	3.24
rest	0.15	0.2	0.24	0.18	0.22	0.23	0.23	0.24	0.24	0.22	0.21	0.24
TOTAL	99.88	99.9	100	100.05	99.99	99.98	99.99	99.97	99.99	100.25	100.19	100.29
Ag	0.1	0.2	0.3	-0.5	0.6	-0.5	0.4	0.2	0.2	-0.1	-0.1	-0.1
As	8.6	3.9	1.2	5.5	0.3	6.4	10.8	4	3.3	7.8	25.4	28
Ba	582	950	1099	729	685	1168	711	869	911	821	550	981
Be	1.8	2.1	2.1	2	2.3	1.9	2.3	1.4	1.9	1.8	1.8	1.7
Bi	-0.1	0.3	0.4	0.3	0.2	-0.1	0.5	0.2	-0.1	0.1	0.2	0.2
Ce	63.5	60	62.1	58.5	63.7	59.2	62.8	62	60.6	62.5	61.3	66.7
Cr	18	14	16	18	18	22	16	15	15	34	55	23
Cs	7.4	1.9	3.2	2.8	2	0.8	2.3	1.8	1.4	8	8.3	2.8
Cu	12	11	3	13	8	10	6	6	11	8	16	5
Dy	4.8	4.7	4.8	4.8	5.2	4.7	4.8	4.7	4.6	5.1	4.9	4.6
Er	2.9	2.9	2.9	3.1	3.1	2.8	2.9	2.9	2.7	3.1	2.9	2.7
Eu	1.4	1.4	1.3	1.4	1.5	1.3	1.4	1.4	1.2	1.3	1.2	1.5
F	587	285	531	500	489	503	296	-200	482	-200	-200	-200
Ga	20.5	16.4	16.9	15.1	17.6	15.8	17.7	16.9	15.1	14.5	17	14.5
Ge	2.5	1.6	1.9	1.3	1.5	1.6	1.5	1.4	3	1.8	1.7	2.5
Gd	5.3	5.2	5.3	5.3	5.6	5	5.3	5.3	5.1	5.5	5.3	5.4
Hf	0	0	0	4	0	0	0	0	0	0	0	0
Ho	1	1	1	1.1	1.1	0.9	1	1	0.9	1.1	1	0.9
La	30.7	28.2	31.9	27.4	30	30	31.1	31.5	33.4	32.4	30.1	32.3
Li	19	16	20.5	7.5	10.5	23.5	25	14	27.5	39	55.5	31.5
Lu	0.4	0.4	0.4	0.4	0.4	0.4	0.4	0.4	0.3	0.4	0.4	0.3
Mo	1.2	1.4	1	1.1	1.2	1	1.4	0.9	1.2	0.1	0.3	-0.1
Nb	7.5	7.6	7.9	7.6	8.1	7.6	7.7	7.5	7.3	11.6	9.2	9.7
Nd	27.9	27.8	28.4	25.8	28.8	26.2	28.9	28.9	28.7	27.9	28.1	29.9
Ni	3	2	2	5	2	1	2	3	2	7	12	3.5
Pb	22	20.5	11	20.5	20	15.5	31.5	21.5	11	20.5	15	19
Pr	7.4	7.2	7.4	6.6	7.5	6.8	7.5	7.6	8.5	7.4	7.3	7.7
Rb	112	89	128	119	84	91	60	63	92	86	89	75
S	950	940	30	420	50	270	170	90	220	210	660	530
Sb	1.1	0.5	0.4	0.3	0.4	0.5	3.4	0.4	1.9	1.1	1.6	1.2
Sc	14	12	13	16	17	13	16	16	12	13	13.5	13
Sm	5.7	5.7	5.7	5.3	6.1	5.4	5.7	5.7	5.4	5.6	5.7	5.9
Sn	2	2.5	2.5	2	2.5	2	2.5	2	2.5	3	3	2.5
Sr	231	245	377	266	467	229	525	324	554	258	177	223
Ta	0.9	1.1	1	0.9	1.1	1	1	0.9	1.4	0.9	0.8	0.7
Tb	0.8	0.8	0.8	0.8	0.8	0.7	0.8	0.8	0.7	0.8	0.8	0.8
Th	10.7	11.3	11.1	10.8	11.3	12.1	11.2	10.5	10.7	11.3	11.4	9.3
U	3.1	3.1	3.2	3.1	3.2	3.1	3.1	3	3	2.5	2.7	2
V	107	97	87	108	120	94	108	105	90	111.5	112	104.5
Y	30.2	29.7	30.5	27.5	31.8	31	30.6	30.9	28.4	36.5	30.5	29.8
Yb	2.7	2.7	2.7	2.6	2.9	2.6	2.7	2.6	2.4	2.8	2.7	2.3
Zn	64	71	54	68	72	44	67	63	43	68	71	67
Zr	169	183	172	190	190	172	184	169	166	234	252	201
Quartz	15.94	23.09	23.21	23.13	26.86	23.17	26.69	21.18	27.73	40.82	41.13	35.36
Corundum	0	0	0.01	0	0	0.12	0	0	0	1.42	4.83	0
Zircon	0.03	0.04	0.03	0.04	0.04	0.03	0.04	0.03	0.03	0.05	0.05	0.04
Orthoclase	19.61	18.46	31.11	23.23	10.21	25.63	9.8	19.38	19.66	11.01	11.97	16.37
Albite	38.3	27.84	17.37	25.63	22.86	25.47	22.67	30.15	31.98	22.66	21.35	23.48
Anorthite	10.68	17.54	15.11	14.84	25.12	12.78	25.01	14.72	12.1	11.05	4.93	11.03
Spodumene	0.05	0.04	0.05	0.02	0.03	0.06	0.07	0.04	0.07	0.1	0.15	0.08
Diopside	4.54	0.72	0	3.62	0.79	0	1.8	5.32	0.94	0	0	3.47
Diopside (Ca)	4.54	0.72	0	3.62	0.76	0	1.73	5.12	0.94	0	0	2.98
Hedenbergite	0	0	0	0	0.03	0	0.07	0.2	0	0	0	0.49
Hypersthene	2.45	4.17	4.59	1.72	4.91	4.73	4.14	1.02	1.3	4.64	5.83	1.97
Enstatite	2.45	4.17	4.3	1.72	4.7	4.28	3.96	0.97	1.3	3.58	4.3	1.66
Ferrosilite	0	0	0.29	0	0.21	0.45	0.19	0.04	0	1.06	1.53	0.31
Magnetite	6.41	6.31	7.04	6.03	7.53	6.6	7.28	6.71	4.78	6.64	8.21	6.52
Chromite	0	0	0	0	0	0	0	0	0	0.01	0.01	0
Haematite	0.39	0.47	0	0.37	0	0	0	0	0.07	0	0	0
Ilmenite	1.14	1.16	1.17	1.17	1.3	1.09	1.22	1.17	1.13	1.61	1.28	1.52
Apatite	0.42	0.45	0.48	0.47	0.49	0.45	0.47	0.45	0.45	0.24	0.33	0.29
Fluorite	0.09	0	0.07	0.09	0.05	0.07	0	0	0.07	0	0	0
Pyrite	0.18	0.18	0.01	0.09	0.01	0.05	0.03	0.02	0.04	0.04	0.12	0.1

SAMPLE	95843061	95843062	95843053	95843064	95843065	95843068	95843069	95843073	95843074	95843103	95843104	95843105
UNIT	Guroba	Guroba	Guroba	Guroba	Guroba	Guroba	Guroba	Guroba	Guroba	Riversdale	Riversdale	Riversdale
	Formation	Formation	Formation	Formation	Formation	Formation	Formation	Formation	Formation	Volcanics	Volcanics	Volcanics
SECTION	G2	G2	G2	G2	G2	G2	G2	G2	G2			
FACIES	sandstone	sandstone	sandstone	sandstone	sandstone	sandstone	conglomerate	CRMS	CRMS	Ignimbrite	Ignimbrite	Ignimbrite
MEMBER												
SiO2	75	75.67	76.13	73.8	74	73.83	62.59	58.23	59.6	75.98	76.43	75.6
TiO2	0.66	0.65	0.63	0.6	0.67	0.31	0.65	0.79	0.9	0.17	0.18	0.19
Al2O3	11.25	10.85	10.7	11.74	11.74	12.4	12.85	17.53	17.79	11.45	10.87	11.62
Fe2O3tot	3.61	3.6	3.38	4.57	4.23	2.87	4.92	7.12	6.16	2.24	2.3	2.85
Fe2O3	0.88	0.98	0.84	1.33	1.2	1	1.55	2.41	2.03	1.15	1.46	2.37
FeO	2.46	2.36	2.29	2.92	2.75	1.41	3.03	4.24	3.72	0.98	0.76	0.43
MnO	0.04	0.04	0.03	0.06	0.06	0.05	0.15	0.15	0.18	0.01	0.01	0.01
MgO	1.23	1.28	1.18	1.54	1.37	0.65	1.96	3.1	2.53	0.21	0.34	0.17
CaO	1.41	1.25	1.24	1.01	1.41	1.92	6.47	5.11	4.32	0.12	0.37	0.2
Na2O	2.51	2.31	2.49	2.03	2.09	3.61	2.16	4.17	4.47	3.42	1.47	2.72
K2O	1.84	1.92	1.83	2.28	2.16	2.45	2.13	1.02	1.38	4.1	5.71	4.5
P2O5	0.12	0.11	0.1	0.11	0.12	0.07	0.13	0.14	0.19	0.02	0.02	0.02
LOI	2.6	2.51	2.47	2.65	2.41	2.25	6.3	3.02	2.87	1.44	1.87	0.95
rest	0.16	0.16	0.16	0.18	0.21	0.17	0.21	0.23	0.25	0.16	0.15	0.34
TOTAL	100.16	100.09	100.09	100.15	100.17	100.12	100.18	100.14	100.23	99.21	99.44	99.12
Ag	-0.1	-0.1	-0.1	-0.1	-0.1	-0.1	-0.1	-0.1	-0.1	-0.1	-0.1	-0.1
As	5.1	7.5	6.7	5.8	25.7	4.4	10.5	11.3	4.7	0.4	1.5	3.1
Ba	487	503	475	581	560	862	594	246	797	636	537	2157
Be	1.6	1.6	1.5	1.6	1.7	2.2	1.9	1.8	1.9	1.4	1.7	2.3
Bi	0.3	0.2	0.2	0.3	0.2	0.4	0.3	0.2	0.2	-0.1	0.1	-0.1
Ce	57.9	56	57.9	51.7	55.7	93.7	60.9	49.5	64.6	73.3	79.5	76.8
Cr	35	36	35	30	56	17	34	37	17	2	-1	-1
Cs	7.2	8.4	7.9	8.3	6.9	6.7	7.7	6.3	3.1	5.7	3.2	2.1
Cu	11	4	7	7	15	9	12	8	3	1	2	2
Dy	4.5	4.6	4.8	4.5	4.6	6.5	5.3	4.1	5.2	4.9	5.2	7
Er	2.6	2.6	2.9	2.7	2.7	3.7	3.1	2.3	2.8	2.8	3.3	4.2
Eu	1.2	1.2	1.3	1.2	1.3	1.2	1.3	1.6	2.1	1.1	1.4	1.6
F	375	418	381	218	-200	1105	229	250	-200	-200	-200	-200
Ga	13.6	13.4	12.7	15.3	15.1	16.8	18.5	21	17.9	13	13.6	17.4
Ge	1.5	1.6	1.5	1.5	1.7	1.7	1.6	1.9	1.3	1.3	1.7	1.4
Gd	4.9	5	5.4	5.1	5	7.3	5.7	4.5	6	5	5.9	6.7
Hf	0	0	0	0	0	0	0	0	0	0	0	0
Ho	0.9	1	1	0.9	0.9	1.3	1.1	0.8	1	1	1.1	1.4
La	29.9	33.1	39.3	35.6	31.3	46.3	32.2	30.2	32.6	29.9	39	39
Li	30	31	29.5	36	33	26	39	37	29	5	3.5	2.5
Lu	0.4	0.3	0.4	0.3	0.4	0.4	0.4	0.3	0.3	0.5	0.5	0.6
Mo	-0.1	-0.1	-0.1	-0.1	-0.1	0.3	-0.1	-0.1	-0.1	0.3	0.2	0.3
Nb	9.2	9	8.7	7.7	9.2	9.3	8.9	7.7	9.2	11.3	10.7	11.8
Nd	25	25.6	28.8	28.7	26.3	40.7	28.3	22.9	30.6	26.5	33.6	33.6
Ni	7.5	11	9.5	8.5	12	4.5	11.5	8	3.5	-0.5	-0.5	-0.5
Pb	17	15	15.5	16.5	16	24	17.5	11	15.5	3.5	14	14.5
Pr	6.9	6.8	7.8	7.6	7	10.9	7.4	5.8	7.7	7.3	9.2	9
Rb	92	91	90	104	104	114	117	55	45	122	122	150
S	70	100	40	40	60	160	50	40	50	80	160	210
Sb	0.5	0.6	0.5	0.6	0.8	0.5	0.9	0.9	0.6	2.7	0.9	1.3
Sc	12.6	12	11.5	11.5	14.5	9	20	20	17.5	9	9	10
Sm	5.2	5	5.5	5.4	5.2	8	5.9	4.8	6.3	5.8	6.9	6.9
Sn	3	2.5	2.5	2.5	2.5	4.5	3	2	2	3	3	3
Sr	113	103	104	110	137	138	294	879	397	76	48	97
Ta	0.8	0.7	0.7	0.7	0.7	0.8	0.7	0.5	0.6	1	0.9	1
Tb	0.7	0.7	0.8	0.7	0.7	1.1	0.9	0.7	0.9	0.7	0.8	1.1
Th	11.8	10.8	10.9	11.9	11.5	17.8	10.2	7	8.4	16.2	14.3	15.3
U	2.5	2.1	2.2	2.3	2.4	3.3	2.2	1.9	2.2	1.8	2.4	2.6
V	93	96	88.5	95	114	31.5	118.5	137.5	71	0.5	-0.5	1.5
W	31.7	37	38.4	31.5	33	39.9	34.1	24.8	29.9	24.1	31.1	41.6
Y	25	25	25	24	25	32	27	21	24	3	3.4	4
Yb	2.5	2.5	2.5	2.4	2.5	3.2	2.7	2.1	2.4	3	3.4	4
Zn	59	60	57	67	67	51	72	97	117	65	85	89
Zr	242	226	225	217	225	183	184	154	253	253	259	266
Quartz	48.49	50.39	50.27	48.33	48.18	39	28.49	14.09	15.18	40.29	46.38	42.4
Corundum	2.84	2.97	2.61	4.28	3.58	0.66	0	0.48	1.39	1.16	1.62	1.61
Zircon	0.06	0.05	0.05	0.04	0.05	0.04	0.04	0.03	0.05	0.04	0.05	0.05
Orthoclase	10.89	11.38	10.85	13.44	12.73	14.63	13.02	5.95	8.07	24.59	34.32	27.11
Albite	21.21	19.54	21.07	17.08	17.58	30.77	18.83	34.73	37.36	29.32	12.63	23.41
Anorthite	6.18	5.42	5.45	4.37	5.37	8.65	19.59	24.35	20.3	0.66	1.89	1.49
Spodumene	0.08	0.08	0.08	0.1	0.09	0.07	0.1	0.1	0.08	0.01	0.01	0.01
Diopside	0	0	0	0	0	0	10.17	0	0	0	0	0
Diopside (Ca)	0	0	0	0	0	0	9.07	0	0	0	0	0
Hedenbergite	0	0	0	0	0	0	1.1	0	0	0	0	0
Hypersthene	3.55	3.51	3.34	4.66	3.86	1.64	0.95	8.43	5.79	0.53	0.86	0.43
Enstatite	3.06	3.19	2.94	3.81	3.39	1.63	0.84	7.5	5.22	0.53	0.86	0.43
Ferrosilite	0.49	0.33	0.41	0.84	0.49	0.01	0.12	0.84	0.56	0	0	0
Magnetite	5.25	5.24	4.92	5.61	6.12	3.76	7.38	10.19	8.84	2.7	1.93	0.81
Chromite	0.01	0.01	0.01	0.01	0.01	0	0.01	0.01	0	0	0	0
Haematite	0	0	0	0	0	0	0	0	0	0.4	1	2.34
Ilmenite	1.25	1.23	1.2	0.94	1.26	0.59	1.27	1.45	1.59	0.33	0.35	0.37
Apatite	0.29	0.27	0.24	0.27	0.29	0.17	0.32	0.33	0.45	0.06	0.05	0.06
Fluorite	0.06	0.07	0.06	0.03	0	0.22	0	0.03	0	0	0	0
Pyrite	0.01	0.02	0.01	0.01	0.01	0.03	0.01	0.01	0.01	0.1	0.03	0.04

SAMPLE	95843106	95843107	95843108	95844004	MUGC0086	Milsted 1	Milsted 2	Milsted 3
UNIT	Riversdale Volcanics	Riversdale Volcanics	Riversdale Volcanics	Riversdale Volcanics	Riversdale Volcanics	Riversdale Volcanics	Riversdale Volcanics	Riversdale Volcanics
SECTION								
FACIES	Ignimbrite	Ignimbrite	Ignimbrite	Ignimbrite	Ignimbrite	Ignimbrite	Ignimbrite	Ignimbrite
MEMBER								
SiO2	75.76	76.24	76.06	77.16	64.4	77.42	75.07	67.86
TiO2	0.2	0.2	0.19	0.18	0.39	0.04	0.22	0.39
Al2O3	11.75	11.57	12.03	11.37	14.4	11.97	13.04	14.56
Fe2O3tot	2.68	2.08	2.52	2.83		0.41	3.01	4.02
Fe2O3	2.34	1.66	2.08	2.31	4.77			
FeO	0.31	0.38	0.4	0.47	3.45	0.04	0.35	0.56
MnO	0	0.01	0	0.01	0.07	0.02	0.02	0.04
MgO	0.09	0.23	0.15	0.15	2.92	0.49	0.62	3.94
CaO	0.27	0.05	0.13	0.16	2.43	0	0.02	0.74
Na2O	3.35	2.1	4.73	2.79	3.31	1.96	0.23	3.29
K2O	4.26	5.48	3.25	4.53	3.52	7.16	7.35	3.83
P2O5	0.02	0.02	0.03	0.02	0.086	0	0	0.02
LOI	0.76	1.17	0.61	0.81	3.59			
rest	0.19	0.16	0.15	0.21				
TOTAL	99.3	99.27	99.81	100.17	99.9			
	-0.1	-0.1	-0.1					
	1.4	-0.2	-0.2					
	808	652	688		428			
	2.1	1.6	1.2					
	0.2	0.1	-0.1					
	77	72.1	76.3		48.2			
	-1	-1	-1		45			
	2.2	2.6	1.2					
	3	2	2		28			
	6	4.8	6.4					
	3.7	3.1	3.8					
	1.4	1.2	1.6					
	-200	-200	-200					
	15.4	15.6	13.5		19			
	1.3	1.5	1.1					
	5.9	5.4	5.7					
	0	0	0					
	1.2	1	1.3					
	35.8	33.3	35.7		27.1			
	2.5	2.5	4.5					
	0.6	0.5	0.5					
	0.2	0.1	0.1					
	11.4	11.3	11.5					
	31	30.9	32.5		19.2			
	-0.5	-0.5	-0.5		17			
	23.5	13	22.5		11			
	8.3	8.3	9.8					
	111	137	56		87			
	50	100	120					
	1.1	1.6	0.6					
	8	9	10		15			
	6.4	6.3	7.1					
	3.5	3.5	1		11			
	113	62	83		195			
	1	1	1					
	0.9	0.8	1					
	14.9	14.6	14.5		10.8			
	2.7	2.6	2.4		2.8			
	0.5	3	5.5		108			
	35.5	28.9	38.2		19			
	3.8	3.3	3.6					
	42	44	11		59			
	275	282	254		121			
	39.71	43.26	35.77					
	1.12	2.11	0.6					
	0.06	0.06	0.06					
	26.55	32.96	19.33					
	28.72	18.07	40.23					
	1.48	0.3	0.66					
	0.01	0.01	0.01					
	0	0	0					
	0	0	0					
	0	0	0					
	0.23	0.58	0.38					
	0.23	0.58	0.38					
	0	0	0					
	0.41	0.65	0.7					
	0	0	0					
	2.43	1.66	2.05					
	0.38	0.39	0.36					
	0.05	0.06	0.08					
	0	0	0					

APPENDIX B3

PETROGRAPHIC ANALYSES

HILL END TROUGH

Quantitative point counts of selected samples of the Turondale, Merrions and Waterbeach Formations are documented in this Appendix. The number of grains counted for each sample is given (n). Other abbreviations are as follows:

- Crystals: Qv = volcanic quartz; Qm = metamorphic quartz; Qgl = composite quartz grains (glomeroporphyritic aggregates); Pl = plagioclase (albite) exhibiting no twinning; Pl(t) = plagioclase exhibiting multiple twinning; Pl(gl) = glomeroporphyritic aggregates of plagioclase; Kp = perthite; Ks = K-feldspar; Mt = opaques (magnetite or ilmenite); Zr = zircon;

- Lithic clasts: Lig = volcanic clasts exhibiting compacted shards and/or angular crystal fragments indicative of a pyroclastic origin (interpreted to be ignimbrite clasts); Lpo = volcanic clasts containing euhedral phenocrysts (interpreted to be porphyries, pumice and/or juvenile vitriclasts); Lch = fine-grained microgranular cherty mosaics which display no remnant volcanic textures or phenocrysts (interpreted to represent groundmass/matrix of volcanic clasts); Lv = undifferentiated volcanic clasts; Lvit = vitriclasts; Lblt = mafic volcanic clasts; Lms = metasedimentary clasts, usually composite quartz-sericite aggregates; Llst = limestone clasts;

- Secondary minerals: Ep = epidote; Cli = clinozoisite; Ca = calcite; Ch = chlorite; Ser = sericite; Bt = biotite;

- Others: Mat = matrix/groundmass; amyg = amygdales.

Total quartz (Q%), feldspar (F%), lithic (L%) and matrix/groundmass (M%) contents, recalculated as a percentage of total count, are also presented.

Sample	n	Q%	F%	L%	Mat%	primary minerals: Qv	Qm	Qgl	Pl	Pl(t)	Pl(gl)	Kp	Ks	Mt	Zr	lithic clasts: Lig	Lpo	Lch	Lv	Lvlt	Lblt	Ls	Lms	Llat	secondary minerals & matrix: Ep	Clt	Cx	Ch	Ser	Bt	clay	Mat	amyg
Turondale Formation: CRVS																																	
Section 1: Type Section																																	
TUR11	500	23.4	23.0	5.4	47.6	66	44	7	97	13	2	3		2	1	4	2	4	10		1	4	1	1	7		3	3	42		1	182	
TUR14	500	31.6	26.8	2.2	39.2	112	46		112	21				2				3	3			4	1		7	5	10					174	
TUR15	500	28.4	23.0	2.6	46.0	64	65	13	98	13	4					6			5			1	1		10		8	4	18			190	
TUR16	500	25.8	23.5	5.0	45.2	43	73	13	94	17	7			2		8	1		10	3		2	1		8		2	3	6			207	
TUR18	500	27.4	15.2	4.0	53.4	41	88	8	51	19	1	5				3	4		5	2		2	1	3	23		8	6	24			206	
TUR19	1000	11.3	11.6	0.3	76.7	73	40		104	10		2		1								3										767	
TUR22	500	35.8	32.4	5.4	25.5	82	67	30	106	43	9	4		4		5	3		7	7		3	2		22	20	9	4			2	71	
TUR23	483	22.2	23.8	0.8	53.4	42	63	2	98	14		3					1					2			2		28					228	
TUR28	500	35.0	16.2	5.0	43.8	56	118	1	63	11	3	4				3		5	3			9	2	3			17	8	22			172	
TUR33	500	26.2	39.2	4.2	30.4	15	112	4	130	60	2	4				5	2		2	6	1	2	3		3			1				148	
TUR35	376	18.6	39.5	2.9	38.6	36	23	11	77	32	33	7		1			5		6						54		1	1	1		11	77	
TUR36	453	25.6	37.1	0.0	37.1	31	69	16	87	75	2	4		1											28		3	1	5		12	121	
TUR40	500	26.4	42.8	4.4	26.0	37	79	16	148	46	11	9		2		1	2		4	10	5				38		6	4	4	17		61	
TUR43	500	34.0	8.2	0.2	55.8	138	24	8	37	3		1		10				1							1		15					262	
TUR44	500	17.0	16.4	0.0	66.4	54	30	1	70	7				5	1										54			16			5	257	
TUR48	250	17.2	16.4	2.0	64.0	42	1		36	2		3		1			1		4						13		3		2		6	136	
TUR51	500	36.2	32.4	6.4	26.0	119	40	17	133	17	4	8				4	9	11	8						4	1					4	121	
TUR55	500	22.6	42.2	5.4	28.2	43	65	5	189	20	1	1		8		1				22		1	2	1	6	3	5	34			23	70	
TUR61	500	33.6	38.0	0.0	28.0	44	121	3	152	6		2		11	1										19	9	6	19	9		12	86	
TUR63	500	27.8	40.2	2.2	28.4	55	81	3	188	12		1		6	1					10		1			7	1		21	1		7	105	
TUR65	500	32.8	30.6	1.4	34.2	29	127	8	135	15	3			5						1		4		2	54	22	12				8	75	
TUR69	500	33.0	31.8	2.8	31.0	41	119	5	131	17	9	2		7						5		8		1	11	5	4	16	2		15	102	
TUR70	500	18.0	43.0	1.2	37.4	21	62	7	171	44				2					1	5					79	3		10	4		17	74	
TUR72	500	24.8	42.2	6.4	25.4	67	48	9	166	27	9	8		6		1	2		4	20		4		1	2	14	3	15			5	88	
TUR73	476	34.5	35.8	5.7	22.5	107	48	9	141	26		2		8		6	5	7	5	1		2		1	16		6		1		2	82	
TUR77	500	20.0	36.0	3.0	40.2	45	52	3	128	35	7	10		3	1		1		6	2		6			23	19	2				14	144	
TUR80	500	21.8	47.4	5.4	25.4	45	63	1	183	37	16	1				7			16	1		3			12	7		2	4		13	89	
TUR82	500	33.8	28.2	3.2	34.0	72	94	3	124	15			2	4		1	2		5			6		2	19		7				16	128	
Section 2:"Kurrajong"																																	
TUR159	505	20.8	21.8	16.4	40.0	88	14	3	90	4	1	15		5		4	3	20	10	35		3	5	3	4		6		1		7	184	
Section 3: "Lorinya"																																	
95843089	500	28.6	30.4	3.0	38.2	110	24	9	126	23		3		9			4			5	2			4	29		5	5				142	
95843090	504	36.5	23.8	3.0	36.3	120	47	17	108	12				2			1		6	8					17		13	9				144	
95843091	500	31.4	29.2	0.0	37.5	89	54	14	134	12				9											32		9	8	1			138	
95843092	500	25.2	37.6	2.4	33.6	69	49	8	142	44		2		6			3		8			1			39			4	10		2	113	
95843093	500	26.2	25.6	3.0	41.4	77	40	24	110	15		3		9			1	8	2			2	1	1	17		6	51	2			131	
Section 4: Crudine Creek																																	
TUR89	500	32.6	21.0	6.2	35.6	60	96	7	100	2	2	1		11	2				40			1			2		95		2		3	76	
TUR90	500	17.2	44.2	2.2	35.8	77	7	2	182	38		1		3			2	1		6		2			6	10	1	20			1	141	
TUR92	500	28.2	36.6	1.2	35.6	94	26	4	169	14				7						6					15	40	10	24				89	
TUR93	500	28.6	29.0	5.6	36.4	73	60	10	129	14	2			7		2		7	4	8	2	6			10	22	2	16	8	1		118	
TUR94	500	12.0	12.6	0.0	75.4	48	12		63																4	32		2	4			335	
TUR96	500	22.0	25.0	2.4	49.6	49	52	9	113	10		2		5				1	3	3		6			8	15	1	15	6			201	
TUR97	500	32.0	28.6	11.6	27.8	42	102	16	123	19				3		3	3	8	3	34	1	5	1	1	7		1	10	3			115	

Sample	n	Q%	F%	L%	Mat%	primary minerals										lithic clasts									secondary minerals & matrix							
						Qv	Qm	Qgl	Pl	Pl(t)	Pl(gl)	Kp	Ks	Mt	Zr	Lig	Lpo	Lch	Lv	Lvlt	Lblt	Ls	Lms	List	Ep	Ctl	Ca	Ch	Ser	Bt	clay	Mat	amyg
Turondale Formation: CRVS																																
Section 5: Fairview Creek																																
95843001	500	18.0	33.4	9.8	37.8	50	37	3	112	49	6			5		11	2	1	9	15		5	3	3	22	1	2	14	10			140	
95843002	500	38.2	31.0	11.6	23.0	77	89		100	46	8	1		5		7	6	15	6	8	3	7	2	2	4		11	9				97	
95843003	500	17.6	36.0	3.6	42.6	41	42	5	125	46	4	5		1		3	1		8		1	2	2	1	1	1	3	5				203	
95843004	500	22.6	34.4	9.0	32.6	38	76		122	42	8			6		5	5	9	5	10		8	3		1		3					159	
95843005	500	9.6	3.2	0.0	87.2	47	1		14	1		1													17		3	6				410	
95843006	500	29.6	34.4	1.8	34.2	62	86		130	37	5					1			2	5		1			10	1	3	13				144	
95843007	500	21.2	21.2	1.6	56.0	57	49		84	19		4							6			2						1				279	
95843010	500	20.0	41.2	4.2	34.2	92	8		167	18	1			2					10			6	2	3	2	9	7	33				120	
95843011	500	40.6	15.0	12.0	31.6	144	59		68	8	1			2	2	5	3	30	12	1	1	4	4		2		16	5				135	
95843012	491	50.3	6.9	19.5	23.6	158	89		30		4			2	1	1	3	60	16		1	3	2	5			14	3				99	
95843013	400	29.0	9.8	3.5	56.8	60	36		36		3				4			9	5								151		1			75	
95843014	500	16.8	36.6	6.8	36.6	72	22		180	2	1			4	2	2		7	13			10		2	1	2	13	56	2			107	
95843015	500	15.8	43.4	4.4	36.4	58	21		203	14				3	2	2		1	13			2		4		25	13	28	2			109	
95843016	500	17.2	43.2	4.4	34.8	64	22		187	24	5			1	1			8	4	8		2				30	1	44				99	
95843017	500	20.4	40.4	0.8	37.6	78	24		189	13				4	1							3			3	22		10				153	
95843018	500	25.8	32.0	1.8	39.8	72	56		140	20				4	1				8							37	2	34				126	
95843019	500	24.8	34.2	0.6	39.0	104	20		162	8	1			6	1							3			2	18		42	1			131	
95843021	500	33.4	27.6	8.0	30.4	101	66		120	17	1			3		6	6	1	21		3	3				18	10	31				95	
95843022	500	28.8	32.0	5.8	34.6	85	49		154	4	2			4		1	9	1	5		2	9	1	1		23	3	36	7			104	
95843023	500	15.4	19.6	0.4	64.4	64	13		83	6												2			1			14				307	
95843024	500	25.6	30.4	5.2	40.4	111	18		137	13	2			1		2	2		7	5					3	6	3	4	3			183	
95843025	500	20.8	30.2	9.2	45.2	82	22		141	7	3			3		3	1	2	6	3		1			1	11			1			213	
95843026	491	29.7	32.4	8.9	29.9	105	41		130	29				5		1	4	10	10	3	1	2	3		2	4	1	13			2		125
95843027	500	27.0	33.6	4.8	28.2	98	37		183	14	1			1	1	4			13	7					16		1	5	4			115	
95843028	500	29.2	30.2	5.0	35.6	98	43		146	5				5				19				2	3		1	13	19	22				123	
95843029	500	22.0	37.8	2.6	37.2	62	48		168	21				1	1	3	3	6	1						4	6		6	2			166	
95843030	500	13.2	6.6	1.8	77.8	57	9		33					3					9						16			3	26			344	
95843031	500	28.6	21.8	5.6	45.0	112	21		98	10	1			5		3	1	14	9					1	6	4	1	15	3			196	
95843032	500	34.4	30.2	4.2	30.8	90	82		136	12	3			2		3		7	9			1	1		6	2	6	26	1			115	
95843034	500	28.0	23.0	25.4	23.6	102	38		110	5						2	5	90	36						1		3		17			97	
Section 8: Turon River, Hill End Anticline																																
TUR113	500	16.5	31.6	0.2	51.2	42	35	6	118	18	20	3		1								1			17				100		139	
TUR114	500	30.2	32.6	1.2	35.8	104	38	9	115	47	2			1				1	2			3			5			2	61		110	
TUR115	500	33.2	41.4	0.8	24.6	79	59	28	159	42	2	4							1		1	2			2		13	2	1	20		85
TUR133	500	35.8	35.8	0.4	28.0	79	48	52	129	48		2							2						23			2				115
TUR134	500	33.8	36.6	0.0	27.6	90	54	25	150	21		22													22		2		60			54
TUR135	545	29.9	33.0	1.1	36.0	65	69	29	90	70		20					2				1	2	1		12		2		2	10		170
TUR136	500	24.2	31.6	1.8	42.2	42	33	46	89	34	1	34		1					6		2	1			1					68		142
TUR137	500	18.6	51.2	1.4	27.8	53	37	8	185	59	2	10					1		5				1		14		5	2		29		89
TUR140	500	28.0	24.2	2.4	47.0	103	16	11	104	17			2				1		10			1			42		19	3		5		166
TUR141	500	33.9	24.4	9.4	32.4	125	31	9	82	30		10	4				5		40			2			15		17	1		22		107
TUR142	500	21.2	23.2	4.0	50.6	76	29	1	99	13		4	5				1		19						111		8					134

Sample	n	Q%	F%	L%	Mat%	primary minerals: Qv	Qm	Qgl	Pl	Pl(t)	Pl(gl)	Kp	Ks	Mt	Zr	lithic clasts: Lig	Lpo	Lch	Lv	Lvlt	Lblt	Ls	Lms	Llst	secondary minerals & matrix: Ep	Chl	Ca	Ch	Ser	Bt	clay	Mat	amyg
Turondale Formation: CRVS																																		
Section 9: Macquarie River, Hill End Anticline																																		
95843082	415	15.4	22.2	0.0	62.4	44	9	11	65	18	6	2													31	5				3	1	219	
95843083	500	6.0	6.0	0.0	88.0	16	8	6	24	3		3													44	1				66		329	
95843085	520	21.3	28.3	6.2	43.5	79	25	7	103	39		5		4			17		15						25	14	44	23			18	102	
TUR143	520	25.8	23.5	1.2	49.6	61	40	33	66	20	1	35					3		1				2		4	17	7			42		188	
TUR144	520	13.3	13.8	1.2	71.7	44	9	16	53	6	6	7					1		5						15	31	6		2	39		280	
TUR145	500	22.4	30.8	0.4	45.8	76	10	26	107	30	3	14		4					2						17	5	3			67	1	135	
TUR146	500	21.2	32.2	3.2	43.4	62	29	15	142	9	1	9					9		7						13	1				53	1	149	
TUR149	500	33.2	38.8	2.2	25.8	121	20	25	156	34		4					4		7						20		8		1	15		85	
TUR150	500	42.8	32.2	1.2	23.8	86	73	55	112	41	1	7					3			2			1		7	1	4		2	31		74	
TUR151	520	11.3	16.0	0.0	72.7	36	9	14	68	5		10							2						37	21	5		1	55	1	258	
TUR152	500	14.8	20.6	0.0	64.8	49	7	17	74	15	2	12													39	1	3			9		272	
TUR153	500	33.8	37.6	0.4	28.2	35	56	78	132	44		12							2						18	2	3			39	1	78	
TUR154	550	17.6	38.9	0.0	42.5	54	10	33	177	33	2	2		5											21	43				74	5	91	
TUR155	520	21.9	41.3	1.5	33.7	73	13	28	177	32		6		8			5		2				1		38	10		17		2	16	92	
TUR156	510	23.9	33.5	4.3	37.8	82	32	8	152	10		9		1	1		5		17						12	11	3	4	2		13	148	
TUR157	540	22.0	57.0	2.0	38.7	59	15	45	172	23	2	3		1			4		2	3		2			32	30	1	9		20	6	111	
TUR158	500	29.4	15.4	2.8	52.2	102	18	27	64	9	1	3			1		5		8				1		19		6			3	5	228	
Section 10: Cudgegong River																																		
95843100	500	33.8	25.8	1.8	40.6	124	17	18	109	17		3		1					6			1	1		37			1		87	9	69	
95843097	500	31.4	10.4	2.4	55.6	89	27	41	26	3	1	22		1				2	10						8		11	2	7	51	4	195	
95843101	500	23.0	20.2	4.6	51.4	78	22	15	84	14		3		4			9		3		2	9			44		3			75	16	119	
95843099	500	26.8	37.6	0.0	33.4	104	14	25	179	7		2		2											52				2		6	107	
Turondale Formation: porphyry																																		
95843115	292	5.1	32.5	0.0	62.0	9	3	3	42	16	34	1		1											21	2			2	52		104	
95843116	500	3.8	31.8	0.0	63.8	7	11	1	54	30	73	2		3											29	1			5	95	3	183	3
95843129	500	6.2	33.2	0.0	59.4	27	4		45	49	71	1		6											10					143		144	
95843132	450	5.1	36.4	0.0	58.2	18	4	1	39	34	90	1		1											34			2		77		149	
94844598B	488	4.3	36.1	0.0	59.6	18	3		49	35	89	3		5											24	2			7	101	9	143	
Merrions Formation																																		
94843522	500	5.8	41.0	0.0	52.8	4	25		174	30	1			2														42	61			181	
94843523	500	34.2	47.0	1.8	17.0	61	110		118	38	2	3	74										9		9			13	1			62	
94843524	500	9.4	35.6	0.4	53.8	6	41		128	45	4		1	4					2						47		2	22	45			153	
Waterbeach Formation																																		
WAT1	510	42.0	7.3	10.0	40.8	125	23	66	26	4		7						4	30			11	6		6		16	1	21	14		150	
WAT2	504	30.6	13.9	0.8	54.4	111	22	22	55	7		8		1								1	3		3		5	1	33	28	1	203	

APPENDIX B4

MEASURED SECTIONS

HILL END TROUGH

The raw data for 12 measured sections are included in Appendix B4. Measured section locations are listed below and illustrated in Figures B4.1, B4.2 and B4.3. T.F. = Turondale Formation; G.F. = Guroba Formation.

Unit	Section	Location	Mapsheet	Mapno.	Mapscale	Base of section		Top of section	
						easting	northing	easting	northing
T.F.	1	Type section	Sofala	8831-1-N	1:25 000	745600	6338250	744700	6338250
T.F.	2	Kurrajong'	Sofala	8831-1-N	1:25 000	744700	6334400	744100	6334500
T.F.	3	Lorinya'	Sofala	8831-1-N	1:25 000	747100	6341100	746200	6341300
T.F.	4	Crudine Creek	Sofala	8831-1-N	1:25 000	747600	6341200	747200	6342650
T.F.	5	Fairview Creek	Tunnabidgee	8832-3-S	1:25 000	752300	6348650	751500	6348500
T.F.	6	Killongbutta'	Gowan	8731-1-S	1:25 000	726500	6323500	727100	6323650
T.F.	7	Monoghan's Bluff	Hill End	8731-1-N	1:25 000	726000	6333100	727000	6332250
T.F.	8	Turon River	Hill End	8731-1-N	1:25 000	726750	6338750	727600	6338750
T.F.	9	Macquarie River	Hill End	8731-1-N	1:25 000	722875	6336500	721850	6336425
T.F.	10	Cudgegong River	Burrendong	8732-I&IV	1:50 000	714000	6493500	713500	6493500
G.F.	G1	Meroo Creek	Windeyer	8832-3-N	1:25 000	736950	6371000	736100	6371000
G.F.	G2	Burrendong Dam	Burrendong	8732I&IV	1:50 000	709500	6387600	708500	6387600

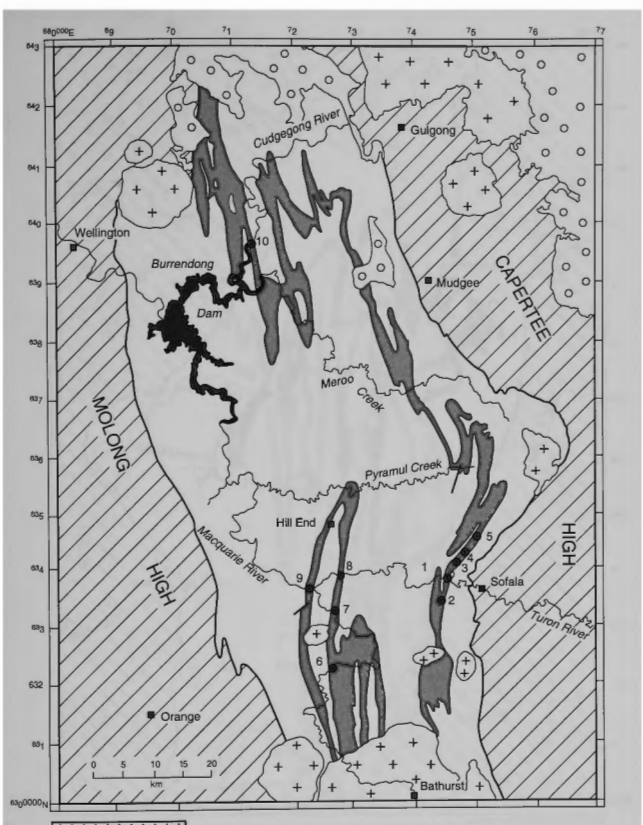

Figure B4.1: Distribution of the Turondale Formation in the Hill End Trough, and the location of measured stratigraphic sections.

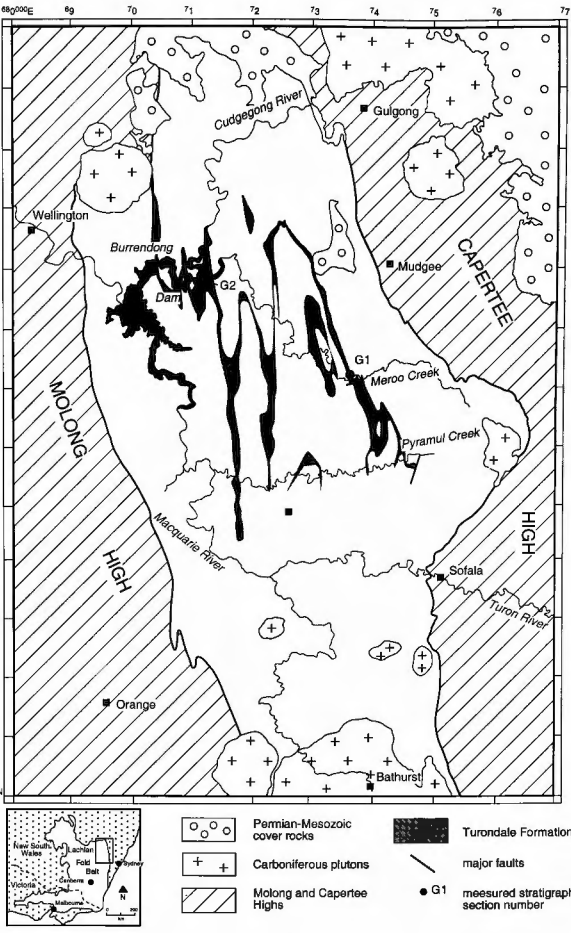

Figure B4.2 Distribution of the Guroba Formation in the Hill End Trough, and the location of measured stratigraphic sections.

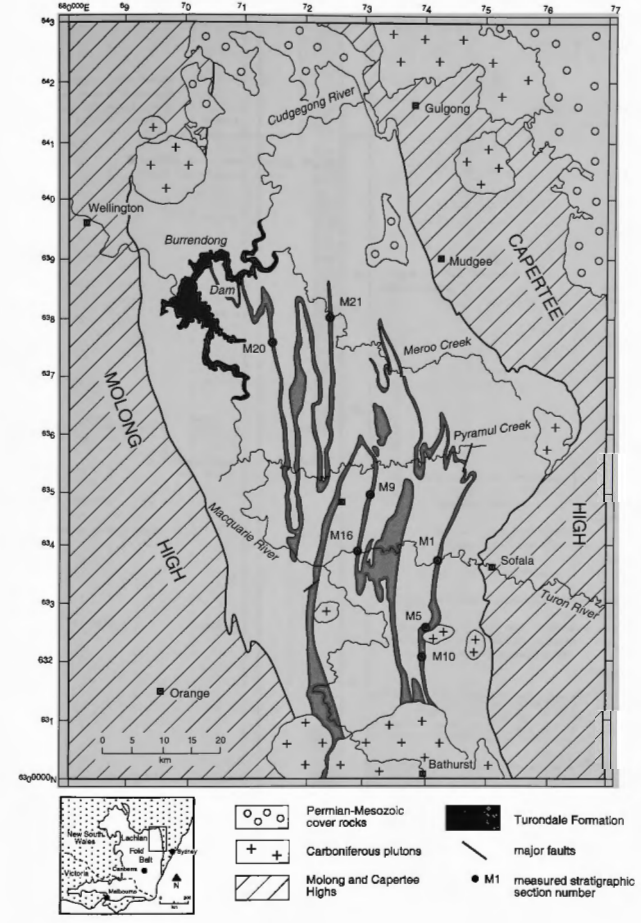

Figure B4.3: Distribution of the Merrions Formation in the Hill End Trough, and the location of measured stratigraphic sections from which samples used in this study were obtained. The measured sections are published in Cas (1978, 1979, 1983a).

Section 1
Turondale Formation
plot 5

Isla

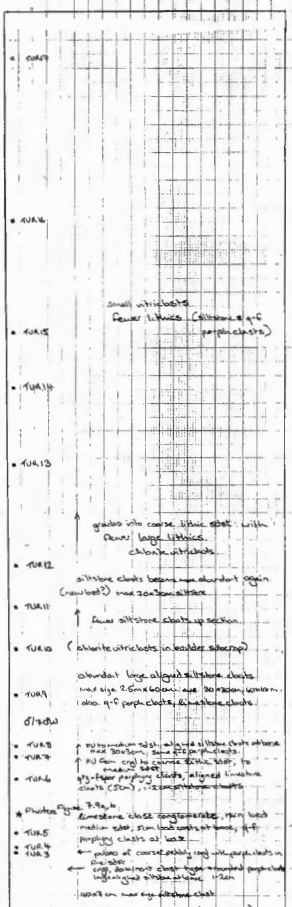

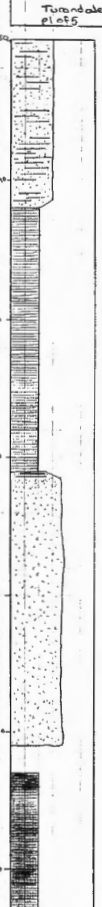

TUR7

TUR6

small utriclasts
fewer lithics (siltstone & q-f porph clasts)

TUR5

TUR4

TUR3

TUR2

grades into coarse lithic sst with fewer large lithics, chlorite utriclasts

TUR12

siltstone clasts become more abundant again (mud bed?) max 20x3cm siltstone

TUR11

fewer siltstone clasts up section

TUR10

(chlorite utriclasts in boulder siltstone)

abundant large aligned siltstone clasts
max size 2.5m x 60cm - ave 30x20cm common
+ abnd. q-f porph clasts, & limestone clasts.

TUR9

07°/S°W

TUR8

↑ FU normal graded siltst - aligned siltstone clasts at base max 30x15cm, below grades into q-f porph clasts

TUR7

↑ FU sm. cycl to coarse lithic sst, to massive sst

TUR6

q-f-porph porphyry clasts, aligned limestone clasts (50cm) - 1.2m siltstone clasts

Plumbton Flysch 3.9m+

limestone clast conglomerate, thin bed
matrix supp, sm rock clasts at base, q-f porphyry clasts at top

TUR5

TUR4

TUR3

← pebble of coarse pebbly sandstone with quartz clasts in matrix

← coarse, dominant clasts have rounded pebble to cobble sized siltstone clasts, 1.2m

laminated sandstone clast

clasts + laminated siltstone (~50cm - 20cm) dominant clast type is limestone / mudstone, blend rare porphyry pebbles

TUR2 (Limestone clast)

rid/80°W

Cowlyman Formation

TUR1

07°/S°W

fine grained, pale laminated, siltstone & mudstone, with common thin (1-10 cm) grey-red... rare very fine sand beds

m f m c gr c b

07°/S°W

medium sstst, massive, diffusedly laminated / normal graded base and planar laminated / graded flow top (15 cm)

TUR26

↑ CU

TUR25

TUR24

TUR23

↑ FU laminated (1m) top 0.5m
fewer cryptoclast

course massive sandstone

TUR22

fine grained pebble clasty sediment
finely planar laminated - no cross bedding

07°/S°W

TUR21

some coarse grained beds with load structures at base.

TUR20

TUR19

TUR18

↑ FU to fine grained conglomerate then fine interbedded clasty sediment

m f m c gr c b

Section 1 (Type Section): Turon River west of Sofala
Torrendale Formation
P2 of 5

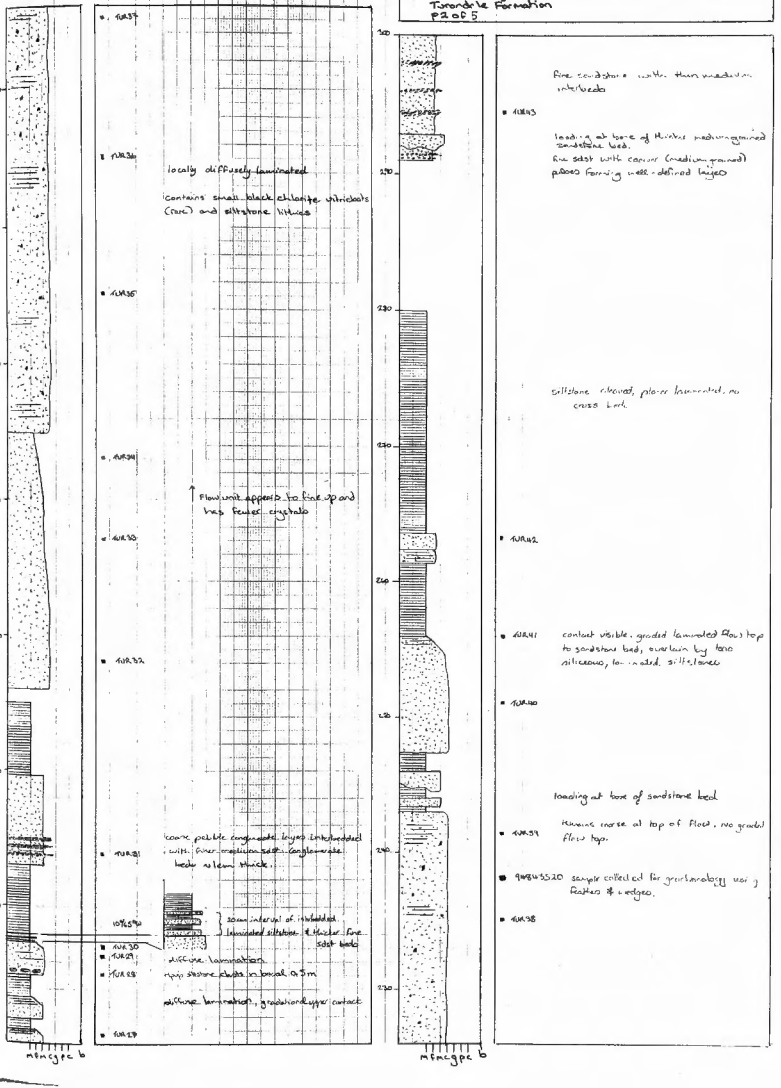

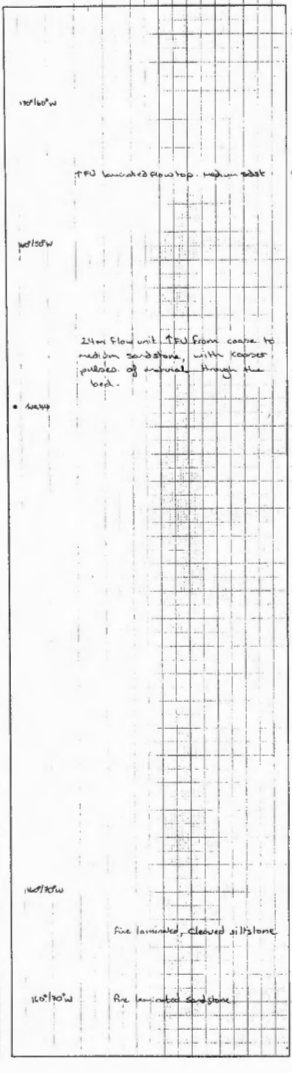

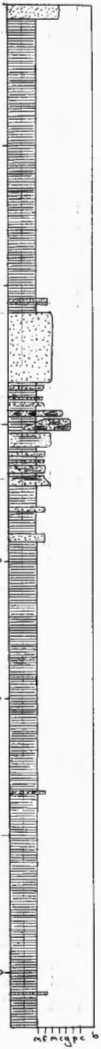

20m ambient sedimentation (siltstone)

130°/60°W

Underside of fine & slightly erosive turbidal fFU into siltstone.

SUR50 5m massive sandstone

Intraformational conglomerate: siltstone rip-up clasts in a coarse sandstone matrix beyond fine-grained sandstone.

SUR49

SUR48

SUR47

SUR46

SUR45

Section 1 (Type Section): Turon River west of Sofala
Turondale Formation
p1 of 5

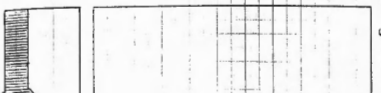

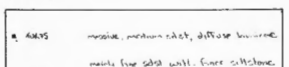

Section 1 U² Turondale Formation P5 of 5

Scale

0.7m massive coarse sand unit

TUR87

amygdaloidal dolerite

TUR86

fine laminated sand

planar laminated siltstones

TUR85

TUR84 diffusely laminated, medium grained sand

TUR83 laminated fine sand

TUR92

TUR91 ← 20cm finer laminated sand at top of bed

TUR80 base loads into underlying laminated sands

* Photo Fig 7.22 a)

TUR81 ↑ FU

TUR78 massive, FU top

TUR77 flaggy FU top to fine sand-sandstone containing large siltstone clasts

planar laminated siltstones

TUR76

metres b

WATERBEACH FORMATION

TUR88 ↑ FU planar laminated flow top

Siltstone rip up clasts at base

3m medium grained sand with FU ↑ planar laminated flow top.

laminated shale, siltstone & fine sandstone

metres b

Section 2: "Kumajong", south of the Type Section
Turnadale Formation
p1 of 2

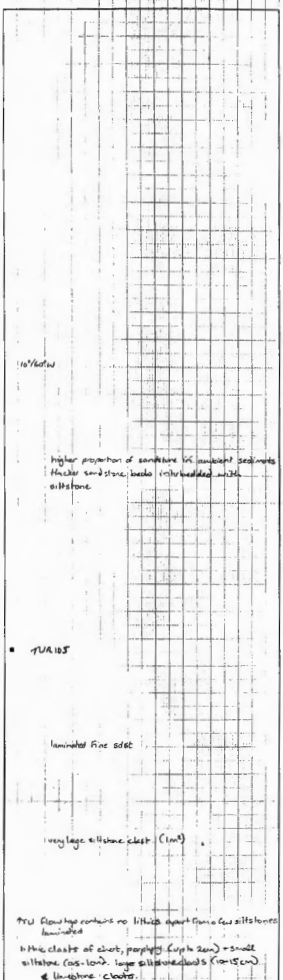

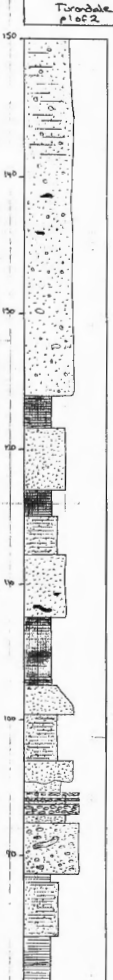

TUR 110

↑ fewer & smaller lithics upsection

diffuse laminations

TUR 107

containing lithic clasts - average 0.5-1.5cm up to 4cm (siltstone), 5cm (rhyolite) ppn of lithics ~5%. & Recrystallised shells.

TUR 108

10°/155°W Fine cherty laminated sediments

TUR 109

Fine cherty laminated sediments now silicified thin siltstones, and does not effervesce

rare siltstone clasts (3cm)

fine cherty sediment with planar laminae at top & base - middle massive

layered fine cherty sediment

thin congl & sdst interbeds

TUR 106 qtz-flspr porph 1-3cm, siltstone up to 5-6cm (ave 0.5-1cm) & limestone (1-3cm)

laminated fine sdst

Section 2: Turnedale Formation
p2 of 2

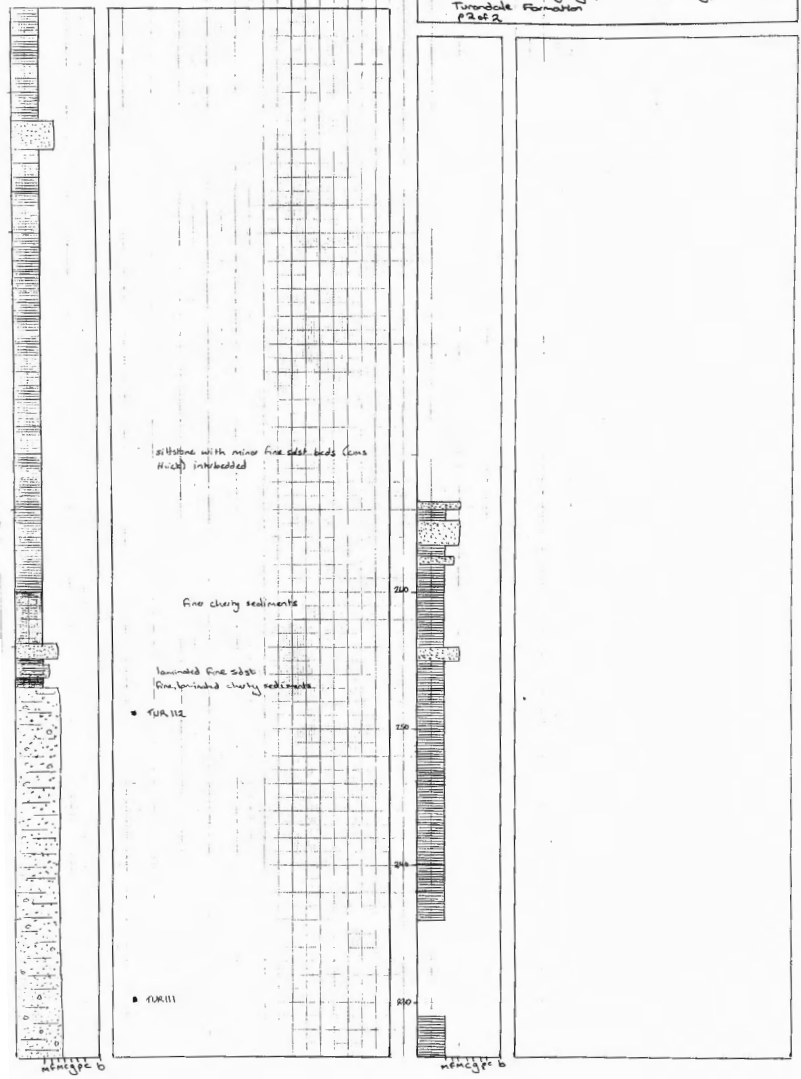

"Loriya" north of Hue Tyre Section, Safala District
Turandale Formation Section 3
p1 of 5

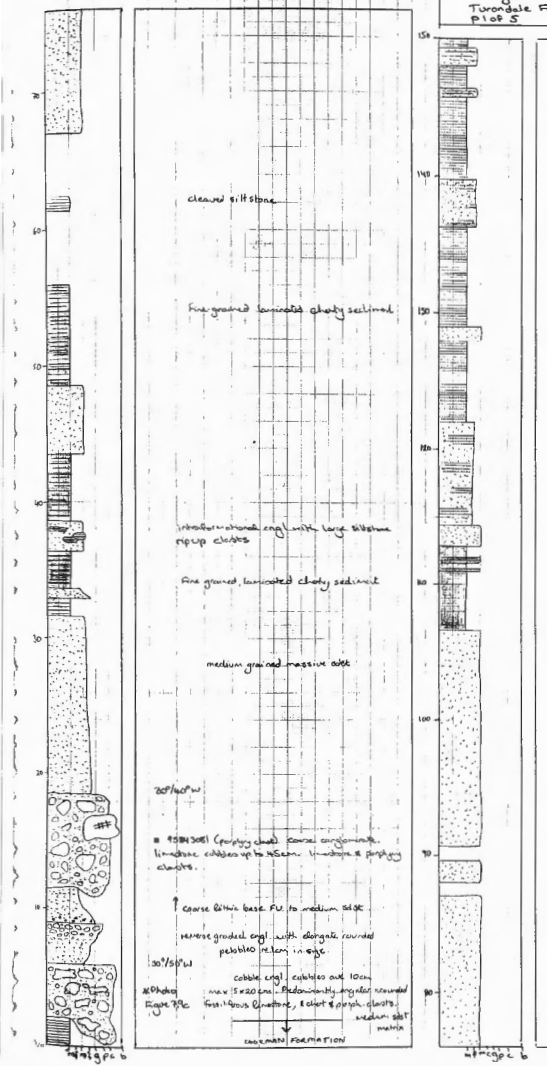

"Loringd" north of the type section, Sofala District
Turondale Formation Section 3
p2 of 5

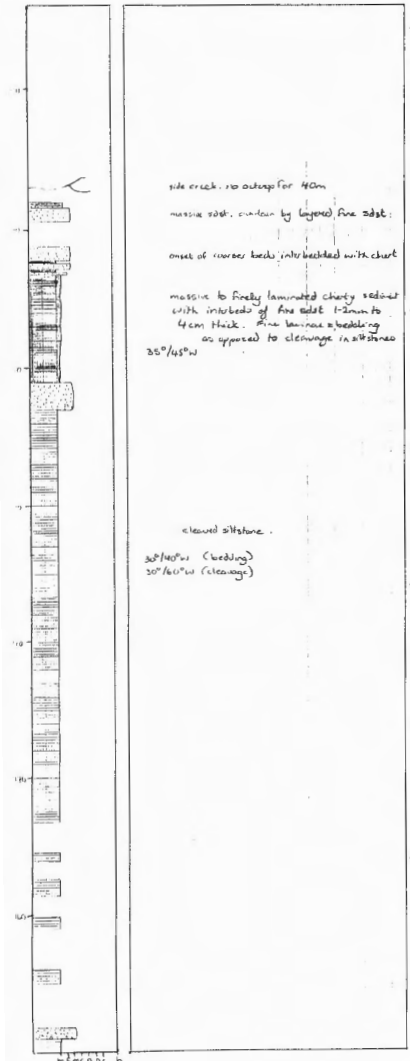

"Loriny" north of the Type Section, Sofala District
Tirandzale Formation
P 808
Section 3

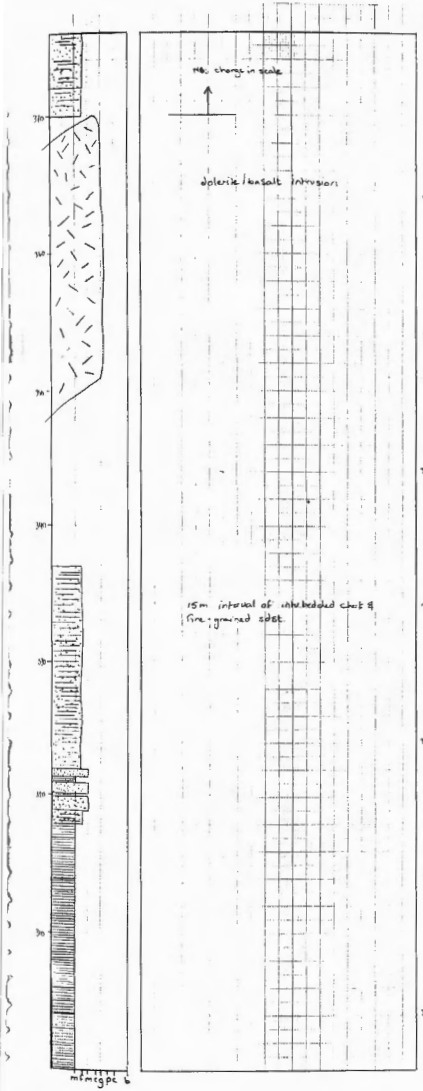

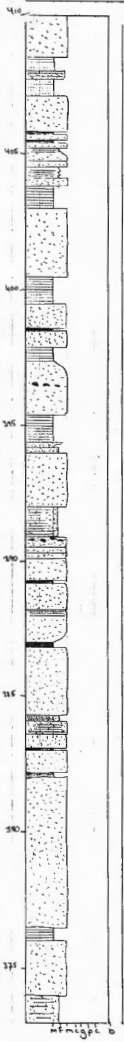

2cm siltstone bands

siltstone

fine grained laminated sdst
small siltstone bands average 1cm upto 15cm

laminated chert nap

interbedded concretion beds (1-2cm) and fine-grained sdst

20°/150°W

fine grained laminated mudstone

"Lorinea [illegible] Turandale Formation Section 3
p 4 of 5

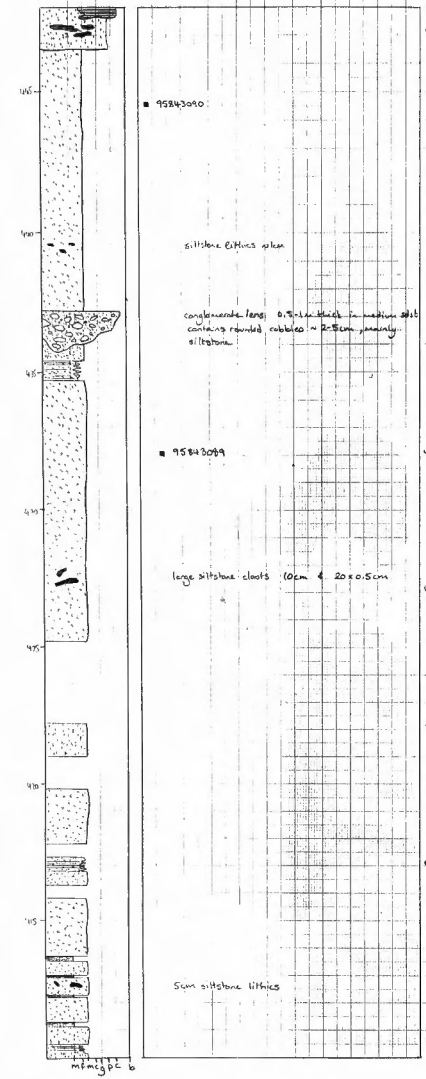

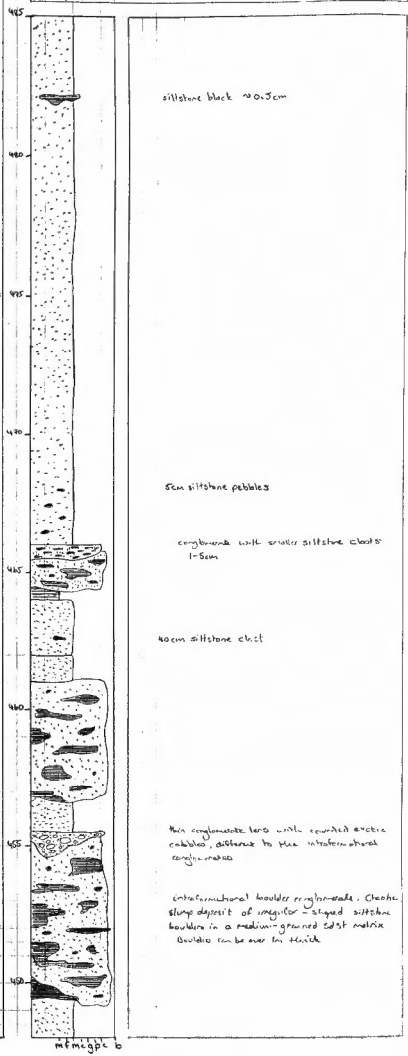

"Laringa" North of the Type Section, Tofala District
Turandale Formation Section 3
P5 of 5

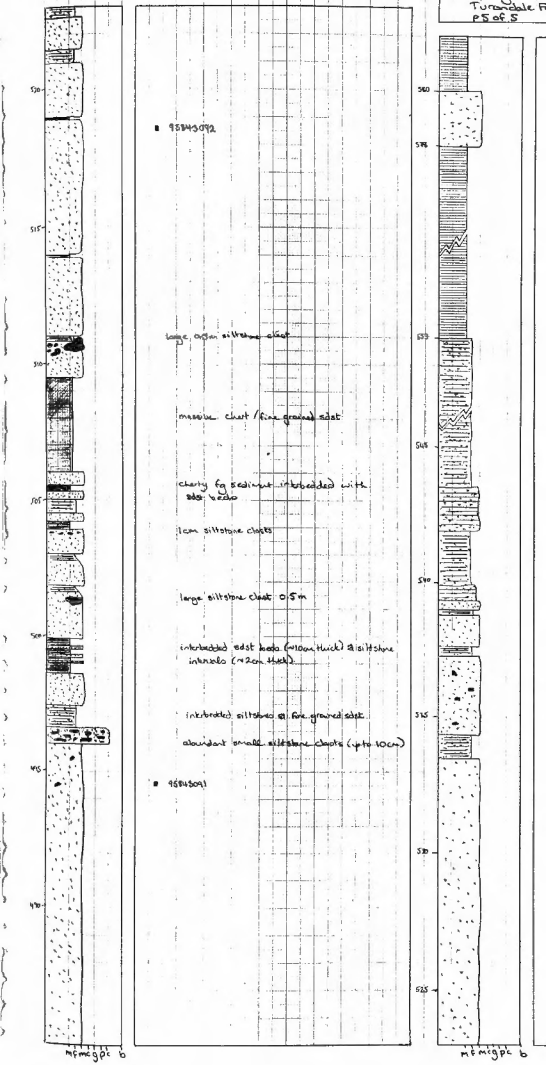

Crudine Creek, north of the [illegible] Section 4 BcFdeDiiM
Tuerdale Formation
p1of4

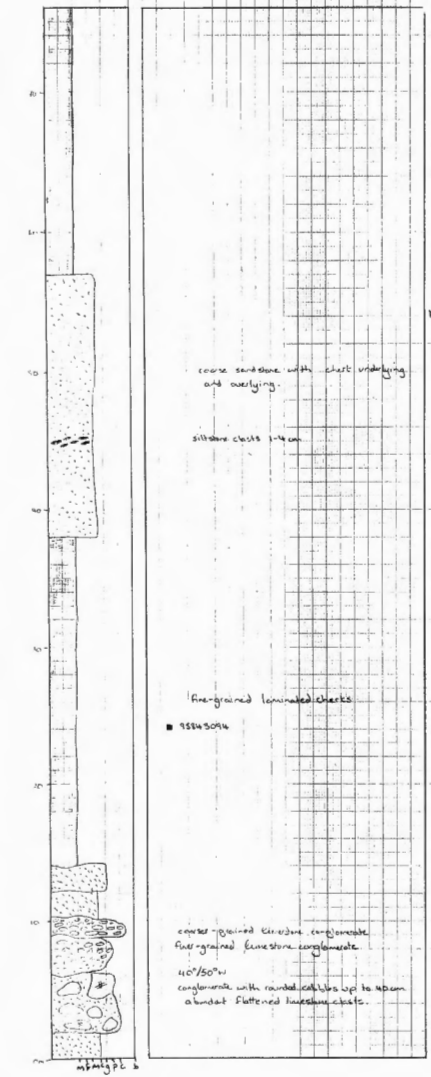

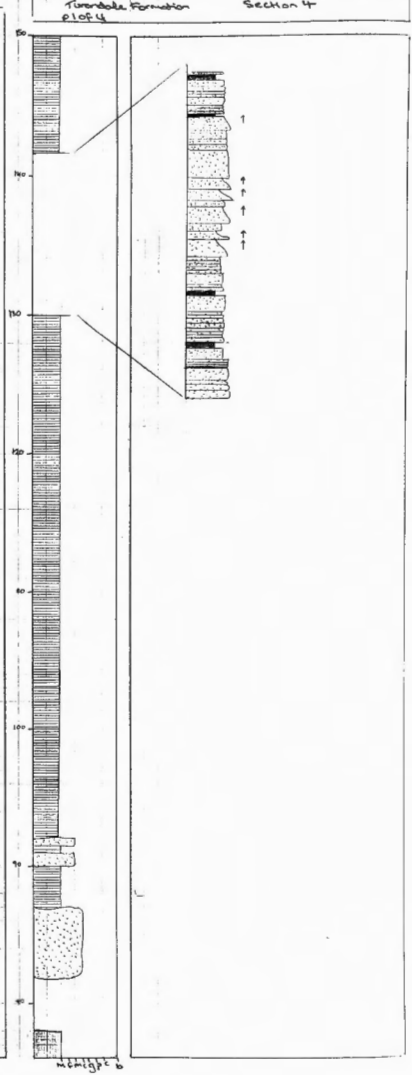

Crudine Creek, north of the Tyne Section, Sofala 1:5000
Torrobolo Formation Section 4
p 2 of 4

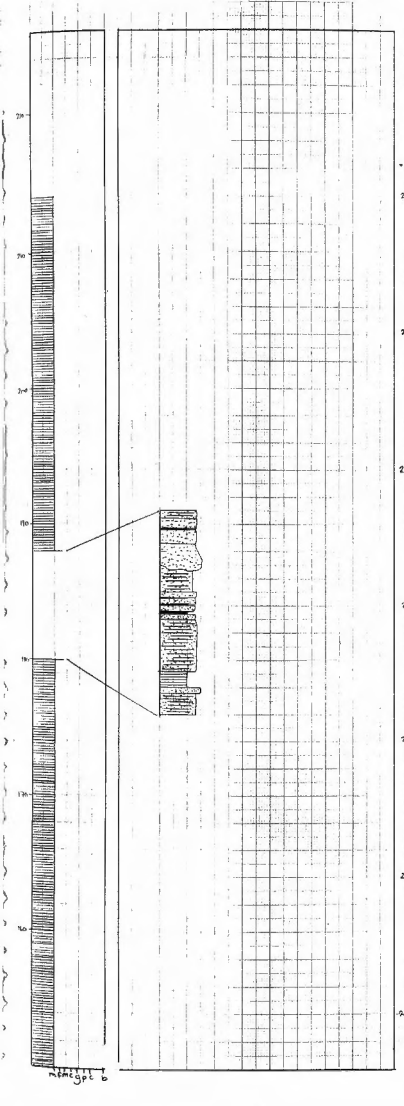

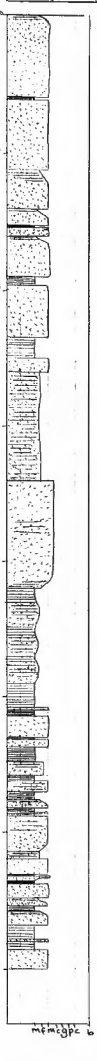

10cm fine sdst laminated flaser top

20°/160°W low-amplitude between 5-6m, massive sdst bed.

UU92

fFU flow top, fines from medium sdst through fine sdst, to siltstone

30cm laminated fFU flow top

massive medium sdst

laminated sdst

laminated fine-medium sdst

UU91

local diffuse laminae

UU90 medium-grained micaceous quartz-feldspathic sdst

reverse-graded, diffusely laminated base 0.4m (fine sdst to medium sdst)

laminated fine siltstone/sdst

↑ FU laminated top
10°/160°W

UU89 massive, diffusely laminated sdst

laminated fine grained sdst

↓ FU massive sdst

↑ FU diffusely laminated flow top

qtz-feldspathic sdst fFU diffusely laminated flow top

10°/160°W

Grading Cross Section
Turondale Formation
Sheet 3 of 4
Section 4

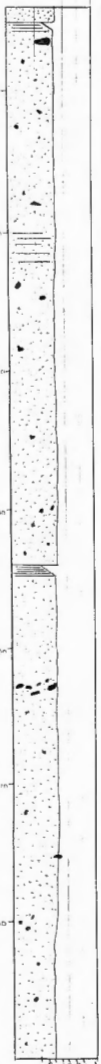

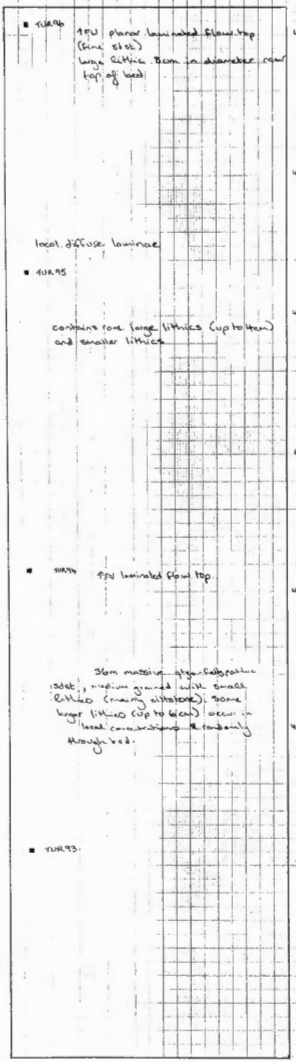

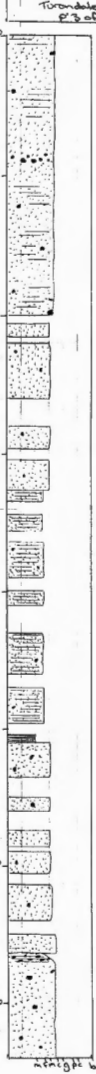

TUR97

where are some coarser pulses in the flows

fine grained laminated sands

1 FU planar laminated flow top with abundant siltstone lithics

Chudine Creek north of Hue Type Section, Sofala District
Tirandalo Formation Section 4
p 4 of 4

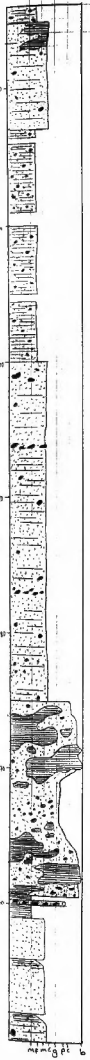

■ TUR 101, 102 chaotic "slump" of sdst & siltstone irregular contact between sdst & siltstone

medium sdst, diffusedly laminated

clasts of siltstone 20x12cm

320°/85°NW laminated sdst with abundant small siltstone clasts

■ TUR 100

diffusely laminated sdst, medium grained contains horizons of lithics (small) and local lithics 5-10cm. lithics mainly siltstone

clarty siltstone boulders sized ~ 1.5 x .5m, 3x1m. they are flattened in shape, suggesting slumping of unconsolidated mudstones and interformation into semi-unconsolidate

■ TUR 99

interformational conglomerate (slump deposit) chaotic mix of large (clearly) siltstone boulders & smaller clasts (20 cm) in medium sdst matrix

↑FU, laminated flow top fine clarty sdst.

■ TUR 98 ↑FU flow top, laminated

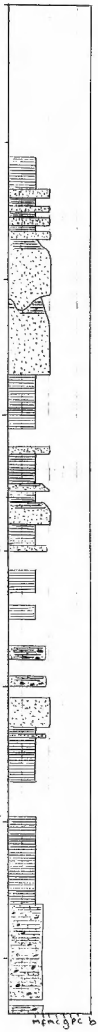

Waterbeach Formation

↑

interbedded fine sdst and siltyvf

loading at base
0.2 diffusely laminated ↑FU flowtop

0.5 fine laminated sdst with horizon of small (<1cm) siltstone rip up clasts

20cm medium grained sandstone bed

20°/60°NW

■ TUR 103 ↑ ferrite into laminated siltstone

Section
Tirrandale formation
pt of S

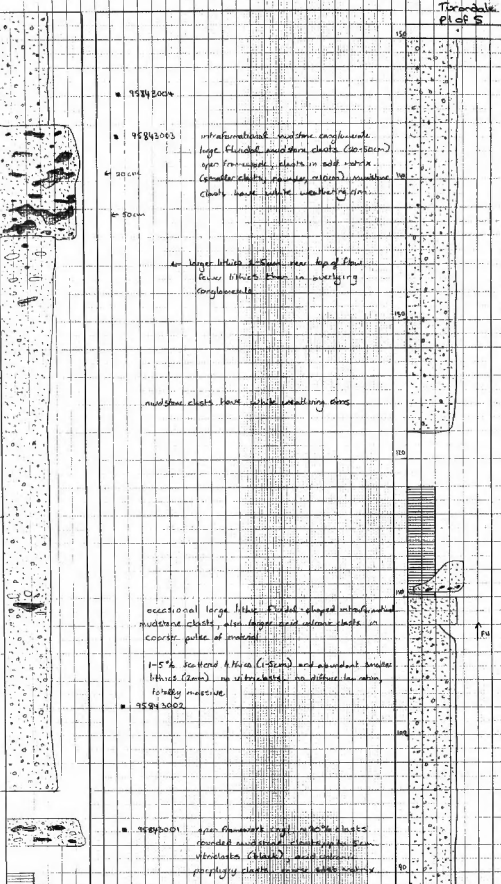

Section 5: Fairview Creek
Tirrendale Formation
P2655

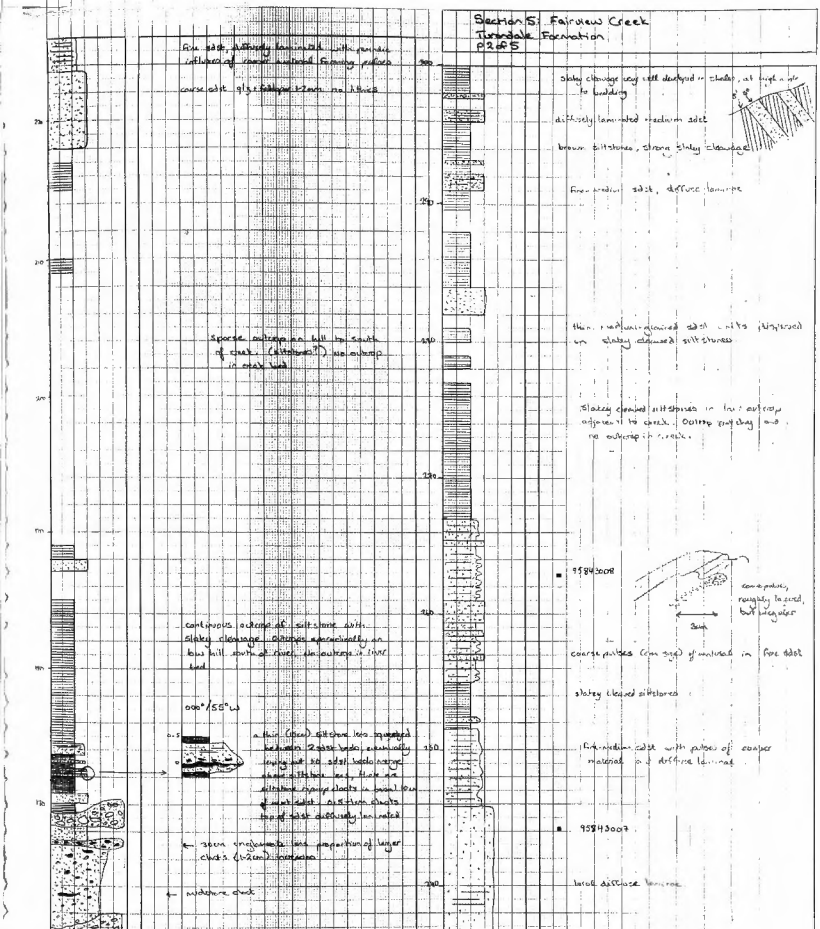

Section
Turondaie formation
P3 of 5

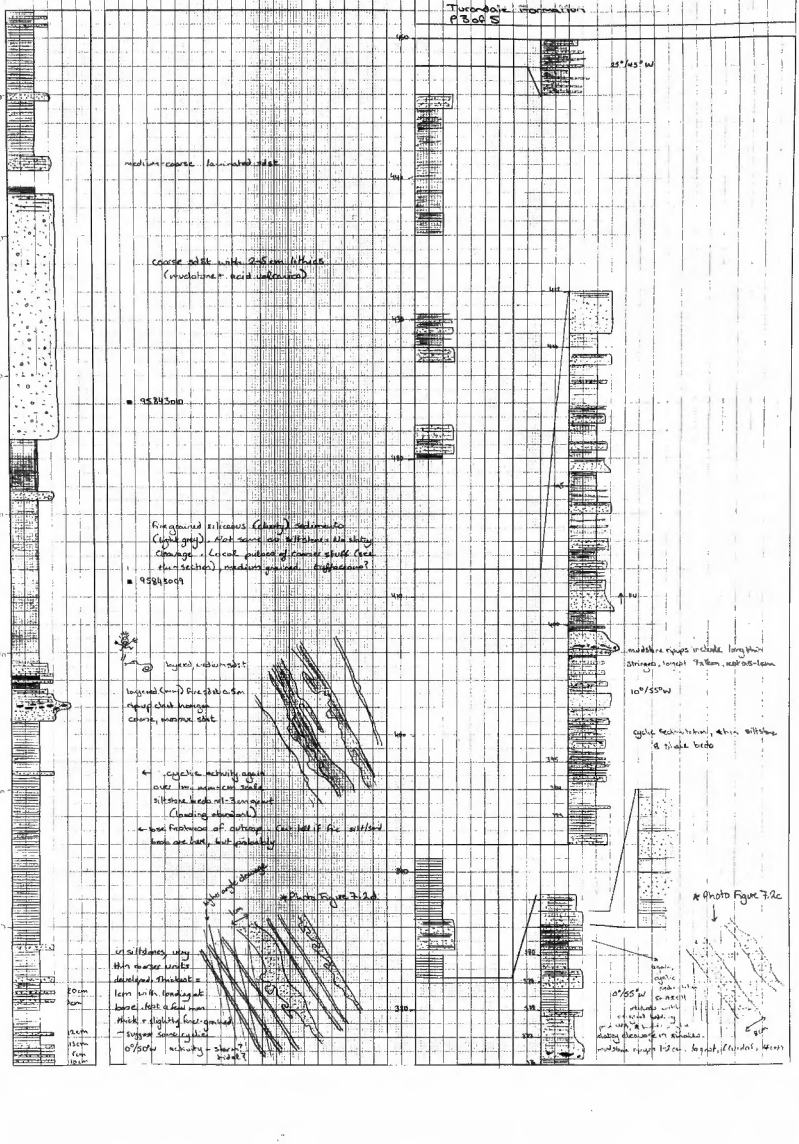

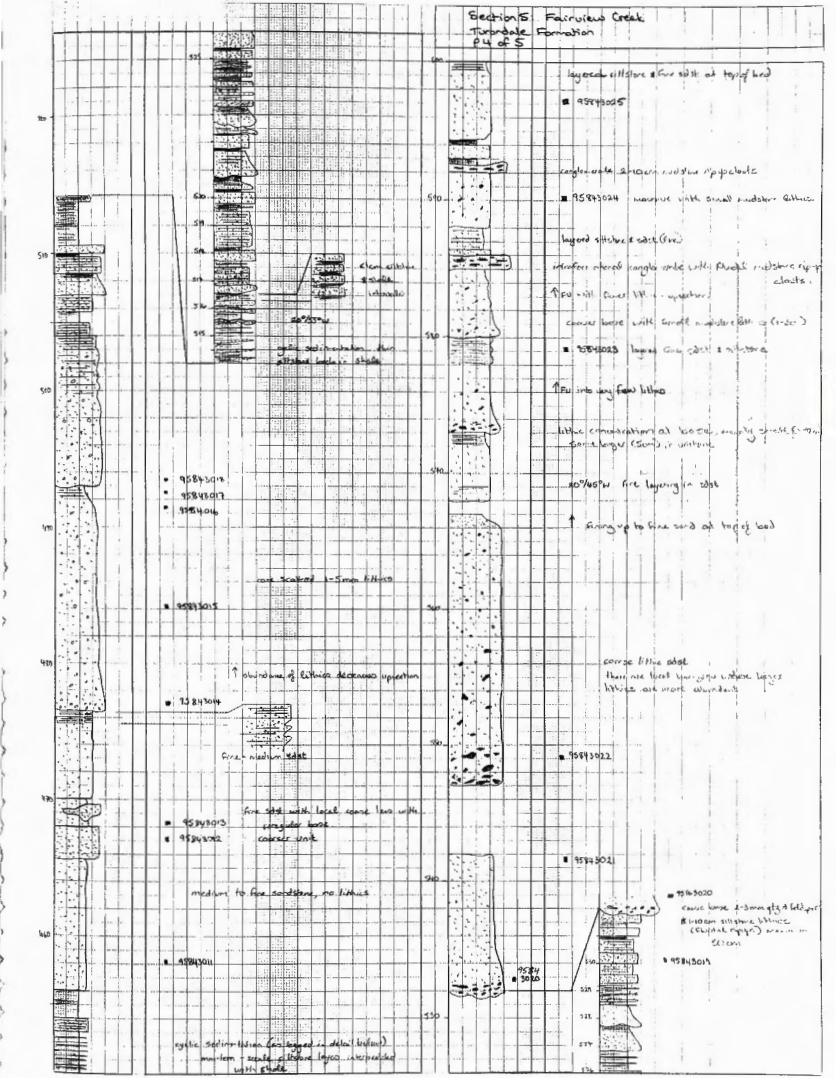

MICADOR A3 297 x 420 mm

Section
Tyrendale formation
p5 of 5

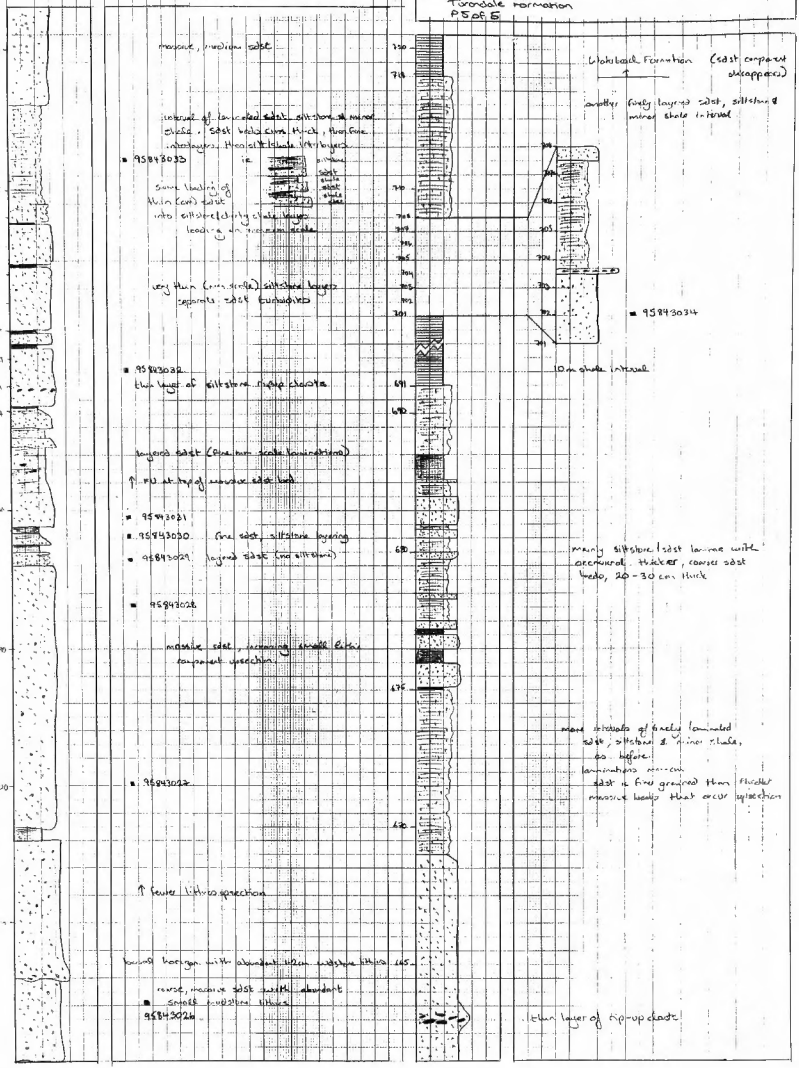

Section 6: "Killorglutta", eastern limb of the Hill End Anticline
Tumbledale Formation
plot 1

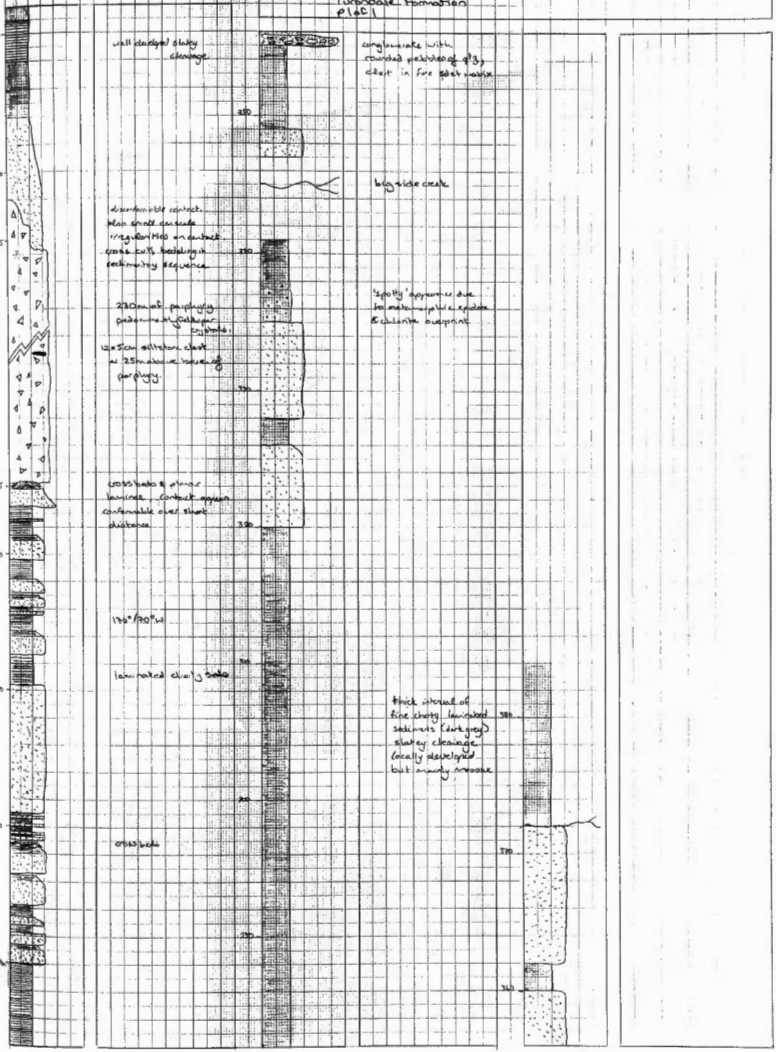

Section 7:
Tinondale formation
pl of 5

Article

fine grained quartzite: coarse-grained thin black clasts and lithic in colour

interbedded lithic clasts and lithic, slightly massive (fine grained tuff) quartzites

- TUR 160
- TUR161
- TUR 162
- TUR 163

massive quartzo-feldspathic tuffs

fine black massive chert

massive quartzo-feldspathic tuff, finer grained than underlying bed

quartzo-feldspathic massive tuff metamorphosed, with biotite

pebble conglomerate with tuff matrix

no distinct layering, looks very massive, hard and siliceous. Clasty (tuffaceous) sediment

contains larger lithic clasts (up to 5cm) - siltstone

very thin siltstone layer

quartz vein

massive quartz-feldspar-lithic tuff with smattered (clay replaced?) biotite clasts.

345°/80°↓

Cookman formation quartzose sediments

150

140

130

120

110

100

90

↑ fine to fine siltstone

diffuse laminae at base top

- TUR16:

- TUR 164 fine clasty sediment, massive laminated chert

fine clasty sediment, no visible bedding

diffuse laminae at base top

clasty sediment, no bedding, but massive

345°/75°E

fine grained clasty tuffaceous sediment, massive

mf mc gpc lo

mf mc gpc lo

Section 7: Monadh's Bluff, main track of the Hill Ed Antelope Turnadale Formation
p2 of 5

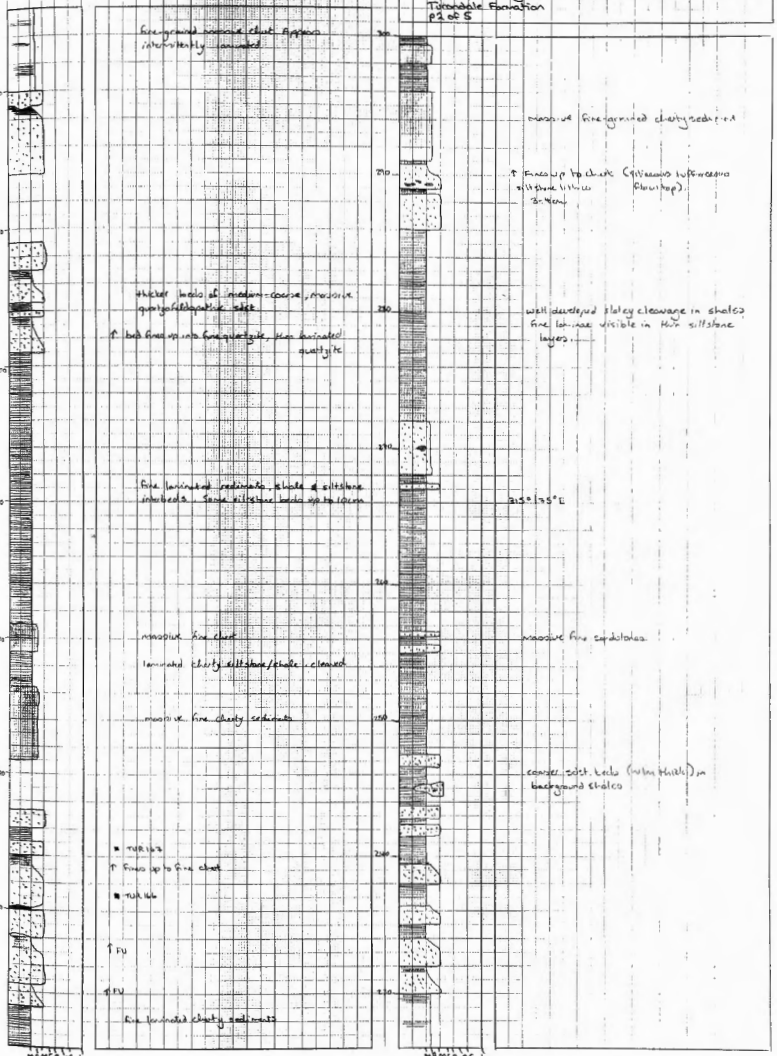

Section 7
Tirrandale Formation
p 3 of 5

Antrelbar

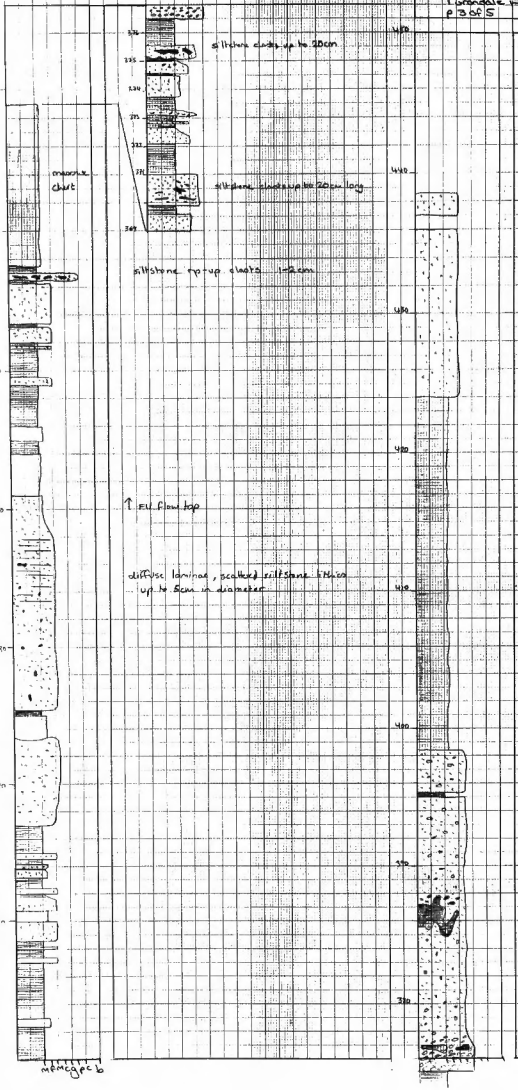

Section 7: Monaghans Bluff, eastern limb of Hillend Anticline
Turnadale Formation
p 4 of 5

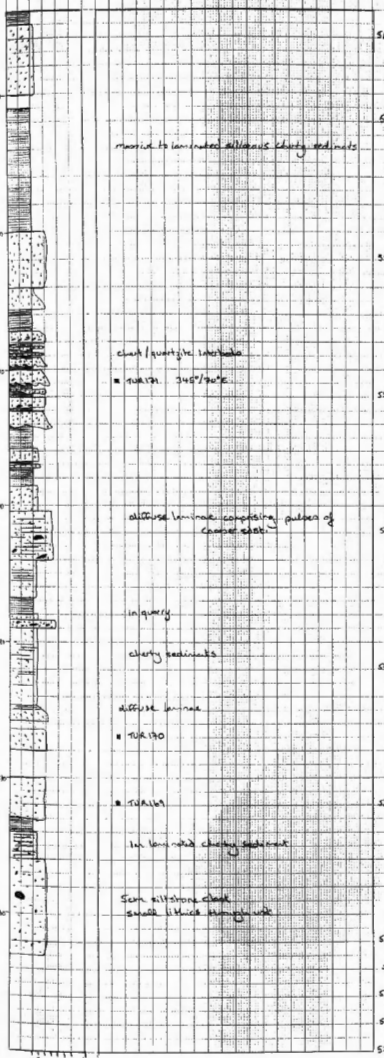

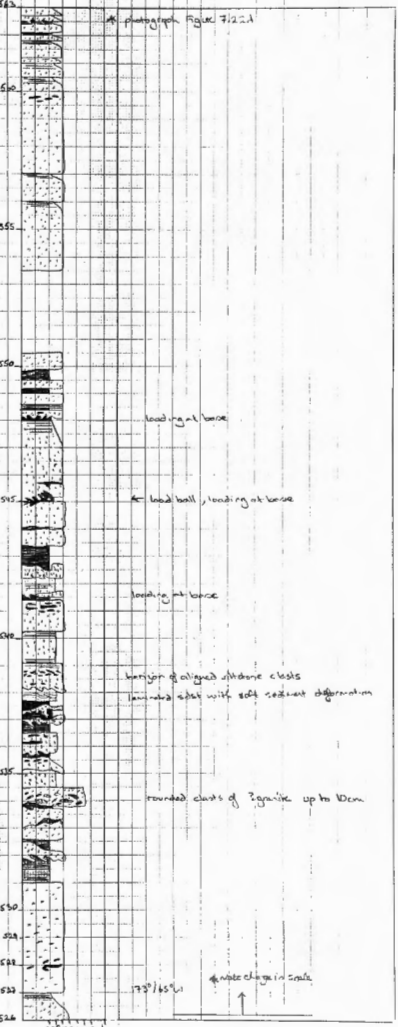

Section 7: Monaghan's Bluff, ea Tyrondale Formation
pg 5 of 5

12m no outcrop

Lithic conglomerate: rounded pebbles of shale up to 3cm within sandst

2-3cm clasts of siltstone as photograph Figure 7.22a

coarser, lithic sdst

quiet tide fine laminae exhibit slumping

diffusely laminated quartzified

* photograph Figure 7.22a

345°/60°E

WATERBEARING FORMATION

Scours of siltstone in coarser sdst

shale and fine bedded sdst ratchets

shale and thin (<5cm) siltstone laminated unit loading at base.

10cm thick siltstone clast

MPMCgpc 6

MPMCgpc 6

MPMCgpc 6

Section B: Turon River, eastern limb of the Hill End Anticline
Turondale & Wolgabrook Formations
01 05 7

TUR115

massive quartz-feldspathic sdst

0°/25°E

local diffuse laminae

TUR114

fine massive to locally laminated sdst

TUR113

Cookman Formation

150

TUR 118

140

Lt. Porphyry - Large fieldspar crystals (4-5mm)

TUR 117

130

TUR 116

150

1m fine thinly sedimented, hardy and more massive. Many undulating silt stones. Possibly a contact metamorphic sequence

vein quartz

adit

110

thin sdst beds in shale

Fine sdst and shale interbeds

100

* photo Figure 7.21a
small mudstone rip-up 10 x 0.5cm

90

20-30 cm fine sdst beds interbedded with 2-3 cm shale interbeds

75 fining fine sdst and shale interbeds

15cm mudstone rip up clast

fining fine sdst/shale interbeds - sdst/shale contacts sharp, shale rip-ups

80

mmegpt

Fieline

Section 8:
Turnadale & Hassendean formations
p 2 of 7

15±5cm chert, either mudstone? or mafic xenolith? Such clasts are very rare

TUR123

TUR122

TUR121

TUR120

TUR119

strong linear fabric is picked out by weathering. May be a brittle preferred orientation or a joint pattern

TUR123

metamorphic overprint: 2-5cm round clasts of epidote/chlorite are abundant in 4m above section (charted by ● on section)

TUR127

becomes more brittle and veined upsection

TUR126

TUR125

9384559E. TUR124

Fragment of petrified wood found. Collected for geochronology

340

330

320

310

300

290

280

270

260

250

240

230

mfmcgpt

mfmcgpt

Section B: Turon River, eastern limb of the Hill End Anticline
Turondale & Waterbeach Formations
p3 of 7

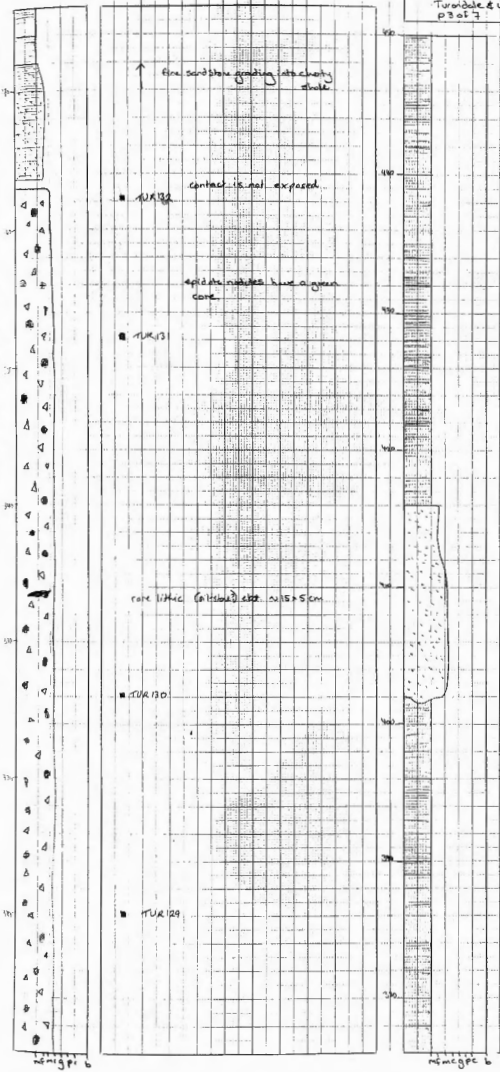

0°/85°E

overlain by cherty sediment which has developed strong bladed cleavage. locally (forming "pencil shales").

Passes up into fine grained sandstone

TUR133

medium, massive quartz + feldspathic silt

locally at base into underlying shale

Section 8: Turonedale Formation & Wasteeam Formation
p4 of 7

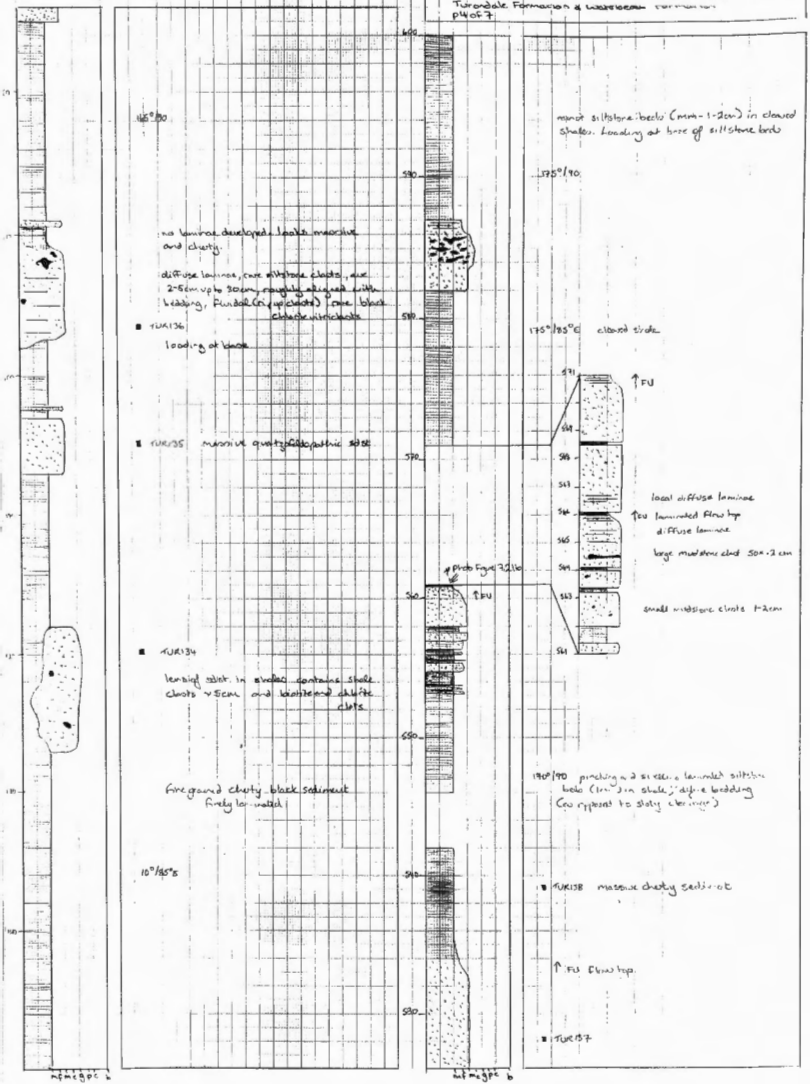

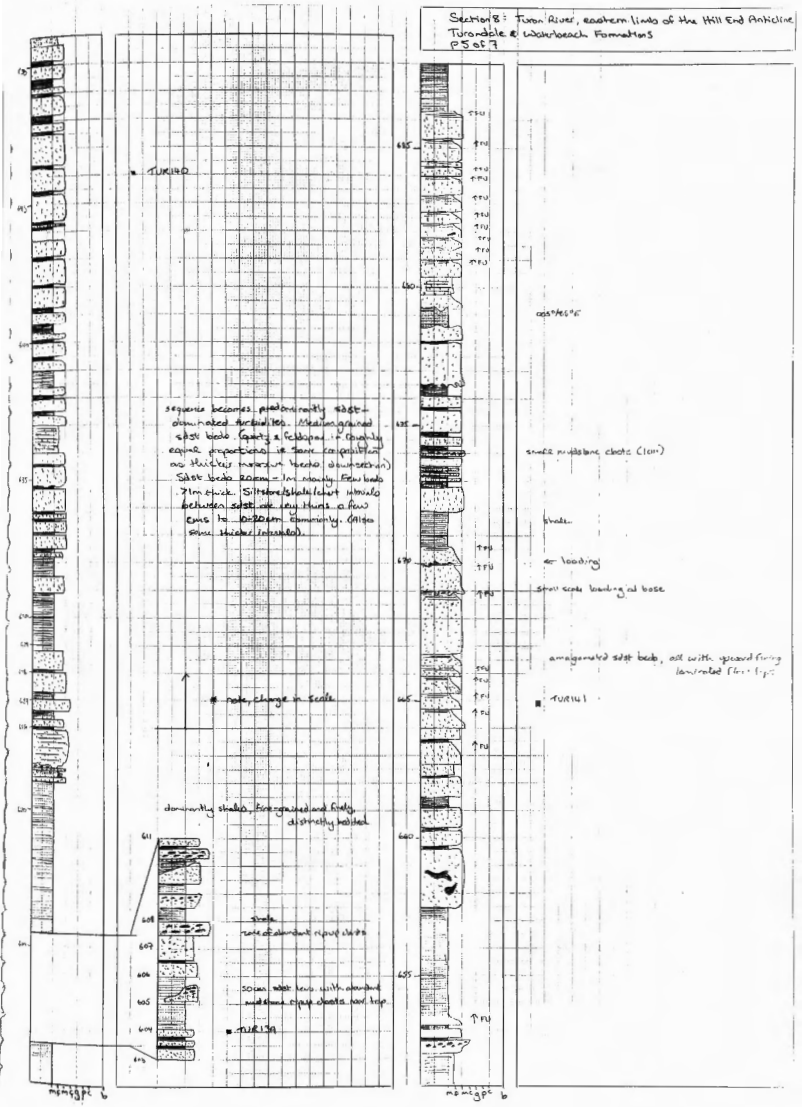

Section 8: Turon River, eastern limb of the Hill End Anticline
Turondale & Waterbeach Formations
p5 of 7

■ TUR140

sequence becomes predominantly sdst-dominated turbidites. Medium grained sdst beds (quartz & feldspar in roughly equal proportions ie same composition as thicker massive beds downsection) Sdst beds 20cm – 1m mainly. Few beds >1m thick. Siltstone/shale/chert intervals between sdst are very thin: a few cms to 10-20cm commonly. (Also some thicker intervals).

* note, change in scale

dominantly shales, fine-grained and finely, distinctly bedded

shale

zone of abundant rip-up clasts

50cm sdst lens with abundant mudstone rip-up clasts near top

■ TUR139

005°/65°E

small mudstone clasts (1cm)

shale

← loading

small scale loading at base

amalgamated sdst beds, all with upward fining laminated fine tops

■ TUR141

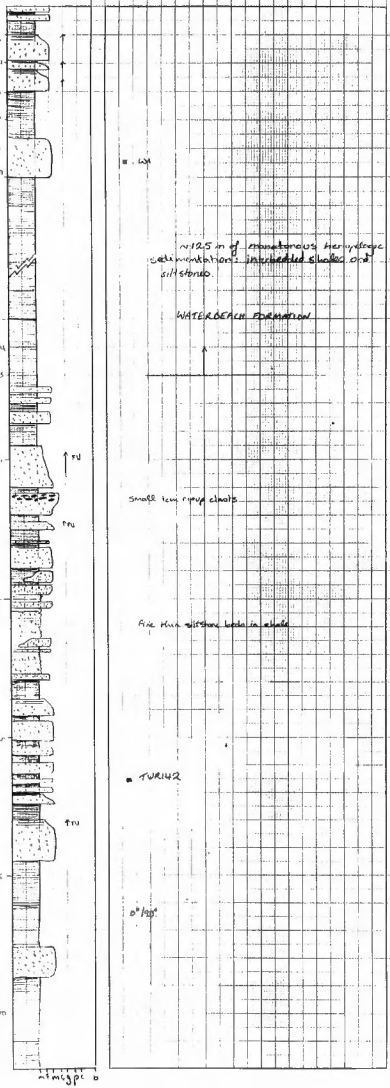

Section [illegible]

Torrandaue & Waterbeach formations

p 6 of 7

-d anticline

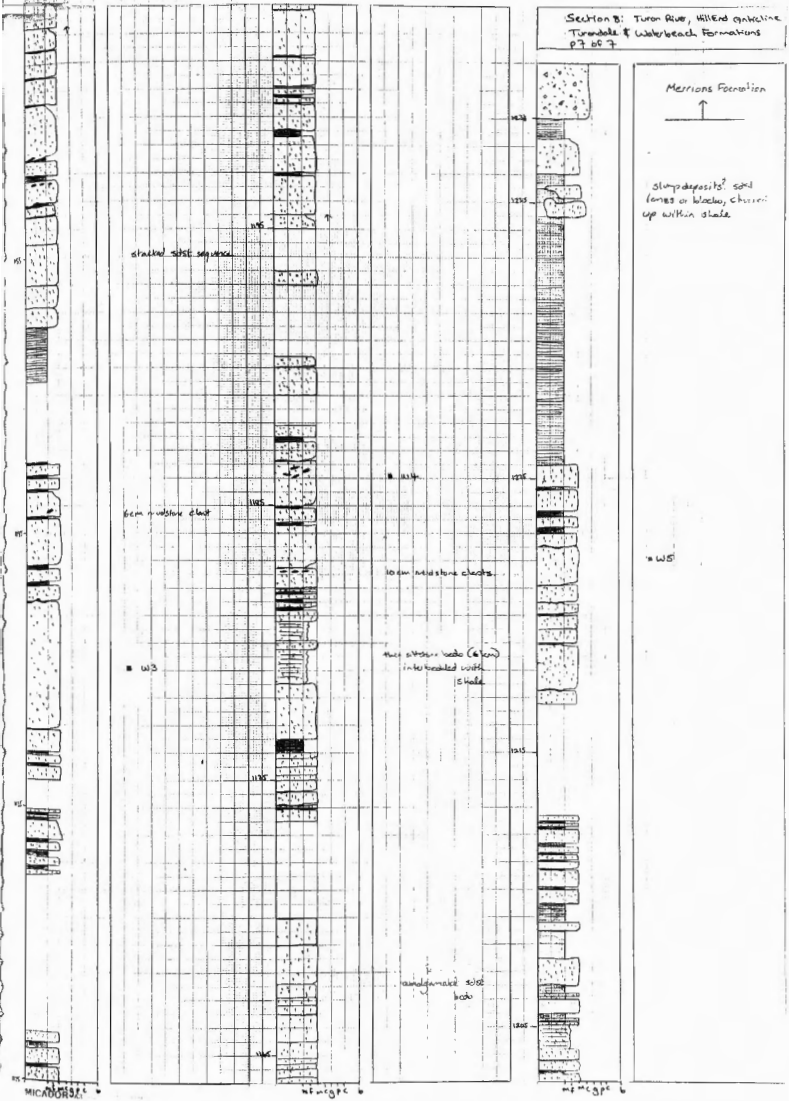
Section B: Turon River, Hillend anticline
Turondale & Waterbeach Formations
p7 of 7
Merrions Formation
slump deposits? sand lenses or blocks, chaotic up within shale
stacked siltst sequence
10cm mudstone clasts
thick siltstone beds (<1m) interbedded with shale
sandy/muddy siltst beds
W3
W5
MICADOROC
NE-SW

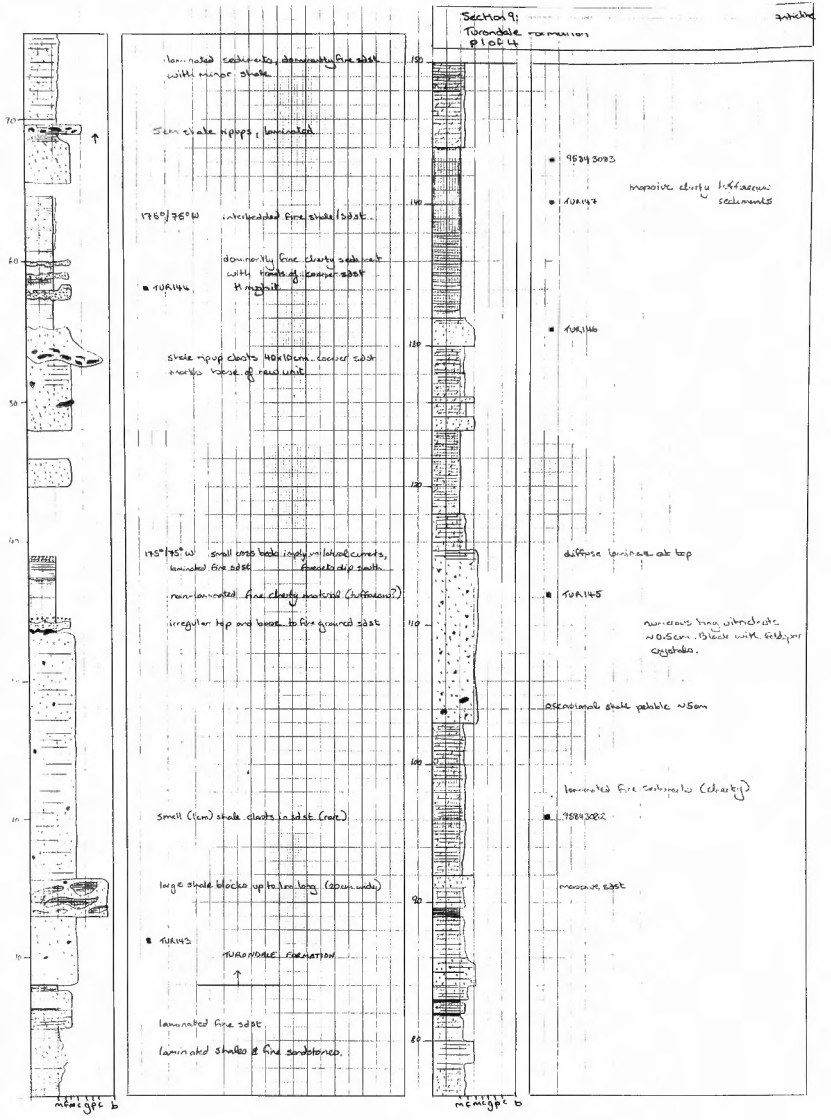
Section 9: Turondale formation
Plot 4
Patching
150
140
130
120
110
100
90
80
70
60
50
40
30
20
10
0
mc mf cg pc b
mc mf cg pc b
laminated sandstone, decreasingly fine sand with minor shale
Sm shale rip-up clasts; laminated
176°/76°W interbedded fine shale/sandst.
dominantly fine clasty sandstone with trends of coarser sand
TUR144
shale rip-up clasts 40x10cm. cocinar sdst marks base of new unit
195°/75°W small cross beds, largely unidirectional currents, laminated fine sdst
Forests dip south.
non-laminated fine clasty sandstone (bioturbated?)
irregular top and base to fine grained sdst
small (1cm) shale clasts in sdst (rare)
large shale blocks up to 1m long (20cm wide)
TUR143
TURONDALE FORMATION
laminated fine sdst
laminated shales & fine sandstones.
9524 3093
massive clasty lithofacies sediments
TUR147
TUR146
diffuse laminae at top
TUR145
numerous tiny, vitric-rich N0.5cm. Block with feldspar crystals.
equidimensional shale pebble 45cm
laminated fine sandstone (clasty)
9589 3082
massive sdst

Section 9: Macquarie River, western limb of Hill End Anticline
Torrondale Formation
P2 of 4

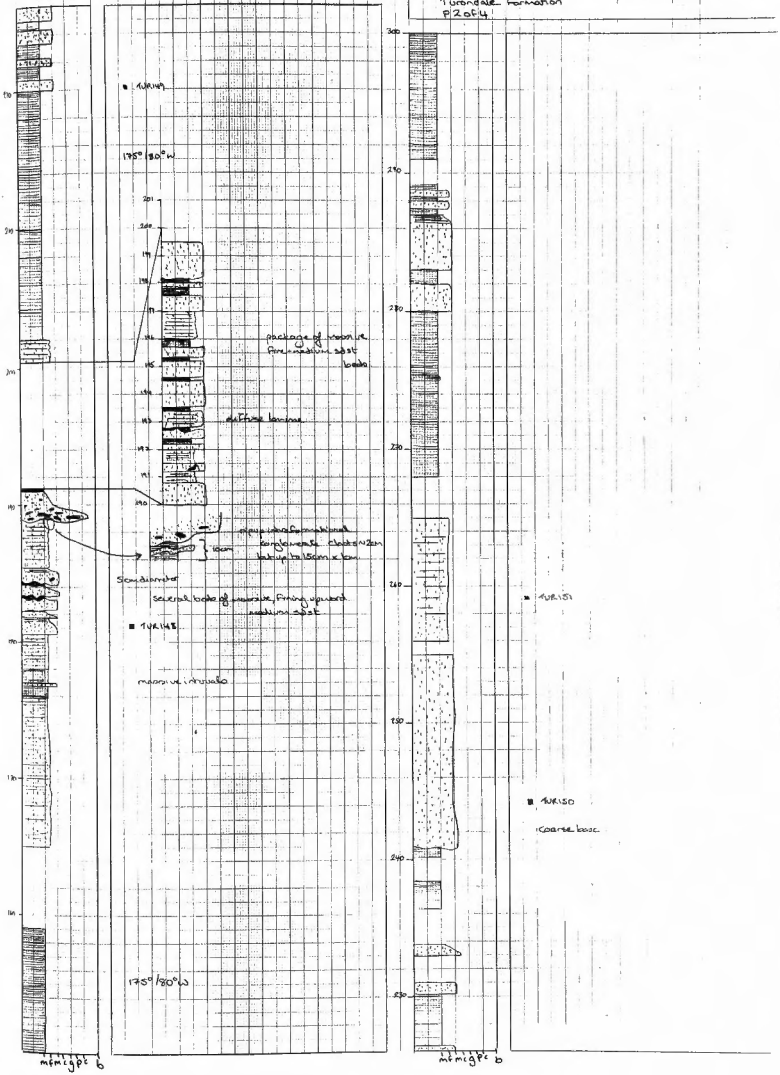

Section 9 — Wildcat
Turondale Formation
P3 of 4

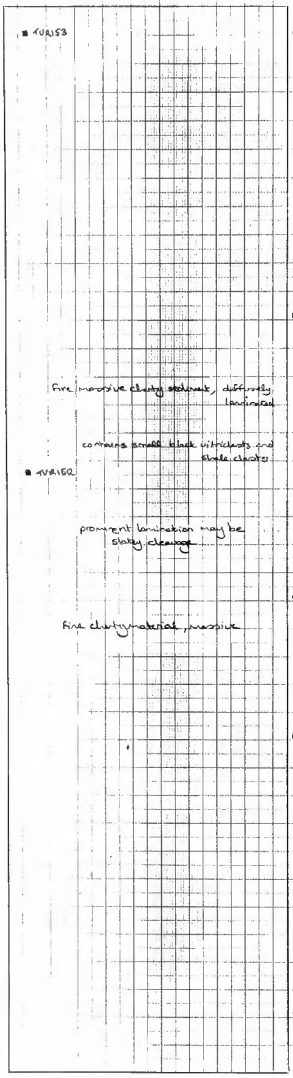

occasional small siltstone clasts 2-3cm

thinner conglomerate

conglomerate as below

* Photograph Figure 7.11
conglomerate, qtz+ fair to crk, rounded clasts some bits of carbon + clasts of shale, coarser sandy

diffuse laminae

Section 9: western limb of Hill End Anticline, Macquarie River
Turondale Formation
P4 of 4

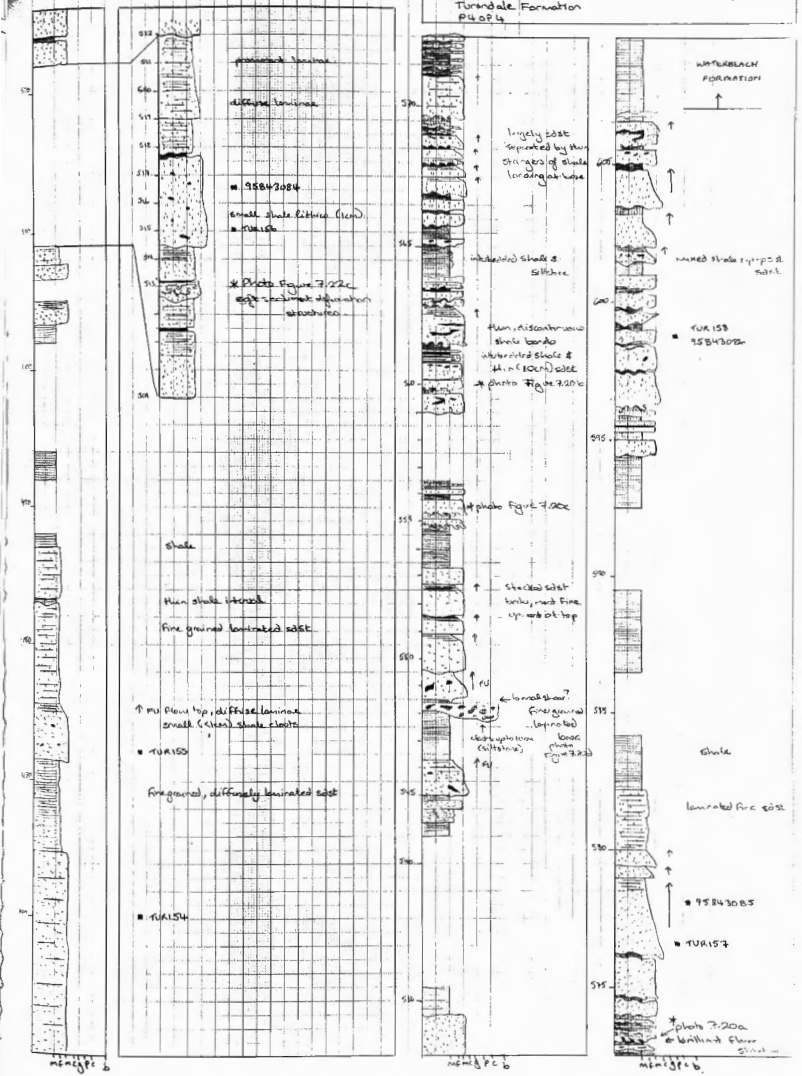

Section 10
Turandale formation
Page 1 of 6

am

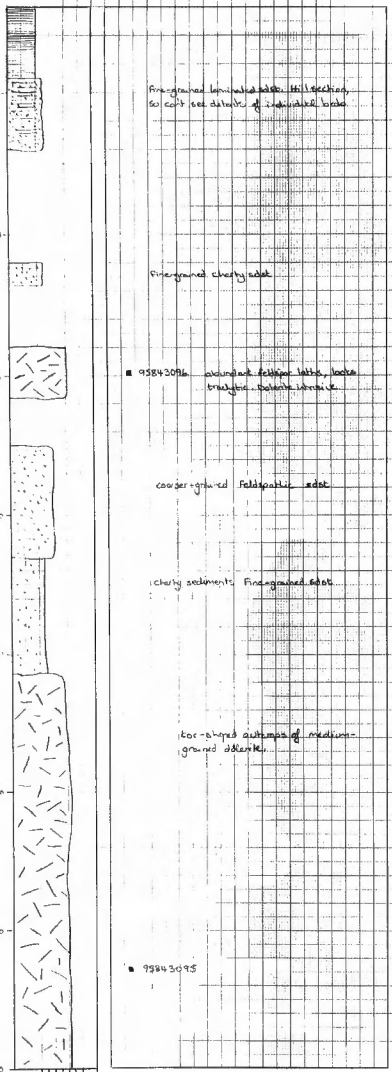

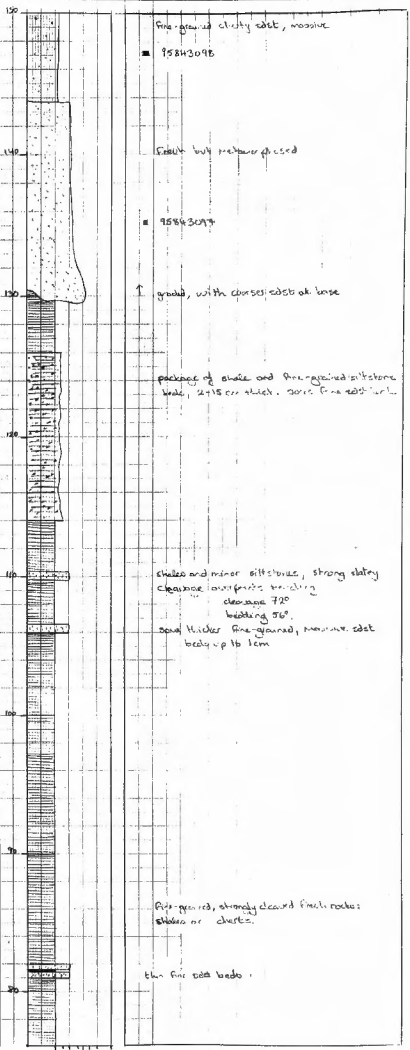

Section 101 Cudgegong River north of Burrendong Dam
Turondale Formation
page 2 of 6

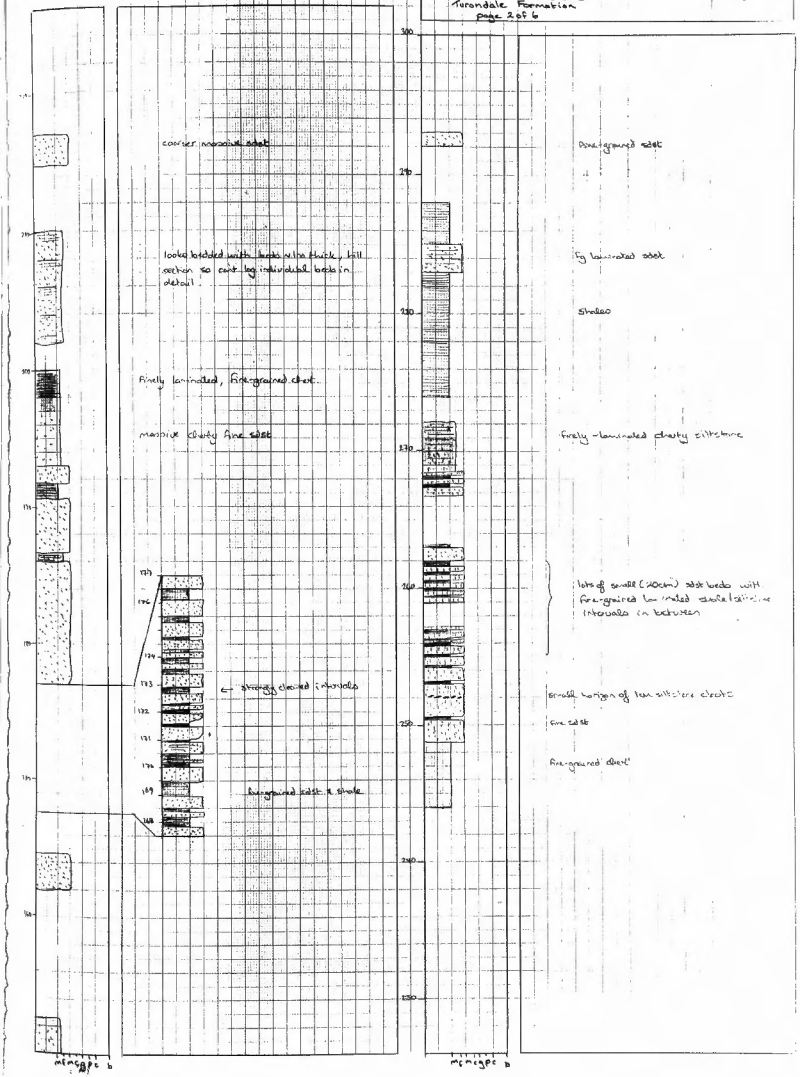

Section 1C:
Turondale Formation
page 3 of 6

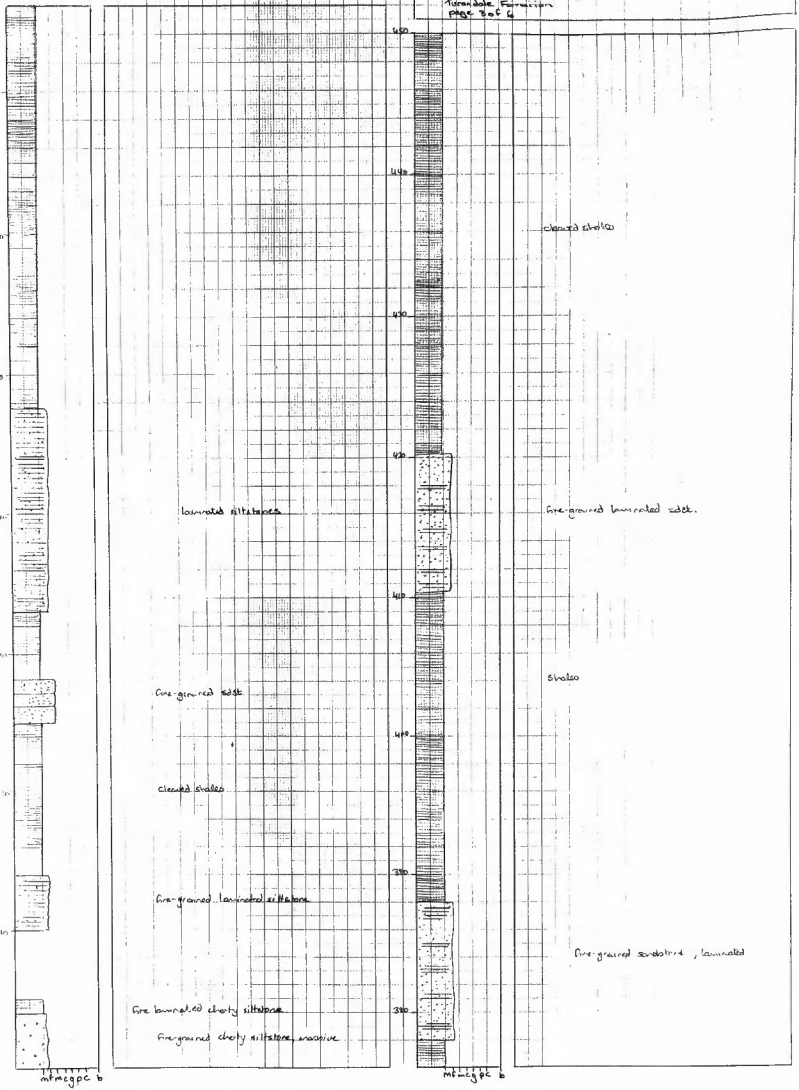

Section 10: Cudgegong River north of Burrendong Dam
Turondale Formation
page 4 of 6

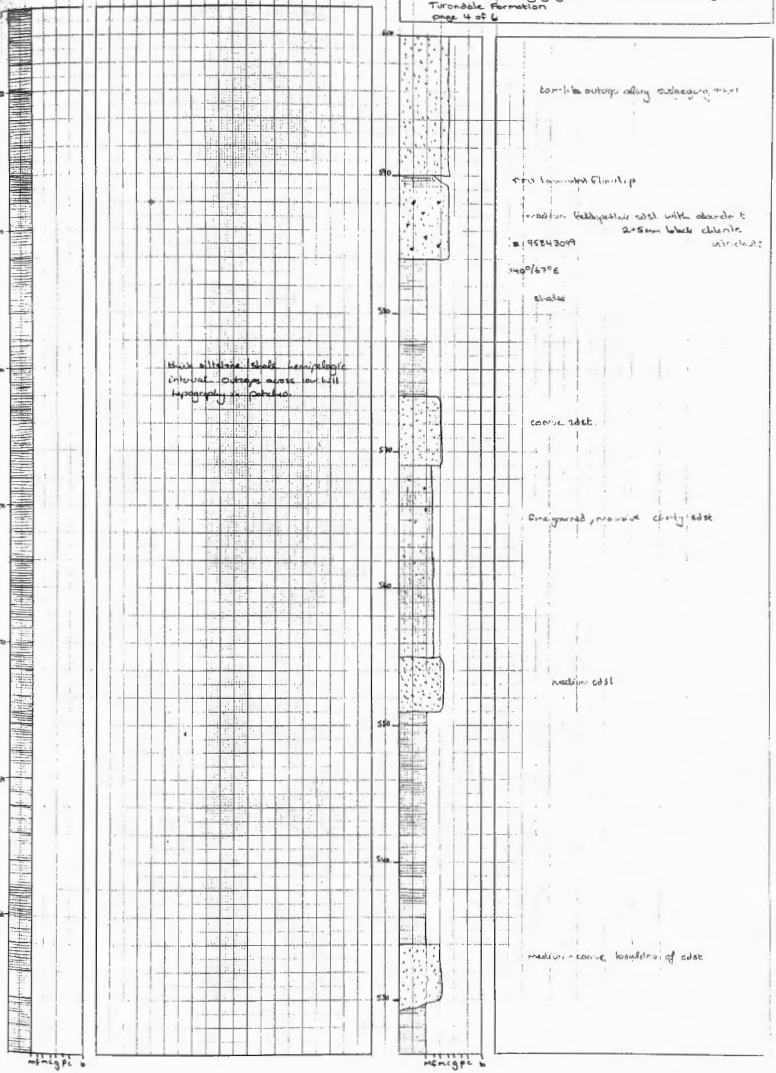

Section 10:
Turnbale Formation
page 5 of 6

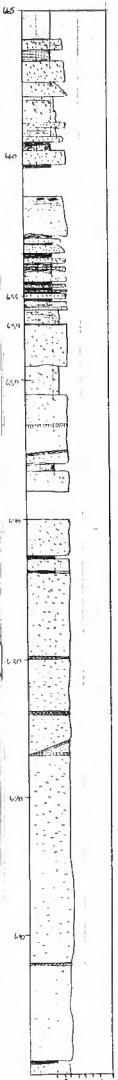

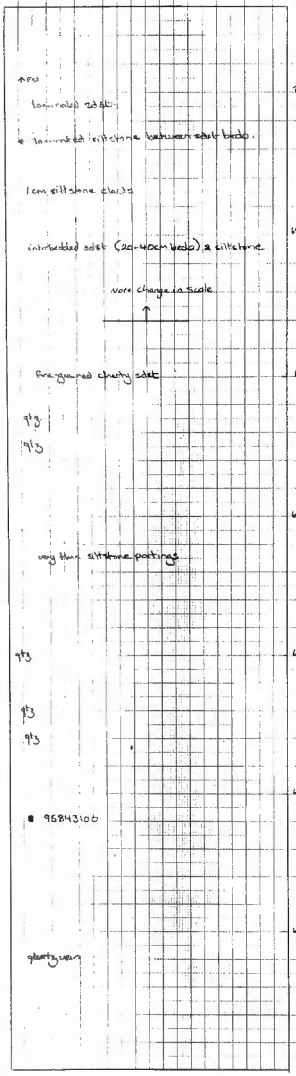

1cm laminated sdst beds

coarse sdst loading on finer sdst

fine-grained laminated cherty sdst.

small 2cm clast clast in siltstone

finely laminated sdst

← abundant 0.5-2cm siltstone clasts at top of sdst bed

loading of sdstone on siltstone

fg layered sdst. layers 1cm

siltstone stringer

5cm siltstone
loading of coarser sdst into underlying finer sdst

siltstone & shale interbeds 5-10cm thick

Section 10: Cudgegong River north of Burrendong Dam
Wiradandle Formation
page 6 of 6

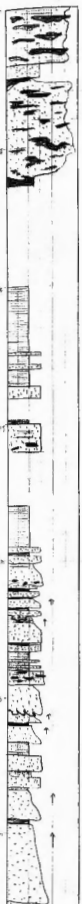

second intraformational conglomerate in fine siltstone matrix
open framework, high proportion of matrix - rounded clasts of dst/
fine grained sdst, angular siltstones, ave 10cm, up to
50x30cm.
- pebble imbrication does not strike with the conglomerate

intraformational conglomerate with siltstone
rip up clasts and stringers, coarse - M/L comp. & clastic
lithic clasts (black, porphyritic, up to 1cm), in a
sdst matrix.
★ Photograph Figure 7.12a, b

small siltstone stringers in shale

chert clasts, 3cm

shale and fine laminated siltstones

2cm siltstone clasts

loading at base

6cm beds of fine & coarse sdst with stringers of
siltstone (10-20cm long x 1cm wide)

loading at base of sdst into underlying sdst.

a series of thicker (fresh) sdst beds showing
distinctive grading - Grading is mainly at top
of bed, fining up to fine grained sdst.

gravelly-sized pebbles at corner base

■ 98843101

mf sltst pbc

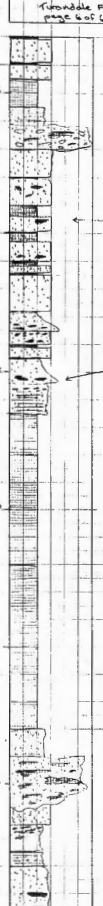

mf sltst pbc

WATERDACH FM.

795

laminated sdst
massive sdst

conglomerate with abundant
rounded clast clasts, mm-3cm,
smaller lithiclasts and fluvial
siltstones 20-30cm

shales

2-10cm siltstone clasts

6cm clasts

770

sand & mudclasts

sand veins/dykes at top
mudstone clasts, 1-5 cm.

small clasts

abundant small siltstone
clasts 1-2cm in fairly thin
layered sdst

laminations of shale, only
very fine sdst beds/lenses - no stringers.

760

diffusely laminated sdst

intraformational conglomerate siltstone rip up clasts
5-10cm up to 50cm boulders in a sdst matrix

750

siltstone mixed with stringers of sdst with 1-2cm of
50:50 1-5cm siltstone clasts.

large a gutter siltstone 10cm
2cm siltstone (black, brecciated, porphyritic)

740

small siltstones 1-2/m

siltstone with fine (<1cm), mic fine grained sdst
stringers

plot 3
* NB: change in Scale
thin silt beds separated by shale intervals
cyclic sediments of thin hard siltstone beds in shale.
~15cm silt beds interspersed with mm-scale carb shale intervals
siltstone clasts 1-3cm
shale with siltstone nodules in its grey matrix.
interbedded shale/siltstone intervals with some massive silt beds <10cm
FU
FU
FU
FU
bedding-parallel calcite veins
bedding-parallel calcite veins filling elongate dissolution cavities in shale matrix
bedding-parallel clay seams
amalgamated silt beds with thin shale/mudstone intervals (1-2cm) at top of each silt bed.
mbmgpc b
mbmgpc B
mbmgpc b

Section 81: Meroo Creek
Gurobo Formation
p2 of 3

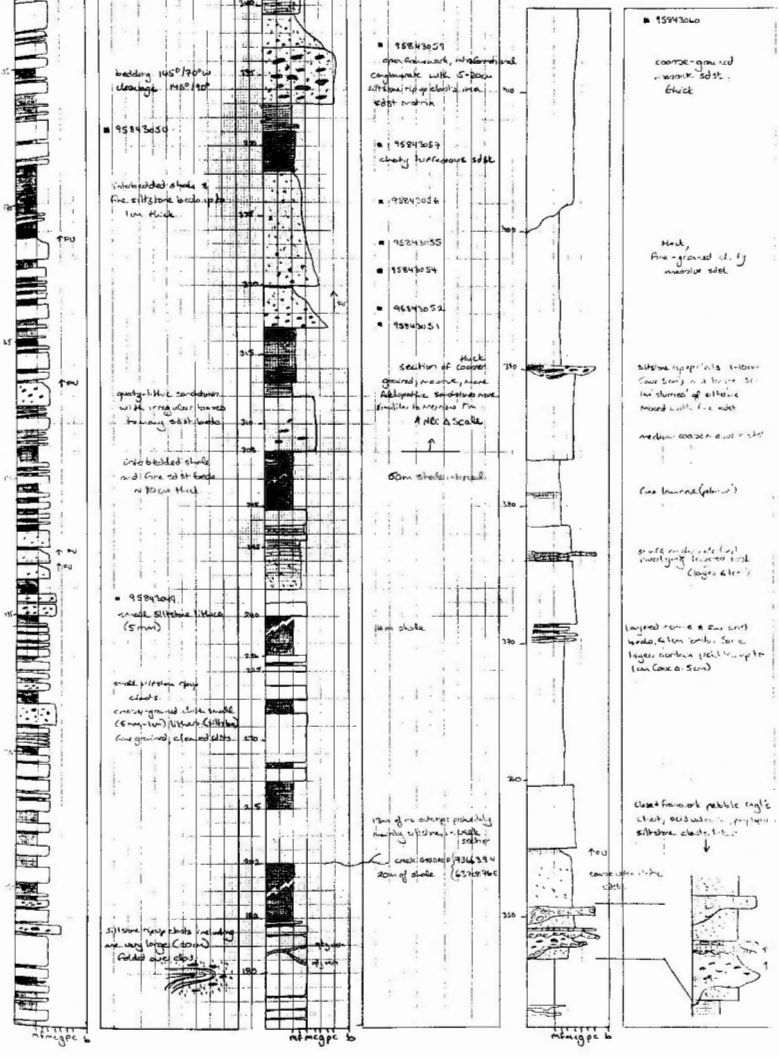

bedding 145°/70°W
cleavage 145°/90°

■ 95843050

interbedded shale & fine siltstone beds up to 1cm thick

quartz-lithic sandstone with irregular bases to many sdst beds

interbedded shale and fine sdst beds ~10cm thick

■ 95843049
small siltstone lithics (5mm)

small siltstone ripup clasts.
coarse-grained with small (5mm-1cm) lithics (siltstone)
fine grained, cleaved sdsts

siltstone ripup clasts including one very large (20cm) folded over clast

qtz vein
qtz vein

■ 95843057
open framework, intraformational conglomerate with 15-20cm siltstone rip up clasts in a sdst matrix

■ 95843057
cherty tuffaceous sdst

■ 95843056

■ 95843055

■ 95843054

■ 95843052

■ 95843051

thick section of coarser grained, massive, more feldspathic sandstone more similar to Merriwa Fm

* NB: Δ Scale

60m shale stream

14m shale

13m of no outcrop: probably mainly siltstone in creek section

creek GRIDREF {9736639 N
20m of shale {6371976E

■ 95843060

coarse-grained massive sdst. thick

thick, fine-grained [illegible] massive sdst

siltstone ripup clasts 1-10cm (ave 5cm) [illegible] 50 [illegible] 'slurries' of siltstone mixed with fine sdst

medium-coarse [illegible] sdst

fine laminae (planar)

several [illegible] [illegible] overlying laminated sdst (layers 6cm)

layered coarse & fine sdst beds, <1cm beds. Some layers contain pebbles up to 1cm (ave 0.5cm)

closed framework pebble cngl's chert, [illegible] [illegible] siltstone clasts [illegible]

↑FU
coarse [illegible] [illegible] sdst.

Section Gr. [illegible]
Gordon Formation
p3 of 3

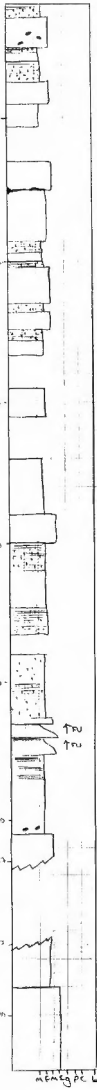

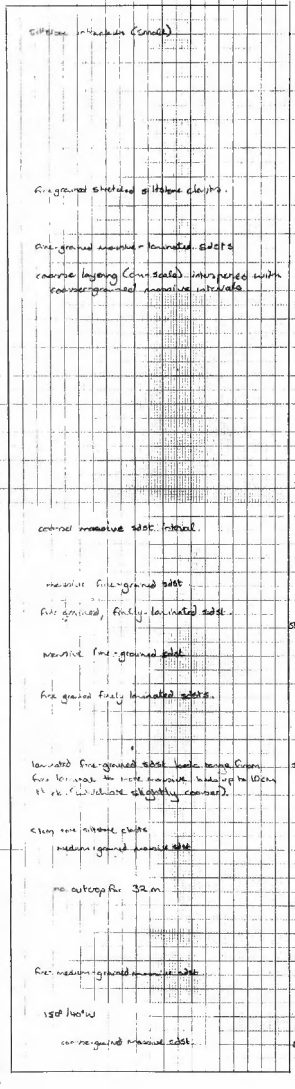

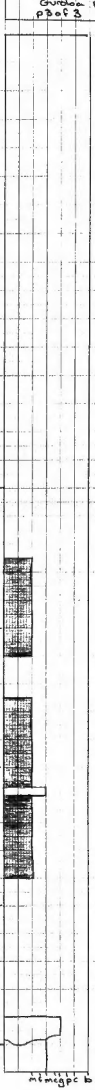

Nerrion 8 Fm

↑

30m of chert-bearing siltstone, finely laminated to bioclastic massive

Section 62: Surrounding Dam Geraldton Formation
Pl of 6
coarse sdst beds
10x3cm
15x5cm
6x2cm
anvil base. Loading of coarse sdst on fine salts, mild laminae flame of mudst below contact
fine coarse basal lamina 20x3cm silt/vfsd
95843063
95843062
coarse sdst, loading of base into underlying laminated silt 20x6cm
160°/70°W
3x1.5cm
15x5cm
20x6cm
mfmcgpc b
mfmcgpc b
mfmcgpc b

Section G2: Bur- Gurbba Formation
P2 of 6

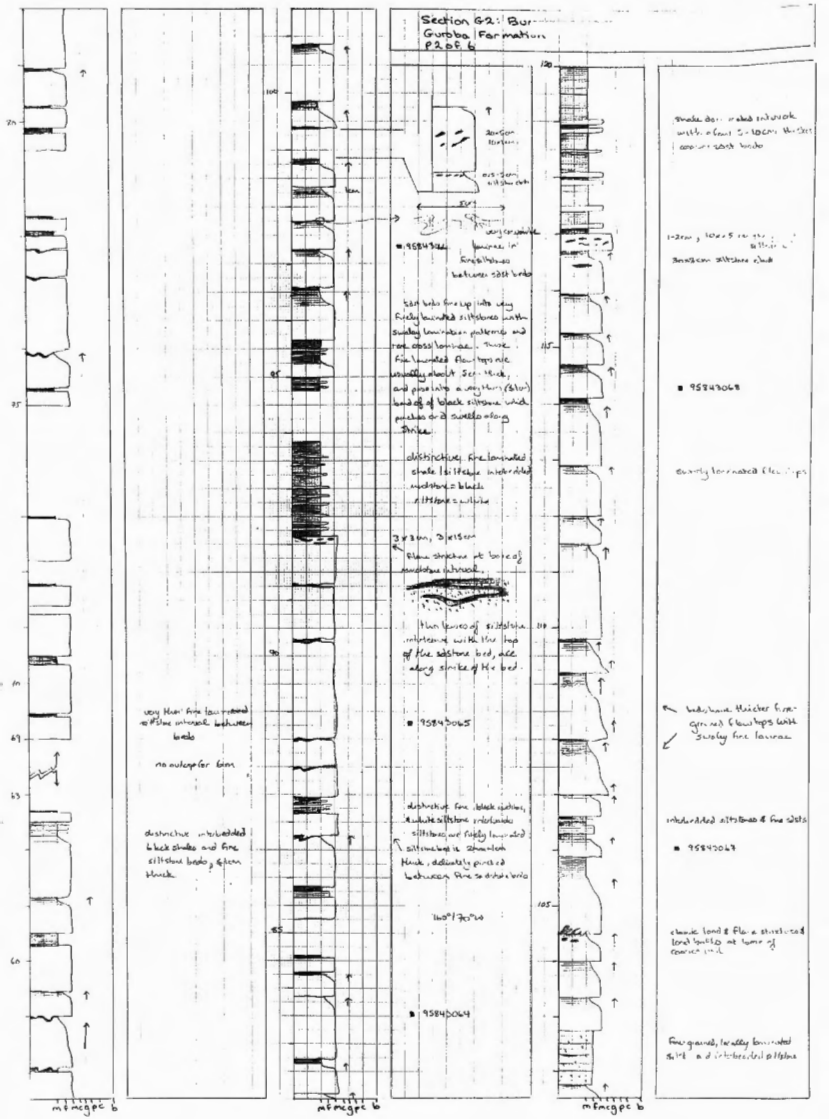

very thin fine laminated siltstone interval between beds

no outcrop for 6m

distinctive interbedded black shales and fine siltstone beds, 5-10cm thick.

■ 95843066 laminae in fine siltstones between sdst beds

sdst beds fine up into very finely laminated siltstones with swaley lamination patterns and rare cross laminae. These fine laminated flow tops are usually about 5cm thick, and pass into a very thin (<1cm) band of of black siltstone which pinches and swells along strike.

distinctive fine laminated shale / siltstone interbedded mudstone = black siltstone = white

3x3cm, 3x15cm

flame structure at base of mudstone interval.

thin lenses of siltstone interleave with the top of the sdstone bed, and along strike of the bed.

■ 95843065

distinctive fine black mudstone, & white siltstone interbeds siltstones are finely laminated siltstone bed is 2mm-1cm thick, delicately pinched between fine sandstone beds

160°/70°W

■ 95843064

shale dominated interval with a few 5-10cm thick coarser sdst beds

1-2cm, 10x5 cm [illegible] siltstone

3x3cm siltstone clasts

■ 95843068

swaley laminated flow tops

beds have thicker fine-grained flow tops with swaley fine laminae

interbedded siltstones & fine sdsts

■ 95843067

classic load & flame structured load balls at base of coarser unit

fine grained, locally laminated silt and interbedded siltstone

Section G2: Burrendong Dam
Gurabe Formation
P3 of 6

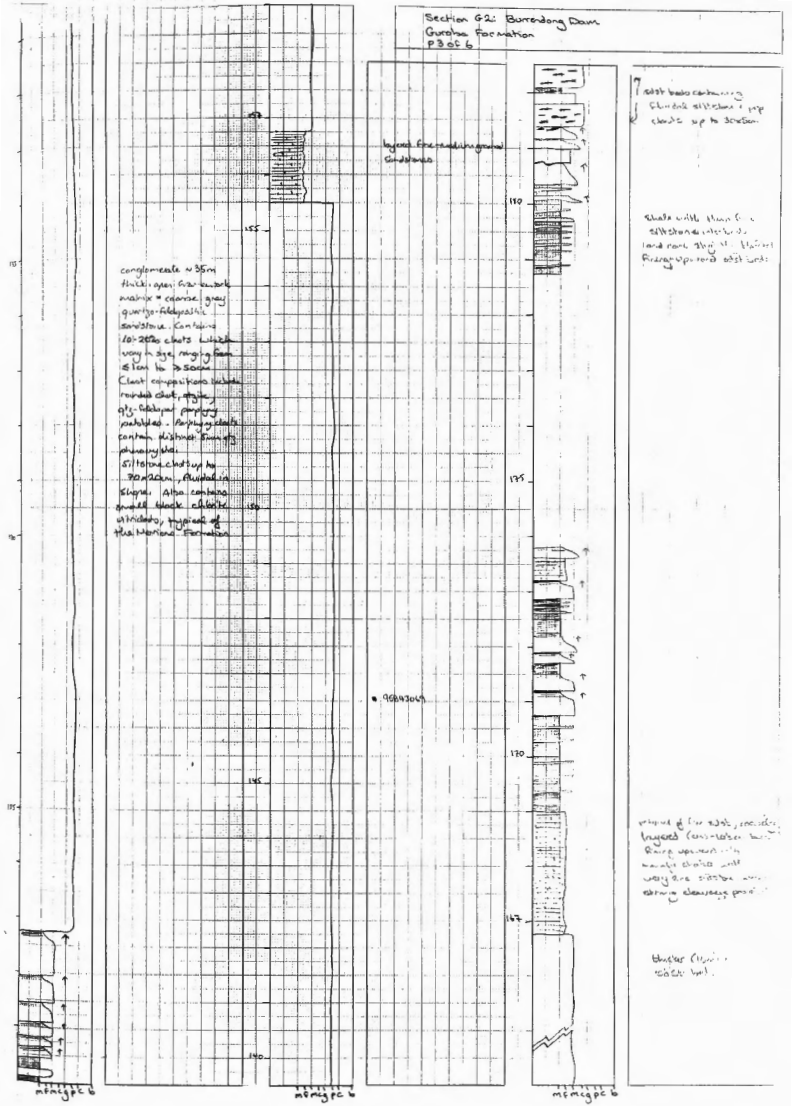

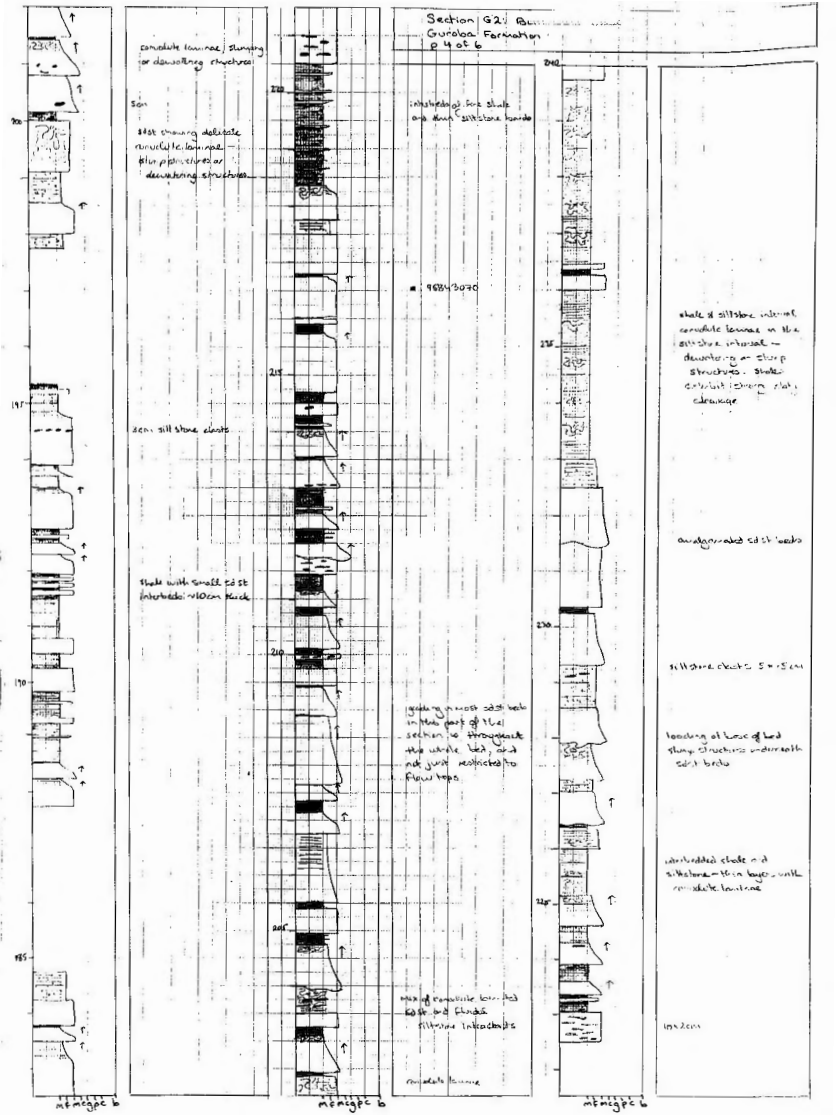
Section G2 Bl...
Gurabol Formation
p 4 of 6
convolute laminae / slumping or dewatering structures
5cm
shale showing delicate convolute laminae / pillow pipe structures or dewatering structures
interbedding of fine shale and thin siltstone bands
shale & siltstone interval convolute laminae in the siltstone interval — dewatering or slump structures. shale: parallel / cross plate cleavage
5cm siltstone sheets
shale with small cm scale interbeds ~10cm thick
amalgamated cm scale beds
siltstone sheets 5 - 15cm
loading of base of bed slump structures underneath sand beds
interbedded shale and siltstone - thin layers with convolute laminae
max of convolute laminated beds by flanks - filtering interbedding
convolute laminae
1m 2cm
metre beds

Section G2 Burrendong Dam
Gurnbo Formation
p5 of 6

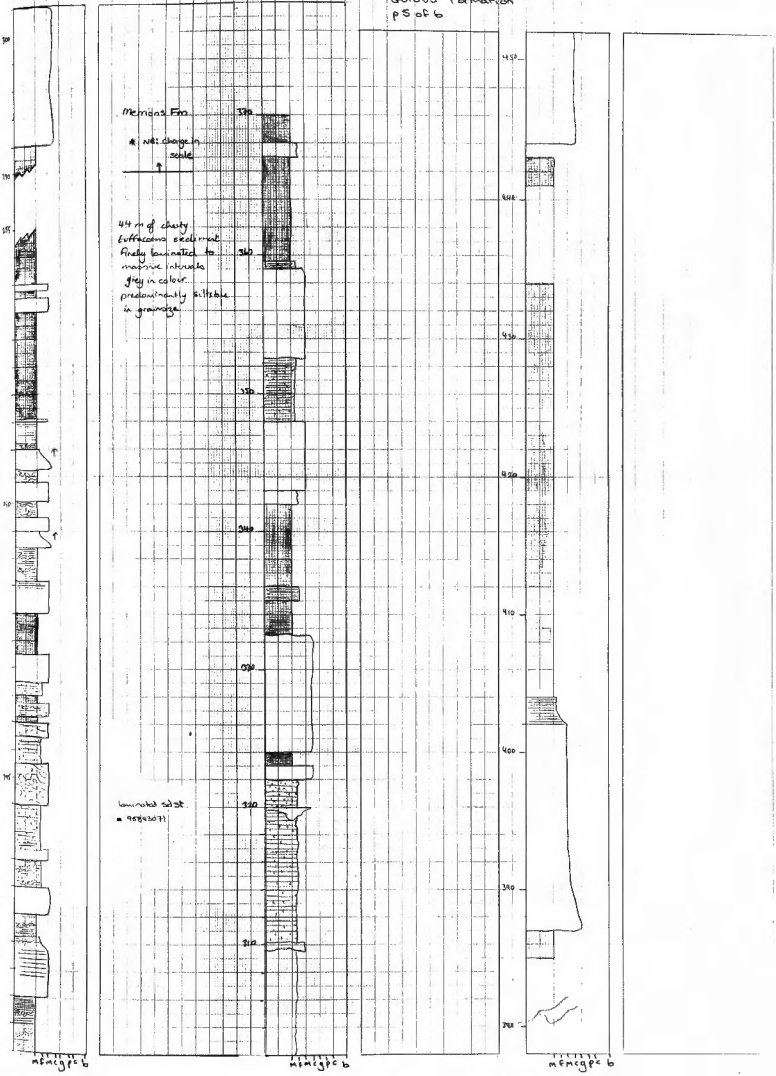

Section G2: Bu Gurdoa Formation
p6 of 6